

PAULO ALEXANDRE GALARCE ZAVALA

**“AEROACOUSTIC SOURCE AND MOVING SOURCE
IDENTIFICATION”**

***“IDENTIFICAÇÃO DE FONTES AEROACÚSTICAS
E FONTES EM MOVIMENTO”***

CAMPINAS
2012

**UNIVERSIDADE ESTADUAL DE CAMPINAS
FACULDADE DE ENGENHARIA MECÂNICA**

PAULO ALEXANDRE GALARCE ZAVALA

**“AEROACOUSTIC SOURCE AND MOVING SOURCE
IDENTIFICATION”**

***“IDENTIFICAÇÃO DE FONTES AEROACÚSTICAS
E FONTES EM MOVIMENTO”***

Doctorate thesis presented to the Mechanical Engineering Postgraduation Program of the Faculty of Mechanical Engineering of the University of Campinas to obtain the Ph.D. grade in Mechanical Engineering in the concentration area of Solid Mechanics and Mechanical Project.

Tese de Doutorado apresentada ao Programa de Pós-Graduação em Engenharia Mecânica da Faculdade de Engenharia Mecânica da Universidade Estadual de Campinas para obtenção do título de Doutor em Engenharia Mecânica na área de concentração de Mecânica dos Sólidos e Projeto Mecânico.

Tutor: Associate Professor José Roberto de França Arruda

Orientador: Prof. Dr. José Roberto de França Arruda

ESTE EXEMPLAR CORRESPONDE A REDAÇÃO FINAL DA
TESE DEFENDIDA POR ..PAULO ALEXANDRE.....
..GALARCE... ZAVALA..... E APROVADA
PELA COMISSÃO JULGADORA EM ..06 / 03 / 2012
.....
ORIENTADOR

CAMPINAS
2012

FICHA CATALOGRÁFICA ELABORADA PELA
BIBLIOTECA DA ÁREA DE ENGENHARIA E ARQUITETURA - BAE - UNICAMP

Z19i Zavala, Paulo Alexandre Galarce
 Identificação de fontes aeroacústicas e fontes em
 movimento / Paulo Alexandre Galarce Zavala. --
 Campinas, SP: [s.n.], 2012.

 Orientador: José Roberto de França Arruda.
 Tese de Doutorado - Universidade Estadual de
 Campinas, Faculdade de Engenharia Mecânica.

 1. Ruído. 2. Medição. 3. Localização. 4.
 Aerodinâmica. 5. Veículos. I. Arruda, José Roberto de
 França. II. Universidade Estadual de Campinas.
 Faculdade de Engenharia Mecânica. III. Título.

Título em Inglês: Aeroacoustic source and moving source identification

Palavras-chave em Inglês: Noise, Measurement, Location, Aerodynamics, Vehicle

Área de concentração: Mecânica dos Sólidos e Projeto Mecânico

Titulação: Doutor em Engenharia Mecânica

Banca examinadora: Arcanjo Lenzi, José Maria Campos dos Santos, Vincent Martin,
 Wim Armand Febronie Bertrand Desmet

Data da defesa: 06-03-2012

Programa de Pós Graduação: Engenharia Mecânica

UNIVERSIDADE ESTADUAL DE CAMPINAS
FACULDADE DE ENGENHARIA MECÂNICA
COMISSÃO DE PÓS-GRADUAÇÃO EM ENGENHARIA MECÂNICA
DEPARTAMENTO DE MECÂNICA COMPUTACIONAL

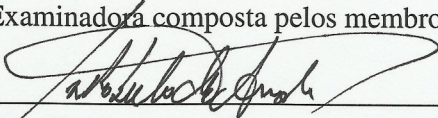
TESE DE DOUTORADO

Identificação de Fontes Aeroacústicas e
Fontes em Movimento

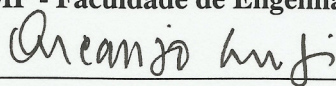
Autor: Paulo Alexandre Galarce Zavala

Orientador: José Roberto de França Arruda

A Banca Examinadora composta pelos membros abaixo aprovou esta Tese:



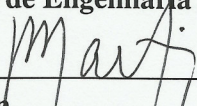
Prof. Dr. José Roberto de França Arruda, Presidente
UNICAMP - Faculdade de Engenharia Mecânica



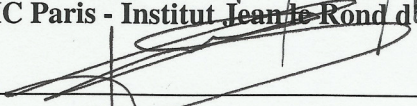
Prof. Dr. Arcanjo Lenzi
UFSC - Departamento de Engenharia Mecânica



Prof. Dr. José Maria Campos dos Santos
UNICAMP - Faculdade de Engenharia Mecânica



Prof. Dr. Vincent Martin
UPMC Paris - Institut Jean le Rond d'Alembert



Prof. Dr. Wim Armand Febronie Bertrand Desmet
KU Leuven - Department of Mechanical Engineering, PMA Division

Campinas, 06 de Março de 2012.

DEDICATÓRIA

Dedico este trabalho ao meu Pai (em memória), à minha Mãe, e à minhas irmãs e sobrinhos, por serem minha inspiração e apoio desde o início desta jornada.

Agradecimentos

Ao meu orientador, Prof. Arruda, por acreditar na possibilidade de realizar um trabalho numa área nova e propiciar o intercâmbio com a Universidade Católica de Leuven, onde viví experiências inesquecíveis de 2009 a 2010, e aos colegas de pós-graduação e professores da Faculdade de Engenharia Mecânica da UNICAMP, que acompanharam com interesse o meu progresso além de conviverem comigo nesses anos de estudo.

Aos meus colegas e professores da Universidade Católica de Leuven, em especial à Wim Desmet, que foi meu orientador em minha estadia nessa Universidade, e também à Paul Sas e Wim De Roeck, que apoiaram meu trabalho e as discussões.

Aos meus colegas da LMS International, em especial à Karl Janssens e Herman Van Der Auweraer, que acreditaram em meu trabalho e apoiaram meu período de 7 meses na LMS International, e a Peter Arnoute que me ajudou com as medições.

À Christophe Schram, Prof. do Instituto Von Kármán (VKI), que me ajudou a entender melhor o que são os fenômenos aeroacústicos.

À Stefan Oerlemans, do National Aerospace Laboratory from The Netherlands (NLR), que se disponibilizou a compartilhar os dados de medição junto com a LMS International e acreditou no potencial do método e do trabalho em geral.

À Maria Brito e Luiz Ferraro da Mercedes-Benz do Brasil, Divisão de Caminhões, que apoiaram este trabalho de pesquisa, e à Fábio Bueno e Gaetano Miranda, que promoveram sua realização e executaram as medições.

Ao Prof. Marcello Faraco e colega Carlos Pagani, que se disponibilizaram a compartilhar medições da USP-São Carlos e à avaliar a aplicação do método deste trabalho, gerando discussões interessantes sobre os resultados, e à Leandro Santana, por ter me colocado em contato com eles.

À Flávio Presezniak, com seu doutorado na VUB (Vrije Univesiteit Brussel), desenvolveu o Beamforming Generalizado Inverso Ponderado e o aplicou nos testes realizados na Universidade de Leuven, gerando um artigo em conjunto e que está em revisão.

À Takao Suzuki, da Boeing, autor do método que escolhi, por ter se interessado por meu trabalho e se disponibilizado a conversar pessoalmente numa conferência em Estocolmo, Suécia.

À minha família que me apóia e acompanha meus estudos na área que escolhi desde minha formação na graduação, aqui na Unicamp.

Ao órgão financiador, FAPESP, pelo apoio financeiro desde o final de 2010 até a defesa, como bolsa de Doutorado.

Acknowledgements

To my supervisor, Prof. Arruda, for believing in the possibility of holding a job in a new area and provided the exchange with the Katholieke Universiteit Leuven, where I lived unforgettable experiences from 2009 to 2010, and to colleagues and professors from the Faculty of Mechanical Engineering at UNICAMP, who followed with interest my progress and socialized with me these years of study.

To colleagues and professors at the Katholieke Universiteit Leuven, in particular, Wim Desmet, who was my supervisor during my stay in this University, and also to Paul Sas and Wim De Roeck, who supported the work and discussions.

To my colleagues at LMS International, especially to Karl Janssens and Herman Van Der Auweraer, who believed in my work and supported my 7 months stay at the LMS International Headquarter in Leuven, and to Peter Arnoute who helped me with the measurements.

To Christophe Schram, Prof. from Von Kármán Institute (VKI), which helped me to better understand what are the aeroacoustic phenomena.

To Stefan Oerlemans, from the National Aerospace Laboratory from The Netherlands (NLR), who offered to share measurement data along with LMS International and believed in the potential of the method and in the performed research work.

To Maria Brito and Luiz Ferraro from Mercedes-Benz of Brazil, Trucks Division, who supported this research, and to Fábio Bueno and Gaetano Miranda, who promoted the work and did the measurements.

To Prof. Marcello Faraco and colleague Carlos Pagani, who agreed to share measurements from USP-São Carlos and evaluate the application of the method developed on this work, generating interesting discussions on the results, and Leandro Santana, for having put me in touch with them.

To Flávio Presezniak, who performed his PhD at VUB (Vrije Univesiteit Brussel), and developed the Generalized Weighted Inverse Beamforming and applied it in test measurements performed at the University of Leuven, generating together an article that is under review.

To Takao Suzuki, from Boeing, author of the method on this work, for having become interested in my work and also available to talk personally at a conference in Stockholm, Sweden.

To my family who supports me and follow my studies in the area since I chose my undergraduate training, here at Unicamp.

To the funding body, FAPESP, for financial support since the end of 2010 to the defense, with a PhD scholarship.

*“Digo-vos: todo o que me reconhecer
diante dos homens, também o Filho do
homen o reconhecerá diante dos anjos de
Deus”*

Lc 12,8

Resumo

Identificação de fontes acústicas é uma ferramenta de análise importante para as melhorias mecânicas necessárias para o atendimento de normas de ruído restritivas, em especial em duas áreas: engenharia de aeronaves e engenharia de veículos. Esses dois setores têm de cumprir com as normas de sobre-vôo de aeroportos e ruído de passagem, respectivamente. Este trabalho tem o objetivo de desenvolver um método de identificação para problemas de fontes aeroacústicas e fontes em movimento. O método baseado no beamforming inverso generalizado tem a vantagem de localizar fontes distribuídas e multipólos e é usado neste trabalho. A estratégia é a de se realizarem verificações em casos simples, com simulações e avaliações experimentais. No teste aeroacústico inicial, um cilindro sob fluxo subsônico, os eventos dominantes de ruído são analisados, e o centro do dipólo e sua orientação são identificados. No teste seguinte, duas-estruturas sob fluxo subsônico, o método híbrido e o mapeamento híbrido inverso generalizado, ambos propostos neste trabalho, permitem uma comparação direta dos níveis de mapeamento com os resultados de beamforming convencional, e uma atenuação das auto-potências da matriz de espectros cruzados é usada para melhorar a resolução. Na identificação de dipólos, uma grade 3D é usada, e a orientação do dipolo é identificada com um componente em direção à malha de microphones, o que é possível devido à utilização de um re-escalamento da matriz de transferência. Avaliações de diretividade para as distribuições de dipólo são realizadas e comparadas com microfones de campo-distante. No terceiro caso aeroacústico, o aerofólio NACA-0012 sob fluxo subsônico, identificações de monopólos são comparados com resultados da literatura obtidos com o DAMAS2. Para os estudos de identificação de fonte em movimento, duas medições são realizadas: ruído de passagem de um veículo de passageiros, e ruído de passagem de caminhão. A de-Dopplerização baseada no centro da grade é adotada, e dois artifícios são desenvolvidos: uso de imagem de fonte na função de transferência; e compensação de foco para fonte de radiação não-esférica. A malha de microfones tem um arranjo especial para melhor resolução horizontal em frequências baixas. Mapeamentos com a contribuição no nível de ruído de passagem são utilizados nas verificações efetuadas de 50Hz a 7kHz, utilizando dois alto-falantes com radiação de ruído tonal e com ruído de banda larga. No final, o desempenho global do método beamforming inverso generalizado é discutido, apresentando suas vantagens, e.g. detecção de fonte multipólo, e suas desvantagens, e.g. sensibilidade a fontes estranhas.

Palavras-chave: Ruído, Medição, Localização, Aerodinâmica, Veículos.

Abstract

Aeroacoustic Source and Moving Source Identification

Identification of acoustic sources is an important analysis tool for the mechanical design improvements required to compliance with restrictive noise regulations, specially on two areas: aircraft and vehicle engineering. These two industries have to comply with the airplane fly-over noise and vehicle pass-by noise limits, respectively. This thesis has the objective to develop an identification method for aeroacoustic and moving source problems. The method based on the generalized inverse beamforming has the advantage to locate distributed sources of multipole type of radiation and is used in this thesis. The strategy is to perform verifications on simple cases, with simulations and experimental assessments. On the aeroacoustic initial testing, with a cylinder under subsonic flow, peak noise events are analyzed, and the dipole center and orientation are identified. In the following test case, two-structures in subsonic flow, the Hybrid Method and the Hybrid Generalized Inverse Mapping, both proposed in this work, allow a direct comparison of mapping levels to the conventional beamforming results, and an attenuation of the auto-powers in the cross-spectral matrix is used to improve resolution. For dipole identification, a 3D grid is used, and its orientation is identified with a component towards array, which is possible due to the use of a transfer matrix re-scaling. Directivity assessments are performed for dipole distributions and compared to far-field microphones. In the third aeroacoustic case, NACA-0012 airfoil under subsonic flow, monopole identifications are compared to DAMAS2 results from the literature. On moving source identification, two measurements are performed: passenger vehicle pass-by noise; and truck pass-by noise test. The de-Dopplerization based on grid center is adopted, and two artifices are developed: image source in transfer function; and focus compensation for source non-spherical radiation. The microphone array has a special design for improved low frequency horizontal resolution. Pass-by noise level contribution mappings are used on verifications performed from 50Hz to 7kHz using two loudspeakers with tonal and broadband noise radiation. Finally, overall performance of the generalized inverse beamforming method is discussed, presenting its advantages, e.g. multipole source detection, and limitations, e.g. sensitivity to extraneous sources.

Keywords: Noise, Measurement, Location, Aerodynamics, Vehicle.

List of Figures

3.1	Acoustic image of A340 at 2kHz with conventional beamforming from (SIJTSMA & STOKER, 2004).	19
3.2	Example of truck testing with conventional beamforming and a spherical source from (GUROVICH <i>et al.</i> , 2009).	21
4.1	Conventional beamforming based on Delay-And-Sum.	26
4.2	Microphone array (blue circles) and target grid positions (black dots).	34
4.3	Monopole source (blue circle) and target grid (black dots).	34
4.4	Monopole source at target center: (a) CB (b) CLEAN-PSF (c) DAMAS2 (d) GIB. Contour levels with 10dB range and 0.5 increment.	35
4.5	Distributed monopole line source (blue circles) and target grid (black dots).	37
4.6	Distributed monopole line source: (a) CB (b) CLEAN-SC (c) DAMAS2 (d) GIB. Contour levels with 10dB range and 0.5 increment.	38
4.7	Dipole source at target grid center with 45° orientation and target grid (black dots).	39
4.8	Dipole source at grid center with 45° orientation: (a) CB (b) CLEAN-SC (c) DAMAS2 (d) GIB. Arrows indicates dipole orientation. Contour levels with 10dB range and 0.5 increment.	40
4.9	Monopole source at (1,0) (blue circle), Dipole source at (-1,0) with 90° orientation and target grid (dots).	41
4.10	Monopole and dipole sources in incoherent radiation: (a) CB with monopole ref. (b) CB with dipole ref. (c) CLEAN-SC (d) DAMAS2 (e) GIB with monopole ref. (f) GIB with dipole ref. Contour levels with 10dB range and 0.5 increment.	42
4.11	Monopole and dipole sources in coherent radiation: (a) CB with monopole ref. (b) CB with dipole ref. (c) CLEAN-SC (d) DAMAS2 (e) GIB with monopole ref. (f) GIB with dipole ref. Contour levels with 10dB range and 0.5 increment.	43
4.12	Monopole source at target center: (a) Residue cost function along regularization on the last iteration (minimum at circle). (b) Optimal regularization factor fraction along iterations.	46
4.13	Monopole source at target center: (a) J_1 cost function and Residue cost function along iterations (minimum at circle). (b) Strength estimation along iterations (J_1 cost function minimum at circle).	47

4.14	Influence of fixed regularization and optimized strategy on single monopole problem: (a) J_1 cost function along iterations (minimum at circle). (b) Strength estimation along iterations (J_1 cost function minimum at circle).	48
4.15	Influence of regularization strategies on single monopole problem: (a) J_1 cost function along iterations (minimum at circle). (b) Strength estimation along iterations (J_1 cost function minimum at circle).	49
4.16	Influence of fixed regularization and optimized strategy on distributed line monopole problem: (a) J_1 cost function along iterations (minimum at circle). (b) Strength estimation along iterations (J_1 cost function minimum at circle).	49
4.17	Influence of regularization strategy on distributed line monopole problem: (a) J_1 cost function along iterations (minimum at circle). (b) Strength estimation along iterations (J_1 cost function minimum at circle).	50
4.18	Influence of fixed regularization and optimized strategy on single dipole problem: (a) J_1 cost function along iterations (minimum at circle). (b) Strength estimation along iterations (J_1 cost function minimum at circle).	50
4.19	Influence of regularization strategy on single dipole problem: (a) J_1 cost function along iterations (minimum at circle). (b) Strength estimation along iterations (J_1 cost function minimum at circle).	51
4.20	Influence of fixed regularization and optimized strategy on coherent sources problem: J_1 cost function along iterations (minimum at circle).	51
4.21	Influence of fixed regularization and optimized strategy on coherent sources problem: (a) Monopole estimation (b) Dipole estimation. J_1 cost function minimum at circle.	52
4.22	Influence of regularization strategy on coherent sources problem: J_1 cost function along iterations (minimum at circle).	52
4.23	Influence of regularization strategy on coherent sources problem: (a) Monopole estimation (b) Dipole estimation. J_1 cost function minimum at circle.	53
4.24	Influence of fixed regularization and optimized strategy on incoherent sources problem, first eigenmode: (a) J_1 cost function along iterations (minimum at circle) (b) Monopole estimation (J_1 cost function minimum at circle).	53
4.25	Influence of regularization strategy on incoherent sources problem, first eigenmode: (a) J_1 cost function along iterations (minimum at circle) (b) Monopole estimation (J_1 cost function minimum at circle).	54
4.26	Influence of fixed regularization and optimized strategy on incoherent sources problem, second eigenmode: (a) J_1 cost function along iterations (minimum at circle) (b) Dipole estimation (J_1 cost function minimum at circle).	55

4.27	Influence of regularization strategy on incoherent sources problem, second eigenmode: (a) J_1 cost function along iterations (minimum at circle) (b) Dipole estimation (J_1 cost function minimum at circle).	55
4.28	Source strength mappings using GIB/IRLS for: (a) Single monopole at target grid center (b) Distributed line monopole. Contour levels with 10dB range and 0.5 increment.	58
4.29	Single and line monopole problem results using GIB/IRLS: (a) J_1 cost function along iterations (minimum at circle) (b) Strength estimation (J_1 cost function minimum at circle).	59
4.30	Source strength mappings using GIB/IRLS(residue weighting) for: (a) Single monopole at target grid center (b) Distributed line monopole. Contour levels with 10dB range and 0.5 increment.	60
4.31	Single and line monopole problem results using GIB/IRLS(residue weighting): (a) J_1 cost function along iterations (minimum at circle) (b) Strength estimation (J_1 cost function minimum at circle).	60
4.32	Source strength mappings using GWIB for: (a) Single monopole at target grid center (b) Distributed line monopole. Contour levels with 10dB range and 0.5 increment.	63
4.33	Source strength mappings using the stabilized GWIB for: (a) Single monopole at target grid center (b) Distributed line monopole. Contour levels with 10dB range and 0.5 increment.	64
4.34	Source strength mappings using GINV for: (a) Single monopole at target grid center (b) Distributed line monopole. Contour levels with 10dB range and 0.5 increment.	67
4.35	Source strength mappings using GINV for: (a) Single monopole at target grid center (b) Distributed line monopole. Contour levels with 10dB range and 0.5 increment.	68
5.1	(a) Microphone array (circles) and target grid (dots); (b) Experimental setup: Array of microphones and single source configuration.	75
5.2	Eigenvalues distribution: (a) One Monopole (b) Two Monopoles.	76
5.3	J_1 cost function for the numerical test in free-field condition: (a) One Monopole (b) Two Monopoles. Optimized: solid; Lower limit: dashed; Higher limit: dash dot. Curve minimum at circle.	78
5.4	J_1 cost function for the numerical test including reflections: (a) One Monopole (b) Two Monopoles. Optimized: solid; Lower limit: dashed; Higher limit: dash dot. Curve minimum at circle.	78

5.5	J_1 cost function for the experimental test: (a) One Monopole (b) Two Monopoles. Optimized: solid; Lower limit: dashed; Higher limit: dash dot. Curve minimum at circle.	79
5.6	Squared strength mapping for the numerical test in free-field condition using the regularization factor at the lower limit: (a) One Monopole (b) Two Monopoles (contour lines are in 10 dB range with 0.5 dB increment).	80
5.7	Squared strength mapping for the numerical test in free-field condition using the regularization factor at the higher limit: (a) One Monopole (b) Two Monopoles (contour lines are in 10 dB range with 0.5 dB increment).	80
5.8	Squared strength mapping for the numerical test in free-field condition using the optimized regularization factor: (a) One Monopole (b) Two Monopoles (contour lines are in 10 dB range with 0.5 dB increment).	81
5.9	Squared strength mapping for the numerical test including reflections using the regularization factor at the lower limit: (a) One Monopole (b) Two Monopoles (contour lines are in 10 dB range with 0.5 dB increment).	81
5.10	Squared strength mapping for the numerical test including reflections using the regularization factor at the higher limit: (a) One Monopole (b) Two Monopoles (contour lines are in 10 dB range with 0.5 dB increment).	82
5.11	Squared strength mapping for the numerical test including reflections using the optimized regularization factor: (a) One Monopole (b) Two Monopoles (contour lines are in 10 dB range with 0.5 dB increment).	82
5.12	Squared strength mapping for the experimental test using the regularization factor at the lower limit: (a) One Monopole (b) Two Monopoles (contour lines are in 10 dB range with 0.5 dB increment).	83
5.13	Squared strength mapping for the experimental test using the regularization factor at the higher limit: (a) One Monopole (b) Two Monopoles (contour lines are in 10 dB range with 0.5 dB increment).	83
5.14	Squared strength mapping for the experimental test using the optimized regularization factor: (a) One Monopole (b) Two Monopoles (contour lines are in 10 dB range with 0.5 dB increment).	84
5.15	Estimations varying radiation frequency for a unitary monopole source.	89
5.16	Monopole with 200Hz radiation: (a) Conventional beamforming (b) Generalized inverse beamforming (contour lines are in 10 dB range with 0.5 dB increment). . .	90
5.17	Monopole with 1kHz radiation: (a) Conventional beamforming (b) Generalized inverse beamforming (contour lines are in 10 dB range with 0.5 dB increment).	90

5.18 Monopole with 5kHz radiation: (a) Conventional beamforming (b) Generalized inverse beamforming (contour lines are in 10 dB range with 0.5 dB increment).	91
5.19 Monopole with 1kHz radiation (mapping on top of photo): Generalized inverse beamforming (contour lines are in 10 dB range with 0.5 dB increment).	91
5.20 Two monopoles in-phase with 1kHz radiation: (a) Conventional beamforming (b) Generalized inverse beamforming (contour lines are in 10 dB range with 0.5 dB increment).	92
5.21 Two monopoles in-phase with 1kHz radiation (mapping on top of photo): Generalized inverse beamforming (contour lines are in 10 dB range with 0.5 dB increment).	93
5.22 (a) Two monopoles in-phase with 1kHz radiation, generalized inverse beamforming (b) Array Point Spread Function for the grid center (contour lines are in 10 dB range with 0.5 dB increment).	95
5.23 Two monopoles in-phase with 1kHz radiation: (a) Conventional beamforming (b) Hybrid mapping based on the generalized inverse beamforming (contour lines are in 10 dB range with 0.5 dB increment).	96
5.24 (a) Microphone array (circles) and target grid positions (dots); (b) Experimental setup.	99
5.25 Two monopoles in-phase free-field (numerical results): (a) Conventional beamforming; (b) Generalized inverse beamforming (Countour lines are in 10 dB range with 0.5 dB increment).	100
5.26 Two monopoles in-phase (numerical results including reflections): (a) Conventional beamforming; (b) Generalized inverse beamforming (Countour lines are in 10 dB range with 0.5 dB increment).	100
5.27 Two monopoles in-phase (experimental results): (a) Conventional beamforming; (b) Generalized inverse beamforming (Countour lines are in 10 dB range with 0.5 dB increment).	101
5.28 Dipole Identification with two horizontal monopoles in anti-phase (numerical free-field results): (a) Conventional beamforming; (b) Generalized inverse beamforming (Countour lines are in 10 dB range with 0.5 dB increment).	103
5.29 Dipole Identification with two horizontal monopoles in anti-phase (numerical results including reflections): (a) Conventional beamforming; (b) Generalized inverse beamforming (Countour lines are in 10 dB range with 0.5 dB increment).	103
5.30 Dipole Identification with two horizontal monopoles in anti-phase (experimental results): (a) Conventional beamforming; (b) Generalized inverse beamforming (Countour lines are in 10 dB range with 0.5 dB increment).	104

5.31	Dipole Identification with two vertical monopoles in anti-phase (experimental results): (a) Conventional beamforming; (b) Generalized inverse beamforming (Countour lines are in 10 dB range with 0.5 dB increment).	104
5.32	Dipole Identification with two monopoles at 135° in anti-phase (experimental results): (a) Conventional beamforming; (b) Generalized inverse beamforming (Countour lines are in 10 dB range with 0.5 dB increment).	105
5.33	Target and measurement grids and source locations	108
5.34	Source identification for: (a)Conventional Beamforming, (b) MUSIC, (c) Generalized Inverse Beamforming (GIB) and (d)Generalized Weighted Inverse Beamforming	109
5.35	Experimental results for: (a)Conventional Beamforming (b) Generalized Inverse Beamforming (GIB) (c) MUSIC and (d)Generalized Weighted Inverse Beamforming (GWIB)	110
5.36	Generalized Weighted Inverse Beamforming (GWIB) after: (a) 1 iteration, (b) 5 iterations, (c) 10 iterations and (d) 15 iterations	111
6.1	Convection and refraction modeling based on Amiet, 1975 (flow from left to right).	119
6.2	Dipole at 45 degrees main plane of radiation: (a) in convected radiation and (b) in convected and refracted radiation, with 0.2M flow from left to right (horizontal lines represents the shear layer).	119
6.3	(a) Jet Experimental Layout (b) 6-arm Spiral with 30 microphones and 1m aperture.	120
6.4	Circular cylinder positioned at 0.4m from the jet outlet (a) Overview (b) Close view.	120
6.5	(a) Array 6-arm spiral microphone positions (b) Target grid points.	121
6.6	Jet speed hot wire measurement results in x-y plane.	121
6.7	Averaged microphone FFT.	122
6.8	Averaged microphone cross-spectra.	123
6.9	Comparison of averaged (blue) and cross-spectral peaks (red).	123
6.10	Time slice on 370Hz with main peak region in red.	124
6.11	Time slice on 510Hz with main peak region in red.	124
6.12	Time slice on 910Hz with main peak region in red.	125
6.13	Dipole identification verification results (a) on case 45° to 90°; and (b) 270° to 315°. Arrows represent dipoles: blue (numerical source); red (identification results). . . .	125
6.14	Dipole at cylinder surface for 370Hz with normal (blue) and tangential (red) components.	126
6.15	Dipole at cylinder surface for 510Hz with normal (blue) and tangential (red) components.	127
6.16	Dipole at cylinder surface for 910Hz with normal (blue) and tangential (red) components.	128

6.17	Equivalent pressure mapping for the identified dipole components at 370Hz.	129
6.18	Equivalent pressure mapping for the identified dipole components at 510Hz.	129
6.19	Equivalent pressure mapping for the identified dipole components at 910Hz.	130
6.20	Amplitude averaging of microphones spectrum.	130
6.21	Dipole identification using experimental data.	131
6.22	Equivalent Pressure Mapping with 1m radius. Horizontal lines represents the shear layer simplification.	132
6.23	Equivalent Pressure Mapping for 1m radius (reduced dB range).	133
6.24	Directivity plot calculated at 1m radius in respect to the cylindrical equivalent radiation.	133
7.1	Airbus A340 landing gears: (a) nose landing gear (b) rear-left landing gear.	136
7.2	Two structures in plane with angle to the main flow direction.	137
7.3	NLR Open Wind Tunnel with Anechoic Test Chamber, illustrated with an airfoil testing setup.	139
7.4	NLR Open Wind Tunnel illustrated with the turntable center bar installed and the 48 microphones array used on measurements.	139
7.5	Schematic top view of test layout (not in scale) (a) Structures angle of 7.5° (b) Structures angle of 20°	140
7.6	Microphones Array distribution and coordinates.	140
7.7	Change in sound pressure level caused by refraction based on Plumblee, 1976. Distances are $R_o = \overline{bd}$, $R_a = \overline{ba}$, $R = \overline{en}$ and $R' = \overline{cn}$	141
7.8	Target grid distribution based in $1/4$ of wavelength width (a) 1kHz (b) 2kHz (c) 4kHz (d) 8kHz.	144
7.9	Conventional beamforming for simulated monopoles with structures at 7.5° angle and flow at 35m/s: single monopole (left); and line distributed monopoles (right). Mappings are source PWL in dB re 1pW.	146
7.10	Conventional Beamforming for Structures with 7.5° angle and flow at 35m/s (results from NLR on left). Mappings are source third octave PWL in dB re 1pW.	148
7.11	Conventional Beamforming for Structures with 20° angle and flow at 35m/s (results from NLR on left). Mappings are source third octave PWL in dB re 1pW.	149
7.12	Conventional Beamforming for Structures with 7.5° angle and flow at 70m/s (results from NLR on left). Mappings are source third octave PWL in dB re 1pW.	150
7.13	Conventional Beamforming for Structures with 20° angle and flow at 70m/s (results from NLR on left). Mappings are source third octave PWL in dB re 1pW.	151

7.14	Conventional beamforming CSM diagonal removal comparison for structures at 7.5° angle and flow at 35m/s: full CSM (left); and diagonal removed (right). Mappings are source PWL in dB re 1pW.	152
7.15	Conventional beamforming microphone weighting comparison for structures at 7.5° angle and flow at 35m/s: without weighting (left); and with weighting (right). Mappings are source PWL in dB re 1pW.	153
7.16	Target grid distribution for the generalized inverse calculations based in 1/4 of wavelength width (a) 1kHz (b) 2kHz (c) 4kHz (d) 8kHz.	156
7.17	Generalized inverse beamforming (without IRLS) for simulated monopoles with structures at 7.5° angle and flow at 35m/s: single monopole (left); and line distributed monopoles (right). Mappings are source PWL in dB re 1pW.	157
7.18	Generalized inverse beamforming with IRLS for simulated monopoles with structures at 7.5° angle and flow at 35m/s: single monopole (left); and line distributed monopoles (right). Mappings are source PWL in dB re 1pW.	158
7.19	Conventional beamforming and Hybrid Mapping comparison for the single monopole simulated case, with grid plane at 7.5° angle and flow at 35m/s: CB (left); and Hybrid (right). Mappings are source PWL in dB re 1pW.	159
7.20	Hybrid generalized inverse beamforming (without IRLS) for simulated monopoles with structures at 7.5° angle and flow at 35m/s: single monopole (left); and line distributed monopoles (right). Mappings are source PWL in dB re 1pW.	160
7.21	Hybrid generalized inverse beamforming with IRLS for simulated monopoles with structures at 7.5° angle and flow at 35m/s: single monopole (left); and line distributed monopoles (right). Mappings are source PWL in dB re 1pW.	161
7.22	Hybrid mappings comparison for the CSM diagonal attenuation for the two structures with 7.5° angle and flow at 35m/s: original CSM (left); and CSM with attenuated diagonal (right). Mappings are source PWL in dB re 1pW.	162
7.23	Generalized Inverse Beamforming for Structures with 7.5° angle and flow at 35m/s (results with IRLS on right). Mappings are source third octave PWL in dB re 1pW.	164
7.24	Generalized Inverse Beamforming for Structures with 20° angle and flow at 35m/s (results with IRLS on right). Mappings are source third octave PWL in dB re 1pW.	165
7.25	Generalized Inverse Beamforming for Structures with 7.5° angle and flow at 70m/s (results with IRLS on right). Mappings are source third octave PWL in dB re 1pW.	166
7.26	Generalized Inverse Beamforming for Structures with 20° angle and flow at 70m/s (results with IRLS on right). Mappings are source third octave PWL in dB re 1pW.	167

7.27	Generalized inverse beamforming with IRLS for the two structures with 7.5° angle and flow at 35m/s: summed over band (left); and extrapolated center frequency analysis (right). Mappings are source PWL in dB re 1pW.	168
7.28	Eigenvalues square root distribution for the simulated line of monopoles in the 4kHz case. Red line indicates the 10dB range from maximum value.	169
7.29	Generalized inverse beamforming with IRLS for the simulated line of monopoles: Source vector solutions to each selected eigenmode and overall. Grid at 7.5° angle and flow at 35m/s. Mappings are source PWL in dB re 1pW.	170
7.30	Eigenvalues square root distribution for the two structures with 7.5° angle and flow at 35m/s. Red line indicates the 10dB range from maximum value.	171
7.31	Generalized inverse beamforming with IRLS for the two structures with 7.5° angle and flow at 35m/s: Source vector solutions to first 5 eigenmodes and overall. Mappings are source PWL in dB re 1pW.	172
7.32	Line Target Grid distribution based in $1/4$ of wavelength width in spanwise direction (a) 1kHz (b) 2kHz (c) 4kHz (d) 8kHz.	176
7.33	3D Target Grid distribution based in $1/4$ of wavelength width in spanwise direction (a) 1kHz (b) 2kHz (c) 4kHz (d) 8kHz.	177
7.34	Far field ($r=2m$) microphones location for directional assessment.	178
7.35	Wall pressure transducers (Kulites) locations: (a) midspan (b) spanwise.	178
7.36	Simulation results for a free-field dipole with 45° in x-z plane. Mappings are source PWL in dB re 1pW.	180
7.37	Directivity for the free-field dipole with 45° in x-z plane.	181
7.38	Simulation results for a free-field dipole with 45° in x-z plane with re-scaling of transfer matrix. Mappings are source PWL in dB re 1pW.	182
7.39	Directivity for the free-field dipole with 45° in x-z plane with re-scaling of transfer matrix.	183
7.40	Directivity results ($r=2m$) for a single dipole with 1kHz in x-z plane using line grid and orientations of: (a) 0° (b) 30° (c) 45° (d) 60° (e) 90° (f) 135°	184
7.41	Directivity results ($r=2m$) for a single dipole with 1kHz in x-z plane using 3D grid and orientations of: (a) 0° (b) 30° (c) 45° (d) 60° (e) 90° (f) 135°	185
7.42	Simulation results for the line grid and dipole with 45° in x-z plane with re-scaling of transfer matrix, 1k (top), 2k, 4k and 8kHz. Mappings are source PWL in dB re 1pW.	186
7.43	Simulation results for the 3D grid and dipole with 45° in x-z plane with re-scaling of transfer matrix: 1kHz (top); 2kHz; 4kHz; and 8kHz. Mappings are source PWL in dB re 1pW.	187

7.44	Directivity results ($r=2m$) for a single dipole with 45° in x-z plane using line grid (top) and 3D grid for frequencies of : (a,d) 2kHz (b,e) 4kHz (c,f) 8kHz.	188
7.45	Simulation results for the 3D grid and line distributed incoherent dipoles with 45° in x-z plane with re-scaling of transfer matrix: 1kHz (top); 2kHz; 4kHz; and 8kHz. Mappings are source PWL in dB re 1pW.	189
7.46	Directivity results ($r=2m$) for the 3D grid and line distributed incoherent dipoles with 45° in x-z plane for frequencies of : (a) 1kHz; (b) 2kHz; (c) 4kHz; and (d) 8kHz.	190
7.47	Dipole direction components level (top and middle) and vectorial representation for the line distributed incoherent dipoles with 45° in x-z plane and 1kHz radiation. Level mappings are source PWL in dB re 1pW and vectorial mappings are strength normalized by maximum absolute level on each direction.	191
7.48	Dipole direction components level (top and middle) and its vectorial representation for the line distributed incoherent dipoles with 45° in x-z plane and 1kHz radiation. Level mappings are source PWL in dB re 1pW and vectorial mappings are strength normalized by maximum absolute level on each direction.	192
7.49	Dipole power level (experimental results) for structures with 7.5° angle and flow at 35m/s: 1kHz (top); 2kHz; 4kHz; and 8kHz. Mappings are source PWL in dB re 1pW.	194
7.50	Dipole power level (experimental results) for structures with 20° angle and flow at 35m/s: 1kHz (top); 2kHz; 4kHz; and 8kHz. Mappings are source PWL in dB re 1pW.	195
7.51	Dipole power level (experimental results) for structures with 7.5° angle and flow at 70m/s: 1kHz (top); 2kHz; 4kHz; and 8kHz. Mappings are source PWL in dB re 1pW.	196
7.52	Dipole power level (experimental results) for structures with 20° angle and flow at 70m/s: 1kHz (top); 2kHz; 4kHz; and 8kHz. Mappings are source PWL in dB re 1pW.	197
7.53	Dipole power level hybrid mapping (experimental results) for structures with 7.5° angle and flow at 35m/s: 1kHz (top); 2kHz; 4kHz; and 8kHz. Mappings are source PWL in dB re 1pW.	200
7.54	Dipole power level hybrid mapping (experimental results) for structures with 20° angle and flow at 35m/s: 1kHz (top); 2kHz; 4kHz; and 8kHz. Mappings are source PWL in dB re 1pW.	201

7.55 Dipole power level hybrid mapping (experimental results) for structures with 7.5° angle and flow at 70m/s: 1kHz (top); 2kHz; 4kHz; and 8kHz. Mappings are source PWL in dB re 1pW.	202
7.56 Dipole power level hybrid mapping (experimental results) for structures with 20° angle and flow at 70m/s: 1kHz (top); 2kHz; 4kHz; and 8kHz. Mappings are source PWL in dB re 1pW.	203
7.57 Dipole estimation (1kHz) with direction components level (top and third row) and vectorial representation for structures with 7.5° angle and flow at 35m/s (experimental results). Level mappings are source PWL in dB re 1pW and vectorial mappings are estimated A_{dip} normalized by maximum absolute level on each direction.	205
7.58 Dipole estimation (2kHz) with direction components level (top and third row) and vectorial representation for structures with 7.5° angle and flow at 35m/s (experimental results). Level mappings are source PWL in dB re 1pW and vectorial mappings are estimated A_{dip} normalized by maximum absolute level on each direction.	206
7.59 Dipole estimation (4kHz) with direction components level (top and third row) and vectorial representation for structures with 7.5° angle and flow at 35m/s (experimental results). Level mappings are source PWL in dB re 1pW and vectorial mappings are estimated A_{dip} normalized by maximum absolute level on each direction.	207
7.60 Dipole estimation (8kHz) with direction components level (top and third row) and vectorial representation for structures with 7.5° angle and flow at 35m/s (experimental results). Level mappings are source PWL in dB re 1pW and vectorial mappings are estimated A_{dip} normalized by maximum absolute level on each direction.	208
7.61 Dipole estimation (1kHz) with direction components level (top and third row) and vectorial representation for structures with 20° angle and flow at 35m/s (experimental results). Level mappings are source PWL in dB re 1pW and vectorial mappings are estimated A_{dip} normalized by maximum absolute level on each direction.	209
7.62 Dipole estimation (2kHz) with direction components level (top and third row) and vectorial representation for structures with 20° angle and flow at 35m/s (experimental results). Level mappings are source PWL in dB re 1pW and vectorial mappings are estimated A_{dip} normalized by maximum absolute level on each direction.	210

7.63	Dipole estimation (4kHz) with direction components level (top and third row) and vectorial representation for structures with 20° angle and flow at 35m/s (experimental results). Level mappings are source PWL in dB re 1pW and vectorial mappings are estimated A_{dip} normalized by maximum absolute level on each direction.	211
7.64	Dipole estimation (8kHz) with direction components level (top and third row) and vectorial representation for structures with 20° angle and flow at 35m/s (experimental results). Level mappings are source PWL in dB re 1pW and vectorial mappings are estimated A_{dip} normalized by maximum absolute level on each direction.	212
7.65	Dipole estimation (1kHz) with direction components level (top and third row) and vectorial representation for structures with 7.5° angle and flow at 70m/s (experimental results). Level mappings are source PWL in dB re 1pW and vectorial mappings are estimated A_{dip} normalized by maximum absolute level on each direction.	213
7.66	Dipole estimation (2kHz) with direction components level (top and third row) and vectorial representation for structures with 7.5° angle and flow at 70m/s (experimental results). Level mappings are source PWL in dB re 1pW and vectorial mappings are estimated A_{dip} normalized by maximum absolute level on each direction.	214
7.67	Dipole estimation (4kHz) with direction components level (top and third row) and vectorial representation for structures with 7.5° angle and flow at 70m/s (experimental results). Level mappings are source PWL in dB re 1pW and vectorial mappings are estimated A_{dip} normalized by maximum absolute level on each direction.	215
7.68	Dipole estimation (8kHz) with direction components level (top and third row) and vectorial representation for structures with 7.5° angle and flow at 70m/s (experimental results). Level mappings are source PWL in dB re 1pW and vectorial mappings are estimated A_{dip} normalized by maximum absolute level on each direction.	216
7.69	Dipole estimation (1kHz) with direction components level (top and third row) and vectorial representation for structures with 20° angle and flow at 70m/s (experimental results). Level mappings are source PWL in dB re 1pW and vectorial mappings are estimated A_{dip} normalized by maximum absolute level on each direction.	217

7.70 Dipole estimation (2kHz) with direction components level (top and third row) and vectorial representation for structures with 20° angle and flow at 70m/s (experimental results). Level mappings are source PWL in dB re 1pW and vectorial mappings are estimated A_{dip} normalized by maximum absolute level on each direction.	218
7.71 Dipole estimation (4kHz) with direction components level (top and third row) and vectorial representation for structures with 20° angle and flow at 70m/s (experimental results). Level mappings are source PWL in dB re 1pW and vectorial mappings are estimated A_{dip} normalized by maximum absolute level on each direction.	219
7.72 Dipole estimation (8kHz) with direction components level (top and third row) and vectorial representation for structures with 20° angle and flow at 70m/s (experimental results). Level mappings are source PWL in dB re 1pW and vectorial mappings are estimated A_{dip} normalized by maximum absolute level on each direction.	220
7.73 Wall pressure transducer (Kulites) SPL for structures with 7.5° angle and flow at 35m/s: 1kHz (top); 2kHz; 4kHz; and 8kHz. Levels in dB re 20 μ Pa.	223
7.74 Wall pressure transducer (Kulites) SPL for structures with 20° angle and flow at 35m/s: 1kHz (top); 2kHz; 4kHz; and 8kHz. Levels in dB re 20 μ Pa.	224
7.75 Wall pressure transducer (Kulites) SPL for structures with 7.5° angle and flow at 70m/s: 1kHz (top); 2kHz; 4kHz; and 8kHz. Levels in dB re 20 μ Pa.	225
7.76 Wall pressure transducer (Kulites) SPL for structures with 20° angle and flow at 70m/s: 1kHz (top); 2kHz; 4kHz; and 8kHz. Levels in dB re 20 μ Pa.	226
7.77 Directivity experimental results (r=2m) for structures with 7.5° angle and flow at 35m/s, far-field microphones level in red, frequencies: (a) 1kHz; (b) 2kHz; (c) 4kHz; and (d) 8kHz.	228
7.78 Directivity experimental results (r=2m) for structures with 20° angle and flow at 35m/s, far-field microphones level in red, frequencies: (a) 1kHz; (b) 2kHz; (c) 4kHz; and (d) 8kHz.	229
7.79 Directivity experimental results (r=2m) for structures with 7.5° angle and flow at 70m/s, far-field microphones level in red, frequencies: (a) 1kHz; (b) 2kHz; (c) 4kHz; and (d) 8kHz.	230
7.80 Directivity experimental results (r=2m) for structures with 20° angle and flow at 70m/s, far-field microphones level in red, frequencies: (a) 1kHz; (b) 2kHz; (c) 4kHz; and (d) 8kHz.	231

7.81	Dipole power level using the line grid (experimental results) for structures with 7.5° angle and flow at 35m/s: 1kHz (top); 2kHz; 4kHz; and 8kHz. Mappings are source PWL in dB re 1pW.	233
7.82	Directivity ($r=2m$) experimental results using the line grid for structures with 7.5° angle and flow at 35m/s, far-field microphones level in red, frequencies: (a) 1kHz; (b) 2kHz; (c) 4kHz; and (d) 8kHz.	234
7.83	Directivity ($r=2m$) experimental results using the line grid for structures with 20° angle and flow at 35m/s, far-field microphones level in red, frequencies: (a) 1kHz; (b) 2kHz; (c) 4kHz; and (d) 8kHz.	235
7.84	Directivity ($r=2m$) experimental results using the line grid for structures with 7.5° angle and flow at 70m/s, far-field microphones level in red, frequencies: (a) 1kHz; (b) 2kHz; (c) 4kHz; and (d) 8kHz.	236
7.85	Directivity ($r=2m$) experimental results using the line grid for structures with 20° angle and flow at 70m/s, far-field microphones level in red, frequencies: (a) 1kHz; (b) 2kHz; (c) 4kHz; and (d) 8kHz.	237
7.86	Dipole power level hybrid mapping comparison for the 8kHz analysis (experimental results) for structures with 7.5° angle and flow at 35m/s: with auto-powers attenuation (top); and without auto-powers attenuation. Mappings are source PWL in dB re 1pW.	238
7.87	Directivity experimental results ($r=2m$) with 3D grid and without attenuation of auto-powers for structures with 7.5° angle and flow at 35m/s, far-field microphones level in red, frequencies: (a) 1kHz; (b) 2kHz; (c) 4kHz; and (d) 8kHz.	239
7.88	Directivity experimental results ($r=2m$) with 3D grid and without attenuation of auto-powers for structures with 20° angle and flow at 35m/s, far-field microphones level in red, frequencies: (a) 1kHz; (b) 2kHz; (c) 4kHz; and (d) 8kHz.	240
7.89	Directivity experimental results ($r=2m$) with 3D grid and without attenuation of auto-powers for structures with 7.5° angle and flow at 70m/s, far-field microphones level in red, frequencies: (a) 1kHz; (b) 2kHz; (c) 4kHz; and (d) 8kHz.	241
7.90	Directivity experimental results ($r=2m$) with 3D grid and without attenuation of auto-powers for structures with 20° angle and flow at 70m/s, far-field microphones level in red, frequencies: (a) 1kHz; (b) 2kHz; (c) 4kHz; and (d) 8kHz.	242
7.91	Directivity experimental results ($r=2m$) with line grid and without attenuation of auto-powers for structures with 7.5° angle and flow at 35m/s, far-field microphones level in red, frequencies: (a) 1kHz; (b) 2kHz; (c) 4kHz; and (d) 8kHz.	243

7.92	Directivity experimental results ($r=2m$) with line grid and without attenuation of auto-powers for structures with 20° angle and flow at 35m/s, far-field microphones level in red, frequencies: (a) 1kHz; (b) 2kHz; (c) 4kHz; and (d) 8kHz.	244
7.93	Directivity experimental results ($r=2m$) with line grid and without attenuation of auto-powers for structures with 7.5° angle and flow at 70m/s, far-field microphones level in red, frequencies: (a) 1kHz; (b) 2kHz; (c) 4kHz; and (d) 8kHz.	245
7.94	Directivity experimental results ($r=2m$) with line grid and without attenuation of auto-powers for structures with 20° angle and flow at 70m/s, far-field microphones level in red, frequencies: (a) 1kHz; (b) 2kHz; (c) 4kHz; and (d) 8kHz.	246
8.1	Test facility, test section and installation layout.	249
8.2	NACA-0012 airfoil and test section with an airfoil test setup.	249
8.3	Array with 106 microphones in spiral distribution: light foam cover (left); and rear view of installation.	250
8.4	Array microphones positions in spiral distribution.	250
8.5	Target grid used on beamforming mappings: 1kHz / 195 points (top); 1.6kHz / 480 points; and 2.5kHz / 1080 points (bottom).	251
8.6	Beamforming results comparison for NACA-0012 with air at 23m/s and 0° angle-of-attack, DAMAS2 (left) and conventional beamforming (DAS): 1000Hz (top); 1600Hz; and 2500Hz (bottom). Mappings are SPL at array plane, and flow from right to left.	252
8.7	Beamforming results comparison for NACA-0012 with air at 35m/s and 0° angle-of-attack, DAMAS2 (left) and conventional beamforming (DAS): 1000Hz (top); 1600Hz; and 2500Hz (bottom). Mappings are SPL at array plane, and flow from right to left.	253
8.8	Beamforming results comparison for NACA-0012 with air at 23m/s and 5° angle-of-attack, DAMAS2 (left) and conventional beamforming (DAS): 1000Hz (top); 1600Hz; and 2500Hz (bottom). Mappings are SPL at array plane, and flow from right to left.	254
8.9	Beamforming results comparison for NACA-0012 with air at 35m/s and 5° angle-of-attack, DAMAS2 (left) and conventional beamforming (DAS): 1000Hz (top); 1600Hz; and 2500Hz (bottom). Mappings are SPL at array plane, and flow from right to left.	255
8.10	Generalized inverse beamforming results comparison for NACA-0012 with air at 23m/s and 0° angle-of-attack, without IRLS (left) and with IRLS: 1000Hz (top); 1600Hz; and 2500Hz (bottom). Mappings are SPL at array plane, and flow from right to left.	257

8.11	Generalized inverse beamforming results comparison for NACA-0012 with air at 35m/s and 0° angle-of-attack, without IRLS (left) and with IRLS: 1000Hz (top); 1600Hz; and 2500Hz (bottom). Mappings are SPL at array plane, and flow from right to left.	258
8.12	Generalized inverse beamforming results comparison for NACA-0012 with air at 23m/s and 5° angle-of-attack, without IRLS (left) and with IRLS: 1000Hz (top); 1600Hz; and 2500Hz (bottom). Mappings are SPL at array plane, and flow from right to left.	259
8.13	Generalized inverse beamforming results comparison for NACA-0012 with air at 35m/s and 5° angle-of-attack, without IRLS (left) and with IRLS: 1000Hz (top); 1600Hz; and 2500Hz (bottom). Mappings are SPL at array plane, and flow from right to left	260
9.1	Simplified moving source modeling.	264
9.2	Test track.	266
9.3	5-arms star antenna layout.	267
9.4	Vehicle and target grid distribution.	267
9.5	Localization error with respect to the number of estimates and using block of 2048 samples (X means error is higher than 0.4m).	268
9.6	Localization error with respect to block size using 3 estimates (X means error is higher than 0.4m).	268
9.7	Localization example using GIB for vehicle at 0m (in front of array).	269
9.8	Localization example using GIB for vehicle at -6m from track center.	269
9.9	CB: Vehicle at 0m (in front of array).	270
9.10	CB: Vehicle at -6m.	270
9.11	Center microphone level along vehicle run.	271
9.12	GIB: Engine 2 nd order (75Hz) localization example for vehicle at 2m from track center.	272
9.13	GIB: Spectrum peak (875Hz) localization example for vehicle at 2m from track center.	272
9.14	CB: Engine 2 nd order (75Hz) localization example for vehicle at 2m from track center.	273
9.15	CB: Spectrum peak (875Hz) localization example for vehicle at 2m from track center.	273
10.1	Track, array of microphones and measured truck at track center (x=0).	277
10.2	Array microphone coordinates, including pass-by noise microphone position at array center.	278
10.3	Array assembly with 61 microphones, including pass-by noise microphone position at array center.	278

10.4	Test track overall range: left and right cones indicate the truck extension coverage during pass-by test.	278
10.5	Loudspeakers position and assembly details: rear (left); and front speaker.	279
10.6	Target grid with 3120 points in square regular distribution.	280
10.7	Identifications of front loudspeaker with tonal 500Hz and Truck at constant speed of 50km/h for various track positions. Mappings are 3 rd oct. SPL (A-Weighted) at pass-by noise microphone position.	282
10.8	Identifications of front loudspeaker with tonal 500Hz using image source in transfer matrix and truck at constant speed of 50km/h for various track positions. Mappings are 3 rd oct. SPL (A-Weighted) at pass-by noise microphone position.	284
10.9	Identifications of front loudspeaker with tonal 300Hz and truck at constant speed of 50km/h for various track positions. Mappings are 3 rd oct. SPL (A-Weighted) at pass-by noise microphone position.	285
10.10	Identifications of front loudspeaker with tonal 300Hz using low frequency focus compensation and truck at constant speed of 50km/h for various track positions. Mappings are 3 rd oct. SPL (A-Weighted) at pass-by noise microphone position. . .	287
10.11	Identifications of front loudspeaker with tonal 200Hz using low frequency focus compensation and truck at constant speed of 50km/h for various track positions. Mappings are 3 rd oct. SPL (A-Weighted) at pass-by noise microphone position. . .	288
10.12	Identifications of front loudspeaker with tonal 100Hz using low frequency focus compensation and truck at constant speed of 50km/h for various track positions. Mappings are 3 rd oct. SPL (A-Weighted) at pass-by noise microphone position. . .	289
10.13	Identifications of front loudspeaker with tonal 50Hz using low frequency focus compensation and truck at constant speed of 50km/h for various track positions. Mappings are 3 rd oct. SPL (A-Weighted) at pass-by noise microphone position. . .	290
10.14	Identifications on 7kHz 3 rd oct. of front and rear loudspeakers with coherent white noise and truck at constant speed of 50km/h for various track positions. Mappings are 3 rd oct. SPL (A-Weighted) at pass-by noise microphone position.	292
10.15	Identifications on 7kHz 3 rd oct. of front and rear loudspeakers with incoherent white noise and truck at constant speed of 50km/h for various track positions. Mappings are 3 rd oct. SPL (A-Weighted) at pass-by noise microphone position.	293
10.16	Identifications of front loudspeaker with tonal 500Hz using IRLS scheme and truck at constant speed of 50km/h for various track positions. Mappings are 3 rd oct. SPL (A-Weighted) at pass-by noise microphone position.	295

10.17	Identifications of front loudspeaker with tonal 300Hz using IRLS scheme and truck at constant speed of 50km/h for various track positions. Mappings are 3 rd oct. SPL (A-Weighted) at pass-by noise microphone position.	296
10.18	Identifications of front loudspeaker with tonal 200Hz using IRLS scheme and truck at constant speed of 50km/h for various track positions. Mappings are 3 rd oct. SPL (A-Weighted) at pass-by noise microphone position.	297
10.19	Identifications on 7kHz 3 rd oct. of front and rear loudspeakers with coherent white noise using IRLS scheme and truck at constant speed of 50km/h for various track positions. Mappings are 3 rd oct. SPL (A-Weighted) at pass-by noise microphone position.	298
10.20	Identifications on 7kHz 3 rd oct. of front and rear loudspeakers with incoherent white noise using IRLS scheme and truck at constant speed of 50km/h for various track positions. Mappings are 3 rd oct. SPL (A-Weighted) at pass-by noise microphone position.	299
10.21	Identifications of front loudspeaker with tonal 500Hz using conventional beamforming and truck at constant speed of 50km/h for various track positions. Mappings are 3 rd oct. SPL (A-Weighted) at pass-by noise microphone position.	301
10.22	Identifications of front loudspeaker with tonal 300Hz using conventional beamforming and truck at constant speed of 50km/h for various track positions. Mappings are 3 rd oct. SPL (A-Weighted) at pass-by noise microphone position.	302
10.23	Identifications on 7kHz 3 rd oct. of front and rear loudspeakers with coherent white noise using conventional beamforming and truck at constant speed of 50km/h for various track positions. Mappings are 3 rd oct. SPL (A-Weighted) at pass-by noise microphone position.	303
10.24	Identifications on 7kHz 3 rd oct. of front and rear loudspeakers with incoherent white noise using conventional beamforming and truck at constant speed of 50km/h for various track positions. Mappings are 3 rd oct. SPL (A-Weighted) at pass-by noise microphone position.	304
10.25	Pass-by noise level along runs with start at 30km/h using 10 th gear (left) and 50km/h using 12 nd gear. Scale on level has 2dBA per division.	305
10.26	Identification for peak frequency level using conventional beamforming (top), generalized inverse without and with IRLS scheme (bottom) for start speed of 30km/h and truck at x=2m track position. Mappings are 3 rd oct. SPL (A-Weighted) in 8dB range at pass-by noise microphone position.	306

10.27	Identification for peak frequency level using conventional beamforming (top), generalized inverse without and with IRLS scheme (bottom) for start speed of 50km/h and truck at x=5m track position. Mappings are 3 rd oct. SPL (A-Weighted) in 8dB range at pass-by noise microphone position.	308
10.28	Identification for 3 rd order level using conventional beamforming (top) and generalized inverse without IRLS scheme for start speed of 30km/h and truck at x=2m track position. Mappings are 3 rd oct. SPL (A-Weighted) in 8dB range at pass-by noise microphone position.	309
10.29	Identification for 3 rd order level using conventional beamforming (top) and generalized inverse without IRLS scheme for start speed of 50km/h and truck at x=5m track position. Mappings are 3 rd oct. SPL (A-Weighted) in 8dB range at pass-by noise microphone position.	310

List of Tables

4.1	Monopole source strength estimation comparison for the monopole at origin case. .	36
4.2	Distributed monopole line source strength estimation comparison.	37
4.3	Dipole estimation comparison.	39
4.4	Monopole and dipole estimations comparison for the incoherent case.	39
4.5	Monopole and dipole estimations comparison for the coherent case.	41
4.6	Time spent on calculations for the monopole problem.	69
4.7	Time spent on calculations phases for the monopole problem.	69
4.8	Time spent with GIB methods on calculations for the monopole problem.	70
4.9	Time spent with GIB methods on calculations phases for the monopole problem. . .	70
5.1	Source strength estimation comparison for the monopole at origin case and different methods: direct; eigenvalue based; regularization factor at minimum limit; regularization factor at maximum limit; and optimized regularization strategy. . . .	85
5.2	Source strength estimation comparison for the two monopoles case and different methods: direct; eigenvalue based; regularization factor at minimum limit; regularization factor at maximum limit; and optimized regularization strategy.	86
5.3	Estimations varying array distance and aperture.	88
5.4	Source strength estimations for three different frequencies.	92
5.5	Strength estimations for two monopoles in-phase example.	93
5.6	Generalized inverse and hybrid estimation for the two monopoles example.	96
5.7	Power estimations for the two monopoles in-phase problem.	101
5.8	Power estimations for the dipole identification using two monopoles in anti-phase problem.	105
7.1	Test cases on NLR measurements.	140
7.2	Coherence length and number of incoherent monopole sources in 0.5m length. . . .	145
11.1	Main practical advantages and limitations on the use of generalized inverse method on aeroacoustic and moving source problems.	319
12.1	Principais vantagens e limitações práticas de engenharia no uso do método inverso generalizado em problemas aeroacústicos e de fonte em movimento.	330

List of Symbols and Abbreviations

Latin Letters

a	- Source strength vector	[m ³ /s]
a_{sph}	- Sphere radius	[m]
a'	- Source vector directly obtained from least squares equation	[m ³ /s]
A	- Transfer matrix	[Pa·s/m ³]
A_{dip}	- Multiplier on dipole radiation expression	
b_s	- Right singular vectors	
c	- Speed of sound	[m/s]
c_{dip}	- Constant to normalize strength of dipole	
c_o	- Speed of sound outside the jet	[m/s]
c_t	- Speed of sound inside the jet	[m/s]
C	- Propagation vector	[Pa]
CB	- Clean beam for replacement of source on cleaned map on CLEAN method	
dA_{θ_i}	- Incremental area	[m ²]
dA_{θ}	- Incremental area	[m ²]
dA_o	- Incremental area	[m ²]
dz	- Complex coefficient	
D_t	- Doppler factor for the amplitude change	
DM	- Dirty map through iterations on CLEAN beamforming method	
f	- Wiener filter or weight	
f_{A_i-dir}	- Transfer function re-scaling factor	
f_{req}	- Frequency	[Hz]
h	- Signals non-coherent noise strength	
h_c	- Spatially coherent component	
H	- Spatial coherent distribution matrix	
I	- Identity matrix	

$I_{\theta'}$	- Acoustic intensities normal to their respective incremental area	$[\text{W/m}^2]$
I_{θ}	- Acoustic intensities normal to their respective incremental area	$[\text{W/m}^2]$
I_o	- Acoustic intensities normal to their respective incremental area	$[\text{W/m}^2]$
k	- Circular wavenumber	
j_1	- Spherical Bessel function of order 1	
J_{ac}	- Jacobian matrix	$[\text{m}^3/(\text{s}\cdot\text{Pa})]$
J_1	- Proposed problem cost function based on ℓ_1 norm	$[\text{m}^3/\text{s}]$
J_1^{alt}	- Alternative cost function based on ℓ_1 norm for testing	$[\text{m}^3/\text{s}]$
J_{1orig}	- Original problem cost function based on ℓ_1 norm	$[\text{m}^3/\text{s}]$
J_{res}	- Residue cost functions	$[\text{m}^3/\text{s}]$
J_{resII}	- Residue cost functions with improved physical units consistency	$[\text{m}^3/\text{s}]$
J_{res}^{alt}	- Alternative residue cost functions	$[\text{m}^3/\text{s}]$
J_2	- Problem cost function based on Euclidean norm	$[\text{m}^6/\text{s}^2]$
J_{w_a}	- Problem cost function using weighted system with minimization of $ a $	$[\text{m}^3/\text{s}]$
J_{WPInv}	- Problem cost function using weighted system with optimized terms	$[\text{m}^3/\text{s}]$
k_c	- DAMAS2 cut-off wavenumber	
ℓ_{coh}	- Spanwise coherence length	$[\text{m}]$
l_i	- Direction cosine of the outward normal \vec{n}	
M	- Mach number	
M_s	- Ratio between the moving source speed and the speed of sound	
n_1	- Spherical Neumann function of order 1	
\vec{n}	- Outward normal from the fluid at boundary with solid obstacle	
N_{grid}	- Number of grid points on the target region	
N_{mic}	- Number of microphones	
N_s	- Number of samples	
N_w	- Rank of the matrix decomposed by singular values	
p	- Problem order of interest	

$Press$	- Pressure	[Pa]
$Press_{dip}$	- Pressure of dipole	[Pa]
$Press_{mic}$	- Pressure calculated for each microphone location	[Pa]
P_{cb}	- Conventional Beamforming estimation	[Pa ²]
P_{cb_M}	- Conventional beamforming in matrix notation	[Pa ²]
P_{Hyb}	- Hybrid beamforming estimation	[Pa ²]
P_{Leg1}	- Legendre function of order 1	
P_{SB}	- Pressure exerted on the fluid by the solid boundaries	[Pa]
q	- Matrix with microphone spectrums	
q_{spec}	- Microphone signal spectrum	[Pa/Hz]
Q	- Monopole strength	[m ³ /s]
$Q_N(x, y)$	- Strength normalized by the maximum mapping value	
r	- Distance between two points of interest	[m]
r_D	- Strength mapping from deconvolution on DAMAS2	
\vec{r}	- Vector from microphone to grid point	[m]
$r_{M.C.}$	- Microphone centroid in number of wavelengths	
r_{aper}	- Array aperture	[m]
res	- System residue	[Pa]
R	- Distance in still air	[m]
R'	- Convected distance	[m]
R_a	- Distance from microphone to apparent noise source	[m]
R_{CSM}	- Cross-Spectrums Matrix (CSM)	[Pa ²]
R_e	- Emission source distance	[m]
R_m	- Distance from the source to the microphone	[m]
R_o	- Distance from microphone to jet centerline	[m]
R_t	- Shear layer distance to the center of the cylindrical flow	[m]
t	- Time	[s]
T	- Lighthill's Stress Tensor	
u_s	- Left singular vectors	
u	- Eigenvector	
U	- Eigenvector matrix	
U_c	- Eddy convection velocity	[m/s]
U_s	- Matrix of left singular vectors	
U_0	- Sphere radial velocity amplitude	[m/s]
U_∞	- Jet air speed	[m/s]

v	- Eigenmode	[Pa]
vel	- Particle velocity	[m/s]
\vec{v}	- Unitary vector with dipole orientation	
V	- Moving source rectilinear movement constant speed	[m/s]
V_s	- Matrix of right singular vectors	
w	- Steering vector or just weighting vector	
W	- Diagonal weighting matrix	
x	- Position coordinates for beamforming calculation	[m]

Greek Letters

α	- Tikhonov regularization factor	
β	- Source terms truncation factor	
ϕ	- Loop gain factor on CLEAN beamforming method	
γ_3	- Dimensionless parameter	
λ	- Eigenvalue	[Pa ²]
λ_{CLEAN}	- dynamic resolution for the clean beam on CLEAN method	
$\lambda_{L.M.}$	- Vector of Lagrange multipliers	
Λ	- Diagonal matrix containing the eigenvalues	[Pa ²]
Π_{mon}	- Monopole Power	[W]
Π_{dip}	- Dipole Power	[W]
ρ	- Air density	[kg/m ³]
ρ_o	- Air density outside the jet	[kg/m ³]
ρ_t	- Air density inside the jet	[kg/m ³]
ρ_0	- Medium density at rest	[kg/m ³]
Σ	- Matrix with singular values	[Pa ²]
θ	- Convected propagation angle in flow	[rad]
θ_o	- Angle from the shear layer to the microphone	[rad]
θ_m	- Angle formed from the source to the microphone	[rad]
θ'	- Emission angle	[rad]
ϑ	- Angle from the polar axis	[rad]

Superscripts

n	- Iteration number
-----	--------------------

Subscripts

i	- Eigenpair number
j	- Microphone index
k	- Grid point index
x	- Dipole source term on x direction
y	- Dipole source term on y direction
s	- Respective to the source location
m	- Microphone number index
max	- Maximum value

Symbols

$ \cdot $ or $ \cdot _2$	- Denotes the Euclidean norm
$ \cdot _p$	- Denotes the ℓ -p norm for vectors
$ \cdot $	- Absolute value for scalars and ℓ_1 -norm for vector
\dagger	- Complex conjugate transpose
$+$	- Pseudo inverse with Tikhonov regularization
δ_{ij}	- Dirac delta
i	- Complex imaginary unit
e	- Exponential function

Abbreviations

ADT	- Azimuthal Decomposition Technique
CB	- Conventional Beamforming
CLEAN	- Beamforming based on conventional method
CLEAN-SC	- CLEAN extension based in source coherence
DAMAS	- Deconvolution Approach for the Mapping of Acoustic Sources
DAMAS2	- Extension of DAMAS for frequency domain approach
DAS	- Delay-And-Sum procedure on conventional beamforming
EESC	- Escola Engenharia de São Carlos (School of Engineering of São Carlos)
GIB	- Generalized Inverse Beamforming
GINV	- Improved Generalized Inverse Beamforming

GWIB	- Generalized Weighted Inverse Beamforming
IRLS	- Iteratively Re-Weighted Least Squares
KUL	- Katholieke Universiteit of Leuven
MBB	- Mercedes-Benz do Brasil
NLR	- National Aerospace Laboratory of The Netherlands
PSF	- Point Spread Function
UNICAMP	- State University of Campinas
VKI	- Von Kármán Institute

Contents

1	Introdução	1
1.1	Objetivos e Escopo da Tese	2
1.2	Organização Geral da Tese	3
2	Introduction	7
2.1	Thesis Objectives and Scope	8
2.2	Thesis Overview	8
3	Literature Review	13
3.1	Introduction	13
3.2	Aeroacoustic Source Identification Techniques	13
3.3	Moving Source Identification Techniques	19
3.4	Summary	21
4	Generalized Inverse Beamforming Methods	23
4.1	Introduction	23
4.2	Generalized Inverse Beamforming Original Method	24
4.2.1	Simplified Algorithm	32
4.2.2	Literature Model Problems	33
4.3	Generalized Inverse Beamforming with Optimized Regularization Strategy	44
4.4	Weighted Least Squares Schemes	56
4.4.1	Iteratively Re-Weighted Least Squares based in Source Vector as Weight	56
4.4.2	Iteratively Re-Weighted Least Squares based in Residue as Weight	59
4.4.3	Generalized Weighted Inverse Beamforming	61
4.4.4	Stabilized Generalized Weighted Inverse Beamforming	63
4.5	Improved Generalized Inverse Beamforming	64
4.6	Computational Effort Analysis	68
4.7	Summary	70
5	Experimental Identification Using Compact Sources	73
5.1	Identification with Optimized Regularization Strategy	73
5.1.1	Introduction	73
5.1.2	Test Setup and Problem Cases Details	74

5.1.3	Eigenvalue Based Strength Estimation	76
5.1.4	J_1 Cost Function Comparison	77
5.1.5	Squared Strength Mappings Comparison	79
5.1.6	Strength Estimations Comparison	81
5.1.7	Summary	86
5.2	Generalized Inverse Beamforming Investigation and Hybrid Estimation	87
5.2.1	Introduction	87
5.2.2	Monopole at Origin	88
5.2.3	Two Monopoles In Coherent Radiation	92
5.2.4	Hybrid Estimation	94
5.2.5	Summary	97
5.3	Monopole and Dipole Identification Using Generalized Inverse Beamforming	98
5.3.1	Introduction	98
5.3.2	Two Monopoles in-Phase	98
5.3.3	Two Monopoles in anti-Phase	102
5.3.4	Summary	105
5.4	Source Identification Using the Generalized Weighted Inverse Beamforming	106
5.4.1	Introduction	107
5.4.2	Numerical Example	107
5.4.3	Experimental Results	108
5.4.4	Summary	112
5.5	Summary	112
6	Aeroacoustic Source Identification: Dipole over Cylinder in Subsonic Jet	115
6.1	Introduction	115
6.2	Aeroacoustic Sources in the Presence of Solid Boundaries	117
6.3	Convection and Refraction Modeling	118
6.4	Aeroacoustic Test Setup	120
6.5	Aeroacoustic Source Peak Emissions	122
6.6	Numerical Investigation On Identification Performance	124
6.7	Dipole Identification on Peak Events	126
6.8	Equivalent Pressure Mappings on Peak Events	128
6.9	Experimental Identification on Averaged CSM	129
6.10	Equivalent Pressure Mappings on Averaged CSM	131
6.11	Directivity Plots on Averaged CSM	132
6.12	Summary	134

7	Aeroacoustic Source Identification: Two Structures in Subsonic Flow	135
7.1	Introduction	135
7.2	Test Setup and General Conditions	138
7.3	Convection and Refraction Modeling	141
7.4	Monopole Identification Using Conventional Beamforming	143
7.4.1	Simulated Identification Verifications	144
7.4.2	Experimental Results and Comparison with Identification from NLR	147
7.4.3	Diagonal Removal Influence in Results	152
7.4.4	Microphone Weighting Influence in Results	153
7.5	Monopole Identification Using Generalized Inverse Beamforming	153
7.5.1	Simulated Identification Verifications	154
7.5.2	Hybrid Generalized Inverse Mapping	155
7.5.3	Auto-Powers Attenuation in CSM	162
7.5.4	Experimental Identification Results and Analysis	163
7.5.5	Eigen-Modes Result Mappings Example	168
7.6	Dipole Identification Using Generalized Inverse Beamforming	173
7.6.1	Dipole Convection and Refraction Modeling	173
7.6.2	Test Setup and General Conditions	175
7.6.3	Transfer Function Re-Scaling for 3D Dipole Identification	178
7.6.4	Simulated Identifications with Convection and Refraction	183
7.6.5	Experimental Results for Dipole Identification	193
7.6.6	Full Hybrid and Hybrid Generalized Inverse Mapping Comparison	199
7.6.7	Dipole Directional Component Level Details	204
7.6.8	Upstream Structure Wall Pressure Transducers Analysis	222
7.6.9	Estimated Directivity Comparison with Far-Field Microphones	227
7.6.10	Line Grid Experimental Results Analysis	231
7.6.11	Auto-Powers Attenuation Influence on Identification	238
7.7	Summary	241
8	Aeroacoustic Source Identification: NACA-0012 Airfoil in Subsonic Flow	247
8.1	Introduction	247
8.2	Test Setup and General Conditions	248
8.3	Beamforming Results Comparison: DAMAS2 and Conventional Beamforming . .	250
8.4	Monopole Identification Using Generalized Inverse Beamforming	256
8.5	Summary	261

9	Moving Source Identification: Passenger Vehicle Pass-by Noise	263
9.1	Introduction	263
9.2	Moving Source Modeling	264
9.3	Test Setup and General Conditions	265
9.4	Experimental Identification Verifications	267
9.5	Passenger Vehicle Noise Identification	271
9.6	Summary	273
10	Moving Source Identification: Truck Pass-by Noise	275
10.1	Introduction	275
10.2	Test Setup and General Conditions	276
10.3	Experimental Identification Verifications	280
10.3.1	Generalized Inverse Beamforming	281
10.3.2	Use of Image Source in Transfer Matrix	283
10.3.3	Use of Low Frequency Focus Compensation	286
10.3.4	Coherent and Incoherent Broadband Sources Identification	291
10.3.5	Generalized Inverse Beamforming with IRLS Scheme	294
10.3.6	Conventional Beamforming	300
10.4	Truck Noise Identification	305
10.4.1	Identification of Peak Noise Emission	305
10.4.2	Identification of Main Engine Order at Peak Noise Emission Position . . .	307
10.5	Summary	309
11	Conclusions	311
11.1	Introduction	311
11.2	Aeroacoustic Source Identification	311
11.2.1	Dipole over Cylinder in Subsonic Jet	312
11.2.2	Two Structures in Subsonic Flow	313
11.2.3	NACA-0012 Airfoil in Subsonic Flow	314
11.3	Moving Source Identification	314
11.3.1	Passenger Vehicle Pass-by Noise	314
11.3.2	Truck Pass-by Noise	315
11.4	Main Contributions to The Research Field	316
11.5	Suggested Future Work	318
11.6	Summary	318

12 Conclusões	321
12.1 Introdução	321
12.2 Identificação de Fontes Aeroacústicas	321
12.2.1 Dipólo sobre Cilindro em Jato Subsônico	322
12.2.2 Duas Estruturas em Fluxo Subsônico	323
12.2.3 Aerofólio NACA-0012 em Fluxo Subsônico	324
12.3 Identificação de Fontes em Movimento	325
12.3.1 Ruído de Passagem de Veículo de Passageiros	325
12.3.2 Ruído de Passagem de Caminhão	325
12.4 Maiores Contribuições para o Campo de Pesquisa	326
12.5 Futuros Trabalhos Recomendados	328
12.6 Resumo	329
Bibliography	331
A DAMAS2	340
B CLEAN-SC	341

1 Introdução

Localização e caracterização de fontes acústicas é uma importante área de investigação desde que a redução do ruído das máquinas vem recebendo atenção especial devido às leis ambientais mais restritivas, problemas de urbanização e expectativas mais exigentes por parte dos consumidores em relação ao conforto acústico. Por exemplo, as restrições ao nível de ruído em sobrevôo para as aeronaves com o objetivo de reduzir a poluição sonora em torno dos aeroportos, e os limites de ruído de passagem veicular com o objetivo de reduzir o ruído de tráfego urbano exigiram melhorias na engenharia de aeronaves e de veículos, respectivamente.

Diferentes técnicas têm sido desenvolvidas para a identificação de fontes de ruído nesses dois tipos de problemas: fontes aeroacústicas e fontes em movimento. A pesquisa em aeroacústica vem desde o final do século XIX, quando Strouhal (1878) publicou seus estudos sobre o ruído produzido à partir do fluxo de ar através de fios, e este campo, aeroacústica, recebeu uma formulação teórica mais tarde por Lighthill (1952). A modelagem de fonte em movimento utilizada neste trabalho foi criada por Morse & Ingard (1968) no século passado, porém o efeito Doppler foi primeiramente descrito teoricamente em 1842 por Johan Christian Andreas Doppler.

A localização de fontes acústicas pode ser obtida utilizando-se vários métodos. Para listar alguns: intensidade do som; avaliação por microfone direcional; holografia acústica; *beamforming*¹ baseado na abordagem convencional e, mais recentemente, *beamforming* com base em métodos inversos.

Todos esses métodos têm características especiais que podem melhor se adaptar em cada tipo de problema. Por exemplo, o uso de microfones direcionais pode ser vantajoso se usado para uma localização mais geral e quando uma solução de baixo custo de medição é necessária. Outro exemplo, para radiação estacionária em campo próximo, a holografia acústica pode ser a escolha mais adequada. Mas para fins gerais, usando-se uma malha de microfones e um curto período de tempo de aquisição, o *beamforming* convencional é a solução preferida para localização de fontes.

Métodos de *beamforming* estão em intensa pesquisa e recentemente, os métodos inversos estão provando ter seu espaço neste campo. Os métodos inversos começam com a definição de uma grade alvo, que corresponde aos locais onde as fontes são procuradas. Um modelo para a função de transferência entre a grade alvo e a malha de medição é definido e o sistema

¹ A tradução para *beamforming*, formação de feixes, não é comum e o termo é mantido em sua linguagem original.

fonte/transferência/receptor é resolvido por mínimos quadrados no caso de problema sobredeterminado (número de pontos candidatos na grade alvo menor que o número de microfones), ou mínimos quadrados e mínima norma para o caso de problema subdeterminado.

Esta metodologia fornece uma representação versátil dos problemas e distribuições complexas de fontes podem ser analisadas, tais como fontes multipolares, comuns nos problemas aeroacústicos. Outra característica importante sobre este método é a melhor resolução em frequências mais baixas de análise quando comparado ao *beamforming* convencional, uma vantagem grande a ser explorada em identificações de ruído de passagem veicular.

1.1 Objetivos e Escopo da Tese

O objetivo primário desta pesquisa é desenvolver um método de identificação que pode ser usado em problemas de geração de fontes aeroacústicas e fornecer uma melhor compreensão destes mecanismos de geração. Dois tipos principais de mecanismos de geração de fonte podem ser distinguidos, a geração de ruído por turbulência do fluxo de ar, por exemplo, encontrado em camada de mistura de jato, e o segundo tipo, o som produzido pela turbulência causada por obstáculos sob fluxo de ar. O escopo da presente investigação é restrito para a verificação do método quando aplicado a fontes aeroacústicas geradas pelo fluxo de ar subsônico por cima de obstáculos compactos. Neste tipo de problema, a radiação pode ser considerada sob certas condições, estacionária, uma condição mais simples de identificação de fontes, e também mais simples porque a geração de som tem eficiência de radiação mais elevada neste tipo de problema, tornando-o uma primeira escolha para a validação de identificação das fontes aeroacústicas.

Um segundo objetivo neste trabalho é desenvolver um método de identificação em problemas de fontes móveis. As aplicações escolhidas são a localização de fontes em veículo de passageiros e em caminhão em procedimento de ruído de passagem. Esse problema de fonte em movimento, em princípio, é muito semelhante em termos de modelagem com a modelagem de fontes em convecção, com alteração na posição da fonte observada em relação à localização verdadeira da fonte, mas os principais desafios são de que o problema não tem radiação estacionária e possui efeito Doppler na frequência observada.

A investigação nesta Tese tem como objectivo levantar as principais vantagens potenciais na utilização do método de identificação *beamforming* inverso, bem como as possíveis inconveniências nestas duas aplicações, fontes aeroacústicas e fontes em movimento.

1.2 Organização Geral da Tese

Primeiro, a literatura relevante usada neste trabalho é apresentada no Capítulo 3. Métodos de identificação utilizados para ambos os problemas aeroacústicos e de fontes em movimento são comparados e avaliados em termos de precisão e versatilidade para abordar fontes multipolares, por exemplo. O *beamforming* baseado no método inverso é selecionado e as principais características são levantadas para serem avaliadas ao longo das verificações de desempenho nas aplicações escolhidas.

O método *beamforming* inverso generalizado e suas variantes são implementados no Capítulo 4, e uma comparação com base em casos numéricos da literatura é feita para os métodos estado-da-arte, tais como CLEAN-SC, e DAMAS2, como também para o *beamforming* convencional. A estratégia de regularização otimizada, proposta de um processo automatizado para escolher o fator de regularização, é introduzida e os resultados apresentados com base em estudos numéricos.

O método inverso é verificado em casos experimentais utilizando fontes compactas em uma sala semi-anecóica nas instalações da Katholieke Universiteit de Leuven (Bélgica), mostrado no Capítulo 5. Ainda que casos simples, levantam os principais aspectos do método, tais como uma melhor faixa dinâmica e melhor capacidade de distinguir fontes próximas de radiação coerente, quando comparado com o *beamforming* convencional. Nesse capítulo, a estimativa de vazão acústica baseada na matriz de espectros cruzados (CSM) e seus autovalores é contrastada com o cálculo direto, tentando ilustrar a sua natureza de representação global da vazão das fontes. Outro desenvolvimento neste capítulo é a metodologia híbrida, que combina a estimativa robusta de vazão direcional do *beamforming* convencional com o mapeamento inverso generalizado, melhorando a sua estimativa de vazão, por vezes deteriorada devido à solução por mínimos quadrados do sistema proposto. Outra característica importante levantada nesse capítulo para o método inverso generalizado é a capacidade de localização em frequências mais baixas quando comparado com o *beamforming* convencional, e isso também é explorado mais adiante nos Capítulos de fontes em movimento.

O sexto capítulo apresenta a identificação de fontes aeroacústicas para um fluxo de jato subsônico sobre uma seção circular de cilindro medido em uma sala semi-anecóica. A modelagem de convecção e refração é aplicada para localizar a formação de dipólos na direção perpendicular ao fluxo e na superfície do cilindro. Duas abordagens são apresentadas, em primeiro lugar a identificação realizada em eventos individuais de pico de radiação, tentando compreender seus mecanismos de geração. A segunda abordagem é a identificação mais comum a partir de um cálculo

de médias mais longo no tempo, o que traz em um mapeamento único, a representação da radiação que corresponderia às principais regiões de geração de fontes aeroacústicas. As regiões detectadas por essas duas abordagens deixa uma importante discussão sobre a natureza da geração de fontes e sua localização.

O sétimo capítulo apresenta a identificação de fontes aeroacústicas sobre duas estruturas sob fluxo de ar subsônico medido em um túnel de vento fechado do Laboratório Aeroespacial Nacional da Holanda (NLR). As estruturas representam uma estrutura de trem de pouso em condição de pouso ou decolagem, onde o ruído é um dos principais contribuintes para a medições de ruído em sobrevôo. Identificações de monopólos feitas pela NLR são comparadas com os resultados gerados pelo *beamforming* convencional, bem como os resultados por método inverso. Identificações de dipólos são realizadas utilizando-se o método inverso e uma avaliação de diretividade é feita em relação aos níveis de microfones em campo distante. Mapeamento híbrido inverso generalizado é desenvolvido e apresentado para a identificação de monopólos e dipólos, um artifício importante para melhorar a resolução dos mapeamentos de identificação por métodos inversos.

No Capítulo 8, a identificação do ruído gerado a partir de um aerofólio de perfil aerodinâmico padrão, NACA-0012, é apresentado e comparado com dados da literatura. As medições foram realizadas no Túnel de Vento Fechado da Escola de Engenharia de São Carlos (EESC) da Universidade Estadual de São Paulo (USP). Resultados para o *beamforming* inverso generalizado são confrontados com o *beamforming* convencional, bem como para o método estado-da-arte, DAMAS2. Esta condição de identificação, túnel de vento fechado, é uma condição desafiadora para qualquer método de localização e, em especial, para os métodos inversos, como discutido ao longo da seção sobre os resultados.

O Capítulo 9 apresenta a primeira aplicação sobre fonte em movimento, juntamente com a modelagem adotada. Um teste experimental é conduzido para o problema de localização de fontes em ruído de passagem com o apoio da LMS International Engineering em sua sede em Leuven (Bélgica). Testes de validação são realizados com uma fonte conhecida colocada sobre um veículo. Após a verificação do método na identificação de uma fonte conhecida, as fontes de ruído do veículos são investigadas. Os resultados apontam para o potencial do método em trazer a localização com uma resolução dinâmica melhor quando comparado ao *beamforming* convencional, também cobrindo frequências mais baixas, mesmo na presença de reflexões no asfalto.

A última aplicação do método, apresentada no capítulo 10, é a identificação de fontes num

teste de ruído de passagem de caminhão. Explorando-se a faixa de frequências mais baixas de análise ao usar-se um arranjo especial de malha de microfones apresentado neste trabalho. Dois artifícios são apresentados, a adoção de uma imagem de fonte para dar conta das reflexões do som no asfalto, e uma compensação de foco para baixas frequências, onde a radiação de onda da fonte é considerada como uma condição intermediária entre a radiação plana e a radiação esférica perfeita. Mapeamentos híbridos inversos generalizados são utilizados para se apresentar o nível de contribuição das fontes no nível medido no microfone do teste de ruído de passagem. Embora tenha uma característica inerente ao *beamforming* de superestimar o nível da fonte sonora, este método apresenta uma estimativa direta da parcela do nível de ruído de passagem relativo à fonte apresentada no mapeamento.

Estes testes mencionados estão longe de esgotar a discussão sobre o desempenho do método inverso generalizado em identificar fontes aeroacústicas e fontes em movimento. No entanto, estes testes levantam as principais possibilidades de análise e novas frentes de pesquisa ao mesmo tempo demonstrando suas melhorias em precisão e versatilidade quando comparados aos métodos tradicionais, como o *beamforming* convencional. Estas contribuições principais estão listadas no Capítulo 11, com uma descrição detalhada das vantagens e desvantagens observadas nesta metodologia, bem como a lista das principais contribuições para os campos de pesquisa sobre esses dois tipos de problemas: fontes aeroacústicas e fontes em movimento.

2 Introduction

Acoustic sources localization and characterization is an important research area since reduction of machinery noise is receiving special attention due to more restrictive environmental regulations, urbanization problems and more demanding acoustic comfort expectation from consumers. For example, airplane fly-over regulations to reduce airport neighborhood noise pollution, and vehicle pass-by noise limits to reduce urban traffic noise. These two examples demand design improvements from aircraft and vehicle engineering, respectively.

Different techniques have been developed to noise source identification on these two problem types: aeroacoustic sources and moving sources. The aeroacoustic research dates from end of XIX century, when Strouhal (1878) published his studies in noise produced from airflow through wires, and this field, aeroacoustics, received later a formal theoretical formulation by Lighthill (1952). The moving source modeling used in this work was established by Morse & Ingard (1968) in the last century, but Doppler effect from moving sources was first described theoretically in 1842 by Johan Christian Andreas Doppler.

The acoustic source localization can be obtained using several methods. To list a few: sound intensity; directional microphone assessment; acoustic holography; beamforming based on conventional approach; and more recently, beamforming based on inverse methods.

All of these methods have special characteristics that may be best suited for particular problems. For example, the use of directional microphones can be advantageous if a rough localization with a low cost measurement solution is required. Another example, for near-field stationary radiation, the acoustic holography may be the most accurate choice. But for general purposes, with the use of an array of microphones and short time of acquisition, conventional beamforming is the preferred solution for source localization.

Beamforming methods are of intense research, and recently, inverse methods are proving their space in this field. The inverse methods start with the definition of a target grid that corresponds to the locations where the sources are to be searched. A model for the transfer function between the target grid and the measurement grid is then defined and the source/transfer/receiver system is solved by least squares on the overdetermined case (when the number of candidate points in the target is smaller than the number of microphones), or least squares and minimum norm for the underdetermined case.

This methodology provides a versatile problem representation and complex source distributions can be analyzed, such as multipole source types, common to aeroacoustic problems. Another important characteristic on this method is better resolution in lower frequency of analysis when compared to conventional beamforming, a big advantage to be explored in pass-by noise identification.

2.1 Thesis Objectives and Scope

The primary objective on this research is to develop an identification method that can be used in problems of aeroacoustic sources generation and provide better understanding to these source generation mechanisms. Two main types of source generation mechanism can be distinguished: the sound generation by pure flow turbulence, for example, found in jet mixing layer; and the second type, the sound produced by the turbulence caused by obstacles in flow. The scope of this research is restricted to the verification of the method when applied to aeroacoustic sources generated by subsonic flow over compact obstacles. On this kind of problem, the radiation can be considered under certain conditions, stationary, a simpler condition for source identification, and also considering that the sound generation and radiation efficiency is higher on this type of problem, making it a first choice for identification validation.

A second objective on this Thesis is to develop an identification method for problems of moving sources. The chosen applications are the source localization in a passenger vehicle and in a truck pass-by noise regulation procedure. This problem of moving source, in principle, is very similar in terms of modeling to source under convective condition, with a change on the observed source position with respect to the true source location, but main challenges are that they have not stationary radiation and that Doppler effect changes the observed frequency.

The investigation on this Thesis aim to improve the current available methodology and raise the main potential advantages on the use of inverse beamforming identification method as well as to raise the possible drawbacks on these two applications, aeroacoustic sources and moving sources.

2.2 Thesis Overview

First, the relevant literature used in this work is presented in Chapter 3. Identification methods used for both aeroacoustic problems and moving sources are compared and evaluated in terms

of accuracy and versatility to address multipole sources for example. The beamforming based on inverse method is selected and main characteristics are raised to be evaluated along the performance verifications with the chosen applications.

The generalized inverse beamforming (GIB) method and its variants are implemented in Chapter 4, and comparison based in numerical cases from the literature is made to the state-of-the-art methods, such as CLEAN-SC and DAMAS2, as long as to the conventional beamforming (CB) method. The optimized regularization strategy, a proposed automated process to chose the regularization factor, is introduced and results presented based in numerical studies.

The inverse method is verified in experimental test cases using compact sources in a semi-anechoic room at the facilities of the Katholieke Universiteit of Leuven (Belgium), shown in Chapter 5. Even though simple cases, they already raise the main aspects of the method, such as a better dynamic range, and capacity to distinguish close sources in coherent radiation, when compared to the conventional beamforming. On this Chapter, the strength estimation based in the Cross-Spectral-Matrix (CSM) eigenvalue is contrasted to a direct calculation, trying to illustrate its nature of overall coherent source strength representation. Another development in this Chapter is the Hybrid Methodology, which combines the robust directional strength estimation from the conventional beamforming to the generalized inverse beamforming mapping, improving its strength estimation, sometimes deteriorated by the inverse least squares and minimum norm resolution of the proposed system. Another important characteristic raised in this Chapter for the GIB method, is the capacity of localization at lower frequencies when compared to the conventional beamforming, and this is also explored later in the moving source Chapters.

The sixth Chapter present the aeroacoustic source identification for a subsonic jet flow over a circular cylinder section measured in a semi-anechoic room. The convection and refraction modeling is applied to locate the dipole formation cross to the flow direction on the impinging cylinder surface. Two approaches are presented, first the identification performed in single events of peak radiation, trying to understand its mechanisms of generation. The second approach is the common identification with a longer time averaging, which brings in one single mapping, the representation of the radiation which would correspond to the main regions of source generation. The regions detected by these two approaches leaves an important discussion about the nature of the source generation and location.

The seventh Chapter present the aeroacoustic source identification for two structures in subsonic airflow measured in an open wind tunnel from the National Aerospace Laboratory from

The Netherlands (NLR). The structures represent a landing gear structure in landing or take-off condition, where its noise is one of the major contributors to the fly-over testings. Monopole identifications from NLR are compared to generated conventional beamforming results as well as to inverse method results. Dipole identifications are performed using inverse method and directional assessment is made and compared to far-field microphone levels. Hybrid Generalized Inverse Mapping is developed and presented for the monopole and dipole identification, an important artifice to improve mapping resolution on inverse identification.

On Chapter 8, the identification of the generated noise from an standard airfoil, NACA-0012, is presented and compared with the literature data. This measurement was performed at the closed wind tunnel from the School of Engineering from São Carlos (EESC) from the State University of São Paulo (USP). Results for the generalized inverse beamforming are confronted to the conventional beamforming as well as to the state-of-the-art method, DAMAS2. This identification condition, closed wind tunnel, is a challenging condition for any localization method, and, in special, for inverse methods, as it is discussed along the results section.

Chapter 9 present the first moving source application, along with the modeling adopted. An experimental test is conducted for a pass-by noise source localization problem with support of LMS International Engineering at the Headquarter in Leuven (Belgium). Validation tests are conducted with a known source placed in top of the vehicle. After verification of the method to identification of the known source, the vehicle noise sources are investigated. The results points to the potential of the method to address the localization with a better dynamic range when compared to conventional beamforming, also covering lower frequencies, even in the presence of reflections on the ground.

The last application, presented in Chapter 10, is a truck pass-by noise identification, exploring the lower frequency of analysis using an special array design presented in this work. Two artifices are presented for this testing, the adoption of an image source to account for the sound reflections on the ground, and a focus compensation for low frequencies, where the source wave radiation is expected to be an intermediate condition between the plane radiation and the perfect sphere radiation. Hybrid generalized inverse mappings are used to present source contribution level to the pass-by noise microphone reading. Although it has the inherent beamforming characteristic of overestimating distributed source level, it present a direct estimate of the source contribution to pass-by level.

These mentioned tests are far from exhausting the discussion of the generalized inverse method performance for aeroacoustic source and moving source identification. However they raise

the main new possibilities of analysis and fronts of research while demonstrating its developed improvements in accuracy and versatility when compared to traditional methods as conventional beamforming. These main contributions are listed in Chapter 11 for aeroacoustic and moving source problems, with a detailed description of observed advantages and disadvantages on this methodology.

3 Literature Review

Source localization and characterization is an important research area in acoustics, and different techniques have been developed to deal with every type of problem. In this Thesis, two problem types are of consideration, aeroacoustic source and moving source identification. In this Chapter, the literature review on these two problem types are discussed, bringing to attention the main characteristics of the already available methods in the literature to address these problems. After this discussion, the rational behind the choice of the method to be developed and applied to aeroacoustic and moving source problems is presented.

3.1 Introduction

First, an overview of the methods more suited to aeroacoustic problems is presented, than an overview of the methods used on moving source problems is presented. The focus on this literature review is on the search of available methods for experimental identification, and brings, in the end, the rational for the choice of research.

This research leaded to six international conference papers, and two journal articles (one published and one under revision). Text and results are extracted from these works, that are cited along the text and listed in the Bibliography.

3.2 Aeroacoustic Source Identification Techniques

Aeroacoustic phenomena can be defined in few words as the sound generation by fluid turbulence. Aeroacoustic problem modeling is an important area of acoustics, initiated by Lighthill (1952) (theoretical foundation), where the acoustic analogy derived from the Navier-Stokes equations for a compressible viscous fluid was first time presented, resulting in an inhomogeneous wave equation, also investigated later in (LIGHTHILL, 1954). The Lighthill Turbulence Stress Tensor contains on its formulation all the possible analytical sources of sound generation respecting Navier-Stokes conservative fluid equations, and there are still recent efforts to understand the aeroacoustic source complexity behind this analogy.

Several other analogies are built for specific cases, for example, moving surfaces. In this

case, the most used aeroacoustic analogy is presented by Ffowcs-Williams (1963), known as FW-H equation, and also referred to in (FFOWCS-WILLIAMS & HAWKINGS, 1969). For the case of solid boundaries, Curle (1955) presented an acoustic analogy which contains the quadrupoles over the fluid volume and the surface distributed dipoles, caused by the interaction of quadrupoles with the solid boundaries.

Two main efforts in aeroacoustic research field could be observed since the analogy from Lighthill was proposed in 1952, one is to confirm the validity of this analogy and the derived ones through experimental assessment, and the second is to resolve the problems numerically, with the Computational Aeroacoustic Analysis (CAA).

Several types of problems have been investigated in the literature, from simple cylinders in moving mediums, with flow over cavities or backward facing steps, to more complex problems, as centrifugal fans, airfoils, wing-slat noise, landing gears, jet engines, etc.

The jet noise problem has been intensely investigated by aeroacoustic researchers since it presents the fundamental flow noise generation mechanism, pure vortex shedding interaction in the mixing layer, as one of the major contributors to the sound radiation. The acoustic sources generated by flow turbulence have been investigated numerically through the application of aeroacoustic analogies directly on the data obtained on the fluid field by simulation with good agreements to the far-field sound measurements.

Detailed models, as vortex pairing models, are used to generate individual sound radiation patterns for closer investigations of source progression characteristics. Those approaches have the advantage to present the internal fundamental source formation and their directivities, but on the other hand, they have complex experimental verification procedures, as developed so far (ELDREDGE, 2007), using for example, Particle Laser Velocimetry (SCHRAM, 2003).

In order to improve experimental verification in aeroacoustic problems, several studies have been carried out with jets to better understand the aeroacoustic sources generation mechanisms, trying to detail as much as possible the strength along axis, directivity pattern, degree of stationarity, etc.

One of the simpler approaches, yet rather accurate, is the polar array technique (TAM, 2007; PAPAMOSCHOU, 2008). This method can be used to reconstruct the strength along jet axis and its directivity, taking into account the convective effects. However, this method is not normally used to

identify if sources are of monopole, or multipole character, and then, more sophisticated methods are required for this purpose.

One of the initial candidate methods is the far-field conventional beamforming technique and derived algorithms, but the source models used initially are mostly based on monopole sources, and the interpretation is limited.

In the work by Jordan & Fitzpatrick (2002), is presented a derivation of the beamforming technique with a signal correction procedure that discriminates different source types, and a source filter process is presented, which detects monopole and dipole in a simplified example.

For more complex source models, near-field array methods developed based on eigenvalue decomposition and regularization techniques were also candidates for aeroacoustic identification (WANG & KAVEH, 1985; YANG, 1994; VISSER, 2004), initiating a series of source model proposals that ultimately allowed the identification of source type, and radiation modes in jet and wind-slat problems.

Recently, the aeroacoustic sources identification efforts have been applied to sound radiation pattern with axisymmetric distribution along the jet axis, normally in low Mach condition. These efforts were initially restricted to study the sound radiation related to large toroidal (axisymmetrical) turbulence structures interaction and therefore restricted to sound emission in peak Strouhal numbers (low frequency). The wave instabilities in these cases are assumed as stationary emissions, and standard approaches for source identification are used to characterize the radiation pattern and source center in respect to jet location and axis, for example, beamforming, near-field acoustical holography, cross-correlation methods, etc.

In the work by Suzuki (2006), a Robust Adaptive Beam-forming Algorithm is derived and applied to a jet problem with low Mach and using a conical microphone array. The method also allows the identification of the zenithal and azimuthal modes in jet problems, and respective source center. The jet problem example used a conical array axisymmetrically distributed around the jet. The example presented results for directivity pattern identification, and this is able by the use of a conical microphone array distributed along the zenithal angle.

The Generalized Inverse Beamforming method, proposed by Suzuki (2008), is applied to a jet-flap interaction problem using a spiral microphone array. The proposed method, in principle, presents the advantage to identify coherent or incoherent, distributed or compact, monopole or

multipole sources. An interesting comparison is done between the proposed method and other state-of-the-art beamforming methods: Conventional Beamforming; Adaptive Beamforming; CLEAN and CLEAN-SC; and DAMAS2. The comparisons done using simple model problems can be used as reference for validation of implementation of the method in source identification.

Acoustic holography is an interesting methodology for source characterization based on inverse problem, recent advances on this approach can be seen in (MARTIN *et al.*, 2011), where a genetic algorithm is also used as an alternative to the resolution of the problem.

Another interesting approach, now for aeroacoustic problems using near-field acoustical holography, is explored by Lee *et al.* (2003); Lee & Bolton (2006, 2007), where a set of reference microphones out-of-flow allows the use of an in-flow circular scanning array for cylindrical radiation assessment along jet axis. This method, shown in depth in (LEE & BOLTON, 2007), has the advantage to present the measured field and extrapolate it in 3D views, with in depth characterization of zenithal and azimuthal modes along the axis. The disadvantage is that in-flow measurements could influence the radiation pattern under investigation. The method permits the far field projection using cylindrical radiation analytical solution. The example problem is a 0.26 Mach jet with 8mm burner, and the measurement used 6x8 reference microphones and a 16 microphones circular array with 0.30m diameter. The paper also presented the relative sound power contribution for monopole, dipole, quadrupole and octopole source types for the shown jet problem example.

Reba *et al.* (2008), used a rotating near-field microphone array, scanning a conical surface surrounding the jet plume, just outside the turbulent shear layer, and a fixed reference array. The near-field pressure statistics were represented by a Gaussian wave-packet model. This modeling allow the reconstruction of far field sound pressure using a Green's function based method and comparisons are shown in the paper with actual far-field measurements, showing some discrepancies only for low and near perpendicular zenithal angles. The jet speed used was 1.5 Mach, and the directivity plots are analyzed against each azimuthal mode. Temperature influence in source location is investigated, showing that with increase in temperature, the peak amplitude moves upstream.

One interesting approach found in recent literature is presented by Kopiev *et al.* (2008), where three circular arrays (6 microphones each) scanning structure (2 arrays in plane and one offsetted) is used to measure the directivity of radiation in a frequency band of 600-2100Hz for jet Mach 0.3 and 0.6. Cross-correlations are used and the Azimuthal Decomposition Technique (ADT) applied on time domain signals in order to reconstruct the azimuthal components. Technical difficulties

were outlined by the author for the ADT implementation using a commercial acquisition system. The azimuthal modes directivity is shown and source location estimated as 5 diameters from jet outlet. Unfortunately, no comparison is done with far field measurements to validate results.

Conventional beamforming is the current primary tool for noise source localization in several fields of engineering. Its principle, sum & delay (DAS), is of easy understanding, and is a natural basis for other techniques development. Conventional beamforming techniques have been widely used in wind tunnel experiments (MUELLER, 2002). However, the sound generated by flow turbulence can present distributed coherent and incoherent source regions, which presents some challenges to the conventional beamforming localization accuracy.

Methods such as CLEAN (HOGBOM, 1974) and DAMAS (BROOKS & HUMPHEREYS, 2006) have been proposed to improve localization accuracy. The CLEAN method proved to be a valuable tool, but as the conventional beamforming, it can be sensitive to coherent distributions. Sijtsma (2007) revised CLEAN to consider spatial coherence function in the CLEAN procedure, leading to CLEAN-SC, increasing its versatility and improving detection of coherent source regions. This method is described in the appendix section.

In DAMAS method, the uncorrelated source distribution is extracted by deconvolution of the generated mapping from conventional beamforming with the point spread function, for example, which represent a monopole source at the target grid. This technique has a substantial computational cost, even though it has improved in the past years. DAMAS procedure was revised by Dougherty (2005), where the deconvolution procedure is simplified to a spatial frequency domain product, and a substantial decrease in computational cost obtained, leading to DAMAS2 and DAMAS3 methods. DAMAS2 algorithm is described in the appendix section for reference.

DAMAS is again revised in (BROOKS & HUMPHEREYS, 2006) to include spatial source coherence, leading to DAMAS-C. Both methods, CLEAN and DAMAS2 are widely used on the field to characterize aeroacoustic sources, however these methods are normally based on monopole type of radiation, restricting the analysis in terms of multipole identification.

Apart from the noise generated by jet, the study of sound generated by air flow through obstacles has also received attention since the establishment of the acoustics fundamentals, and it is first subject of scientific scrutiny on the work performed by Strouhal (1878), where tonal noise was observed in some particular flow conditions over slender objects. This phenomenon was called Aeolian tones and is still object of investigation by important research centers, for

example, as illustrated by King & Pfizenmaier (2009) on his work, where several obstacle profiles are subjected to flow speeds on the range of Mach 0.1 to 0.2. Evaluations of Strouhal frequencies and sound-pressure levels relationships are obtained and commented for different diameters and length characteristics.

Several efforts have been made also on the prediction of sound generation on these problems, for example, Takaishi *et al.* (2007), presented the source regions based on vortex sound theory close to the flow separation regions. On this work, the acoustic mappings and directivity plots indicate a dipole radiation transversal to the flow for low frequencies, and aligned to the flow for higher frequencies. Another interesting work is presented by Martinez-Lera *et al.* (2007) using Curle's Analogy (CURLE, 1955), where again, the dipole like radiation pattern is obtained cross to the flow direction. Similar results are also obtained by numerical analysis by Guasch & Codina (2007); Seo & Moon (2007), and Müller (2008), obtaining by different methods the dipole like directivity, cross to the flow, for lower frequencies.

In order to verify the numerical results, more complex identifications are required, which could for example, assess the dipole radiation pattern in flow through compact obstacles. On these cases, the dipole radiation is more significative than the other multipole sources created by the flow turbulence, and identification methods could in principle be focused primary on the dipole radiation.

In aircraft design, the landing gear is one of the major contributors to the noise in landing and take-off. This is investigated by conventional beamforming in (SIJTSMA & STOKER, 2004), where a A-340 is assessed. Figure 3.1 shows the mapping result for one of the analyzes. The landing gear aeroacoustic problem can be simplified by substituting it by two regular profile structures. This is investigated in detail later in this thesis.

Among the recent research methods, one in particular promises the advantage to identify sources that could be of compact or distributed nature, in coherent or incoherent radiation, with monopole or multipole source patterns, as already mentioned, the Generalized Inverse Beamforming (GIB) (SUZUKI, 2008). Recently, this method integrated the Iteratively Re-Weighting Least Squares Scheme in (SUZUKI, 2010), and the 2008 results are revised in (SUZUKI, 2011).

The rational for choosing this method, with the aim of application to an aeroacoustic problem: sound generation by subsonic flow over a compact obstacle, is that it can deal with dipole identification with a substantial dynamic range improvement compared to the conventional

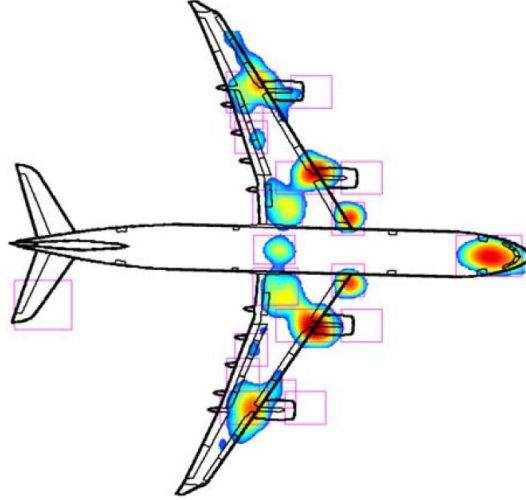


Figure 3.1: Acoustic image of A340 at 2kHz with conventional beamforming from (SIJTSMA & STOKER, 2004).

beamforming. This problem is chosen since it presents easier detection conditions when compared to the pure jet noise, such as: a more intense radiation from sources (dipole compared to quadrupole radiation efficiencies); stationary source center regions with respect to the obstacle surfaces in contrast to moving sources in jet noise; and source distributions related to obstacles geometry than related to complex flow mixing layer turbulence properties. This type of problem is a first choice for verification, but the method, in principle, could be later used to more complex problems as well.

The method proposed by Suzuki is based on the microphone array cross-spectral matrix (CSM) eigen-structure, and the response is represented by eigenmodes, each one related to an orthogonal source distribution. This source distribution is calculated by the inversion of the transfer function matrix, built based on a candidate source type. In the case that this transfer function matrix is ill-conditioned, regularization techniques, such as Tikhonov's regularization, can be used. An automated process for the definition of the regularization factor is proposed in Zavala *et al.* (2011d) and adopted in this work.

3.3 Moving Source Identification Techniques

Once the method of source localization is developed to problems with convection effects in the propagated wave, it can be easily applied to problems of moving sources with few modifications. This initiated a second activity on this research that is to develop and investigate the generalized

inverse beamforming method on the localization of moving sources. The chosen problem is the vehicle pass-by noise.

Pass-by noise testing is one of the most important requirements on vehicle development, and one that is subject of government regulation. Fully understand on the vehicle performance on this testing demands a lot of effort in terms of measurements, and when improvement is required, other techniques are used to locate the proper system that dominates the pass-by noise level. One of these techniques is the Transfer Path Analysis (TPA) (JANSSENS *et al.*, 2011), which is able to rank the main system contributions in the vehicle emitted noise.

Another approach in understanding system contributions in the pass-by level is to use numerical transfer paths and synthesize the noise at the regulation microphone position. An example of numerical determination of the radiation path is found in (ZAVALA & PAVANELLO, 1998), using finite element method.

The most common approach to localization of sources is the use of array techniques such as beamforming, and it offers some advantages on source localization and quantification, for example, the simultaneous acquisition during passages allows the detailed analysis in a post-processing phase, and indications on the region that is generating the noise can be done in short period.

General studies using conventional beamforming (CB) on the localization of moving sources are performed by Cigada *et al.* (2007) and Castellini & Sassaroli (2010), this later in reverberant environment, but the Delay-And-Sum (DAS) application on moving sources can be better illustrated in the work by Cigada *et al.* (2007), where a line of microphones is used to locate a loudspeaker placed on a vehicle. The CB application to pass-by noise problems can also be observed in the work by Gerges *et al.* (2009), where a vehicle was used to exemplify the localization performance for several processing techniques, such as CB, DAMAS2 and TIDY, for a known vehicle source.

A complete study on the use of conventional beamforming in truck pass-by noise source mapping is done by the Transportation Research Board (US) and reported in (GUROVICH *et al.*, 2009). In this extensive report, the array development is presented in detail, but fails to prioritize the detection on the horizontal direction. Image source created by the reflections on the ground are discussed, and full truck testings are presented, but with the limitation of poor resolution in low frequency.

The use of the generalized inverse method to moving sources is a new application of the

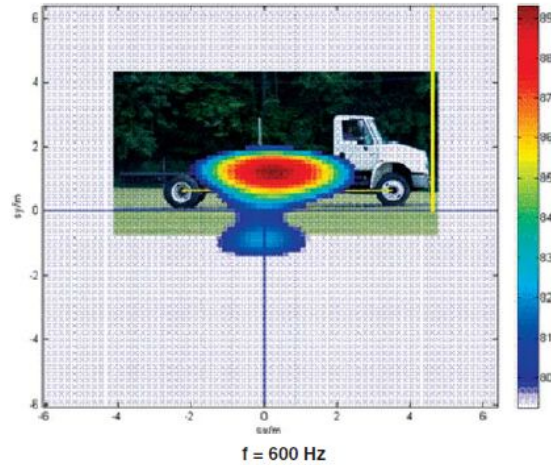


Figure 3.2: Example of truck testing with conventional beamforming and a spherical source from (GUROVICH *et al.*, 2009).

method in the literature, and face the challenge to perform identifications considering the non-stationarity of the simultaneously recorded signals, the presence of Doppler effect on these recorded signals, and also the application of identifications in fast transient problems, such as the vehicle accelerating conditions in pass-by noise testing. These and other challenges are to be investigated throughout this work in the moving sources chapter.

3.4 Summary

Aeroacoustic identification is one of the most challenging scenarios for source localization, and the literature is still lacking of research on general methods capable to deal with fast sound emission events, with coherent and incoherent source regions, and complex transfer paths with convection and refraction. This work is certainly an important step with this objective, to develop standard problems that can be repeated in laboratory and also by simulations, and better understand the aeroacoustic sources generation, remembering that the proposed identification methodology can be easily applied to simulation results.

In moving sources, the available literature is short in detailed identification performance evaluation, for example, in dealing with low frequency content, and in overcoming the difficulties brought by the presence of reflections, as in the case of pass-by noise testing. These two obstacles can be of major importance in the adoption of inverse methods on this type of scenario.

The simplifications required by the application of localization techniques that are developed, in principle, to stationary problems are introduced and discussed. De-Dopplerization of the signals, spectrum and mapping averaging, also related to the block size or frequency resolution, poses an important aspect on the localization, normally not discussed in detail in the available literature for moving sources, but discussed here throughout the moving source Chapters.

4 Generalized Inverse Beamforming Methods

In this Chapter, the generalized inverse beamforming method (GIB) with the original algorithm proposal is presented along with a simplified version. Also, more recent developments for the GIB are described: Iteratively Re-Weighted Least Squares (IRLS) scheme; Generalized Weighted Inverse Beamforming (GWIB); and Improved Generalized Inverse Beamforming (GINV). Literature model problems are used to illustrate the GIB method's performance compared to conventional beamforming (CB) and to state-of-the-art beamforming methods: CLEAN; and DAMAS2. In the end, the computational effort for each of the methods are compared using as basis, the fast conventional beamforming method.

4.1 Introduction

The generalized inverse beamforming method is first introduced by Suzuki (2008), with the advantage of resolving coherent or incoherent, distributed or compact, mono or multipole sources. This potentially versatile and broad method, GIB, in principle, uses the same array information as used on conventional beamforming but also can provide a better source localization dynamic range when compared to CB. These characteristics represent a real improvement in comparison to methods based on the conventional approach, which suffer of resolution on distributed coherent source cases.

The generalized inverse method can be described in few words as a least squares problem with objective to find a source distribution that fits the array response. This source distribution is refined by truncations of the least significative source positions until a pre-condition is reached, for example, the problem cost function is minimized or the source region minimum size is reached. The original generalized inverse beamforming algorithm is presented in section 2 and a simplified version is also shown. Results for this simplified algorithm are obtained for the model problems originally presented by Suzuki in 2008 and compared to conventional beamforming (PILLAI, 1989), as well as, to CLEAN-SC (SIJTMA, 2007) and DAMAS2 (DOUGHERTY, 2005).

The definition of the Tikhonov regularization factor is a key step in the algorithm performance, and an automated strategy, the optimized regularization strategy is proposed in section 3. This strategy is based on the search of the regularization that minimizes the residue at each

algorithm iteration. This strategy also provides the identification of the optimum strength estimation along the iterations (ZAVALA *et al.*, 2011D). Results obtained with fixed regularization and the optimized for the literature model problems are used to demonstrate the versatility in this approach.

Weighted least squares schemes can improve significantly the dynamic range in localization and some methods are described in section 4, the Iteratively Re-Weighted Least Squares, Suzuki (2010), and the Generalized Weighted Inverse Beamforming, by Presezniak (2011). These methods are presented along with results for the model problems used by Suzuki (2008). Another recent development is the Improved Generalized Inverse Beamforming, proposed by Dougherty (2011), with the objective of developing a better estimation when the sparsity of the cross-spectral matrix is no longer a valid assumption. This formulation, shown in section 5, also provides a powerful link between the conventional beamforming and the generalized inverse method. Model problems are also used to illustrate the GINV performance compared to the original GIB.

At the end of this Chapter, in section 6, the computational effort for each of the methods in discussion is compared to the conventional method, which is still considered as one of the fastest available methods of localization based on array information. Computational efforts for pre, post and processing phases are presented and the impact on increased processing time for the GIB methods is discussed in comparison to the methods based on the conventional beamforming approach.

In the summary section, the main advantages and disadvantages of the generalized inverse methods compared to the conventional beamforming, as well as to the state-of-the-art methods are outlined and discussed based on the presented results.

4.2 Generalized Inverse Beamforming Original Method

Following the work from Suzuki (2008), each microphone simultaneous signal, considered in blocks with N_s samples, can be used to generate their spectrum, q_{spec_j} , with N_p points each, and

be arranged in matrix form, q , as:

$$q = \begin{bmatrix} q_{spec1} \\ q_{spec2} \\ \vdots \\ q_{specN_{mic}} \end{bmatrix}, \quad (4.1)$$

where N_{mic} is the number of microphones, leading to a matrix of $N_{mic} \times N_p$.

The averaged Cross-Spectral Matrix (CSM) can be generated by the averaging of the product of the spectra matrix:

$$R_{CSM} = \overline{(qq^\dagger)}, \quad (4.2)$$

where † is the complex conjugate transpose; the bar over the product denotes average estimate; and the size of R_{CSM} is $N_{mic} \times N_{mic}$.

Each term of the CSM have the information of phase and amplitude relationship between microphones averaged throughout several spectrums. This matrix averaging retains the stationary characteristics between microphones, increasing the signal-to-noise ratio on the subsequent estimation. Another advantage on the use of CSM is its compactness for data storage and processing, requiring only $N_{mic} \times N_{mic}$ data space for the full test period. The CSM can be built for the full spectrum products, just band wise, or even per frequency line. The strategy depend on the type of sources in analysis, tonal or random, for example, and the power assessment of interest, for example, a power density (per Hz), source power per band, or overall source power level. Throughout the text, the most common assessment is the third octave band analysis, as standard in aeroacoustic measurements and also in automotive applications.

The conventional beamforming uses the CSM to obtain the source mapping by applying the

steering vector or just weighting vector, w (PILLAI, 1989), with the phase delays:

$$P_{cb} = w^\dagger R_{CSM} w, \quad (4.3)$$

where w can be defined as:

$$w = \frac{C}{\|C\|}, \quad (4.4)$$

where C is the propagation vector from each microphone to the target grid point at (x, y) ; and $\|\cdot\|$ denotes the Euclidean norm.

This form of the conventional beamforming is also known as Sum-And-Delay (DAS) procedure (PILLAI, 1989), and is represented schematically in Figure 4.1.

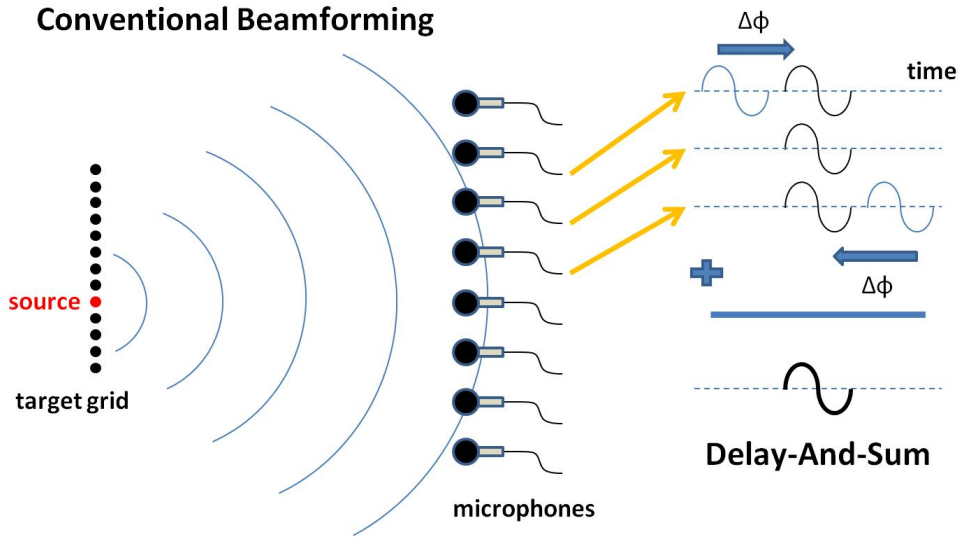


Figure 4.1: Conventional beamforming based on Delay-And-Sum.

This procedure corresponds in obtaining the average signal power from all microphones in the array. Another variant of the conventional beamforming is the focus beamforming, where the signals are projected towards the source position and then averaged. In this case, the steering vector

is calculated as:

$$w = \frac{1}{C}, \quad (4.5)$$

The generalized inverse beamforming method starts from the Cross-Spectral Matrix, but instead of applying weighting vectors to this matrix, as used on the conventional beamforming technique, the method decomposes this matrix in eigenvectors and eigenvalues:

$$R_{CSM} = U\Lambda U^\dagger, \quad (4.6)$$

where U is the eigenvector matrix, Λ is the diagonal matrix containing the eigenvalues.

The use of methods based on the array cross-spectral eigenvectors and eigenvalues is considered a robust method for source localization (SCHMIDT, 1986; MUELLER, 2002). Each eigenvalue represents the overall strength related to a coherent source distribution and the eigenvectors are associated to the sensors phase responses to these coherent source distributions.

After retrieving the number of eigenvalues and eigenvectors that represents the relevant source distributions, the i^{th} ‘eigenmode’ is defined as:

$$v_i = \sqrt{\lambda_i} u_i, \quad (4.7)$$

where v_i is the eigenmode, λ_i and u_i are the corresponding eigenvalue and eigenvector.

The noise source localization problem can be formulated as finding the source vector, a_i , that

solves the following source/transfer-path/receiver equation:

$$Aa_i = v_i, \quad (4.8)$$

where A is the transfer matrix, containing the radiation patterns from each target grid point to every sensor position, with size $N_{mic} \times N_{grid}$, and the latter, the number of grid points on the target region.

The A_{jk} can be calculated as follows for a monopole source candidate at (x, y) target grid point k and response at sensor j .

$$A_{jk} = \frac{\rho c k}{4\pi r_{jk}} e^{-ikr_{jk}}, \quad (4.9)$$

where ρ is the air density; c is the speed of sound; k is the circular wavenumber; and r_{jk} is the distance between the grid point k and the sensor j .

For a dipole source the simplified transfer matrix can be calculated according to Suzuki (2008):

$$A_{jk} = \frac{\rho c c_{dip}}{4\pi r_{jk}} \frac{\vec{r}_{jk} \cdot \vec{v}}{r_{jk}^2} (-1 + ikr_{jk}) e^{-ikr_{jk}}, \quad (4.10)$$

where c_{dip} is a constant suggested by Suzuki to normalize the strength of the source types; \vec{r}_{jk} is the vector from sensor j to grid point k ; and \vec{v} is the unitary vector with dipole orientation.

The introduced constant is calculated as $c_{dip} = \sqrt{|r_{M.C.}|/(kr_{aper})}$, where the distance from the origin to the microphone centroid is $|r_{M.C.}| = 10$, in number of wavelengths, and r_{aper} is the array aperture. According to Suzuki, this constant is introduced to overcome the ‘radiation efficiency’ differences between monopoles and dipoles, that would affect the ordering of the source vector terms, and the eigenvectors structure too.

On the case of dipoles oriented in the plane parallel to the array plane, the transfer matrix contains transfer functions for dipole components in the orthogonal directions, parallel to array, and which overall peak surface velocity would be the result of the Euclidean norm of the components. In principle, the transfer matrix could contain as many reference source solutions, and their components, as required to be solved simultaneously.

In order to calculate the source vector, a_i , the generalized inverse, or pseudo-inverse, equations are used. When a larger number of target grid points and source reference solutions than sensors are used, an underdetermined system is obtained and the following equation is used (SUZUKI, 2008):

$$a_i \approx A^\dagger (AA^\dagger)^{-1} v_i . \quad (4.11)$$

In the case of an overdetermined system, the following equation is used:

$$a_i \approx (A^\dagger A)^{-1} A^\dagger v_i . \quad (4.12)$$

Since the matrix AA^\dagger is generally ill-conditioned, a Tikhonov regularization is used (SUZUKI, 2008) to solve equation (4.11) or (4.12). This adds an artificial diagonal term on the matrix to be inverted and results in the following equations for, respectively, the underdetermined and the overdetermined formulation:

$$a_i \approx A^\dagger (AA^\dagger + \alpha^2 I)^{-1} v_i , \quad (4.13)$$

$$a_i \approx (A^\dagger A + \alpha^2 I)^{-1} A^\dagger v_i , \quad (4.14)$$

where α is the Tikhonov regularization factor, and I is the Identity matrix.

The square of the regularization factor is suggested to be a fraction of the greatest eigenvalue of AA^\dagger or $A^\dagger A$, depending if the system is underdetermined or overdetermined. The regularization improves the condition number on the matrix to be inverted. The condition number is the ratio between the largest and smallest singular value of this matrix and is used to indicate the expected quality on the inversion, for example, close to unity condition numbers, means that accurate inversion results are expected.

Using the generalized inverse techniques, the cost function to be minimized can be written, according to Suzuki, as:

$$J_2 \equiv \frac{1}{2} \|a_i\|^2 + \lambda_{L.M.}^T (v_i - Aa_i). \quad (4.15)$$

where $\|\cdot\|$ denotes the Euclidean norm; and $\lambda_{L.M.}$ is the vector of Lagrange multipliers, or constraint adopted in the search for the solution.

According to Suzuki (2008), the square of the regularization factor could be chosen as a fraction of the greatest eigenvalue of the matrix AA^\dagger or $A^\dagger A$, with suggested range from 0.1% to 5%. The overall source distribution is recovered by summing the source distributions related to each eigenmode. However, the solution brought by equations (4.13) and (4.14) are least squares approximations. The use of a least squares approach to find the source vector is not accurate, since distributed sources have their contributions squared and then summed. To illustrate this characteristic, consider a unitary source retrieved by two grid points, the source vector summation using a ℓ_2 -norm approach is $(1/2)^2 + (1/2)^2 = 1/2$, which results in an incorrect total, while the overall strength of the source vector using a ℓ_1 -norm, $(1/2) + (1/2) = 1$, would be the desired result.

The choice of the source vector norm to be minimized is directly linked to the eigen-decomposition of the CSM and consideration of the eigenmode in the system to be resolved. This means that if a coherent response is to be fitted by an arrangement of sources, these sources are necessarily in coherent radiation, and because of this, the linear superposition of source radiations is the best choice to represent the overall intensity.

It is suggested to redefine the source detection problem as a minimization of the source vector ℓ_1 norm constrained by the minimization of the residue, and represented by the following cost function:

$$J_{1_{orig}} \equiv |a_i| + \lambda_{L.M.}^T (v_i - Aa_i), \quad (4.16)$$

where $|\cdot|$ is the ℓ_1 -norm (for vectors), representing the direct summation of the vector terms module.

Since no direct approach can be adopted to solve this minimization problem in ℓ_1 norm, the proposed method searches the minimum of the $J_{1_{orig}}$ cost function using the least squares equations and iteratively truncating the source vector terms, discarding the least significative terms on each iteration. This process is applied until a predefined criterion is fulfilled, for example, a minimum number of remaining terms on the source vector.

Considering the truncation factor as β , which is the percentage of terms to be kept after truncation. A reduced transfer matrix, with size $N_{mic} \times \beta N_{grid} N_{types}$, is used to recalculate the source vector a'_i using equations 4.13 or 4.14, and an update version of a_i is obtained by linear combination with the obtained a'_i .

$$a_i^{n+1} = \left(1 - \frac{dz}{|dz|}\right) a_i^n + \frac{dz}{|dz|} a'_i, \quad (4.17)$$

where superscript n denotes the iteration counter; dz is a complex coefficient to be determined as to minimize $|a_i^{n+1}|$; and here $|\cdot|$ represent the absolute value of dz .

A Gaussian spatial filter is applied on each iteration result mapping to suppress spurious peaks. The iterations are repeated until a predefined number of grid points in the source vector is reached.

The original algorithm version is summarized as follows:

- 1) Generate the Cross-Spectral Matrix and perform the eigenvalue decomposition;
- 2) Select the number of coherent modes to be processed;
- 3) Generate the corresponding eigenmodes v_i ;
- 4) Define the source types and target domain, calculate the transfer matrix, A ;
- 5) Calculate the initial amplitude distribution, a_i ;
- 6) Reorder and truncate the source vector a_i , and reform a reduced transfer matrix A' ;
- 7) Solve a'_i using equations (4.13) or (4.14);
- 8) Determine dz using for example, Newton-Raphson method, and update a_i ;
- 9) Apply the Gaussian spatial filter for each source map;
- 10) Repeat from 6) to 9) until a predefined number of source terms is reached;
- 11) Generate source maps of all selected eigenmodes and superpose source intensity for each source type.

The Gaussian spatial filter is applied on the mappings with the mere purpose of improving the mapping visualization, since the estimated strength remains unchanged between the mappings.

This algorithm proposed by Suzuki, although complete and stable, can be improved to a faster simplified version without significative changes on results.

4.2.1 Simplified Algorithm

First, as also suggested by Suzuki, the dz factor can be simplified to unity without major problems, and then, the update source vector a_i is simply taken as the result of the least squares equations a'_i . Another simplification, since no combination is done for the new source vector on each iteration, the gaussian spatial filter is applied only on the final mapping, after the last iteration.

With these simplifications, the algorithm becomes:

- 1) Generate the Cross-Spectral Matrix and perform the eigenvalue decomposition;
- 2) Select the number of coherent modes to be processed;
- 3) Generate the corresponding eigenmodes v_i ;
- 4) Define the source types and target domain, calculate the transfer matrix, A ;
- 5) Calculate the source vector, a_i , using the generalized inverse equations (4.13) or (4.14);
- 6) Reorder and truncate the source vector a_i , and reform a reduced transfer matrix A' ;
- 7) Repeat item 5 and 6 until a defined number of source terms is reached;
- 8) Apply the Gaussian spatial filter for each source map.
- 9) Generate source maps of all selected eigenmodes and superpose source intensity for each source type.

In order to verify the implementation of the simplified algorithm, the model problems used by Suzuki in 2008 are used for comparison with the original results.

4.2.2 Literature Model Problems

Suzuki (2008) used 5 problems to illustrate the methods performance in comparison to conventional beamforming, CLEAN-PSF and CLEAN-SC, DAMAS2, and others. CLEAN-SC and DAMAS2 are described in more details on appendix section.

Here, the same problems are used to compare the simplified algorithm results to these mentioned methods. A 60 microphones 6-arm spiral is placed 10 wavelengths from the target region plane. A Target grid is adopted with extension of 6×6 wavelengths, and a grid division of $1/4$ of wavelength is used, leading to 25×25 grid points. The array and spiral distribution are plotted on top of each other in Figure 4.2.

On this problem, velocity and length scales are normalized by speed of sound and wavelength respectively. The wavenumber is set as $k = 2\pi$. Noise is added directly to the Cross-Spectral Matrix, with random complex values corresponding to approximately 50% of the pressure amplitude added to the off-diagonal part of the CSM, and random real values corresponding to 100%, added to the diagonal part.

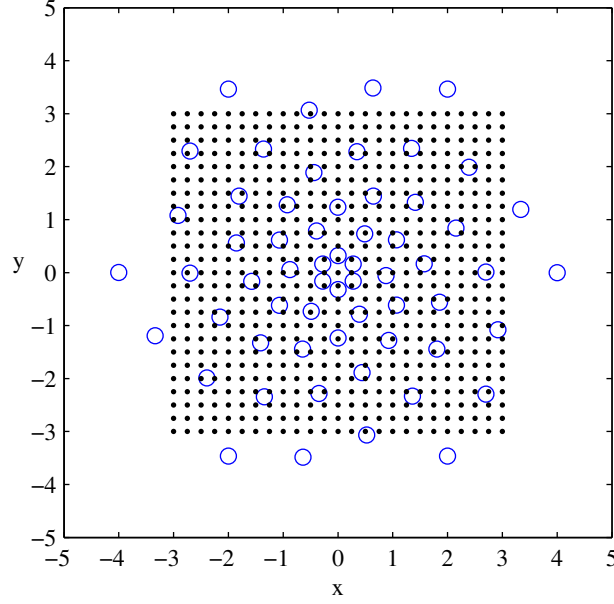


Figure 4.2: Microphone array (blue circles) and target grid positions (black dots).

The generalized inverse algorithm is set with truncation factor β of 90%, and iterations terminated when the number of grid points left in source vector reaches $N_{mic}/2$. The regularization factor adopted in the GIB algorithm is constant throughout the iterations, in the limits suggested in previous section, and defined as to better approximate the obtained results to the ones reported in the literature. The first problem consist of a monopole at the center of the target grid, and its position on top of the target grid is shown in Figure 4.3.

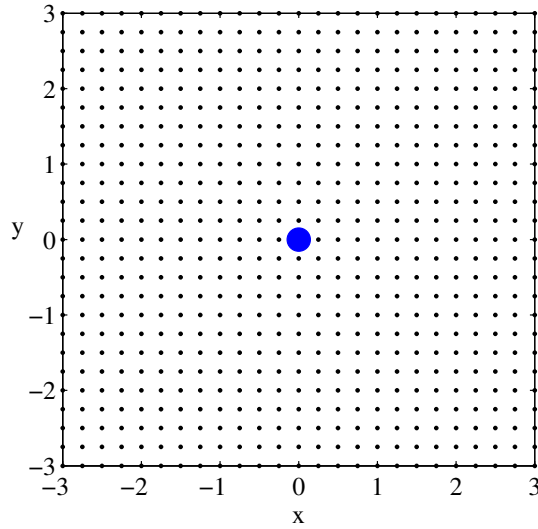


Figure 4.3: Monopole source (blue circle) and target grid (black dots).

Results obtained for conventional beamforming, CLEAN-PDF, DAMAS2 and GIB, are shown in Figure 4.4, where mappings are based on the strength normalized by the maximum mapping value, $Q_N(x, y)$, and shown in dB scale, calculated as $Q_{dB}(x, y) = 20 \text{Log}_{10}(Q_N(x, y))$. CLEAN method presented identical results for CLEAN-PSF and CLEAN-SC, and one iteration was applied, with loop gain factor, $\phi = 1$. In DAMAS2, the cut-off wavenumber is set to be $k_c^2 = (\pi/\delta x \times \pi/\delta y)/(2 \log 2)$, and algorithm stopped after 30 iterations for the single monopole case. DAMAS2 algorithm requires a translational shift invariant Point Spread Function, and the coordinates transformation shown in (DOUGHERTY, 2005) is adopted when the algorithm is applied. This coordinates transformation will be showed in detail and applied to GIB in a latter section. GIB algorithm is stopped after 32 iterations on the single monopole case, and one eigenmode used.

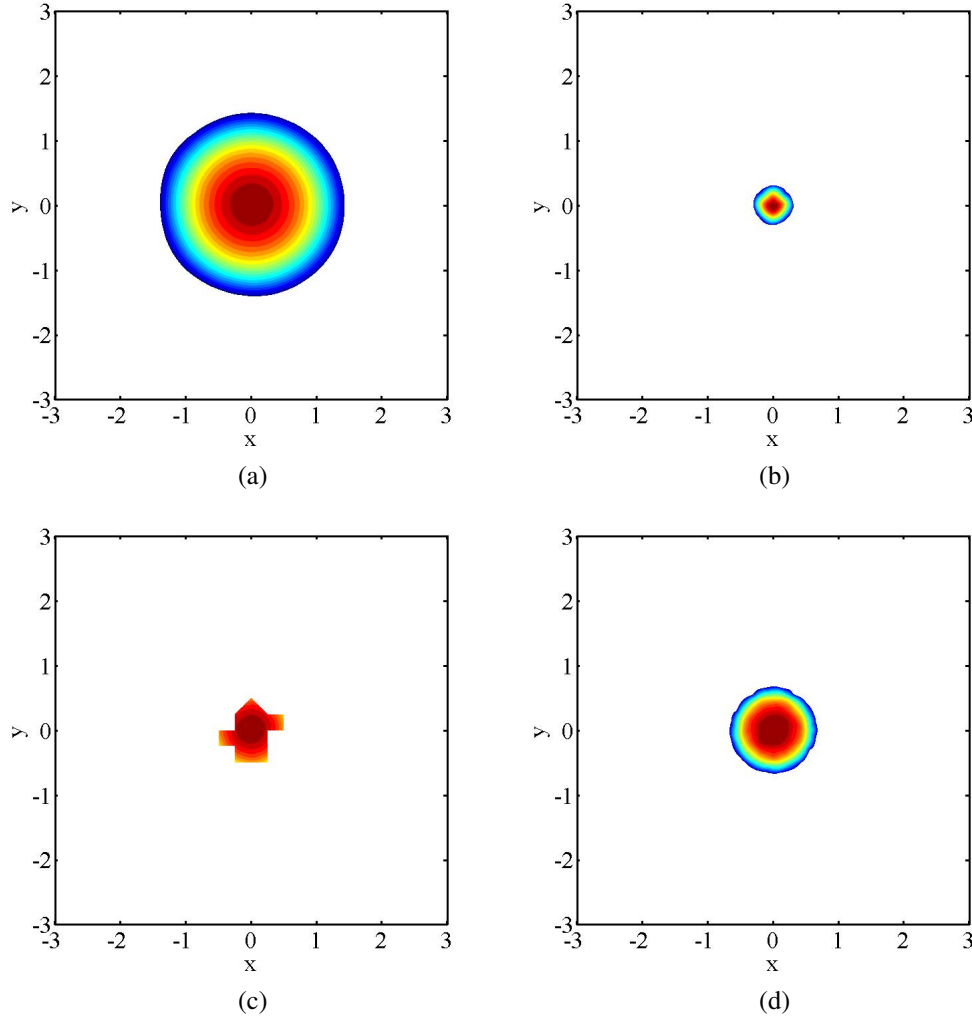


Figure 4.4: Monopole source at target center: (a) CB (b) CLEAN-PSF (c) DAMAS2 (d) GIB. Contour levels with 10dB range and 0.5 increment.

All methods are able to locate the source center, the conventional beamforming presenting the worst dynamic range, about 1.5 wavelength radius for a 10dB range. CLEAN presented the best dynamic range, but in fact, it is artificially adjusted for addition of a peak back on the cleaned mapping. DAMAS2 results is somewhat irregular, and its dynamic range seems to vary a lot between near grid points, indicating maybe the need for a spatial filter to improve and produce a smoother localization. The generalized inverse beamforming presented a dynamic range of about half wavelength radius for 10dB range, which is significantly better than the conventional beamforming. The strengths obtained are shown in Table 4.1:

	CB	CLEAN-PSF	DAMAS2	GIB
Strength estimation	1.00	1.00	1.03	1.00

Table 4.1: Monopole source strength estimation comparison for the monopole at origin case.

All four methods estimated accurate strengths, with only DAMAS2 presenting a small overestimation. Conventional beamforming and CLEAN estimations are obtained at the location with peak strength, and DAMAS2 and GIB are the summed strengths for the grid points in the 10dB range.

Following the model problems, and to investigate the potential to address distributed sources, a line of monopoles is used with 1.5 wavelength, and consisting actually by a sequence of 20 equally spaced monopoles. The source distribution can be observed in Figure 4.5. Results for the chosen methods are observed in Figure 4.6, where CLEAN-SC uses 1 iteration and ϕ factor of 1. DAMAS2 used 30 iterations, and GIB, 32 iterations (one eigenmode).

Comparing the localizations for the line source, the conventional beamforming and CLEAN are not able to clearly identify the distributed sources. CLEAN actually erases all neighboring coherent contributions to the peak so as it fails totally in devising the region of distributed sources. DAMAS2 and GIB are able to locate the source line but GIB presents a clear advantage in fully characterizing the source region from end to end. The strengths estimations are presented in Table 4.2.

Conventional beamforming and CLEAN have the same estimation since CLEAN uses the conventional beamforming as starting point to a cleaner mapping. DAMAS2 and GIB, are closer to

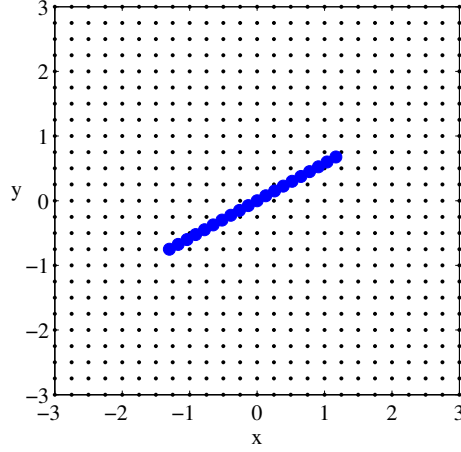


Figure 4.5: Distributed monopole line source (blue circles) and target grid (black dots).

	CB	CLEAN-PSF	DAMAS2	GIB
Strength estimation	0.70	0.70	0.98	0.94

Table 4.2: Distributed monopole line source strength estimation comparison.

the actual unitary strength. The estimation on GIB is sensitive to the regularization factor adopted and here is used one that reproduces approximately the obtained value in the literature. In next section, the regularization influence on estimation and also an optimized procedure is presented in details.

The next model problem is a single dipole with 45° orientation. The source diagram is presented in Figure 4.7. Results obtained for beamforming mappings are shown in Figure 4.8, where conventional beamforming, and GIB used a dipole reference solution and CLEAN and DAMAS2, used monopole reference solution. CLEAN used 6 iterations with ϕ factor equal to 0.5, iterations are stopped when cleaned mapping has higher peak value than previously cleaned mapping. DAMAS2 used 40 iterations and GIB, 42 iterations (one eigenmode).

CLEAN and DAMAS2 method fails to locate the dipole source since they are based on monopole radiation type. Conventional beamforming and GIB are able to locate source center and orientation, but GIB presents a significantly better dynamic range, with no sidelobes as found in the conventional beamforming. The estimation for the peak dipole surface velocity (CB and GIB) and strength (CLEAN and DAMAS2) are shown in Table 4.3.

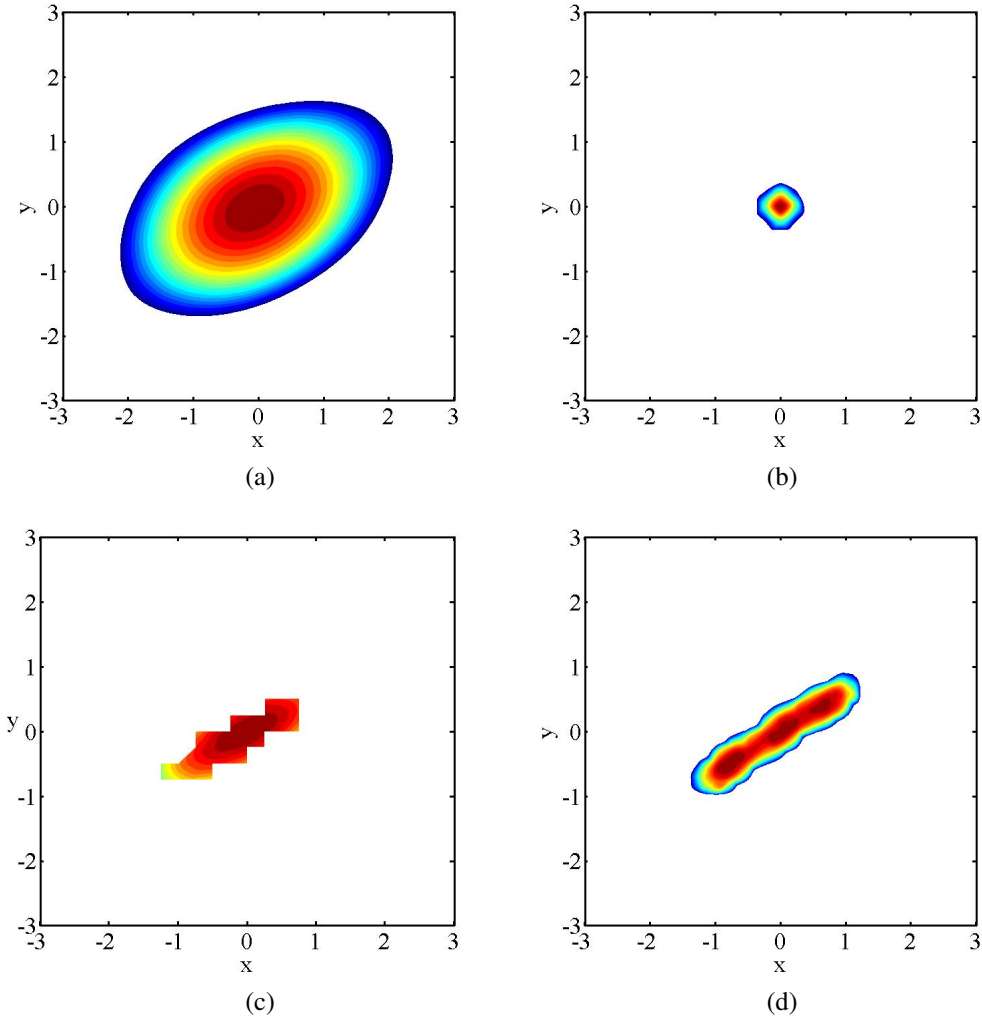


Figure 4.6: Distributed monopole line source: (a) CB (b) CLEAN-SC (c) DAMAS2 (d) GIB. Contour levels with 10dB range and 0.5 increment.

Conventional beamforming, as well as, GIB, are able to estimate the dipole peak velocity, with a small advantage to CB on this case. The GIB estimation reproduces the literature result using a fixed regularization factor.

The last two model problems are based on the same source configuration, one monopole source at coordinates (0,1) and one dipole source at (-1,0), and with 45° orientation. The configuration is shown in Figure 4.9. The first problem consider the monopole and dipole sources in an incoherent radiation, leading to two significant eigenvalues, and then, two eigenmodes are used in the GIB calculations. The GIB algorithm used 42 iterations, the CLEAN-SC is limited to 10 iterations with ϕ factor as 0.5, and DAMAS2 used 40 iterations. The results for the conventional beamforming, using monopole and dipole reference solution, CLEAN-SC and DAMAS2 using

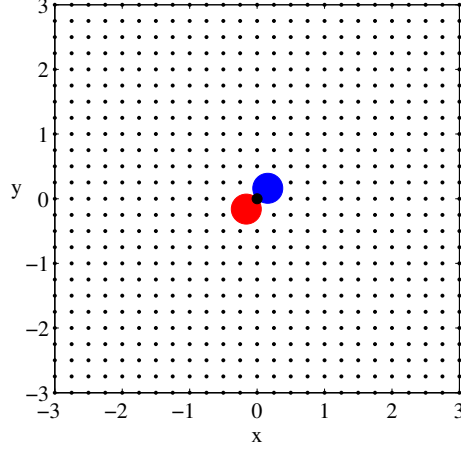


Figure 4.7: Dipole source at target grid center with 45° orientation and target grid (black dots).

	CB	CLEAN-PSF	DAMAS2	GIB
Estimation	1.00	0.18	0.74	0.94

Table 4.3: Dipole estimation comparison.

monopole reference solution, and GIB using monopole and dipole reference solutions are shown in Figure 4.10.

On conventional beamforming, the monopole reference solution brings the monopole identification only, and the dipole reference solution brings a distorted center region of the dipole center, with correct orientation around the true center but also distorted when approximate to the monopole source region. The CLEAN and DAMAS2 just captures the monopole source center. The GIB is able to locate the monopole source and dipole source without interference despite the proximity of two wavelengths between sources. The dipole identification for GIB also brings the correct orientation. The strength and peak velocity estimates for each of the methods are shown in Table 4.4.

	CB (mon.)	CB (dip.)	CLEAN-PSF	DAMAS2	GIB (mon.)	GIB (dip.)
Estimation	1.00	1.18	1.00	1.38	0.91	0.90

Table 4.4: Monopole and dipole estimations comparison for the incoherent case.

The estimation results are accurate for the monopole source center on the conventional and CLEAN, but GIB is more accurate when considering both monopole and dipole estimations.

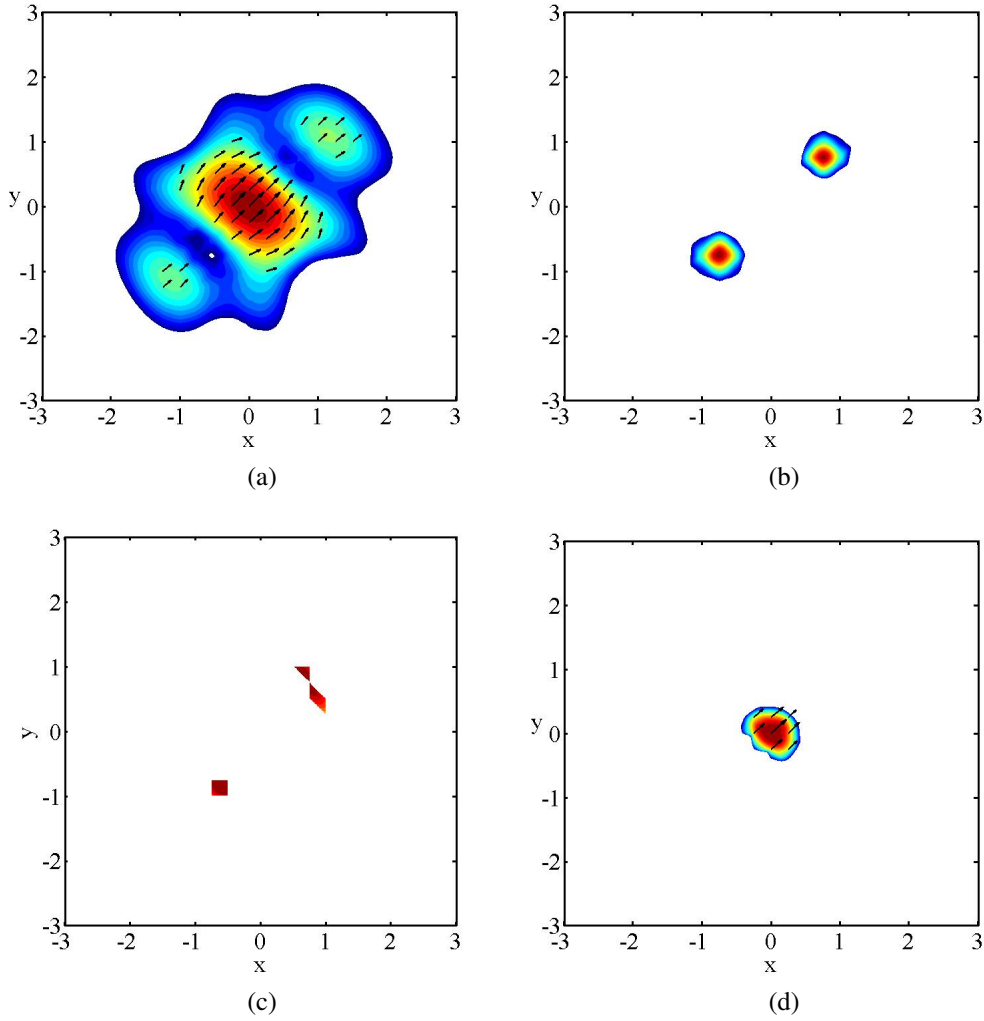


Figure 4.8: Dipole source at grid center with 45° orientation: (a) CB (b) CLEAN-SC (c) DAMAS2 (d) GIB. Arrows indicates dipole orientation. Contour levels with 10dB range and 0.5 increment.

DAMAS2 seems to suffer from the combination of both sources radiation, overestimating the monopole type of radiation.

The second case using the monopole and dipole configuration is with a coherent radiation, and with dipole shifted $\pi/2$ in time, the same model problem as in the considered literature (SUZUKI, 2008). Results obtained for the conventional method, CLEAN-SC with 6 iterations and ϕ factor of 0.5, DAMAS2 with 40 iterations, and GIB with 42 iterations, are shown in Figure 4.11.

The monopole identification using conventional beamforming is somewhat distorted but brings correctly the monopole center, but the dipole is now more distorted towards the side of the monopole and is rather difficult to locate its center. The CLEAN and DAMAS2 locates the

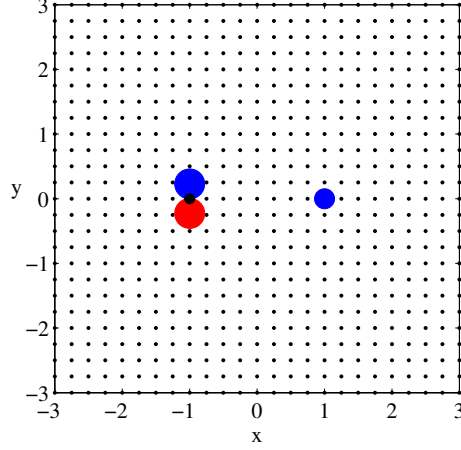


Figure 4.9: Monopole source at (1,0) (blue circle), Dipole source at (-1,0) with 90° orientation and target grid (dots).

monopole source center, but DAMAS2 seems to be more influenced by the dipole interference. The GIB is again able to locate both sources without deterioration or interference between radiations, capturing also the dipole orientation. The estimation results are shown in Table 4.5.

	CB (mon.)	CB (dip.)	CLEAN-PSF	DAMAS2	GIB (mon.)	GIB (dip.)
Estimation	0.99	1.39	0.97	0.99	0.98	1.00

Table 4.5: Monopole and dipole estimations comparison for the coherent case.

The conventional, CLEAN and DAMAS2 are accurate to estimate the monopole strength, as well as the GIB, but for the dipole, the conventional fails in bringing an overestimate, while the GIB is accurate. Both methods are able to capture dipole orientation without problems.

In summary, the GIB demonstrated a superior performance in source centers localization and estimation, even for the distributed case, in coherent and incoherent multipoles scenarios, identifying the correct source type and orientation when applicable. This in contrast to the limitations found with the reference methods, conventional beamforming, CLEAN, and DAMAS2.

Despite the simplicity of the used model problems, they already indicate the full potential for investigation and development. The first development investigated is the need for an automated procedure for the regularization factor definition.

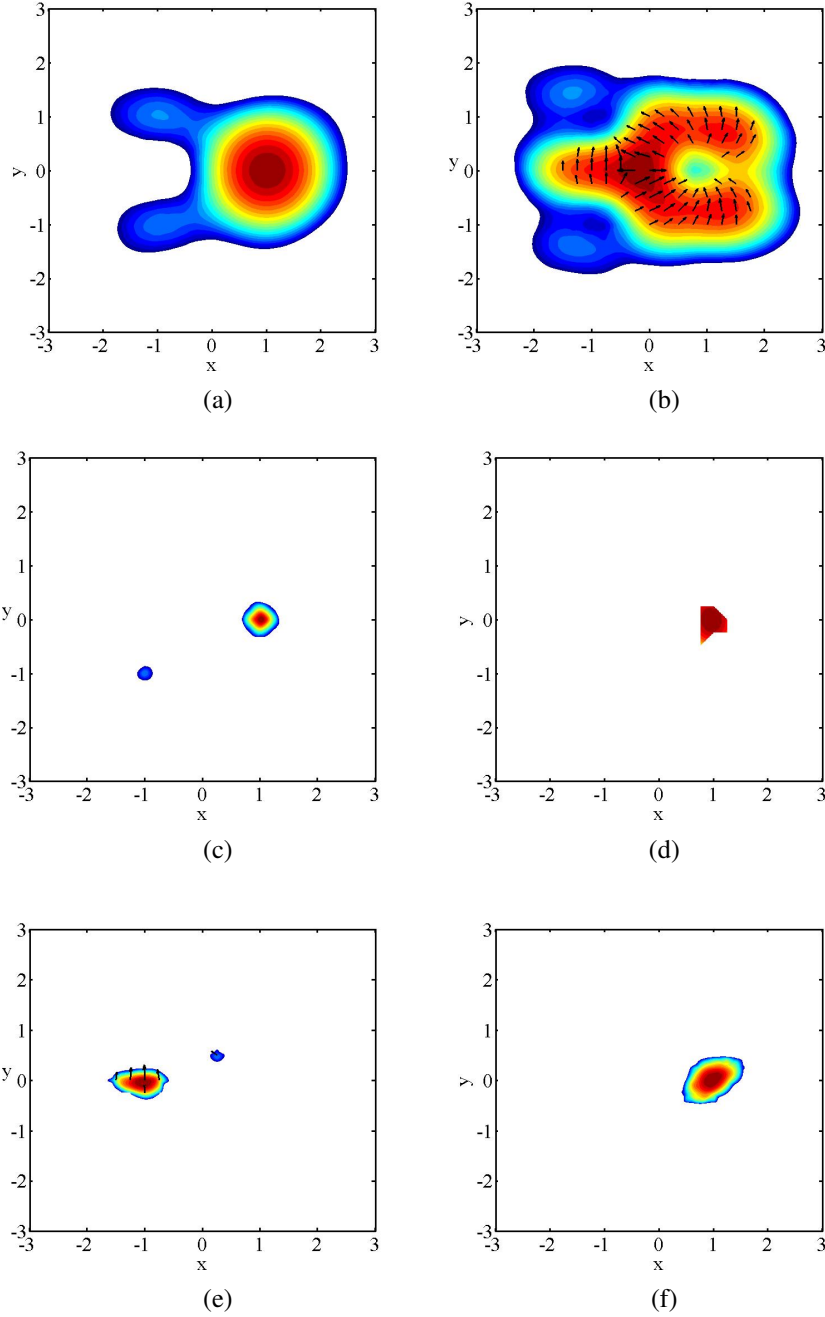


Figure 4.10: Monopole and dipole sources in incoherent radiation: (a) CB with monopole ref. (b) CB with dipole ref. (c) CLEAN-SC (d) DAMAS2 (e) GIB with monopole ref. (f) GIB with dipole ref. Contour levels with 10dB range and 0.5 increment.

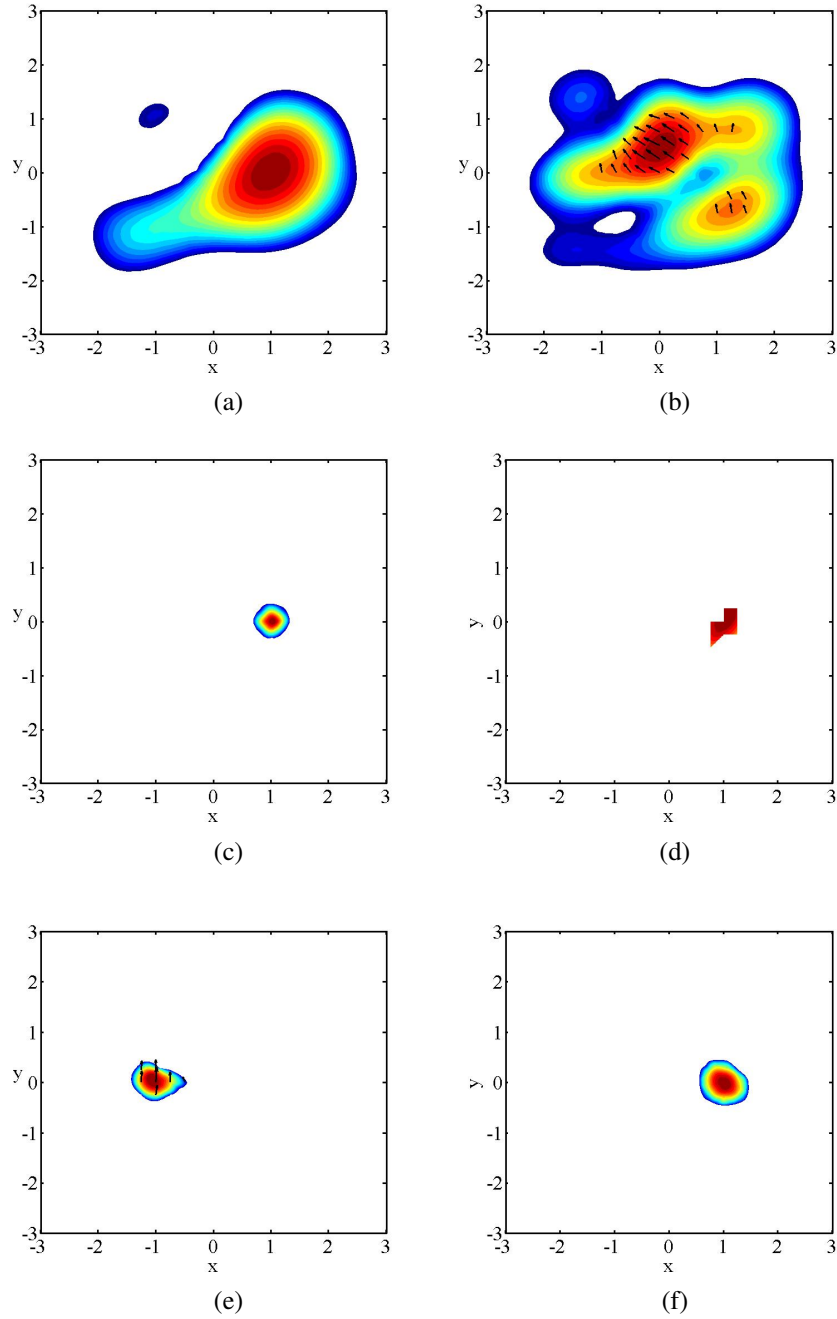


Figure 4.11: Monopole and dipole sources in coherent radiation: (a) CB with monopole ref. (b) CB with dipole ref. (c) CLEAN-SC (d) DAMAS2 (e) GIB with monopole ref. (f) GIB with dipole ref. Contour levels with 10dB range and 0.5 increment.

4.3 Generalized Inverse Beamforming with Optimized Regularization Strategy

The generalized inverse beamforming algorithm can be summarized as the search of the source strengths vector which minimizes the $J_{1_{orig}}$ cost function. The iterative truncation process is used along with the least squares generalized inverse equations on this search. The Tikhonov regularization used to improve the condition of the problem introduces an artificial diagonal term to the system and strongly influences the estimation strength.

On Suzuki (2008), the square of the regularization factor is suggested as a fraction of the greatest eigenvalue of the matrix to be inverted, with a limit range of 0.1% to 5%, but little is said about the criteria for its definition in this range and the the influence on estimation results.

In this section, an automated procedure to define the regularization factor is proposed using the literature model problems as reference. Different regularization strategies are compared: the fixed regularization factor over estimations using the fraction limits suggested by Suzuki; an intermediate fixed regularization that reproduces the literature result; and a regularization factor definition based on the minimization of a specific cost function on each iteration .

The use of Tikhonov regularization on equations 4.13 and 4.14 corresponds to the minimization of the following cost function based on the ℓ_2 norm:

$$J'_2 \equiv ||\alpha a_i||^2 + ||v_i - Aa_i||^2. \quad (4.18)$$

In order to obtain an explicit expression to equation 4.16, the equation 4.18 is rearranged and used with ℓ_1 norm instead of ℓ_2 norm. Two alternative expressions for the J_1 cost function are formulated as:

$$J_1 \equiv |a_i| + \alpha^{-2}|v_i - Aa_i|^2; \quad (4.19)$$

or

$$J_1^{alt} \equiv |a_i| + \alpha^{-1}|v_i - Aa_i|^2. \quad (4.20)$$

These two expressions are used and compared to another strategy for the definition of the regularization factor at each iteration, the minimization of the residue terms on the alternative J_1 cost functions. This strategy considers the source vector ℓ_1 norm invariant with respect to the regularization factor, leading again to two expressions for investigation:

$$J_{res} \equiv \alpha^{-2}|v_i - Aa_i|^2; \quad (4.21)$$

or

$$J_{res}^{alt} \equiv \alpha^{-1}|v_i - Aa_i|^2. \quad (4.22)$$

These Residue Cost Functions, are based on the ℓ_1 -norm, direct summation of the module of the residue terms.

The original generalized inverse algorithm search for the minimum of the J_1 cost function along iterations is kept the same, but a specific regularization factor is defined at each iteration which minimizes either the J_1 or the Residue cost function proposed. These alternative approaches are confronted em terms of estimation progress over iteration and advantages and disadvantages are listed in the end. The four tested approaches are:

- a) Minimize J_1 over iterations and minimize J_1 at each iteration;
- b) Minimize J_1^{alt} over iterations and minimize J_1^{alt} at each iteration;
- c) Minimize J_1 over iterations and minimize J_{res} at each iteration;
- d) Minimize J_1^{alt} over iterations and minimize J_{res}^{alt} at each iteration.

Results are obtained for each of the model problems presented in the literature, and only strategy *a*) is not able to converge to right sources location in all model problems, failing in coherent sources case, and by this reason, being discarded from the comparison.

The first model problem is the single monopole at the center of the target grid, an example of the Residue cost function curve, J_{res} , using strategy *c*), in the considered range of regularization factor, for the last iteration in the GIB algorithm, is presented in Figure 7.10. This strategy, based in the minimization of the Residue cost function at each iteration, was first presented in (ZAVALA *et al.*, 2011D) and here is extended later to dipole and also to the combined monopole and dipole, coherent and incoherent model problems.

With the regularization factor defined on each iteration, the source vector is defined, and the J_1 cost function evaluated. The J_1 cost function is in fact, the summation of the residue cost function with the source vector ℓ_1 -norm on each of the strategies. The optimal strength estimation is obtained at the J_1 cost function minimum, and represents the best fit along the iterations. Figure 4.12b shows an example of the regularization factor fraction used on each iteration and Figure 4.13 shows the J_1 cost function and J_{res} cost function, and strength along iterations for the single monopole model problem.

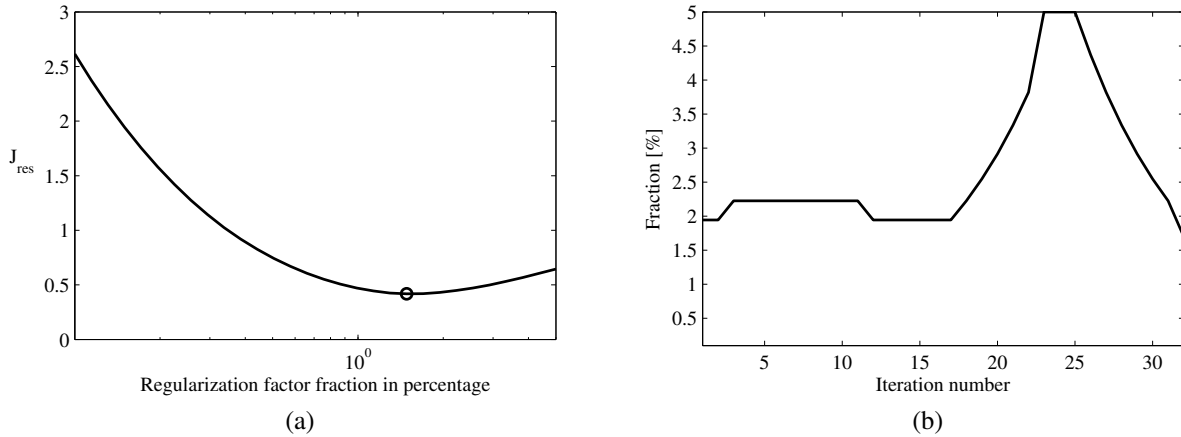


Figure 4.12: Monopole source at target center: (a) Residue cost function along regularization on the last iteration (minimum at circle). (b) Optimal regularization factor fraction along iterations.

Even after the J_1 minimum is reached, the iteration procedure described above can be carried on, and a further narrowing of the source region can still be achieved until the source region is clearly identified. The criteria to stop the iterations can be reaching a minimum number of source vector terms. In this way, the strength estimation related to the narrowed map can be influenced by an increased residue when compared to the optimal estimation. The monitoring of the estimated

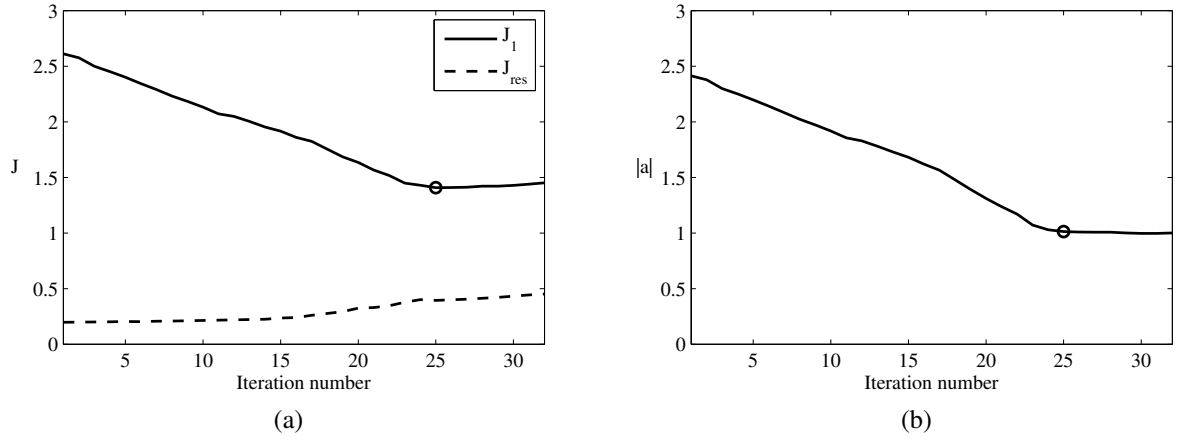


Figure 4.13: Monopole source at target center: (a) J_1 cost function and Residue cost function along iterations (minimum at circle). (b) Strength estimation along iterations (J_1 cost function minimum at circle).

strength and cost functions along the iterations is a quality measure of the identification.

The first comparison is made with the strategy *c*), called optimized regularization strategy in (ZAVALA *et al.*, 2011D), and the fixed regularization factors, in the range limits suggested by Suzuki or with the intermediate factor that reproduces the literature results at the end of the iterations. These curves are shown in Figure 4.14, for the J_1 cost function along iterations and the monopole strength estimation ($|a|$) over the iterations. Each estimation is performed with a different CSM, where random noise is added according to the same strategy mentioned in the previous section.

The first observation from the comparison in Figure 4.14 is that the minimum regularization factor (0.1%), yields the highest J_1 and strength estimation, and the maximum regularization (5%), the opposite, which is coherent with the expected influence of the regularization factor, underestimating the correct strength if it is too big, and overestimating it in the case when it is too small. This influence of the Tikhonov regularization is maybe better illustrated if the matrix to be inverted is decomposed in its singular values and vectors. The representation of the solution vector in this case can be expressed by Equation 4.23:

$$a_i = \sum_{j=1}^N f_j \frac{u_j^T v_i}{\sigma_j} b_j, \quad (4.23)$$

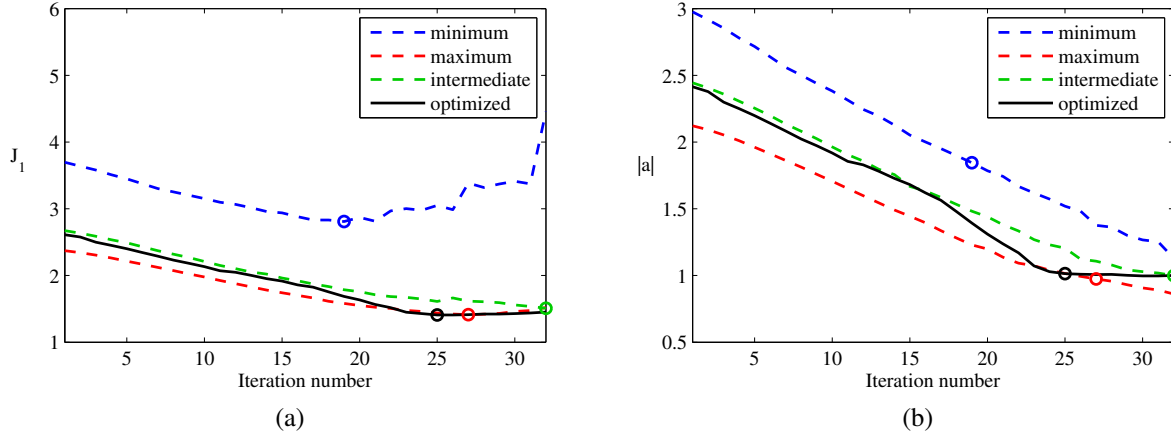


Figure 4.14: Influence of fixed regularization and optimized strategy on single monopole problem: (a) J_1 cost function along iterations (minimum at circle). (b) Strength estimation along iterations (J_1 cost function minimum at circle).

where N_w is the rank of the matrix to be inverted; f_j are the Wiener weights ($f_j = \frac{\sigma_j^2}{\sigma_j^2 + \alpha^2}$); u_{s_j} are the left singular vectors, and b_{s_j} the right singular vectors. With this expression, the influence of the regularization factor α on the Wiener filter weights, and consequently, on the estimations is clear.

Still in terms of the fixed regularization strategies, the intermediate factor, presents the same trend along the iterations as the limit ones, the only difference is that the final iteration is at the correct estimation, on this case, a unitary strength monopole. On the other hand, the optimized strategy, starts its estimation very close to the intermediate fixed factor but later in the iterations, it presents a clear platform around the correct strength, since the iteration number 25 on this case, when it reaches its J_1 cost function minimum. This demonstrating clearly the estimation stabilization when compared to the fixed regularization results.

Now, if we compare the optimized strategy with the other alternative strategies in b) and d), shown in Figure 4.15, different behaviors are observed. First, the strategy b) which minimizes J_1^{alt} , present abrupt changes in J_1 and also in the strength estimation, which can confuse the search of the J_1 global minimum with a local one. Second, the strategy d, or the one which minimizes J_{res}^{alt} , don't present a clear estimation stabilization as the optimized strategy, which minimizes J_{res} . Strategies b) and d) also doesn't present a clear minimum in the J_1 cost function, making it more difficult to judge when to stop iterations in the case of unknown source strength. With these results, it is clear that the strategy c) which minimizes J_{res} is the better choice.

Considering now the second model problem, a line distributed monopole source, results are

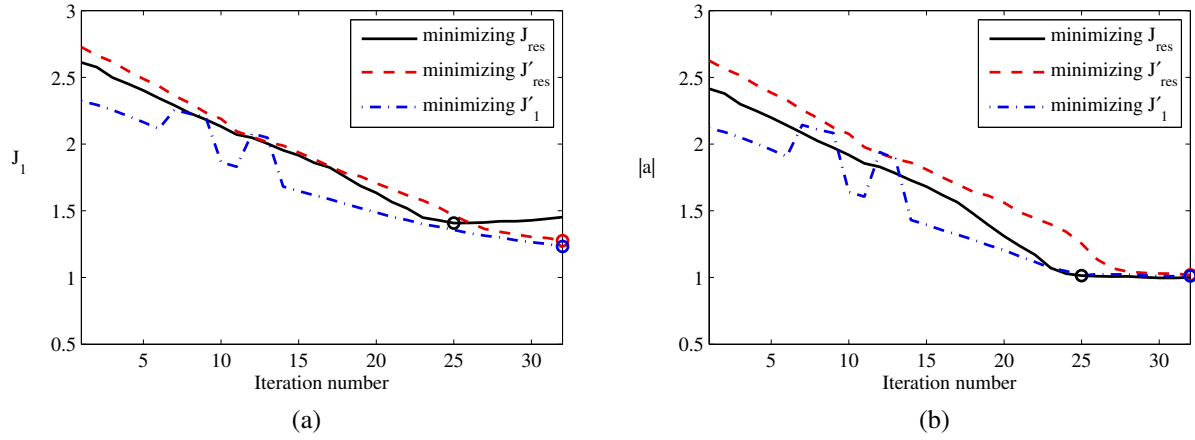


Figure 4.15: Influence of regularization strategies on single monopole problem: (a) J_1 cost function along iterations (minimum at circle). (b) Strength estimation along iterations (J_1 cost function minimum at circle).

presented for the fixed regularization factors and the optimized strategy in Figure 4.16. A similar behavior is found in this case when compared to the monopole case, again, where the strategy based on the minimization of the J_{res} function at each iteration clearly present a distinct J_1 minimum over the iterations, as well as the estimation strength present a clear stabilization around the correct strength. The J_1 minimum being reached after 21 iterations in this case.

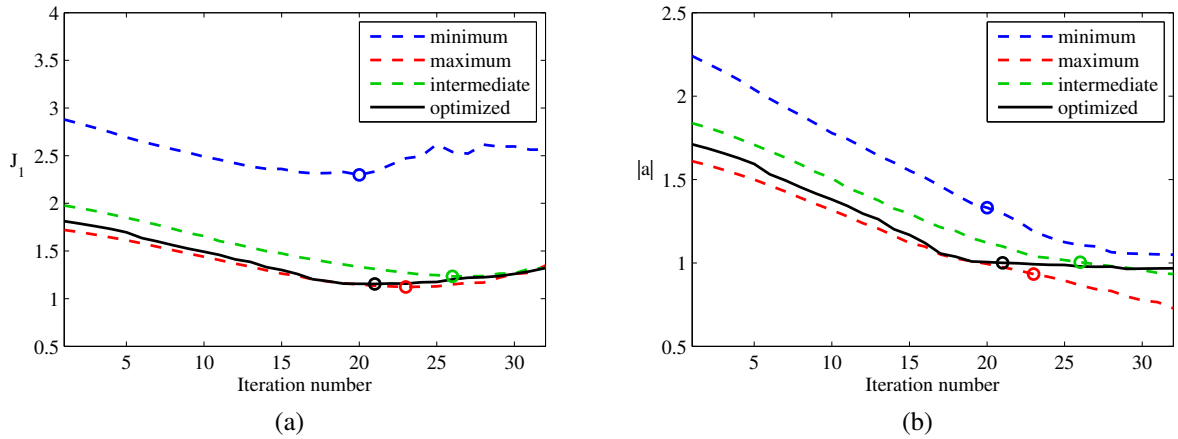


Figure 4.16: Influence of fixed regularization and optimized strategy on distributed line monopole problem: (a) J_1 cost function along iterations (minimum at circle). (b) Strength estimation along iterations (J_1 cost function minimum at circle).

On the comparison of the optimized strategy with the other approaches, shown in Figure 4.17, the clearer J_1 minimum is brought by the optimized strategy, which also present the more stabilized strength estimation around the correct unitary strength, and the sooner too.

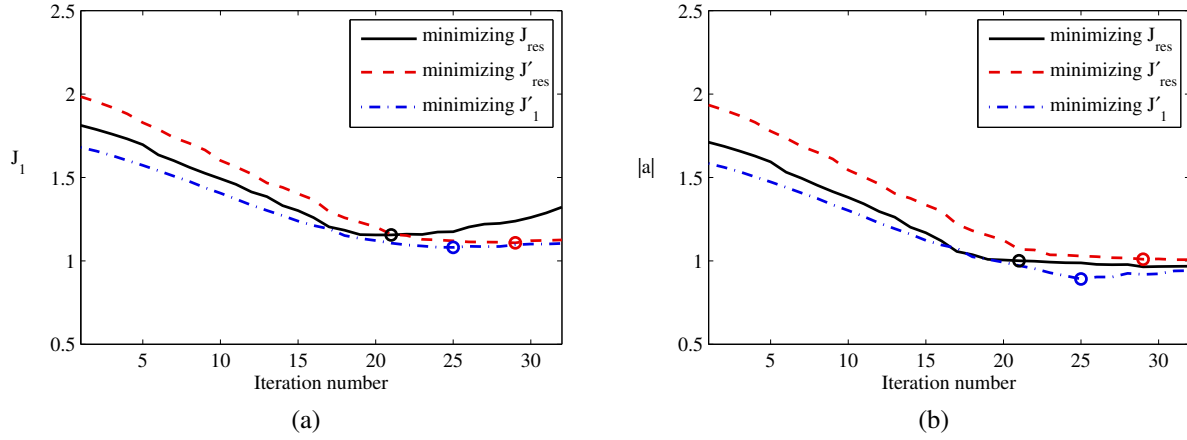


Figure 4.17: Influence of regularization strategy on distributed line monopole problem: (a) J_1 cost function along iterations (minimum at circle). (b) Strength estimation along iterations (J_1 cost function minimum at circle).

The third model problem from the considered reference literature is the single dipole at the target center. The comparison for the optimized strategy and the fixed regularization factor are shown in Figure 4.18. Here, in the case of dipole, the source vector ℓ_1 norm, $|a|$, is based on the Euclidean norm of the dipole components: $|a| = \sqrt{|a_x|^2 + |a_y|^2}$. The results for the J_1 cost function and dipole peak (or axial) surface velocity demonstrates again the advantages in the optimized strategy over the fixed factors, with clear J_1 minimum and stabilization around the correct estimation.

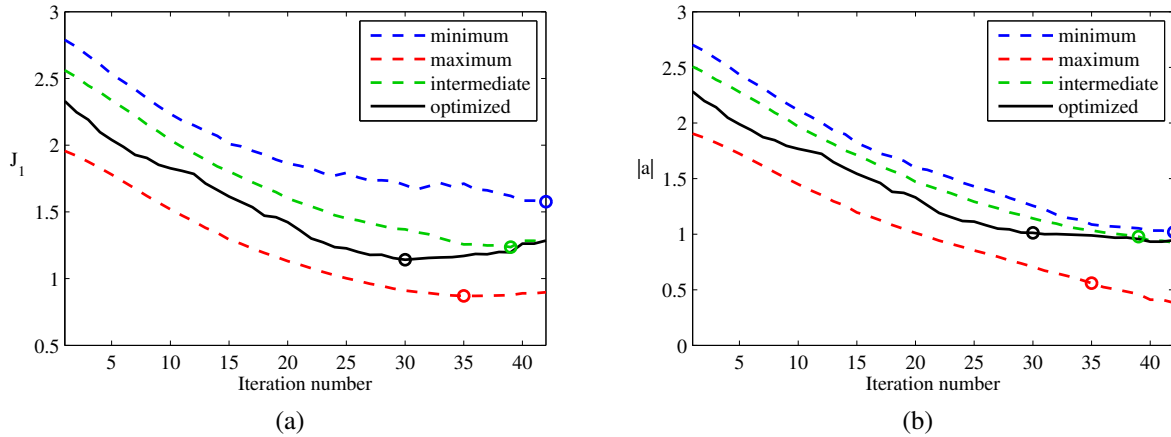


Figure 4.18: Influence of fixed regularization and optimized strategy on single dipole problem: (a) J_1 cost function along iterations (minimum at circle). (b) Strength estimation along iterations (J_1 cost function minimum at circle).

Figure 4.19 presents the comparison between the considered strategies, and the one that

brings the sooner and clearer J_1 minimum, and more stabilized estimation is the optimized strategy. On this case, the worst estimation is found with the minimization based on the J_1^{alt} cost function at each iteration.

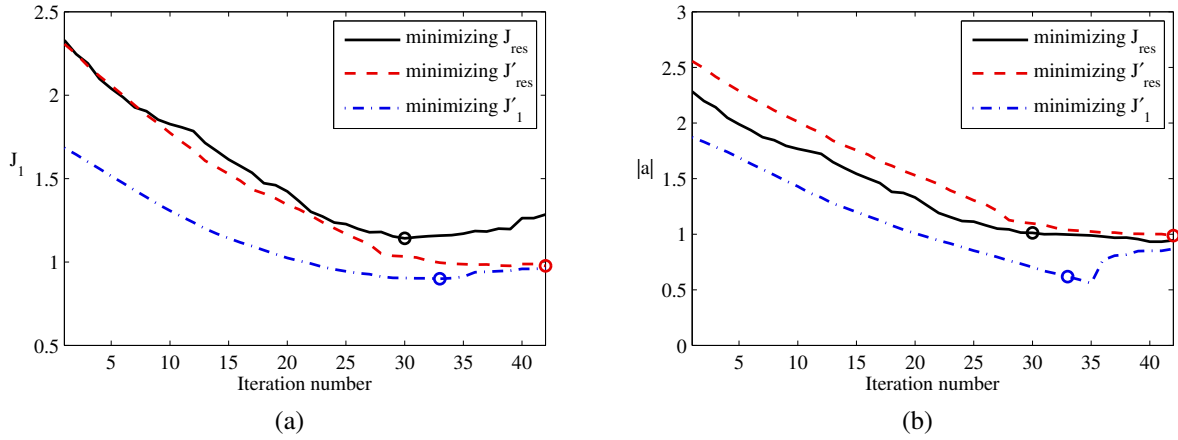


Figure 4.19: Influence of regularization strategy on single dipole problem: (a) J_1 cost function along iterations (minimum at circle). (b) Strength estimation along iterations (J_1 cost function minimum at circle).

The more complex considered literature cases, the simultaneous monopole and dipole, separated by two wavelengths, in coherent and incoherent radiation are investigated. First, on the coherent case, the results for the J_1 cost function comparing the fixed regularization factors and the optimized strategy are found in Figure 4.20. Results for the estimations on the monopole reference solution source vector terms and the respective dipole terms are shown in Figure 4.20.

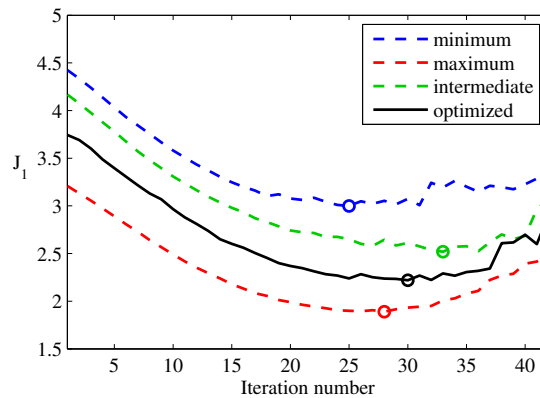


Figure 4.20: Influence of fixed regularization and optimized strategy on coherent sources problem: J_1 cost function along iterations (minimum at circle).

Is interesting to observe that the monopole estimation quickly stabilizes around the correct

unitary strength whilst the dipole estimation slowly decay to reach the unitary peak axial estimation. While the monopole part shows small differences between the optimized strategy and the minimum and intermediate fixed factors, on the dipole part, the optimized strategy is the only one to bring a certain stabilization when reaching the maximum predefined number of iterations.

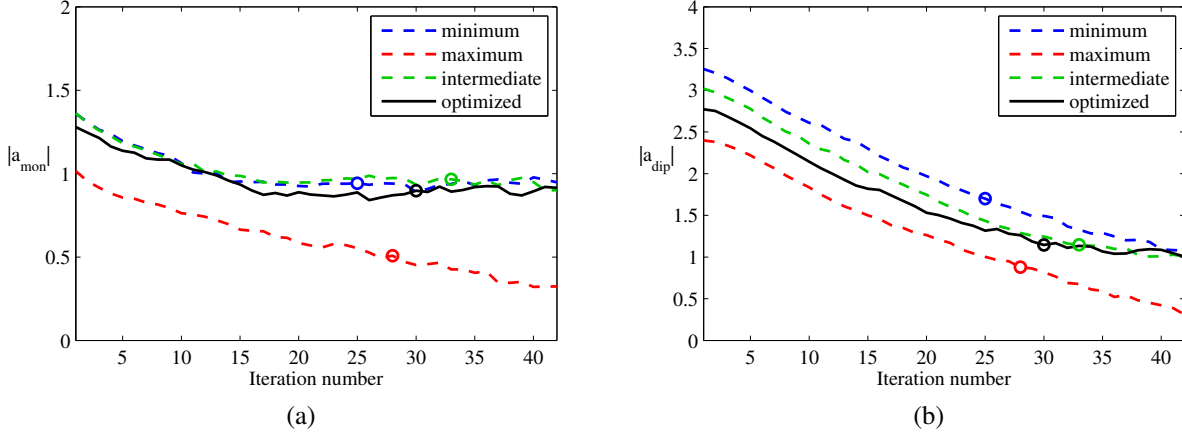


Figure 4.21: Influence of fixed regularization and optimized strategy on coherent sources problem: (a) Monopole estimation (b) Dipole estimation. J_1 cost function minimum at circle.

Now considering the other strategies in comparison for the coherent case, results are shown in Figure 4.22 for the J_1 cost function and in Figure 4.23 for the estimation on monopole and dipole parts. The optimized strategy is the only one to bring a distinct minimum, and with a smoother estimation variation along iterations compared to strategies based on minimization of J_1^{alt} and $J_{\text{res}}^{\text{alt}}$ at each iteration.

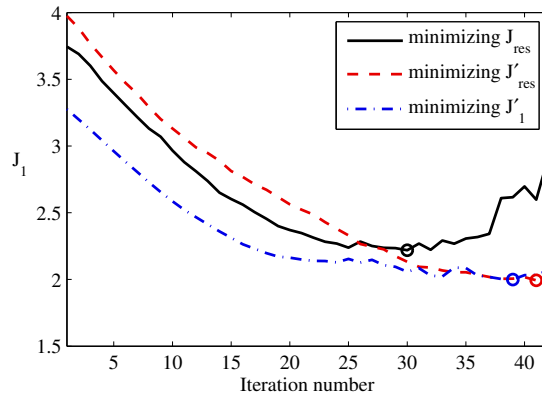


Figure 4.22: Influence of regularization strategy on coherent sources problem: J_1 cost function along iterations (minimum at circle).

On the second simultaneous monopole and dipole case, the incoherent radiation model

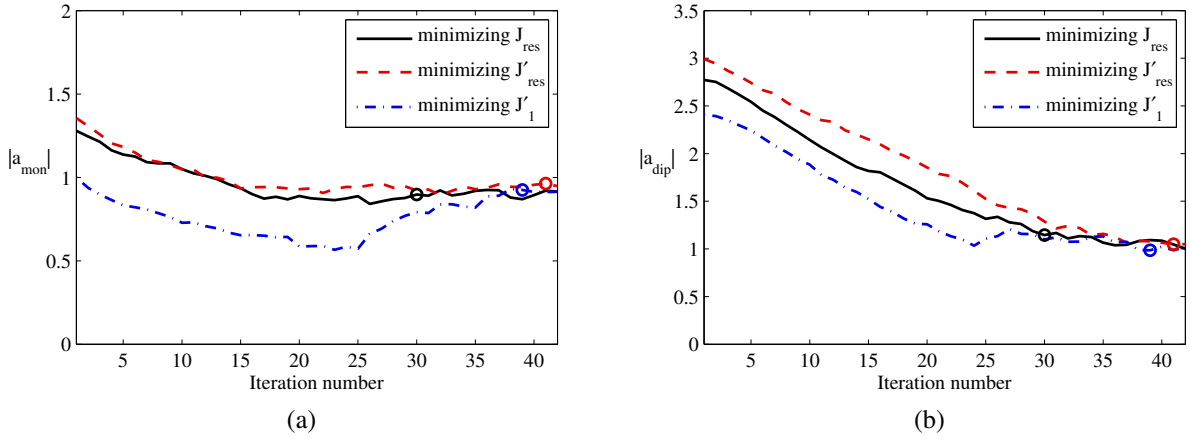


Figure 4.23: Influence of regularization strategy on coherent sources problem: (a) Monopole estimation (b) Dipole estimation. J_1 cost function minimum at circle.

problem, the response is split in two eigenmodes, and systems are assembled with transfer matrix containing both monopole part as well as dipole part, but since monopole present a higher radiation efficiency, the first eigenmode (arranged in descent order of eigenvalue magnitude) corresponds to the monopole radiation and the second, consequently to the dipole. Each response vector, or eigenmode v_i , has a specific J_1 cost function associated, as well as, a source vector $|a_i|$. Results for the first response vector J_1 cost function and monopole part source vector terms are shown in Figure 4.24. A deeper analysis and interpretation of CSM eigen-structure is found in (MUELLER, 2002), and in Appendix section: Eigenvalue Based Estimation.

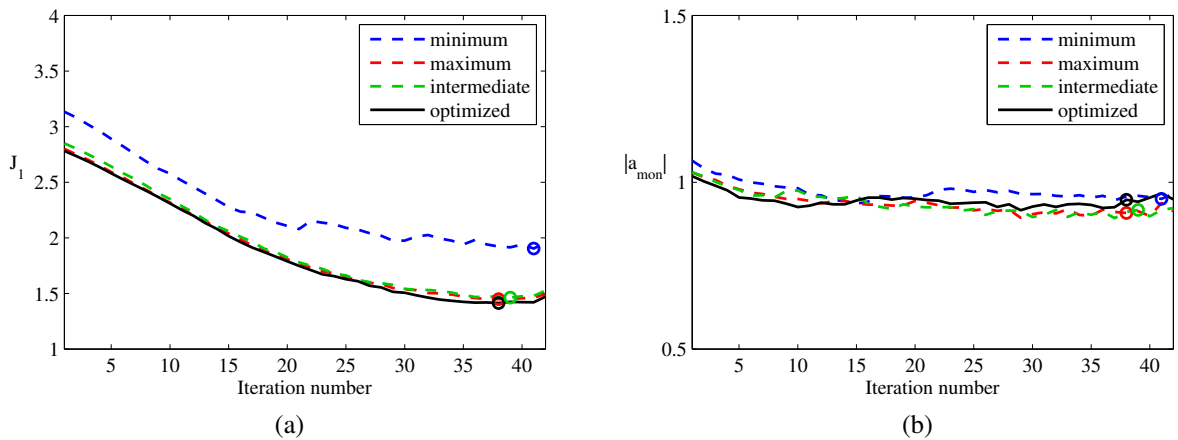


Figure 4.24: Influence of fixed regularization and optimized strategy on incoherent sources problem, first eigenmode: (a) J_1 cost function along iterations (minimum at circle) (b) Monopole estimation (J_1 cost function minimum at circle).

Although the monopole part in solving the system for the first eigenmode is quite stabilized,

the J_1 cost function reaches its minimum only close to the predefined iterations number limit. In this case, similar estimations are found for all the fixed factors and the optimized strategy. If comparing now the other strategies to the optimized one, again for the first eigenmode, small advantage is found for the optimized one, with a sooner minimum, found after 38 iterations, when compared to the other strategies.

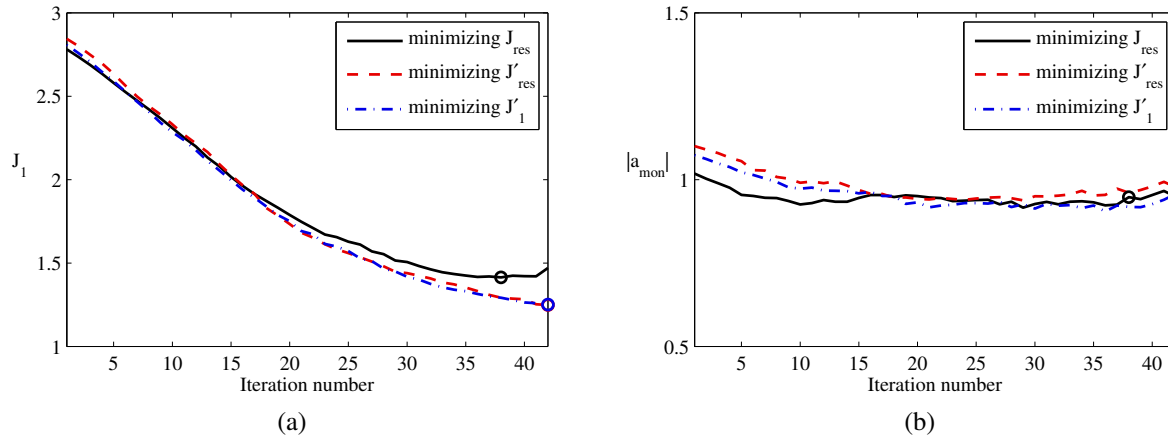


Figure 4.25: Influence of regularization strategy on incoherent sources problem, first eigenmode: (a) J_1 cost function along iterations (minimum at circle) (b) Monopole estimation (J_1 cost function minimum at circle).

The resolution of the system with the second eigenmode, and considering the dipole radiation part, results for the J_1 cost function and estimation are shown in Figure 4.26 for the comparison of the optimized regularization strategy and the fixed regularization factors. Again, the minimum of the J_1 cost function over the iterations is found in general close to the predefined maximum number of iterations, and the estimation present a smooth decay no clear stabilization for any of the curves. This demonstrates the more complex situation in finding a source vector fit to the sources response, but the optimized strategy is still able to mark the minimum at the 41st iteration, with an accurate estimation of the unitary strength monopole source.

Considering now the results comparing the strategies based in minimization of J_1^{alt} and J_{res}^{alt} at each iteration, and the optimized one, which minimizes J_{res} at each iteration, shown in Figure 4.27, again the J_1 cost function minimum is found closer to the end of iterations, and no clear stabilization is found for the estimation. Although not clear, the optimized strategy is able to mark the minimum after 41 iterations with an accurate dipole axial surface velocity estimation.

The objective on this comparisons is to list the main advantages and disadvantages of each approach to finding the most accurate estimation using the reference model problems found in the

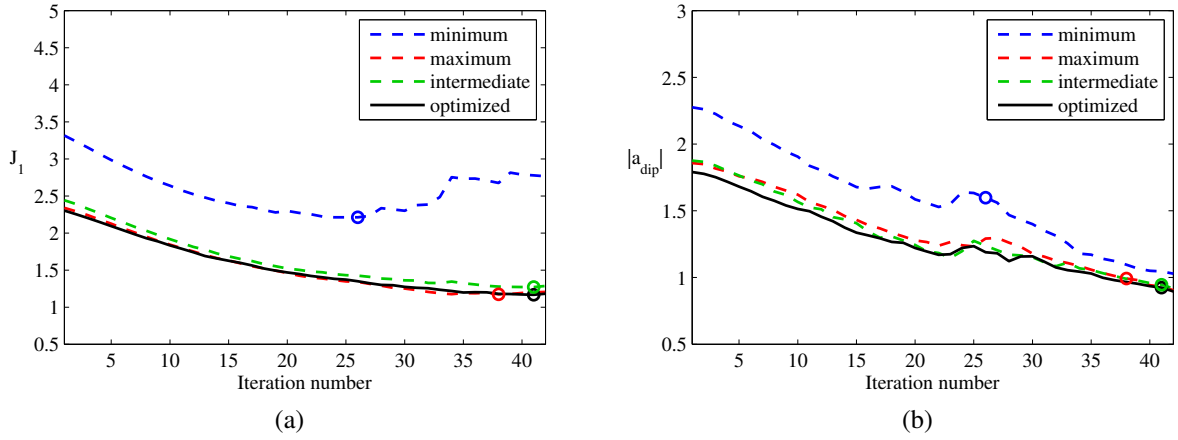


Figure 4.26: Influence of fixed regularization and optimized strategy on incoherent sources problem, second eigenmode: (a) J_1 cost function along iterations (minimum at circle) (b) Dipole estimation (J_1 cost function minimum at circle).

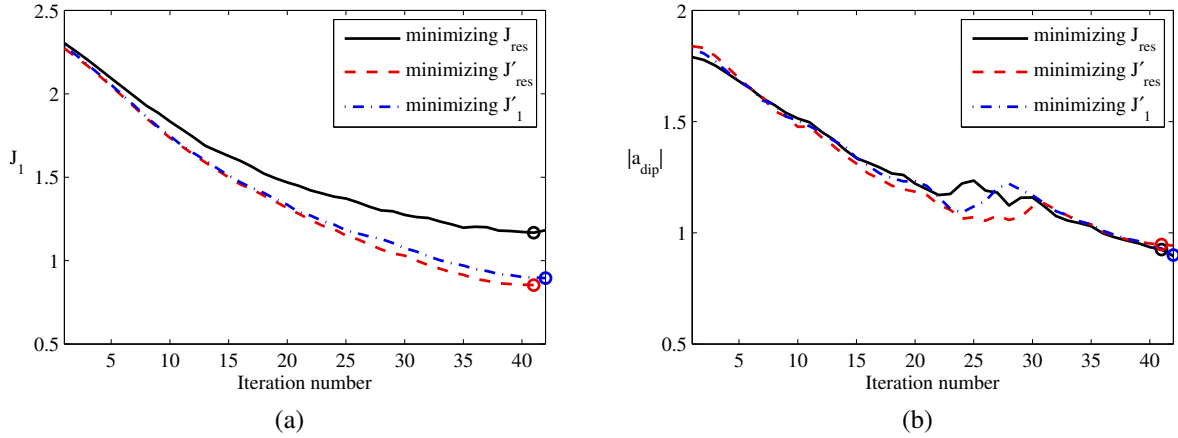


Figure 4.27: Influence of regularization strategy on incoherent sources problem, second eigenmode: (a) J_1 cost function along iterations (minimum at circle) (b) Dipole estimation (J_1 cost function minimum at circle).

original method's proposal literature. Using the fixed regularization, the only one advantage is the effort to obtain the source vector estimate, requiring only one resolution of least squares equations 4.13 or 4.14. In the other hand, they provide a blind estimate, with observed inaccuracy of almost 100% if considered the estimation at the J_1 cost function minimum over the iterations.

The strategy which minimizes J_1^{alt} at each iteration, described in item b), present the disadvantage of some abrupt changes in J_1 cost function (in this case, also adopted the J_1^{alt} for evaluation over the estimations), which causes local minimums along the iterations and could

confuse the algorithm in finding the best estimation. The advantage observed is that it approximates to the optimized behavior but in general with a worst estimation approximation. The strategy which minimizes J_{res}^{alt} at each iteration, described in item *d*), present a slightly better performance the previous strategy, with a better estimation, but with a later stabilization on the estimation platform around the correct unitary strength, for example, see monopole or line mode problems.

The strategy which best indicate the estimation is the, so-called, Optimized Regularization Strategy, described in item *c*), which corresponds to minimize the J_{res} at each iteration, still evaluating the J_1 function over the estimations to find the best source vector fit. This strategy demonstrated a clear J_1 cost function minimum, and sooner than the other strategies, with also a better stabilization of the estimation with a platform around the correct estimation. One possible disadvantage when compared to the fixed regularization is the effort to search for the minimum of the J_{res} function. Considering this, this method is only recommended when the estimation accuracy is of foremost importance. If the estimation is no longer critical importance, but the localization, then is recommended that a fixed regularization is used. A more detailed computational effort comparison is presented in a later section in this Chapter.

4.4 Weighted Least Squares Schemes

In this section, three different approaches using weighted least squares schemes are presented, and the reference literature model problems are used to illustrate their results. The first method is the Iteratively Re-Weighted Least Squares (IRLS) scheme, first presented in combination with the generalized inverse beamforming by Suzuki (2010). Following the same strategy, the use of IRLS, a second weighting is proposed, the residual based weighting IRLS, method applied as found in Huber (1981), chapter 7. The third method is the Generalized Weighted Inverse Beamforming, first proposed in (PRESEZNIAK, 2011), where the weighting matrix is created in the search to minimize the source terms that doesn't influences the result.

4.4.1 Iteratively Re-Weighted Least Squares based in Source Vector as Weight

The work by Suzuki in 2010 introduced the Iteratively Re-Weighted Least Squares scheme in combination with the generalized inverse beamforming, and used it to solve a jet-noise study using a ℓ_p norm where $p = 3/2$. Later, Day & Suzuki (2011) used this method again to solve a in-duct noise identification.

This method, IRLS, is directly combined with the iterative algorithm from the original generalized inverse beamforming with modifying only Equations 4.13 or 4.14, for underdetermined or overdetermined systems, respectively.

These Equations become:

$$a_i^{(n+1)} \approx W^{(n)} A^\dagger (A W^{(n)} A^\dagger + \alpha^2 I)^{-1} v_i, \quad (4.24)$$

$$a_i^{(n+1)} \approx (A^\dagger A + \alpha^2 (W^{(n)})^{-1})^{-1} A^\dagger v_i, \quad (4.25)$$

where $W^{(n)}$ is a diagonal matrix with components of $w = |a^{(n)}|^{2-p}$; and (n) or $(n+1)$ denotes the iteration number superscript.

Normally in IRLS applications, the residue is used as weighting, but Suzuki opted to use the source vector as weighting input in the generation of the next iteration source vector. Later in this section, the residue weighting is also investigated and results compared to this application proposed in 2010. The weighted least squares problem using the source vector term calculated in the previous iteration can be interpreted as the minimization of the following cost function:

$$J_{w_a} \equiv ||diag(|a_i|)(v_i - A a_i)||^2, \quad (4.26)$$

where $diag(|a|)$ is the diagonal matrix formed with the source vector terms module. The advantage on this formulation is that it searches directly the simultaneous minimization of the norm of the source vector and the residue.

Again, the Tikhonov regularization can be adopted to improve inversion of transfer matrix, and the regularization factor squared is set to be 1% in the work from 2011 and suggested as 1% of the greatest eigenvalue of AA^\dagger or $AW^{(n)}A^\dagger$. Now with smaller influence in the result, the

regularization is set as minimum as possible, and fixed over iterations.

Two problems are chosen from the literature model problems to illustrate the results obtained with this method, the single monopole and the distributed line monopole. The regularization factor squared adopted is 1% as suggested in literature. Mappings for the strength obtained after 8 iterations are shown in Figure 4.28.

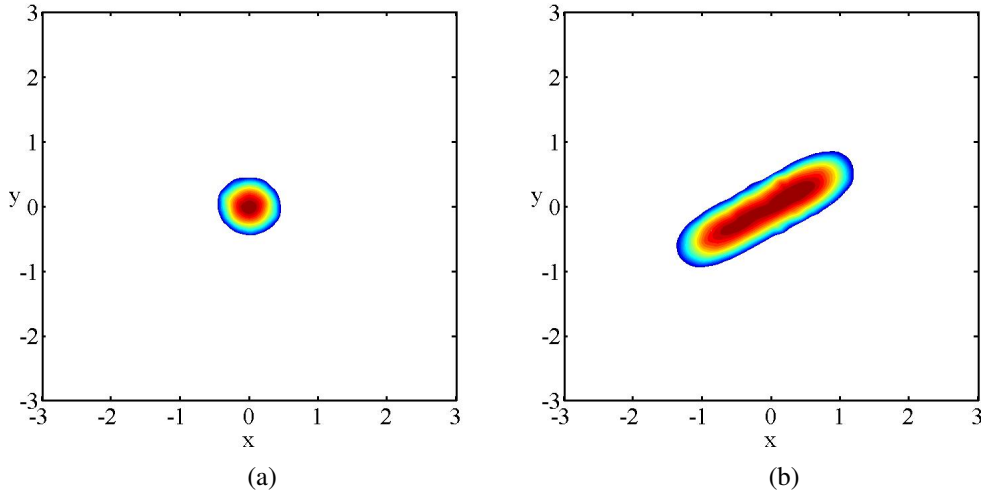


Figure 4.28: Source strength mappings using GIB/IRLS for: (a) Single monopole at target grid center (b) Distributed line monopole. Contour levels with 10dB range and 0.5 increment.

These results show the increased dynamic range obtained with a lower number of iterations. The distributed line mapping also indicates a smoother localization when compared to the original methods results, shown in Figures 4.4 and 4.6 for the single and distributed monopole original results respectively. The strength estimation and J_1 cost function over iterations are shown in Figure 4.29.

From the estimation curve and J_1 cost function is difficult to assess the correct estimation, or the J_1 cost function minimum, for example, on the case of the monopole model problem, the minimum is after 8 iterations, but in the distributed line monopole, the minimum is at the first iteration. The estimations obtained are 0.98 for the monopole and 1.11 for the distributed line, both reasonably accurate, but in the case of the line source, less accurate than the GIB without IRLS, which estimation is 0.94 according to literature and 1.01 with the optimized regularization strategy. In summary, if the estimation is not of foremost importance, this method is much faster than the original least squares scheme, since it requires fewer iterations and a fixed low factor regularization is enough to provide convergence in the source localization. A deeper performance analysis is carried out in a further section in this chapter, comparing among others the original GIB and the

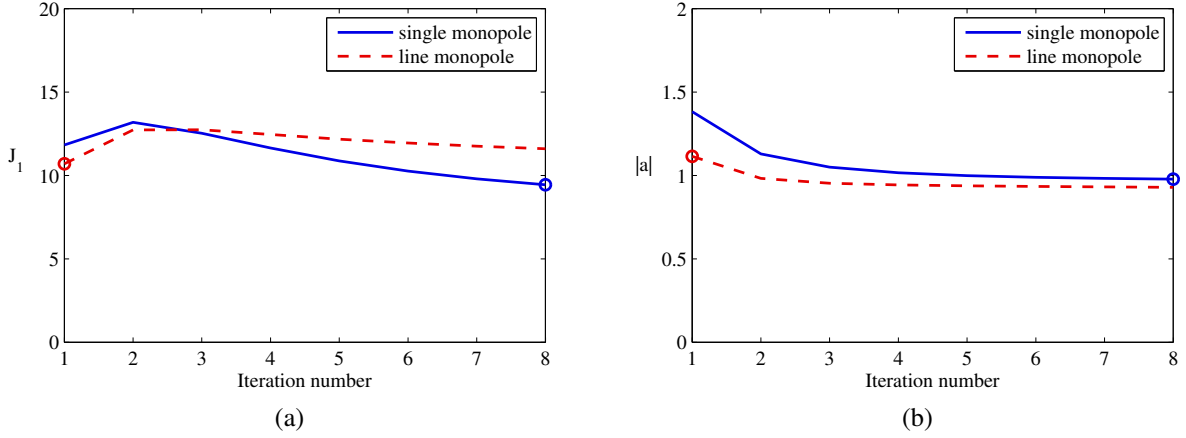


Figure 4.29: Single and line monopole problem results using GIB/IRLS: (a) J_1 cost function along iterations (minimum at circle) (b) Strength estimation (J_1 cost function minimum at circle).

GIB/IRLS.

4.4.2 Iteratively Re-Weighted Least Squares based in Residue as Weight

As already mentioned, and found in (HUBER, 1981), or (BJORCK, 1996), the normal approach is to use the p-norm of the residue in the weighted least squares problem, leading to a minimization of the following cost function:

$$J_{w_r} \equiv ||diag(|r_i|)^{(p-2)/2}(v_i - Aa_i)||^2, \quad (4.27)$$

where r_i is the residue associated to the source vector a_i and eigenmode v_i .

To investigate the results with this approach and compare to the method proposed by Suzuki, the single monopole and distributed line are again used to illustrate the IRLS weighted by residue and with norm $p = 1$. Despite in literature is known that $p = 1$ is of slow convergence, the advantage on this case is to apply the ℓ_1 norm also in the residue minimization. Results obtained after 28 iterations are presented in Figure 4.30 and 4.31, for the mappings, and J_1 cost function and source strength estimation, respectively. The regularization fraction adopted is 5% of the greatest eigenvalue of the matrix to be inverted.

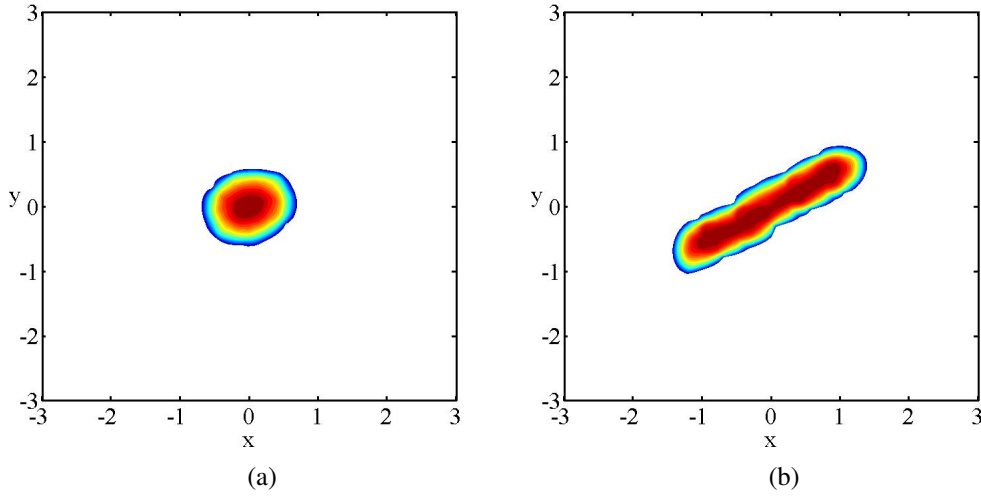


Figure 4.30: Source strength mappings using GIB/IRLS(residue weighting) for: (a) Single monopole at target grid center (b) Distributed line monopole. Contour levels with 10dB range and 0.5 increment.

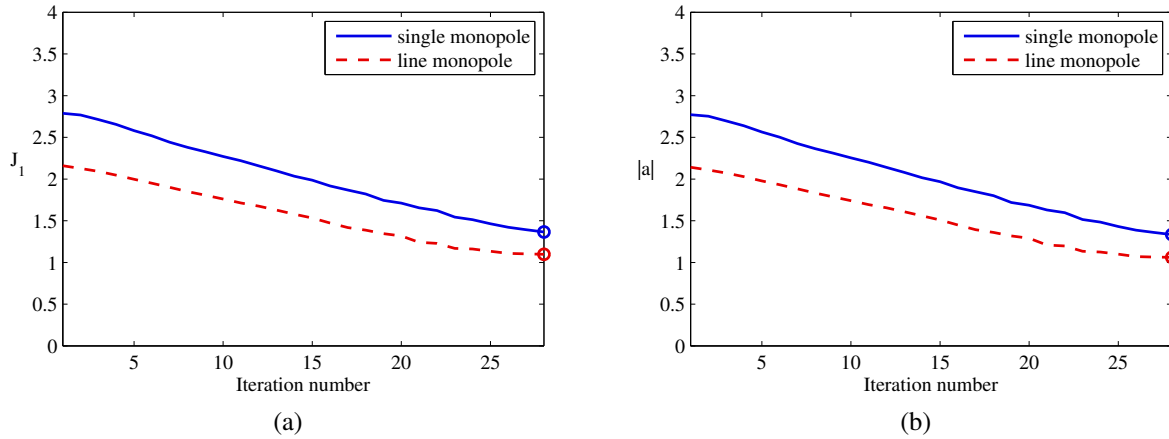


Figure 4.31: Single and line monopole problem results using GIB/IRLS(residue weighting): (a) J_1 cost function along iterations (minimum at circle) (b) Strength estimation (J_1 cost function minimum at circle).

As already mentioned in literature, small differences are observed in the results, and a slight increase in dynamic range with a reduced number of iterations are obtained. The disadvantage on this case is the strength estimation, which are 1.30 for the single monopole and 1.05 for the line source. No clear minimization is observed in J_1 cost function or estimation strength, being difficult to judge which is the correct estimation along iterations.

4.4.3 Generalized Weighted Inverse Beamforming

Another approach that can be applied in the generalized inverse beamforming is the so-called, Generalized Weighted Inverse Beamforming (PRESEZNIAK, 2011), based in the Iteratively Weighted Pseudo Inverse technique (WPInv) (GUILLAUME *et al.*, 2002; PARLOO *et al.*, 2003). The system to be solved can be written as:

$$a_i = (A)_W^+ v_i, \quad (4.28)$$

where

$$(A)_W^+ = W(AW)^+ \quad (4.29)$$

and W is the diagonal matrix with terms $|w|$; and $(AW)^+$ means the pseudo inverse of AW , using for example the Tikhonov regularization:

$$(AW)^+ = (AW)^\dagger ((AW)(AW)^\dagger + \alpha^2 I)^{-1}. \quad (4.30)$$

In this technique, the diagonal weighting matrix is optimized to minimize the ℓ_p -norm of the source vector, according to the following cost function:

$$J_{WPInv} = \|a_i\|_p^p, \quad (4.31)$$

with p a value close to zero and considering $|a|_p^p = (\sum |a_k|^p)^{(1/p)}$.

The cost function in Equation 4.31 can be written as a quadratic cost function:

$$J_{WPI_{nv}} = \frac{1}{p} |res_i|^2, \quad (4.32)$$

with

$$res_i = |a_i|^{\frac{p}{2}}. \quad (4.33)$$

This quadratic cost function can be minimized using the Gauss-Newton optimization algorithm, considering that an analytical expression for the Jacobian matrix ($Jac_{jk} = \partial res_{i_j} / \partial w_k$) can be obtained as:

$$\frac{\partial res_{i_j}}{\partial w_k} = \frac{p}{2} |a_{i_j}|^{\frac{p}{2}-2} \left(\text{Re}(a_{i_j}) \text{Re} \left(\frac{\partial a_{i_j}}{\partial w_k} \right) + \text{Im}(a_{i_j}) \text{Im} \left(\frac{\partial a_{i_j}}{\partial w_k} \right) \right), \quad (4.34)$$

with the derivatives $\partial a_{i_j} / \partial w_k$ calculated as:

$$\frac{\partial a_{i_j}}{\partial w_k} = (I - W(AW)^+ A) W^+ \text{diag}(|a_i|), \quad (4.35)$$

Since the Jacobian matrix can be computed analytically using Eq. 4.34 and Eq. 4.35, a fast minimization on the $J_{WPI_{nv}}$ cost function is obtained.

In order to illustrate the method's performance, the single monopole and the distributed line monopole is again used. The GIB algorithm is with 8 iterations, and resultant source vector is then used as input to the optimization procedure using the weighted pseudo inverse Equation

4.29. The Gauss-Newton optimization is performed with a maximum of 5 iterations, the Tikhonov regularization factor squared as 1% of the greatest eigenvalue of $AW(AW)^\dagger$, and $p = 1$, so searching the ℓ_1 -norm of the source vector terms $|a|$. Results can be observed in Figure 4.32

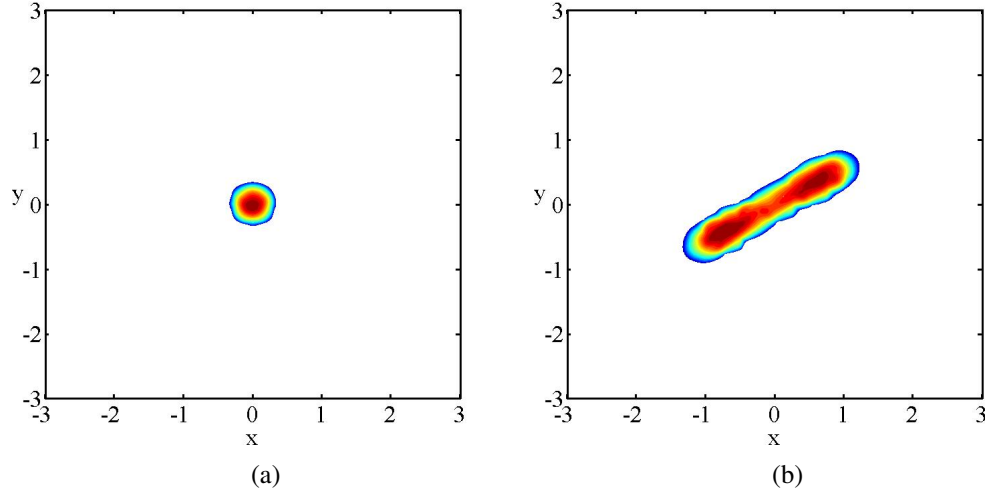


Figure 4.32: Source strength mappings using GWIB for: (a) Single monopole at target grid center (b) Distributed line monopole. Contour levels with 10dB range and 0.5 increment.

Resolution in the single monopole case seems to present a slight increase in dynamic range when compared to the best dynamic range so far, the Suzuki's GIB/IRLS based in the source vector as weighting, and for the line monopole, it presents a concentration closer to the extremes of the line when compared to the GIB/IRLS result mappings. The strength estimations are 1.01 and 1.06 for the single monopole and the line monopole respectively, which indicates a slightly better result to the unitary strengths. In this case, is difficult to define a criteria of stopping the algorithm iterations and define the appropriate mapping when the source is of unknown spread. The use of smaller p-norms in a sequential optimization is recommended in the work of Presezniak (2011), but in these model problems it leaded to unstable and incorrect mappings, possibly due to errors in the calculation of the Jacobian terms influenced by small terms in the source vector. To overcome this difficulty a novel and simple artifice method is proposed.

4.4.4 Stabilized Generalized Weighted Inverse Beamforming

It is observed in the Jacobian calculation for the previous section model problems, that small terms in the source vector could lead to abnormal Jacobian estimations, then affecting the subsequent iteration result with an abnormally increased weighting factor at that source term.

This can be easily avoided if the Jacobian terms related to the source terms smaller than 20dB are nulled, for example. If this approach is used, with three subsequent weighting optimizations using $p = (1/2)^n$ where $n = 0, 1, 2$, on the model chosen problems, results can be obtained as shown in Figure 4.33.

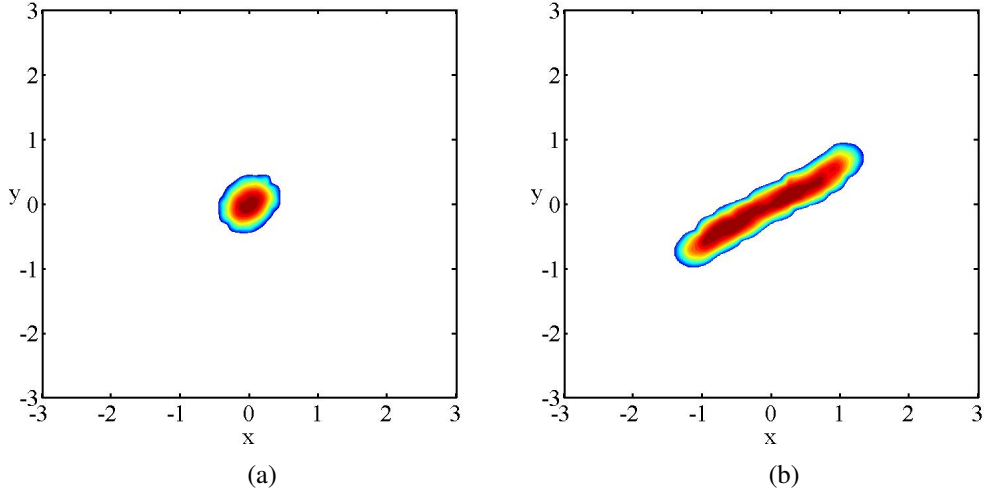


Figure 4.33: Source strength mappings using the stabilized GWIB for: (a) Single monopole at target grid center (b) Distributed line monopole. Contour levels with 10dB range and 0.5 increment.

The distributed line monopole identification is slightly improved, marking more continuously the line. On the other hand, the monopole seems to have lower dynamic range when compared to previous result obtained with $p = 0$. The strengths estimation are 1.17 and 1.08, for the single monopole and line monopole sources respectively. These results indicates a less accurate estimation, remembering that the best norm to represent the linear superposition of radiation would be the $p = 0$, confirmed by the presented results.

In summary, the GWIB present similar results to the IRLS based in source vector as weighting, with the disadvantage that it requires the optimization of the weighting factors after the last iteration of the GIB, used as input to the GWIB. A detailed computational effort analysis is performed at the end of this chapter.

4.5 Improved Generalized Inverse Beamforming

A recent development in the generalized inverse techniques is the Improved Generalized Inverse Beamforming (GINV) by Dougherty (2011). This technique is applied to jet noise

problem and is claimed to improve resolution in case of extended sources, not requiring an eigen-decomposition of the Cross-Spectral Matrix, and by this, less sensitive to non-sparsity in the CSM. The formulation presented has the advantage to relate the conventional beamforming approach to the generalized inverse techniques in a direct equation using the CSM and transfer matrix singular value, its reciprocal and its singular left and right vectors.

The GINV method starts from the assumption that for a slowly-varying in time, block-by-block basis, the average of the microphone signals Fourier transform can be used to build the following system:

$$a = A^+ q, \quad (4.36)$$

where A^+ means the pseudo inverse with Tikhonov regularization, for example; and q is the microphones spectrum matrix. With this, the following equation can be assembled:

$$aa^\dagger = (A^+ q)(A^+ q)^\dagger \quad (4.37)$$

or

$$aa^\dagger = A^+ q q^\dagger A^{+\dagger}. \quad (4.38)$$

Substituting the CSM matrix:

$$aa^\dagger = A^+ R_{CSM} A^{+\dagger}, \quad (4.39)$$

which is the GINV equation. To obtain the source vector, just considering the square root of the

diagonal terms of aa^\dagger is enough.

According to Dougherty (2011), the conventional beamforming equation in matrix formulation can be given by:

$$P_{cb_M} = A^\dagger R_{CSM} A, \quad (4.40)$$

where P_{cb_M} has in its diagonal the auto-powers for each source grid, $P_{cb_M} = aa^\dagger$.

The relationship between the GINV equation and the conventional beamforming is better expressed if the singular value decomposition is applied to the transfer matrix:

$$A = U_s \Sigma V_s^\dagger, \quad (4.41)$$

where U_s is the matrix of left singular vectors; Σ the matrix with singular values; and V_s is the matrix of right singular vectors. The generalized inverse becomes:

$$A^+ = V_s \Sigma^{-1} U_s^\dagger. \quad (4.42)$$

The Equation 4.40 can be reformulated as:

$$P_{cb_M} = V_s \Sigma U_s^\dagger R_{CSM} U_s \Sigma V_s^\dagger, \quad (4.43)$$

while the expression for GINV can be reformulated as:

$$aa^\dagger = V_s \Sigma^{-1} U_s^\dagger R_{CSM} U_s \Sigma^{-1} V_s^\dagger. \quad (4.44)$$

This shows that the only difference between the methods, conventional and GINV, are the use of the singular values non-reciprocal or reciprocal, respectively (apart from possible normalization differences in the transfer matrix build).

To illustrate the dynamic range and localization in case of distributed sources the single monopole and the distributed line source model problems from literature are again used. The regularization adopted is the Tikhonov with regularization factor squared calculated as 5% of the greatest eigenvalue of AA^\dagger . Results are shown in Figure 4.34.

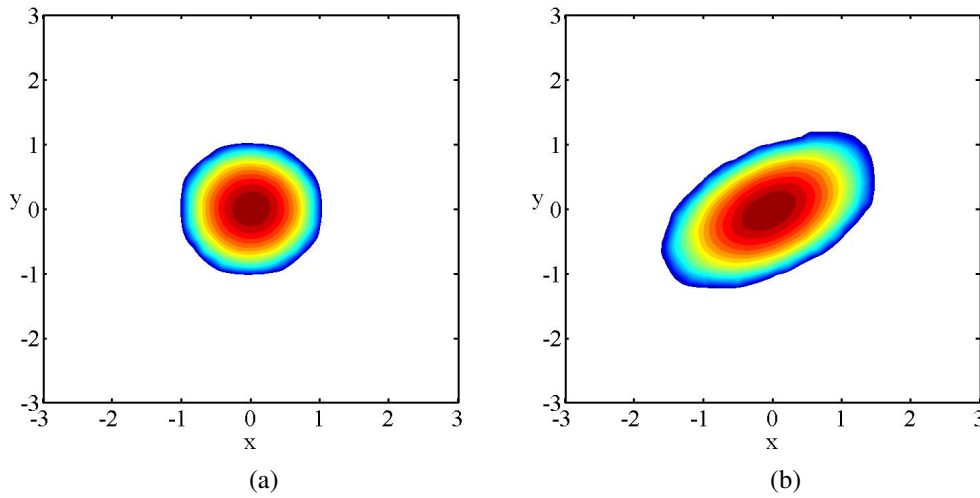


Figure 4.34: Source strength mappings using GINV for: (a) Single monopole at target grid center (b) Distributed line monopole. Contour levels with 10dB range and 0.5 increment.

It is clear from the mappings that is achieved a much better dynamic range when compared to the conventional beamforming, but they present a worst dynamic range than GIB (Figures 4.4 and 4.6). In fact, they approximately corresponds to the mappings obtained if the GIB equations are used to calculate only the first source vector, no truncation. Results for the first calculation in the GIB are shown in Figure 4.35.

Even then, the results for GIB in the first calculation present a smoother mapping and slightly

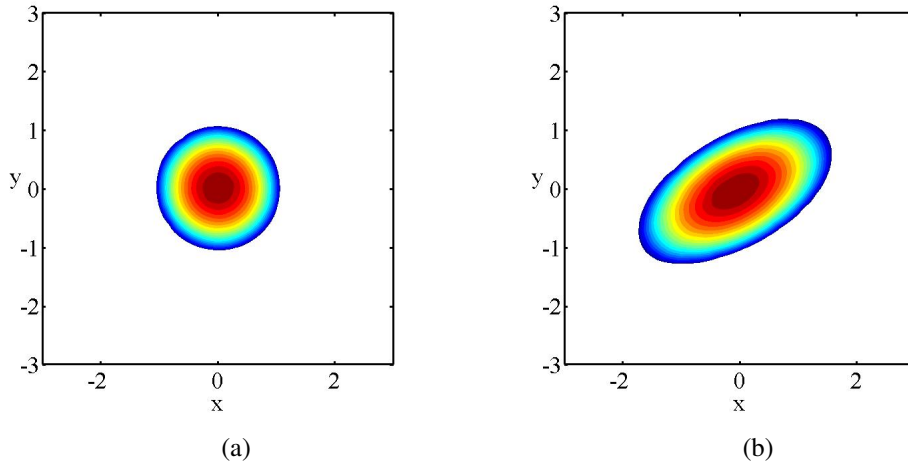


Figure 4.35: Source strength mappings using GINV for: (a) Single monopole at target grid center (b) Distributed line monopole. Contour levels with 10dB range and 0.5 increment.

better in dynamic range too. The strength estimations for the GINV are 1.09 and 1.04, for the single monopole and the line monopole, respectively, and they can be considered reasonably accurate estimations, but worst than GIB (with truncations). The performance of this method in terms of comprising multiple incoherent responses in one single evaluation is performed later in the aeroacoustic applications chapter.

The localization could be enhanced if the truncation process used in the GIB is applied with the GINV, but very similar results are expected, and the differences would be caused mainly by the consideration of the eigenmode in the GIB instead of the full CSM in the GINV.

4.6 Computational Effort Analysis

The objective in this section is to provide an overview of the necessary computational effort involved in the use of each of the described methods: GIB; GIB/IRLS; GWIB; and GINV; as well as the state-of-the-art methods: CLEAN and DAMAS2; compared to the conventional beamforming and using a reference identification problem, the single monopole case from literature (SUZUKI, 2008). The objective is not to provide a full, and in depth analysis for computationally optimized procedures, since the implementation used is not optimized for that purpose but for research of different methods and specific test cases. The analysis brings the overall time consumed for each of the methods using the CB as basis, as well as a breakdown in each method, for the time spent in preparation, calculation, iteration step when applicable, and post-processing (including

visualization and reports generation).

The first comparison is the total time consumed, comparing the CLEAN-PSF, DAMAS2, GIB using a fixed regularization factor and the GIB with the optimized regularization strategy, shown in Table 4.6.

	CB	CLEAN-PSF	DAMAS2	GIB (fix.reg.)	GIB (opt.)
Time	100%	113%	101%	145%	177%

Table 4.6: Time spent on calculations for the monopole problem.

The first observation is that CLEAN and DAMAS2 have very similar effort than conventional beamforming, which is expected. The GIB method takes approximately half to 3/4 more time than CB, for the fixed and optimized regularization, respectively. Considering that these methods use iterative procedures, this impact in time would be expected to be higher, but if we analyze each calculation phase in more detail, shown in Table 4.9, is clear that the processing calculation proportion increases significantly, from 4% in CB to 60% in GIB with optimization. So, the overall time impact by the use of iterative methods is smaller if considered together with the pre and post-processing time, despite that the post-processing in the GIB doesn't requires any special feature when compared to CB.

	CB	CLEAN-PSF	DAMAS2	GIB (fix.reg.)	GIB (opt.)
Pre-processing	18 %	16 %	18 %	17 %	15 %
Processing	4 %	6 %	5 %	52 %	60 %
Post-processing	78 %	78 %	77 %	31 %	25 %

Table 4.7: Time spent on calculations phases for the monopole problem.

Another comparison is made for CB to all GIB methods described previously in this Chapter, GIB/IRLS, GWIB, and GINV, and results are presented in Figure 4.8. The results for the GIB/IRLS with source vector or residue as weighting are considered as with the same algorithm effort for simplification, and using a fixed regularization with 8 iterations, it approximates in time, to the GIB with fixed regularization but with 32 iterations. The GWIB, which uses the optimized regularization strategy until the 8th iteration and the weighting optimization afterwards, is similar to the GIB with optimized regularization strategy with 32 iterations. The GINV is the fastest,

but remembering that its results is equivalent to use the GIB with only one calculation, and less accurate than GIB with 32 iterations.

	CB	GIB (fix.reg.)	GIB (opt.)	GIB/IRLS	GWIB	GINV
Time	100%	145%	177%	154%	174%	120%

Table 4.8: Time spent with GIB methods on calculations for the monopole problem.

The processing steps proportions for the GIB methods, shown in Figure 4.9, confirms the increase in the main processing phase, but weighted schemes presented less impact than expected, which could be analyzed as an important decision factor to the use of these methods, with no or insignificant impact in total computational effort.

	CB	GIB (fix.reg.)	GIB (opt.)	GIB/IRLS	GWIB	GINV
Pre-processing	18 %	17 %	15 %	16 %	15 %	18 %
Processing	4 %	52 %	60 %	57 %	61 %	11 %
Post-processing	78 %	31 %	25 %	27 %	24 %	71 %

Table 4.9: Time spent with GIB methods on calculations phases for the monopole problem.

These comparisons done for a single monopole can hide important differences in computational effort when more complex problems are considered, such as distributed sources, multiple radiation type sources, or multiple incoherent sources scenarios. This would require an analysis with respect to accuracy and computational effort, and is beyond the scope of this preliminary study. A more detailed analysis on some of these cases is discussed later in Chapters with Aeroacoustic problems and Moving source problems.

4.7 Summary

The GIB methods have superior performance when compared to CB and the state-of-the-art methods, CLEAN and DAMAS2, with a small penalty in computational effort, for the reference problems from literature. Between the GIB methods, the weighted inverse methods are important developments in dynamic range, but they still lack in a clear metric to support the decision to stop iterations and define the correct strength, demanding a higher judge skill by the analyst.

The GIB/IRLS with residue as weighting is a novel contribution, and presented a slightly better mapping when compared to the other weighted methods, but in general they can be considered as with similar results. The generalized inverse beamforming techniques are receiving important contributions to its development, and improvements to its accuracy and reliability for this latest developments are demonstrated in these simple examples. A deeper performance analysis for GIB methods is performed in the next Chapter.

The GINV present worse results than the original GIB for the chosen literature reference problems, but this is expected since it has been created for non-sparse problems, according to the original author.

5 Experimental Identification Using Compact Sources

Generalized Inverse Beamforming is a relatively new method, and little is known about its performance and requirements. In this Chapter, numerical and experimental tests are confronted using compact sources and a 30 microphones spiral array in a semianechoic room. Results are compared for cases of single monopole and two monopoles in coherent radiation (in phase and in anti-phase). With two monopoles in anti-phase, an induced dipole is also identified experimentally, recovering radiation center and main axis direction. Strength estimations are compared to the numerical and experimental identifications as well as to eigenvalue based strength estimation. A novel method, Hybrid Estimation, is also presented, combining the estimation obtained by conventional beamforming to generalized inverse beamforming to improve accuracy and reliability. These investigations generated three presented conference papers and two articles (one under review), cited along text.

5.1 Identification with Optimized Regularization Strategy

A promising recent development on acoustic source localization and source strength estimation is the Generalized Inverse Beamforming, which is based on the microphone array cross-spectral matrix eigen-structure. This method presents several advantages over the conventional beamforming, including a higher accuracy on the source center localization and strength estimation even with distributed coherent sources. This paper aims to improve the strength estimation of the generalized inverse beamforming method with an automated regularization factor definition. Also in this work, a virtual target grid is introduced, and source mapping and strength estimation are obtained disregarding, as much as possible, the reflections influence. Two simple problems are used to compare the generalized inverse performance with fixed regularization factor to performance obtained using the the optimized regularization strategy. Numerical and experimental data are used, and two other strength estimation methods are also evaluated for reference.

5.1.1 Introduction

This section applies the optimized regularization strategy also in experimental identification and is reported in (ZAVALA *et al.*, 2011D). The strategy is based on the search of the minimum of the regularization residue for each algorithm iteration. This means that the best source map fit

is used on each algorithm iteration. The strategy also provides the identification of the optimum strength estimation along the iterations, which represents the best source map fit along the iterations, or truncations of the source map.

This section also proposes a simple method to calculate direct and indirect source strength in the presence of reflections using the generalized inverse beamforming by the adoption of a virtual grid. This virtual grid is positioned on the source image "location", and the respective contributions are then separated from the direct contribution.

These two proposals are used on two problems: A single monopole radiation; and Two monopoles radiation in in-phase radiation. Numerical and experimental data are used, and results for the generalized inverse beamforming using fixed regularization factors on the limits proposed on literature are compared to the optimized strategy. Numerical analysis is initially presented for the free-field condition, and since the experimental data is obtained in semi-anechoic environment, with hard floor reflections, numerical analysis is also performed with a secondary source region placed symmetrically in respect to ground floor to simulate the reflections.

Two reference strength estimations are used in comparison to the generalized inverse results, the cross-spectral matrix eigenvalue based estimation, and a direct analytical based estimation. The analytical estimation is presented to demonstrate the nature of the eigen-value based estimation.

5.1.2 Test Setup and Problem Cases Details

The array used consists of a 30 microphones 6-arm spiral distribution. The array aperture is 2m in diameter and the distance from the array to the source plane is 2.5m. The experiments are conducted in a semi-anechoic room, and measurements are carried-out with compact sources emitting sine wave at 1kHz. On the two monopoles test, the compact sources are positioned two wavelengths from each other, horizontally aligned, and in-phase signal input.

The target grid points are chosen to cover ± 3 wavelengths in a regular pattern around the source location (origin), in the x-y plane (parallel to array plane) with a grid spacing equal to $1/4$ of the wavelength. The grid distribution adopted in this work is similar to the grid adopted by Suzuki (2008) on his model problems. The array sensors position, target grid points, and the experimental setup overview are shown in figure 5.1.

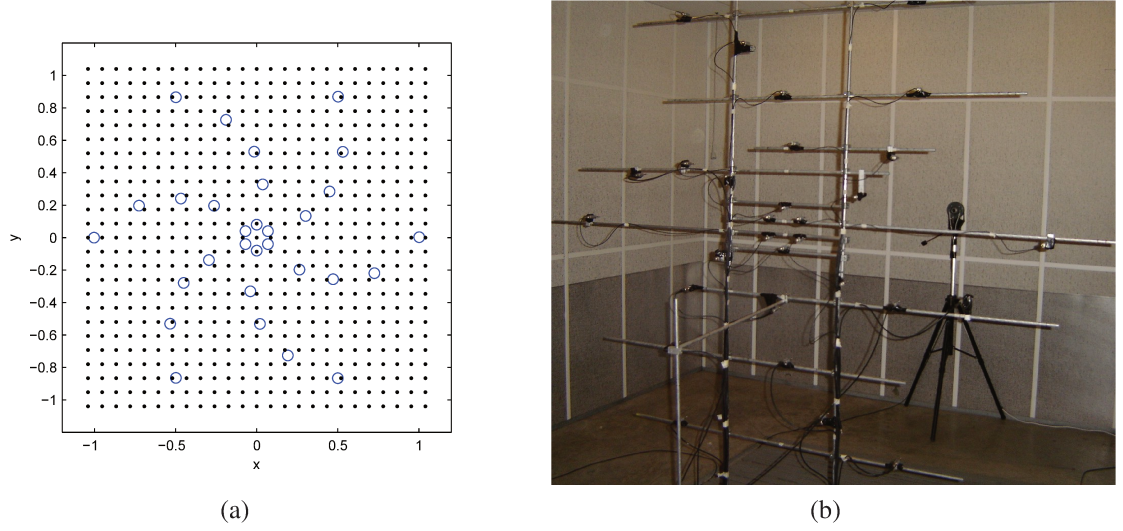


Figure 5.1: (a) Microphone array (circles) and target grid (dots); (b) Experimental setup: Array of microphones and single source configuration.

The measurements are conducted using a simultaneous acquisition system, and the sampling frequency was set to 20.48kHz, also used on the numerical simulations. Time blocks with 1024 samples are used to obtain the strength estimations and mappings.

For the numerical simulations, source responses on microphones are created using the analytical radiation equation, and noise is added according to the same strategy used by Suzuki (2008) on his model problems, but a factor of 10% is adopted to simulate a less aggressive noise and bring a more compatible noise distribution when compared to the measured noise in the semi-anechoic room. Numerical simulations considered a unitary source strength for each compact source, and experimental signals are normalized to unitary sources by considering the averaged analytical response at the array microphone locations. Figure 5.2 shows the normalized eigenvalue distribution for one and two monopole cases. Eigenvalues are normalized by $(\rho ck)^2$ and presented results have unit of m^4/s^2 .

The eigenvalue distribution indicates that only one significant source distribution is present on the data, for all tests, one monopole and two monopoles. The remaining and least significant eigenvalues demonstrate a low level of noise on the experiments and on the simulated signals. Another observation is that the main eigenvalues present a higher level on experimental and on the numerical with reflections results, compared to the numerical free-field result for both tests, one monopole and two monopoles. This is related to the presence of the reflections on the tests.

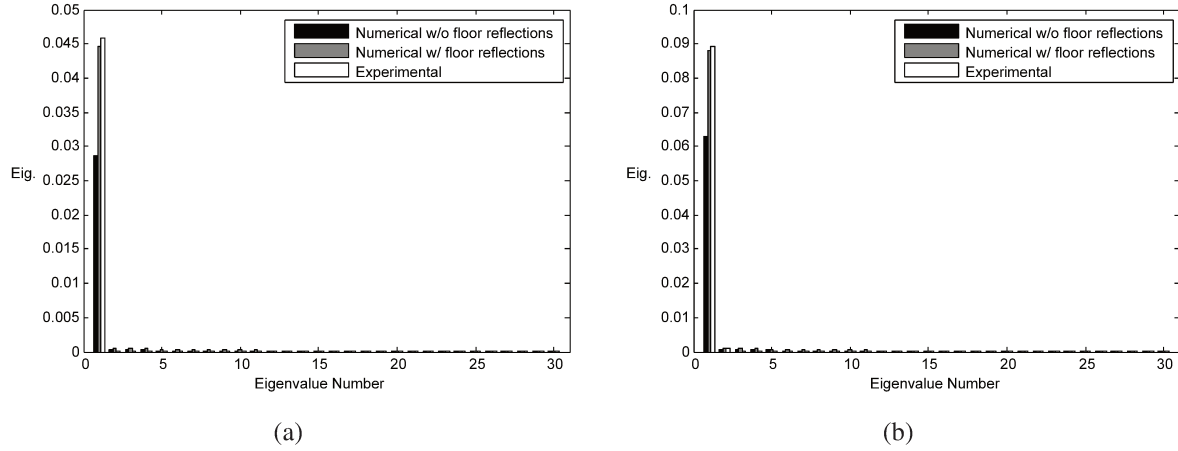


Figure 5.2: Eigenvalues distribution: (a) One Monopole (b) Two Monopoles.

5.1.3 Eigenvalue Based Strength Estimation

Cross-spectral matrix eigenvalue based strength estimation is a recent method to assess source strengths present in the measured array signals. The eigenvalues are related to the source strength according to the following equation (MUELLER, 2002):

$$\lambda_i = C^2 M Q_{eig,i}^2 + h, \quad (5.1)$$

where C is the propagation factor, M is the number of sensors, $Q_{eig,i}$ is the source strength, and h is the signals non-coherent noise strength, which can be assumed as the least significant eigenvalue (MUELLER, 2002).

Considering a monopole radiation as described below (MORSE, 1948):

$$Press = \rho c k \frac{a_{mono}}{4\pi r} e^{-jkr}, \quad (5.2)$$

where a_{mono} is the monopole source strength, r is the distance from the source to each sensor, and k , the wavenumber. The propagation factor shown in equation (5.1) for a unitary monopole

source is described as:

$$C = \frac{\rho c k}{4\pi r} . \quad (5.3)$$

The eigenvalue based estimation for a unitary source strength monopole can be described as:

$$Q_{eig,i} = \sqrt{\frac{(4\pi r)^2(\lambda_i - h)}{(\rho c k)^2}} . \quad (5.4)$$

One of the limitations on the source strength estimation based on the cross-spectral matrix eigenvalues is that it is an overall estimation. On the case of indirect contribution from reflections, for example, this estimation is no longer able to differentiate direct from indirect strength contributions. This limitation is illustrated through the problems in this work. Another limitation is the sensitivity to close sources and radiation interferences over the microphone array signals, leading to incorrect overall estimations on these cases.

5.1.4 J_1 Cost Function Comparison

On this section, the J_1 cost functions obtained for the proposed regularization strategy are compared to the fixed regularization factors, using the limits of 0.1% and 5%. Examples of the J_1 cost function progress along iterations for the numerical simulation considering a free-field condition, are shown in figure 5.3, for the one monopole and two monopoles cases.

The first observation is that the cost function minimum is reached at different iteration number for each regularization strategy adopted, optimized and the fixed ones. All of them arrives to a similar cost function value, but only the optimized strategy present a more stable behavior around the minimum. The higher regularization factor present the smoother curve, and the lower factor, the more irregular one. In general, the optimized seems to be an intermediate value between these two curves.

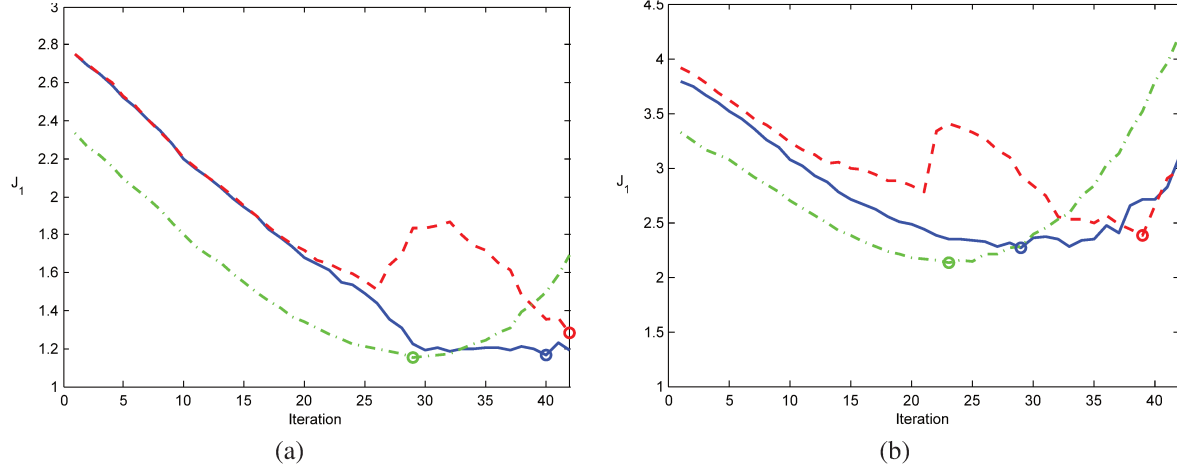


Figure 5.3: J_1 cost function for the numerical test in free-field condition: (a) One Monopole (b) Two Monopoles. Optimized: solid; Lower limit: dashed; Higher limit: dash dot. Curve minimum at circle.

On figure 5.4, the cost functions obtained on the numerical simulations considering reflections are presented. Again, the optimized strategy presents a more stable behavior around it's minimum. But, the addition of reflections on the numerical test seems to require a higher regularization factor, since the curve related to the optimized strategy is now closer to the upper regularization factor limit. The experimental tests cost functions are shown in figure 5.5.

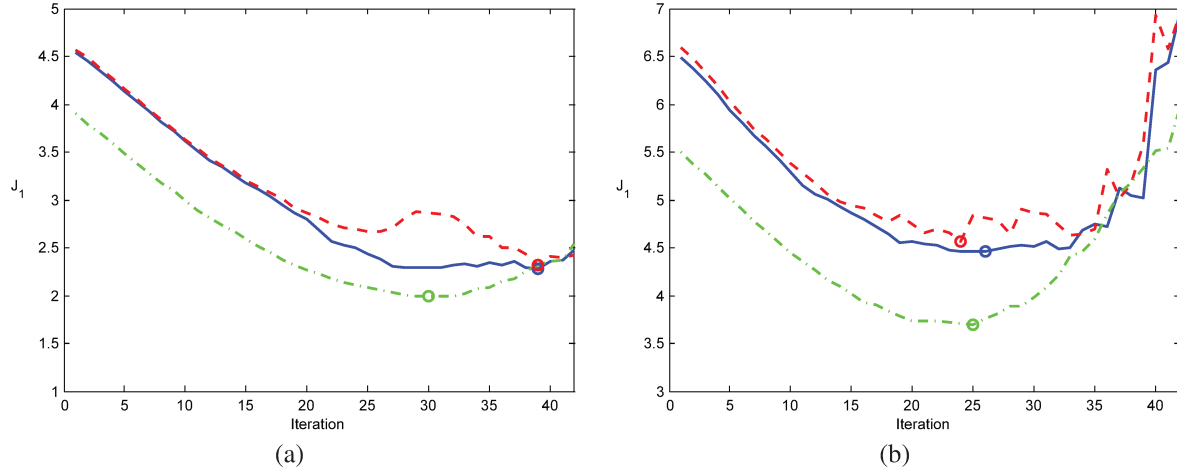


Figure 5.4: J_1 cost function for the numerical test including reflections: (a) One Monopole (b) Two Monopoles. Optimized: solid; Lower limit: dashed; Higher limit: dash dot. Curve minimum at circle.

Now, the optimized regularization strategy presents an equivalent behavior as to adopt the upper limit of fixed regularization factor. This means that the experimental data strength calculation

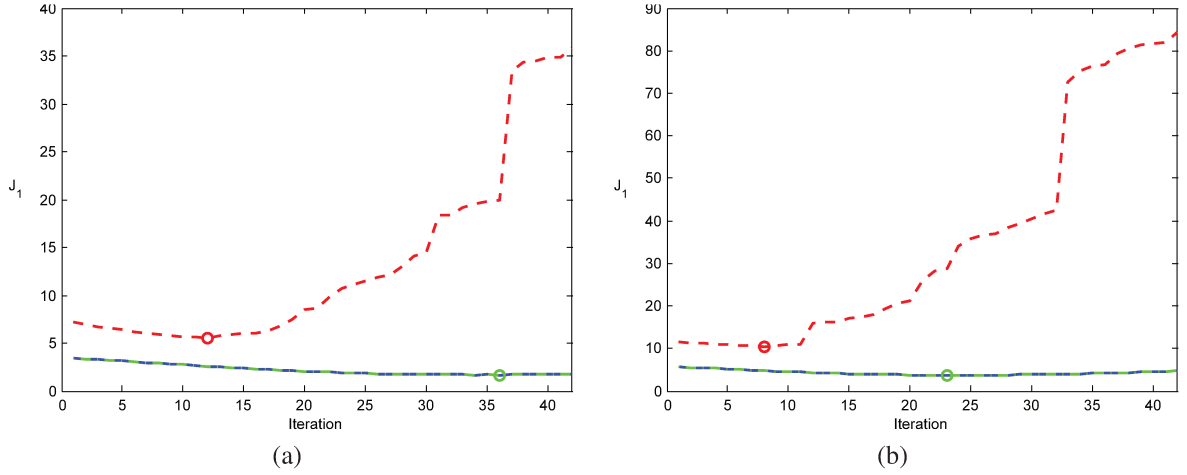


Figure 5.5: J_1 cost function for the experimental test: (a) One Monopole (b) Two Monopoles. Optimized: solid; Lower limit: dashed; Higher limit: dash dot. Curve minimum at circle.

required a bigger regularization. The adoption of a small regularization factor led to a higher residue, which explain the high values achieved for this cost function. Another observation is that very similar behavior is observed in both test cases, one monopole and two monopoles, both requiring a high regularization factor.

5.1.5 Squared Strength Mappings Comparison

Mappings are obtained after averaging of 10 estimations, and each estimation calculated at the J_1 cost function minimum. For the numerical simulation in free-field condition, the results for the fixed and the optimized strategy are shown on figures 5.6 to 5.8. The amount of terms left on the source vector depends on the number of iterations where the cost function minimum is found.

The mappings for the numerical simulation including reflections are presented on figures 5.9 to 5.11. The mappings on the numerical predictions with reflections are very similar to the free-field predictions. The small differences can be attributed to the cost function minimum being reached in a different iteration. The adoption of a virtual grid on the numerical simulation with reflections present results that are effective in neglect the reflections from the ground.

The experimental mappings are shown on figures 5.12 to 5.14. The experimental results calculated at the cost function minimum, for each strategy, optimized and fixed, shows that the adoption of the lower limit of regularization brings the experimental algorithm search to a minimum

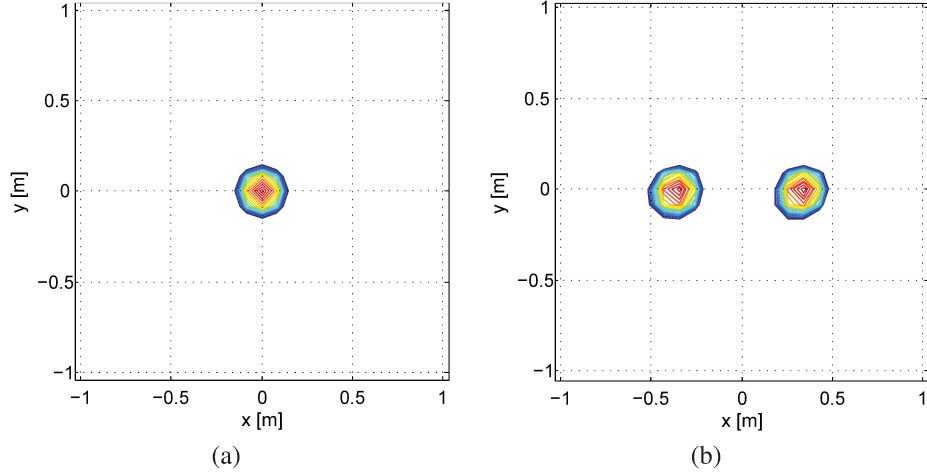


Figure 5.6: Squared strength mapping for the numerical test in free-field condition using the regularization factor at the lower limit: (a) One Monopole (b) Two Monopoles (contour lines are in 10 dB range with 0.5 dB increment).

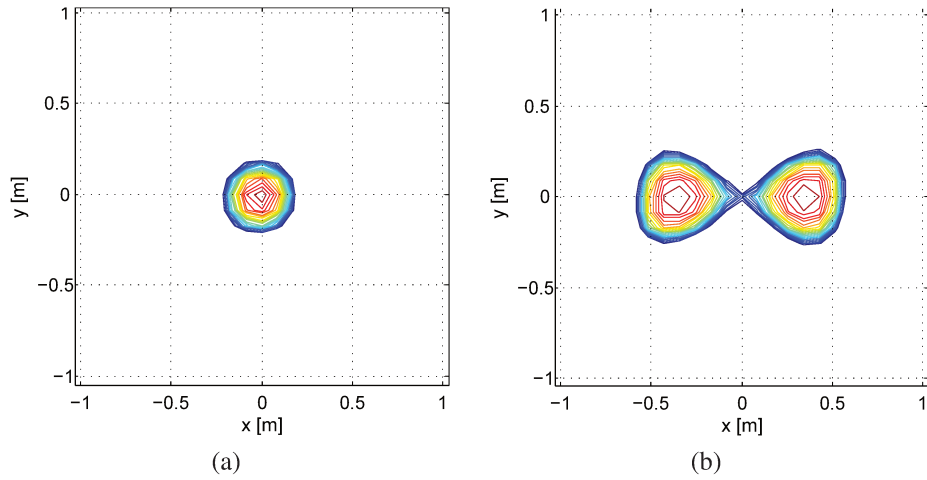


Figure 5.7: Squared strength mapping for the numerical test in free-field condition using the regularization factor at the higher limit: (a) One Monopole (b) Two Monopoles (contour lines are in 10 dB range with 0.5 dB increment).

with a small number of truncations, leading to a mapping with a high number of terms. The best mapping on this case is obtained with the upper regularization limit which coincides with the optimized strategy. The mappings obtained at the cost function minimum are the ones that best represent the source distribution, also being related to the best compromise between the calculated strength vector and the system residue.

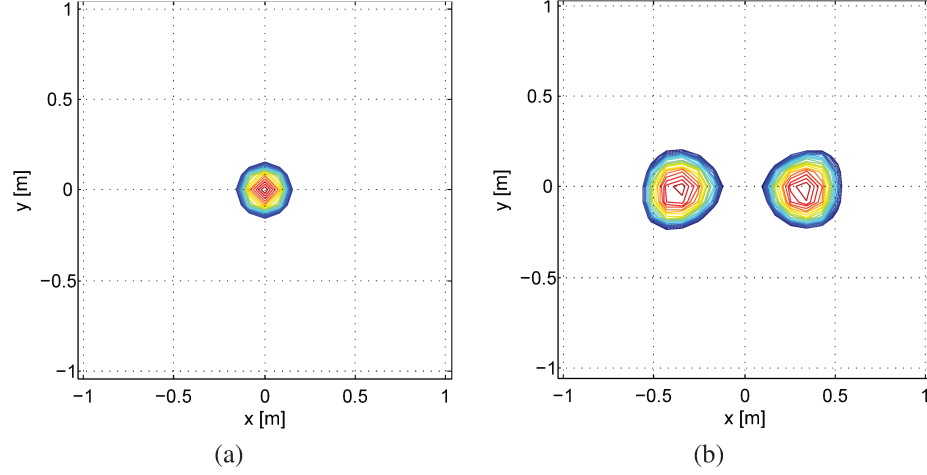


Figure 5.8: Squared strength mapping for the numerical test in free-field condition using the optimized regularization factor: (a) One Monopole (b) Two Monopoles (contour lines are in 10 dB range with 0.5 dB increment).

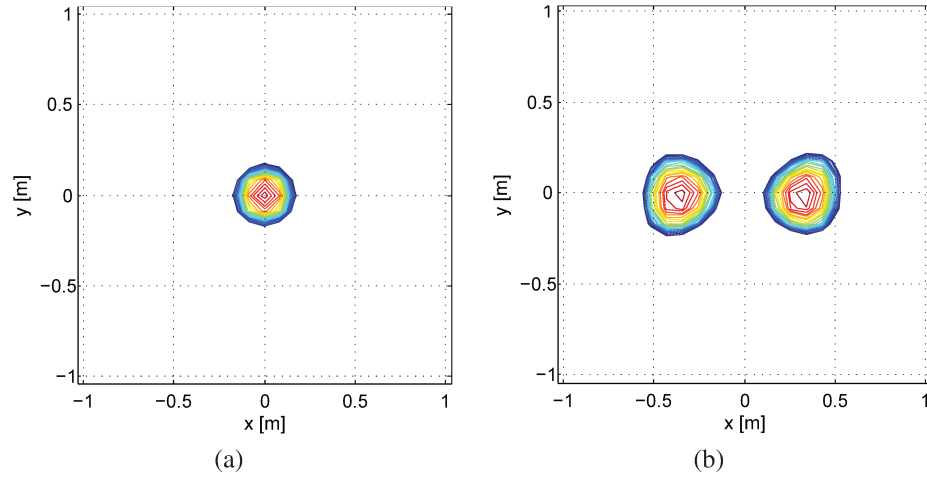


Figure 5.9: Squared strength mapping for the numerical test including reflections using the regularization factor at the lower limit: (a) One Monopole (b) Two Monopoles (contour lines are in 10 dB range with 0.5 dB increment).

5.1.6 Strength Estimations Comparison

In order to compare the strength estimation retrieved by the generalized inverse method, the eigenvalue based estimation equation is rewritten as:

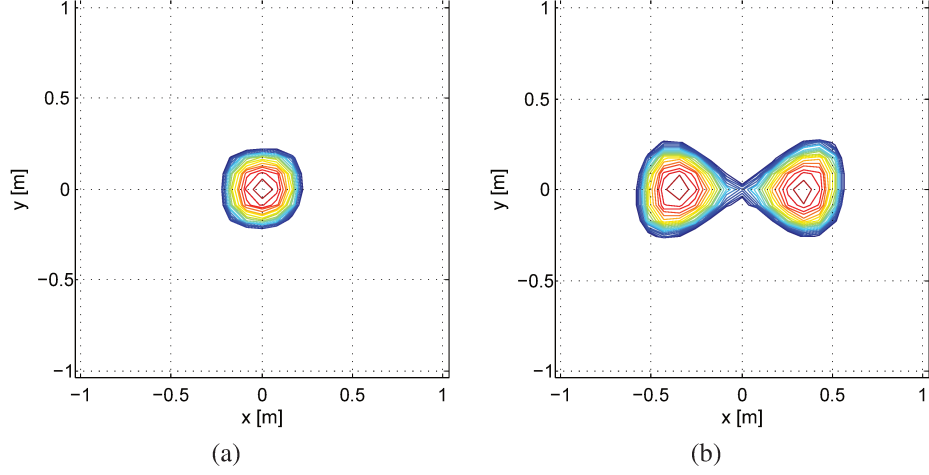


Figure 5.10: Squared strength mapping for the numerical test including reflections using the regularization factor at the higher limit: (a) One Monopole (b) Two Monopoles (contour lines are in 10 dB range with 0.5 dB increment).

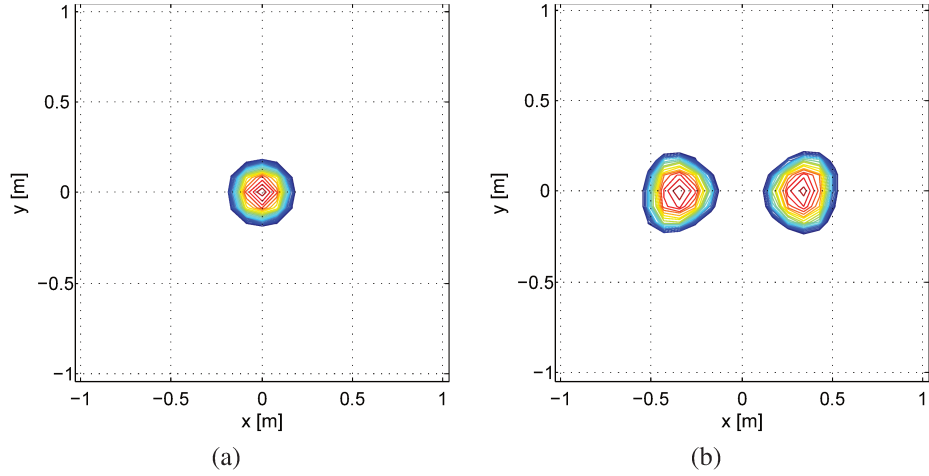


Figure 5.11: Squared strength mapping for the numerical test including reflections using the optimized regularization factor: (a) One Monopole (b) Two Monopoles (contour lines are in 10 dB range with 0.5 dB increment).

$$Q_{eig,i} = \sqrt{\frac{(4\pi r_{mean})^2 (\lambda_i - h)}{M(\rho ck)^2}}, \quad (5.5)$$

where r_{mean} is the average of sensor distances to the target grid center.

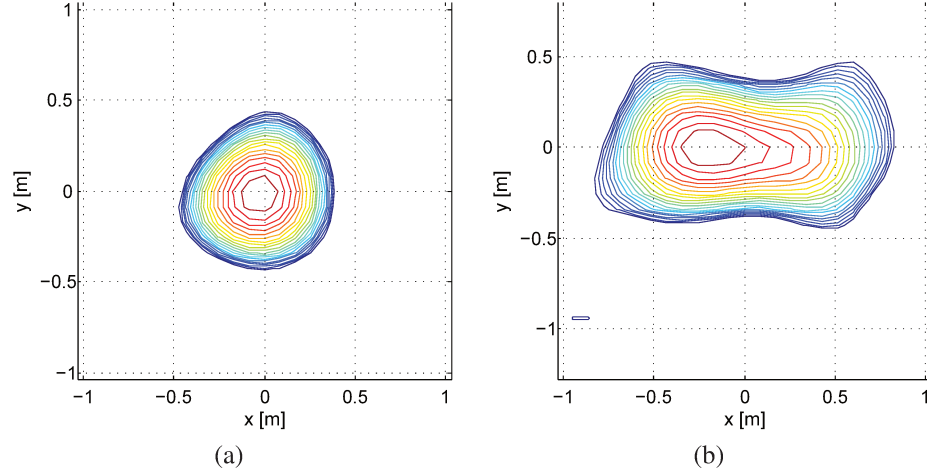


Figure 5.12: Squared strength mapping for the experimental test using the regularization factor at the lower limit: (a) One Monopole (b) Two Monopoles (contour lines are in 10 dB range with 0.5 dB increment).

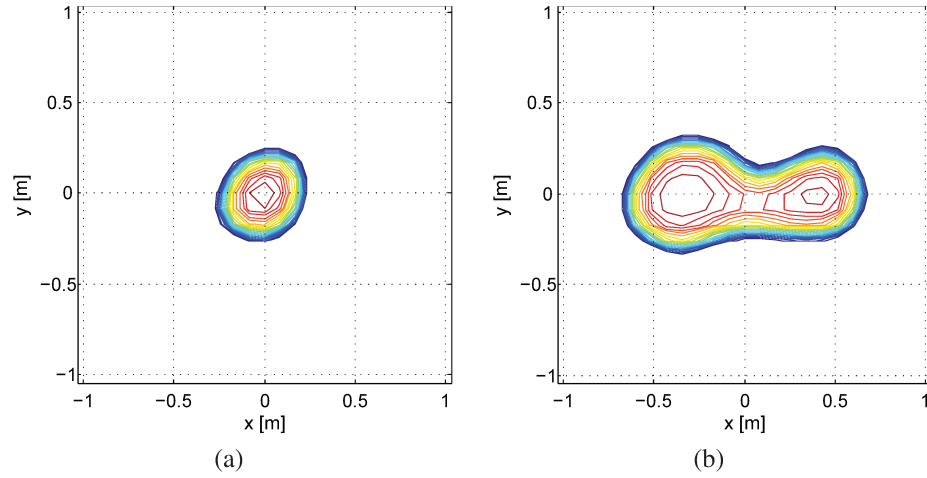


Figure 5.13: Squared strength mapping for the experimental test using the regularization factor at the higher limit: (a) One Monopole (b) Two Monopoles (contour lines are in 10 dB range with 0.5 dB increment).

Another estimation, a direct analytical source strength estimation, is also introduced. This direct source strength calculation is based on the averaged sensor signal power. The analytical radiation equation for a unitary strength source at the target grid origin is used to simulate the sensors' readings for the monopole case, and two unitary sources for the two monopoles case.

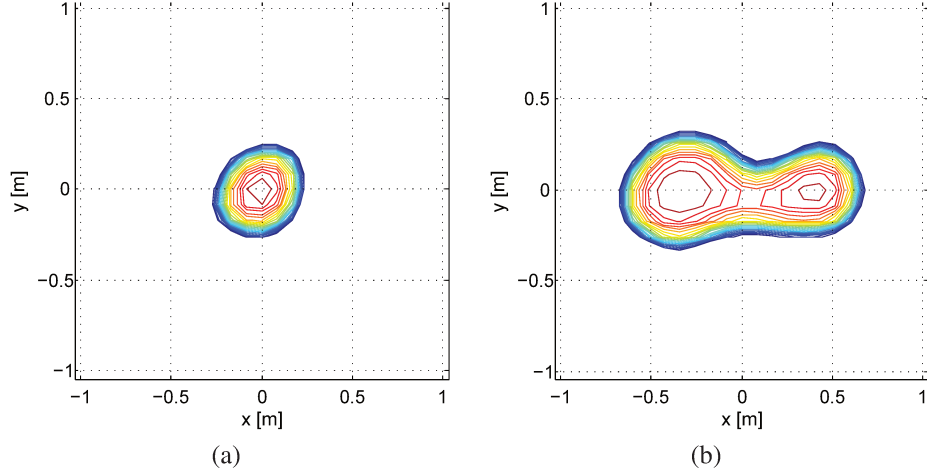


Figure 5.14: Squared strength mapping for the experimental test using the optimized regularization factor: (a) One Monopole (b) Two Monopoles (contour lines are in 10 dB range with 0.5 dB increment).

The direct calculation for the one monopole case can be described by the equation below:

$$Q_{dir} = \frac{(4\pi r_{mean})^2}{M} \sum_{n=1}^M \left(\frac{1}{4\pi r_n} e^{-jkr_n} \right)^2, \quad (5.6)$$

where Q_{dir} is the direct strength, with unit of m^3/s .

The direct calculation presented for the experimental test case, uses the measured signals strength instead of the analytical prediction.

On the case of reflections on the ground, the analytical direct calculation is shown on the following equation:

$$Q_{dir} = \frac{(4\pi r_{mean})^2}{M} \sum_{n=1}^M \left(\frac{1}{4\pi r_n} e^{-jkr_n} \right)^2 + \frac{(4\pi r_{v,mean})^2}{M} \sum_{n=1}^M \left(\frac{1}{4\pi r_{v,n}} e^{-jkr_{v,n}} \right)^2, \quad (5.7)$$

where, the virtual position, r_v , corresponds to the image source location, below the ground,

and $r_{v,mean}$ corresponds to the average distance from the image source and the sensors position.

The analytical radiation equation used for two unitary sources with 2 wavelengths distance from each other can be described by the equation below for the free-field condition:

$$Q_{dir} = \frac{(4\pi r_{l,mean})^2}{M} \sum_{n=1}^M \left(\frac{1}{4\pi r_{l,n}} e^{-jkr_{l,n}} \right)^2 + \frac{(4\pi r_{r,mean})^2}{M} \sum_{n=1}^M \left(\frac{1}{4\pi r_{r,n}} e^{-jkr_{r,n}} \right)^2, \quad (5.8)$$

where $r_{l,n}$ is the distance from each sensor to the source located on the left, and $r_{r,n}$ is the distance from each sensor to the source located on the right, $r_{l,mean}$ and $r_{r,mean}$ are average distances for left and right sources, respectively.

On the case of reflections on the floor, the direct analytical calculation adds the contribution from the image sources in similar approach as adopted in equation (5.7).

The strength estimations for the one monopole case are shown in comparison in table 5.1. The generalized inverse beamforming results are the average of 10 estimations retrieved at the J_1 cost function minimum of each estimation. The three regularization strategies used are shown, the minimum and maximum regularization factor limits and the proposed optimized strategy.

Test	Q_{dir}	Q_{eig}	$Q_{\alpha_{min.}}$	$Q_{\alpha_{max.}}$	$Q_{\alpha_{optimized}}$
Numerical without reflections	1	1	1.02	0.89	1.01
Numerical with reflections	1.56	1.56	1.02	1.05	1.02
Experimental	1.60	1.60	1.75	0.77	0.77

Table 5.1: Source strength estimation comparison for the monopole at origin case and different methods: direct; eigenvalue based; regularization factor at minimum limit; regularization factor at maximum limit; and optimized regularization strategy.

The first observation is that the direct and the eigenvalue based strength estimations have similar results, indicating that the eigenvalue based estimation is in fact, an averaged signal power estimation. Another observation considering these two estimate methods, is that the experimental data present results that are very close to the numerical results. However, these two estimations, direct and eigenvalue based, are highly influenced by the presence of reflections, and both fail to

estimate the source strength, on this case, a unitary strength, as found in the free-field calculations.

Among the generalized inverse estimations, the optimized regularization strategy presents the best result, even with the presence of reflections. The optimized strategy seems to approximate to the lower or the upper regularization limit, but in an automated process. The results for the two monopoles case are shown in table 5.2.

Test	Q_{dir}	Q_{eig}	$Q_{\alpha_{min.}}$	$Q_{\alpha_{max.}}$	$Q_{\alpha_{optimized}}$
Numerical without reflections	2.15	2.20	2.00	1.71	2.00
Numerical with reflections	3.04	3.07	2.20	2.26	2.13
Experimental	3.09	3.14	3.20	1.98	1.98

Table 5.2: Source strength estimation comparison for the two monopoles case and different methods: direct; eigenvalue based; regularization factor at minimum limit; regularization factor at maximum limit; and optimized regularization strategy.

On the case of two monopoles, similar observations can be done for the direct and eigenvalue based estimations as done for the one monopole case, and all these estimations fail to retrieve the actual combined source strength on the case of reflections from the ground.

The generalized inverse beamforming using the proposed optimized strategy presents the best strength estimation result among all approaches. The optimized strategy result for the numerical free-field condition is the best approximation.

The experimental result is close to the actual combined source strength. Again showing a good agreement of the experimental result to the numerical prediction, both considering a virtual grid to differentiate the direct from the image source contributions.

5.1.7 Summary

The problems discussed in this section, a single monopole and two monopoles in-phase, demonstrate that the optimized regularization strategy used on the generalized inverse beamforming retrieves the best strength estimation even without prior information on the problem. This is verified, numerically and experimentally, for the overall strength estimation and also for the source center localization.

The results shown in the work from Zavala *et al.* (2011d), also illustrate an important advantage of the generalized inverse method in estimating combined source strength despite of interferences on sensor signals. This advantage on accurate combined source estimation, along with the possibility to calculate the strength on partial regions, allows the adoption of a virtual target grid, and estimates can then be obtained for direct and indirect source radiation on the presence of reflections or on the presence of other undesired sources in the measurement area, and open a wide range of engineering applications. This artifice don't require a priori knowledge of the undesired sources, but only the possible reflection regions, and their contribution is then identified and separated from the region of interest.

5.2 Generalized Inverse Beamforming Investigation and Hybrid Estimation

In this section, the performance of the GIB method is investigated for two simple cases in comparison to conventional beamforming (ZAVALA *et al.*, 2010B). This section is a preliminary investigation in regards of two characteristics: The frequency range for a monopole identification; and the localization accuracy for two compact sources in coherent radiation. The results are presented for the generalized inverse beamforming and the conventional beamforming. In the end, a hybrid approach is proposed to illustrate the correspondence between the generalized inverse beamforming and the conventional beamforming. The hybrid estimation gives a secondary estimation that can be used to assess the quality of the generalized inverse beamforming.

5.2.1 Introduction

The first test case, a simple monopole, illustrates the frequency range accuracy, and the second test case, two monopoles in coherent radiation, illustrates the different performance in coherent scenarios. Numerical investigation is used to define the test array aperture and distance to the target region. In order to improve the generalized inverse estimation on the coherent case, a new hybrid estimation is proposed. This consists in creating a source mapping that is comparable to the conventional mapping based on the generalized inverse mapping and the array Point Spread Function. The offsetting between the hybrid mapping and the conventional mapping indicates the quality of the generalized inverse estimation and the hybrid estimation points to the actual sources overall strength. This confirms the consistency of the generalized inverse algorithm in preserve the relevant source information even after truncation of the initial source vector.

5.2.2 Monopole at Origin

This first example is used to illustrate the performance in identification in terms of frequency range. But first, numerical tests are used to define the appropriate array configuration in terms of aperture and distance to the target plane. The array configuration is a 6-arm spiral layout, similar to the array used on (SUZUKI, 2008), but with 30 microphones, the same used in previous section. The target grid points distribution adopted in this work is similar to what is adopted in (SUZUKI, 2008) for the numerical models tests, target grid range is 6 wavelengths, and spacing is $1/4$ of a wavelength, again the same as previous section. The generalized inverse algorithm is stopped after the source vector reaches a minimum size of 21 terms. All results are average of 5 estimations. Estimations used signal blocks with 1024 samples.

The numerical tests for a unitary strength 1kHz monopole source in free-field located at the target grid center, varying the array aperture and distance to target, is shown in table 5.3. The source signal included noisy according to the same strategy used by Suzuki (2008), but with a factor of 0.5 to have a less aggressive noise and comparable to what is found in the experiments. The sampling frequency covered 10 wavelengths per block.

		Distance to Target in wavelengths						
		1	2	5	10	15	20	50
Aperture in wavelengths	1	1.05	1.00	0.96	0.96	0.96	0.96	0.96
	2	1.18	1.02	0.98	0.96	0.96	0.95	0.95
	4	1.69	1.36	1.00	0.99	0.97	0.96	0.96
	6	1.77	1.55	0.99	0.99	0.98	0.97	0.96
	8	1.83	1.51	1.26	0.99	0.99	0.98	0.96
	10	1.82	1.60	1.40	1.00	0.99	0.98	0.96
	12	1.74	1.72	1.49	1.02	1.00	0.99	0.96
	14	1.80	1.71	1.47	1.09	1.01	0.99	0.97

Table 5.3: Estimations varying array distance and aperture.

According to the results, good estimates (with error less than 10%) are found with ratio between the distance to the aperture starting around on 1. It is clear from the results, that estimates can be done as close as 1 wavelength, and in general, ratios above 1 generates good estimates. For convenience, the ratio for the experiments was chosen to 1.25, and tests done with spiral at 2.5m

distance to the source, and aperture diameter of 2m. The chosen microphones positioning and test configuration for the monopole testing can be observed in Figure 5.1 from previous section.

For the chosen configuration, numerical tests are performed varying the source frequency, from 100Hz to 5kHz. The results are presented on figure 5.15.

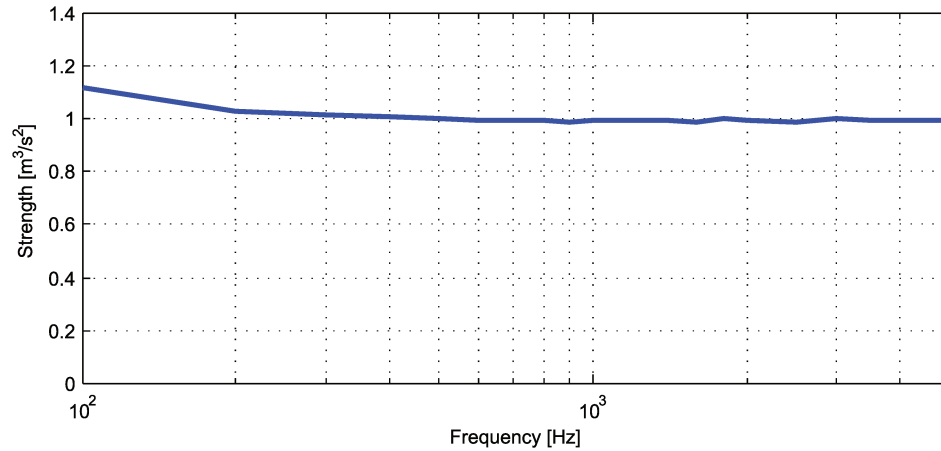


Figure 5.15: Estimations varying radiation frequency for a unitary monopole source.

Estimations above 100Hz are expected to have more accurate results, with error smaller than 10%, according to the numerical simulations. This result already demonstrates the broad frequency range of this method, the generalized inverse beamforming.

Three frequencies are chosen for the experiments. The source mappings for a unitary source at 200Hz, 1kHz, and 5kHz, are presented, respectively, in figures, 5.16, 5.17, and 5.18, for conventional beamforming and the generalized inverse beamforming methods. Acquisition uses 20.48kHz sampling rate for the 200 and 1kHz tests, and 102.4kHz for the 5kHz test.

From the results, is observed that the conventional beamforming is not capable to locate source at 200Hz, while the generalized inverse beamforming produces a mixed identification with the reflections on the floor, considering that the source was located at approximately 1.6m from the ground.

For the 1kHz result, it is clear the advantage of the generalized inverse beamforming in dynamic range, presenting the source location with 10dB range with around 1/2 wavelength radius, compared to the conventional beamforming result of around 1 wavelength radius.

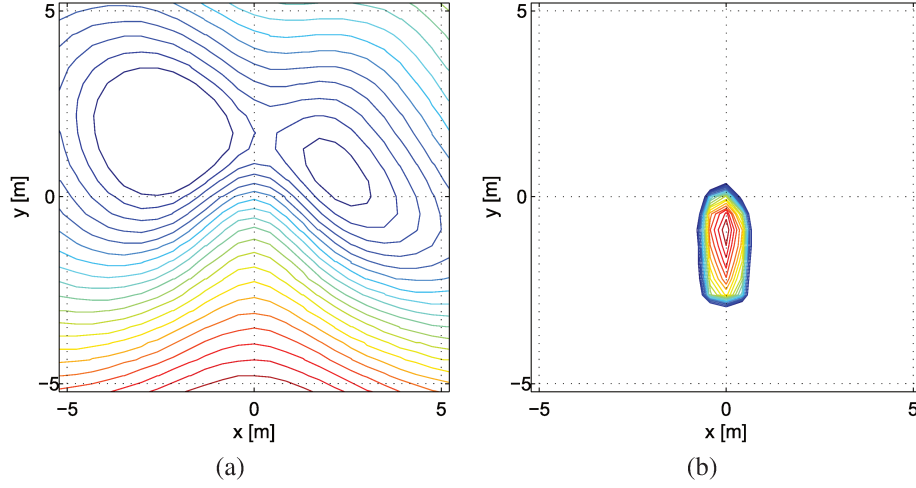


Figure 5.16: Monopole with 200Hz radiation: (a) Conventional beamforming (b) Generalized inverse beamforming (contour lines are in 10 dB range with 0.5 dB increment).

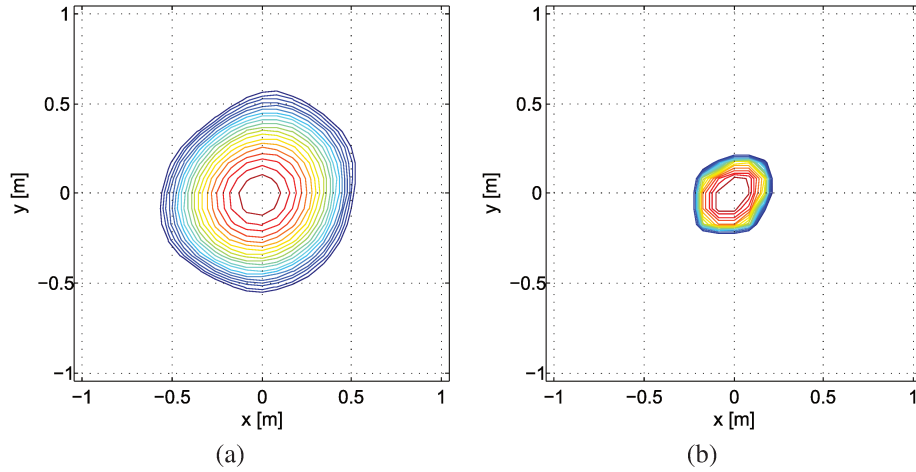


Figure 5.17: Monopole with 1kHz radiation: (a) Conventional beamforming (b) Generalized inverse beamforming (contour lines are in 10 dB range with 0.5 dB increment).

For the 5kHz source radiation case, both methods present a source center, but the higher dynamic range for the generalized inverse beamforming is also clear. Both results indicate a small offset for the source center, and this is attributed to the array positioning errors, with estimated offset of about 30mm from the correct location, which is low compared to the test involved dimensions.

The generalized inverse mapping present a spurious peak on the range of 10dB, and this also can be explained by the array positioning error. The expected limitation to go beyond 5kHz is only the array positioning error. The generalized inverse mapping can be observed on top of the photo of the source in figure 5.19.

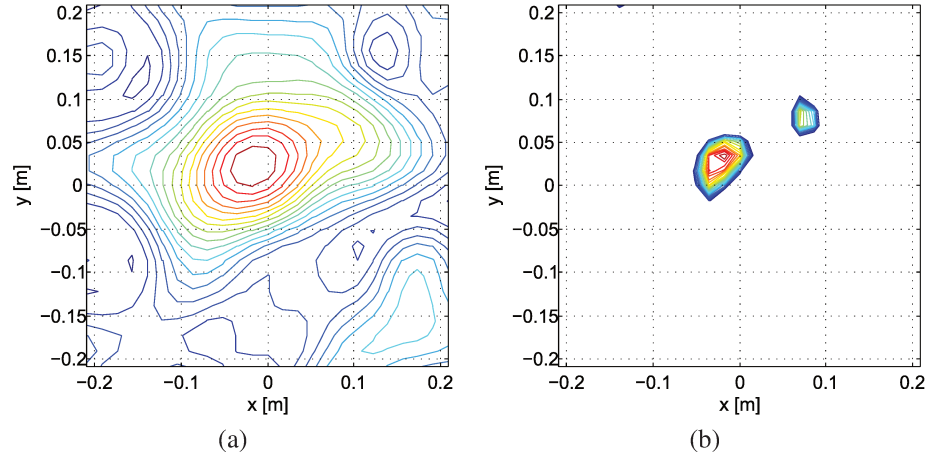


Figure 5.18: Monopole with 5kHz radiation: (a) Conventional beamforming (b) Generalized inverse beamforming (contour lines are in 10 dB range with 0.5 dB increment).

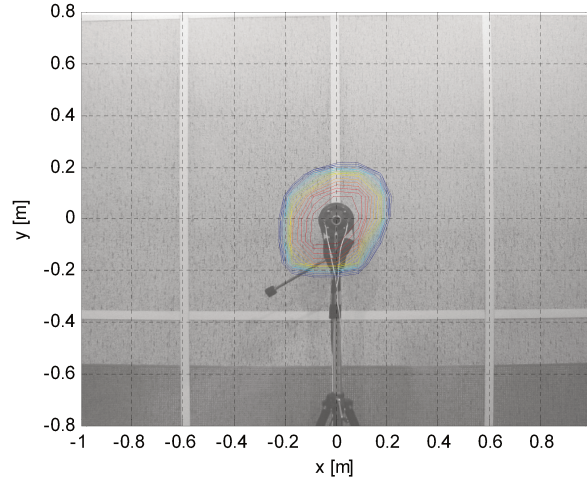


Figure 5.19: Monopole with 1kHz radiation (mapping on top of photo): Generalized inverse beamforming (contour lines are in 10 dB range with 0.5 dB increment).

The strength estimations for the conventional beamforming and the generalized inverse beamforming are presented in table 5.4. The results for the conventional beamforming are calculated at the maximum value on the mapping.

The generalized inverse beamforming present more accurate or similar estimations than conventional beamforming for all three tested frequencies. This indicates that the generalized inverse beamforming has a broader frequency range in respect to lower frequencies. For higher frequencies, the indication is that estimations are affected by the same amount of error for both

Frequency	Conventional beamforming	Generalized inverse beamforming
200Hz	2.10	1.06
1kHz	1.11	0.92
5kHz	0.63	0.63

Table 5.4: Source strength estimations for three different frequencies.

methods. A better microphone positioning accuracy is expected to enhance results for higher frequencies.

5.2.3 Two Monopoles In Coherent Radiation

Now, to illustrate the generalized inverse superior performance in coherent scenarios, a simple test using two compact sources separated by two wavelengths is used. The sources are set to radiate in-phase at 1kHz. The array configuration, aperture, distance to target plane, target grid range, and target grid spacing, are all the same as on previous example.

The mappings for the conventional beamforming and generalized inverse beamforming are presented in figure 5.20.

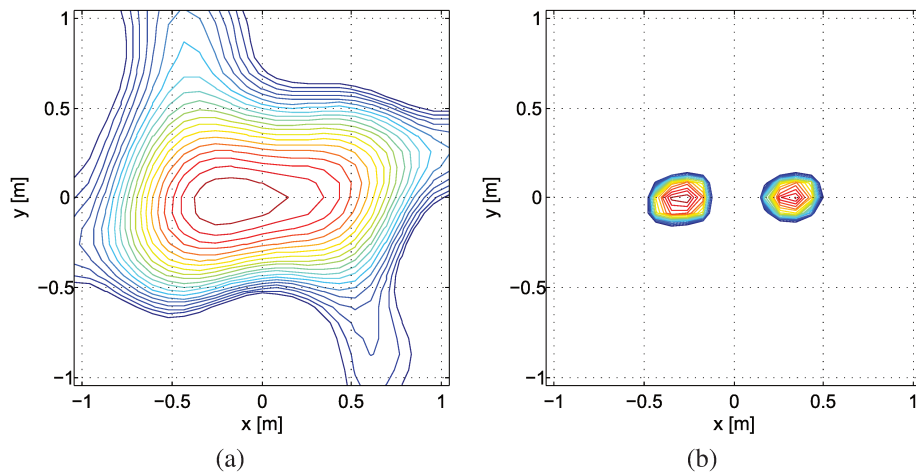


Figure 5.20: Two monopoles in-phase with 1kHz radiation: (a) Conventional beamforming (b) Generalized inverse beamforming (contour lines are in 10 dB range with 0.5 dB increment).

Is clear from the results that the generalized inverse beamforming is capable to identify two monopole sources, and that the conventional beamforming does not present a clear identification.

The number of terms on the source vector is still 21 terms, and this leads to a reduced radius than $1/2$ wavelength for the 10dB range, since the 21 terms are now distributed in two sources. The conventional beamforming asymmetric result could be related to the array distribution, with peak closer to the region with more microphones. The generalized inverse mapping can be observed on top of the photo of the sources in figure 5.21.

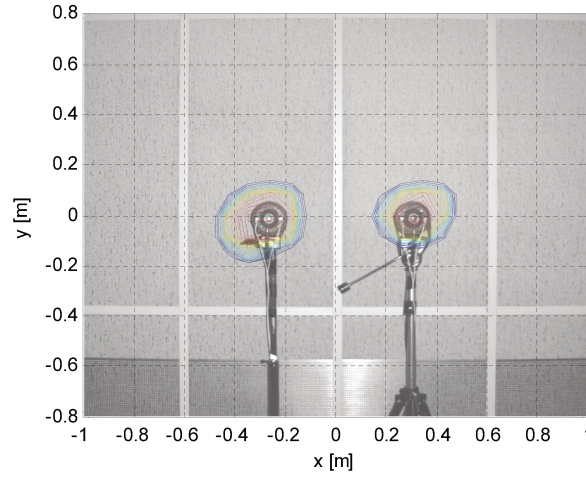


Figure 5.21: Two monopoles in-phase with 1kHz radiation (mapping on top of photo): Generalized inverse beamforming (contour lines are in 10 dB range with 0.5 dB increment).

The estimations are presented on table 5.5. The conventional beamforming result is obtained at the mapping peak.

Frequency	Conventional beamforming	Generalized inverse beamforming
1kHz	1.26	1.41

Table 5.5: Strength estimations for two monopoles in-phase example.

The result for the generalized inverse beamforming is the best approximation to the expected response, $Q = 2$. But still not accurate enough, and an improved methodology is required.

5.2.4 Hybrid Estimation

Conventional beamforming is based on the delay & sum principle, and can be stated as shown in the equation below:

$$P_{cb} = w^\dagger R_{CSM} w, \quad (5.9)$$

where w is the vector with the weighting factors (or delays).

The estimation retrieved by conventional beamforming is equivalent to a directional microphone with the same dynamic characteristics of the Point Spread Function of the array. The Point Spread Function can be described by the equation below:

$$PSF_s = |w^\dagger w_s|^2, \quad (5.10)$$

where w_s is the weighting vector related to source at the point, s .

The conventional beamforming is a robust estimation technique, with signal to noise ratio improved according to the number of microphones on the array. The hybrid estimation is based in the conversion of the generalized inverse mapping, using the array point spread function, to an equivalent mapping. This process takes advantage of the more accurate source mapping from the generalized inverse method, and the less sensitive to noise conventional mapping. The conversion is described as:

$$P_{Hybo} = \left| \sum_{j=1..N_{grid}} a_{ij} PSF_{oj}^{\frac{1}{2}} \right|^2, \quad (5.11)$$

where P_{Hybo} is the power or strength (depending on the unit of a_i) at a particular target grid point, o . This expression relate the directional sensitivity of the conventional method by its

PSF to the source distribution from the GIB, producing a degraded localization, but now directly comparable to the conventional beamforming straight result.

On figure 5.22 is shown the original generalized inverse beamforming from the two monopoles in coherent radiation example, and the array Point Spread Function for the grid center.

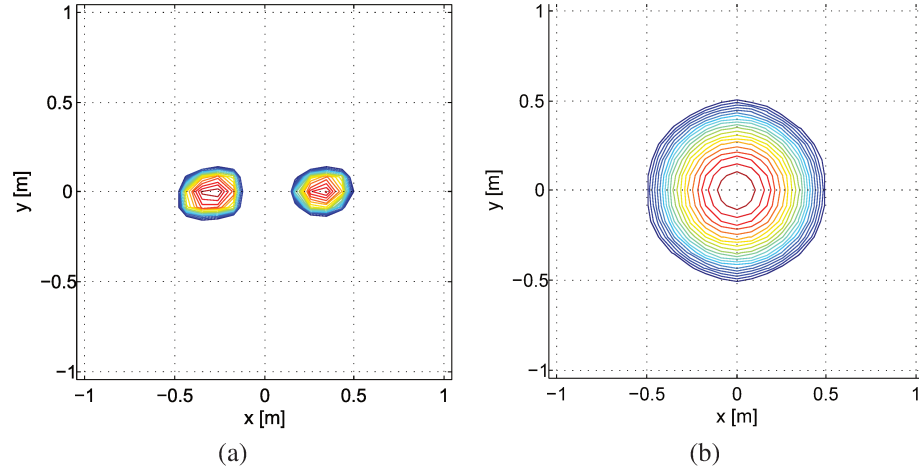


Figure 5.22: (a) Two monopoles in-phase with 1kHz radiation, generalized inverse beamforming (b) Array Point Spread Function for the grid center (contour lines are in 10 dB range with 0.5 dB increment).

This converted mapping, or hybrid mapping, is then compared to the conventional mapping, and the averaged strength offsetting is used to estimate the difference between the two mappings.

In figure 5.23, the conventional mapping for the two monopoles case and the hybrid mapping is presented.

The similarity between the two mappings is clear from the results. However, since the generalized inverse mapping is a distributed mapping, there is an expected difference from the hybrid mapping to the conventional mapping. This is caused by the point spread function being applied to a distributed source mapping, and the sum over this results is lower than the actual source strength multiplied by the point spread function at the source center location. Or, in other words, if the generalized inverse mapping would be a concentrated source mapping instead of the distributed, the hybrid mapping would be equal to the conventional mapping.

The offsetting between the conventional mapping and the hybrid mapping, when applied to the generalized inverse results, lead to a mapping that is the closest approximation to the original

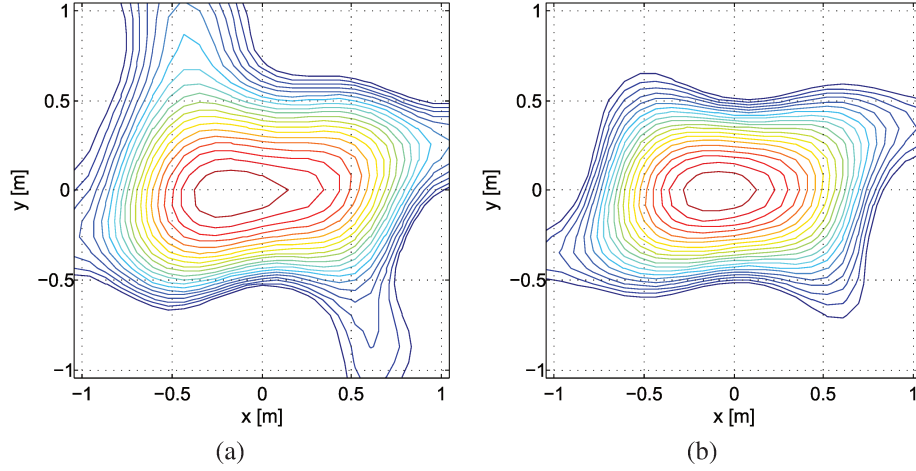


Figure 5.23: Two monopoles in-phase with 1kHz radiation: (a) Conventional beamforming (b) Hybrid mapping based on the generalized inverse beamforming (contour lines are in 10 dB range with 0.5 dB increment).

conventional mapping. This offsetting when added to the generalized inverse results, includes the error due to the distributed nature of the generalized inverse beamforming. Causing the hybrid estimation to be an overestimation of the source mapping. The proposal here is that the hybrid offsetting is a limit of probable estimation, and the best approximation would be an intermediate value between the original generalized inverse estimation and the value with added offsetting. On table 5.6, the generalized inverse estimation, hybrid offsetting and the hybrid estimation estimation, are presented.

Generalized inverse beamforming	Offsetting [%]	Hybrid estimation
1.41	48	2.08

Table 5.6: Generalized inverse and hybrid estimation for the two monopoles example.

Even considering that the hybrid estimation is closer to the combined source strength, $Q = 2$, it has inherent error due to the distributed nature of the generalized inverse mapping. Another aspect is that the conventional beamforming estimation also has some errors related to the presence of noise on the measurements. This two aspects, explains the remaining gap from the hybrid estimation to the actual combined source strength. Taking these aspects into consideration, the hybrid offsetting certainly indicates the quality of the generalized inverse beamforming estimation by comparison to the conventional beamforming, and certainly points to the range of a more

accurate estimation.

5.2.5 Summary

The investigations used a 6-arm spiral array configuration, and two cases of monopole sources: One monopole at target grid center; and two monopoles in coherent radiation. The first test case is used to illustrate the array characteristics, array aperture and distance to target grid, influence on estimation, and also the frequency range accuracy in estimation and mapping.

Some characteristics can be pointed out from the investigation performed. First, that using the 6-arm spiral configuration, a ratio about one or higher, between the distance from the array to the source target plane, and the array aperture, leads to an accurate monopole source strength estimation. Even with the array as close as one wavelength from the target plane, the generalized inverse method is capable to give an accurate estimation.

The investigation performed also demonstrated the superior performance on frequency range for localization of a compact source, with a broader low frequency range in respect to mapping. This is an important advantage of the generalized inverse method since one of the drawbacks on the conventional beamforming is the restricted low frequency accuracy.

The second test example, two monopoles in coherent radiation, is used to illustrate the higher accuracy on coherent scenarios in locating source centers compared to the conventional beamforming. The higher dynamic range on the generalized inverse method allowed the individual source center detection while the conventional beamforming is not able to locate the individual source centers.

Despite the estimation using the generalized inverse method being already more accurate than the conventional beamforming on the presented case, a new method is applied to the generalized inverse result, and a hybrid estimation between the conventional beamforming method and the generalized inverse method, presented. This hybrid estimation points to the region of a more accurate estimation, and indicates the quality of the original generalized inverse method's result.

These findings confirm the potential of the generalized inverse beamforming method to be used in more complex problems, with advantages such as: broader frequency range; lower array

distance limit to region of interest, with respective lower array size; higher spatial accuracy in coherent cases; accurate source strength estimation; and the possibility to apply a less sensitive to noise estimation, the hybrid estimation.

5.3 Monopole and Dipole Identification Using Generalized Inverse Beamforming

Aeroacoustic problems pose some challenges to the conventional techniques normally used to source localization and identification. The main difficulties are that sources are normally distributed, with coherent and incoherent regions, and with simultaneous mono and multipole radiation patterns. Among the most recent ones, the Generalized Inverse Beamforming method has the promise to meet these challenges. In this work, reported in (ZAVALA *et al.*, 2010C), the potential for identification of compact sources in close vicinity, similar to a distributed source, and the potential to identify a dipole center and orientation, induced by two compact sources, are illustrated in two no-flow tests.

5.3.1 Introduction

This section investigate for simple problems using monopole sources the performance of the generalized inverse beamforming technique in comparison to the conventional beamforming technique as found in Pillai (1989). Results obtained in semi-anechoic room are compared to numerical predictions. The objective of the present work is the development of a simple reference configuration for the performance evaluation of the generalized inverse beamforming technique in identifying close in-phase monopole sources, and in detecting an induced dipole by two monopoles in anti-phase. With this comparison some of the method limitations and potentials will be outlined. This validation is a preparation for the application of the method to aeroacoustic problems.

5.3.2 Two Monopoles in-Phase

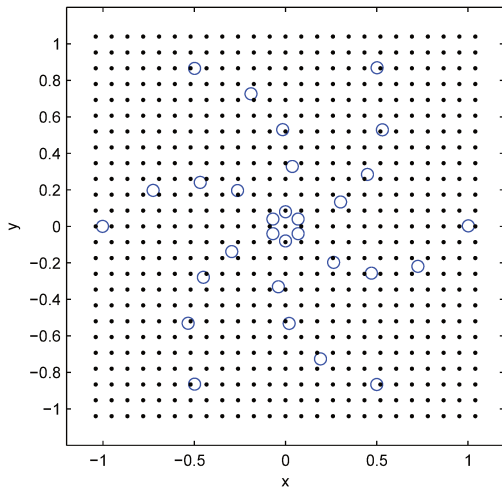
The first set of problems intend to investigate the potential of the generalized inverse beamforming compared to the conventional beamforming in identifying two coherent compact sources located in the close vicinity of each other. In addition to the experimental results, numerical tests are conducted to reproduce the experimental scenario for both the free-field and semi-anechoic

results.

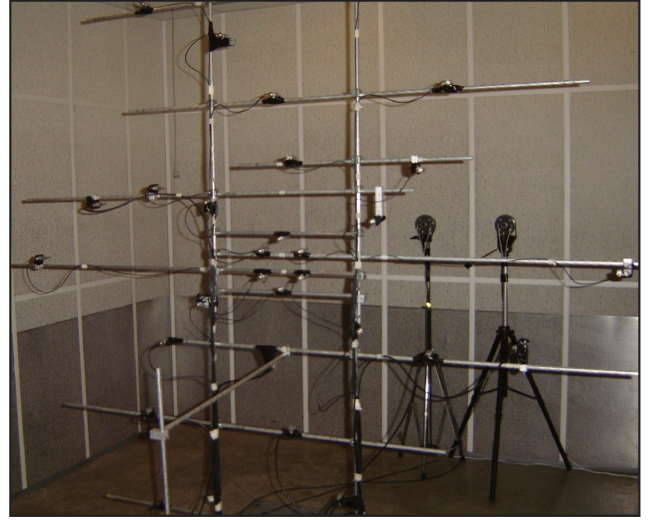
The main test characteristics are an array with 30 microphones distributed in a 6-arm spiral configuration, Figure 5.24a; Sources radiation frequency of 1kHz and with a distance of $3/2$ wavelength from each other; Array distance to sources plane of 2.5m; and array aperture of 2m diameter. Simultaneous acquisition with 20.48kHz sampling frequency is adopted, and 1024 time samples used for each estimation.

The results are averages over 10 estimations. In the numerical predictions, noise is included, similar to what is used in the model problem section in Suzuki (2008).

The target grid region is chosen as ± 3 wavelengths from the origin, with an interval width of $1/4$ of wavelength. Figure 5.24a shows the array sensors positions and target grid points distribution.



(a)



(b)

Figure 5.24: (a) Microphone array (circles) and target grid positions (dots); (b) Experimental setup.

At first, the sources are positioned horizontally. On figure 5.25 the conventional beamforming mapping and the generalized inverse beamforming mapping for the numerical free-field condition are presented. All generalized inverse results presented in this work are obtained for 32 iterations. For the monopole source identification, this corresponds to 21 remaining terms in the source vector. From this result, it is clear that conventional method fails to identify the individual source centers compared to the generalized inverse results, where the source centers are clearly depicted.

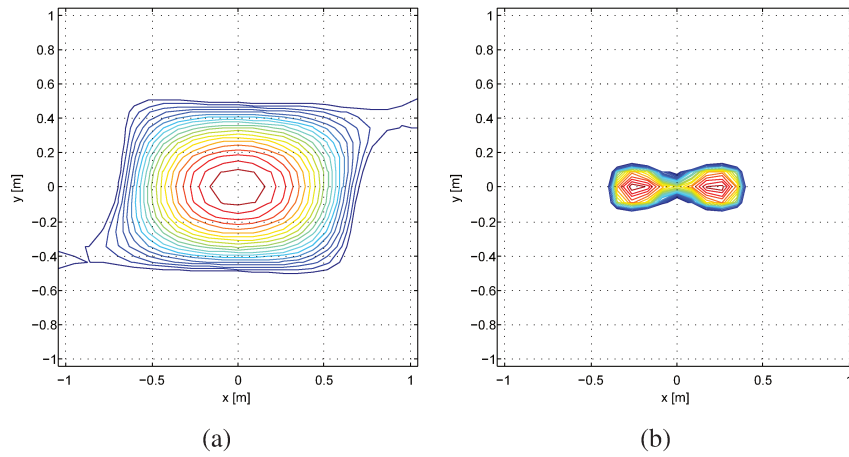


Figure 5.25: Two monopoles in-phase free-field (numerical results): (a) Conventional beamforming; (b) Generalized inverse beamforming (Countour lines are in 10 dB range with 0.5 dB increment).

Including floor reflections in the numerical set-up (shown in figure 5.26), the conventional beamforming shows an even more concentrated source peak detection. In this case, the generalized inverse beamforming also presents a single peak region instead of locating the individual source centers. This indicates that the method is rather sensitive to reflections for this sources proximity. Nevertheless, the generalized inverse method identifies with high power the region of the source centers.

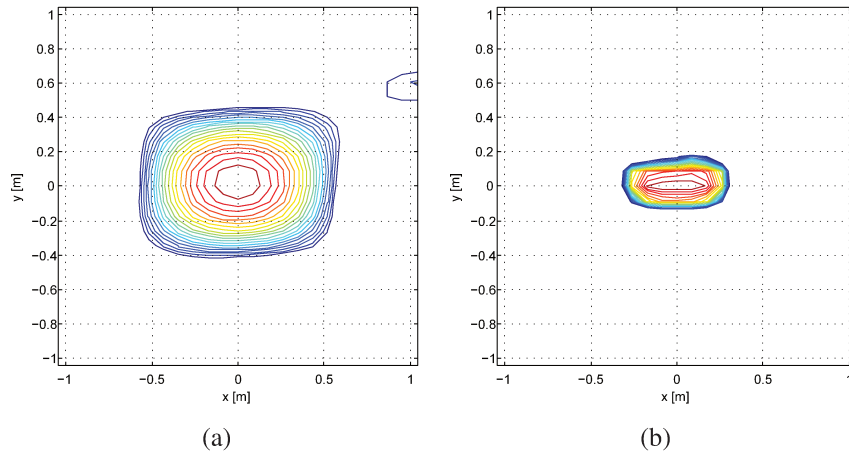


Figure 5.26: Two monopoles in-phase (numerical results including reflections): (a) Conventional beamforming; (b) Generalized inverse beamforming (Countour lines are in 10 dB range with 0.5 dB increment).

The experimental results for this configuration are shown in figure 5.27. Both sources are

supplied with the same signal and no attention is paid to the specific radiation efficiency of each loudspeaker. Based on the results of the conventional beamforming mapping the right loudspeaker possibly presents a higher radiation efficiency, moving the center of the noise map in this direction, but still failing to clearly detect the individual source centers.

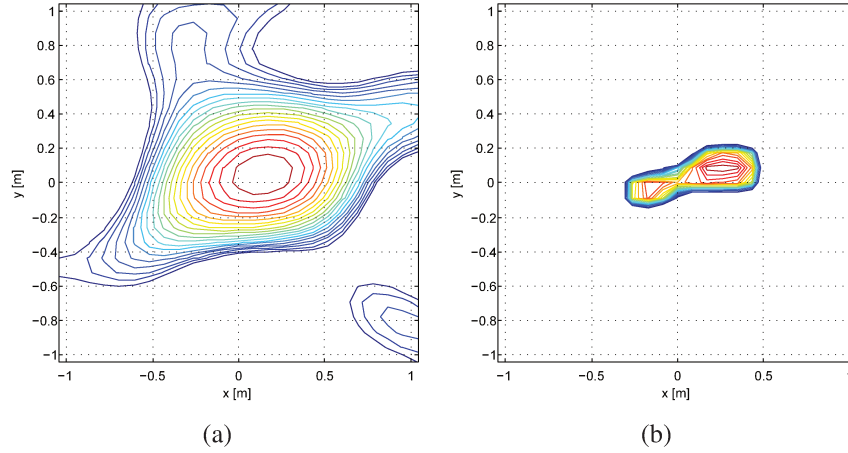


Figure 5.27: Two monopoles in-phase (experimental results): (a) Conventional beamforming; (b) Generalized inverse beamforming (Countour lines are in 10 dB range with 0.5 dB increment).

With the generalized inverse beamforming, the individual source centers are identified with some distortions. Similar as for conventional beamforming results, the right source presents a higher radiation power. Secondly, the positions in terms of height are distorted, which is possibly caused by the array configuration. The power detection would be higher on regions where you have more density of microphones, for example, along the microphones spiral arm.

Table 5.7 summarizes the results for the sound power estimations obtained with the configurations discussed above. Conventional beamforming results calculated at mapping center, and power estimations for the generalized inverse beamforming are retrieved after 32 iterations.

Test	Conventional	Generalized Inverse
Numerical free-field	2.21	2.97
Numerical including reflections	2.53	1.78
Experimental	1.84	1.74

Table 5.7: Power estimations for the two monopoles in-phase problem.

It can be noticed that conventional and generalized inverse results indicate a possible destructive interference at the sensors array related to the floor reflections, and this leads to a lower power estimation than on the free-field case. The experimental results are in good agreement with numerical prediction for the generalized inverse beamforming.

An important difference between both methods is the power calculation. For the conventional beamforming, this value is obtained at the mapping center location, while for the generalized inverse it is the summation over all remaining source grid points. This causes the estimation to be independent of any assumption regarding the source center location, which is an important advantage compared to the conventional beamforming.

5.3.3 Two Monopoles in anti-Phase

As for the second test case, two monopoles with anti-phase excitation are used to validate the dipole identification. Numerical tests are used to investigate the possible monopole source locations which result in dipole radiation on the source plane parallel to the array plane, resulting in the distance of $3/2$ wavelength between the loudspeakers. This configuration generates a dipole source with center located between the sources and in orientation aligned with the sources. Small deviations are expected for the dipole identification using two monopoles in the semi-anechoic test condition, since reflections could alter the radiation symmetry.

The conventional beamforming technique can also be used to detect dipole type of sources, and the implementation here followed what is presented by Suzuki (2008).

In figure 5.28, the numerical free-field results, show that both methods are capable to detect the induced dipole at the center of the grid region, and that the orientation is retrieved with a reasonable accuracy. The major difference is attributed to the lower dynamic range in the mapping retrieved by the conventional method, resulting in spurious peaks. The detection area is similar to the monopoles test case: a radius of approximately $1/2$ wavelength. The arrows on the mappings indicate the dipole orientation.

For the numerical prediction including ground reflections (figure 5.29). More spurious peaks are encountered for both methods, and the orientation obtained with the generalized inverse beamforming is slightly influenced. The dynamic range of the generalized inverse is, however,

still superior.

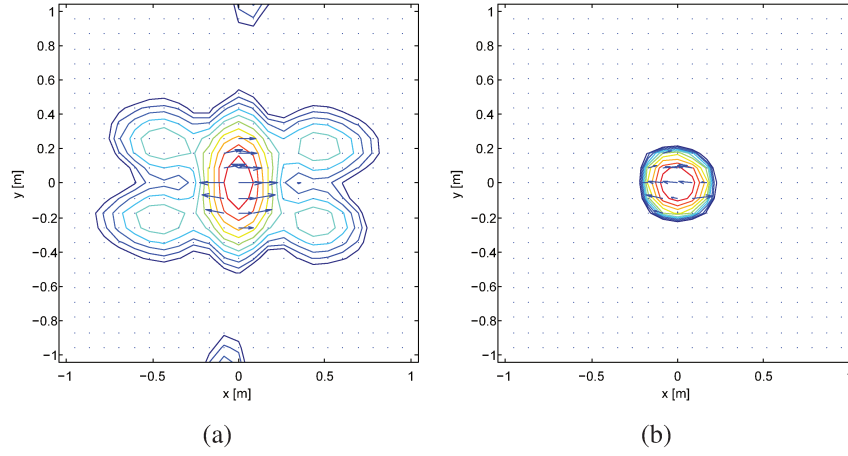


Figure 5.28: Dipole Identification with two horizontal monopoles in anti-phase (numerical free-field results): (a) Conventional beamforming; (b) Generalized inverse beamforming (Countour lines are in 10 dB range with 0.5 dB increment).

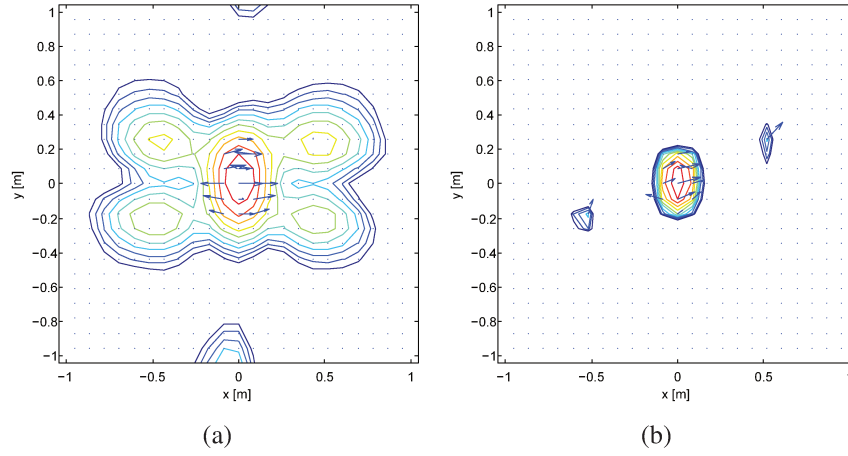


Figure 5.29: Dipole Identification with two horizontal monopoles in anti-phase (numerical results including reflections): (a) Conventional beamforming; (b) Generalized inverse beamforming (Countour lines are in 10 dB range with 0.5 dB increment).

The experimental results, shown in figure 5.30, show a similar result to the numerical predictions, with the presence of some spurious peaks in the induced dipole mapping.

Following other experiments are performed, one with the monopoles displaced vertically, and the other with the monopoles placed at 135° . The results are shown in figures 5.31 and 5.32. The advantage for the generalized inverse beamforming in dynamic range compared to conventional

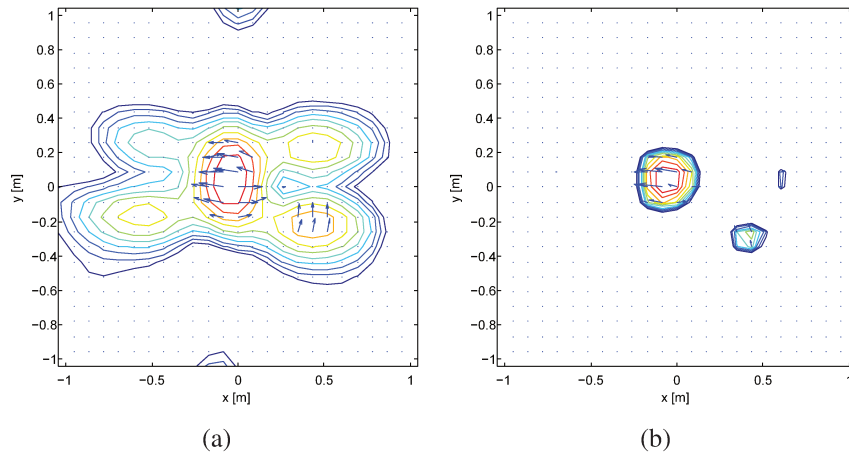


Figure 5.30: Dipole Identification with two horizontal monopoles in anti-phase (experimental results): (a) Conventional beamforming; (b) Generalized inverse beamforming (Countour lines are in 10 dB range with 0.5 dB increment).

beamforming can be clearly noticed. The dipole orientation is retrieved by both methods, even in the presence of the reflections from semi-anechoic room floor.

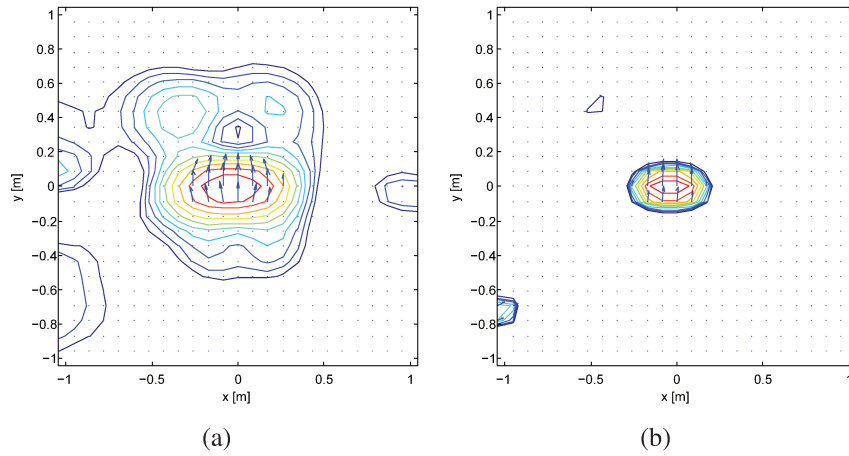


Figure 5.31: Dipole Identification with two vertical monopoles in anti-phase (experimental results): (a) Conventional beamforming; (b) Generalized inverse beamforming (Countour lines are in 10 dB range with 0.5 dB increment).

Table 5.8 summarizes the results for the sound power estimations obtained with the configurations discussed above. Conventional beamforming results calculated at mapping center, and power estimations for the generalized inverse beamforming are retrieved after 32 iterations.

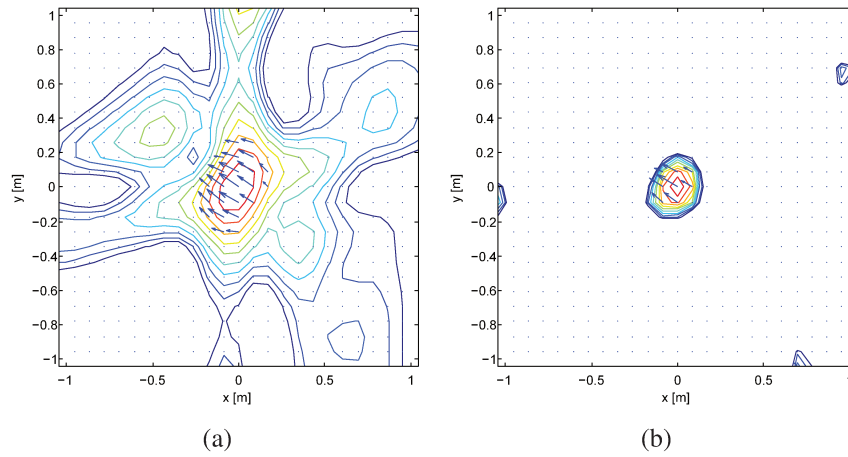


Figure 5.32: Dipole Identification with two monopoles at 135° in anti-phase (experimental results): (a) Conventional beamforming; (b) Generalized inverse beamforming (Countour lines are in 10 dB range with 0.5 dB increment).

Test	Conventional	Generalized Inverse
Numerical free-field / Horizontal	1.06	1.12
Numerical including reflections / Horizontal	1.39	0.32
Experimental / Horizontal	10.2	2.63
Experimental / Vertical	2.51	0.64
Experimental / 135°	1.01	0.49

Table 5.8: Power estimations for the dipole identification using two monopoles in anti-phase problem.

The horizontal monopole distribution presents a higher power radiation for both the conventional and generalized inverse beamforming methods. This can be related to the symmetry of the sources in respect to the floor, which is not the case for the vertical or the inclined case, creating a more complex radiation field. The retrieved power estimates are found around unity for both free-field numerical results, but interactions with the mirrored sources results in a lower power estimation for the generalized inverse beamforming in comparison to the conventional method.

5.3.4 Summary

It is demonstrated for a dual monopole in-phase configuration that the generalized inverse beamforming retrieves the source center location with higher accuracy and dynamic range than the

conventional beamforming method. Based on these test cases results it can be estimated that the capacity for the generalized inverse method to identify two close compact sources is at the limit on the case of $3/2$ of wavelengths between two source centers in coherent radiation. The experimental results illustrates that the method is able to locate the individual source centers with a power estimation in good agreement with the numerical results. The generalized inverse beamforming presents an advantage with respect to the sound power estimation compared to conventional method since it is not dependent on a source center assumption.

The induced dipole identification case shows that both methods are capable to locate the center of radiation with a good agreement between numerical and experimental results. For both methods, the dipole orientation is retrieved with a reasonable accuracy. Similar as for the first test case, the generalized inverse beamforming exhibits a better dynamic range detection but includes some spurious peaks on the mappings. The power estimations using the conventional method, present a higher discrepancy between the numerical and experimental predictions. The generalized inverse estimations for the vertical and inclined source disposition show an intermediate level between the numerical free-field and the numerical perfect reflective floor test. This indicates that the experimental tests conducted in a semi-anechoic room lead to an intermediate condition between free-field and semi-anechoic, with radiation interference at the sensors.

These reference tests can be used as in-situ calibration, before full aeroacoustic wind-tunnel measurements and to check the influence from wall reflections on detection accuracy.

5.4 Source Identification Using the Generalized Weighted Inverse Beamforming

Identification of acoustic sources gained attention through the years in the search to improve noise emitted by modern machinery. Beamforming techniques based in microphone array measurements are of common use since they normally demand affordable data acquisition effort while producing fairly clear source identification in most of the applications. However, for aeroacoustic applications, this method is challenged by the coherent distributed nature of aeroacoustic sources. This work presents a method, based on the Generalized Inverse Beamforming, but with a weighted pseudo inverse approach and an optimization procedure for the weight definition, the Weighted Generalized Inverse Beamforming. A simple example is used to illustrate the advantages of this method to perform source identification on closely spaced compact source. Numerical and

experimental assessment are presented and the results with GWIB are compared to Conventional Beamforming, Multiple Signal Classification (MUSIC) and GIB results. The conclusion and remarks are presented at the end.

5.4.1 Introduction

To improve solution of general inverse problems, the weighted pseudo inverse technique (GUILLAUME *et al.*, 2002) is widely adopted. This method pre and pos-multiply the transfer function matrix by a diagonal weight matrix. The weight values are then optimized in order to minimize the number of relevant sources.

A simple case of two compact sources in close vicinity in coherent radiation is investigated by numerical and experimental assessment. Weighted generalized inverse results are compared to the ones obtained by conventional beamforming, Multiple Signal Classification, and the generalized inverse beamforming. In the end, the advantages of the proposed method are outlined as well as the computational effort increase when compared to the generalized inverse beamforming. Text and results extracted from (PRESEZNIAK *et al.*, 2012).

5.4.2 Numerical Example

In this section a numerical example is presented to show the advantages of this method. The example consists of two monopole sources radiating at 1 kHz and separated by 1.5 wavelength distance. The array is adopted with 30 microphones distributed over a 6-arm spiral configuration and 2 m aperture. The array distance to the source plane is 2.5 m . The target grid region is chosen as 3 wavelengths from the target center, with a rectangular grid with $1/4$ of a wavelength spacing and 25 points, as indicated in Fig. 5.33

In this paper, four identification methods are compared: conventional beamforming, Multiple Signal Classification (MUSIC), Generalized Inverse Beamforming (GIB) and the proposed Generalized Weighted Inverse Beamforming (GWIB). The GIB result is shown after 32 iterations using 10% truncation, this means that after each iteration, 10% of the possible source locations are discarded. In the GWIB method, the optimal result is obtained after 15 iterations. The results for all the identification methods are shown in the Fig. 5.34.

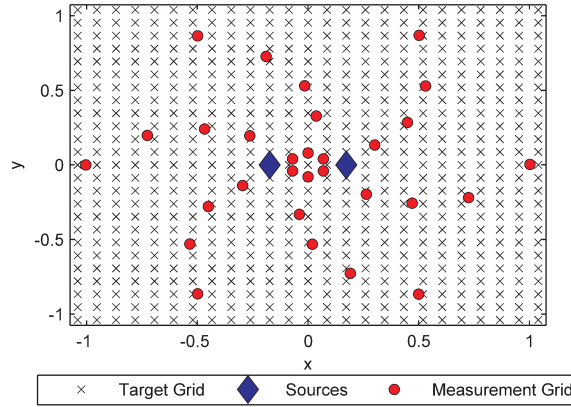


Figure 5.33: Target and measurement grids and source locations

All the plots are shown in a $10dB$ range. From Figure 5.34 it is possible to draw the following conclusions:

- All the methods converged to the source areas;
- The conventional beamforming technique correctly identified the zone, but was not able to identify both sources separately;
- The MUSIC method presented results comparable to the conventional beamforming method but with a better dynamic range;
- The Generalized Inverse Beamforming (GIB) showed a better result, identifying both sources;
- The Generalized Weighted Inverse Beamforming (GWIB) improved the GIB results, specially when it refers to the dynamic range.

5.4.3 Experimental Results

To validate the proposed methodology, an experiment was performed using the same configuration as the numerical example. The setup used is the same presented in a previous section and is shown in Figure 5.24.

As adopted in the numerical example, two compact sources radiate an in-phase sine wave at 1 kHz with a distance of 1.5 of a wavelength from each other. The measurements used a

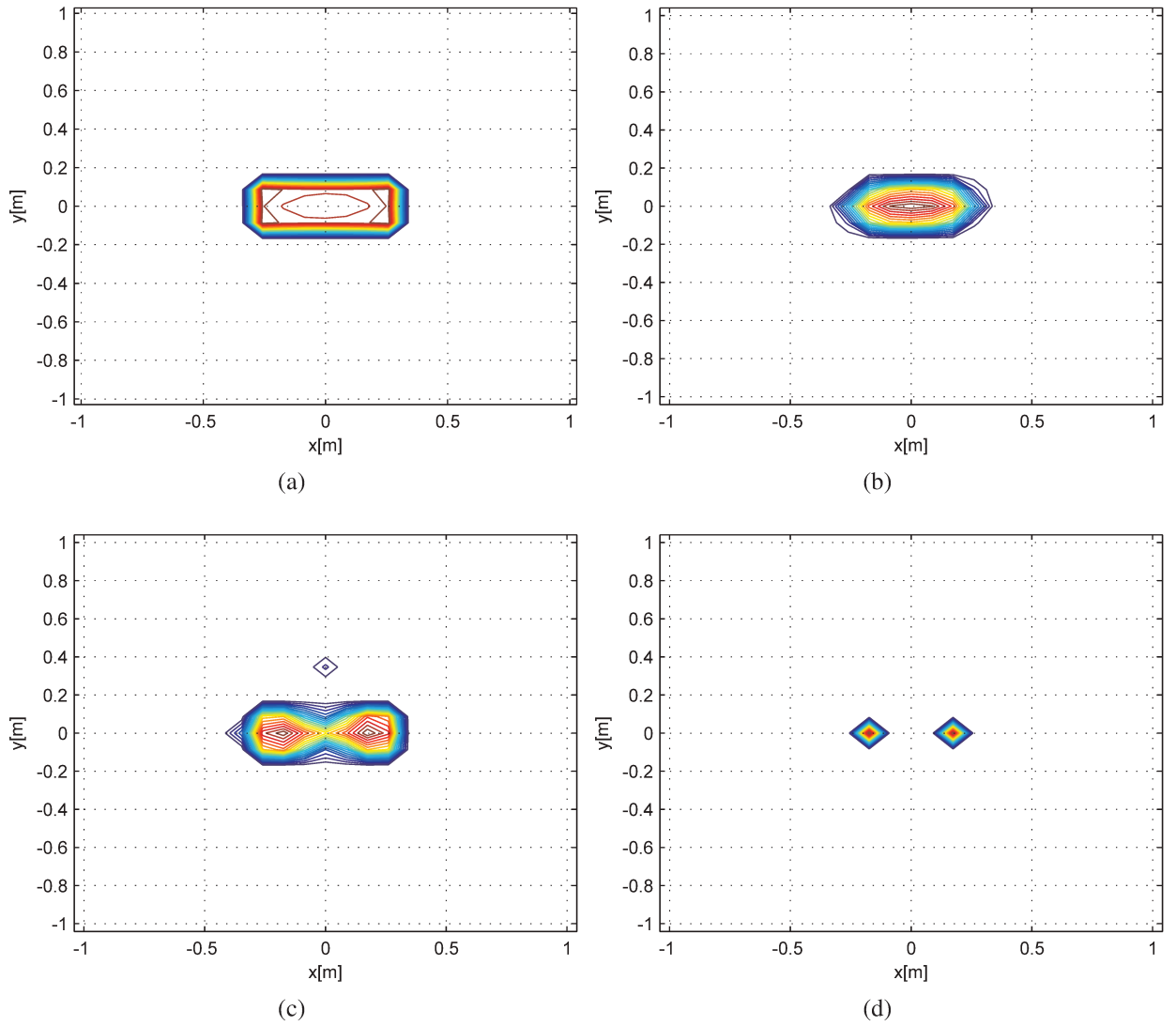


Figure 5.34: Source identification for: (a) Conventional Beamforming, (b) MUSIC, (c) Generalized Inverse Beamforming (GIB) and (d) Generalized Weighted Inverse Beamforming

simultaneous acquisition with 20.48 kHz sampling frequency. Blocks with 1024 time samples per microphone are used for each acquisition. The target grid region is chosen as 3 wavelengths from the target center, with a grid spacing of $\frac{1}{4}$ of wavelength. The results are shown in Fig. 5.35

The Generalized Inverse Beamforming (GIB) result is obtained after 32 iterations using 10% truncation. In the Generalized Weighted Inverse Beamforming (GWIB) method, the optimal results is obtained after 15 iterations, but with the optimization procedure, the computational time is still almost the same, 1.526 s for the GIB versus 2.081 s for the GWIB.

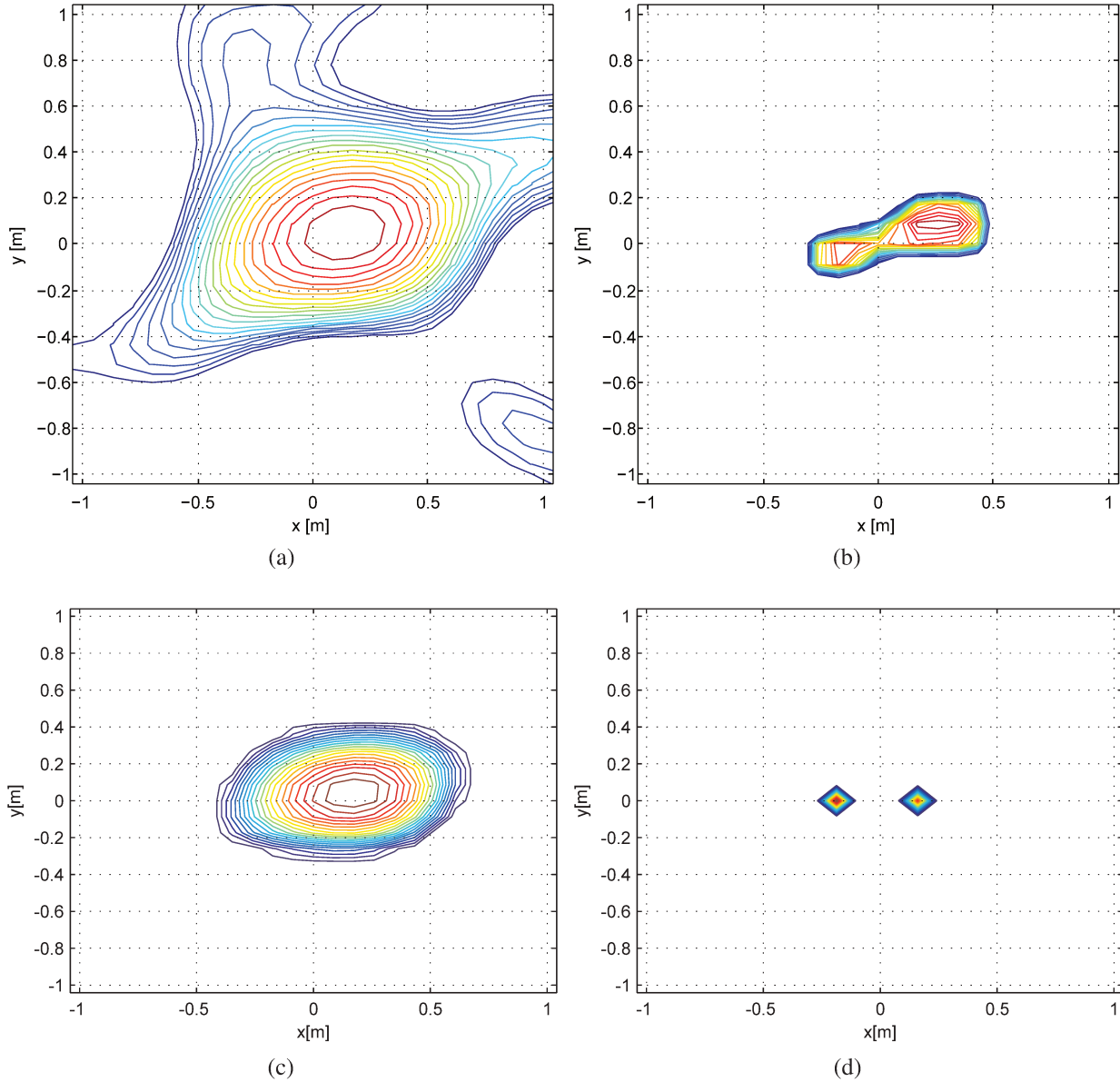


Figure 5.35: Experimental results for: (a)Conventional Beamforming (b) Generalized Inverse Beamforming (GIB) (c) MUSIC and (d)Generalized Weighted Inverse Beamforming (GWIB)

Experimental results using GIB are very similar to the numerical prediction, and the method was able to capture the individual source locations, in contrast to the conventional beamforming and the Multiple Signal Classification (MUSIC) that presented one single source center. The beamforming and the MUSIC results are almost the same but the MUSIC algorithm indicates a source center more to the right, possibly steered to a slightly louder speaker.

The maps indicate some level differences in the source radiations which led the GIB to keep

more source grid terms on the side of the higher emission. The GWIB was able to capture individual source locations with substantial increase in dynamic range and no clear influence of the higher level of one loudspeaker.

To better show the convergence of the proposed method, Fig. 5.36 shows the results for 1, 5, 10 and 15 iterations.

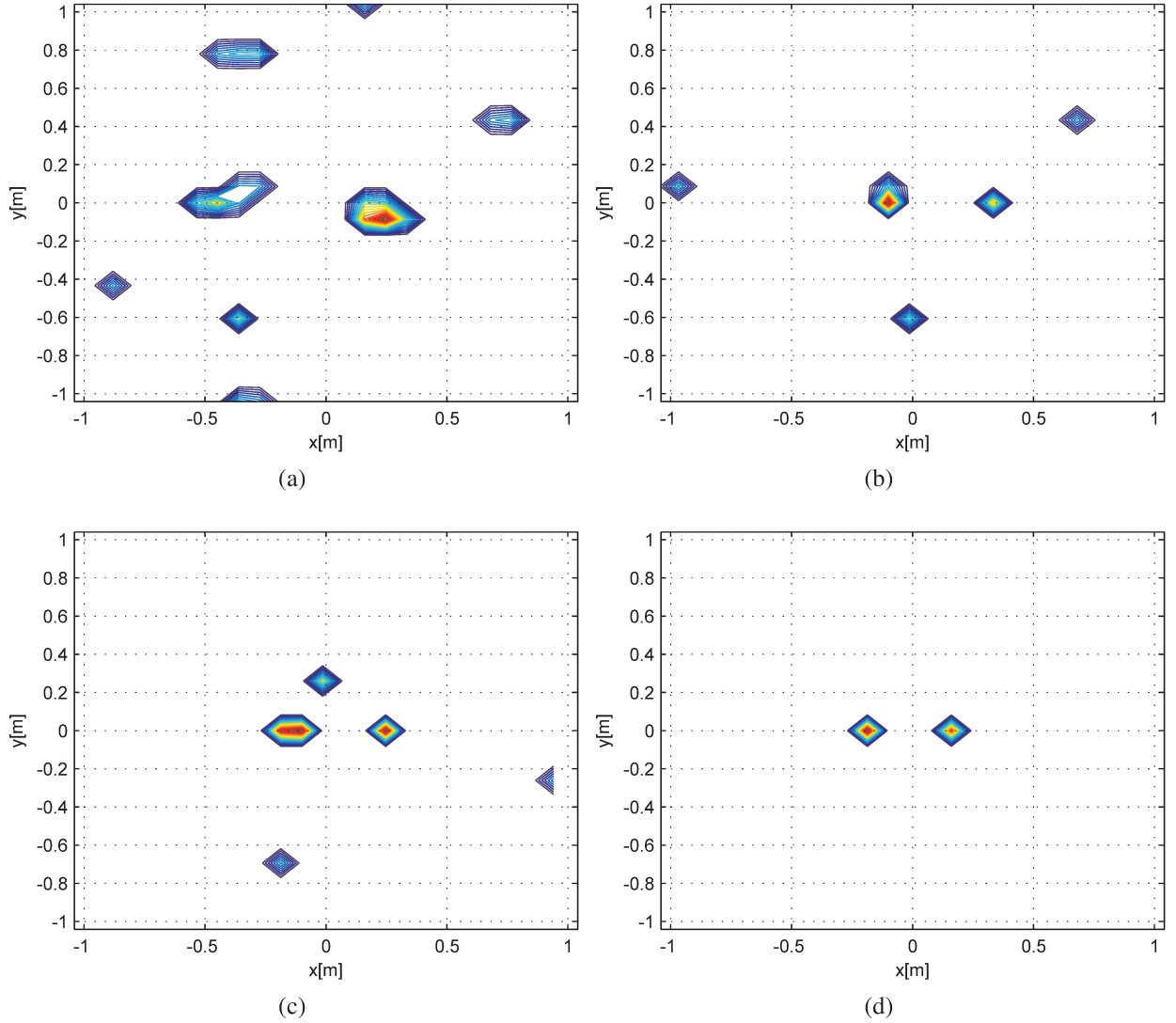


Figure 5.36: Generalized Weighted Inverse Beamforming (GWIB) after: (a) 1 iteration, (b) 5 iterations, (c) 10 iterations and (d) 15 iterations

The progression along iterations for the GWIB shows that sources identification changed over the iterations, and even that one of the sources was not clearly present in the first iteration. It was detected on subsequent iterations, showing the robust performance on the proposed method to

separate the source centers in coherent radiation.

5.4.4 Summary

This section presents results for a new beamforming technique based on the Generalized Inverse Beamforming but using a weighted pseudo inverse approach and an optimization procedure for the weight definition. The objective of this optimization is to minimize the number of sources with a higher sensitivity to generate the response. This method, called Generalized Weighted Inverse Beamforming (GWIB), increases the dynamic range of the GIB, making it possible to identify closely spaced sources, as close as 1.5 wavelength in the example treated, supported by numerical and experimental investigation.

The results show that this new method converges faster than the Generalized Inverse Beamforming, but the computational effort is somewhat equivalent, since an optimization procedure is required for the weight definition at each iteration.

Thus, considering the computational effort and the obtained results, the advantage of this proposed method, GWIB, is evident, since it improves significantly the dynamic range on the identification with approximately the same processing effort as the GIB.

5.5 Summary

These experimental identification tests and comparisons to numerical results clearly indicates the advantages on inverse methods in beamforming mapping generation. Problems considering compact sources in a semi-anechoic room demonstrated the advantage in dynamic range when compared to conventional beamforming, and capability to distinguish better two close sources (closer than two wavelengths). The estimation in GIB also can be checked by the use of the hybrid estimation proposed, and interpretation of the eigenvalue based strength estimation indicate that all radiation contributions, direct and indirect, are present in its value, posing some difficulties to the GIB strength estimation. In the other hand, the use of a virtual grid was capable to reduce this effect as well as to decompose the reflected contribution from the direct one, a possible big advantage in some complex source scenarios.

The identification of a dipole radiation by the use of two compact sources in anti-phase also demonstrated the capability to identify radiation center and main axis direction even in the presence of reflections. In the end, the use of weighting procedures in the inversion problem increases significantly the dynamic range, demonstrated by simple experimental cases and also in the presence of reflections.

These results, presented in four reports, are a verification and validation of the GIB method and preparation to application to more complex experimental cases, as aeroacoustic sources and moving sources identification.

6 Aeroacoustic Source Identification: Dipole over Cylinder in Subsonic Jet

Aeroacoustic source identification poses some challenges to conventional techniques such as conventional beamforming. The challenges can be summarized as the distributed nature of the aeroacoustic sources, in coherent or incoherent radiation, with multipole radiation characteristics. In order to cope with these difficulties, Generalized Inverse Beamforming (GIB) is adopted. This method allows the simultaneous identification of compact or distributed, coherent or incoherent, mono or multipole sources, with a reduced number of sensor signals. The method is applied to an aeroacoustic test using a simple geometry as obstacle in a low Mach number jet. The result focuses on the dipole formation on the circular cylinder surface. Convection and refraction influence are included in the identification using a simplified approach for retarded time calculation. Equivalent pressure mappings and directivity plots are generated to help visualization of radiation field. This work investigates the performance obtained on the use of GIB method on this simple aeroacoustic source identification problem.

6.1 Introduction

Several efforts have been made in the field of aeroacoustics to understand sound generation and propagation. New experimental techniques have been applied in order to characterize the phenomena involved in these problems. In this work, the generalized inverse beamforming is used to identify the dipole distribution formed on top of a cylinder section in a subsonic air jet flow. The jet impinges asymmetrically on the cylinder, causing higher speeds on one side of the obstacle. This configuration could be representative for landing gear tire noise generation. The identification is validated through numerical cases. With the dipole distribution identified, equivalent pressure mappings are built and estimated directivity plot generated for the main plane of radiation.

This Chapter presents the preliminary investigations done for an aeroacoustics simplified problem, a circular cylinder section impinged by a low Mach number cold jet in a semi-anechoic room. Although simple, the proposed problem evaluates the consistency on the source identification using the generalized inverse beamforming.

According to Curle (1955), the expected sources are basically quadrupoles distributed over

the flow volume and dipoles formed at the solid boundary, with a higher radiation efficiency for the latter, and being the focus of investigation. The dipole reference solution adopted in the identification is restricted to the plane parallel to the array. The convection and refraction modeling adopted in this work is summarized, two examples are presented: convection only; and convection and refraction pressure mappings for a 45° single dipole. The aeroacoustic test setup details are introduced, including the jet speed profile related to the measurement flow condition.

The aeroacoustic source peak emissions are located using averaged spectra and averaged cross-spectra. The aim is to locate specific source emissions that present a reasonable coherence among all the array microphone signals, and produce a better identification. In this work, initially, three of the main peak emissions are considered to investigate related source distributions, as presented in (ZAVALA *et al.*, 2010A).

The identification results for these three chosen peak emissions are presented, and its representation is introduced: a contour mapping with arrows representing magnitude and direction along the cylinder surface.

In order to illustrate the pressure field for the identified dipole formation, an equivalent pressure mapping for the cylinder transversal plane is introduced. Although the results of only three individual emissions are not sufficient to represent the broadband radiation problem, it allows the identification of interesting relationships on radiation directivity related to the frequency of emission.

Numerical investigation is performed to illustrate the identification capabilities for the chosen frequencies. Equivalent pressure mappings are presented for the main radiation plane, according to the identified source distributions, and the directivity plot is showed and discussed.

After the peak emissions investigation, the traditional identification approach based on long averaging of the cross-spectral matrix is presented, along with the directivity plots and equivalent pressure mappings, as presented in (ZAVALA *et al.*, 2011A).

In the end, the main conclusions from this preliminary investigation are outlined. They confirm some advantages of the applied method. Also mentioned are the possible future investigations for this simple problem.

6.2 Aeroacoustic Sources in the Presence of Solid Boundaries

The presence of solid boundaries in flow results in aerodynamic sound produced by a dipole field distributed over the solid boundaries, which are the limits of Lighthill's quadrupole distribution, according to Curle (1955). The presented dimensional analysis in the same classical work showed that the dipoles should be more efficient generators than the quadrupoles distributed over the turbulent flow region if the Mach number is small enough.

The variation in air density accounting for the radiation from the distributed quadrupoles and the distributed dipoles considering zero normal velocity at the solid boundaries can be expressed as (CURLE, 1955):

$$\rho - \rho_0 = \frac{1}{4\pi c^2} \frac{\partial^2}{\partial x_i \partial x_j} \int_V \frac{T_{ij}(y, t - \frac{r}{c})}{r} dy + \frac{1}{4\pi c^2} \frac{\partial}{\partial x_i} \int_S \frac{P_{SB_i}(y, t - \frac{r}{c})}{r} dS(y), \quad (6.1)$$

where ρ_0 is the medium density at rest; T_{ij} is the Lighthill's stress Tensor (LIGHTHILL, 1952) given by:

$$T_{ij} = \rho v_{el_i} v_{el_j} + p_{cst_{ij}} - c^2 \rho \delta_{ij}, \quad (6.2)$$

which represents the difference between the effective stresses in the real flow and the stresses in the uniform acoustic medium at rest (considering $c^2 \rho \delta_{ij} = Press \delta_{ij}$). Indexes i and j here represent directions x and y . $p_{cst_{ij}}$ is the compressive stress tensor.

In Equation 6.1, $P_{SB_i} = -l_j p_{cst_{ij}}$ represents the distributed dipole strength per unit area, and note also that P_{SB_i} is exactly the force per unit area exerted on the fluid by the solid boundaries in the x_i direction, considering that l_i is the direction cosine of the outward normal from the fluid ($(l_1, l_2, l_3) = \vec{n}$).

Physically, the sound field is the sum of the sound generated by a volume of quadrupoles and by a surface distribution of dipoles at the solid boundaries, this field subjected to convection.

6.3 Convection and Refraction Modeling

The free-field dipole radiation equation is no longer representative in the case of a source in flow. With the observer outside the flow, the refraction representing the interaction of the outgoing radiation waves from the sources on the boundary shear layer has to be taken into account. These can be done in a simplified approach using the modeling presented by Amiet (1975) and also shown in (MUELLER, 2002).

The simplified modeling consists of a source at the center of a cylindrical tubular jet profile, and the propagation to the outside observer is treated as a 2D problem. Figure 6.1 illustrates the relationship between the emission direction, the convection direction, and the refraction direction according to this modeling and equation 6.3 below shows the relationships between these directions:

$$R_m \cos \theta_m = R_t \cot \theta + (R_m \sin \theta_m - R_t) \cot \theta_o, \quad (6.3)$$

where R_m is the distance from the source to the microphone; θ_m is the angle formed from the source to the microphone; R_t is the shear layer distance to the center of the cylindrical flow; θ is the propagation angle in flow and θ_o is the angle from the shear layer to the microphone.

The relationship between the emission path R and convected path R' is:

$$R' = \frac{R}{-M \cos \theta + \sqrt{M^2 \cos^2 \theta - M^2 + 1}}, \quad (6.4)$$

where M is the open-jet Mach number, relationship between the jet air speed and speed of sound inside the jet: $M = U_\infty / c_t$; θ is the convected wave normal angle. The convected and refracted wave path is the sum of R' and the still air path to the microphone based in the θ_o refracted angle.

On Figure 6.2, two examples of radiation using this simplified 2D modeling are presented, a 45 degrees dipole radiation in convection, and this dipole in convection and refraction radiation.

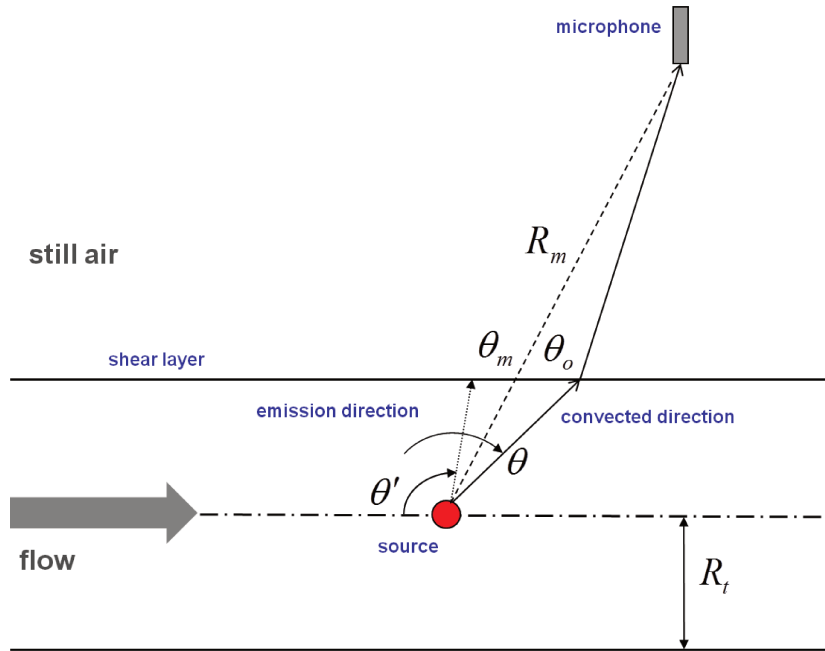


Figure 6.1: Convection and refraction modeling based on Amiet, 1975 (flow from left to right).

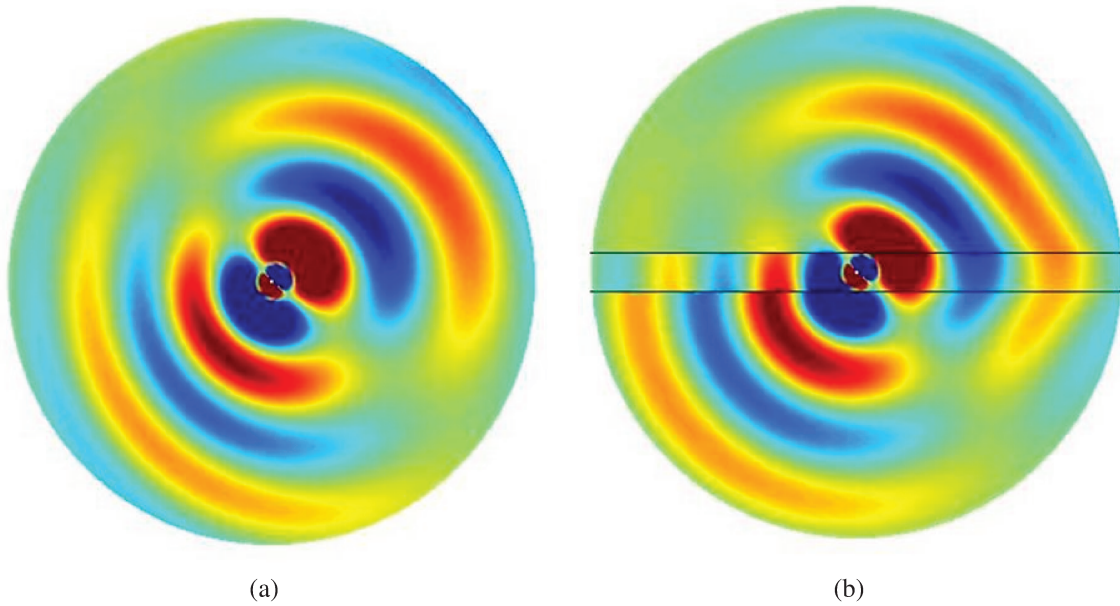


Figure 6.2: Dipole at 45 degrees main plane of radiation: (a) in convected radiation and (b) in convected and refracted radiation, with 0.2M flow from left to right (horizontal lines represents the shear layer).

In the second example, is illustrated the importance of the shear layer influence on the propagated waves retarded time calculation. This modeling is used on the calculation of the transfer functions between the possible source points (target grid) and the observers (microphone array).

6.4 Aeroacoustic Test Setup

The test setup can be observed on figure 6.3, at the semi-anechoic room of the Katholieke Universiteit of Leuven (in Belgium), along with the array used on this test. The adopted array consists of a 6-arm spiral configuration based on the Underbrink multi-arm spiral design, with 30 microphones. The array has 1m aperture and is positioned at 1.25m from the jet axis. The circular cylinder section is 40mm in diameter, and 20mm in length. The cylinder is positioned 0.4m from the outlet pipe. The array center is aligned with the cylinder center. Details can be observed in figure 6.4. The array microphone positions and target grid points can be seen in figure 6.5.

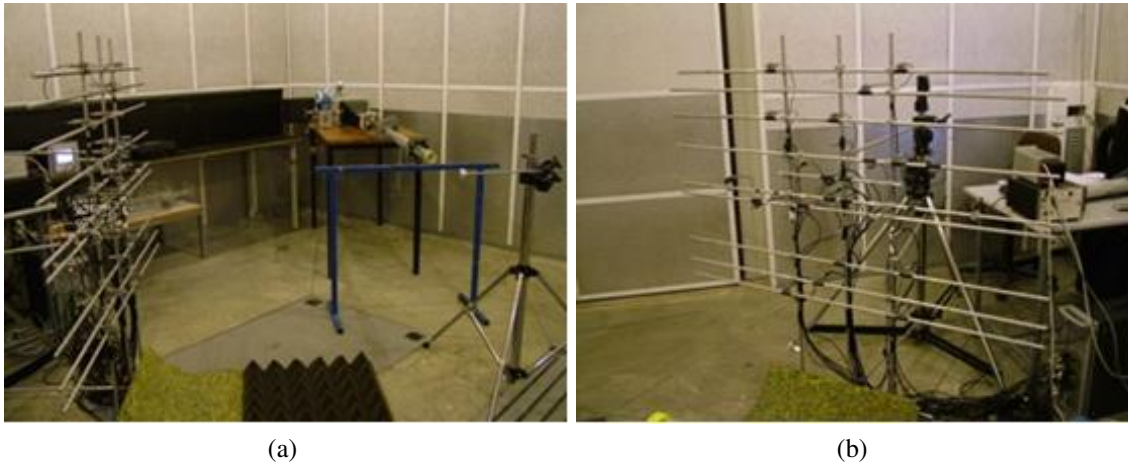


Figure 6.3: (a) Jet Experimental Layout (b) 6-arm Spiral with 30 microphones and 1m aperture.

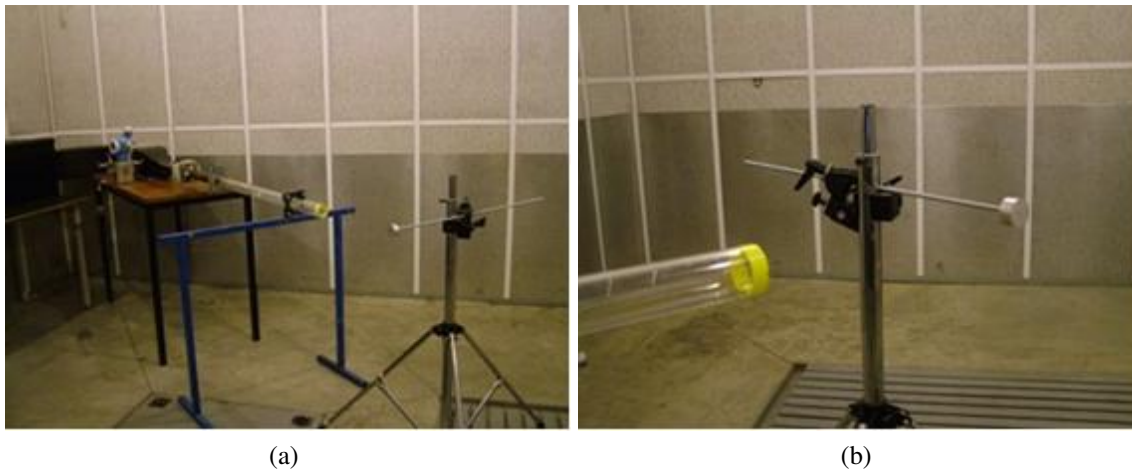


Figure 6.4: Circular cylinder positioned at 0.4m from the jet outlet (a) Overview (b) Close view.

The target grid consist of 72 points, 5 degrees interval, distributed over the x-y plane. The jet

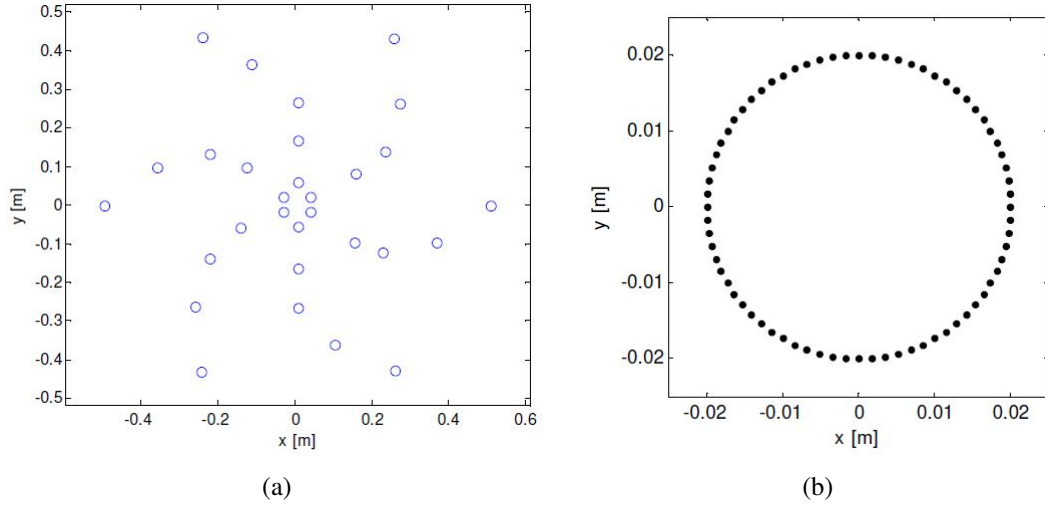


Figure 6.5: (a) Array 6-arm spiral microphone positions (b) Target grid points.

axis is positioned with approximately 2 degrees of inclination, and this produced a non-symmetric speed profile. The measurements are done with a flow speed at the outlet pipe of approximately 0.2M, and a hot wire measurement without the cylinder is presented in figure 6.6.

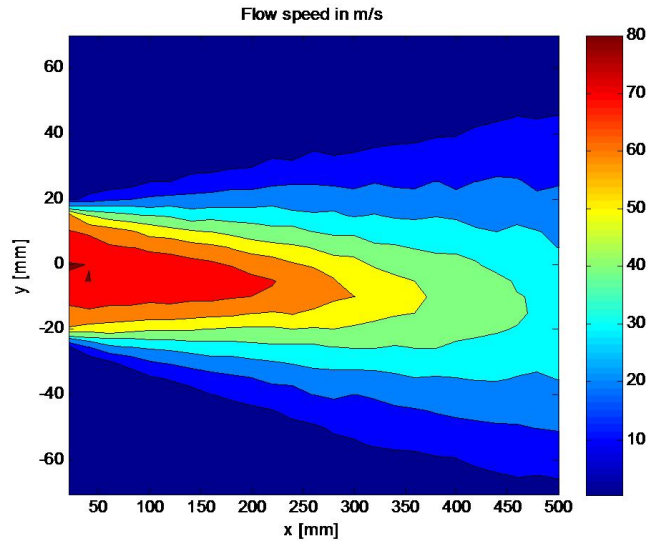


Figure 6.6: Jet speed hot wire measurement results in x-y plane.

The x-y plane is at the jet axis and parallel to the array. The estimated flow speed at the cylinder position ($x=400\text{mm}$) is adopted as 0.07M, and refraction shear layer is estimated at 40mm from the jet axis. The adopted refraction modeling considered a cylindrical speed profile around the source region, and also, the source located at the jet axis, those are simplifications to the real

situation, where the source is distributed and not concentrated.

The cylinder section dimensions were chosen to produce a concentrated source region, compact, to help the identification effort by the proposed method. However, the ratio between the diameter and length, on this case, 2, already indicate that a tonal noise would not be observed, and more broadband random character would be observed.

6.5 Aeroacoustic Source Peak Emissions

With the acquisition of 30 simultaneous microphone signals from the spiral array, the next step is to investigate the best approach to identify the sources from the temporal information. The broadband non-stationary emission is well-known to pose a challenge to techniques used to identify source types and locations. In this work, the aim is to investigate individual and specific frequency emissions that could be related to fast coherent turbulent structure formations. In order to locate these events, two different approaches are used, simple averaging of all microphone spectra, and averaging of all possible microphone cross-spectra. The results for a 1.2 sec. recording interval are shown in figures 6.7 and 6.8. The signals' sampling frequency is 102kHz, and spectra on the mappings are calculated with the highest frequency resolution, of about 10Hz in this case, and for every 7ms along the recorded interval.

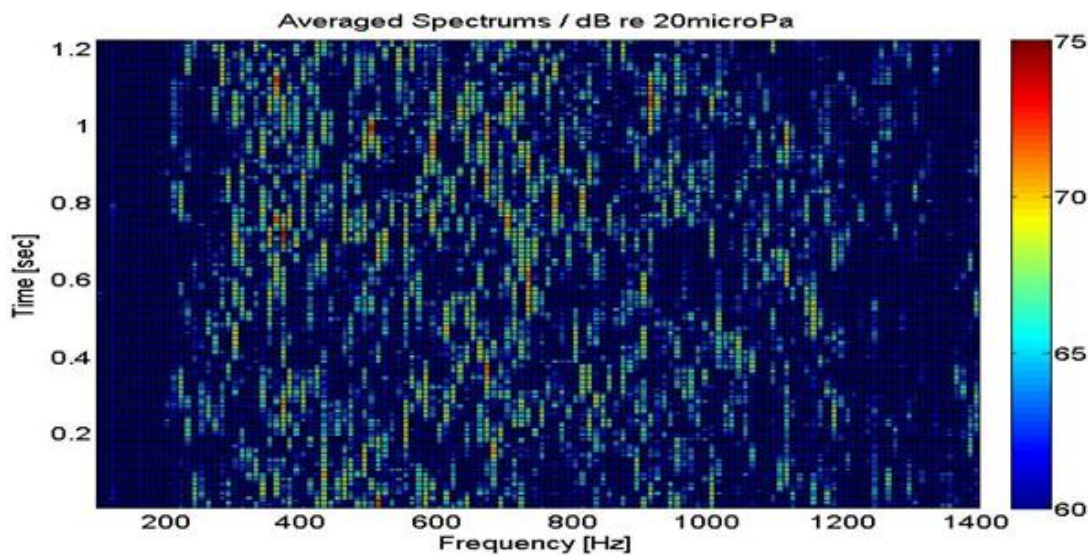


Figure 6.7: Averaged microphone FFT.

A random generation is clear from these graphs in terms of frequency, and the main frequency

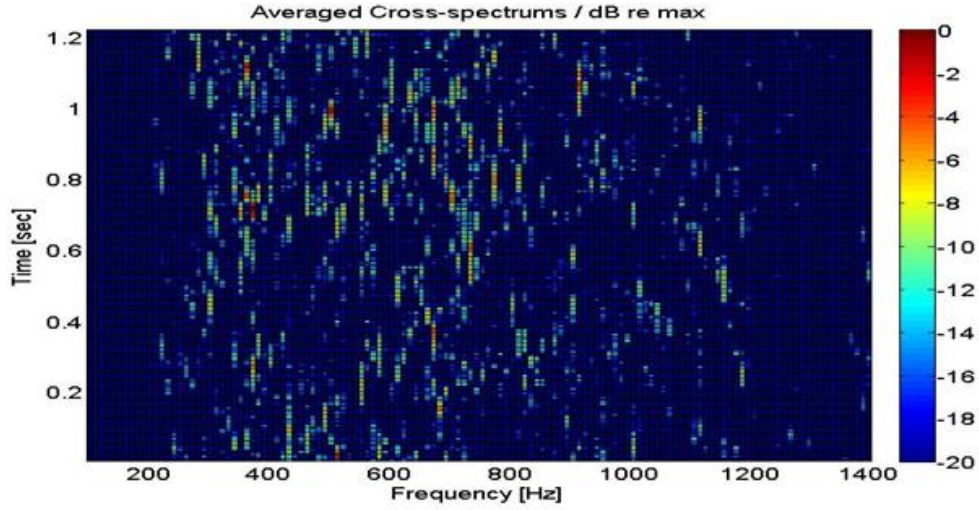


Figure 6.8: Averaged microphone cross-spectra.

range of emission is observed from 200 to 1200Hz in this problem. Both representations are able to capture the main peaks, with some dynamic range advantage to the cross-spectrum averaging approach. The peak on each frequency line is shown in figure 6.9, comparing the FFT averaging and the cross-spectral averaging.

From these graphs, three frequencies are chosen for investigation: 370Hz; 510Hz; and 910Hz. The temporal response for these three frequencies is shown in figures 6.10 to 6.12, with the peak emission region shown in red.

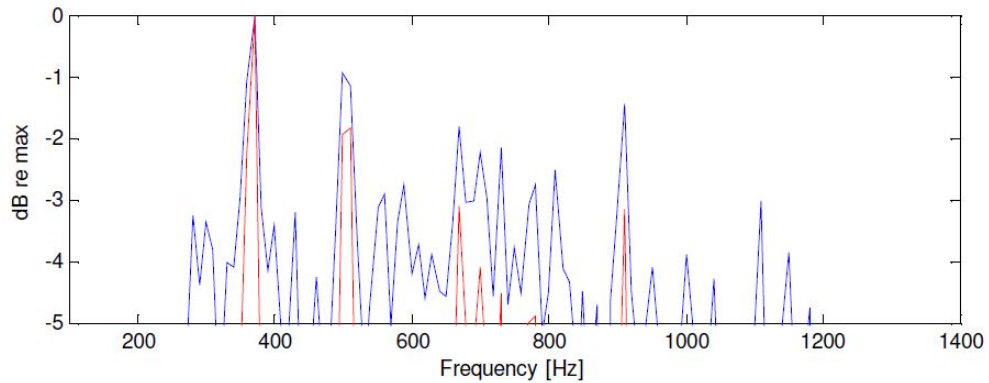


Figure 6.9: Comparison of averaged (blue) and cross-spectral peaks (red).

Blocks with 10240 samples are used around the peak region to the cross-spectral matrix calculation. On this work, no averaging is adopted to the cross-spectral matrix calculation.

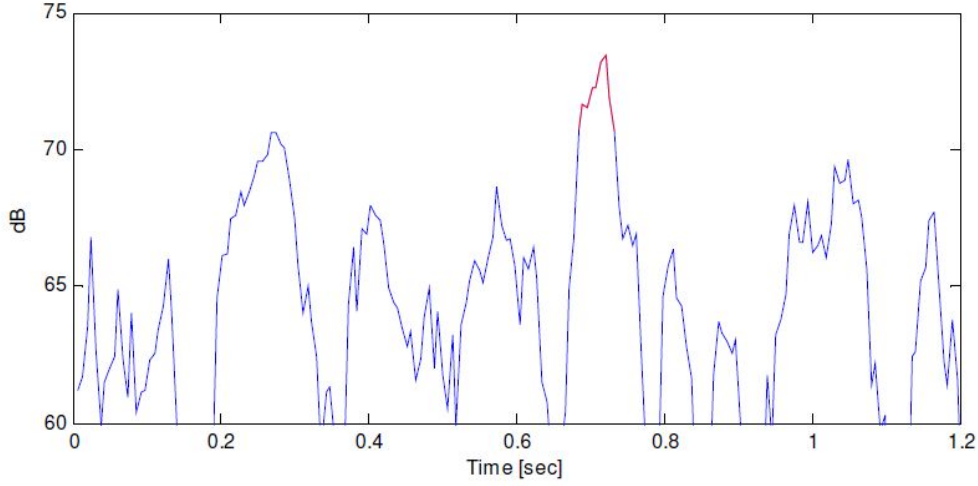


Figure 6.10: Time slice on 370Hz with main peak region in red.

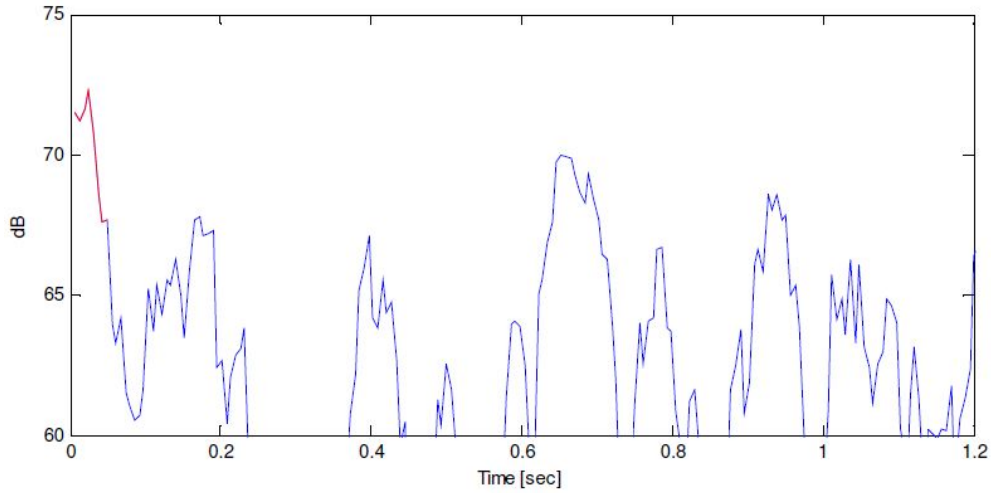


Figure 6.11: Time slice on 510Hz with main peak region in red.

6.6 Numerical Investigation On Identification Performance

Before applying the identification directly to the experimental data, a simulation is build with objective to verify if the method is able to separate and identify source regions considering that the obstacle in quite small compared to the wavelength for 370Hz emission.

Two cases are adopted, the first with dipoles uniformly distributed from 45° to 90° , and the second from 270° to 315° , both with normal to the cylinder surface orientation and in the x-y plane. The identification is performed with artificial noise added to the CSM, similar to the strategy adopted by Suzuki (2008). The iteration stop criteria is adopted as to reach 25% or less of the grid

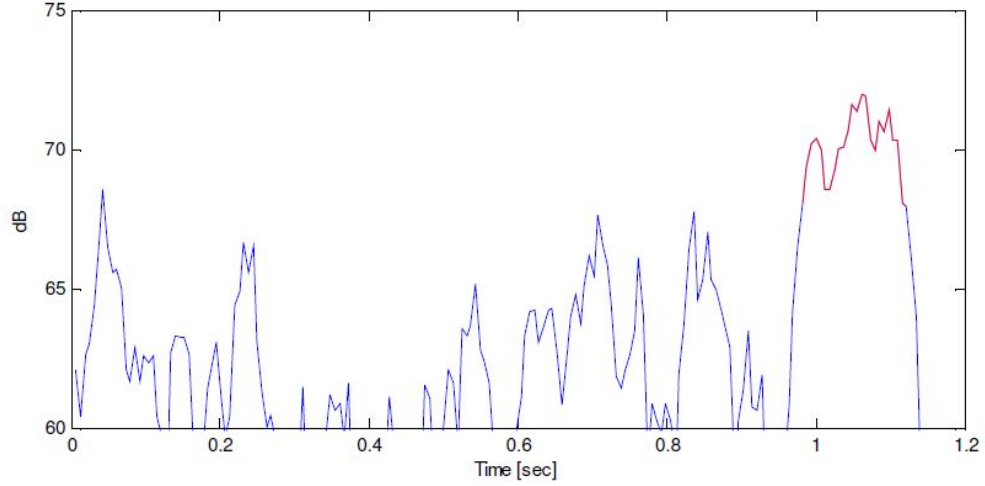


Figure 6.12: Time slice on 910Hz with main peak region in red.

points, and iterations stopped with 16 source terms. Identification results are presented in Figure 6.13. Arrows are adopted to represent dipoles strength and orientation on the x-y plane.

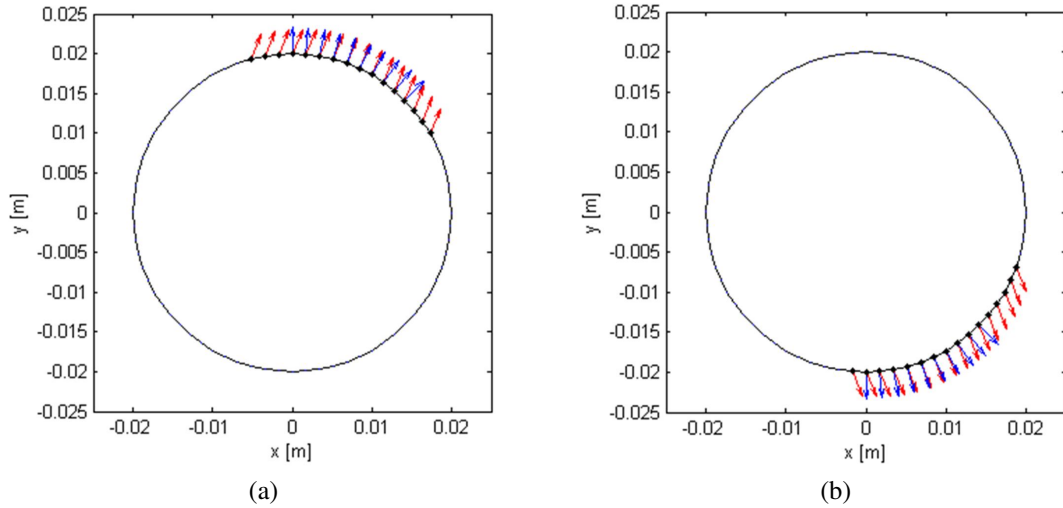


Figure 6.13: Dipole identification verification results (a) on case 45° to 90° ; and (b) 270° to 315° . Arrows represent dipoles: blue (numerical source); red (identification results).

The results shows good agreement on the general location of the dipole distribution despite the region size compared to the wavelength. However, the identification results seem to adopt a general orientation, not being able to capture the small orientation changes in the source region. Even though those results can be considered satisfactory for the main objective on this work that is to characterize the main source regions and general orientations on those regions.

6.7 Dipole Identification on Peak Events

The target grid consists of a line of dipoles distributed on the circular cylinder surface on the middle transversal plane. The dipole reference solution considered in this identification is restricted to the x-y plane. The other dipole directions are neglected on this preliminary analysis.

The dipole components in the transfer matrix are calculated for normal and tangential direction, and consider the convection and refraction modeling. The grid interval is 5 degrees, and the iterations stops after half of the grid points are truncated.

No special attention to the absolute strength of the dipoles is done on this work, but only the relative strength distribution along the cylinder surface between the normal and tangential components.

The results are presented in two types of representation. The first, a contour mapping with arrows representation, where the arrows represent only the orientation of the dipole, with normal and tangential components. A symmetric field is expected for both sides of the identified dipole, even above the cylinder, considering the compactness of the obstacle compared to the wavelengths in analysis.

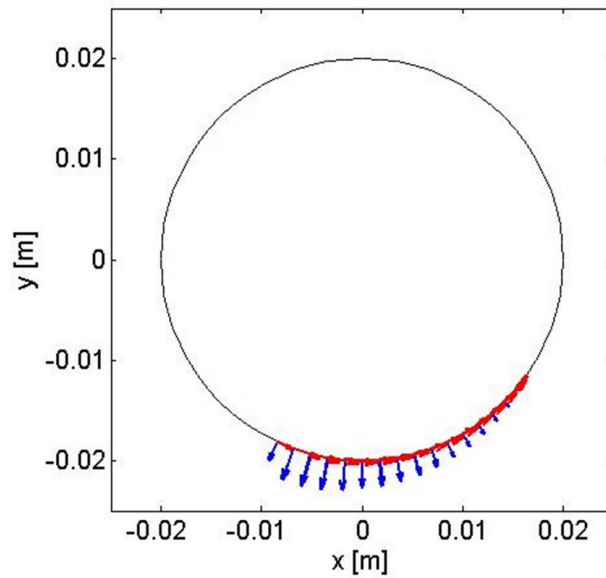


Figure 6.14: Dipole at cylinder surface for 370Hz with normal (blue) and tangential (red) components.

The first observation is that the normal component presents the higher contribution compared to the tangential. This is expected considering the moderate speed condition for the measurements, where the viscous related turbulence is present but less important.

The second observation is that the region where the dipoles are identified is at the bottom of the cylinder, with normal peak around 250 and 280 degrees. This is also expected since the flow highest speeds are directed to the bottom of the cylinder, and the expected separation region would be on this sector.

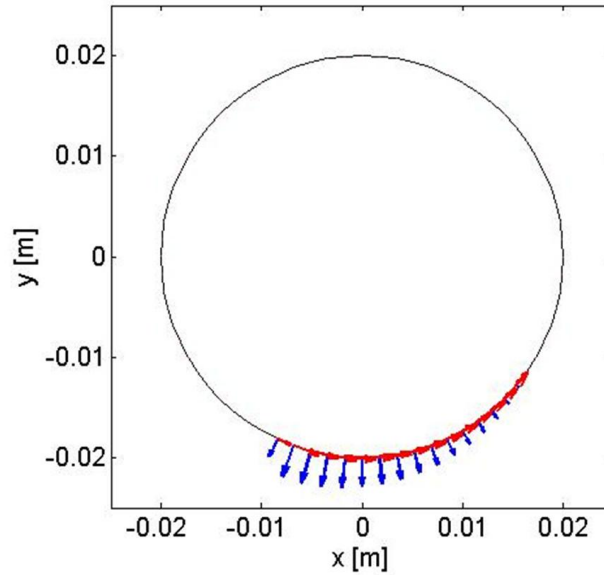


Figure 6.15: Dipole at cylinder surface for 510Hz with normal (blue) and tangential (red) components.

The tangential component presents a more constant distribution, and this is related to the viscous effects from the interaction of the flow with the cylinder surface on the main separation region.

One important observation is that for highest investigated frequency, the dipole distribution moved downstream and presents part of the contributions from the top of the cylinder too (figure 6.16).

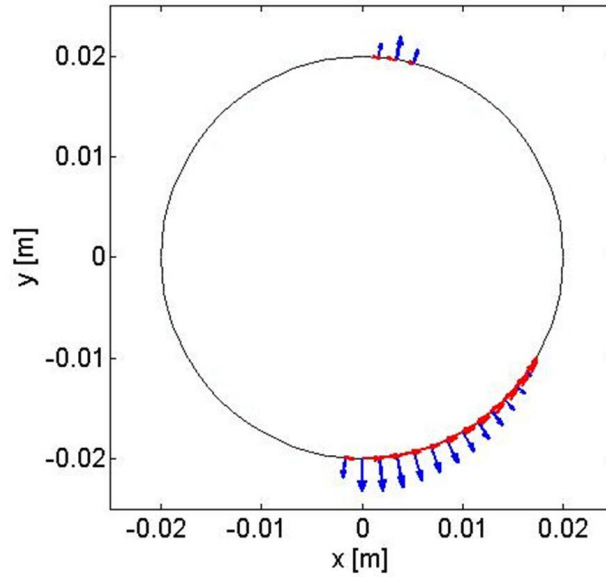


Figure 6.16: Dipole at cylinder surface for 910Hz with normal (blue) and tangential (red) components.

6.8 Equivalent Pressure Mappings on Peak Events

An equivalent pressure mapping can be built for the x-y plane radiation using the identified dipole distribution to support the interpretation of the results. Figures 6.17 to 6.19 show the equivalent mappings considering a radiation from the center of the target region, disregarding the cylinder surface, and being coherent with the convection and refraction modeling.

The scale of the mappings is not proportional to their overall contribution on the emitted sound, but only represents the instantaneous dipole radiation field created at the moment when the peaks are produced, including the convection and refraction influences. From the equivalent mappings it is clear that the convection and refraction influences are small compared to the wavelengths under analysis, with just small deviations from the free-field expected response. One important observation is that the main axis of radiation, or pressure maxima, seems to be related to the frequency, where the higher frequency presented almost a horizontal resultant directionality. This result is aligned with the expected pressure fluctuation distribution being moved downstream on the cylinder surface.

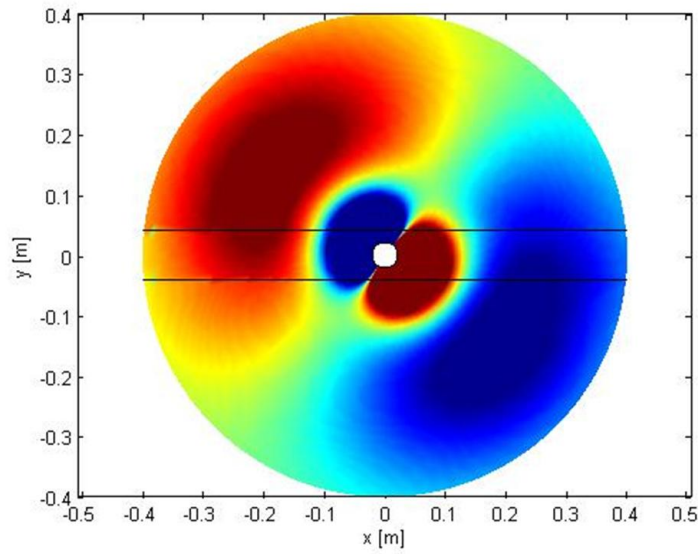


Figure 6.17: Equivalent pressure mapping for the identified dipole components at 370Hz.

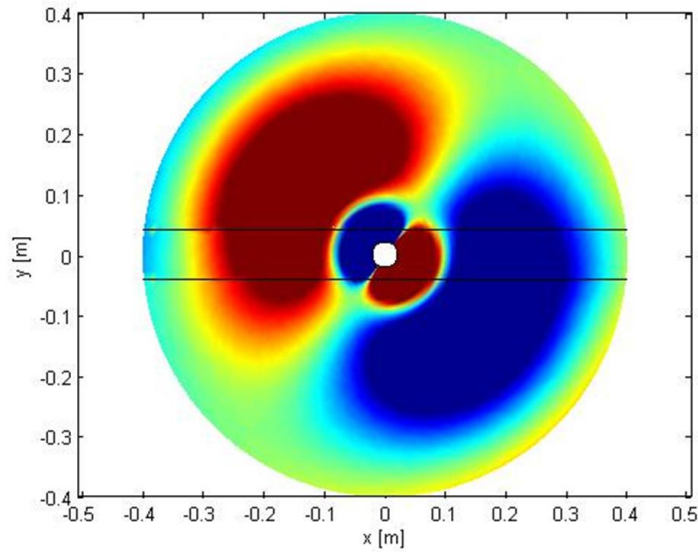


Figure 6.18: Equivalent pressure mapping for the identified dipole components at 510Hz.

6.9 Experimental Identification on Averaged CSM

Using a 102.4kHz sampling acquisition system, spectrums can be built using blocks with 10240 samples, and frequency resolution of 10Hz. The microphones spectrums amplitude averaging over approximately 4 seconds is presented on Figure 6.20. The averaging used 100 spectrums and approximately 60% overlap. This graph would represent the most important frequency

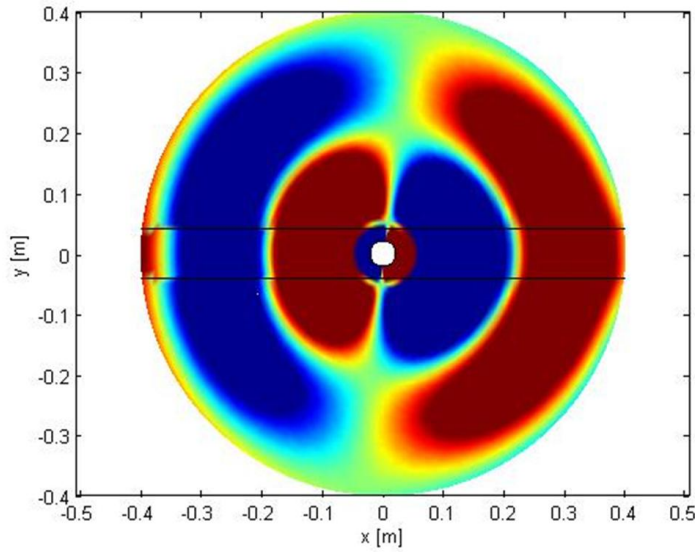


Figure 6.19: Equivalent pressure mapping for the identified dipole components at 910Hz.

emissions, and the peak is detected at 370Hz. This frequency is then chosen for the investigation.

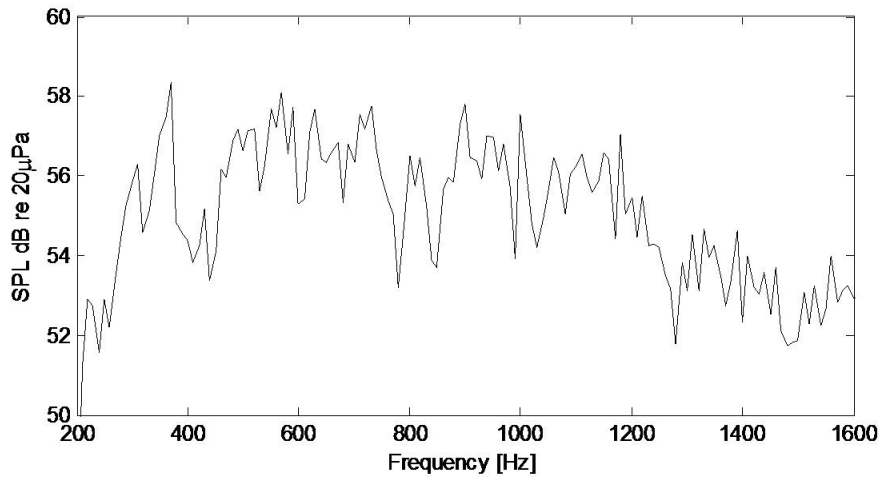


Figure 6.20: Amplitude averaging of microphones spectrum.

Using the same strategy for the spectrums averaging, 100 spectrums over 4 seconds (60% overlap), using one microphone in the array inner circle as reference for the averages, the CSM is built and the identification performed. Stop criteria is chosen again as to reach 25% grid region, keeping in the end, 16 source points. The dipole identification results can be observed on Figure 6.21. Contrary to the objective in previous sections where the identification is performed in a single peak event, the averaging represent an overall estimation in location and orientation for that particular frequency. The identification is performed to assess the dipole orientation on the x-y

plane only.

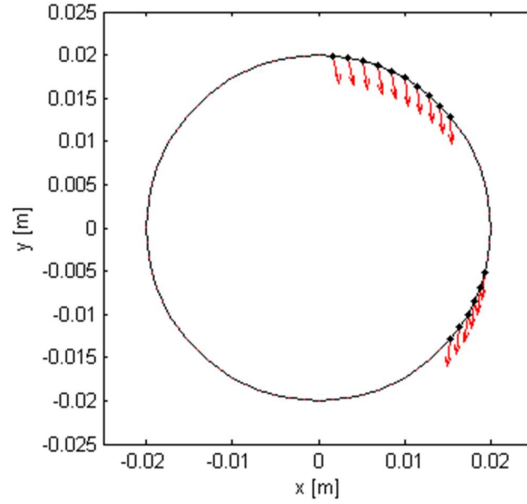


Figure 6.21: Dipole identification using experimental data.

The result shows two regions of distributed dipoles, with similar orientations, close to vertical direction. Considering that the flow impinges the cylinder section asymmetrically, with higher speeds on the bottom area, the regions of separation of fluid is in accordance to the expected flow speed profiles. The pressure fluctuations due to these separations would be the main influence on the source region generation. These locations and orientation are in accordance to the work of Takaishi *et al.* (2007), even considering that in this paper, the flow is slightly asymmetric and the cylinder diameter to section length ratio is smaller, may causing other 3D effects on source location.

6.10 Equivalent Pressure Mappings on Averaged CSM

With the identification results showed in Figure 6.22, Equivalent Pressure Mappings can be generated for the main plane of radiation, x-y plane, shown in Figure 6.23.

The distributed dipole configuration with two regions and similar orientations led to a spiral like type of propagation, not presenting a clear radial zero-pressure intermediate region between the two dipole main axis of emission. This interesting result is confirmed if a smaller dynamic range is adopted for the visualization of the same result, shown in Figure 6.23.

This kind of radiation pattern can also be observed in dipoles subjected to rotation, which indicates that one possible interpretation of the result is that the captured dipole radiation using the

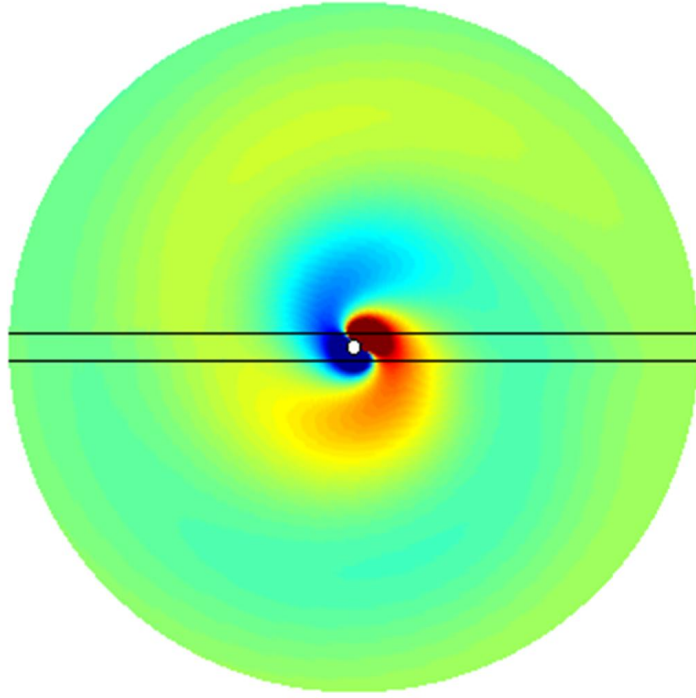


Figure 6.22: Equivalent Pressure Mapping with 1m radius. Horizontal lines represents the shear layer simplification.

averaging in fact would correspond to a rotating dipole radiation, which is not observed when using a single event identification. This difference could be explained considering that for one particular emission, the oscillations in pressure are normally instantaneously symmetric in respect of top and bottom regions for cylinder in flow simulations and acoustic radiation. The averaged identification represent not only the dipole main direction, cross-flow, but also the change in phase between the bottom and upper regions.

6.11 Directivity Plots on Averaged CSM

In order to investigate the main radiation directions, the directivity is build according to the definition from Kinsler *et al.* (1982), shown in Figure 6.24.

Despite the spiral like pressure mapping for the identified dipole distributions, the directivity confirms the cross-flow expected orientation for low frequencies, as mentioned in Takaishi *et al.* (2007). The directivity seems to deviate according to the low asymmetry on the flow (2°), with higher speeds on the bottom of the cylinder.

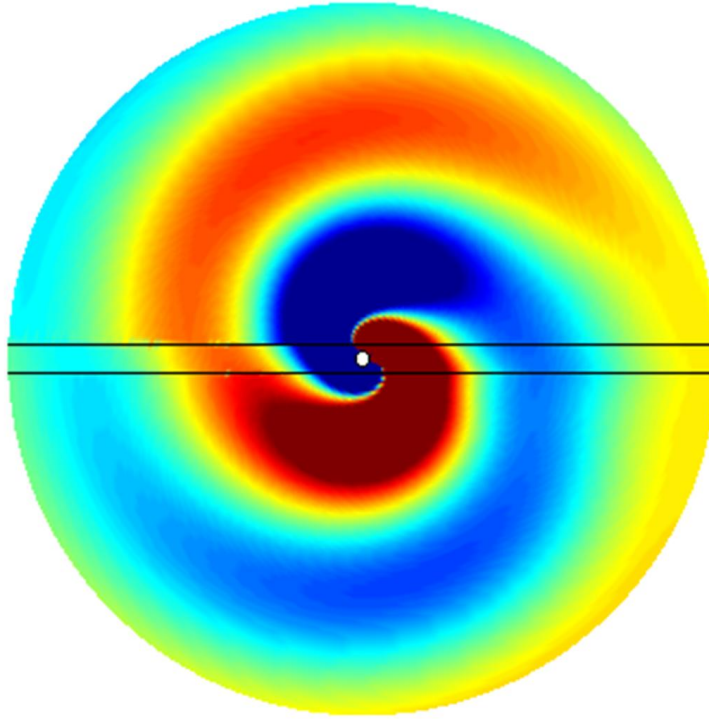


Figure 6.23: Equivalent Pressure Mapping for 1m radius (reduced dB range).

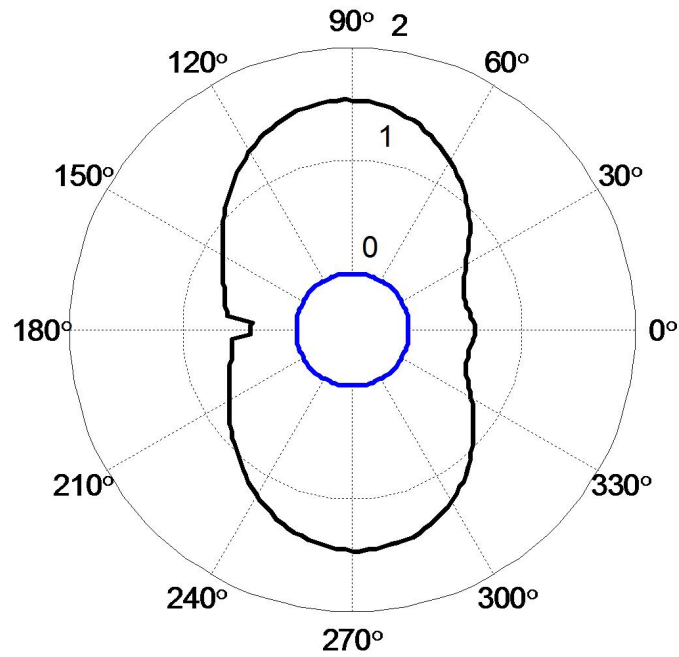


Figure 6.24: Directivity plot calculated at 1m radius in respect to the cylindrical equivalent radiation.

The regions around 0° and 180° shows the convection effects, since they are on the flow region. The spiral like radiation causes still important radiation even close to 90° from the main radiation directions.

6.12 Summary

The selection of the peak emissions by cross-spectral averaging, and individual identification is an important tool to support the understanding of source generation and radiation characteristics. This preliminary investigation of dipole formation on the cylinder section transversal plane is restricted to just three of the main peaks in a 1.2 seconds interval. This does not intent to represent the overall dipole distribution but the adopted approach can be later used with that objective. The equivalent mapping can be used to assess far-field wavefront and points to regions of higher pressure amplitudes.

The generalized inverse beamforming method is able to capture the source region with high accuracy, and point to the pressure fluctuation relationship with frequency. The method implemented only considered the dipole formation in the plane parallel to the array, and future work is planned to address other different directions and also accurate absolute strength estimations.

This work present a new approach to the aeroacoustic sources identification, such as dipole distributions over compact obstacles in subsonic jet flows. Microphone spectrums averaging leaded to slightly different results when compared to single event identifications. The spiral like radiation pattern suggests that the dipole would be rotating, despite that no rotation is considered on the transfer matrix modeling. This rotation in fact would be the representation of the pressure oscillation between the two identified regions. The directivity obtained on the experimental setup is in fully agreement with the numerical cases studied in literature, even considering that those problems differs in diameter/length ratio to the tested obstacle.

7 Aeroacoustic Source Identification: Two Structures in Subsonic Flow

In this Chapter, noise generated by two structures at an angle with respect to a subsonic flow main direction is investigated experimentally with identifications of monopole and dipole types of aeroacoustic source. Initially, monopole identification results from the National Aerospace Laboratory of The Netherlands (NLR) in collaboration with UNICAMP are confronted with results obtained from application of conventional beamforming as well as the generalized inverse method. The Hybrid Generalized Inverse mapping is proposed based on the Hybrid estimation. Then, dipole identification is performed with Generalized Inverse Beamforming and a special technique is proposed to situations where dipoles have important radiation towards array direction. A line and a 3D grid are adopted to represent structures and perform the identifications of source centers of generation of sound. Wall pressure measurements are performed in one of the structures simultaneously to the array acquisition. On dipole estimation, directivity assessment is also made and far-field sound pressure level compared to estimated value.

7.1 Introduction

Noise generated by structures in flow has been investigated since acoustics fundamentals were established. As already mentioned, one of the first aeroacoustic phenomena to receive a scientific approach is the aeolian tones generation by wires or thin structures subjected to moderate or high air flow speeds by Strouhal (1878). Since then, experimental testing has evolved to the use of complex facilities and transducers. Currently these efforts involve microphone array techniques or similar configurations with the aim of aeroacoustic sources localization and characterization.

One of the key industry research fields concerns aircraft noise, related to comfort for passengers as well as, more recently, related to attend demanding airports neighborhood noise pollution restrictions. For example, the adoption of fly-over limits, a noise level recording procedure over taking off or landing manoeuvre, created a necessity to understand noise generation mechanisms, and improve design process by improving simulation capabilities.

Considering these specific aircraft noise emission conditions in take off or in landing manoeuvre, experimental sources characterization has demonstrated, for example, that the landing

gears is one of the top regions concerning sound power generation, as shown in previous works (SIJTSMA & STOKER, 2004). Experimental assessments also demonstrated that the interaction between different portions of the structures can significantly amplify the noise generation, posing an extra difficulty to find noise reduction counter measures with low cost impact on design. The Airbus A340 landing gears are shown in Figure 7.1.

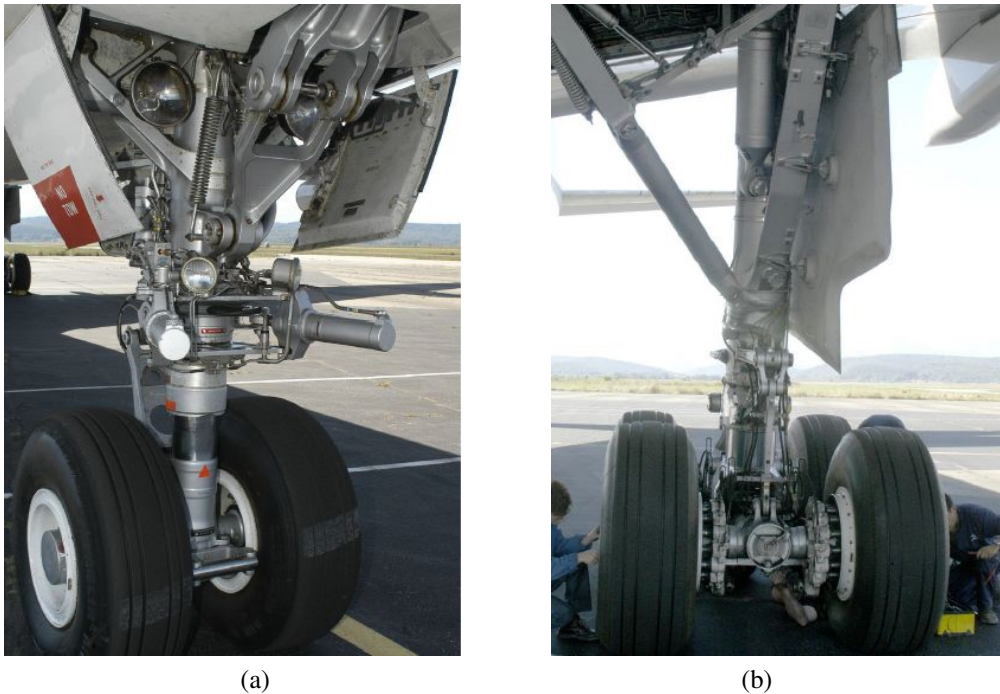


Figure 7.1: Airbus A340 landing gears: (a) nose landing gear (b) rear-left landing gear.

With the objective to develop a simple problem that would represent a landing gear noise generation, two bars with square profiles are mounted in sequence and subjected to subsonic airflows. Two angle configurations are studied with respect to the flow direction. This problem aims to reproduce simple turbulence conditions that could be assessed as a stationary problem. The simplified problem can be observed in Figure 7.2.

Measurements are taken in an open wind tunnel test facility at the Holland Aerospace National Laboratory (NLR), with an array of microphones, surface pressure transducers at the bars surface at some points of interest, and also some far-field microphone readings distributed in the anechoic test chamber in polar arrangement.

Conventional beamforming Delay-and-sum mappings are also provided from NLR research group in order to check measurements results and allow comparisons to different identification

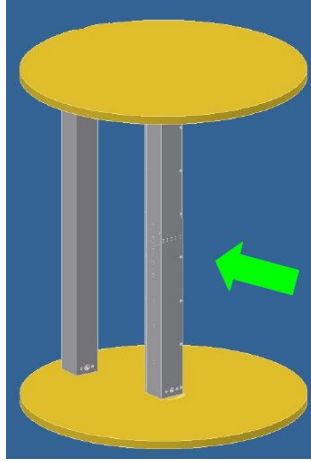


Figure 7.2: Two structures in plane with angle to the main flow direction.

techniques as the inverse methods. So, initially, reference identification simulations based in conventional beamforming using a regular distribution of monopoles in line are performed with the objective of supporting the experimental mappings analysis. Experimental results for monopole sources screening are confronted with the mappings received by NLR and discussed. Influence of CSM diagonal removal and microphone weighting, used to improve the mappings accuracy, are illustrated for one of the test conditions.

Simulated sources are used to illustrate the mappings obtained by the conventional method for regular line distribution of monopoles. Simulated line distributions are also used to verify the Generalized Inverse Beamforming mappings and develop the Hybrid Generalized Inverse Mapping that can be directly compared to conventional beamforming mappings.

Generalized inverse beamforming is initially applied to the reference problems, a single monopole and a distribution of monopoles in line, so as to discuss the nature of the original mappings and present the proposed hybrid methodology, that creates a comparable source power level mapping to the conventional beamforming mappings. The eigen-modes individual source mappings results are also presented for one of the cases to illustrate and discuss their distribution and importance.

Dipole identification is performed for two types of grids, in line at the bars centers, and a full 3D grid on bars surfaces, and results are presented and discussed along with the directivity assessment based in the equivalent pressure built from the estimation of sources.

The hybrid generalized inverse mappings are obtained for the experimental tests and results presented for the generalized inverse with the Iteratively Re-Weighted Least Squares scheme and without, on the monopole case).

The Auto-Power Attenuation in the Cross-Spectral Matrix is proposed so as to improve generalized inverse mappings dynamic range, and an example of its influence is presented for both identifications.

7.2 Test Setup and General Conditions

The tests were conducted in an Open Wind Tunnel with Anechoic Test Channel of the National Aerospace Laboratory of The Netherlands (NLR) as part of an European Union 7th Framework Programme: VALidation and Improvement of Airframe Noise prediction Tools, VALIANT. This research is part of LMS International contribution to the consortium, with Generalized Inverse Beamforming Analysis of the two structures case, and part of KUL and LMS cooperation with the Faculty of Mechanical Engineering of the State University of Campinas (UNICAMP) in this research topic.

The test chamber has $5 \times 5 \times 3 m^3$ dimensions and walls are covered with foam wedges, considered with more than 99% absorption above 500Hz. The wind tunnel nozzle has $0.38 \times 0.51 m^2$ and top and bottom end plates have $0.90 \times 0.70 m^2$, see Figure 7.3 and 7.4 for reference.

Two square profile bars with 40mm width are placed in sequence with 160mm distance between them, in a turntable device, with front structure in the turntable axis, which is 265mm from the nozzle exit plane. Two configurations are chosen for the testings, structures with angle in respect to airflow direction of 7.5° (with rear structure farther from array) and structures with angle of 20° . These layouts can be seen schematically in Figure 7.5.

Four test cases are used, for two structures angle and two airflow speeds, 35m/s and 70m/s, approximately Mach 0.1 and 0.2, respectively. The test cases are listed on Table 7.1. The airflow speeds and structures dimensions are chosen so as to reproduce Reynolds numbers close to the ones related to a landing gear in aircraft approaching or taking off maneuvers.

The array has 48 microphones of 1/2-inch type, and is approximately 0.8m wide and 0.6m

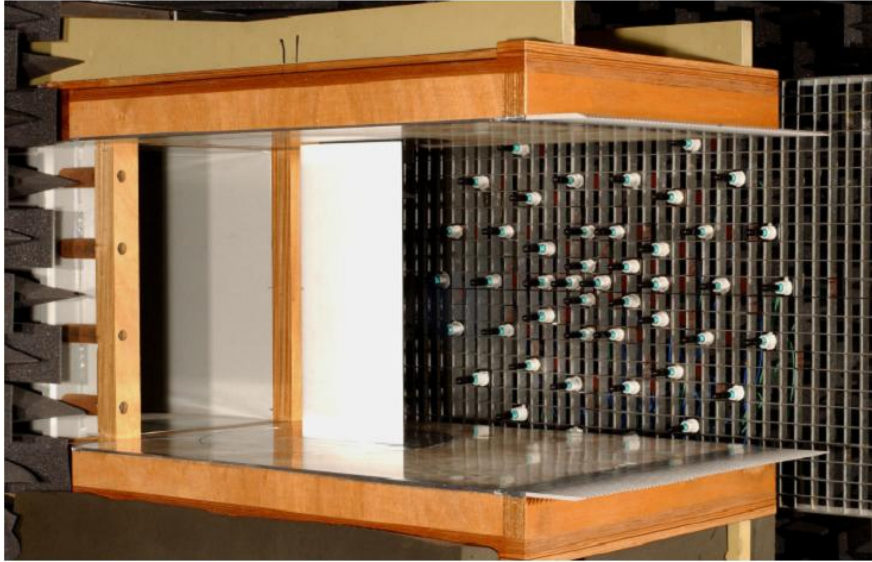


Figure 7.3: NLR Open Wind Tunnel with Anechoic Test Chamber, illustrated with an airfoil testing setup.

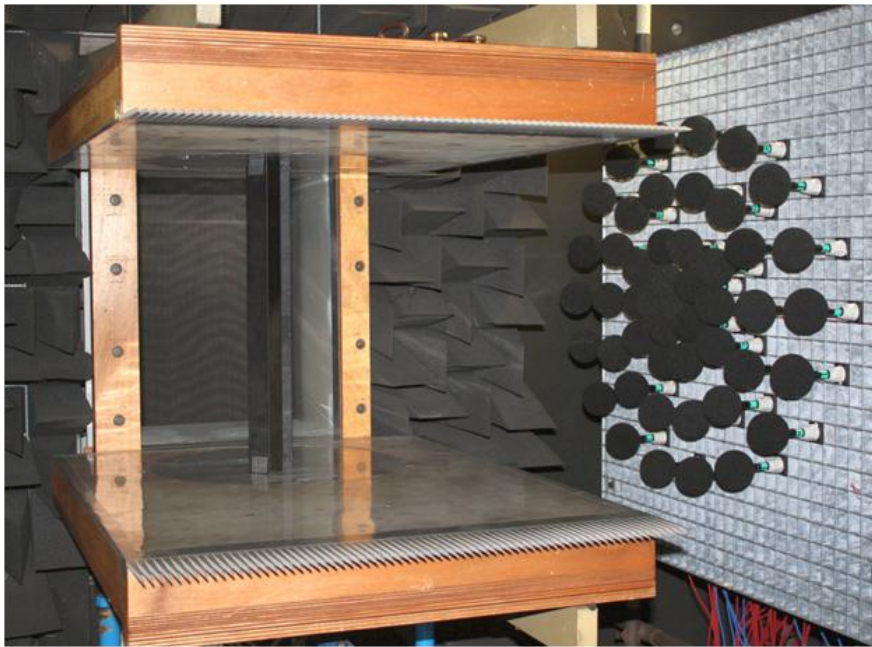


Figure 7.4: NLR Open Wind Tunnel illustrated with the turntable center bar installed and the 48 microphones array used on measurements.

height with its center positioned in front of the center of the two structures. The distance from the array plane to tunnel axis is 0.7m. These array dimensions are chosen to have high resolution in the low frequency range and obtain maximum signal-to-noise ratio. The coordinate system adopted has its origin at the center of the front structure and turntable axis, with x axis in flow direction,

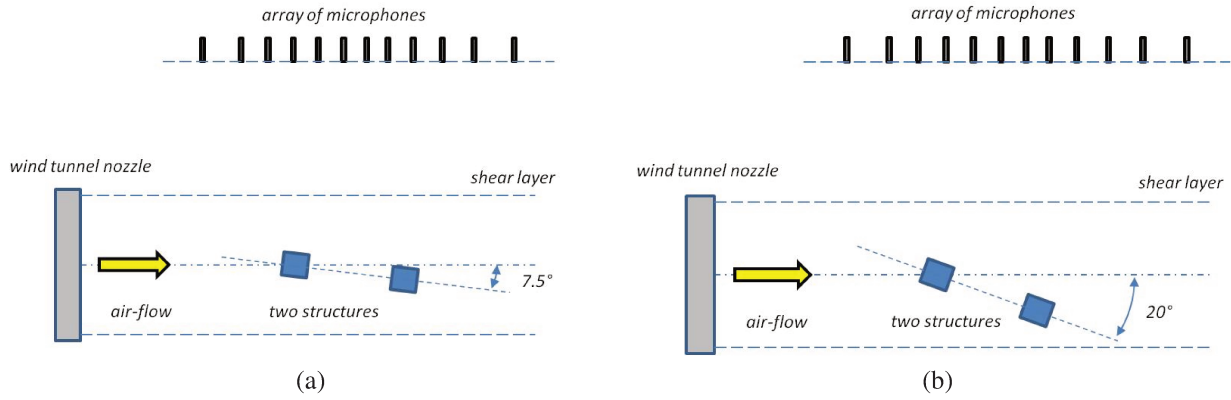


Figure 7.5: Schematic top view of test layout (not in scale) (a) Structures angle of 7.5° (b) Structures angle of 20°.

Test	Two-structures angle [°]	Airflow speed [m/s]
Case 1	7.5	35
Case 2	20	35
Case 3	7.5	70
Case 4	20	70

Table 7.1: Test cases on NLR measurements.

and y in vertical direction. The array distribution and microphones xy coordinates can be seen in Figure 7.6.

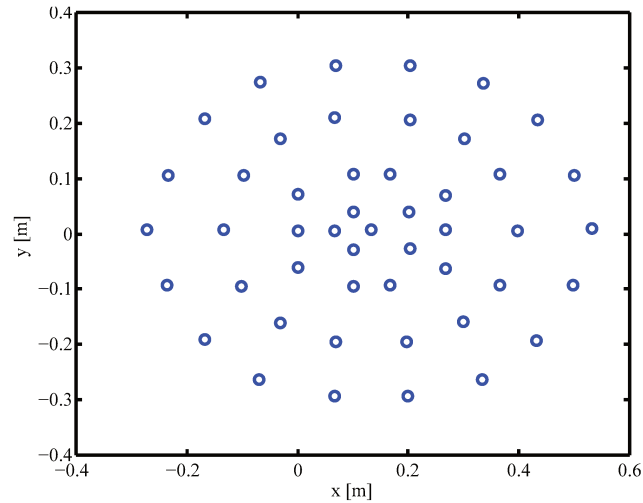


Figure 7.6: Microphones Array distribution and coordinates.

Measurements were taken with a simultaneous data system acquisition system with 102.4kHz sampling rate, and time signals recorded for 20 seconds. A high-pass filter is used at 500Hz and

an anti-aliasing low-pass filter used at 51.2kHz. Time blocks with 4096 samples are adopted to calculate each spectrum using Hanning window, and Cross-Spectral Matrix results are averaged with 50% overlap, allowing 1000 averages and 25Hz frequency resolution.

7.3 Convection and Refraction Modeling

The identifications considered the shear layer at 0.19m from tunnel axis, propagation model of Amiet (1975), and included change in sound pressure level by refraction according to Plumblee (1976), and referred to in (MUELLER, 2002), Chapter 1.

The pressure level is changed by the wave spread through the shear layer as shown in Figure 7.7.

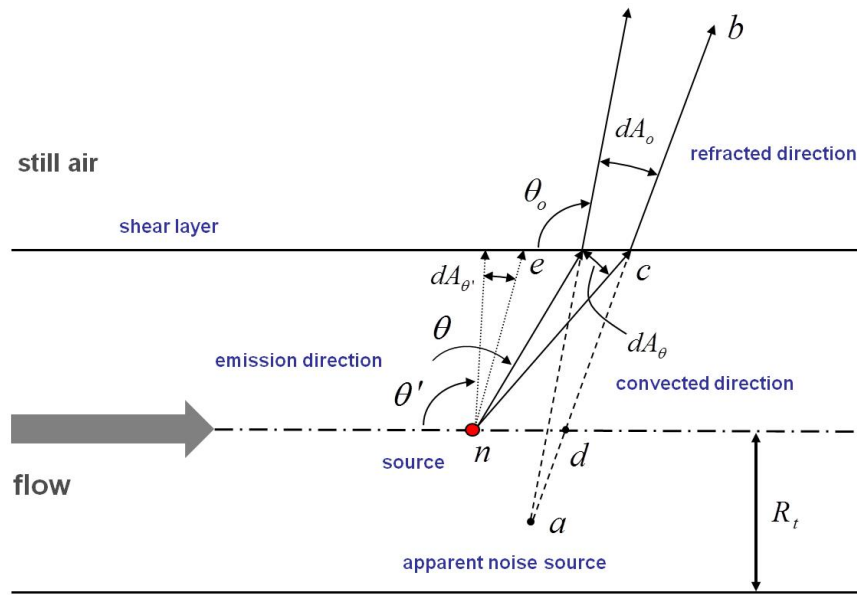


Figure 7.7: Change in sound pressure level caused by refraction based on Plumblee, 1976. Distances are $R_o = \overline{bd}$, $R_a = \overline{ba}$, $R = \overline{en}$ and $R' = \overline{cn}$.

To determine the pressure level change, the energy propagated normally to the incremental areas $dA_{\theta'}$, dA_{θ} and dA_o are equated:

$$I_{\theta'} dA_{\theta'} = I_{\theta} dA_{\theta} = I_o dA_o, \quad (7.1)$$

where $I_{\theta'}$, I_{θ} and I_o are the acoustic intensities normal to their respective incremental areas.

As a result of refraction, the pressure level at b varies with distance as (PLUMBLEE, 1976):

$$I_o \propto Press_b^2 \propto (R_o R_a)^{-1}, \quad (7.2)$$

where R_o and R_a are the distances from b to the jet centerline and the apparent noise source, respectively.

Inside the jet the variation of pressure level with distance follows the usual spherical spreading relationship:

$$I_{\theta'} \propto Press_c^2 \propto R'^{-2}. \quad (7.3)$$

The pressure measured at point b (Figure 7.7) is related to predicted level at point c by the following equation (PLUMBLEE, 1976):

$$\frac{Press_c^2}{Press_b^2} = \left(\frac{\rho_t D_t^{-4}}{\rho_o} \right) \left(\frac{R_o R_a}{R'^2} \right), \quad (7.4)$$

where ρ_t and ρ_o are the air density inside and outside of the jet, respectively; and the Doppler factor for the amplitude change is:

$$D_t = \left[1 - \left(\frac{U_{\infty}}{c_t} \right) \cos \theta' \right], \quad (7.5)$$

where the U_{∞} is the air speed inside the jet; c_t is sound speed inside the jet, and θ' is the emission angle.

The above equations correct data measured at point b for spherical spreading, shear-layer refraction spreading, and the change in the acoustic intensity caused by wave convection. The distances R_o and R_a are calculated according to the following expressions:

$$R_o = R_m \left(\frac{\sin \theta_m}{\sin \theta_o} \right) ; \quad (7.6)$$

$$R_a = R_o + \left(\frac{R_t}{\sin \theta_o} \right) \left[\left(\frac{\cot \theta'}{\cot \theta_o} \right) \left(\frac{c_o}{c_t} \right)^2 - 1 \right] . \quad (7.7)$$

The above distances are shown in Figure 7.7, considering $R_o = \overline{bd}$, $R_a = \overline{ba}$, $R = \overline{ne}$ and $R' = \overline{nc}$.

With these relationships, the source level assessment can be compensated for the wave refraction spreading and the true source level inside jet stream estimated. Normally, the change in pressure level is small, and its influence in localization is almost neglectful. Anyhow, it is considered in the source localization for improved accuracy.

7.4 Monopole Identification Using Conventional Beamforming

Four 1/3-octave bandwidths are chosen for analysis, with center frequencies of 1k, 2k, 4k and 8kHz. A regularly spaced target grid distribution is adopted for each band center frequency with 1/4 wavelength width between grid points. The grid distribution can be seen in Figure 7.8 for each band center frequency.

Conventional beamforming based in strength is calculated with Cross-Spectral Matrix diagonal (Auto-powers terms) removed, since this improves significantly the dynamic range on the localization, a common practice in aeroacoustic analysis since it decreases the influence of coherence loss on the cross-spectrums between microphones, disregarding, the higher in level, auto-power from the beamformer summation (OERLEMANS, 2009). The influence of this artifice is demonstrated for one of the experimental results in a later section.

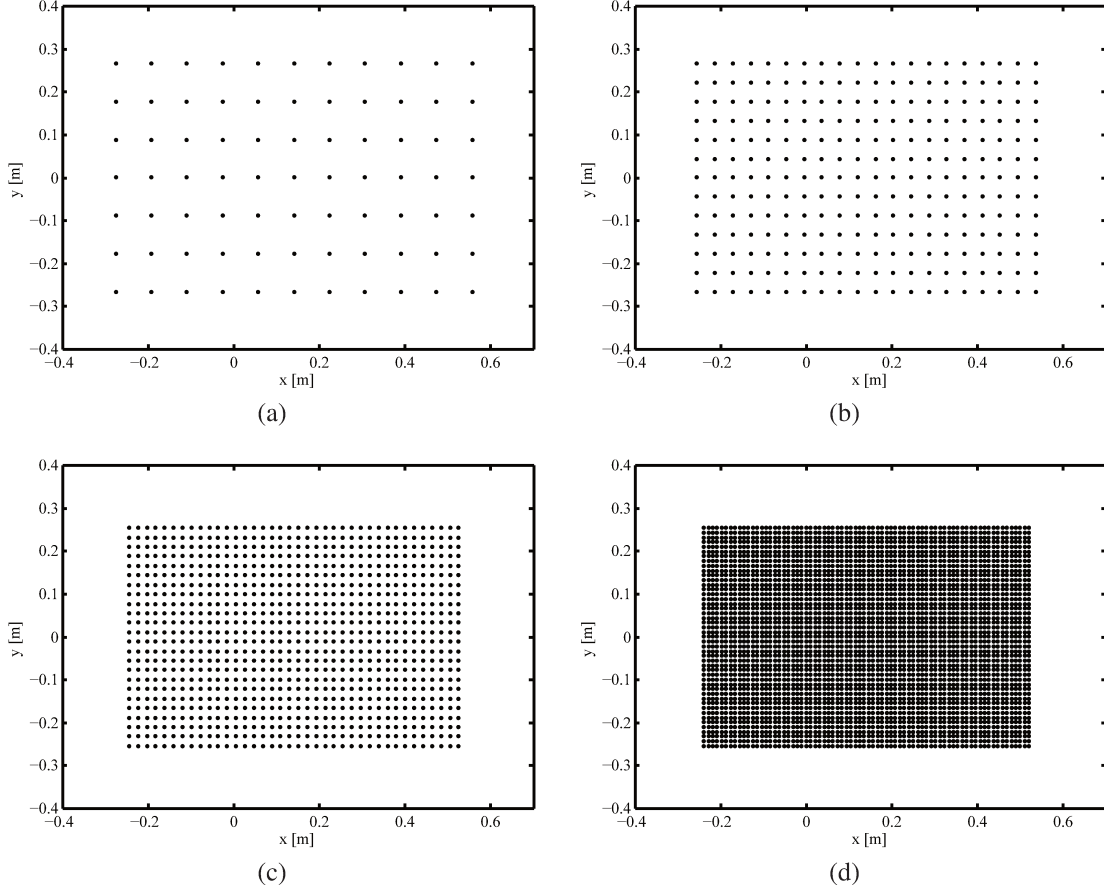


Figure 7.8: Target grid distribution based in $1/4$ of wavelength width (a) 1kHz (b) 2kHz (c) 4kHz (d) 8kHz.

7.4.1 Simulated Identification Verifications

In order to provide some reference identification mappings to the experimental results analysis, two cases are simulated for identification, one single monopole at the coordinate $(0.10, 0)$, and one line distribution of monopoles with $x = 0.10m$, from $y = -0.25m$ to $y = 0.25m$. The distance between monopoles is chosen as to reproduce the expected spanwise coherence length beneath an attached turbulent boundary layer (BLAKE, 1986), that can be estimated as:

$$\ell_{coh} = \frac{U_c}{2\pi\gamma_3 freq}, \quad (7.8)$$

where $U_c \approx 0.7U_\infty$ is the eddy convection velocity in m/s ; $\gamma_3 \approx 0.8$ is a dimensionless parameter, and $freq$ is the frequency in Hz, which leads to coherence lengths and number of considered incoherent monopole sources as shown in Table 7.2.

Frequency [Hz]	Coherence Length [mm]	Number of sources in 0.5m
1k	4.8	104
2k	2.4	208
4k	1.2	417
8k	0.6	833

Table 7.2: Coherence length and number of incoherent monopole sources in 0.5m length.

The coherence length is very small compared to the wavelength, and an increased level is expected on the conventional beamforming mappings, since several sources are considered in the sight of the mainlobe range for each assessed grid point. Simulations used unitary time-average square strength for each monopole, and the configuration of the first data set: grid with 7.5° angle and airflow with 35m/s.

Identification mappings are source PWL (Power in Watt Level) in dB re 1pW, for the monopole and line of sources, shown in Figure 7.9. The expression of the total power from a monopole source can be described as shown in Equation 7.9:

$$\Pi_{mon} = \frac{\rho c k^2 Q^2}{4\pi}. \quad (7.9)$$

Note that the estimated monopole strength, Q , is considered in the expression as the time-averaged squared strength.

The single monopole mappings are able to capture the correct strength value, while the line distribution increased about 20dB on the correct unitary strength monopoles as expected. For a low frequency such as 1kHz, the chosen dynamic range of 12dB indicates a relatively big region, and small differences are found between the single and distributed line case. Starting at 2kHz and higher at 8kHz, are the effects of sidelobes, since no sidelobe cancelation procedure is adopted in the conventional beamforming algorithm used in this study. Even if the distributed line source is fairly captured in the 4kHz and 8kHz mappings, the levels are somewhat increased in the corners

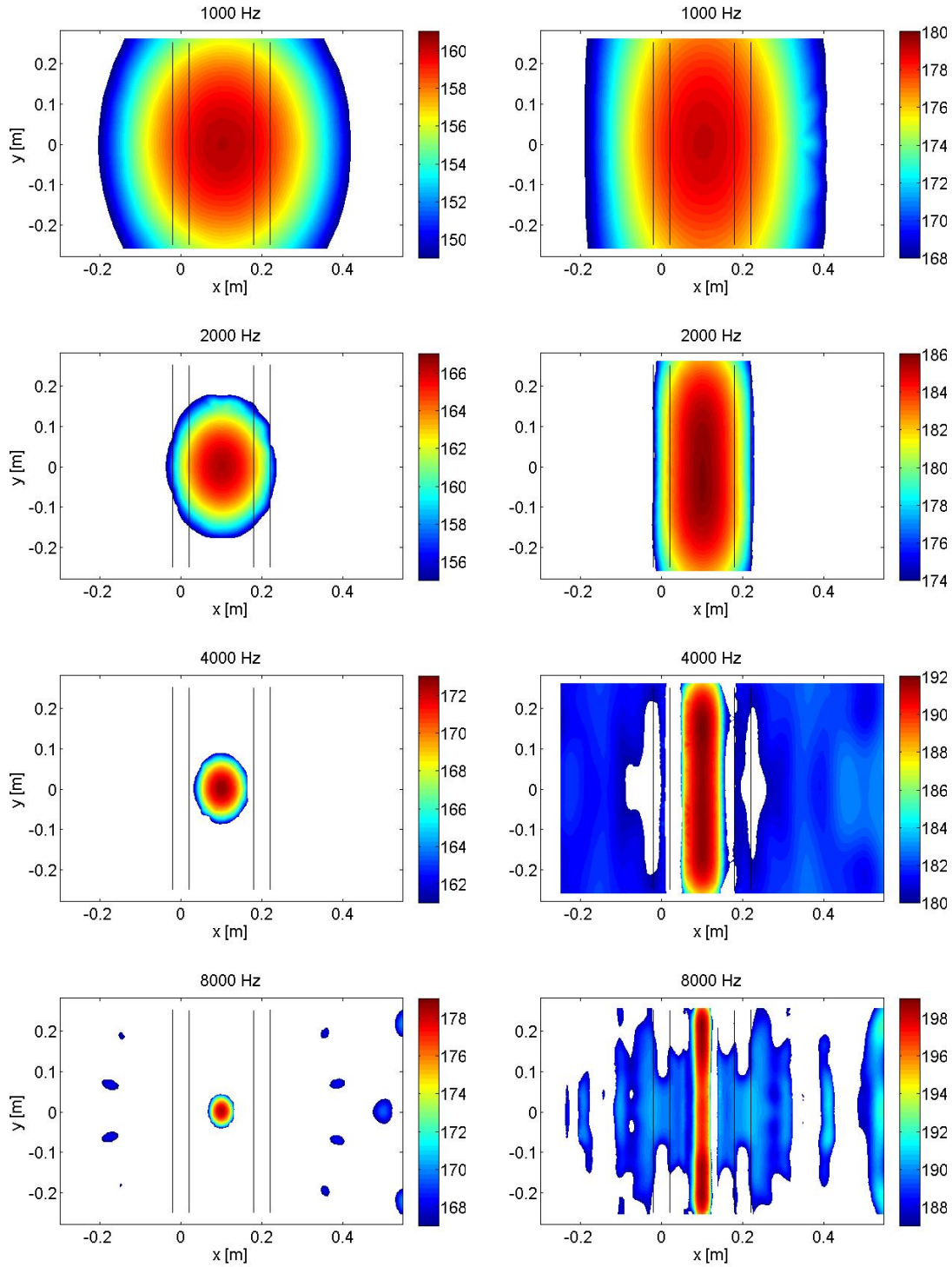


Figure 7.9: Conventional beamforming for simulated monopoles with structures at 7.5° angle and flow at 35m/s: single monopole (left); and line distributed monopoles (right). Mappings are source PWL in dB re 1pW.

for the 8kHz case, which can pose some difficulty to assess how constant a distribution is, only referring to this mapping.

7.4.2 Experimental Results and Comparison with Identification from NLR

Experimental identification mappings are built considering conventional beamforming with CSM diagonal removal for third-octave bands centered in 1k, 2k, 4k and 8kHz. The conditions are two structures angles: 7.5° and 20° ; and 35m/s and 70m/s airflow speeds. Results are presented in Figures 7.23 to 7.26. The mappings calculation adopted Amiet convection and refraction modeling, sound pressure level change by refraction, grid passing through structures centers and microphone weighting, influence on results to be shown in a later section.

The agreement between the mappings received from NLR research group and the ones calculated in this investigation confirms the validity of the spectra averaging procedure and conventional beamforming that was implemented. The agreement is both in general mapping resemblance as well as in power level for the chosen third-octave bands. The small differences found in the mappings seem to be related to the presence of higher side lobes in the mappings, since there haven't been used any suppression technique in this study.

The general localization of regions of high emissions indicate a regular line distribution in the bars direction, and dynamic range are similar to what was found in the performed simulations used as reference, indicating the validity of the coherence length throughout boundary layers.

The main line regions are located near the downstream structure for the bars plane angle of 7.5° , for either 35m/s and 70m/s airflow speeds. This indicates that the created turbulence by the upstream bar is probably hitting directly the downstream bar, and causing higher emission. In the 70m/s test, this effect at the higher frequency band is decreased, probably due to higher turbulence and small flow turbulent structures sizes. The region of emission is located in front of the downstream bar in contrary to the expected region of flow separation, after the bar, and this indicates that the interaction between bars creates an inner turbulent region.

For the measurements with bars plane angle of 20° , the upstream bar is causing the higher emission line, with region located after the bar, and with small or no presence of high emission close to the downstream bar. On the other hand, the overall center of emission for the 1k to 4kHz

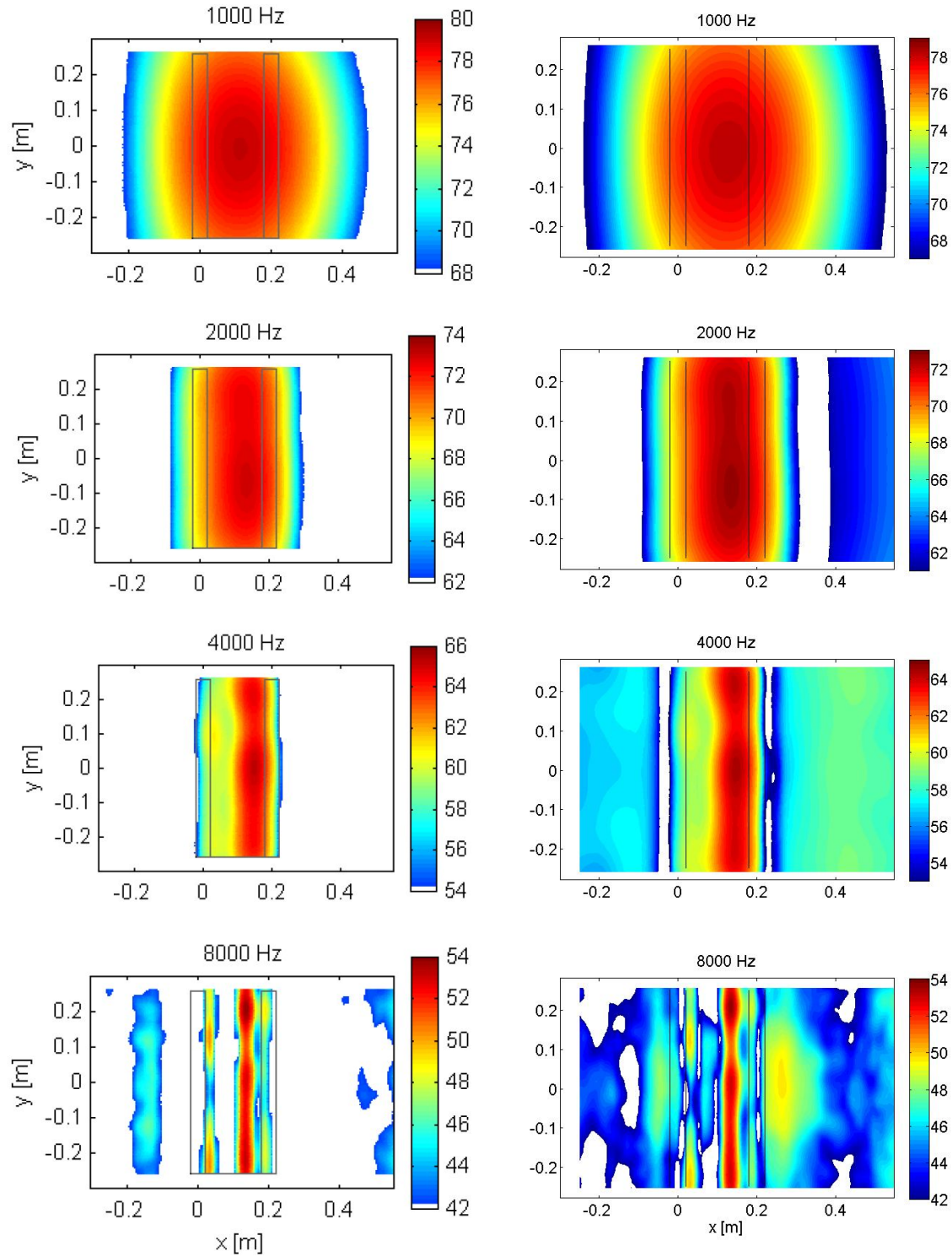


Figure 7.10: Conventional Beamforming for Structures with 7.5° angle and flow at 35m/s (results from NLR on left). Mappings are source third octave PWL in dB re 1pW.

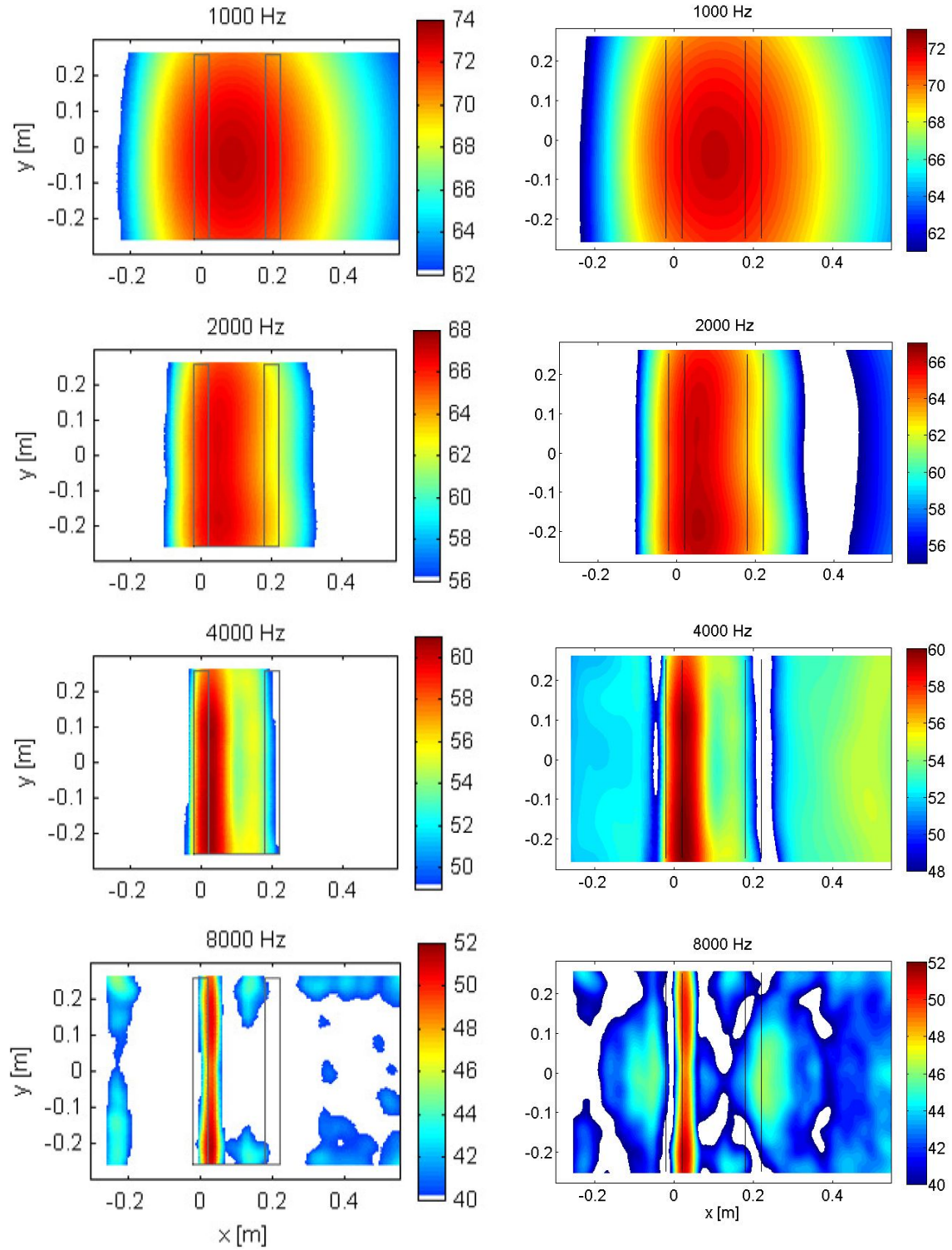


Figure 7.11: Conventional Beamforming for Structures with 20° angle and flow at 35m/s (results from NLR on left). Mappings are source third octave PWL in dB re 1pW.

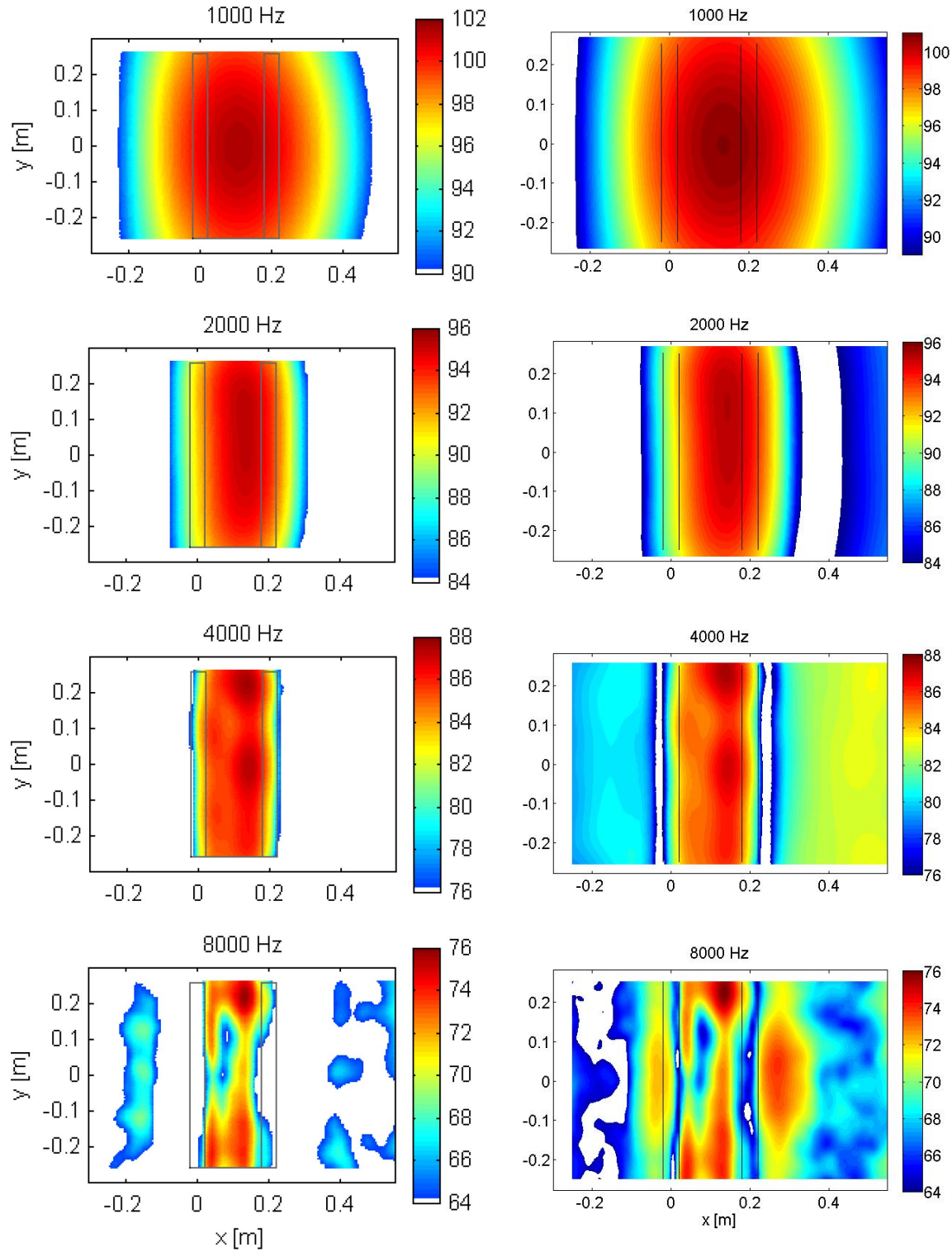


Figure 7.12: Conventional Beamforming for Structures with 7.5° angle and flow at 70m/s (results from NLR on left). Mappings are source third octave PWL in dB re 1pW.

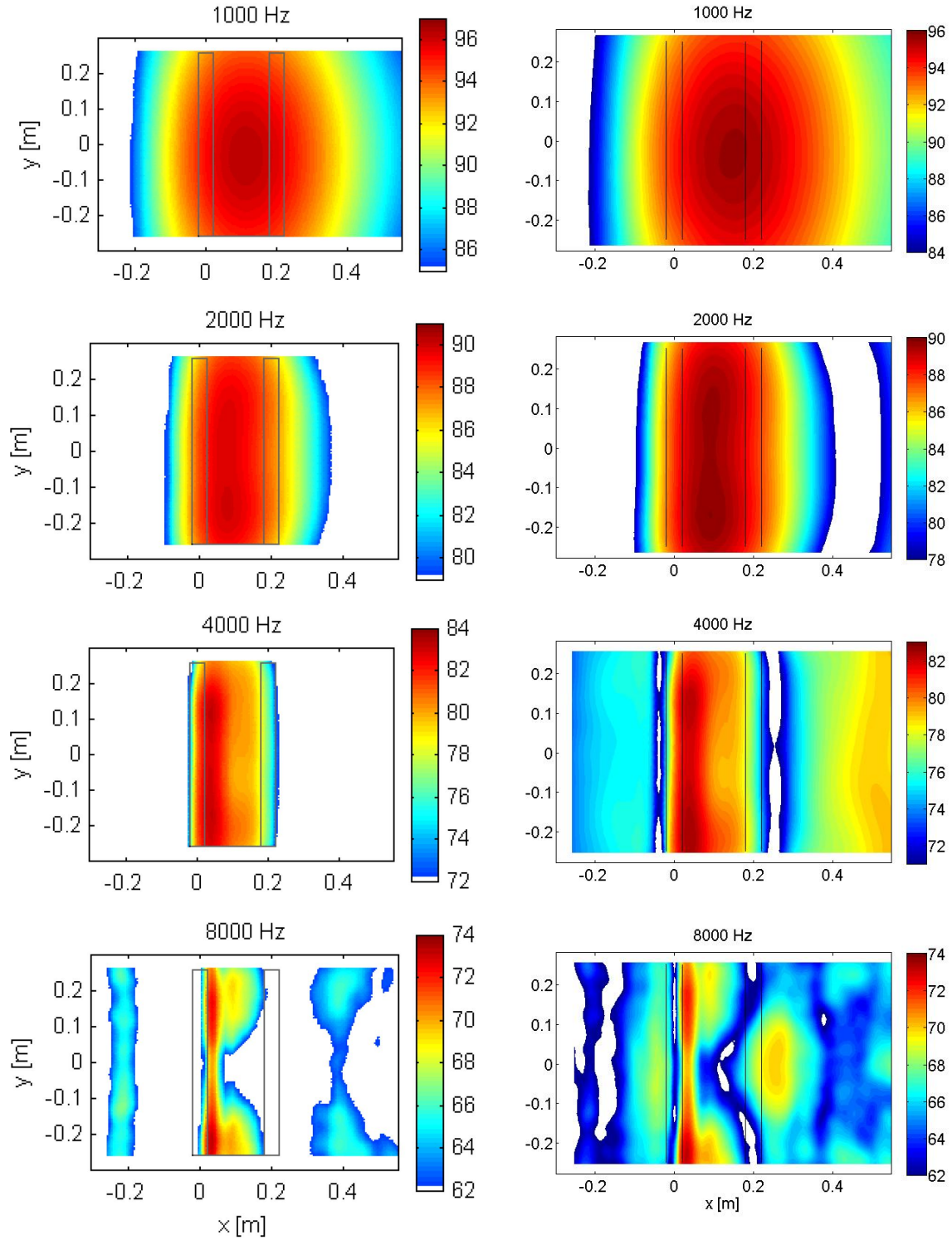


Figure 7.13: Conventional Beamforming for Structures with 20° angle and flow at 70m/s (results from NLR on left). Mappings are source third octave PWL in dB re 1pW.

indicate the full region in between bars as dynamically relevant, demonstrating again an interaction of flow dynamics and sound emission between the structures.

The conventional beamforming seems to present a fairly accurate mapping for higher frequencies, but loses capacity to depict the center of radiation in the lower frequency range, with the 1kHz mapping almost not able to distinguish a compact source region from a distributed line region.

7.4.3 Diagonal Removal Influence in Results

To illustrate the influence of diagonal removal in the identified mappings, or in other words, the influence of auto-powers level in the beamformer summation, the first data set, 7.5° angle and 35m/s airflow speed is used, and mappings are confronted in Figure 7.14.

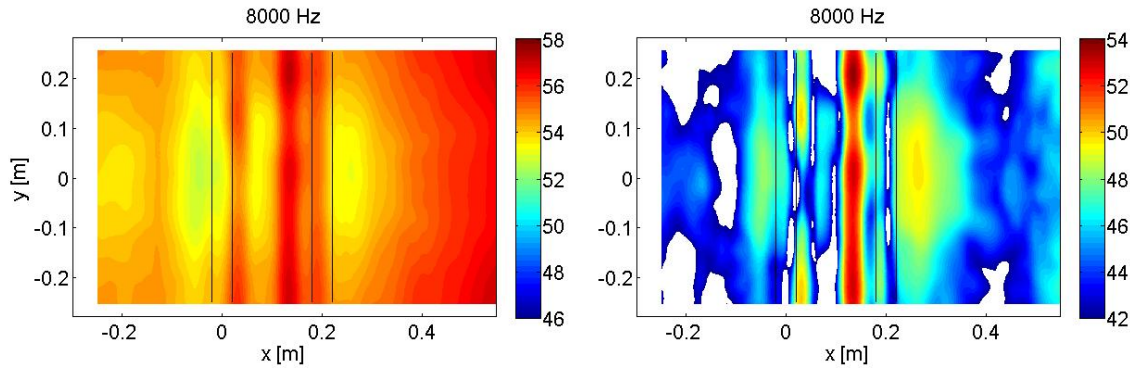


Figure 7.14: Conventional beamforming CSM diagonal removal comparison for structures at 7.5° angle and flow at 35m/s: full CSM (left); and diagonal removed (right). Mappings are source PWL in dB re 1pW.

The advantage in removing the diagonal from the CSM on this aeroacoustic problem is evident since the auto-powers, as known in the literature (MUELLER, 2002), raise the overall mapping level and decrease the relative importance of the cross-spectrum terms, decreasing the resolution of main regions of emissions detection. The removal of CSM diagonal also is of easy implementation in the beamformer calculation, just requiring a small adjustment in the number of terms on the power levels average.

7.4.4 Microphone Weighting Influence in Results

Another known artifice to improve conventional beamforming is the adoption of microphone weighting factors relative to their effective power contribution to the antenna overall power averaging, and thus function of each microphone surrounding area compared to the overall antenna aperture area. The influence in the adoption of microphone weighting is shown in Figure 7.15.

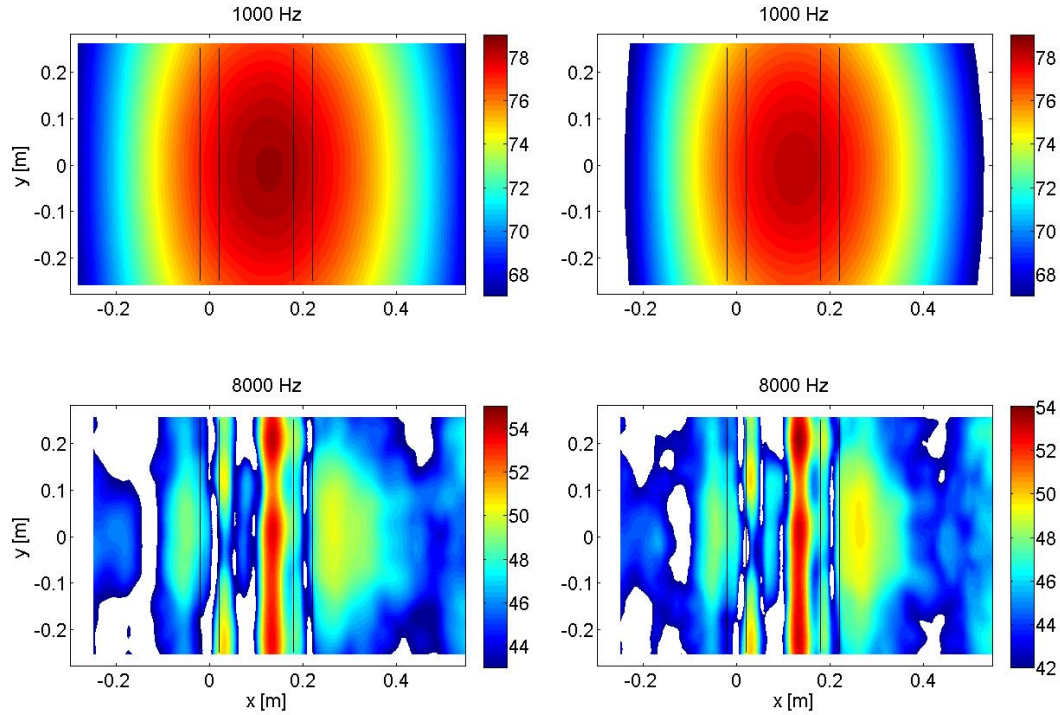


Figure 7.15: Conventional beamforming microphone weighting comparison for structures at 7.5° angle and flow at 35m/s: without weighting (left); and with weighting (right). Mappings are source PWL in dB re 1pW.

Despite the small influence in the main source regions, there is some reduction in the lower dynamic response region, reducing the main lobe and also reducing the influence of sidelobes.

7.5 Monopole Identification Using Generalized Inverse Beamforming

The Generalized Inverse Beamforming is a relatively recent method and little is known about its performance compared to other methods, like the conventional beamforming. In this

section, results are obtained for the generalized inverse method with and without the Iteratively Re-Weighted Least Squares scheme (IRLS) (SUZUKI, 2011), and discussed in comparison to the shown conventional beamforming mappings.

In order to perform the comparison, first it is required to investigate and develop the generalized inverse mappings as a directional mapping instead of the norm based quantitative assessment, thus creating a common basis for comparison. For this, simulations of a single monopole and a line of monopoles are used to develop the common basis comparison.

7.5.1 Simulated Identification Verifications

Using the same simulation cases used on the conventional beamforming investigation, a single monopole at the $x = 0.10m$ and $y = 0$ coordinates, and the line of monopoles at the $x = 0.10m$, and with y varying from $y = -0.25m$ to $y = 0.25m$ coordinates. for the line distribution, the number of incoherent monopole sources is as shown in Table 7.1.

The generalized inverse algorithm without IRLS is set to stop truncation when the J_1 cost function reaches its minimum or the number of terms in the source vector reaches 12 grid points. The residue cost function adopted in this study is an alternative to the expression shown in Chapter 2, and can be described as follows:

$$J_{resII} \equiv \alpha^{-1} |v_i - Aa_i|. \quad (7.10)$$

This expression presents very similar results to the one used in Chapter 2 while keeping a coherent relationship between physical units in the residue cost function to be compared to the $\ell - 1$ norm of the source vector.

The generalized inverse algorithm with IRLS is set to stop after 10 iterations. Both methods use the eigenmodes of which the square root of the eigenvalues are in the 10dB range from the maximum value. The optimum regularization strategy is adopted for the generalized inverse without IRLS and for the first calculation in the IRLS case. As shown in a previous Chapter, the optimum regularization is set to minimize the residue cost function on each iteration.

On the IRLS method, after the first calculation, the regularization factor adopted is 5% of the greatest eigen-value of $A^\dagger W_i A$, where kept fixed throughout the subsequent IRLS iterations.

The grid adopted for the generalized inverse calculations is still based in $1/4$ wavelength spacing between grid points, but its limits are spaced shorter in the x direction to avoid extra computational cost in a low source level region and is spaced longer in the y direction to consider regions of reflected emissions in the end plates which can carry energy that should be correctly captured in the inversion of the system, otherwise it is counted as from the central part of radiation. This characteristic could imply in slightly decreased level readings in lower frequencies, since the reflections are somewhat separated from the central part.

The target grid distributions are presented in Figure 7.16, for the center frequencies of 1k, 2k, 4k and 8kHz, with respectively: 80, 270, 986 and 3762 grid points.

Simulated identifications using the generalized inverse beamforming for the single monopole and line distribution of monopoles is shown in Figure 7.17 for the analysis performed without IRLS and in Figure 7.29 for the analysis performed with IRLS.

Despite that the summation of the terms over the mappings recover the strength level for the single monopole case, this level is not clear on the distributed source mappings.

The distribution of source levels in the line of monopoles simulation doesn't seem to recover the constant distribution of strength. The generalized inverse with IRLS mappings are substantially improved in terms of localization of the line source but the levels along the line are even more irregular and distant from the expected constant source strength distribution. These observations demanded that an intermediate process is adopted to develop a mapping that could better represent and be compared to the conventional mapping.

7.5.2 Hybrid Generalized Inverse Mapping

With the objective of developing a comparable mapping for the conventional beamforming, a Hybrid generalized inverse mapping based on the Hybrid mapping is developed here. It consists of the Hybrid mappings levels being adopted at the source terms which presents higher levels, for example, in a 10dB range from the highest term. The Hybrid Method was first presented

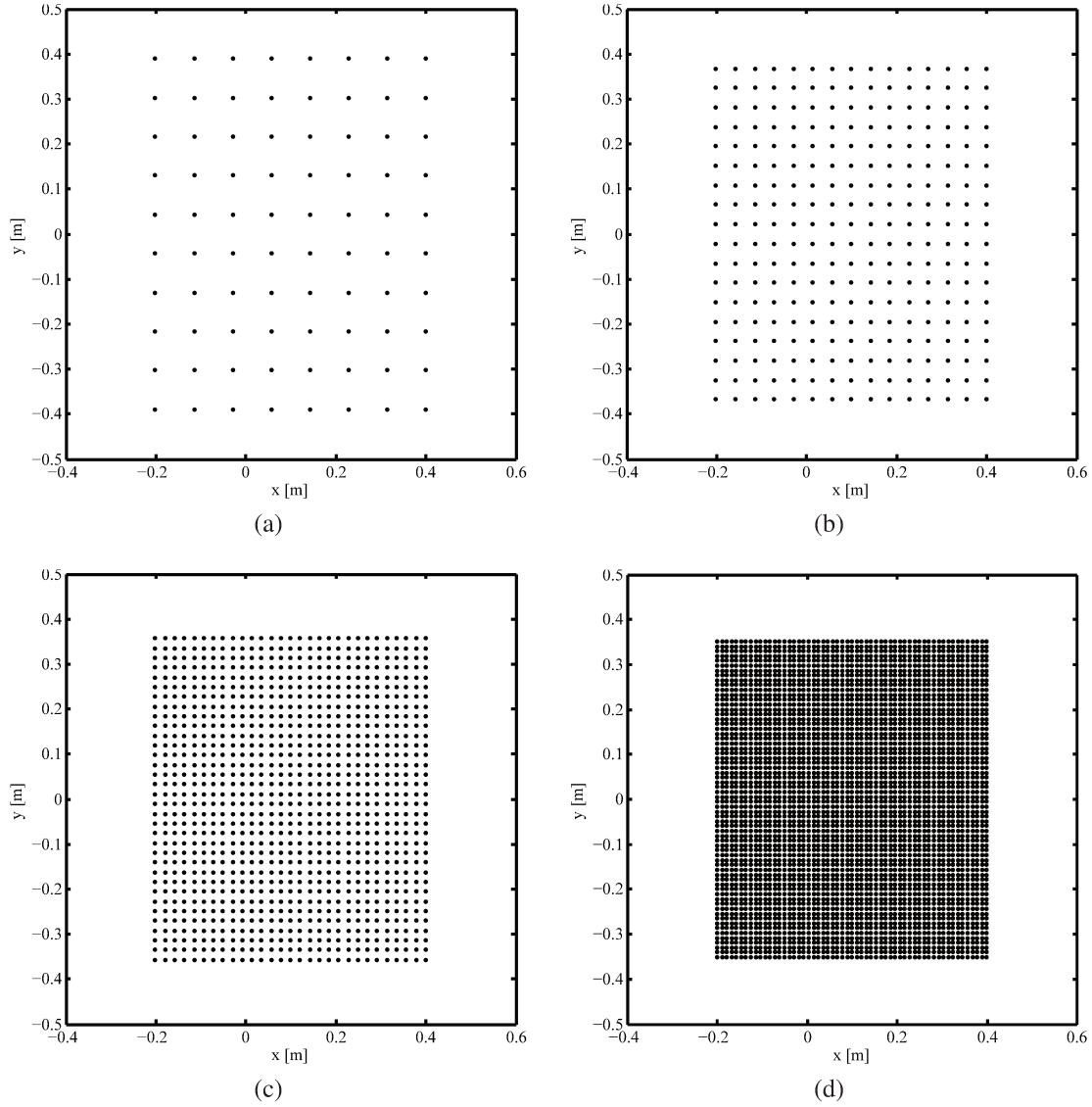


Figure 7.16: Target grid distribution for the generalized inverse calculations based in $1/4$ of wavelength width (a) 1kHz (b) 2kHz (c) 4kHz (d) 8kHz.

in (ZAVALA *et al.*, 2010B), and also detailed in the Experimental Identification Using Compact Sources Chapter, Section 5.2.

The Hybrid method, developed in previous works (ZAVALA *et al.*, 2010B) and presented in Chapter 3, relates the generalized inverse mapping to the correspondent conventional beamforming mapping by a convolution of the generalized inverse mapping with the Point-Spread Function of the array, and in principle, recover the conventional mapping directional source level. An example of the Hybrid mapping is shown in Figure 7.19

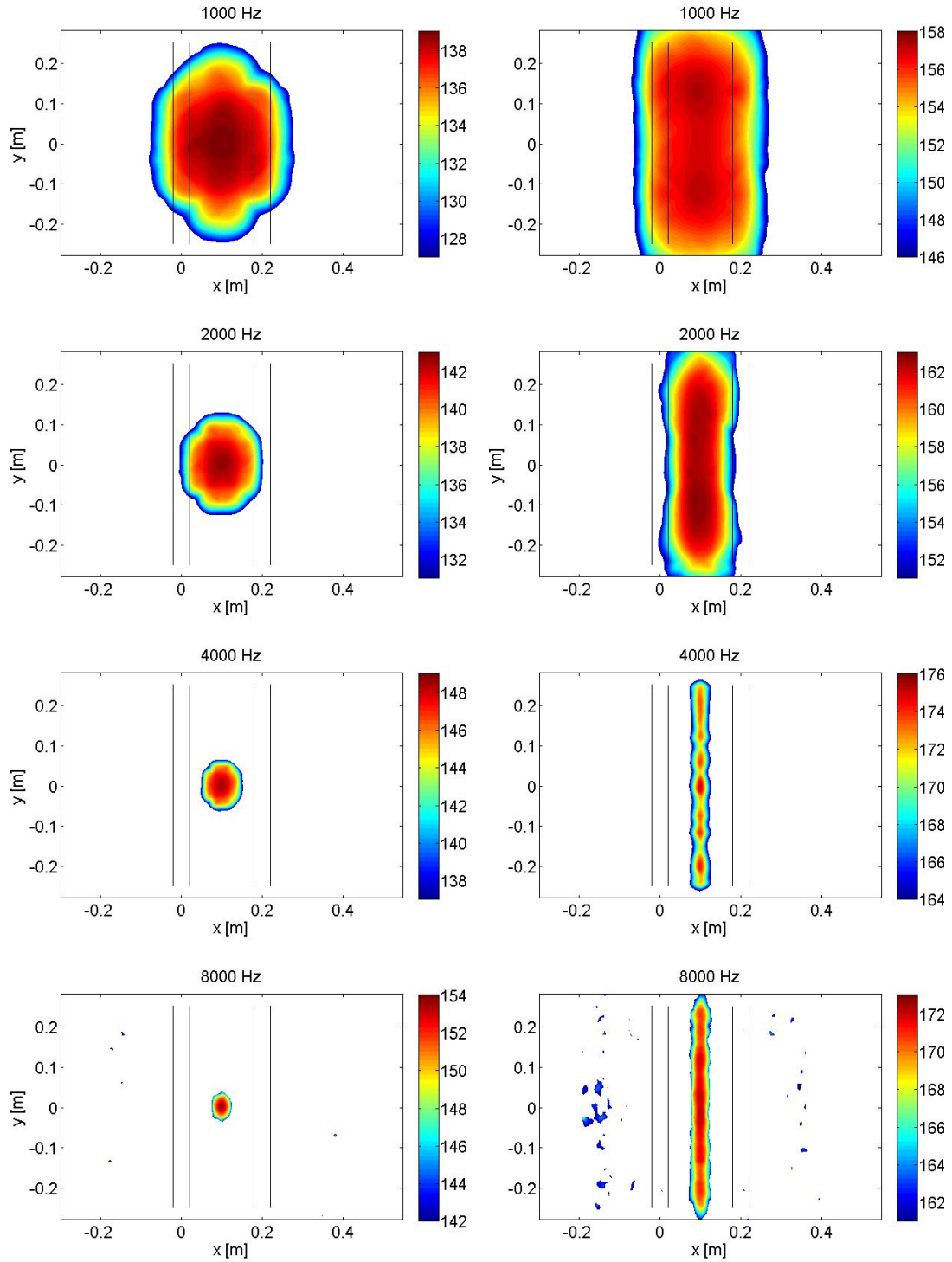


Figure 7.17: Generalized inverse beamforming (without IRLS) for simulated monopoles with structures at 7.5° angle and flow at 35m/s: single monopole (left); and line distributed monopoles (right). Mappings are source PWL in dB re 1pW.

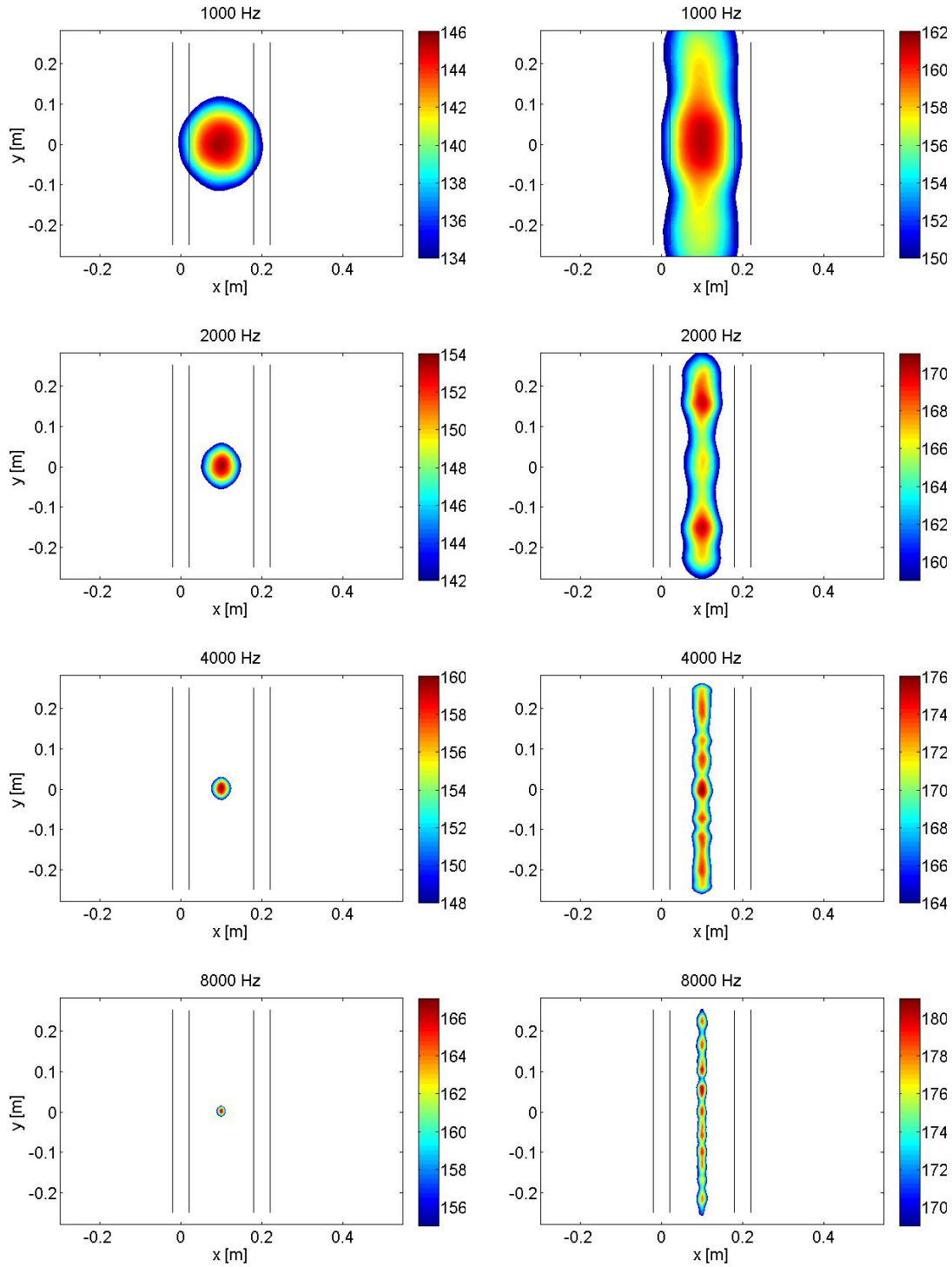


Figure 7.18: Generalized inverse beamforming with IRLS for simulated monopoles with structures at 7.5° angle and flow at 35m/s: single monopole (left); and line distributed monopoles (right). Mappings are source PWL in dB re 1pW.

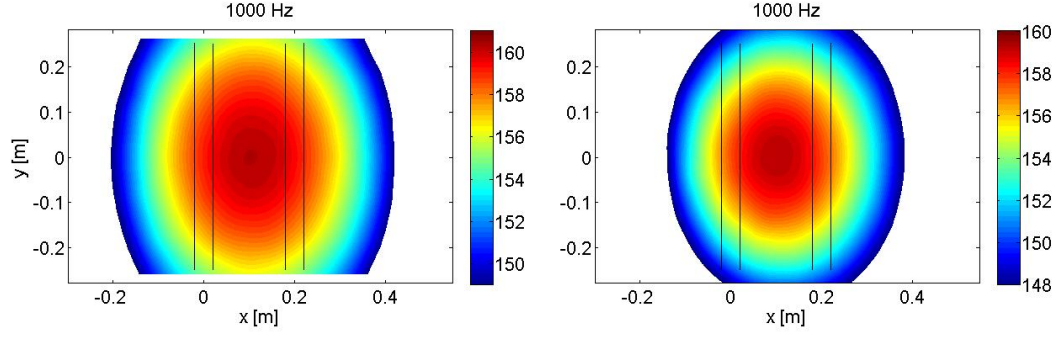


Figure 7.19: Conventional beamforming and Hybrid Mapping comparison for the single monopole simulated case, with grid plane at 7.5° angle and flow at 35m/s: CB (left); and Hybrid (right). Mappings are source PWL in dB re 1pW.

Despite the fact that not an exact conventional mapping is recovered, a fair approximation is obtained, and, most importantly, the directional source level mapping is approximately obtained. The small reduction in peak level could be explained since the generalized inverse mapping source distribution is not a perfectly concentrated source representation.

With the aim to build a comparable source level mapping but with the advantage of source region localization of the generalized inverse source vector, a Hybrid generalized inverse mapping is proposed, which consists of keeping the Hybrid levels at the grid points in the inverse source vector that are greater than a certain level, for example, 10dB range from the maximum source vector term. Actually, the square of the point-spread-function is adopted to improve localization of the main sources without significant change in level compared to the use of the original PSF, and a sharp gaussian filter is used to improve visualization.

This proposed mapping is presented for the simulated cases of single monopole and line of monopoles using the first data set configuration, grid with 7.5° angle and 35m/s airflow speed, which can be seen in Figure 7.20 for the Hybrid mappings based in the generalized inverse without IRLS and in Figure 7.21 for the ones based on the generalized inverse with IRLS.

Now, the mappings approximately recover the unitary strength results for the single monopole case and similar results to the conventional beamforming results for the line of monopoles, with an advantage for the GI with IRLS, with respect to the level and to the region of source location. Although the mappings present only a slightly bigger region of source location when compared to the generalized inverse mapping without the hybrid level, they present a much better representation

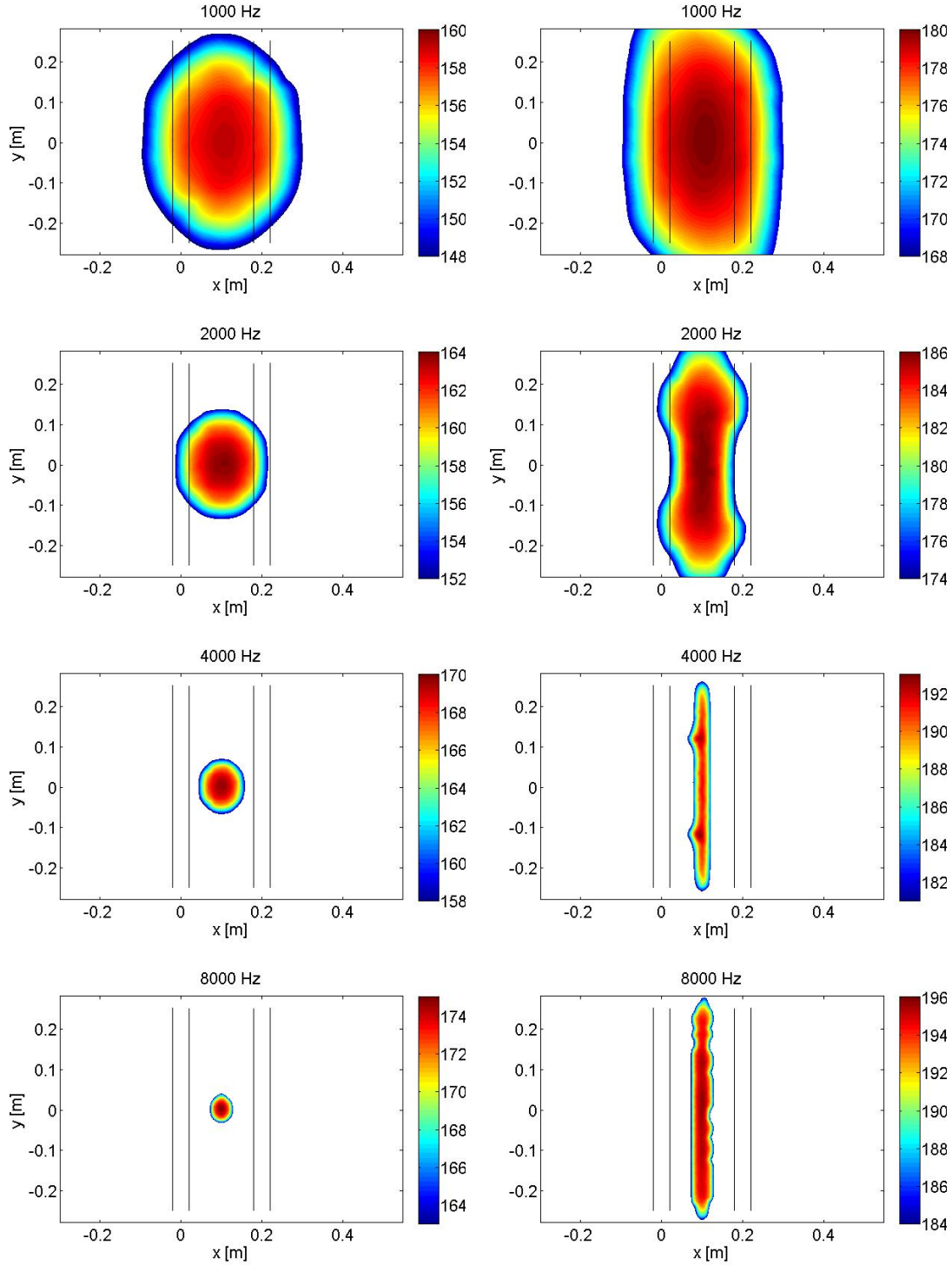


Figure 7.20: Hybrid generalized inverse beamforming (without IRLS) for simulated monopoles with structures at 7.5° angle and flow at 35m/s: single monopole (left); and line distributed monopoles (right). Mappings are source PWL in dB re 1pW.

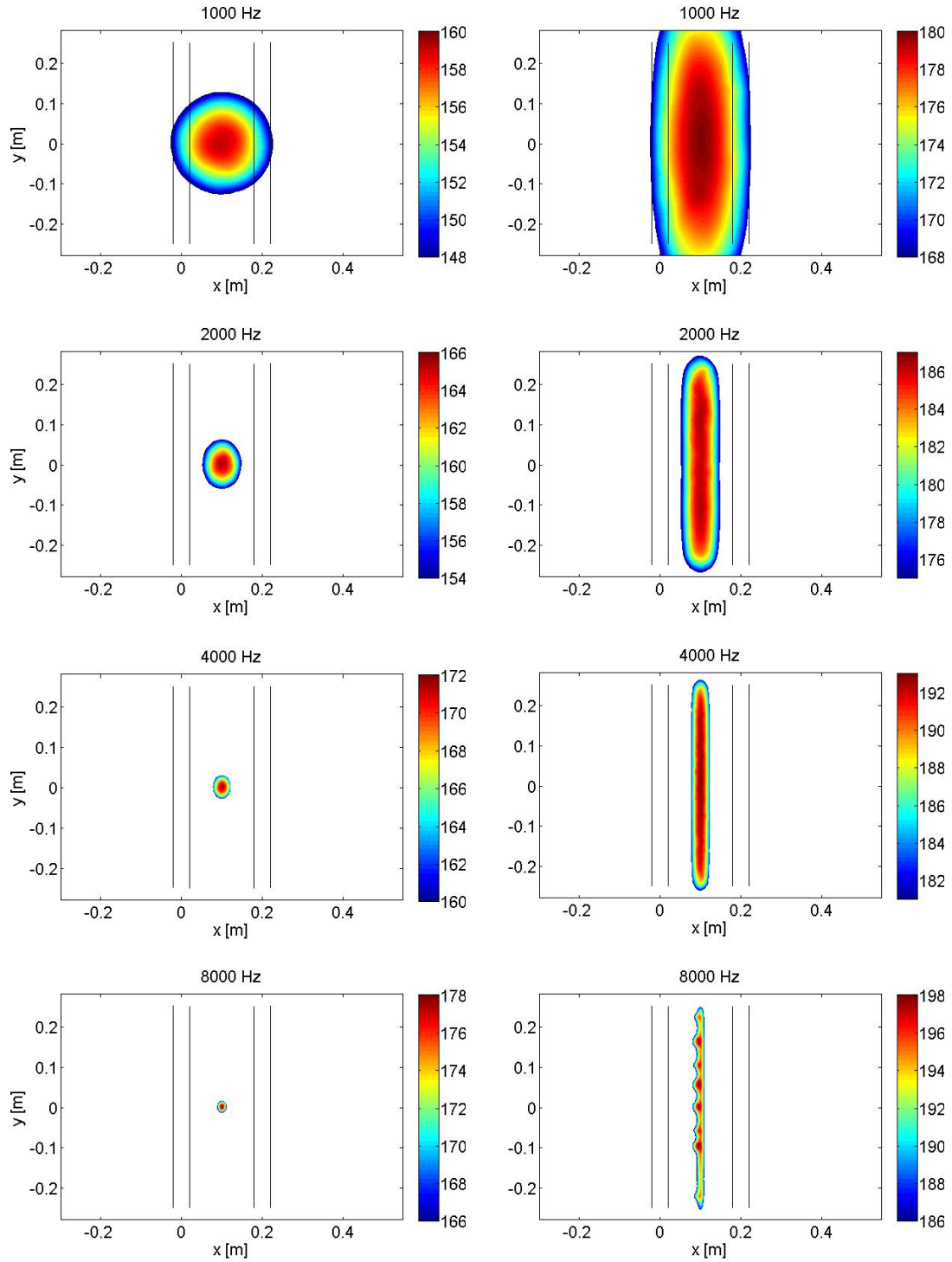


Figure 7.21: Hybrid generalized inverse beamforming with IRLS for simulated monopoles with structures at 7.5° angle and flow at 35m/s: single monopole (left); and line distributed monopoles (right). Mappings are source PWL in dB re 1pW.

of the source level distribution than the direct inverse result.

7.5.3 Auto-Powers Attenuation in CSM

As previously shown, the influence of the auto-powers in the CSM can be detrimental to the mapping resolution, and the same happens with the generalized inverse mapping. To overcome this difficulty, a proposed method is presented here so that the auto-powers levels in the CSM diagonal are attenuated before the eigen-decomposition to obtain the eigen-modes. This artificial attenuation is based in the reduction of the diagonal terms based in the comparison of the average levels of cross-spectral terms to the diagonal ones. This reduction allows an increased resolution of the mapping but brings an inconvenient side effect, the split in positive and negative eigen-values. On the other hand, disregarding the negative eigen-values seems not to affect the overall performance in obtaining a better resolution.

To demonstrate the effect of the attenuation of CSM diagonal terms in the generalized inverse mappings, the first data set is calculated for the 8kHz frequency band by the generalized inverse with IRLS and by the Hybrid mapping, with analyzes presented in Figure 7.22.

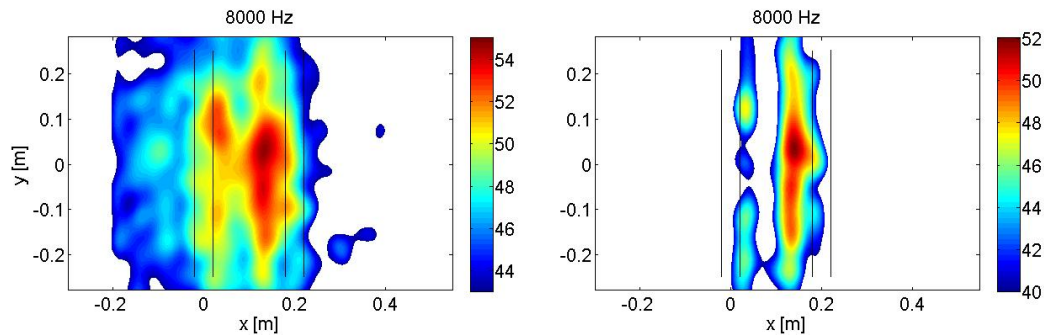


Figure 7.22: Hybrid mappings comparison for the CSM diagonal attenuation for the two structures with 7.5° angle and flow at 35m/s: original CSM (left); and CSM with attenuated diagonal (right). Mappings are source PWL in dB re 1pW.

The CSM diagonal attenuation improves significantly the spatial dynamic resolution, and presenting a similar mapping to the conventional beamforming result. The reduction in level is observed again, similar to the result from the previous section.

7.5.4 Experimental Identification Results and Analysis

With the CSM diagonal attenuation artifice, presented in the previous section, hybrid generalized inverse mappings are generated without IRLS and with IRLS for comparison to the conventional mappings presented earlier. Results can be observed in Figures 7.23 to 7.26

Mappings for 1k, 2k and 4kHz, are generated by summation over the third octave band frequency lines, but the presented 8kHz mapping corresponds to the analysis at the center frequency, and extrapolated to the third octave band. This is chosen so as to keep the high resolution found at this frequency range, which is somewhat destroyed if a summation is performed over 75 frequency lines (25Hz resolution). To illustrate this result, the average mapping for the first data set is shown in Figure 7.27.

It is clear the advantage of using the center frequency analysis at higher frequencies as in the 8kHz band, and this averaging distortion can be in fact result of the higher localization resolution, which can be deteriorated if a wide band such as in the third octave band at 8kHz case is summed. At least, this can be an option to the analyst.

Regarding the results observed in all data sets using the hybrid generalized inverse beamforming, they all are in agreement with the conventional mappings both in main source localization as well as in the source power estimation, considering that the adopted approach tends to reduce about 1 to 2dB. The localization regions are all accurately depicted in the mappings with a significant advantage to the generalized inverse method with IRLS, which presents outstanding results in the medium and lower frequency range to separate the localized region as from a distributed source in line to the response from a compact region. The result is also very similar to the simulated line of monopoles, again confirming the assumption of coherence length to calculate the number of incoherent spanwise regions.

The impressive resolution on the IRLS results can, on the other hand, hide some details and nuances from the source scenario, and again, this can be an option to the analyst to consider always results from both approaches for comparison.

The 2kHz and 4kHz mappings often presented centers of radiation instead of regular line distributions, and this has to be taken carefully, remembering that the original generalized inverse mapping tends to concentrate levels in some regions, as observed on the simulation results.

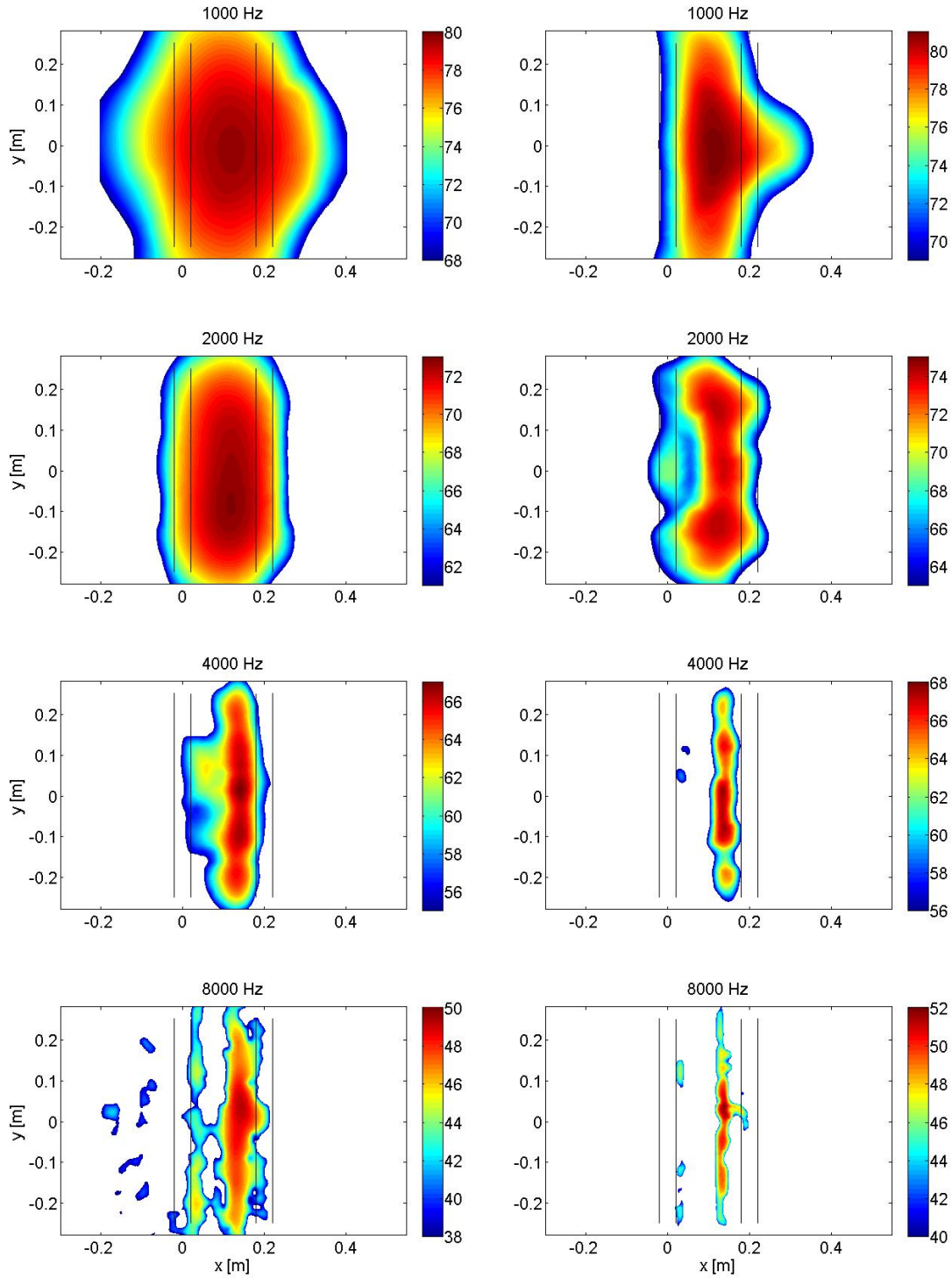


Figure 7.23: Generalized Inverse Beamforming for Structures with 7.5° angle and flow at 35m/s (results with IRLS on right). Mappings are source third octave PWL in dB re 1pW.

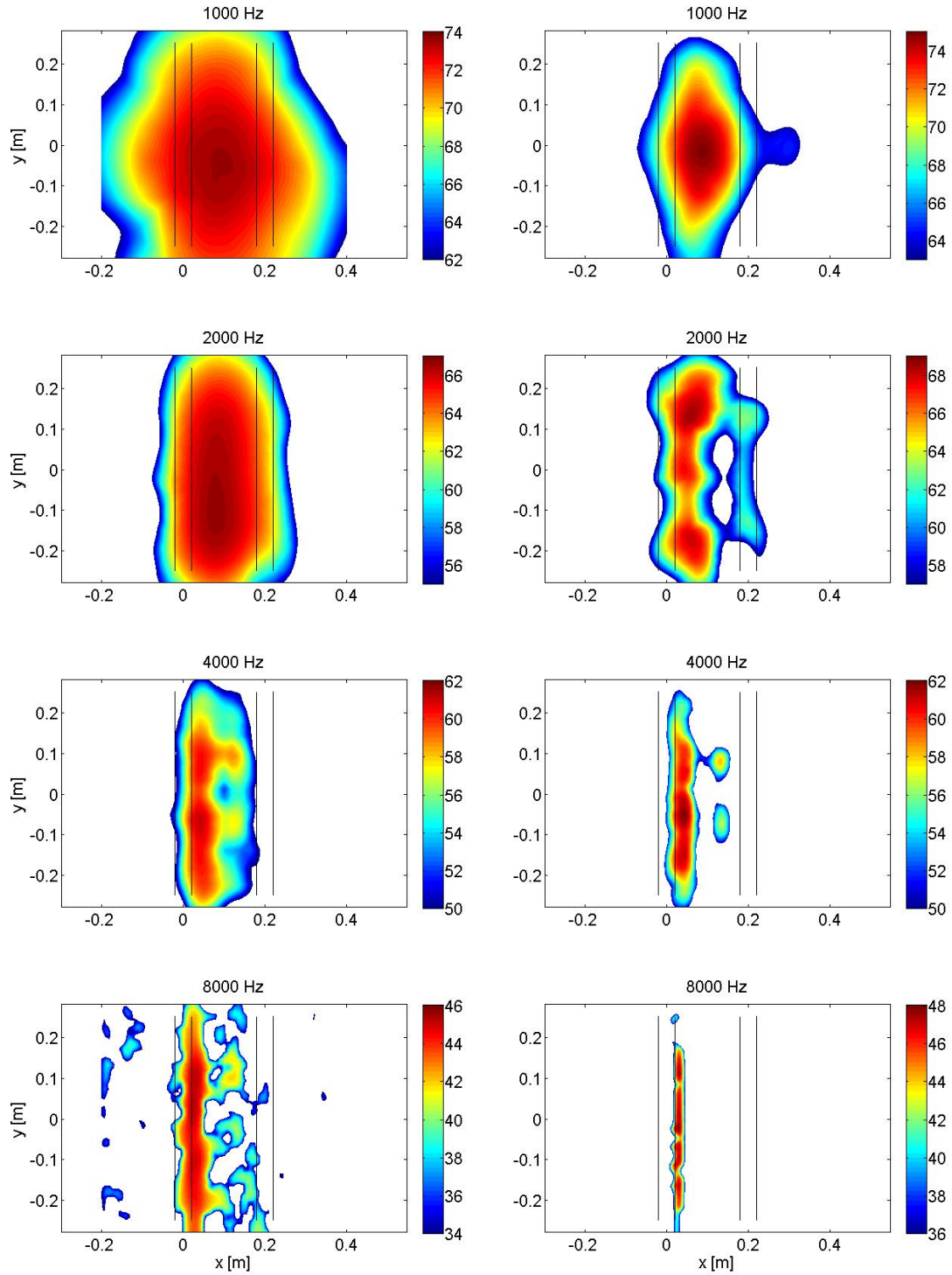


Figure 7.24: Generalized Inverse Beamforming for Structures with 20° angle and flow at 35m/s (results with IRLS on right). Mappings are source third octave PWL in dB re 1pW.

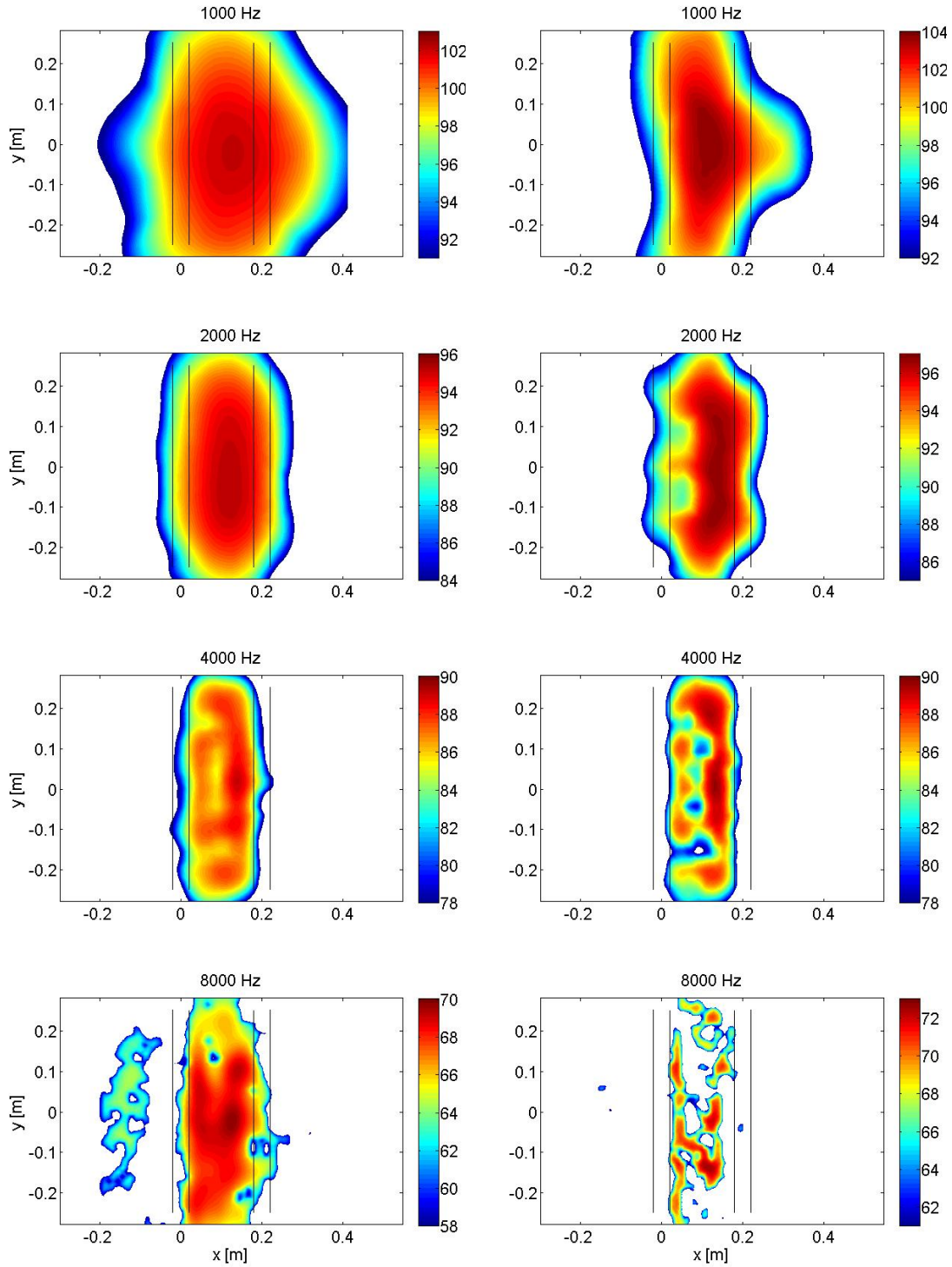


Figure 7.25: Generalized Inverse Beamforming for Structures with 7.5° angle and flow at 70m/s (results with IRLS on right). Mappings are source third octave PWL in dB re 1pW.

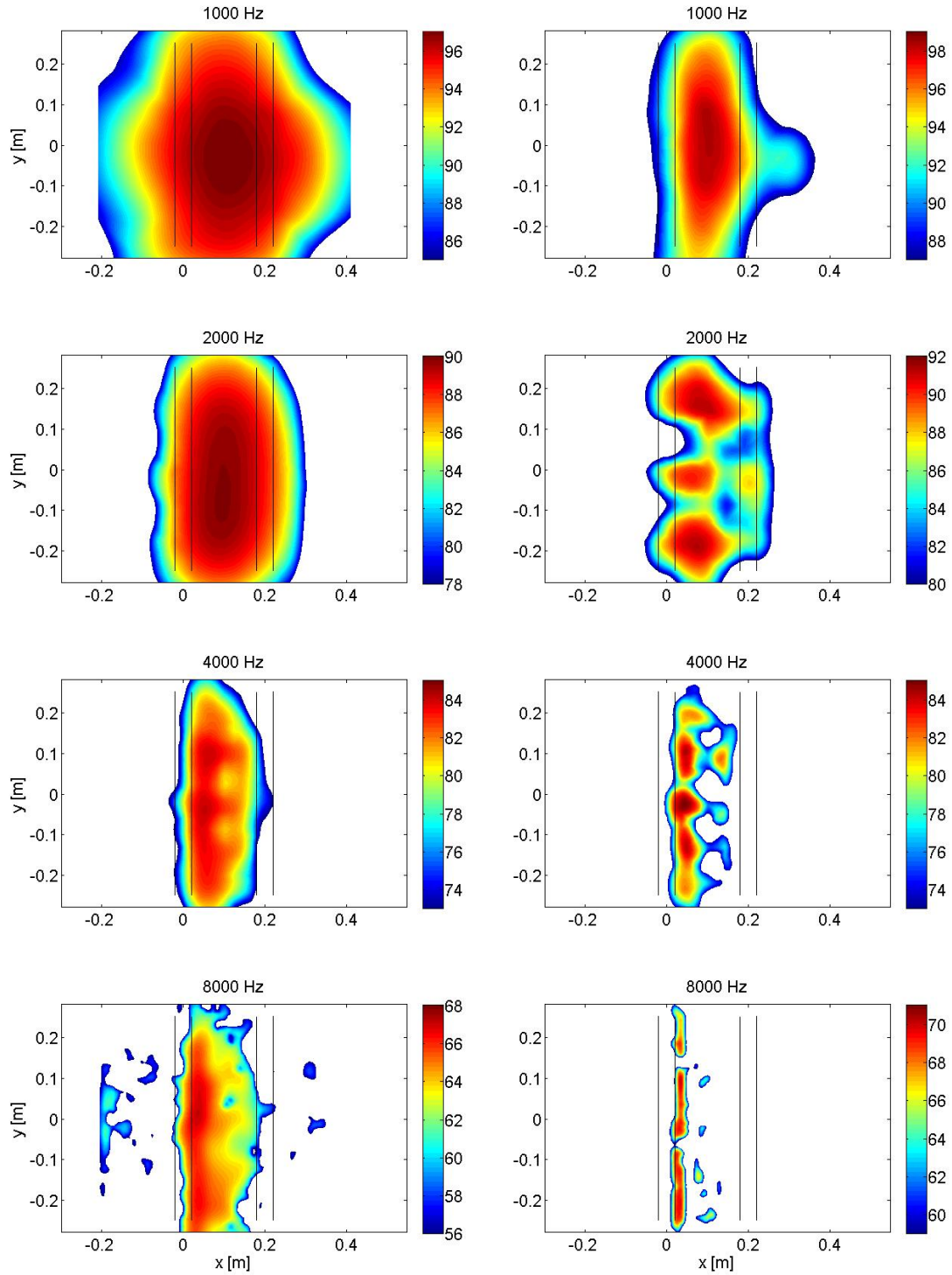


Figure 7.26: Generalized Inverse Beamforming for Structures with 20° angle and flow at 70m/s (results with IRLS on right). Mappings are source third octave PWL in dB re 1pW.

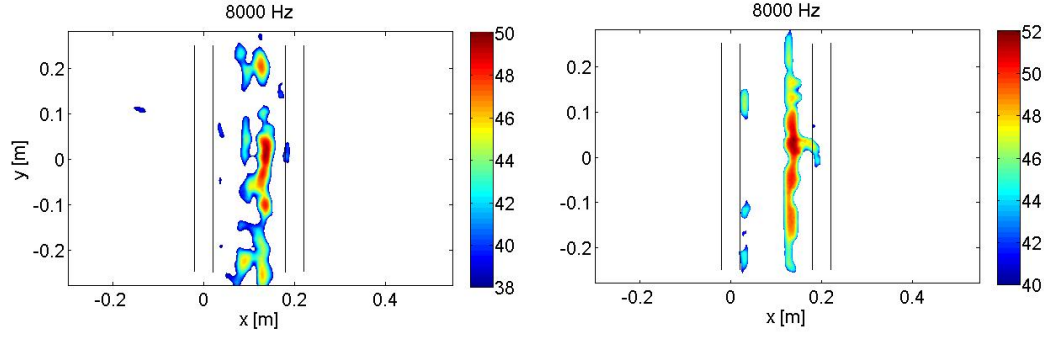


Figure 7.27: Generalized inverse beamforming with IRLS for the two structures with 7.5° angle and flow at 35m/s: summed over band (left); and extrapolated center frequency analysis (right). Mappings are source PWL in dB re 1pW.

Considering all these observations, the results from the hybrid generalized inverse mapping increases significantly the information from the source location without the presence of excessive sidelobe effects or spurious peaks.

7.5.5 Eigen-Modes Result Mappings Example

To illustrate the representation and importance of the eigen-modes respective source vector solutions, first, the line source simulation is again used for the 4kHz case, grid at 7.5° angle and flow at 35m/s. The square root of the eigenvalues is presented in Figure 7.28. Individual source vector results for each selected eigenmode are presented in Figure 7.29.

It is interesting to observe that the eigenvalue magnitude sequence order doesn't necessarily correspond to the order if the maximum absolute value of the source vector is considered, since the eigenvalue magnitude is related to the source vector $\ell - 1$ norm, an overall estimation.

As it can be seen from the individual source vector solutions to each eigenmode, despite that all the 417 monopole sources distributed in line from -0.25 to 0.25m are incoherent, just 5 modes are in the 10dB range from the maximum value, and their source distributions are somewhat regularly distributed. The interpretation that arises from the mappings is that the solutions are split into orthogonal spatial representations without a necessary fully separation in individual coherent regions, or, in other words, an individual source vector to each incoherent region. Also, it seems to represent regions with spatial symmetry, in an effort to represent the overall level distribution.

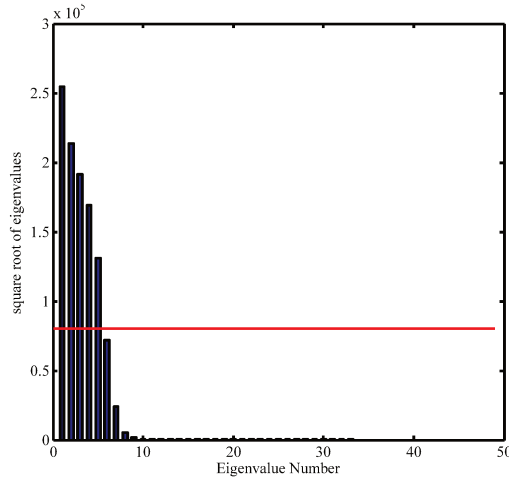


Figure 7.28: Eigenvalues square root distribution for the simulated line of monopoles in the 4kHz case. Red line indicates the 10dB range from maximum value.

In this sense, the individual source vector representations loses its direct physical meaning or importance, being more a mathematical smoothed representation in orthogonal basis of the overall source vector.

To illustrate again these characteristics, the experimental case for the 4kHz frequency band is chosen, the square root of the eigenvalues is shown in Figure 7.30 and the source mappings presented in Figure 7.31. The CSM diagonal attenuation is used, and eigenvalues below zero are nulled.

The eigenvalue distribution has 11 values in the 10dB range, and these 11 source vector solutions are used to form the overall source vector. Analyzing the first 5 source vectors, it is observed that the modes number 3, 4 and 5, bring the correspondent peak level to the overall source vector, and their individual regions seem to separate better the incoherent regions than in the simulated constant strength distribution case, maybe due to the non-constant source distributions in the experimental scenario.

In summary, the individual source vectors related to each eigenmode could be of interest, but their physical correspondence in the identification is not clear, and may lead to false conclusions if they are considered as isolated incoherent source mappings.

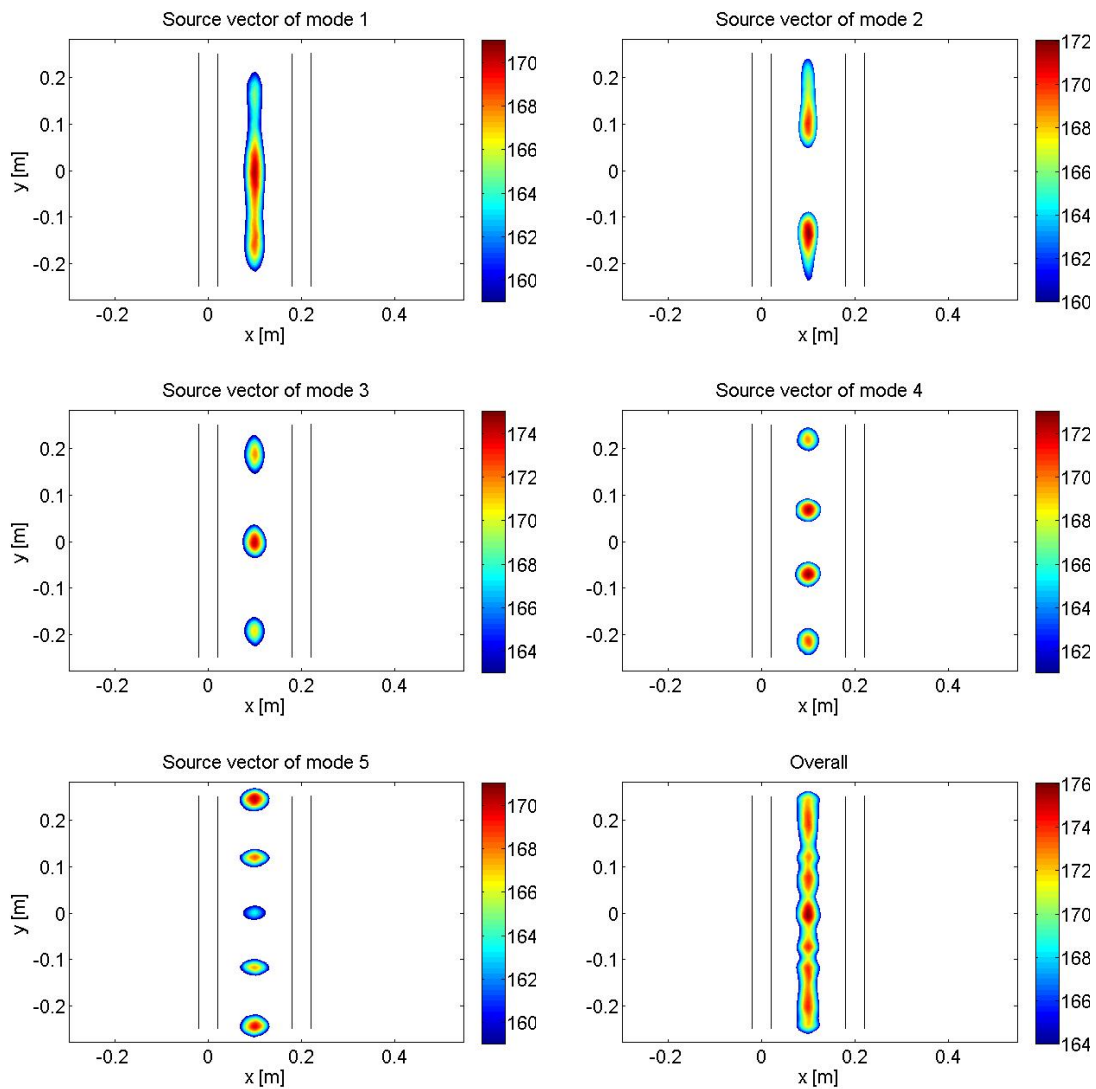


Figure 7.29: Generalized inverse beamforming with IRLS for the simulated line of monopoles: Source vector solutions to each selected eigenmode and overall. Grid at 7.5° angle and flow at 35m/s. Mappings are source PWL in dB re 1pW.

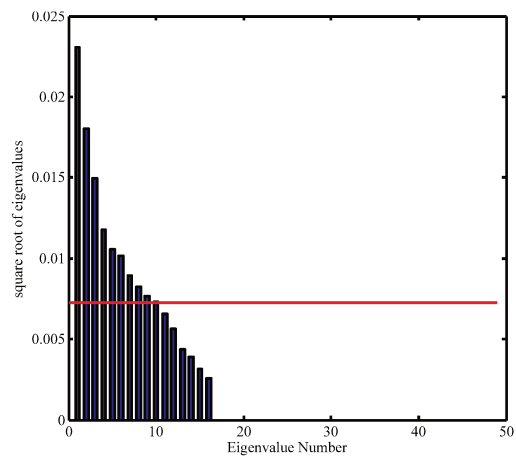


Figure 7.30: Eigenvalues square root distribution for the two structures with 7.5° angle and flow at 35m/s. Red line indicates the 10dB range from maximum value.

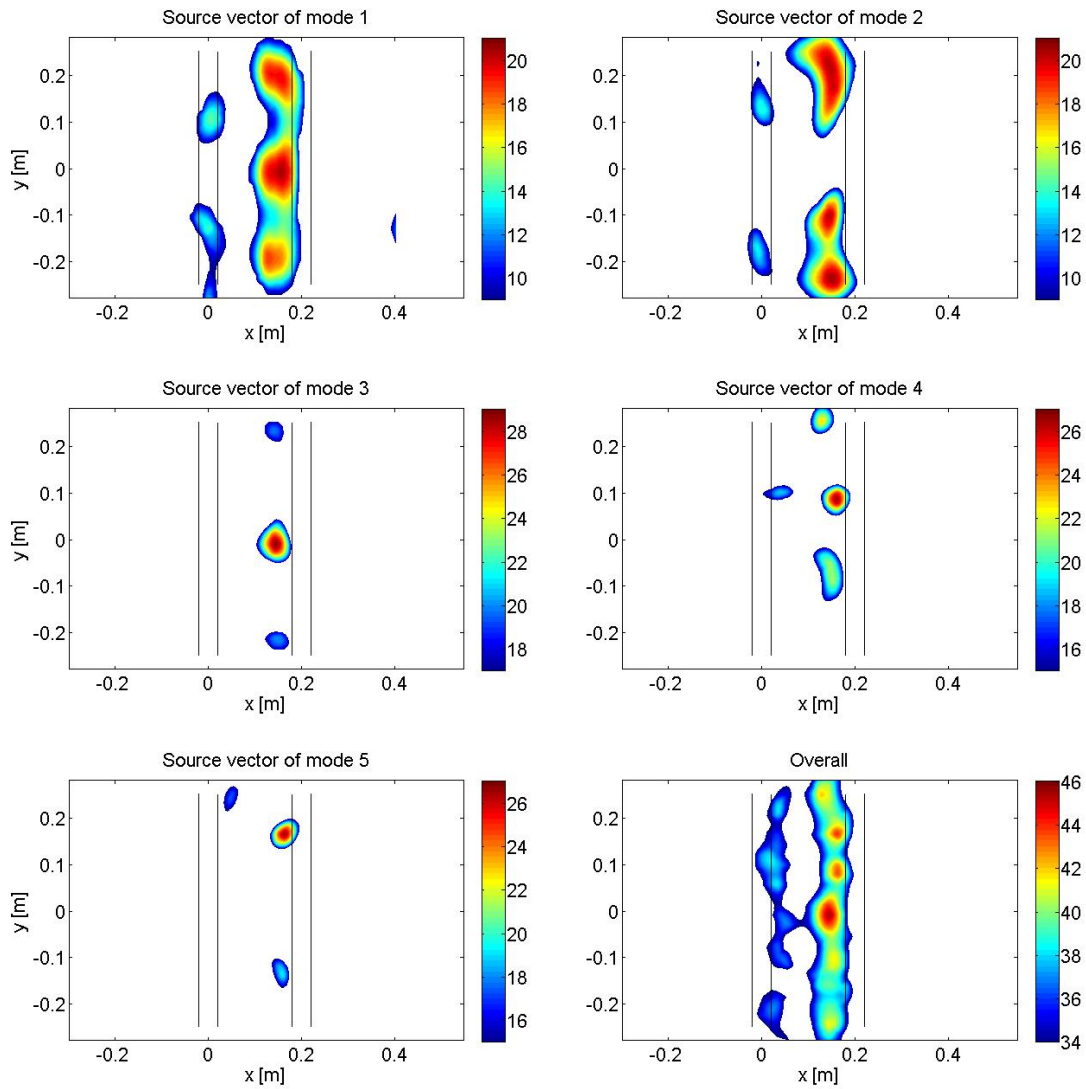


Figure 7.31: Generalized inverse beamforming with IRLS for the two structures with 7.5° angle and flow at 35m/s: Source vector solutions to first 5 eigenmodes and overall. Mappings are source PWL in dB re 1pW.

7.6 Dipole Identification Using Generalized Inverse Beamforming

In this section, the aeroacoustic sources for the two structures are investigated using the reference solution of a dipole radiation type. This is done in accordance with the expected dipole distribution over the structures as stated by Curle (1955). The free-field dipole radiation is used along with the effects of convection and refraction in the retarded propagation distance, and directions propagation. Simulation is used to investigate the identification of a 3D dipole with component of its orientation also orthogonal to the array plane. For this, is developed a transfer matrix re-scaling method, to overcome the anisotropic nature of dipole radiation, with satisfactory results.

Simulations with single dipole and two types of grids, in line (bars centers) and a full 3D grid on the bars surface, are used and their results compared. As shown in the monopole section, a distributed line of incoherent dipoles is also investigated according to the coherent length from the literature, and estimation performance is discussed.

After the verifications of estimation performance done with simulation, the method is applied to the experimental data, airflow of Mach 0.1 and 0.2, with bars plane of 7° and 20° . Results are discussed and the influence of the use of auto-powers attenuation procedure, as well as the Hybrid Generalized Inverse mappings are exemplified. Results for directivity are also compared to experimental far-field measurements, and wall pressure transducers placed in one of the bars. The obtained results for dipole identification are compared to the monopole identification and its advantages are outlined.

7.6.1 Dipole Convection and Refraction Modeling

In this work, the free-field dipole radiation is considered based on the radiation from a sphere of radius a , whose center vibrates along the polar axis with a velocity $U_0 e^{-i\omega t}$, according to Morse (1948). The radial velocity of the surface of the sphere is $U_0 \cos\vartheta e^{-i\omega t}$ where ϑ is the angle from

the polar axis. The pressure wave can be described by:

$$Press_{dip} = A_{dip} P_{Leg_1}(\cos\vartheta) [j_1(kr) + in_1(kr)] e^{i\omega t}, \quad (7.11)$$

where P_{Leg_1} is the Legendre function of order 1; j_1 and n_1 are the spherical Bessel and Neumann functions of order 1, representing the oscillating sphere radiation. The above expression reduces to:

$$Press_{dip} = A_{dip} \cos\vartheta \left(\frac{-1 + ikr}{k^2 r^2} \right) e^{i(\omega t - kr)}. \quad (7.12)$$

The above expression is used in the identification, and A_{dip} estimated. The multiplier A_{dip} can be determined from the radial particle velocity expression on the limit of $r \rightarrow 0$ as:

$$\lim_{r \rightarrow 0} u_r = \lim_{r \rightarrow 0} \left(\frac{2A_{dip}}{\rho c} \right) \left(\frac{1}{kr} \right)^3 \cos\vartheta e^{i\omega t} = U_0 \cos\vartheta e^{i\omega t}. \quad (7.13)$$

For $r = a_{sph}$, the sphere radius, the expression for A_{dip} is:

$$A_{dip} \approx \left(\frac{\rho c k^3 a_{sph}^3 U_0}{2} \right), \quad (7.14)$$

and the expression for the radiation wave becomes:

$$Press_{dip} = \left(\frac{\rho c k a_{sph}^3 U_0}{2} \right) \cos\vartheta \left(\frac{-1 + ikr}{r^2} \right) e^{i(\omega t - kr)}. \quad (7.15)$$

The total power radiated is:

$$\Pi_{dip} = \frac{\rho c \pi k^4 a_{sph}^6 U_0^2}{6}. \quad (7.16)$$

But the above expression is not suitable for identification, since the sphere radius a_{sph} is not known, and for this, the total power can be calculated as function of the estimated variable A_{dip} :

$$\Pi_{dip} = \frac{2\pi A_{dip}^2}{3\rho c k^2}, \quad (7.17)$$

and this expression now is conveniently independent of the sphere radius a and the peak radial particle velocity amplitude U_0 .

The wave decay from a dipole is higher since it is proportional to $1/r^2$ in comparison to the monopole decay of $1/r$, but on the other hand, its power increases as function of the fourth power of the wave number k , increasing its relative importance for higher frequencies when compared to monopole power. To account for the convection and refraction, the same strategy used for the monopoles can be used for the dipoles, and the propagated distance is substituted by the retarded distance, calculated according to the same wave normal principles presented in the earlier section on the monopole.

7.6.2 Test Setup and General Conditions

The test setup and conditions are the same as for the monopole identification previously showed. For the target grid, now considering the objective of locating the main sources of aeroacoustic sound generation, one can expect to locate the centers of radiation at the centers of the bars (considering its compactness) or, more precisely, one can expect to have dipoles distributed over the bar surfaces.

Two source location candidate strategies are considered, one along bars centers, and the second, at each squared profile bar surface. The objective is to assess the dipole power and its

orientation in each studied condition. Both grid strategies have discretization in spanwise direction as $1/4$ of wavelength per regularly spaced grid points, but for the grid at the surfaces, 4 grid lines per bar side (spaced by 4mm) are adopted. The target grids used for the chosen frequencies are presented in Figures 7.32 and 7.33.

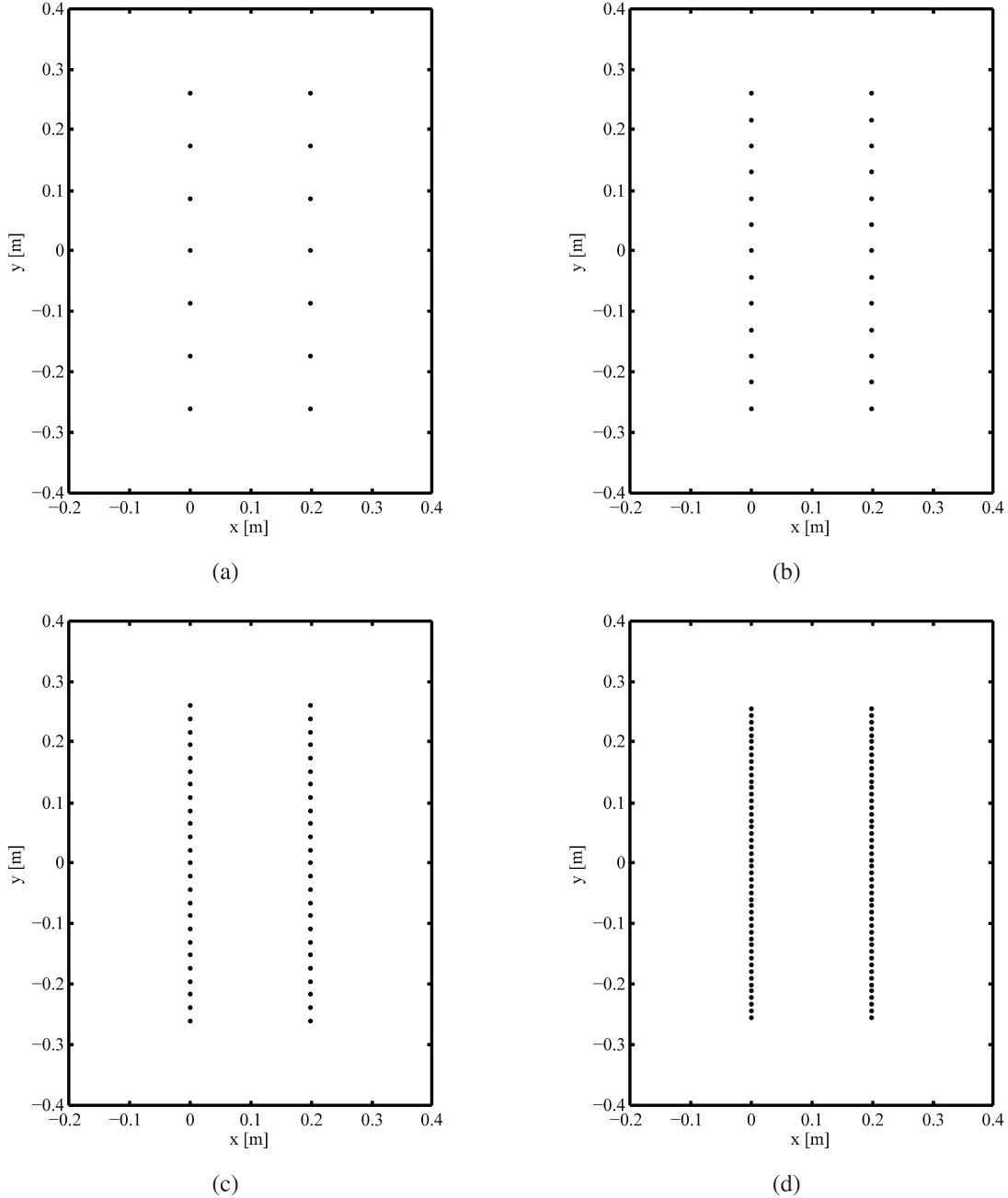


Figure 7.32: Line Target Grid distribution based in $1/4$ of wavelength width in spanwise direction (a) 1kHz (b) 2kHz (c) 4kHz (d) 8kHz.

The line grids have 14, 26, 50 and 96 points in the 1k, 2k, 4k, 8kHz analysis respectively,

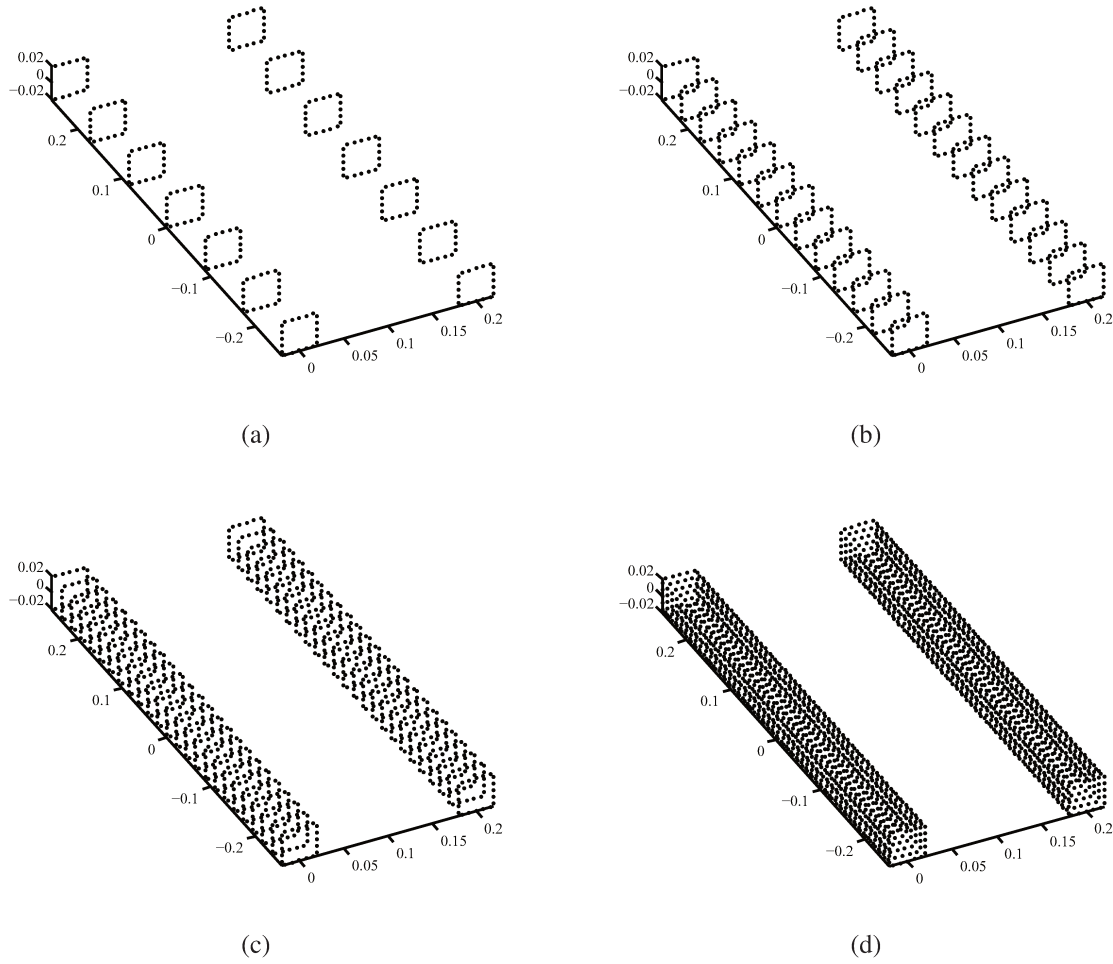


Figure 7.33: 3D Target Grid distribution based in $1/4$ of wavelength width in spanwise direction (a) 1kHz (b) 2kHz (c) 4kHz (d) 8kHz.

and the 3D grid has 280, 520, 1000 and 1920 points for the same frequencies. The grid, as on the monopole study, is rotated by 7° or 20° , with rear bar placed farther from the array plane for the respective identifications. The expected region of sound sources generation, in the flow separation region, is exposed with these arrangements.

Directional assessments based on the identified dipole distribution are confronted to six far field microphones pressure responses ($1/2$ -inch type), placed at a radius of 2m from the front bar center. The far field microphones location are illustrated in Figure 7.34.

Also, wall pressure transducers (Kulite sensors) are used distributed over the front bar only (limited due the the number of available channels for simultaneous recordings). The objective is to

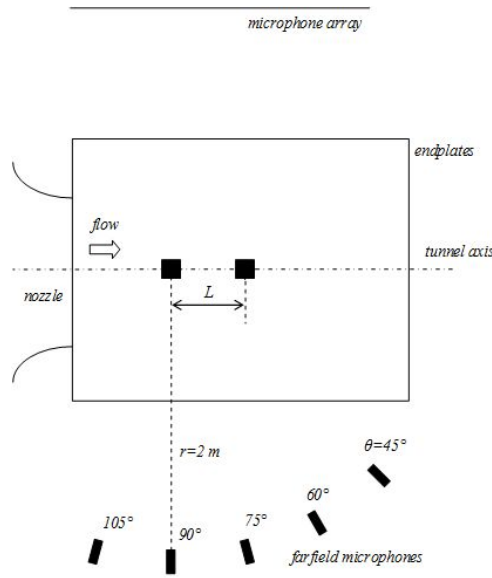


Figure 7.34: Far field ($r=2\text{m}$) microphones location for directional assessment.

assess the pressure distribution in spanwise direction and also in cross-bar direction, for front and rear bar surfaces (spanwise), and midspan section (cross-bar) assessment. The sensors locations can be observed in Figure 7.35.

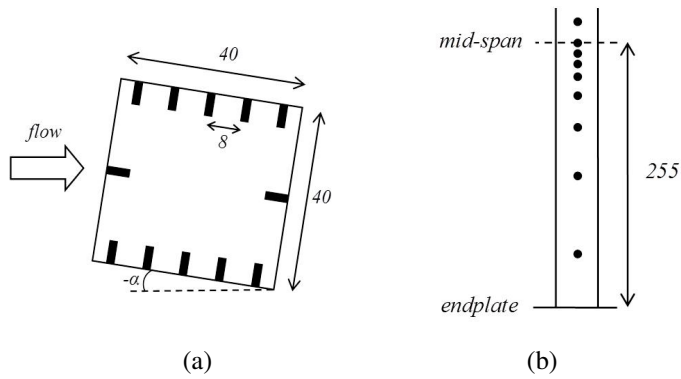


Figure 7.35: Wall pressure transducers (Kulites) locations: (a) midspan (b) spanwise.

7.6.3 Transfer Function Re-Scaling for 3D Dipole Identification

The generalized inverse beamforming as proposed in (SUZUKI, 2008), presented the identification of dipoles with main axis in the plane parallel to the array plane. Now, in this work, is presented the identification of dipoles with main axis oriented in any direction. Simulation is used

to demonstrate its performance.

The line grid is used (without grid plane rotation) to locate a dipole at coordinates (0,0) that corresponds to the upstream bar, middle section. The dipole is implemented with orientation of 45° with respect to the x-direction (flow direction), and with positive angle corresponding to the quadrants that are on the far-field microphones side, opposite to the array location. The dipole radiation considered a frequency of 1kHz, and in this first analysis, no flow convection is considered.

The source Power in Watt Level (PWL) is calculated using the same method presented for the monopole mappings, a Hybrid Generalized Inverse Mapping, which corresponds to the source locations identified by the generalized inverse method, with the level obtained by the Hybrid Mapping, that is obtained by applying the square of the Point-Spread-Function to the GIB mappings as discussed in the monopole section. Indeed, on the dipole identification, the gaussian filter used in the monopole is not applied, and locations are true correspondents to the generalized inverse results in the 12dB range from maximum source term result with the Hybrid mapping values. This method provides a visualization comparable to the directional response of a conventional beamforming mapping, with sources level directly read from the plots.

For the simulations, the dipole considered a sphere radius of $1/10$ of wavelength, and the identification results obtained using IRLS scheme with 18 iterations and 4 grid points left in the source vector. The identification only considered dipole components in x and z direction, main interest on the experimental analysis is in the identification of these two components.

The identification also used the auto-powers attenuation as shown in the monopole section, and a comparison is made in the experimental results discussion. The regularization strategy is the same used on the monopole tests: the optimum regularization strategy is adopted for the first calculation, and on the first iteration, the regularization factor adopted is 5% of the greatest eigenvalue of $A^\dagger W_i A$, and kept fixed throughout the subsequent IRLS iterations. The method uses the eigenmode which the square roots of the eigenvalues are within the 10dB range from the maximum value.

Simulated results for the dipole with 45° orientation in x-z plane are shown in Figure 7.36, with plots for overall magnitude, x and z-component level, with line grid results plotted at each bar face. The directivity, here considered as the time-averaged pressure amplitude calculated for

a radius of 2m from the front bar center, is shown in Figure 7.37 for this simulated dipole identification without any change in the transfer matrix.

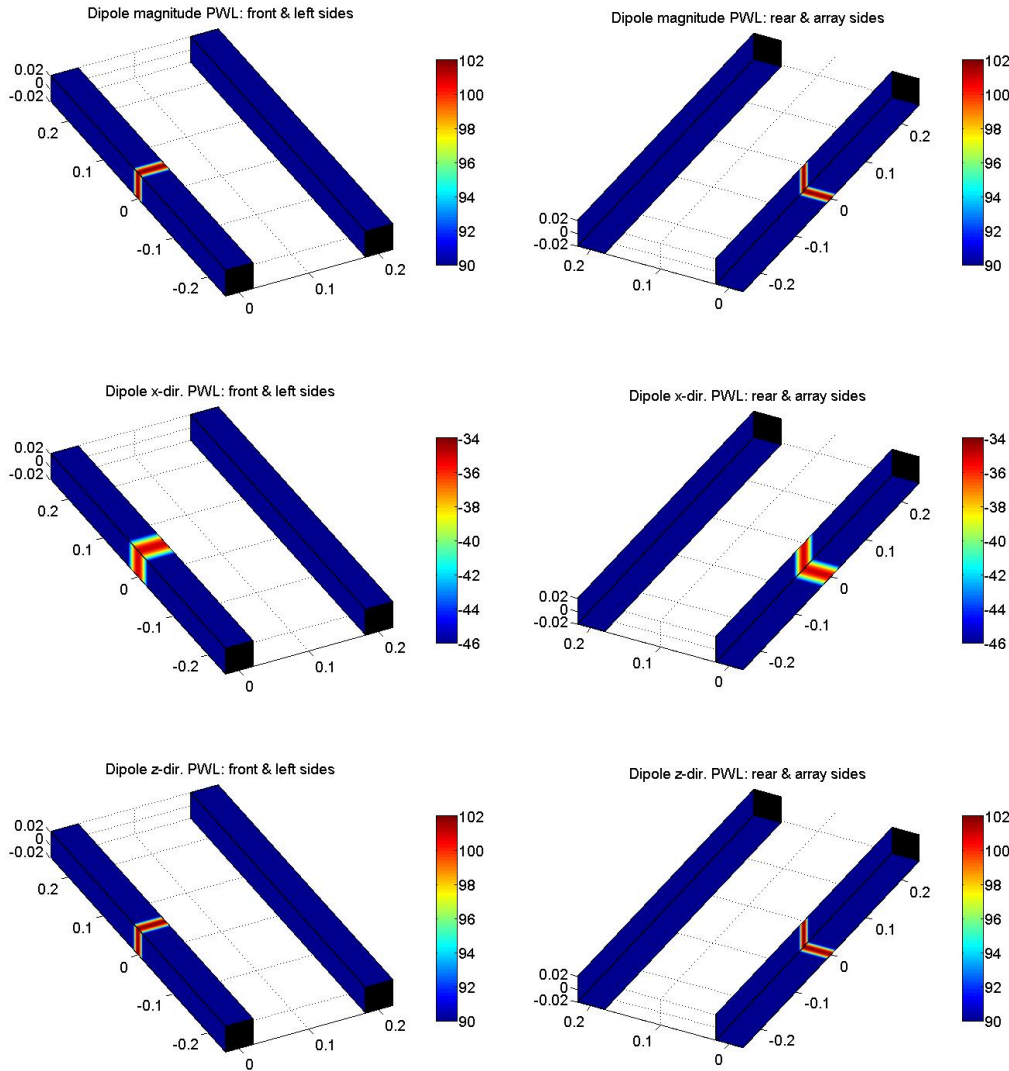


Figure 7.36: Simulation results for a free-field dipole with 45° in x-z plane. Mappings are source PWL in dB re 1pW.

The generated dipole power is 106dB for a unitary time-averaged peak radial particle velocity amplitude, and the identification brings the overall power level of 102dB, and x and z-component power levels of 35 and 102dB, showing clearly that it failed to capture the direction of the dipole, excessively attributed to the z-direction, orthogonal to the array plane.

In this result, the excessive power level in the z-direction is probably related to the anisotropic

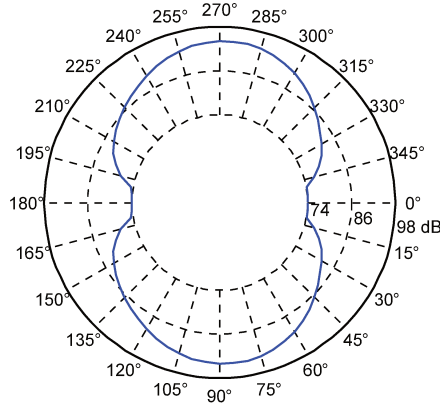


Figure 7.37: Directivity for the free-field dipole with 45° in x-z plane.

character of dipole radiation, with a higher valued transfer function for the z-direction, causing an uneven distribution of source direction components, since the least squares solution distributes the residue over the component terms, minimizing the error with a higher z-component.

A proposed re-scaling of the transfer function terms related to each direction is tested and results are obtained for the dipole simulation. The re-scaling factor can be expressed as:

$$f_{A_{i-dir}} = \frac{1}{N_{mic}N_{grid}} \sum_{\substack{m=1..N_{mic} \\ n=1..N_{grid}}} |A_{i-dir,mn}|, \quad (7.18)$$

with the re-scaling factor defined for each direction, each transfer matrix term is divided by the respective direction factor. Since this is a linear transformation of the transfer matrix, the source vectors are altered, and their results have to be re-scaled back to the original factor by dividing the results by the respective direction factor. This is an artifice to improve estimation approximation and counterweight the influence of the anisotropic dipole nature.

The results obtained for the simulated dipole using the transfer matrix re-scaling is presented in Figure 7.38 for the power levels and in Figure 7.39 for the directivity. Now, the overall power level is estimated as 105dB, with components of 100dB and 103dB for x and z direction respectively. The ratio between the factor for the z-direction and the x-direction is about 4 on the presented results.

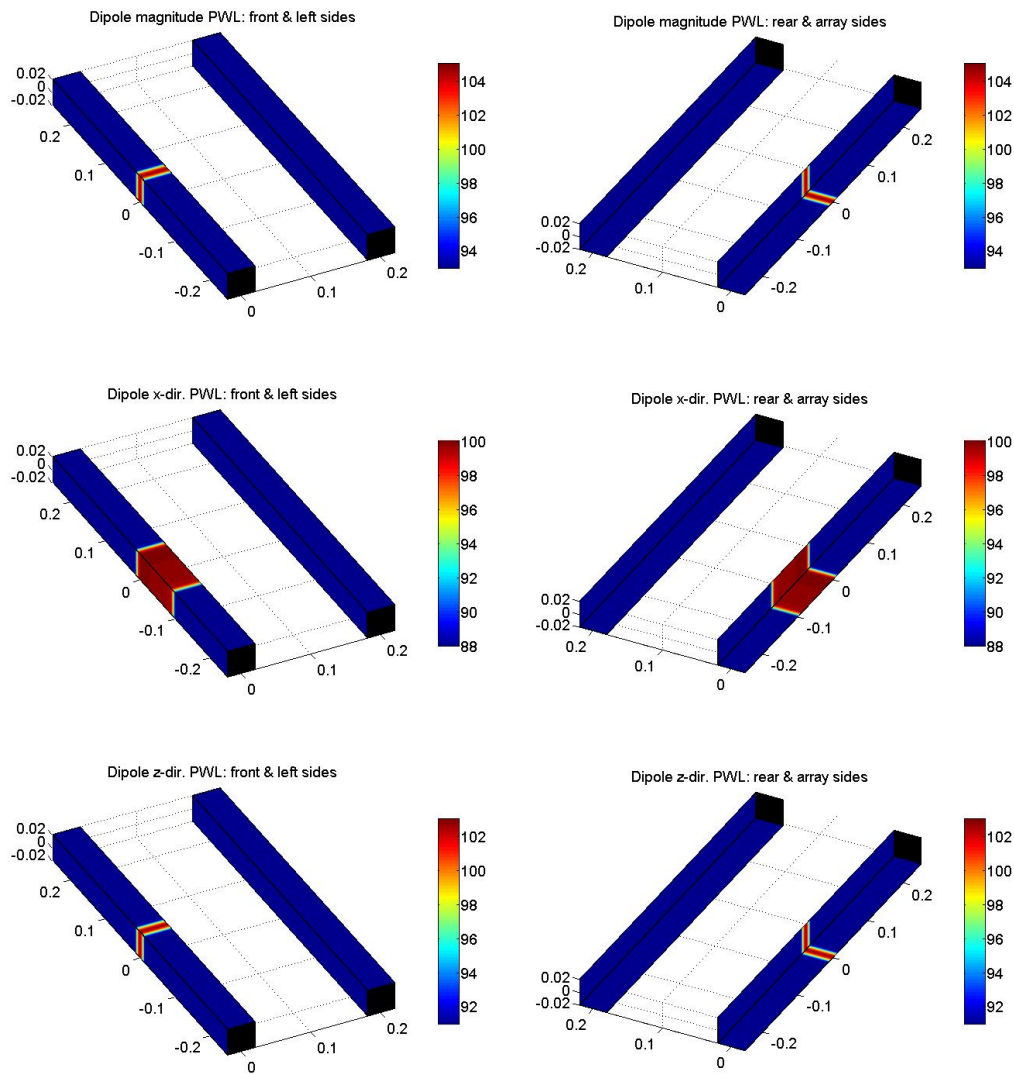


Figure 7.38: Simulation results for a free-field dipole with 45° in x-z plane with re-scaling of transfer matrix. Mappings are source PWL in dB re 1pW.

Despite the fact that the overall level estimation improved significantly, with only 1dB difference to the generated 106dB dipole power, the direction components still present some differences in level, and the main direction is still slightly deviated towards the z-direction, with higher original transfer values. The directional error is lower than 10° , and is considered as a reasonable approximation.

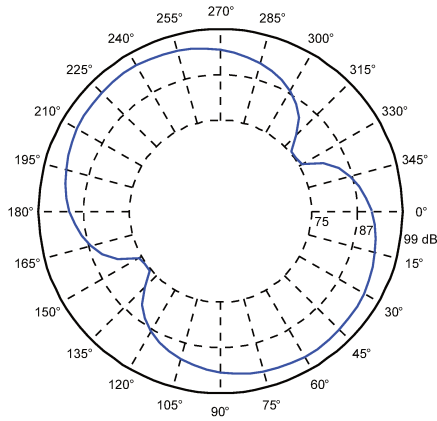


Figure 7.39: Directivity for the free-field dipole with 45° in x-z plane with re-scaling of transfer matrix.

7.6.4 Simulated Identifications with Convection and Refraction

Considering the first measurement condition: bars plane with 7° and airflow speed of 35m/s (Mach of 0.1), the simulation considered again 1 dipole at coordinates (0,0) and the line grid. Results of directivity for radiation with 1kHz and various dipole orientations in the x-z plane are presented in Figure 7.40 using the transfer matrix re-scaling.

the influence of convection and refraction in the directivity plots is clear, dislocating the wave towards the x-direction, with convection in the region near 0° or 180° . The re-scaling is also effective in the single dipole identification using the line grid. The same results can be generated for the 3D grid, using 30 iterations, and are shown in Figure 7.41.

The directivity plots for the line grid and for the 3D grid presented very similar results, with a small advantage to the 3D grid in terms of curve smoothness, and both agree very well in level too. The estimation of dipole orientation can be considered valid in the case of flow, with convection and refraction using the same conditions as for the measurements.

Estimations are performed for both target grids, line and 3D, varying the frequency of the single dipole with orientation of 45° . The results of dipole power level are shown in Figure 7.42 and Figure 7.43 for the line and 3D grid, respectively.

The line grid case estimation used a minimum of 4 terms left in the source vector or 30

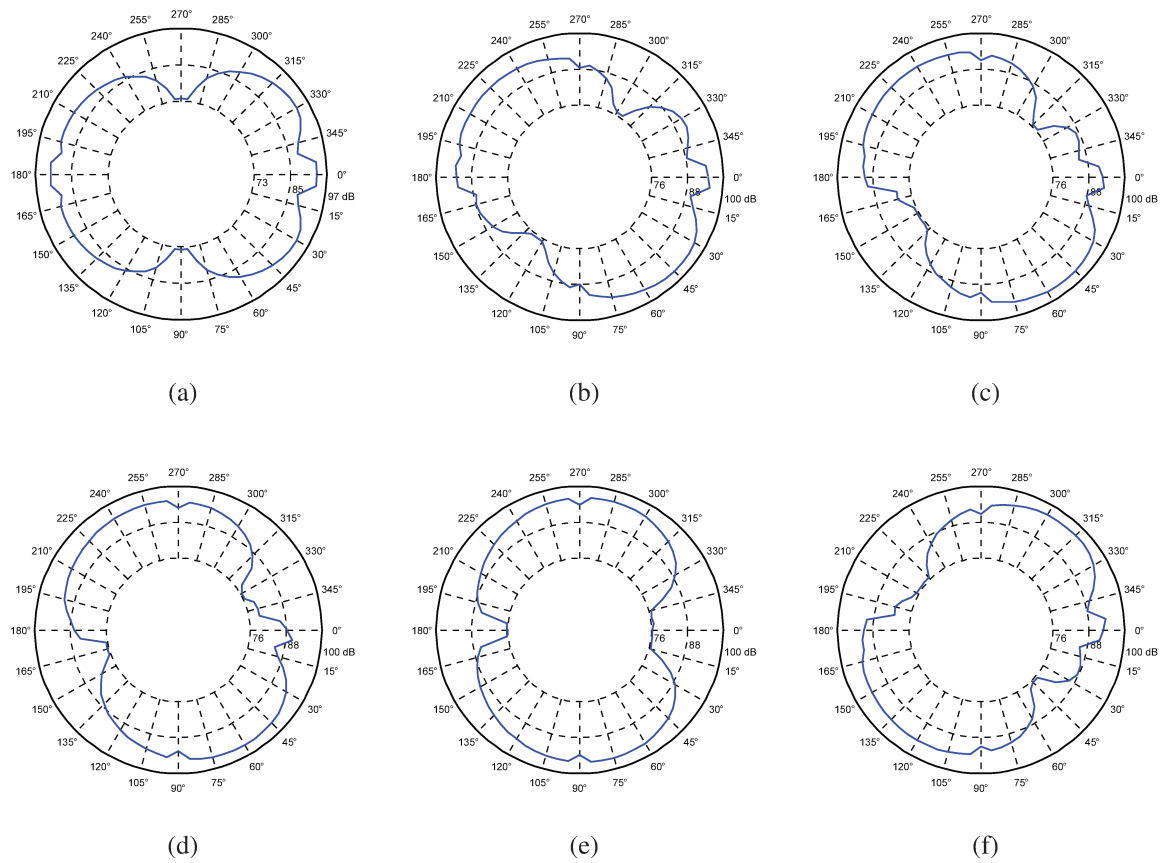


Figure 7.40: Directivity results ($r=2\text{m}$) for a single dipole with 1kHz in x-z plane using line grid and orientations of: (a) 0° (b) 30° (c) 45° (d) 60° (e) 90° (f) 135°

iterations otherwise. Results of source level are quite close to the generated dipole powers of: 106dB (1kHz); 100dB (2kHz); 94dB (4kHz); and 88dB (8kHz). The localization region is precisely the location of the simulated dipole at (0,0).

The 3D grid results are even better in terms of power estimation, and also in terms of localization, considering that with the bars plane rotated by 7° , with rear bar farther from the array, the points that are closer to the dipole location and closer to the array are the ones brought by the estimation.

The directivity plots for the line grid and 3D grid results, for 2k, 4k and 8kHz, are presented in Figure 7.46.

The directivity results agree well between the line grid and 3D grid, with a small difference

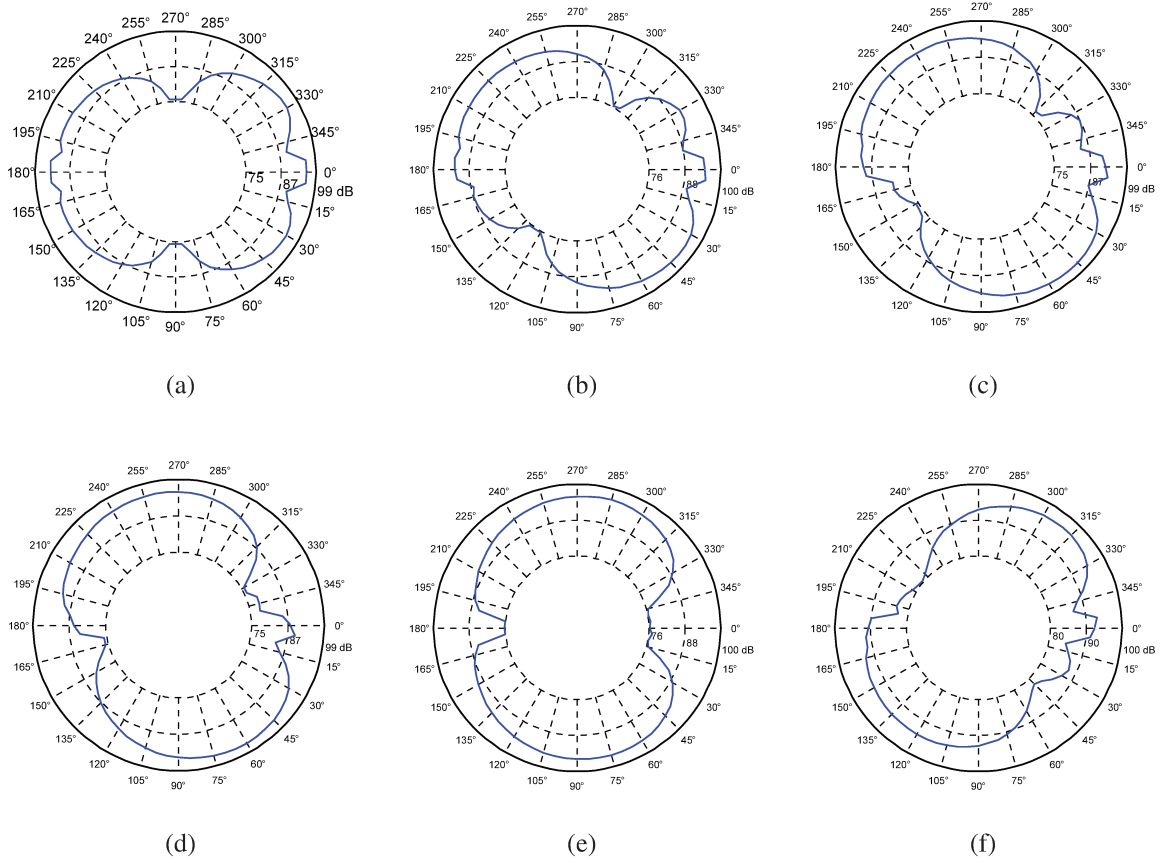


Figure 7.41: Directivity results ($r=2m$) for a single dipole with 1kHz in x-z plane using 3D grid and orientations of: (a) 0° (b) 30° (c) 45° (d) 60° (e) 90° (f) 135°

in the 8kHz case, showing a small flattening in the dipole main direction of radiation.

In order to simulate a closer situation to the real sources distribution, a line of incoherent dipoles with orientation of 45° is used along with the 3D grid for identifications with 1k, 2k, 4k and 8kHz. The sources are evenly distributed spanwise, with x and y coordinates as (0,0). The number of distributed sources is the same used in the monopole simulations in the previous section, see Table 7.1 for reference. The generalized inverse beamforming with IRLS scheme is used, with 10 iterations for 1k, 2k and 4kHz, and 20 iterations for the 8kHz analysis. Power level results using the Hybrid generalized inverse mappings are presented in Figure 7.45. The directivity plots are presented in Figure 7.46.

In all frequencies, the localization spots correctly the closest point in the grid and the array, with the advantage that for higher frequencies, the full distribution is captured along the bar.

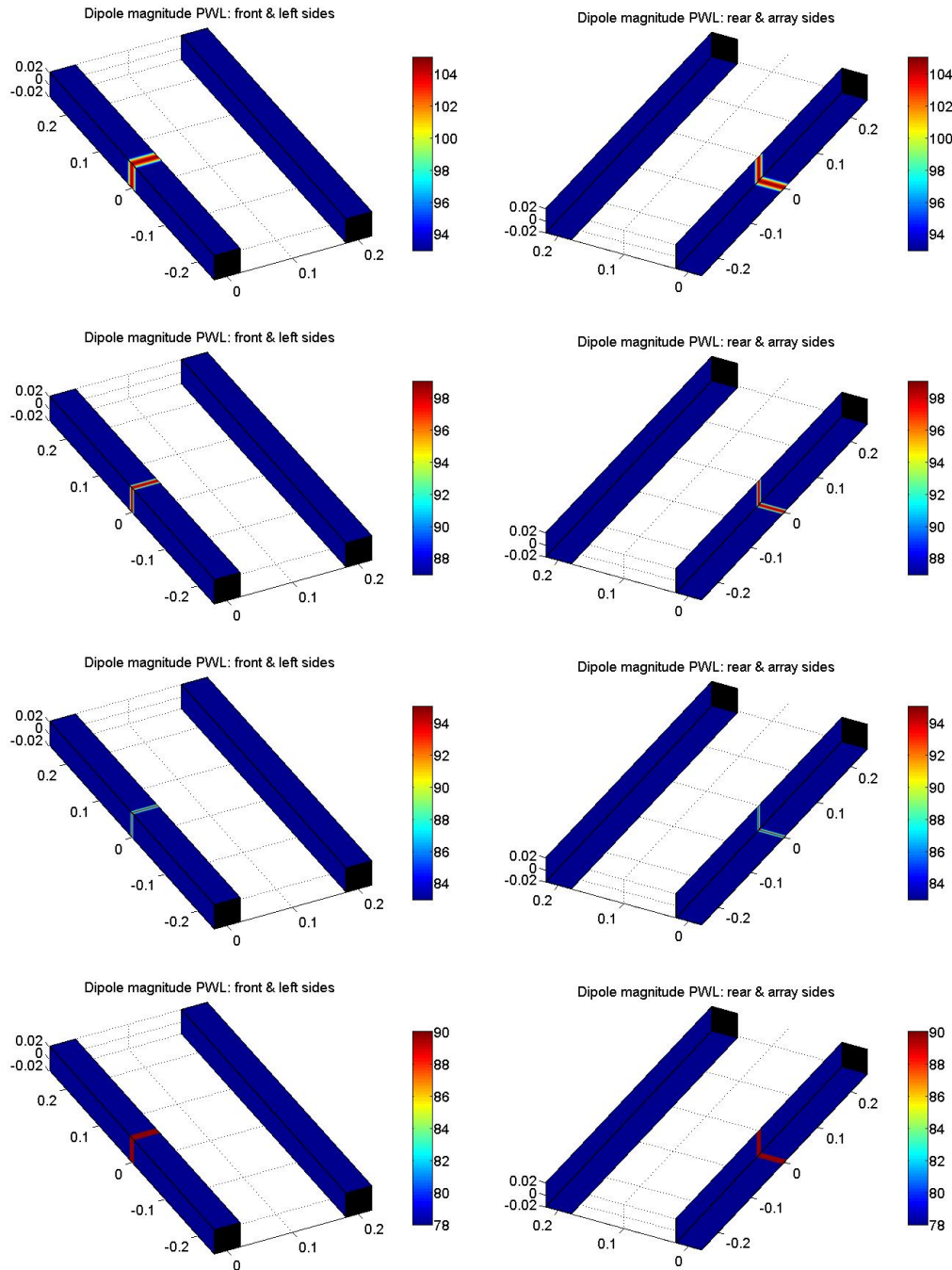


Figure 7.42: Simulation results for the line grid and dipole with 45° in x-z plane with re-scaling of transfer matrix, 1k (top), 2k, 4k and 8kHz. Mappings are source PWL in dB re 1pW.

The levels are increased in the same manner as the monopole mappings increased for the line distribution as well. The directional behavior seems to tend more to the z-direction than on the single dipole cases, but the error of 15% is considered acceptable, also considering the presence of

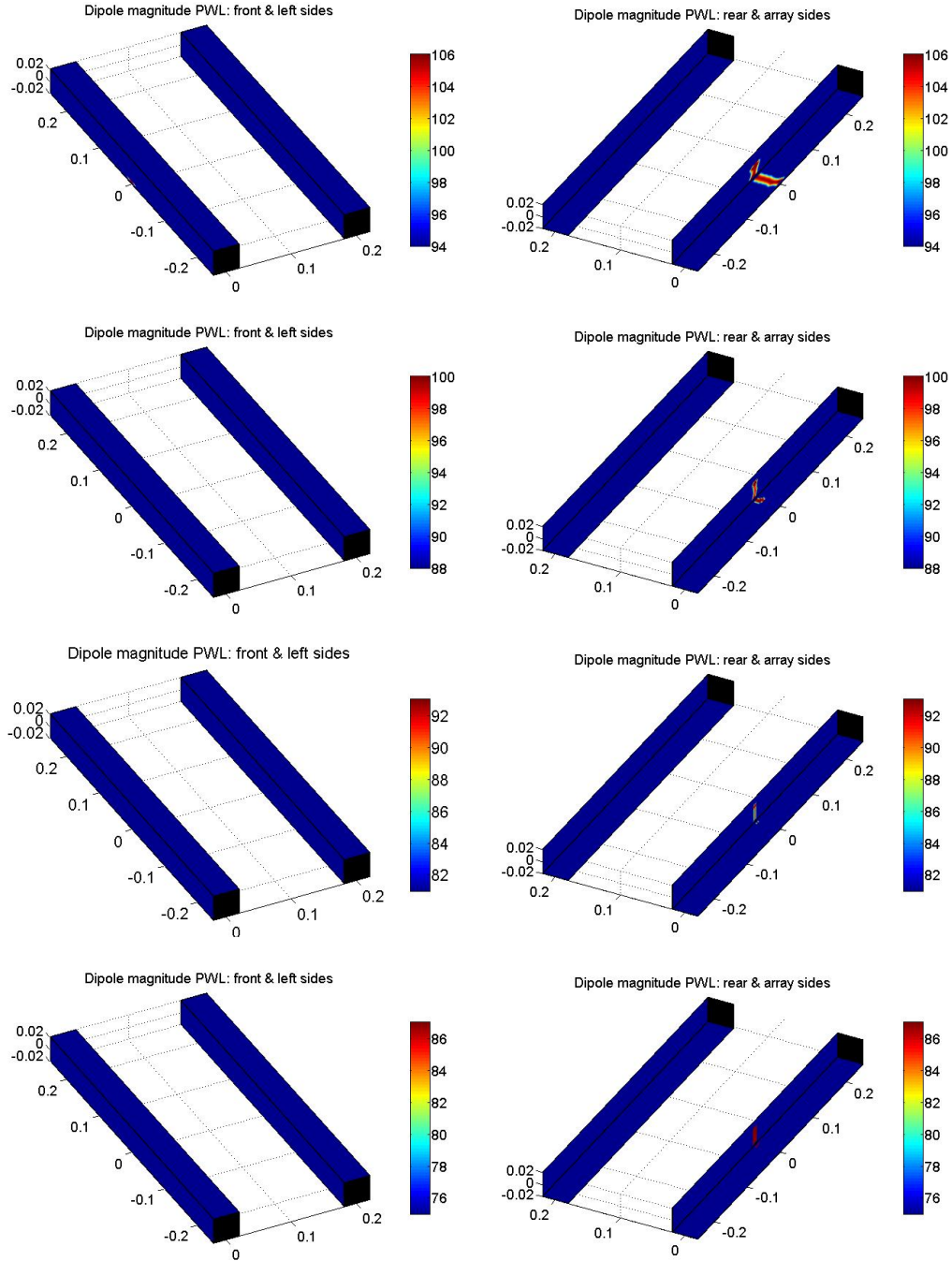


Figure 7.43: Simulation results for the 3D grid and dipole with 45° in x-z plane with re-scaling of transfer matrix: 1kHz (top); 2kHz; 4kHz; and 8kHz. Mappings are source PWL in dB re 1pW.

the flow in the estimations. The directional plot for the 8kHz is the one that presented the highest difficulty to identify the correct orientation, with a flattening of the main axis, as shown in the single dipole case.

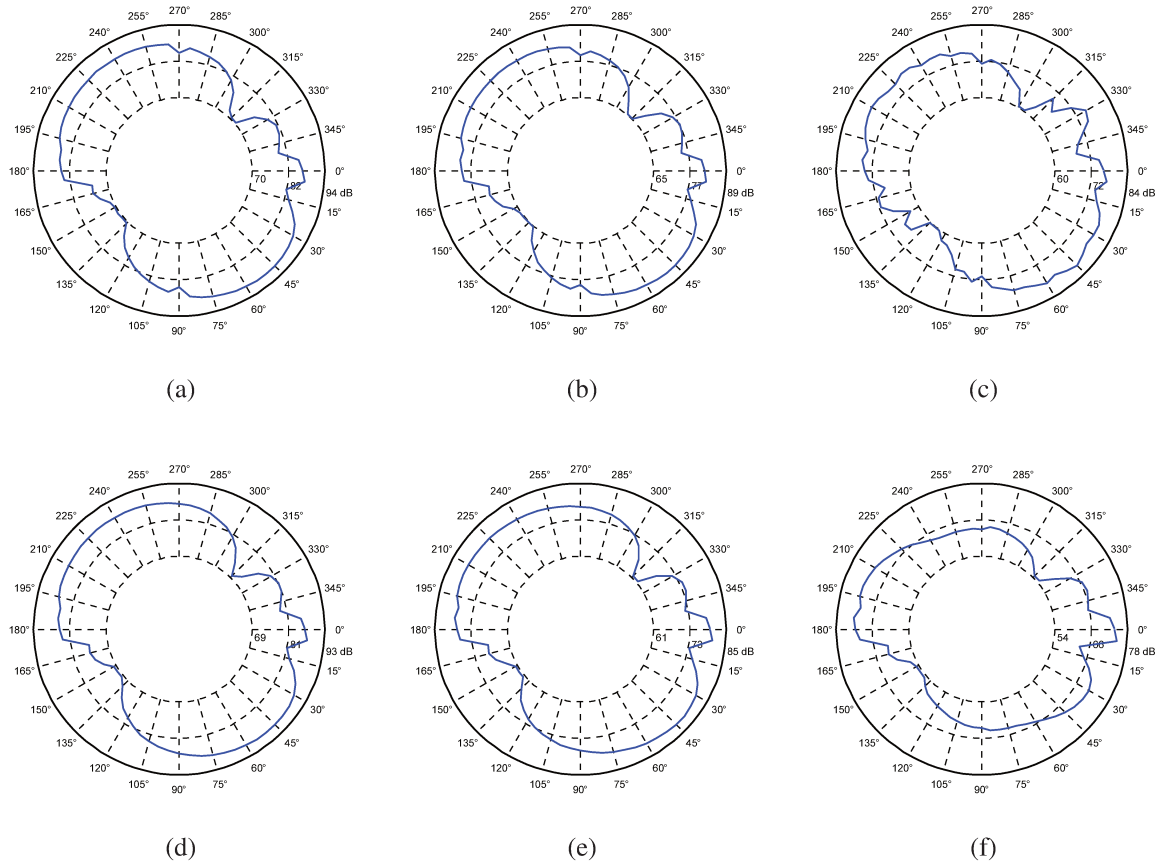


Figure 7.44: Directivity results ($r=2m$) for a single dipole with 45° in x-z plane using line grid (top) and 3D grid for frequencies of : (a,d) 2kHz (b,e) 4kHz (c,f) 8kHz.

Another possible representation of the dipole mappings is a vectorial representation of the estimated direction component source vector terms, remembering that on this representation, opposite vectors (i.e.: x and z components positive, or x and z negative) are in fact representing the same dipole orientation. The results for the line of incoherent dipoles in the 1kHz and 8kHz cases are presented with the component levels and the vectorial dipole representation, normalized by the maximum absolute level in each direction. The Figures 7.47 and 7.48 show the results for the 1kHz and 8kHz cases, respectively.

It is clear from the 1kHz results that in the main region (center of upstream bar), the vectors are in the first/third quadrant, with correct dipole orientation representation, but on the 8kHz case, it is more difficult to assess the correct overall dipole orientation. On the other hand, this representation can be helpful to identify the coherence length distribution, in this case very small.

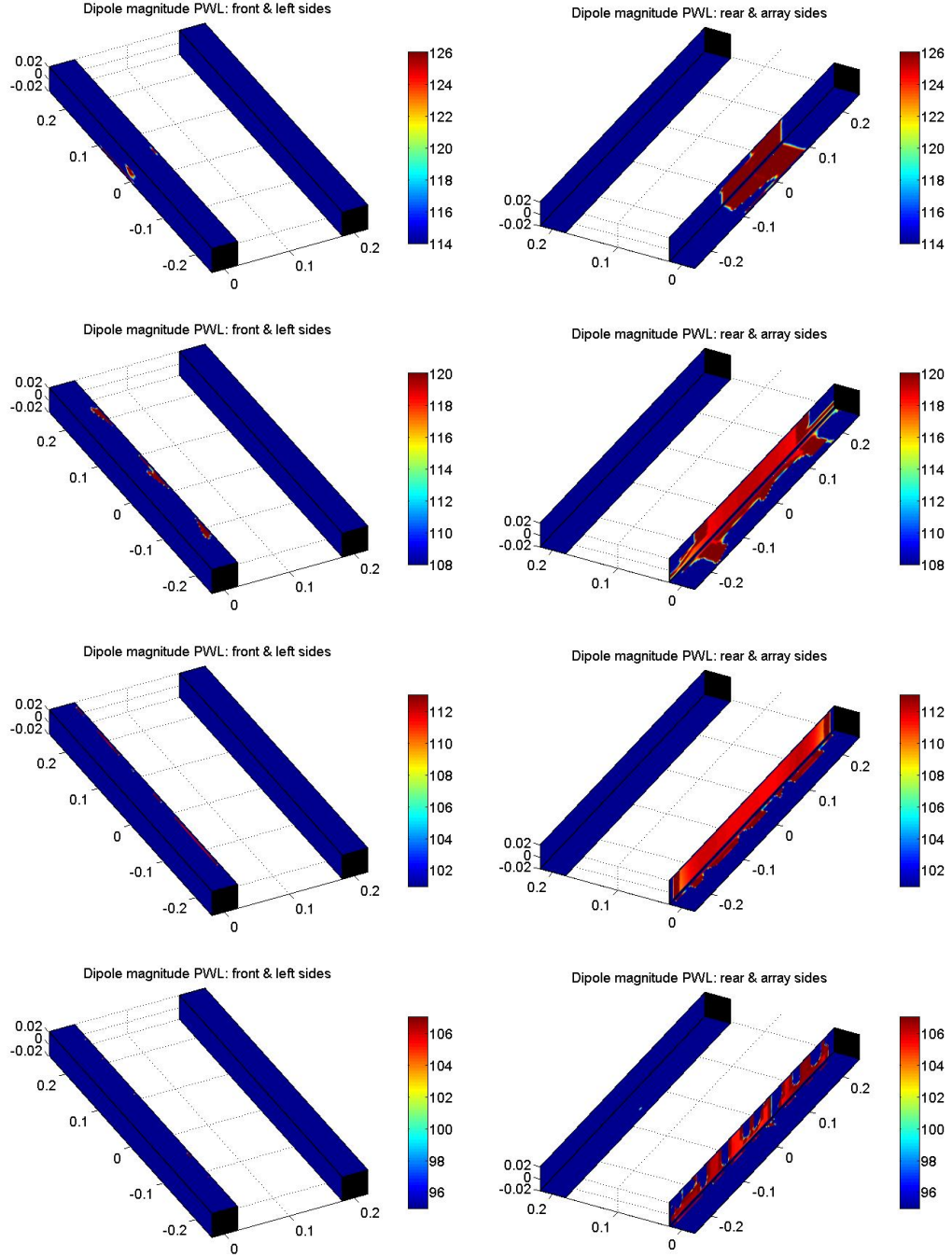
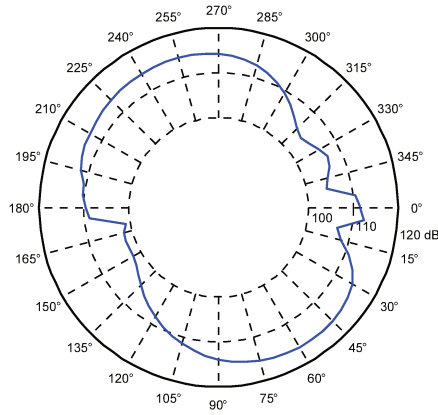
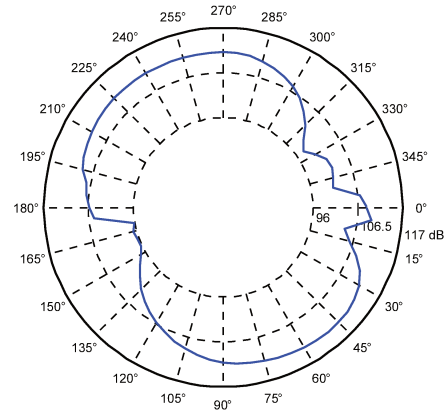


Figure 7.45: Simulation results for the 3D grid and line distributed incoherent dipoles with 45° in x-z plane with re-scaling of transfer matrix: 1kHz (top); 2kHz; 4kHz; and 8kHz. Mappings are source PWL in dB re 1pW.

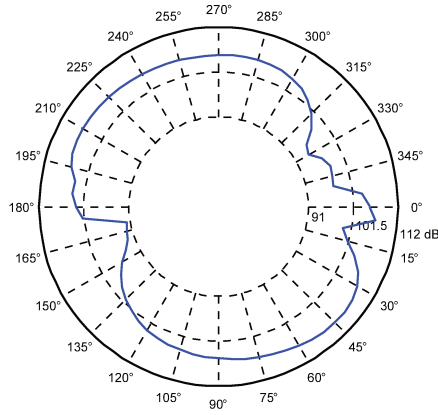
Once verified the general performance on identification of distributed dipoles using the generalized inverse method and IRLS scheme, visualization of results with the Hybrid generalized



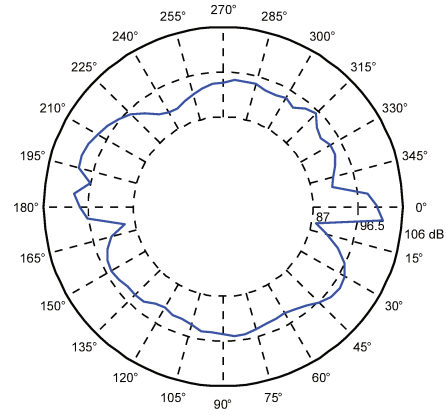
(a)



(b)



(c)



(d)

Figure 7.46: Directivity results ($r=2\text{m}$) for the 3D grid and line distributed incoherent dipoles with 45° in x-z plane for frequencies of : (a) 1kHz; (b) 2kHz; (c) 4kHz; and (d) 8kHz.

inverse mapping, and construction of directional assessment and vectorial representation, the experimental assessments can be presented and discussed.

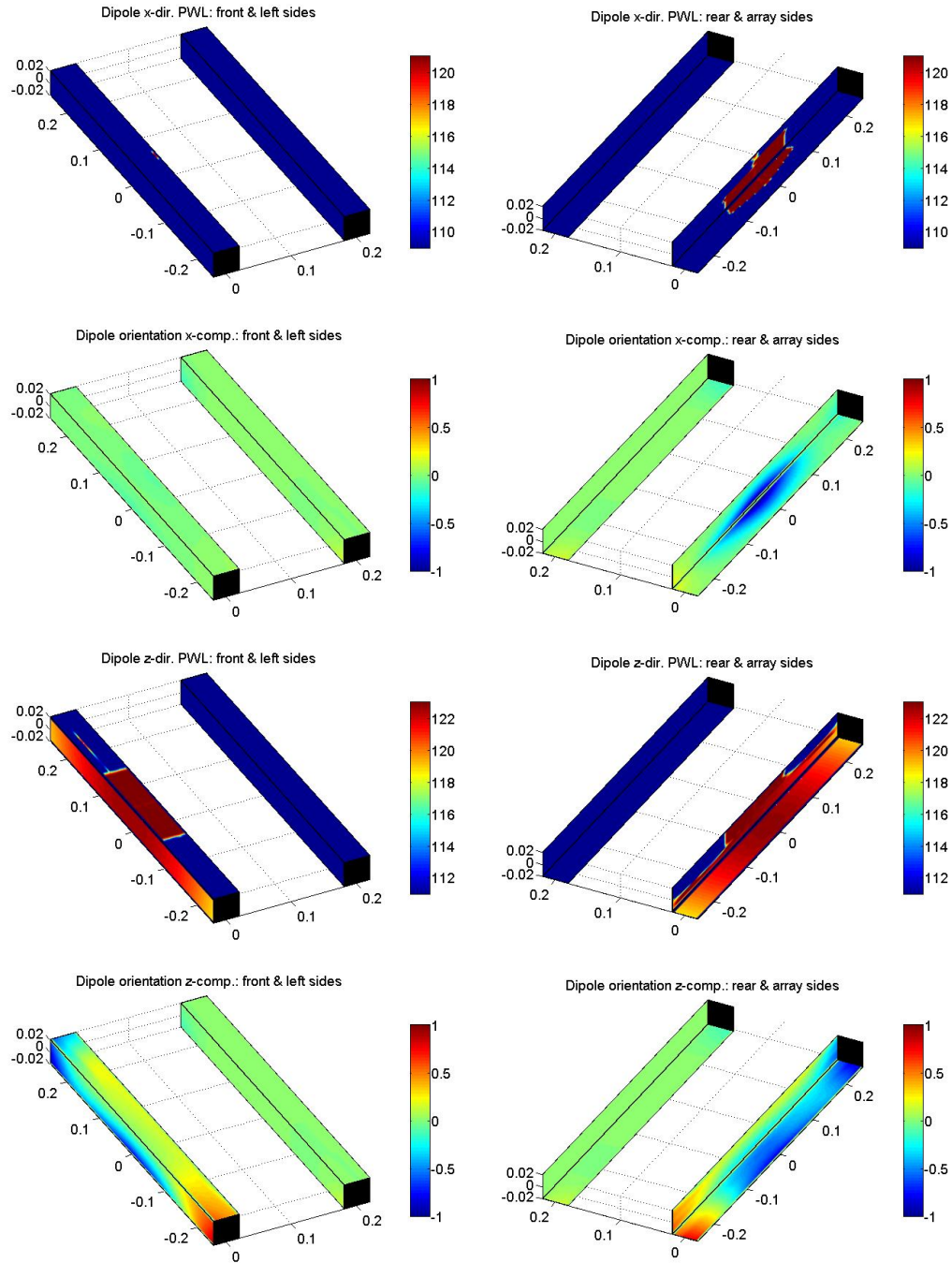


Figure 7.47: Dipole direction components level (top and middle) and vectorial representation for the line distributed incoherent dipoles with 45° in x-z plane and 1kHz radiation. Level mappings are source PWL in dB re 1pW and vectorial mappings are strength normalized by maximum absolute level on each direction.

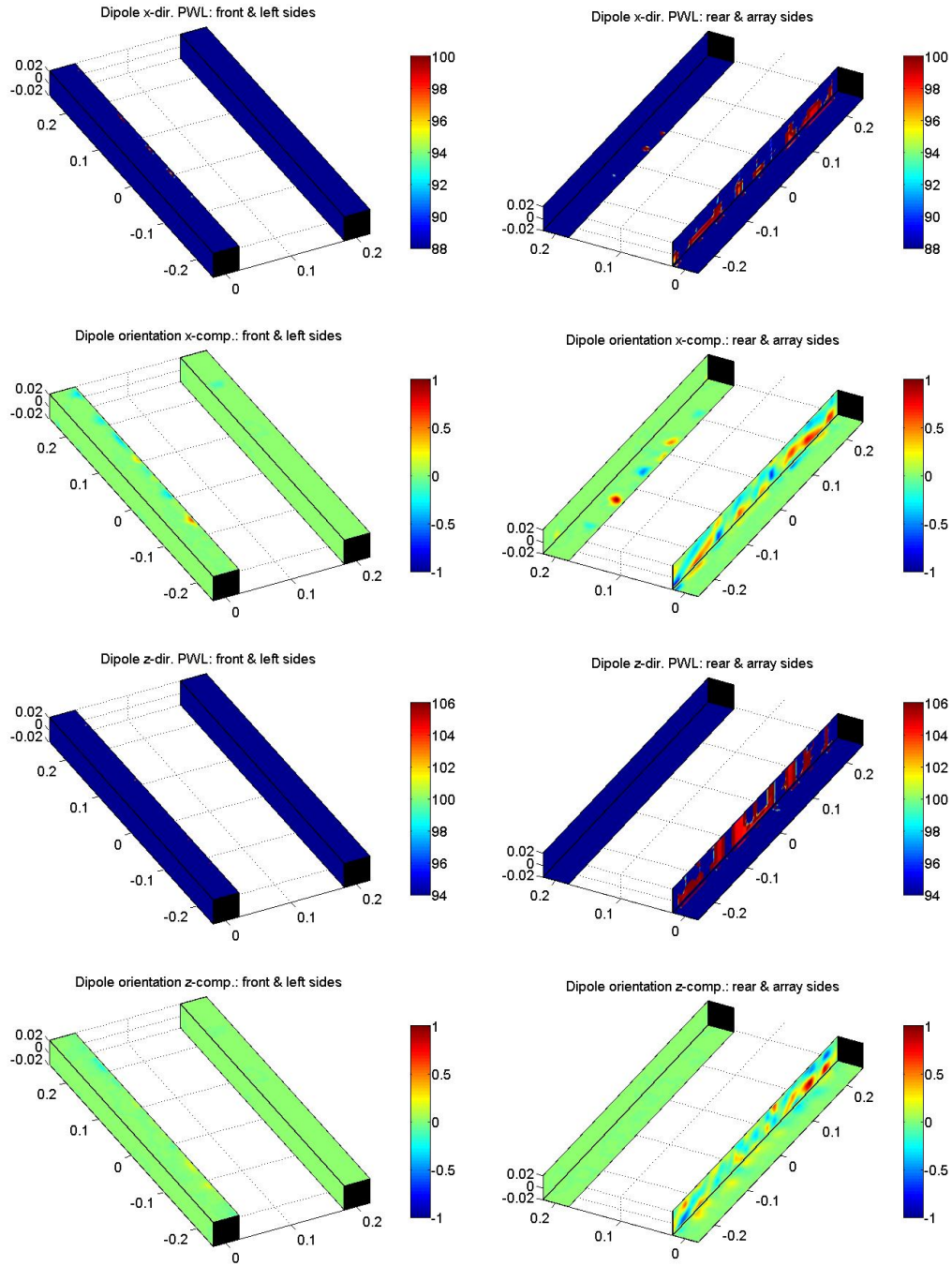


Figure 7.48: Dipole direction components level (top and middle) and its vectorial representation for the line distributed incoherent dipoles with 45° in x-z plane and 1kHz radiation. Level mappings are source PWL in dB re 1pW and vectorial mappings are strength normalized by maximum absolute level on each direction.

7.6.5 Experimental Results for Dipole Identification

The measurements consisted of four conditions, two with airflow speed at 35m/s (approximately Mach 0.1), and two with speed of 70m/s (Mach 0.2). Each speed condition is measured with the structures at an angle of 7.5° and 20° , to assess the turbulence generated by the upstream structure hitting the downstream structure, and producing aeroacoustic sound. The expected sources to dominate the sound radiation on this low Mach number speed are of dipole type, and distributed over the structure surfaces predominantly. The expected direction is cross-flow, in x and z directions, predominantly. The objective of the identification is to assess the distribution of the dipole and their orientation. A secondary objective is to provide easy visualizations of the sources, and their directivity.

For this, the Generalized Inverse Beamforming with the IRLS scheme is adopted again, and for the visualizations of dipole source level, the Hybrid generalized inverse mapping is used. This mapping, uses the locations in the 10dB range from the GIB mappings but with the levels from the Hybrid Mappings, which is the transformation of the generalized inverse mapping by the point-spread-function (squared) to a mapping that is comparable to the conventional beamforming in its directional behavior. This directional behavior means that the mapping value at a certain point corresponds to the source level at that point and the sources in the neighborhood defined by the PSF. The algorithm is set to perform 10 iterations for the 1kHz analysis, and 3 for the rest with one exception, the second data set in the 4kHz analysis, which used only one iteration to keep a minimum visualization of the sources. The regularization is the same as used in the simulations, optimized strategy on the first calculation and on the first iteration, the regularization factor adopted is 5% of the greatest eigen-value of $A^\dagger W_i A$, and kept fixed throughout the subsequent IRLS iterations. The method uses the eigenmodes of which the square root of the eigenvalues are within the 10dB range from the maximum value.

The mappings presented in this section are obtained without the application of a gaussian filter, as used in the monopole mappings, and they present a more sharp progression between the no-sources to the sources region. Later, the Full Hybrid mapping is presented and discussed in comparison to the hybrid generalized inverse used in this section. The experimental identifications are presented in Figures 7.49 to 7.52, with dipole power level (PWL).

The first data set, flow at 35m/s and angle of 7.5° , the results shows the downstream structure

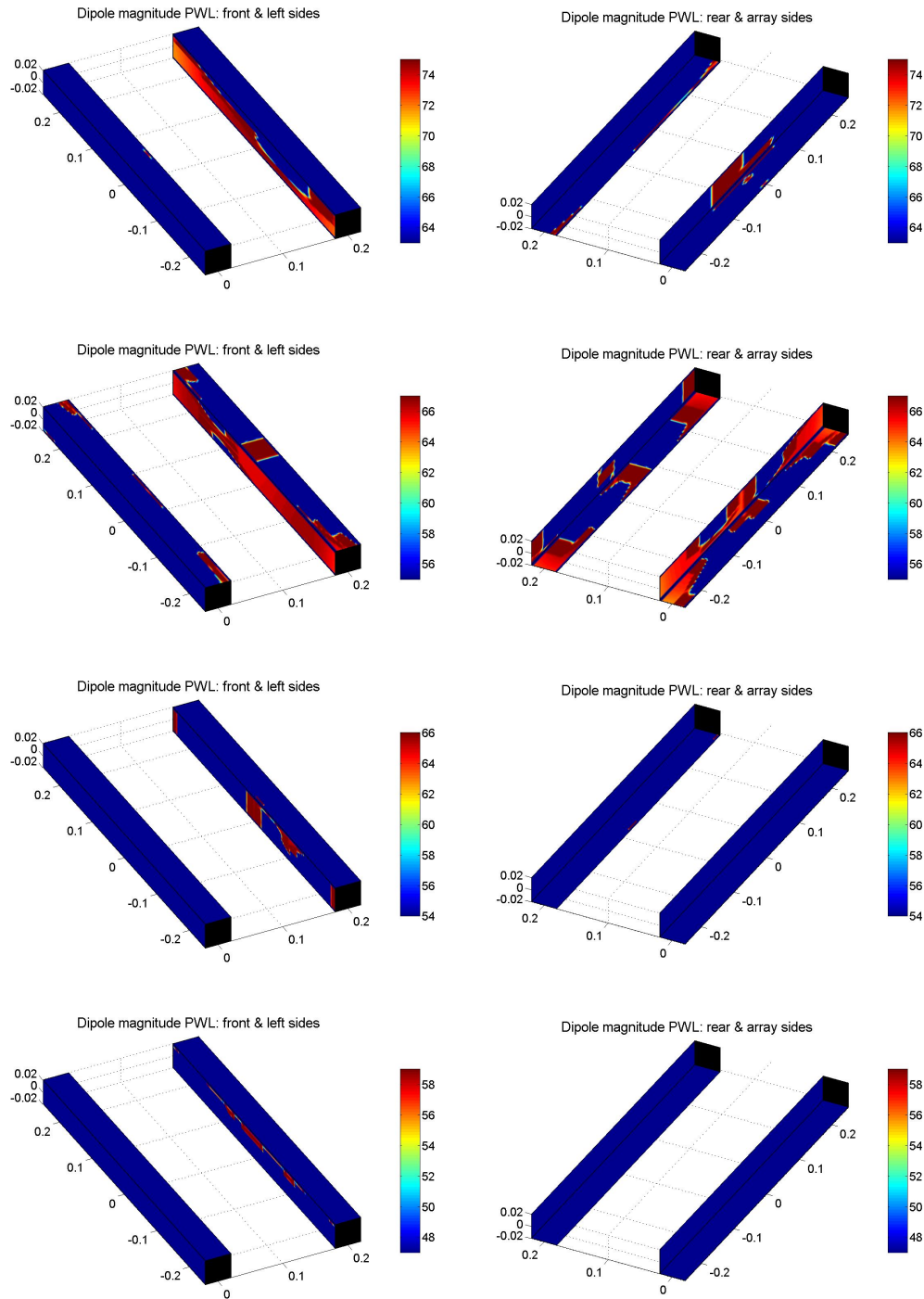


Figure 7.49: Dipole power level (experimental results) for structures with 7.5° angle and flow at 35m/s: 1kHz (top); 2kHz; 4kHz; and 8kHz. Mappings are source PWL in dB re 1pW.

as the main location of sources. For 1kHz, there is a small location of sources in the upstream structure too, and the distribution is in inner faces, and along the bar. The 2kHz mapping also

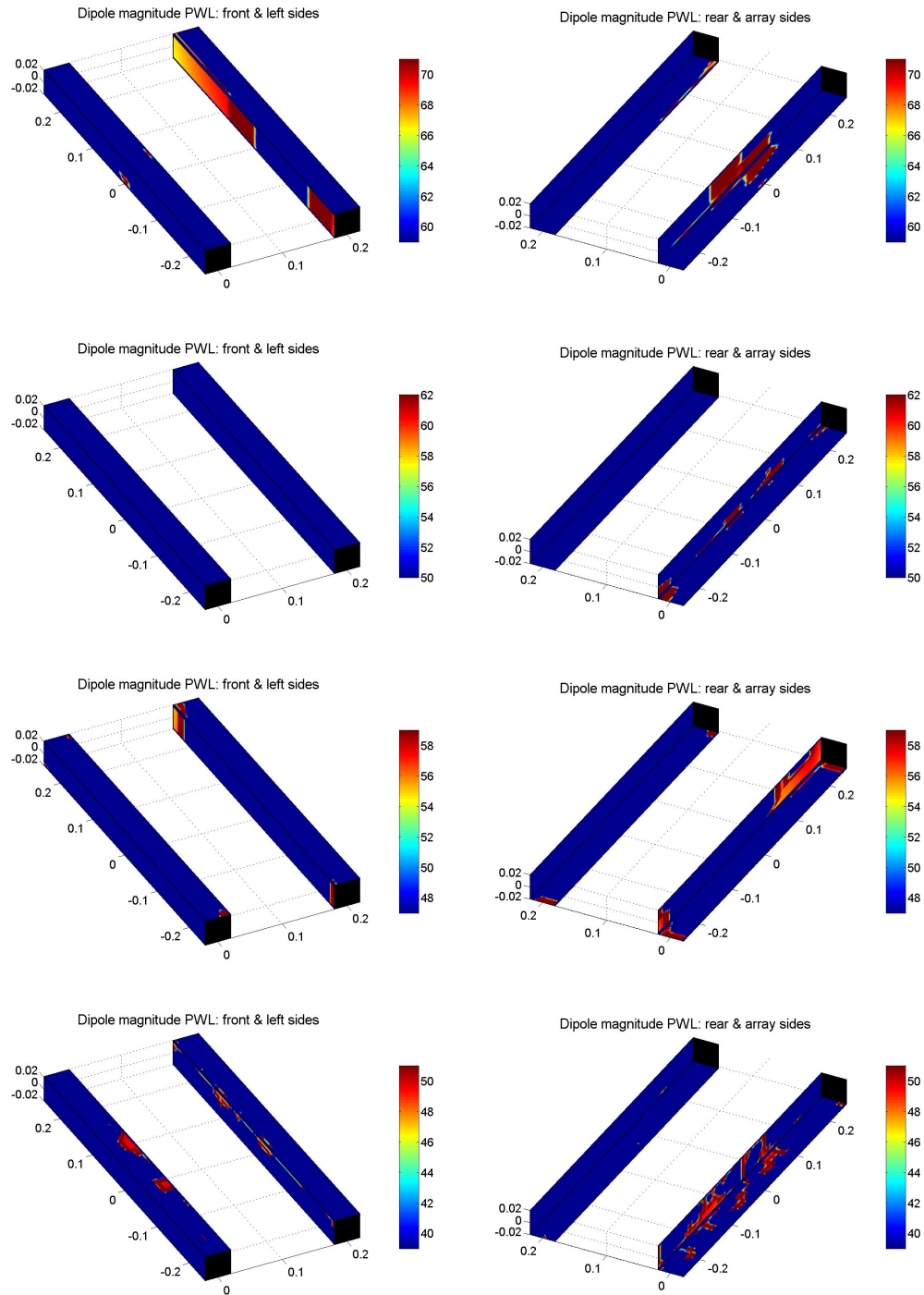


Figure 7.50: Dipole power level (experimental results) for structures with 20° angle and flow at 35m/s: 1kHz (top); 2kHz; 4kHz; and 8kHz. Mappings are source PWL in dB re 1pW.

presents sources in inner faces, but now they are more concentrated in the extremities and in the center. The 4kHz case only present sources at the inner face, in the extremity and in the center.

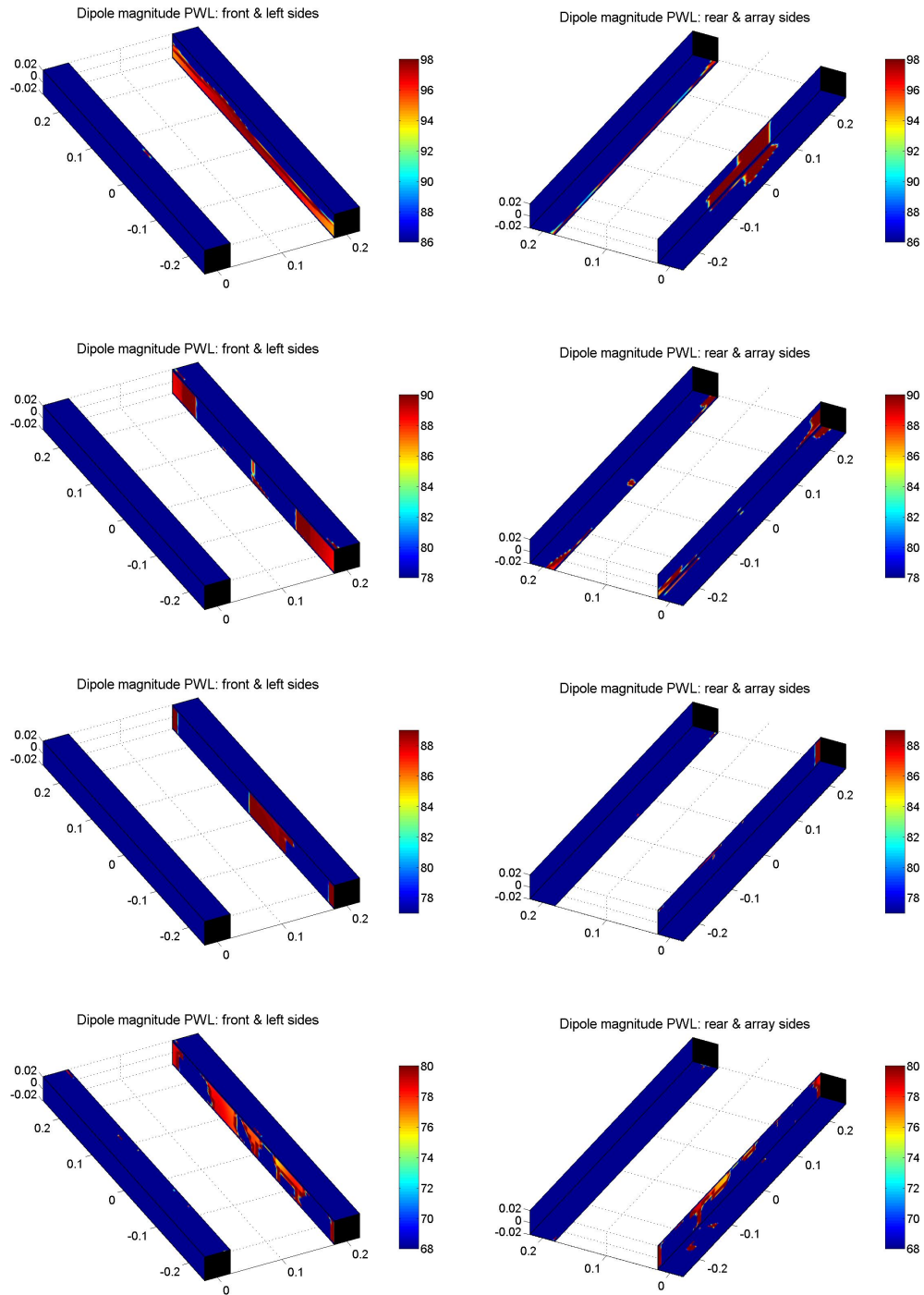


Figure 7.51: Dipole power level (experimental results) for structures with 7.5° angle and flow at 70m/s: 1kHz (top); 2kHz; 4kHz; and 8kHz. Mappings are source PWL in dB re 1pW.

The 8kHz case, brings sources only in the corner of the rear structure that faces the far-field microphones, and is farther from the array, which is also the corner that hits the turbulent flow

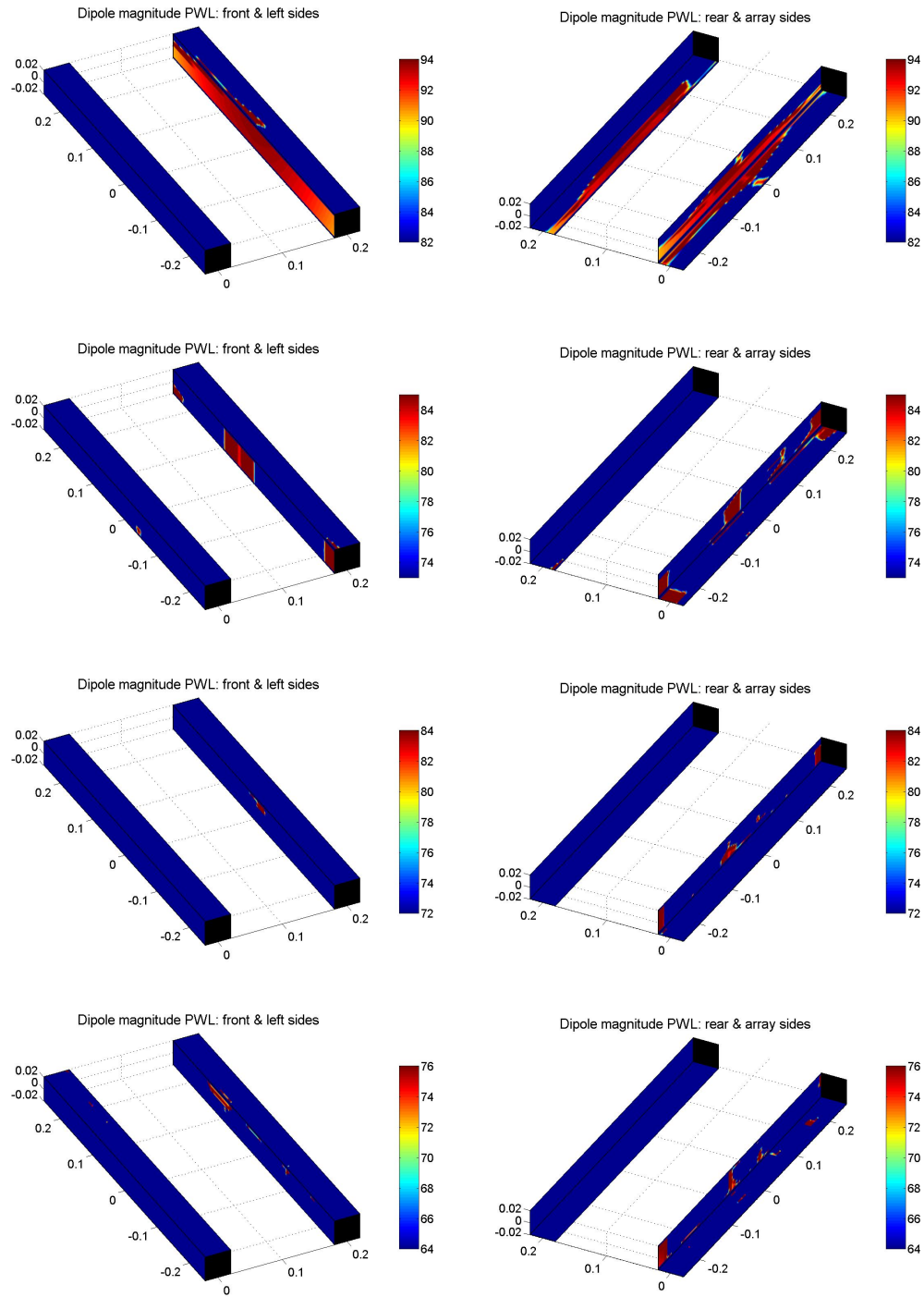


Figure 7.52: Dipole power level (experimental results) for structures with 20° angle and flow at 70m/s: 1kHz (top); 2kHz; 4kHz; and 8kHz. Mappings are source PWL in dB re 1pW.

from the first bar.

These first results are all in accordance to the conventional and generalized inverse mappings for all frequencies, and showing the rear bar as main location. But the detection of the corner that hits the turbulence can only be depicted from the dipole hybrid generalized inverse mappings.

For the second data set, flow at 35m/s and angle of 20° , the results show more sources at the upstream structure. For 1kHz, they are again distributed at the inner faces. At 2kHz, sources are detected mainly in the upstream structure. For 4kHz, the sources are located more on the extremities, higher in the upstream structure. In the 8kHz analysis, there are more sources in the upstream bar, but there are still some in the corner that hits the turbulence in the second bar.

The increase of sources in the upstream bar could be related to a more aggressive flow detachment from the bar with the angle of 20° . Again, the results are in accordance to the monopole mappings from conventional and generalized inverse beamforming.

The third data set, flow at 70m/s and angle of 7.5° , present sources at both structures. In the 1kHz case, again they are in the inner structures faces, more distributed in the rear bar. For 2kHz, there are more sources on the extremities, at the inner face of the rear bar and on the corners that separate the flow for the first bar, and the one that probably faces the higher turbulence in the second bar. Note that coordinates in the mappings are not rotated for an easy visualization. For 4kHz, sources are more located at the second bar inner face. On the 8kHz analysis, the inner faces are also the main locations, seemingly more present in the rear structure, but both presenting sources at the extremities. The mappings are coherent between the conventional and generalized inverse beamforming using monopole source type results.

The fourth data set, flow at 70m/s and angle of 20° , present the rear face or inner face of the first bar as the main location of sources. On the 1kHz case they are more intense in the corner that detaches the flow from the first bar, and in the inner face and the corner that probably faces the turbulence from the first bar on the second bar. In the 2kHz mappings, again extremes and the center of the inner faces are the main locations. The 4kHz case presents sources in the inner face, at extremities and in the center of the front structure. The 8kHz case, again presents sources in the upstream bar, with sources in the inner face and in the corner that first hits the flow from the first bar. The mappings in general are in agreement between the conventional and generalized inverse mappings using monopole type of source.

In terms of source levels, here the dipole powers are calculated for the band center frequencies

of analysis, and results extrapolated to the band level. This is done to avoid losing details on the summation process as previously demonstrated in the monopole generalized inverse mapping simulated example.

The level on the dipole mappings are not directly comparable to the monopole mappings, but considering the radiation type difference, they are on the same order of magnitude, but raising in proportion for higher frequencies, due to the dipole nature. This mapping could help in decision making process, while considering the correct power of radiation, and consequent far-field estimations.

The 3D grid, seemed to provide important hints from the source centers of radiation, and a comparison to a line grid is presented later on this section.

7.6.6 Full Hybrid and Hybrid Generalized Inverse Mapping Comparison

The visualization using the generalized inverse locations and the hybrid mapping values can be somewhat sharp in nature in a first look, and because of this, to support the comparison to the monopole beamforming results, the full hybrid mappings, while a result of transforming the generalized inverse result by the point-spread function (on this analysis it is used the square of the PSF), can be presented for the same measurements presented in the previous section. Results are shown in Figures 7.53 to 7.56.

Now the overall power level progression is closer to the ones found in the monopole conventional mappings, which yield very similar results in terms of localization of the main region. For example, on the first data set, the higher level is on the second bar, while on the second data set, the main region is on the first bar. Is important to emphasize that they are the same result, but with the PSF transformation.

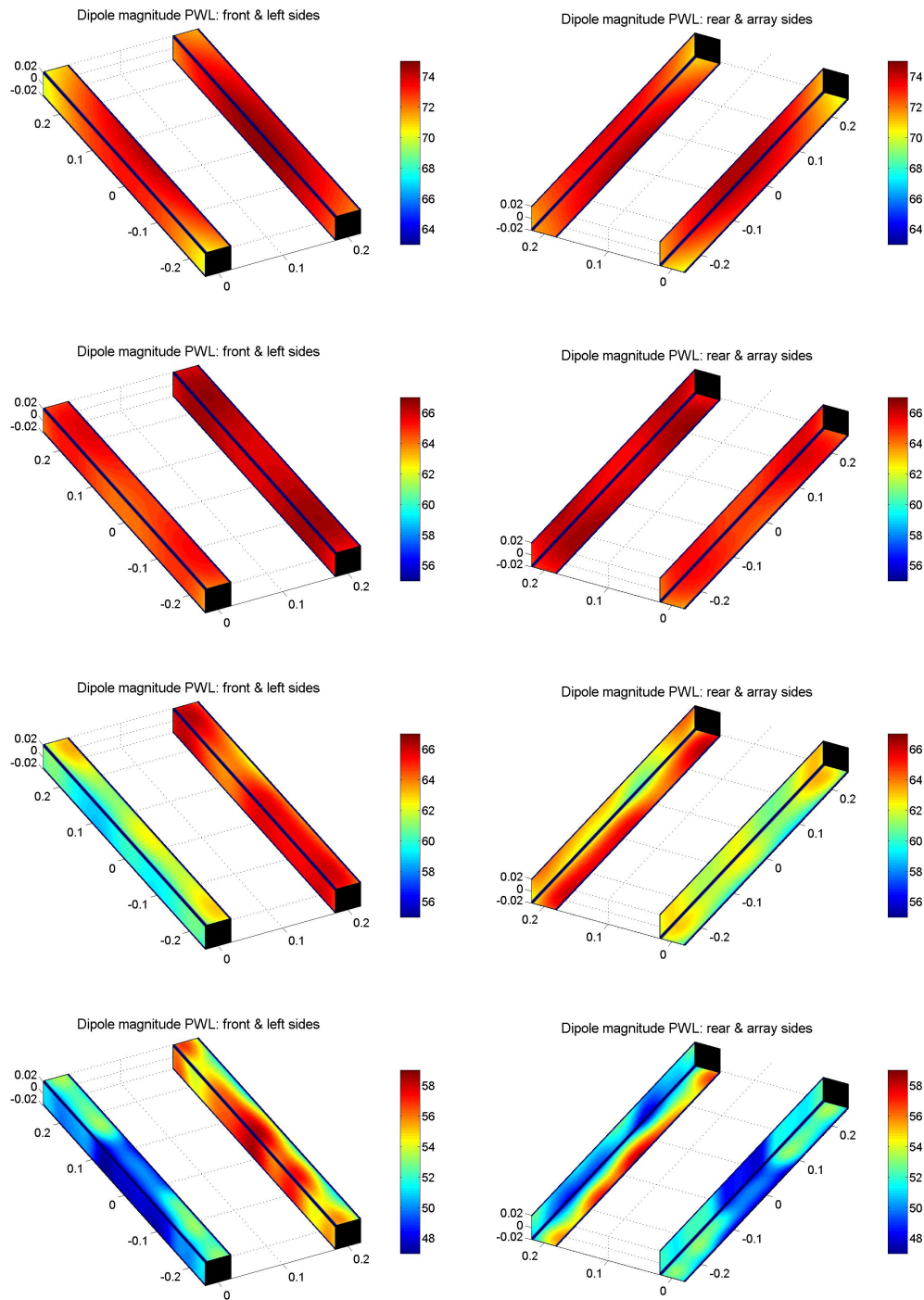


Figure 7.53: Dipole power level hybrid mapping (experimental results) for structures with 7.5° angle and flow at 35m/s: 1kHz (top); 2kHz; 4kHz; and 8kHz. Mappings are source PWL in dB re 1pW.

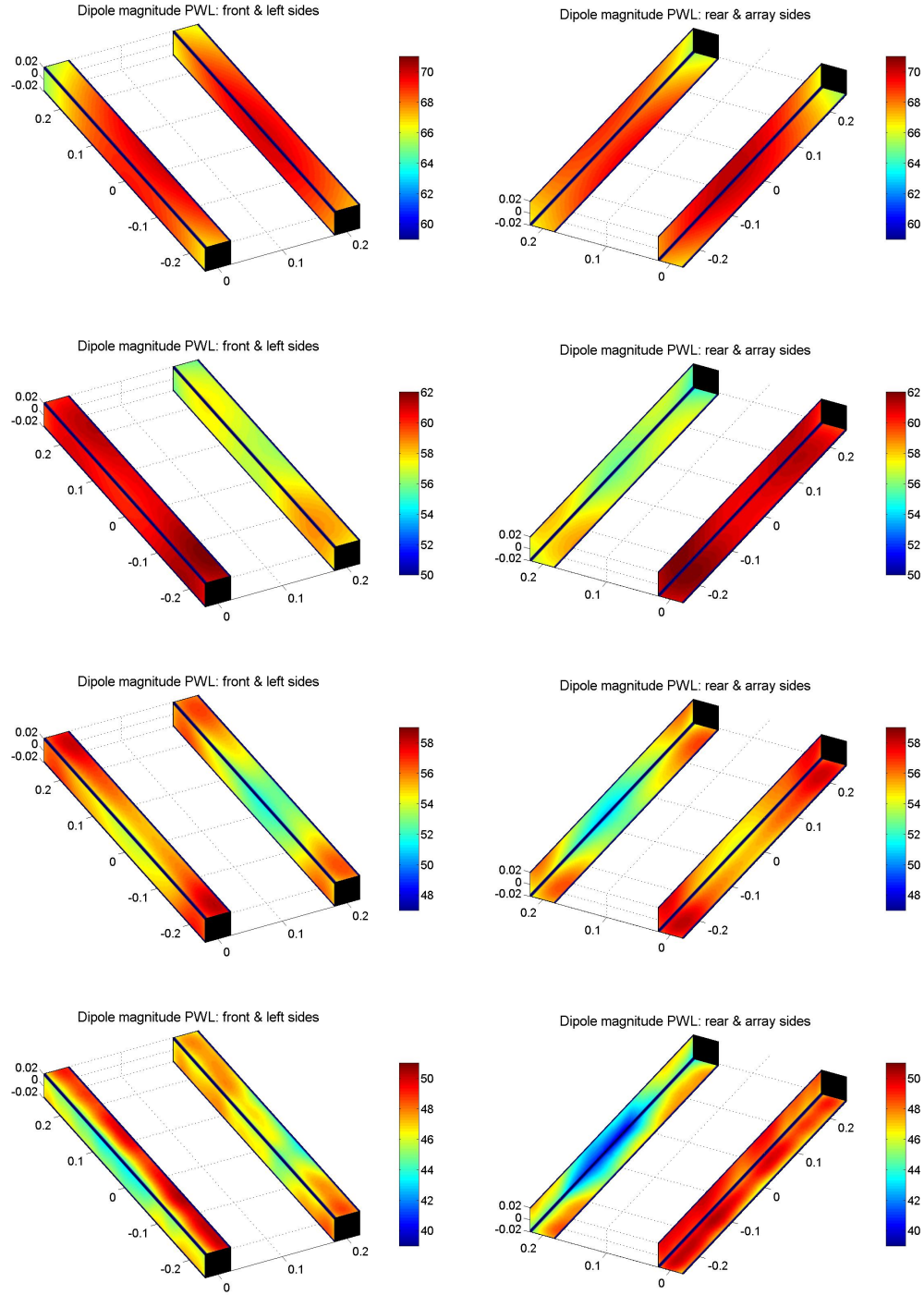


Figure 7.54: Dipole power level hybrid mapping (experimental results) for structures with 20° angle and flow at 35m/s: 1kHz (top); 2kHz; 4kHz; and 8kHz. Mappings are source PWL in dB re 1pW.

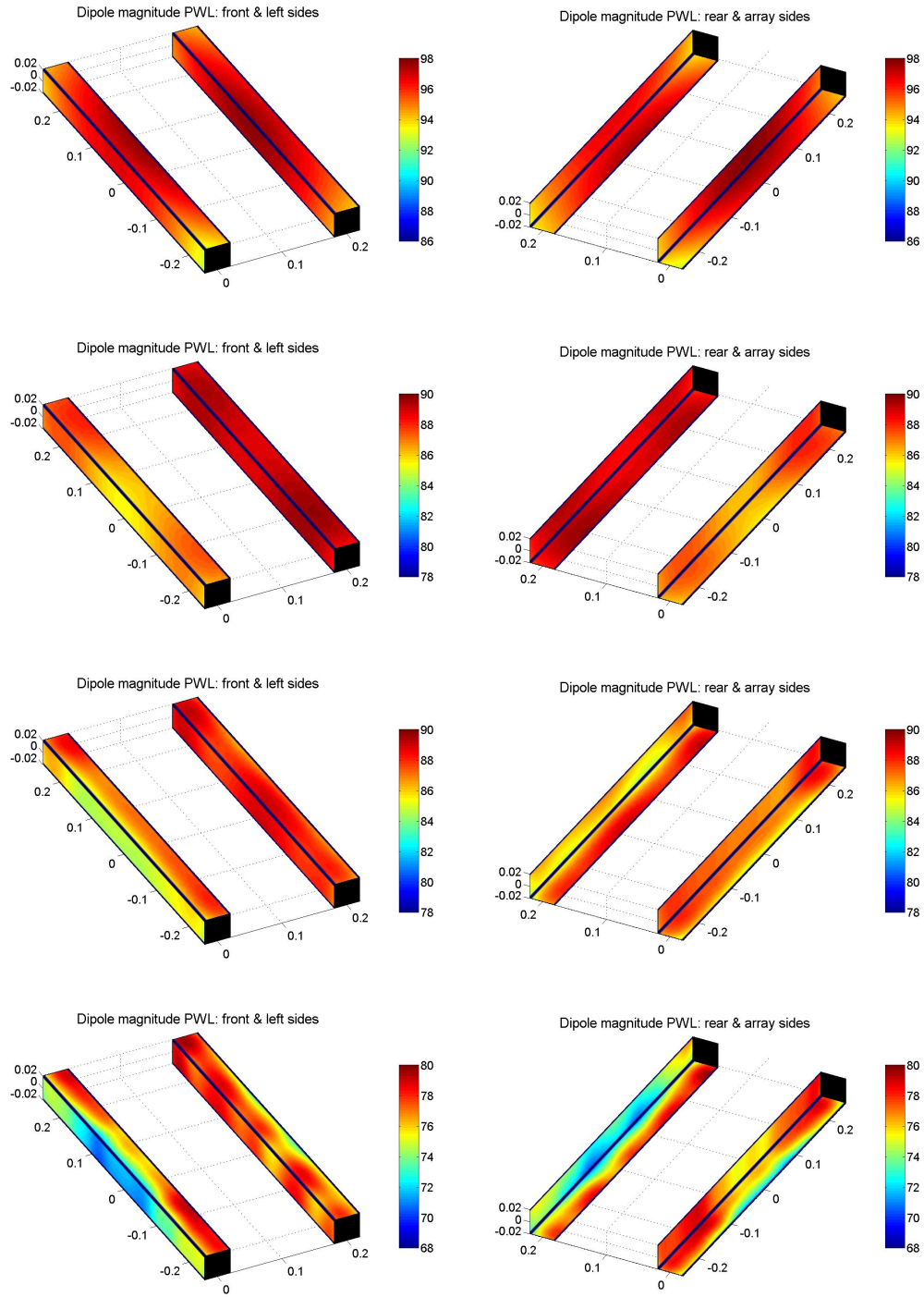


Figure 7.55: Dipole power level hybrid mapping (experimental results) for structures with 7.5° angle and flow at 70m/s: 1kHz (top); 2kHz; 4kHz; and 8kHz. Mappings are source PWL in dB re 1pW.

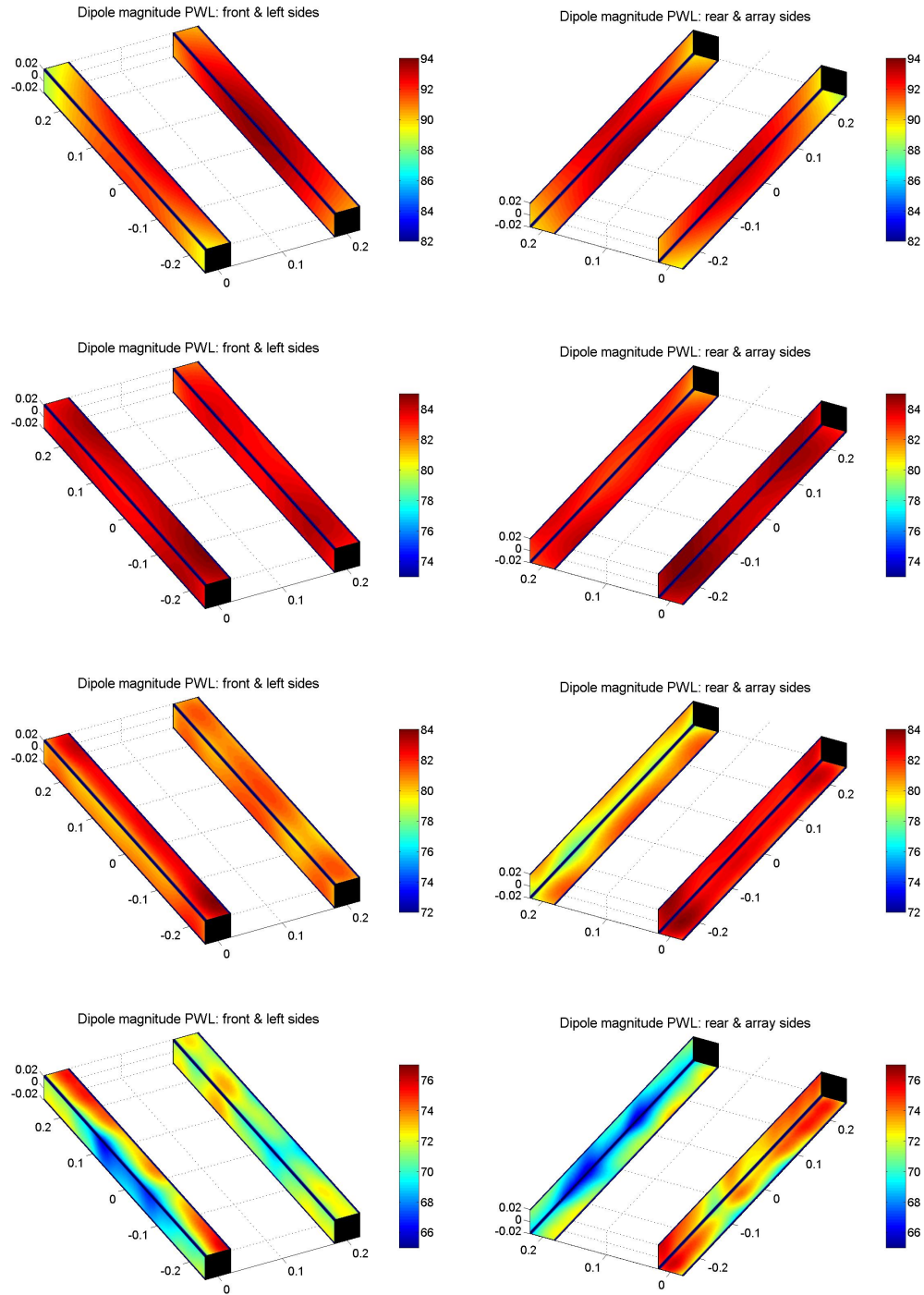


Figure 7.56: Dipole power level hybrid mapping (experimental results) for structures with 20° angle and flow at 70m/s: 1kHz (top); 2kHz; 4kHz; and 8kHz. Mappings are source PWL in dB re 1pW.

The use of this visualization is helpful for an overall sense, but the details are hidden by the filtering effect from the PSF convolution with the generalized inverse result. For example, is not easy to assess in the full hybrid mapping that, in the first data set, in the 8kHz analysis, the main region of source centers of radiation is located in the corner of the second bar that hits the turbulence from the first bar as shown in the previous section with the hybrid generalized inverse mapping.

In summary, it is suggested to have this mapping as aid to the sources main regions determination, but the details are only clear on the hybrid generalized inverse mapping.

7.6.7 Dipole Directional Component Level Details

The dipole identification in the generalized inverse algorithm is retrieved by the determination by least squares of the orthogonal components of the dipole, represented as a vector. With this calculation, the presented result is the magnitude of the vector, and there is also valuable information on the components of the dipole that determine its orientation. Two visualizations are provided, the first based in the component power levels, calculated in the same manner as the dipole magnitude, and the second, the in-phase part of the estimated component level, plotted in linear scale, and normalized to the maximum source component value of the respective mapping, the estimated component level in fact, being the multiplier A_{dip} , as named by Morse (1948), and described in a previous section. There are multiple definitions of dipole strength, and to avoid confusion, this term is not used in this text.

The results for the four data sets are presented for each of the analysis frequencies from 7.57 to 7.72. They refer to the same calculations shown in the previous sections.

The first important observation is the relative participation of the x-direction (in the flow direction) in comparison to the z-direction (cross-flow). Their level dictate the orientation of the resultant dipole. Note that the exact quadrant is determined by the vectorial representation.

On the first data set, flow at 35m/s and angle of 7.5° , the levels of components are approximately the same in the 1 and 2kHz analysis, and the x-component increases in proportion in the 4 and 8kHz analysis, which is in accordance to the general expected dipole orientation for higher frequencies, and also observed in the flow over cylinder identifications in a previous Chapter.

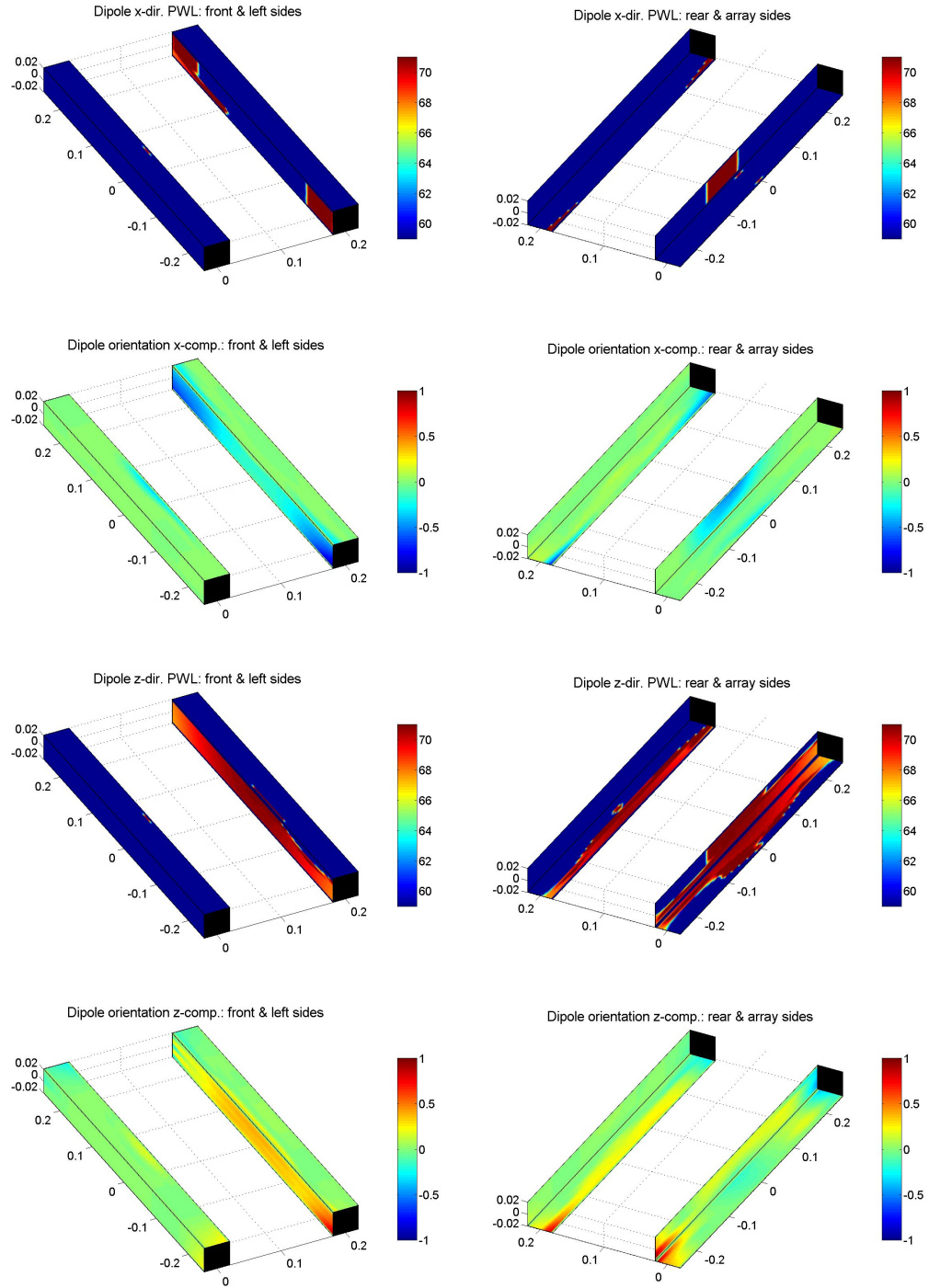


Figure 7.57: Dipole estimation (1kHz) with direction components level (top and third row) and vectorial representation for structures with 7.5° angle and flow at 35m/s (experimental results). Level mappings are source PWL in dB re 1pW and vectorial mappings are estimated A_{dip} normalized by maximum absolute level on each direction.

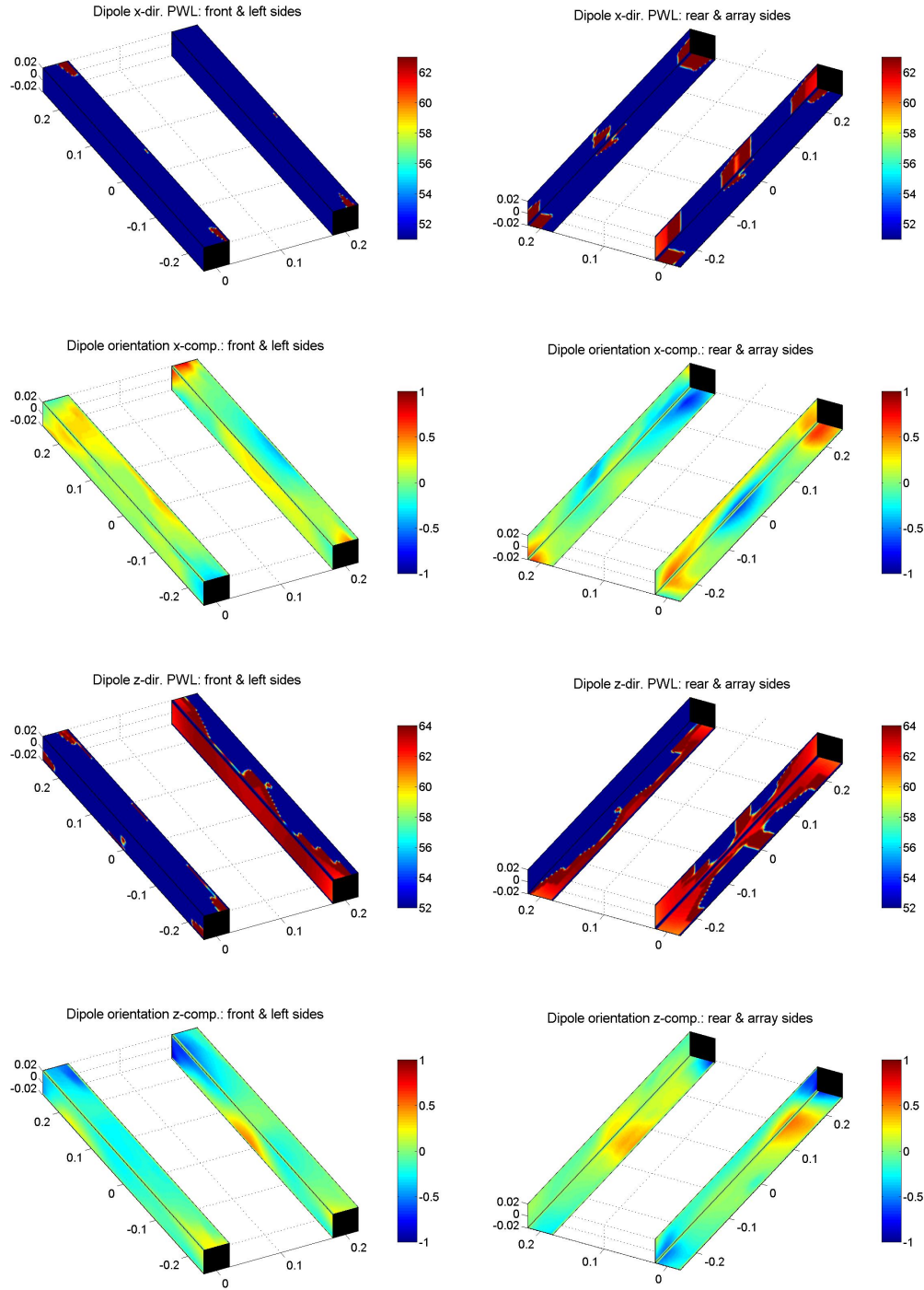


Figure 7.58: Dipole estimation (2kHz) with direction components level (top and third row) and vectorial representation for structures with 7.5° angle and flow at 35m/s (experimental results). Level mappings are source PWL in dB re 1pW and vectorial mappings are estimated A_{dip} normalized by maximum absolute level on each direction.

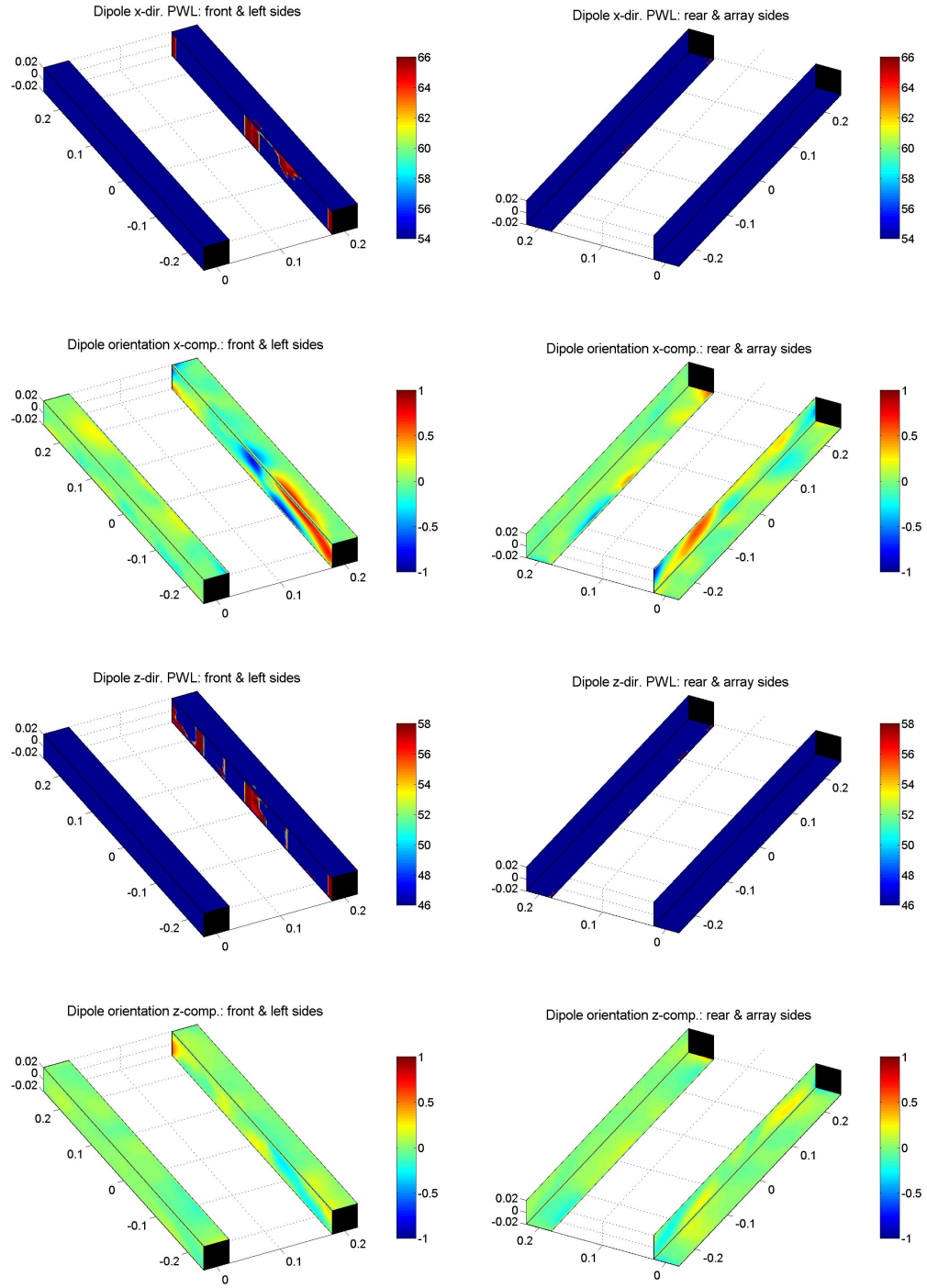


Figure 7.59: Dipole estimation (4kHz) with direction components level (top and third row) and vectorial representation for structures with 7.5° angle and flow at 35m/s (experimental results). Level mappings are source PWL in dB re 1pW and vectorial mappings are estimated A_{dip} normalized by maximum absolute level on each direction.

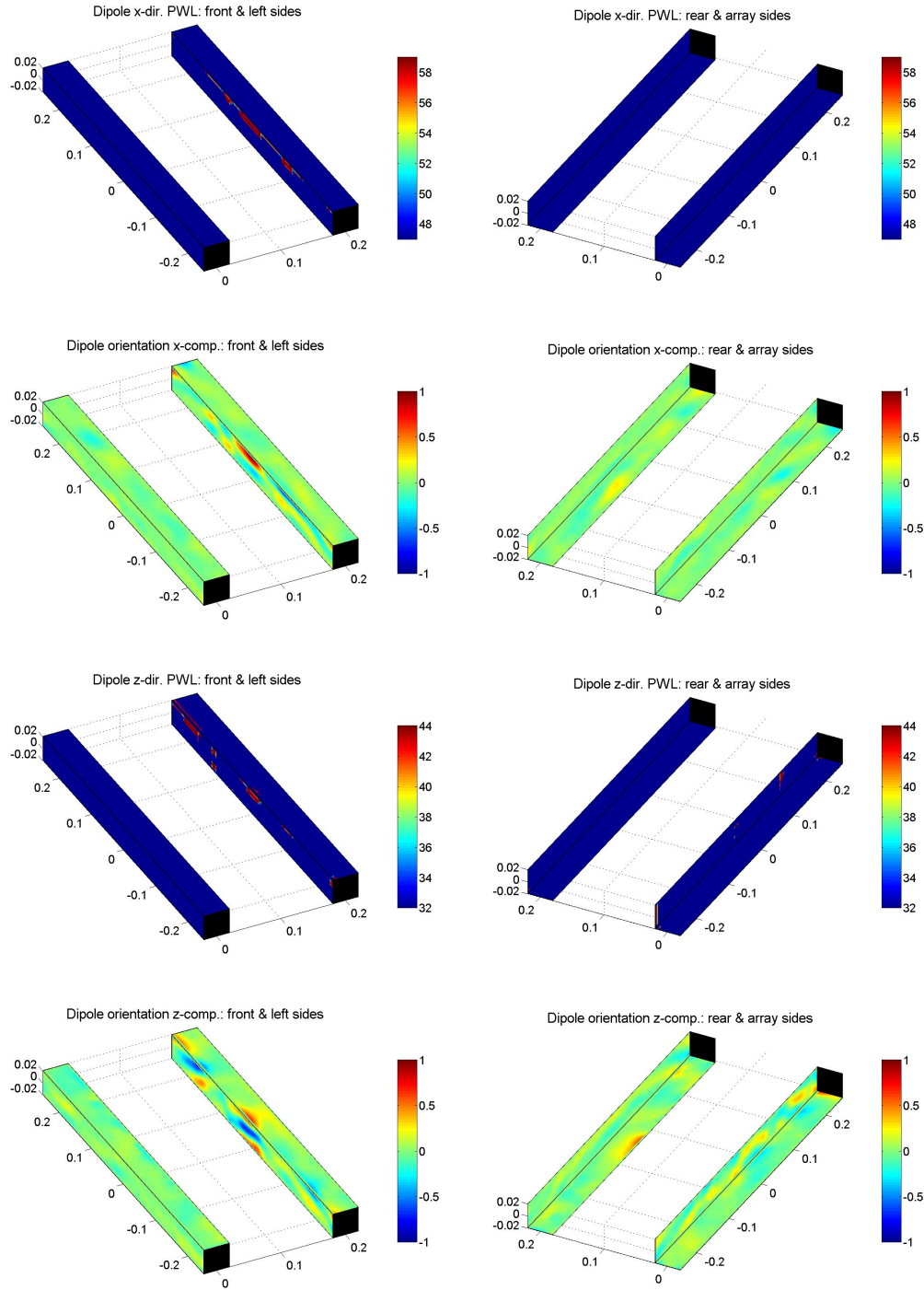


Figure 7.60: Dipole estimation (8kHz) with direction components level (top and third row) and vectorial representation for structures with 7.5° angle and flow at 35m/s (experimental results). Level mappings are source PWL in dB re 1pW and vectorial mappings are estimated A_{dip} normalized by maximum absolute level on each direction.

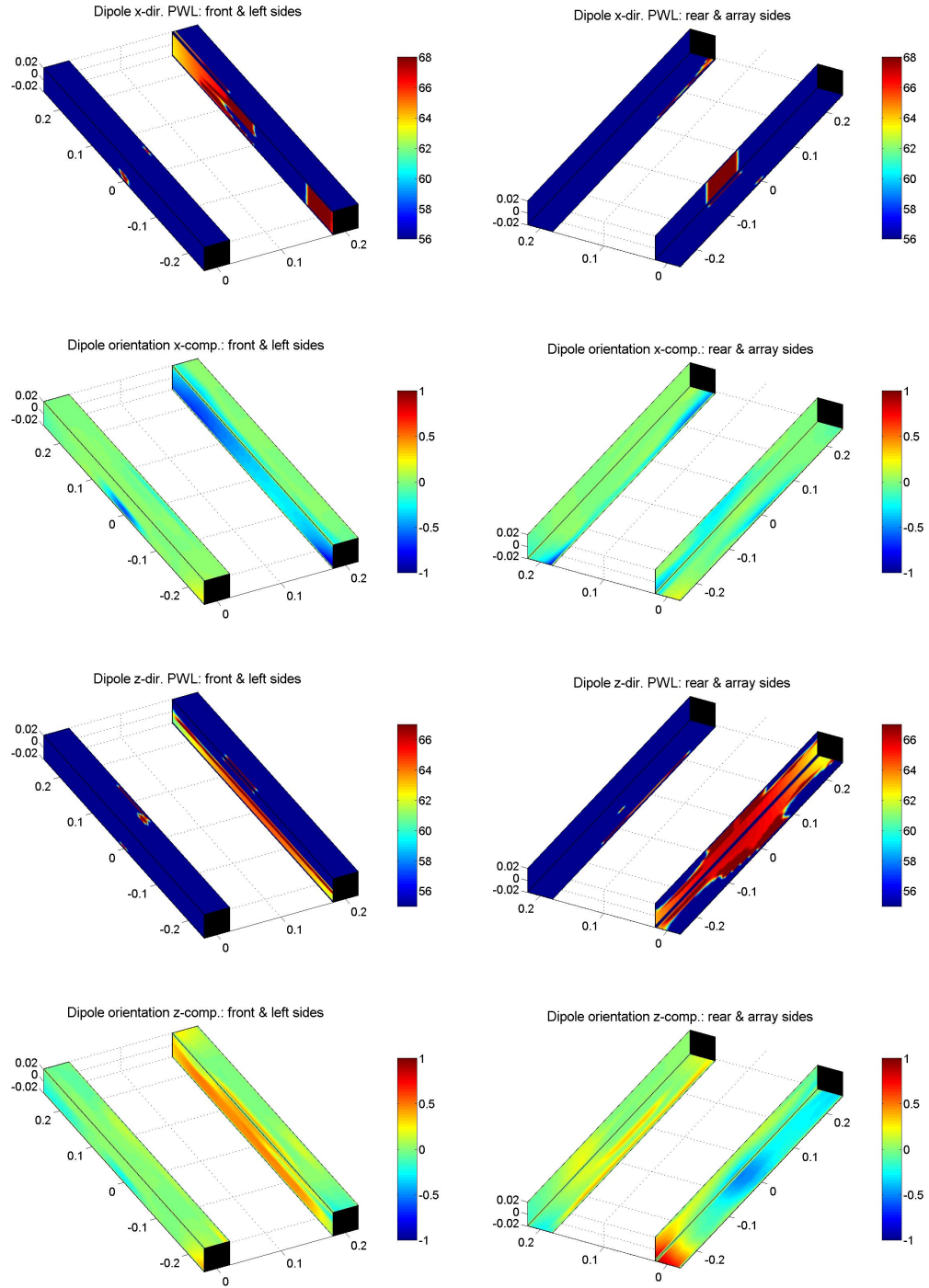


Figure 7.61: Dipole estimation (1kHz) with direction components level (top and third row) and vectorial representation for structures with 20° angle and flow at 35m/s (experimental results). Level mappings are source PWL in dB re 1pW and vectorial mappings are estimated A_{dip} normalized by maximum absolute level on each direction.

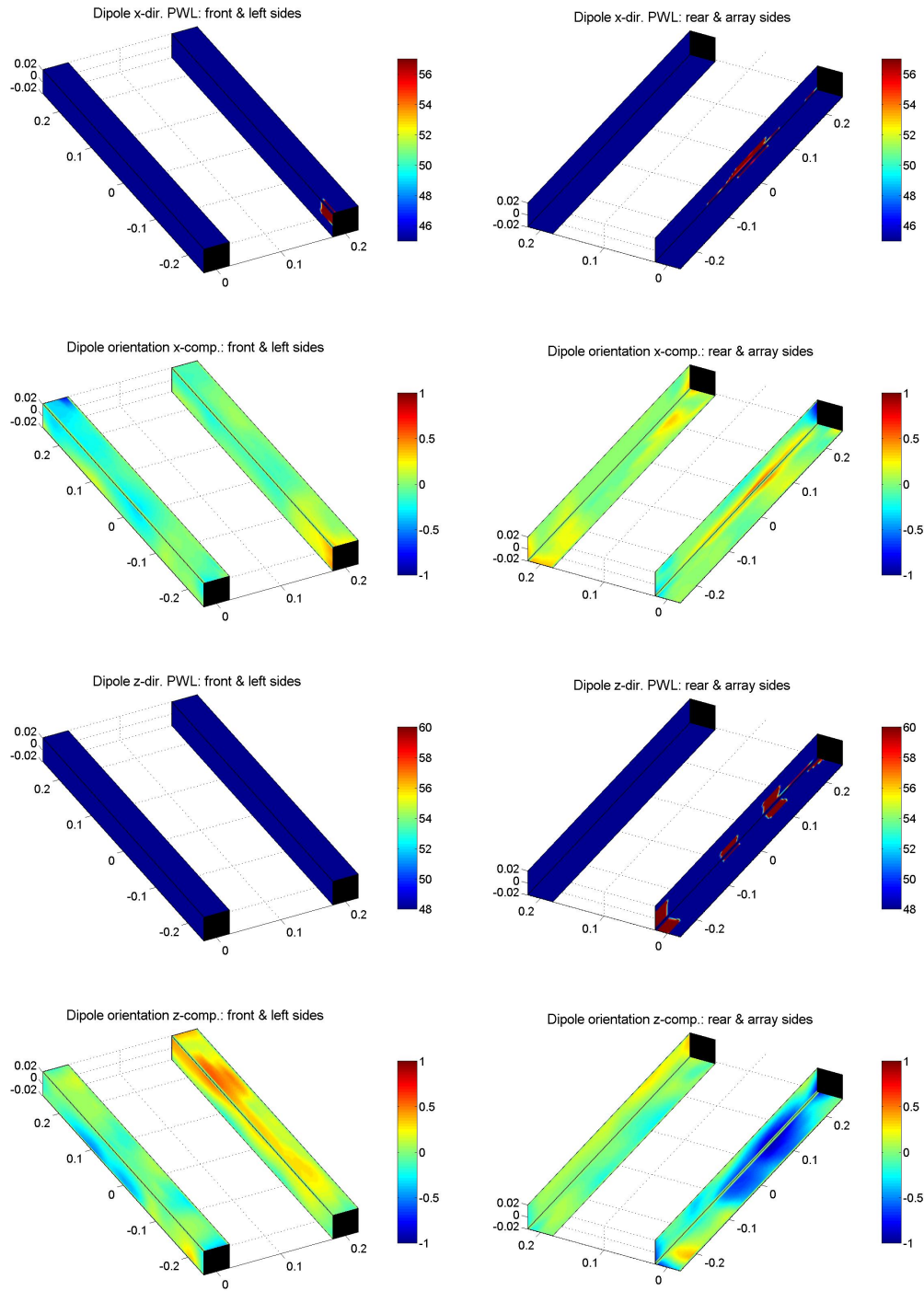


Figure 7.62: Dipole estimation (2kHz) with direction components level (top and third row) and vectorial representation for structures with 20° angle and flow at 35m/s (experimental results). Level mappings are source PWL in dB re 1pW and vectorial mappings are estimated A_{dip} normalized by maximum absolute level on each direction.

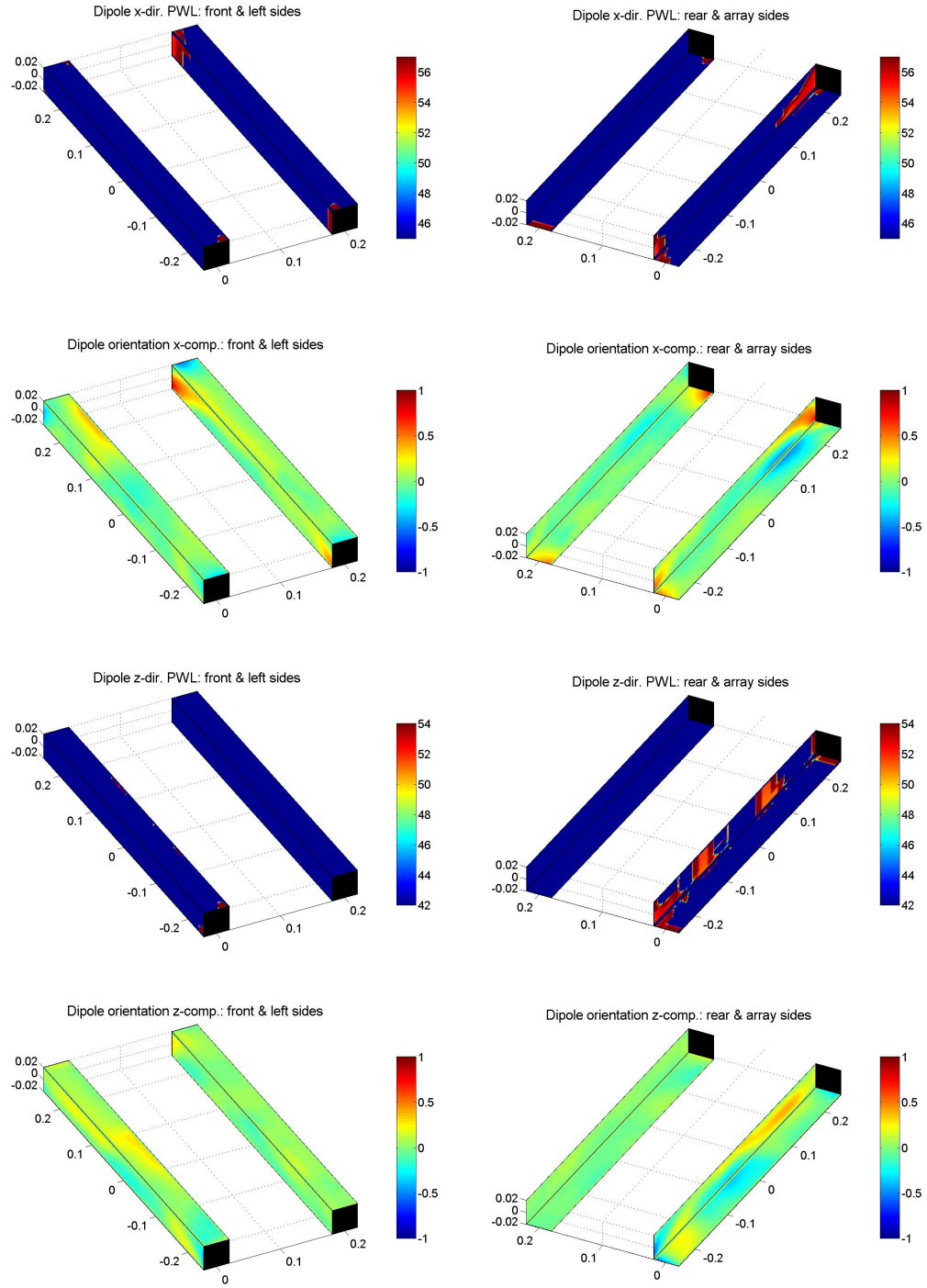


Figure 7.63: Dipole estimation (4kHz) with direction components level (top and third row) and vectorial representation for structures with 20° angle and flow at 35m/s (experimental results). Level mappings are source PWL in dB re 1pW and vectorial mappings are estimated A_{dip} normalized by maximum absolute level on each direction.

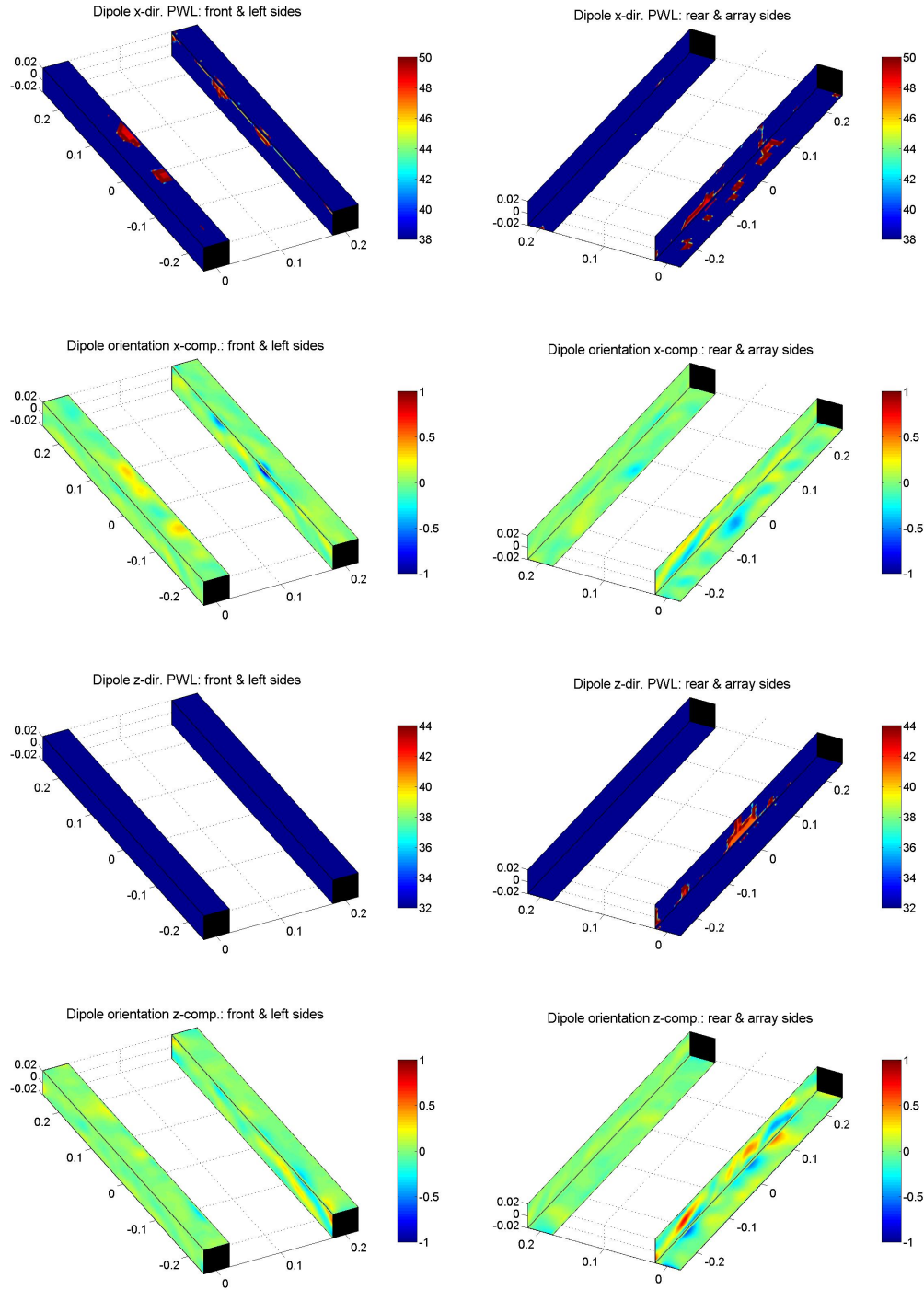


Figure 7.64: Dipole estimation (8kHz) with direction components level (top and third row) and vectorial representation for structures with 20° angle and flow at 35m/s (experimental results). Level mappings are source PWL in dB re 1pW and vectorial mappings are estimated A_{dip} normalized by maximum absolute level on each direction.

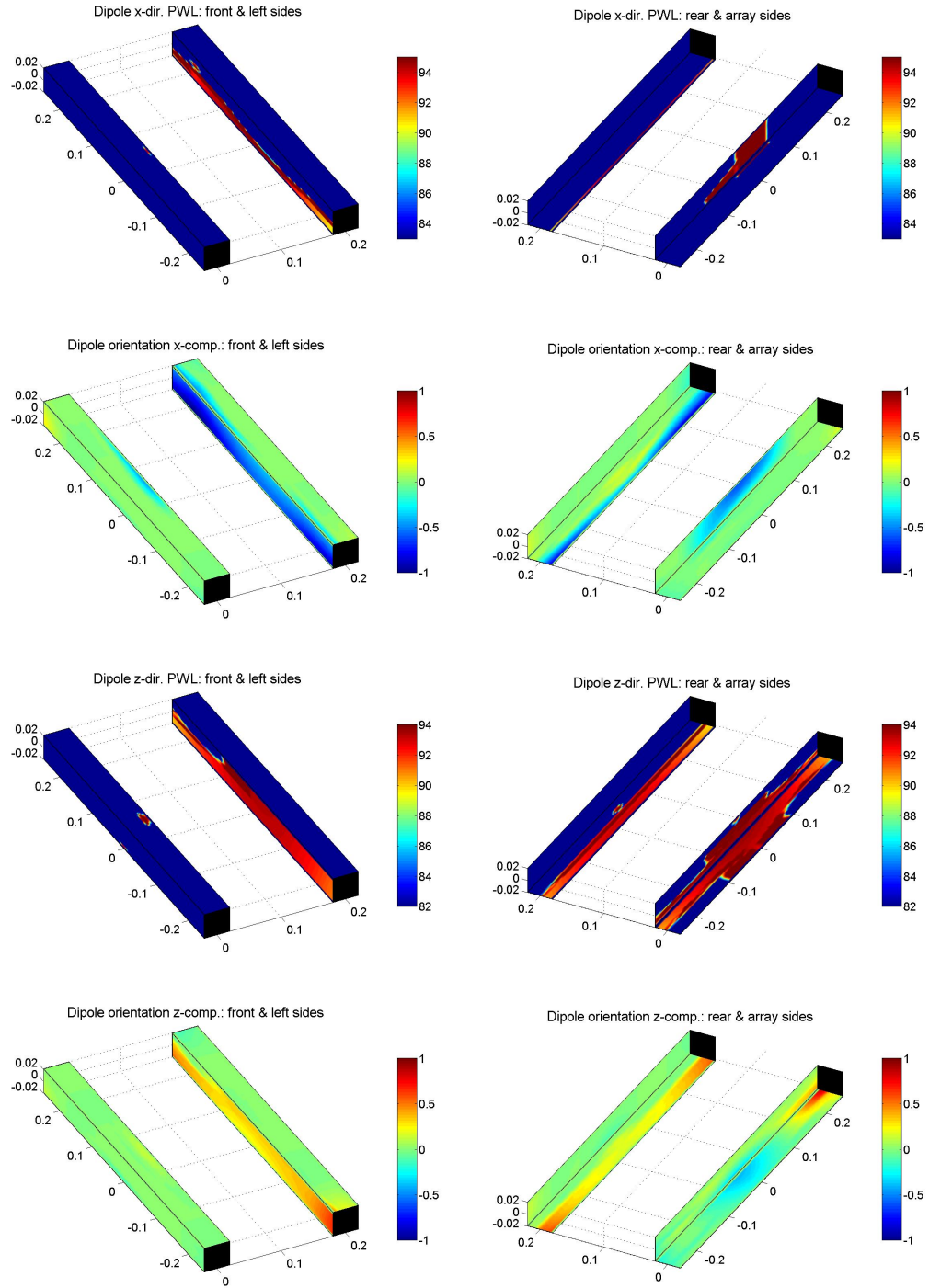


Figure 7.65: Dipole estimation (1kHz) with direction components level (top and third row) and vectorial representation for structures with 7.5° angle and flow at 70m/s (experimental results). Level mappings are source PWL in dB re 1pW and vectorial mappings are estimated A_{dip} normalized by maximum absolute level on each direction.

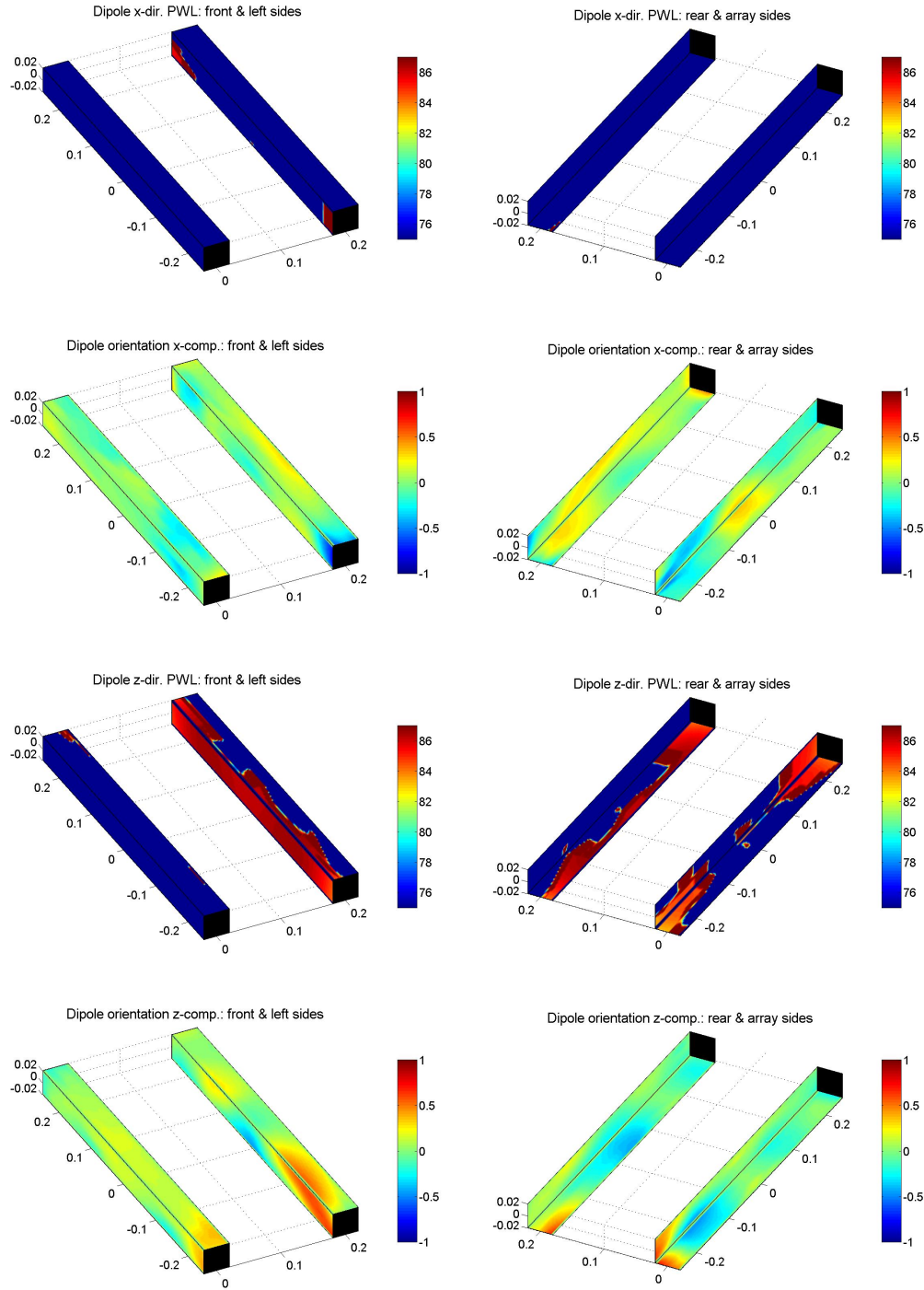


Figure 7.66: Dipole estimation (2kHz) with direction components level (top and third row) and vectorial representation for structures with 7.5° angle and flow at 70m/s (experimental results). Level mappings are source PWL in dB re 1pW and vectorial mappings are estimated A_{dip} normalized by maximum absolute level on each direction.

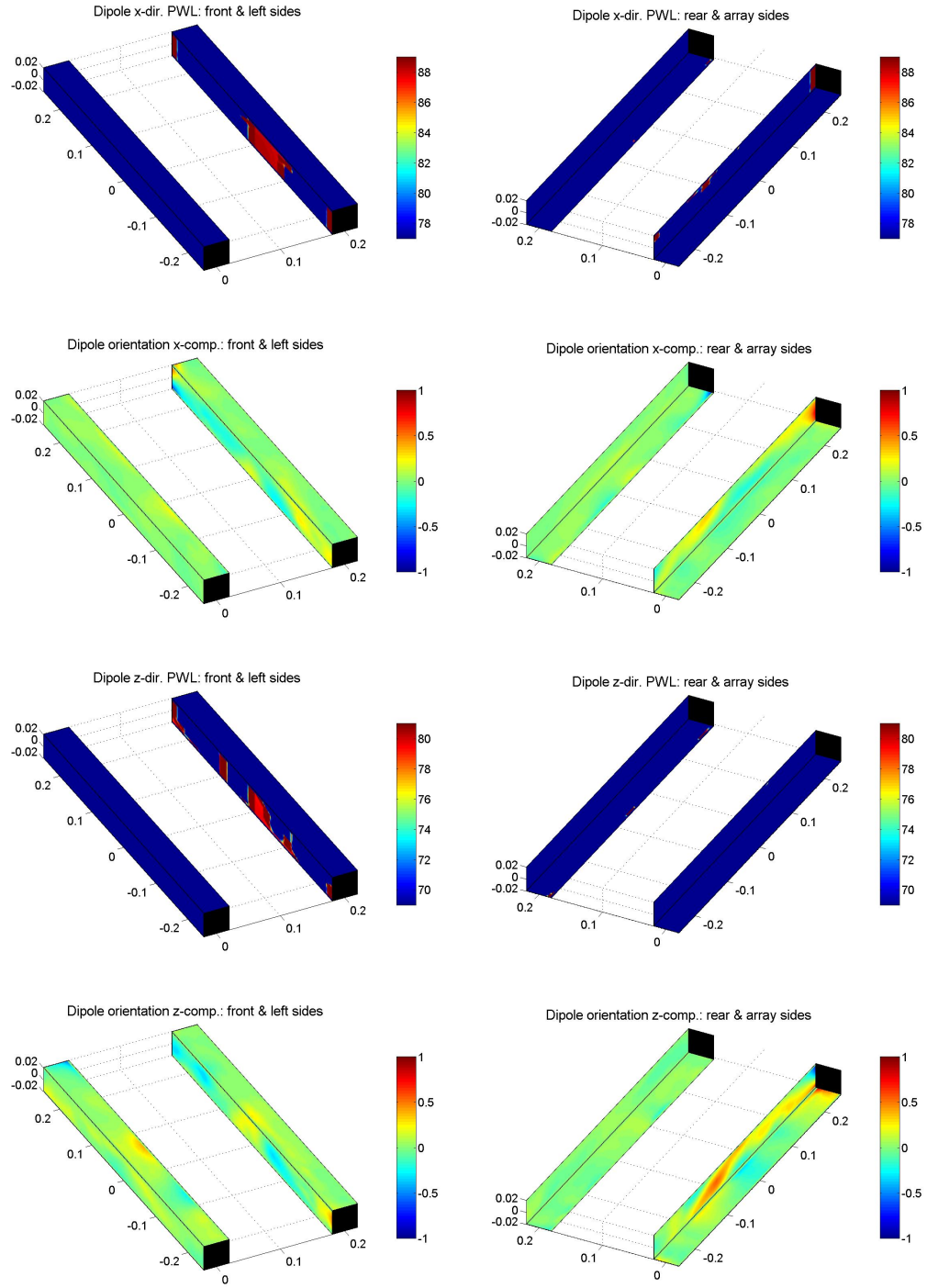


Figure 7.67: Dipole estimation (4kHz) with direction components level (top and third row) and vectorial representation for structures with 7.5° angle and flow at 70m/s (experimental results). Level mappings are source PWL in dB re 1pW and vectorial mappings are estimated A_{dip} normalized by maximum absolute level on each direction.

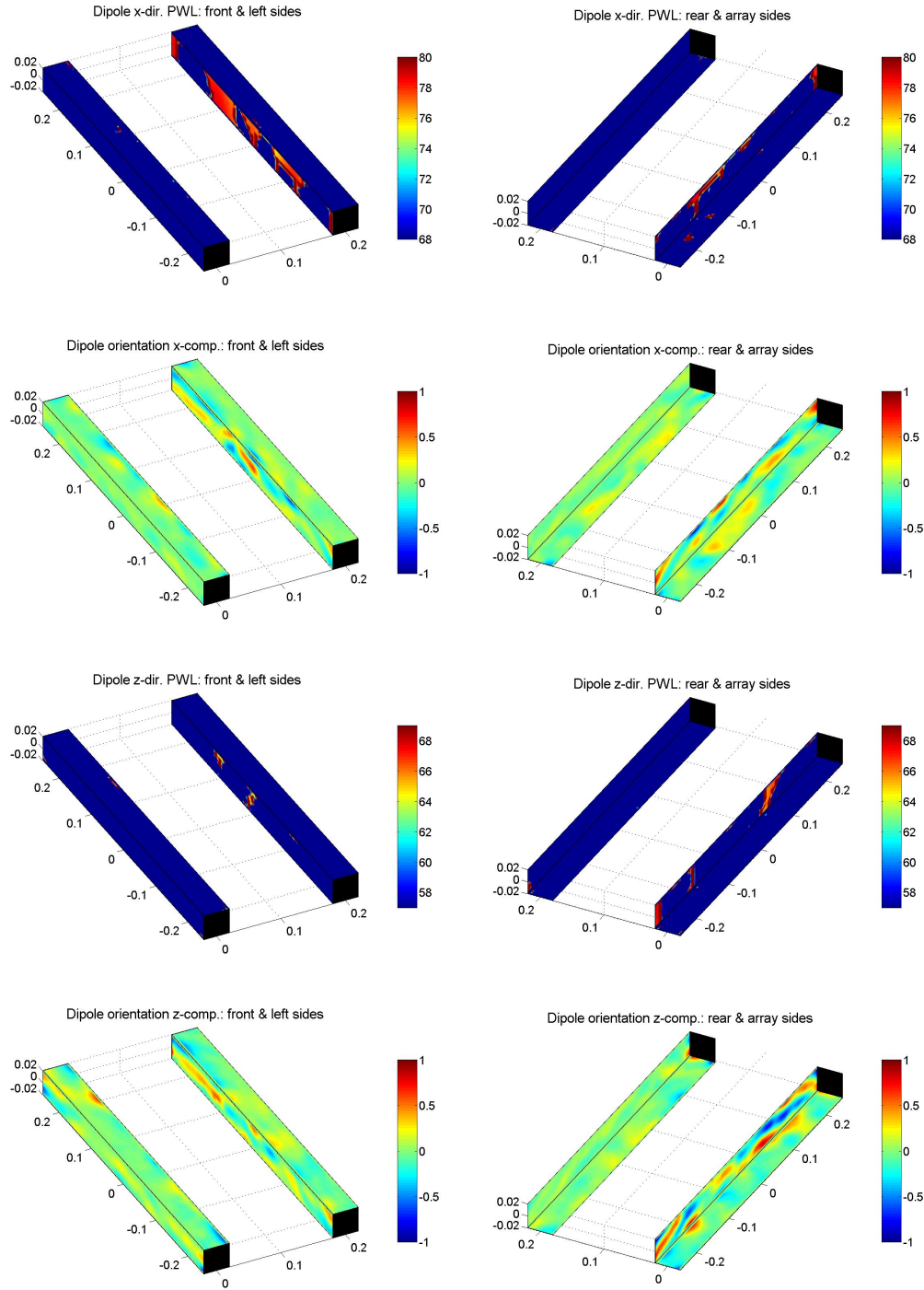


Figure 7.68: Dipole estimation (8kHz) with direction components level (top and third row) and vectorial representation for structures with 7.5° angle and flow at 70m/s (experimental results). Level mappings are source PWL in dB re 1pW and vectorial mappings are estimated A_{dip} normalized by maximum absolute level on each direction.

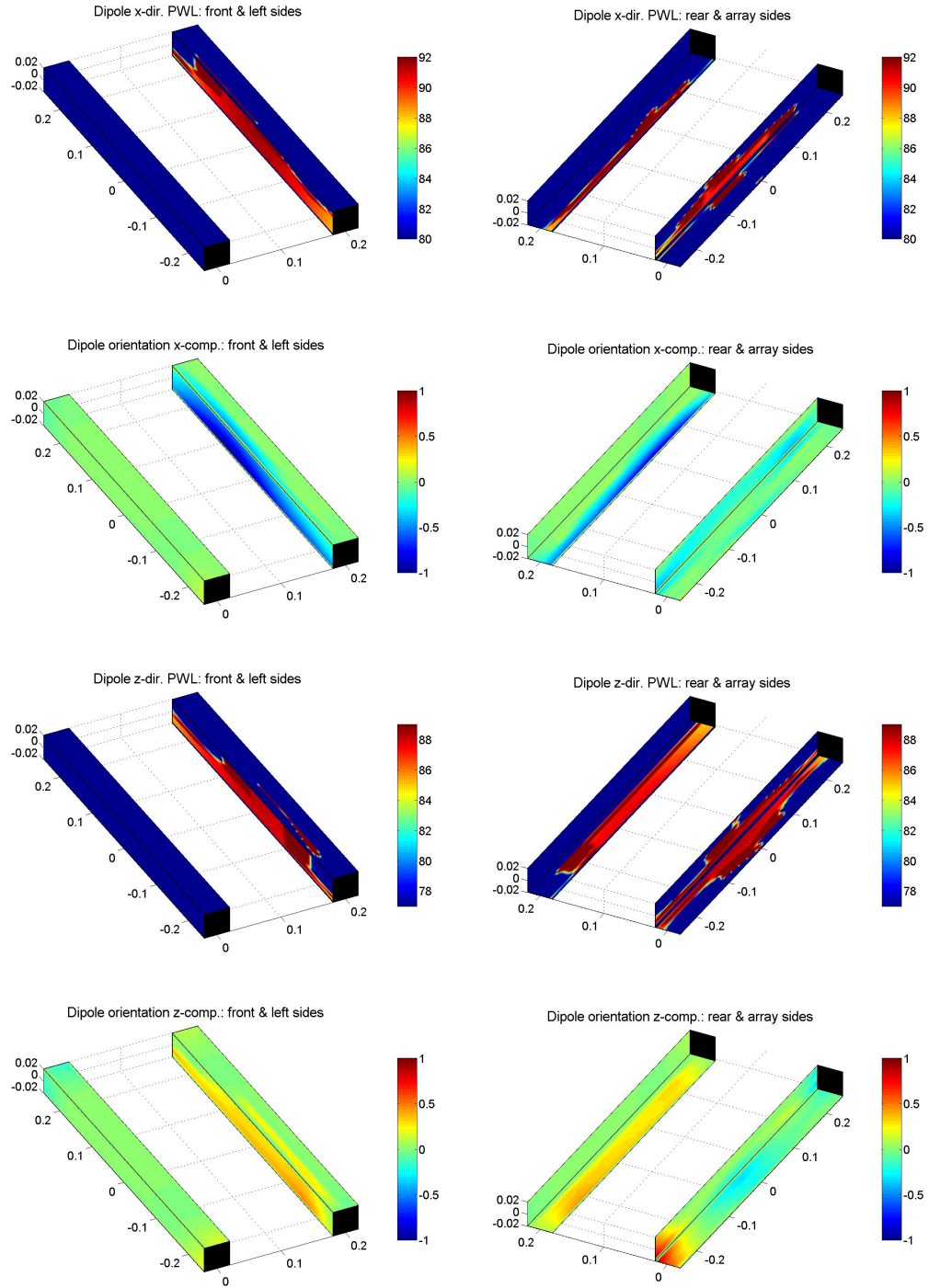


Figure 7.69: Dipole estimation (1kHz) with direction components level (top and third row) and vectorial representation for structures with 20° angle and flow at 70m/s (experimental results). Level mappings are source PWL in dB re 1pW and vectorial mappings are estimated A_{dip} normalized by maximum absolute level on each direction.

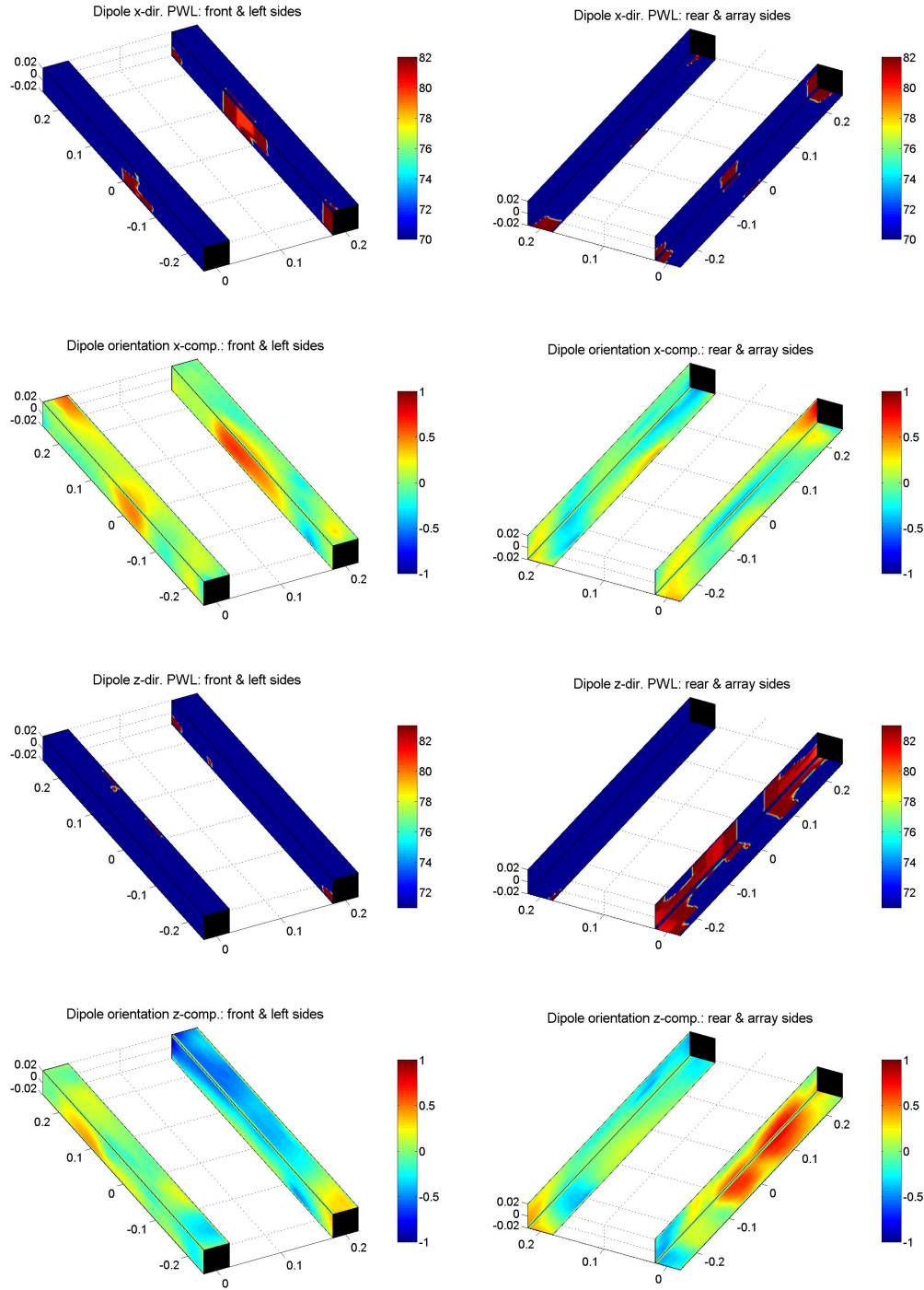


Figure 7.70: Dipole estimation (2kHz) with direction components level (top and third row) and vectorial representation for structures with 20° angle and flow at 70m/s (experimental results). Level mappings are source PWL in dB re 1pW and vectorial mappings are estimated A_{dip} normalized by maximum absolute level on each direction.

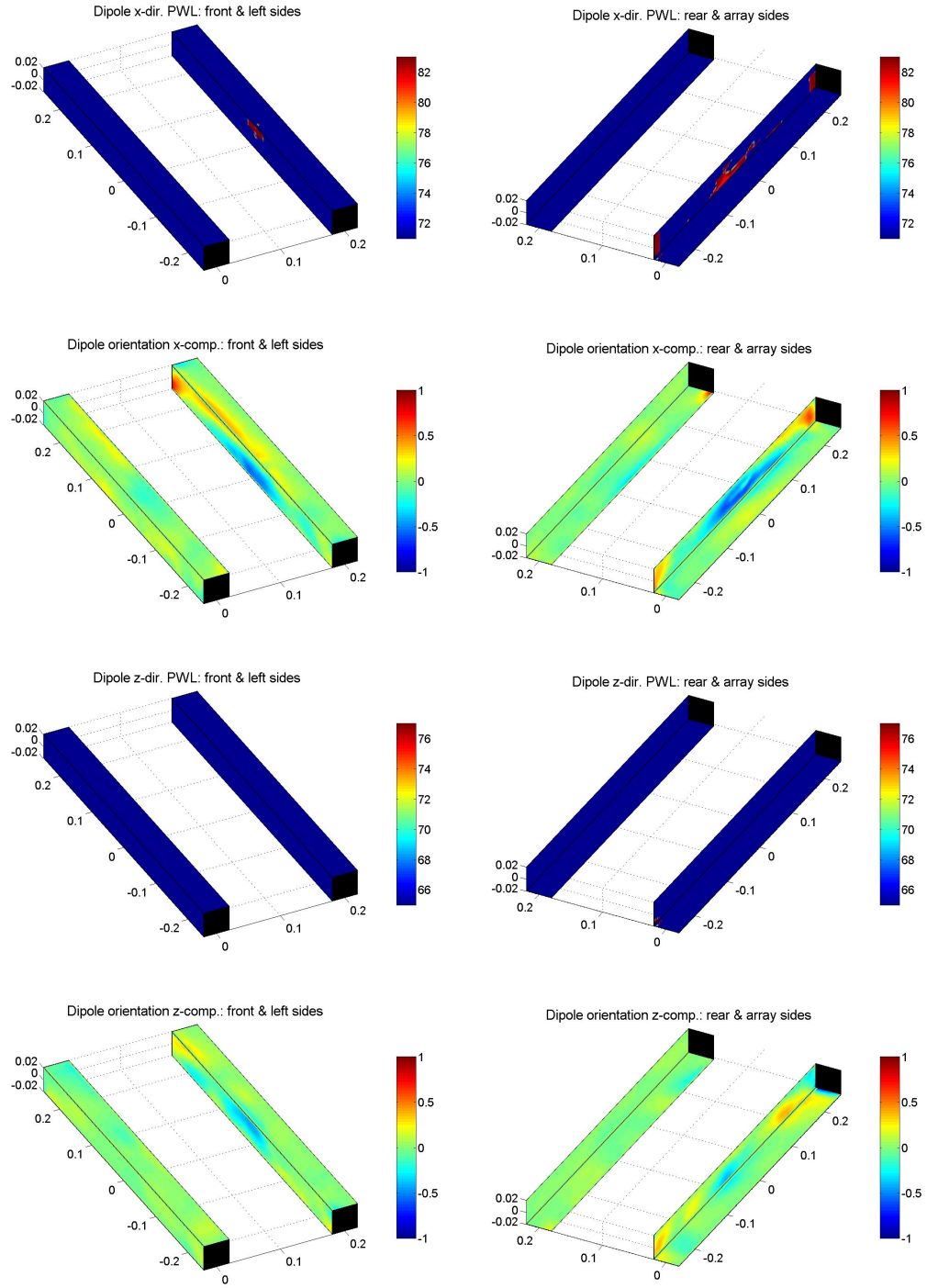


Figure 7.71: Dipole estimation (4kHz) with direction components level (top and third row) and vectorial representation for structures with 20° angle and flow at 70m/s (experimental results). Level mappings are source PWL in dB re 1pW and vectorial mappings are estimated A_{dip} normalized by maximum absolute level on each direction.

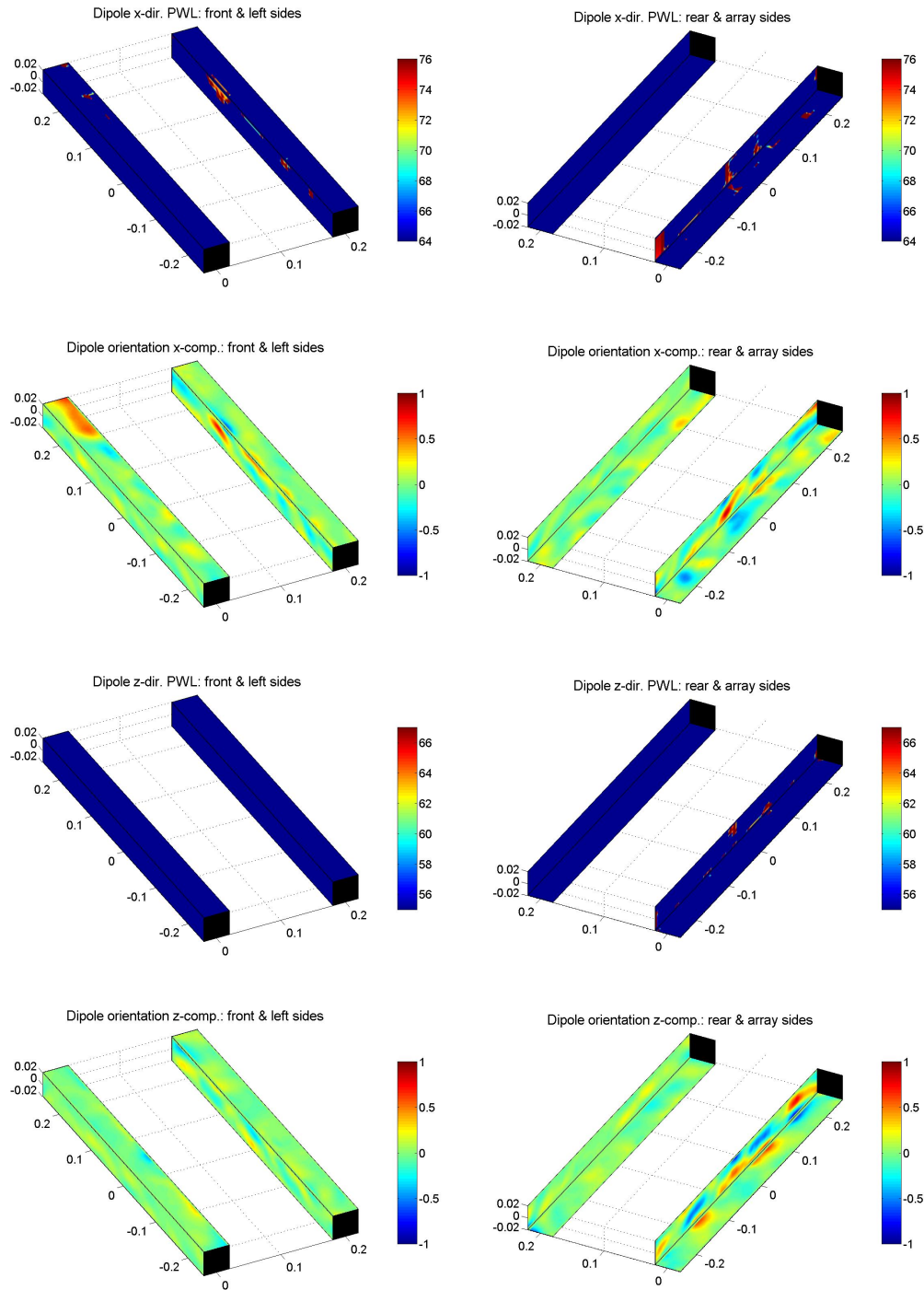


Figure 7.72: Dipole estimation (8kHz) with direction components level (top and third row) and vectorial representation for structures with 20° angle and flow at 70m/s (experimental results). Level mappings are source PWL in dB re 1pW and vectorial mappings are estimated A_{dip} normalized by maximum absolute level on each direction.

This behavior is found in general throughout all the data sets, with a slightly higher importance of the z-component (cross-flow) for the lower frequencies on the higher speed data sets (70m/s).

This already indicates that the dipoles radiation is closer to the z-axis for lower frequencies, and closer to the x-axis for higher frequencies, but the exact directional behavior of the resultant of all the dipole sources and their contributions, to be assessed later in the Directivity Assessment section.

In terms of phase shift on regions of source localization, the first observation is smooth transition in the lower frequencies of analysis, 1 and 2kHz, showing that in terms of radiation, large surfaces are in coherent radiation (in-phase). In other words, the coherence length could be assessed as of received from the microphones. For higher frequencies, abrupt phase changes are found, smaller regions of coherent radiation and more intense changes close to the corners of the bars.

For example, see Figure 7.60, where a dipole region is formed in the middle of the downstream structure, and with interesting phase shifts, from the corner, through the inner face, and ending and the other corner. This may indicate, in this case, a coupling of the dipole formation with the dimensions of the bars in terms of wavelengths, with a higher radiation as result.

The corner phase shift seems to happen throughout all the data sets in the 8kHz analysis, but for the higher airflow speeds, 70m/s, it seems that a kind of wake effect appears in the dipole phase shift distribution, certainly related to the specific flow turbulence formed in these conditions. This is easily observed in Figure 7.68. This level of detail rivals the ones obtained by PIV (Particle Image Velocimetry).

The coherence length at higher frequencies also seems to be significantly reduced, and non-regularly distributed along bar extension, here the coherence length is estimated from the regions with homogeneous orientation distribution. The conventional method seems to bring more regular distributions of sources than the generalized inverse beamforming. This could be attributed in part to the decomposition of the spectral matrix in orthogonal representations, and the recombination of the overall by the summation (in intensity) of each source vector result. This process seems to produce centers of radiation more pronounced than on the conventional mappings. This specific study is somewhat beyond the scope of this work and is mentioned as a suggestion for future work on this method.

7.6.8 Upstream Structure Wall Pressure Transducers Analysis

The wall pressure in the upstream structure is measured with Kulite sensors, along the positions shown in Figure 7.35. Kulites XCS-093 and 062 are used, with diameters of 2.4 and 1.7, respectively. The sensors are able to measure the static and fluctuating pressure variation. However, in this analysis, only the fluctuating pressure is considered and is reported as sound pressure level (re $20\mu\text{Pa}$).

Results are presented in Figures 7.73 to 7.76, for the four data sets measured. Note that the plots represents the pressure values along the bar width for visualization aid, but it is respective only to the central line as shown on the diagrams.

The first observation is that on the measurements with structures angle of 7.5° , the sound pressure levels are higher in the front structure face on the array side, and for the other case, the maximum pressures are found in the front face and on the array side face. It is important to remember that the location of higher pressure is not necessarily the location of the dipole center of radiation.

If these plots are compared to the hybrid generalized inverse or the full hybrid mapping results, shown in Figures 7.49 to 7.52 and in Figures 7.53 to 7.56, some similarities are observed, such as the higher pressure at the corner for the midspan measurements on the array side.

Another example of similarity, can be observed on the first data set, flow at 35m/s and angle of 7.5° , comparing to the hybrid generalized inverse mapping, frequencies of 1 and 2kHz. The inner face also shows a higher power level in the middle of the bar, and possibly reflected in pressure, on the wall transducers. This is also observed, for example, in the fourth data set, flow at 70m/s and angle of 20° , for frequency of 1kHz, where there is some increment in the middle of the bar in the inner face.

The last observation, relevant to mention is that in this last condition these sources at the middle of the bar, spotted in the hybrid generalized inverse beamforming, could explain the higher pressure on the front face, although no dipole sources are identified on that location.

In summary, some general trends are in agreement between the source mappings and the wall pressure transducers with the interpretation of radiated pressure from the identified dipole sources.

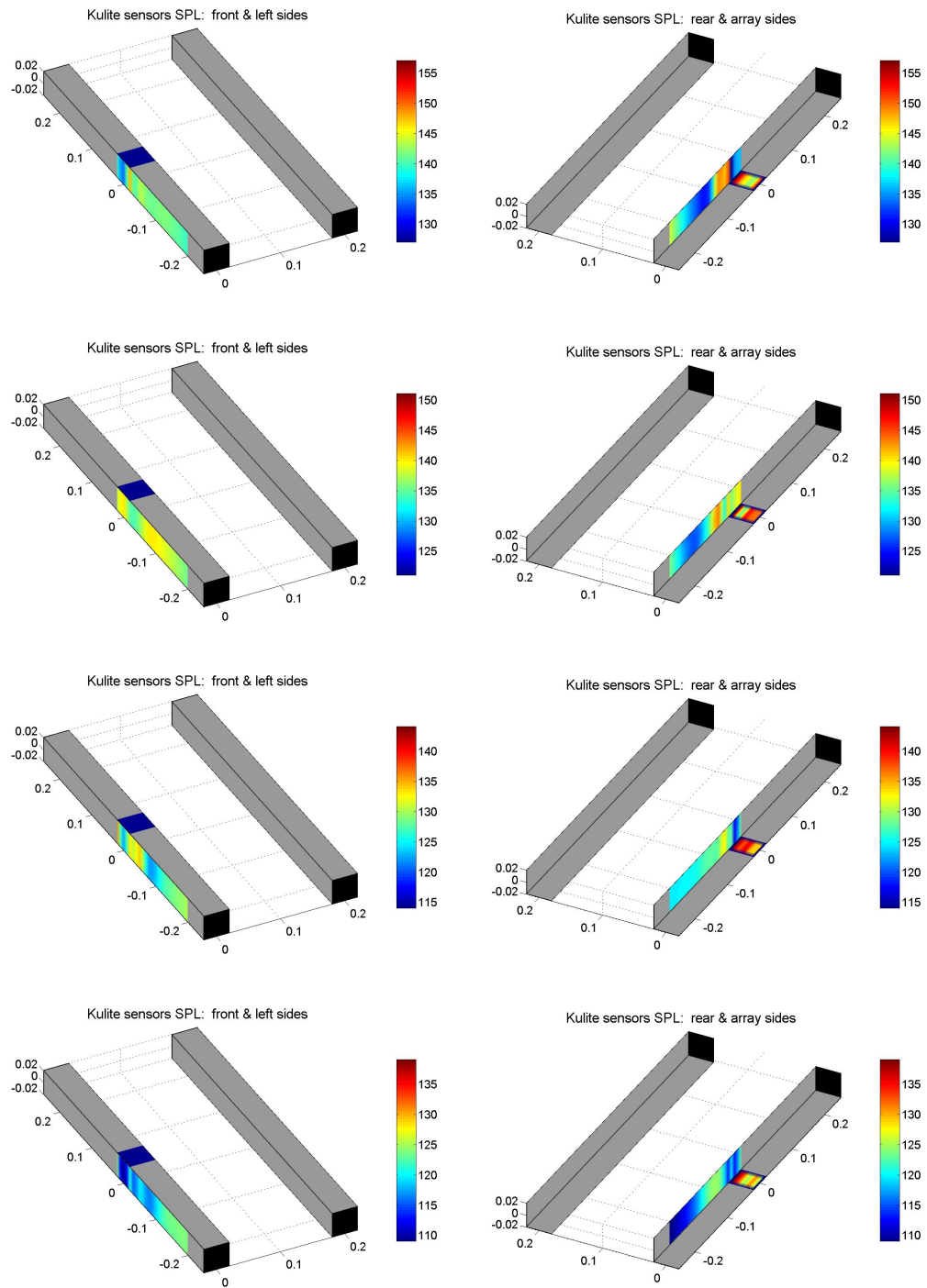


Figure 7.73: Wall pressure transducer (Kulites) SPL for structures with 7.5° angle and flow at 35m/s: 1kHz (top); 2kHz; 4kHz; and 8kHz. Levels in dB re $20\mu Pa$.

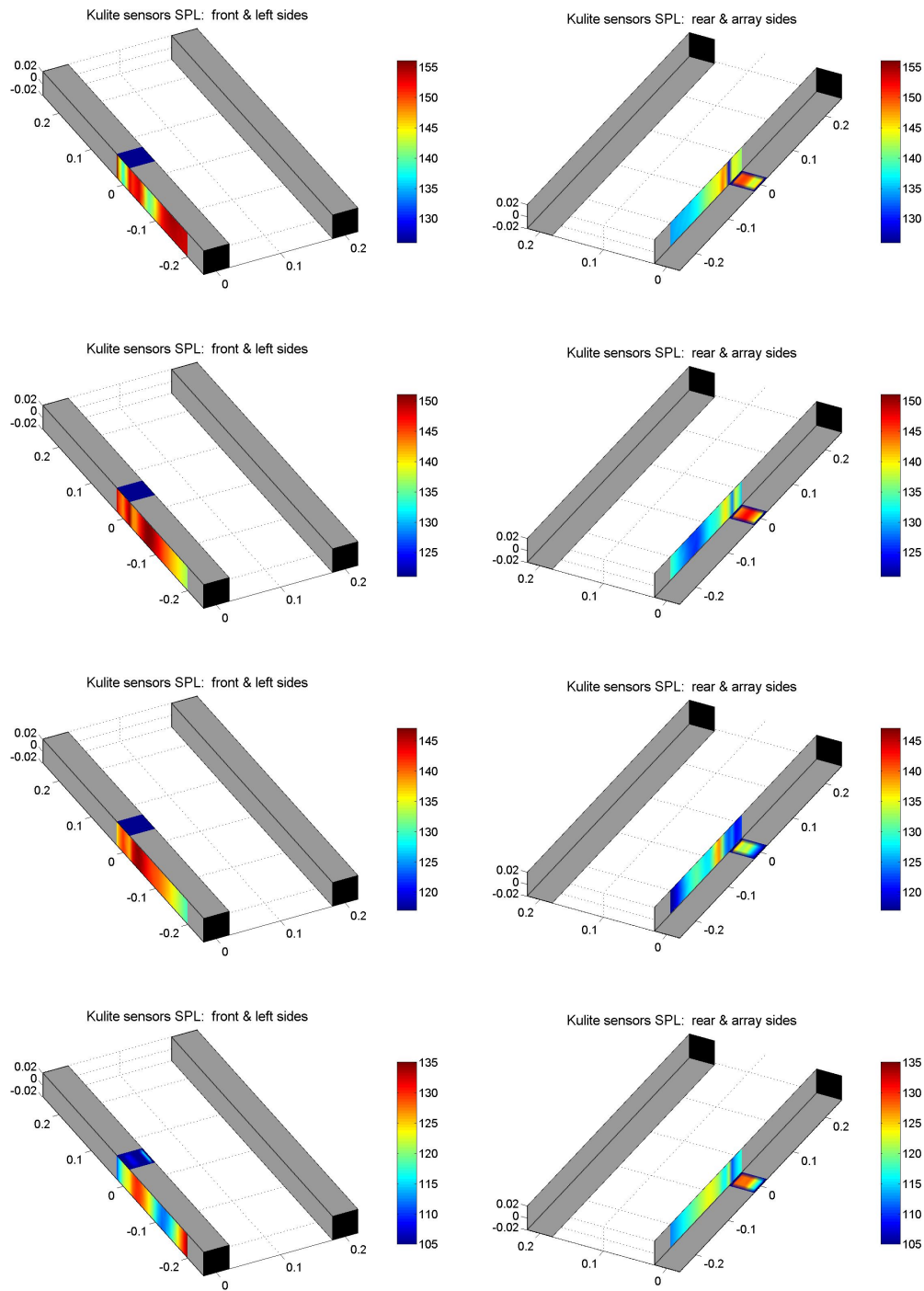


Figure 7.74: Wall pressure transducer (Kulites) SPL for structures with 20° angle and flow at 35m/s: 1kHz (top); 2kHz; 4kHz; and 8kHz. Levels in dB re 20 μPa .

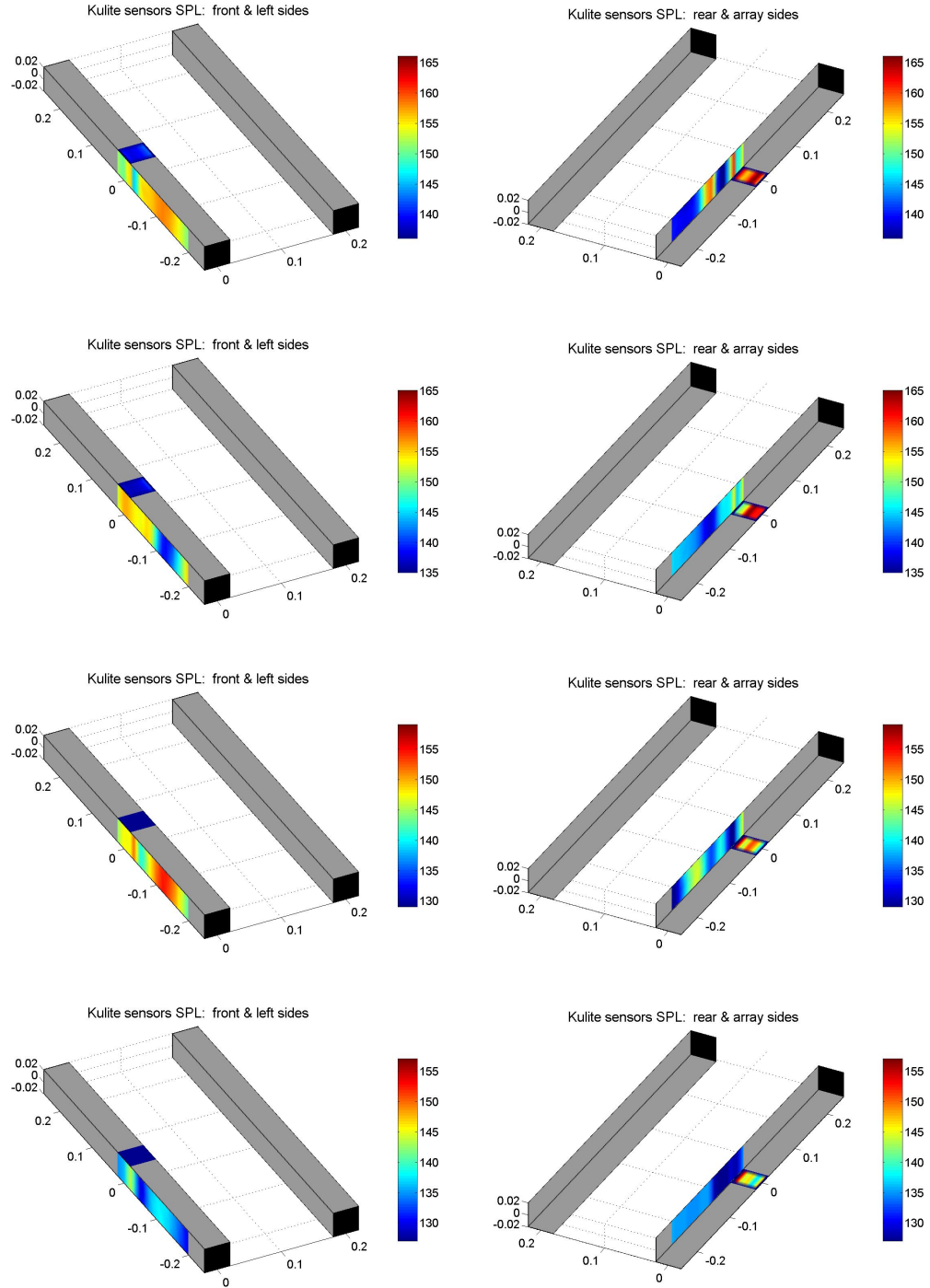


Figure 7.75: Wall pressure transducer (Kulites) SPL for structures with 7.5° angle and flow at 70m/s: 1kHz (top); 2kHz; 4kHz; and 8kHz. Levels in dB re $20\mu Pa$.

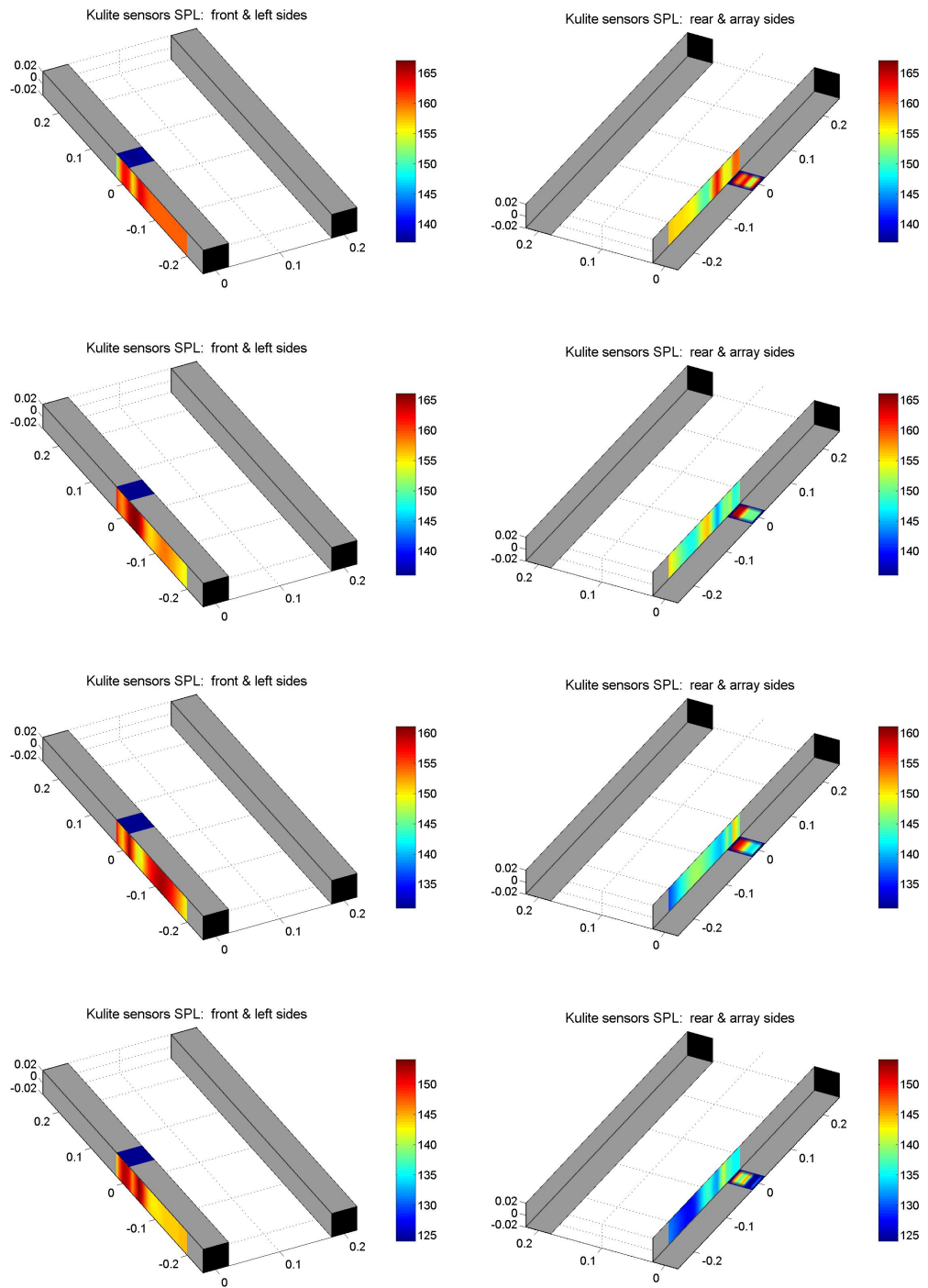


Figure 7.76: Wall pressure transducer (Kulites) SPL for structures with 20° angle and flow at 70m/s: 1kHz (top); 2kHz; 4kHz; and 8kHz. Levels in dB re 20 μPa .

7.6.9 Estimated Directivity Comparison with Far-Field Microphones

From the presented results of estimated dipole components for all data sets, the equivalent pressure for a distribution of dipoles in flow and without consideration of the reflection and scattering effects from the presence of the structures, can be built and compared to the far-field microphone readings, placed at a radius of 2m from the upstream bar. This methodology was first presented in (ZAVALA *et al.*, 2010A), and was presented also in the previous Chapter on Dipole formation over a cylinder section in subsonic flow.

The analysis considered only the sound pressure level over a frequency resolution of 25Hz, at the frequencies of interest: 1, 2, 4 and 8kHz. No third octave summation is performed since it decreases significantly the spatial resolution for analysis. The microphone positions are shown in Figure 7.34 for reference.

The results are presented from Figure 7.77 to 7.80, for each data set. These results are obtained with the auto-powers attenuation procedure in the transfer matrix, and its influence is discussed in an later section.

The first observation is that the directivity assessment at 1kHz presents the closest results to the far-field microphones, this can be in part explained by the expected coherence loss through the flow turbulence, and also on the shear layer refraction, modeled as thin and perfect. This effect is less pronounced in lower frequencies, explaining the better results.

The second observation is that the convection effects are well represented, this observed again more clearly in the lower frequency of 1kHz. For angles that would represent being inside the flow, only the convection is calculated to provide a 360° assessment.

On the first data set, flow at 35m/s and angle of 7.5°, the dipole main axis is apparently aligned perpendicular to the two structures plane, with the lobe in the far-field microphones side being convected with the flow, presenting maxima at approximately 90°. The angle convention is following the measurements plan, with first two quadrants in the far-field microphones side, and 0° at the x-axis. The far-field microphone sound pressure levels are in general accordance with the estimated pressure, but with deviations of up to 5dB.

For higher frequencies the deviations of the far-field microphone levels are even higher,

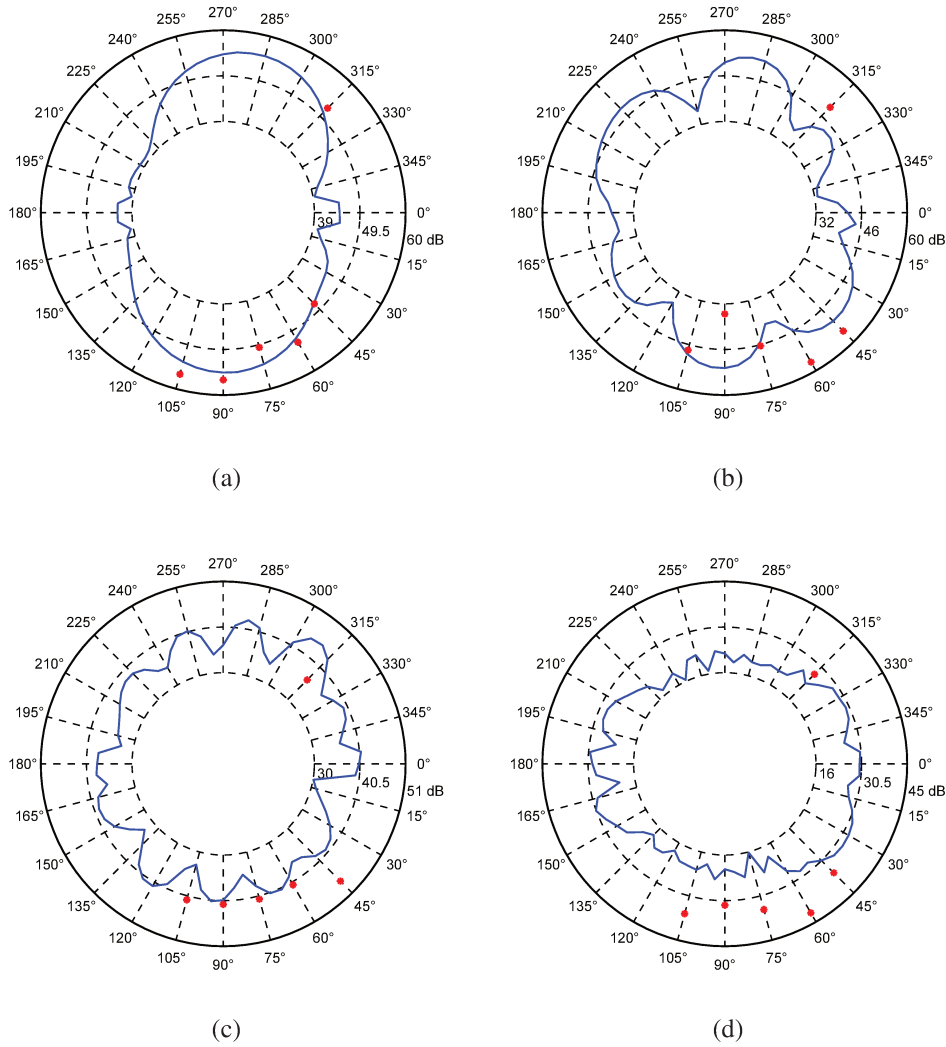


Figure 7.77: Directivity experimental results ($r=2m$) for structures with 7.5° angle and flow at $35m/s$, far-field microphones level in red, frequencies: (a) $1kHz$; (b) $2kHz$; (c) $4kHz$; and (d) $8kHz$.

being up to approximately $15dB$ in the $8kHz$ case. But the general estimated directivity could be considered similar to the indicated directivity from the far-field microphones. It is important to remember that the end plates influence in sound radiation is not taken into account on the equivalent pressure mapping, which considers a free-field radiation out of the flow.

The $4kHz$ and $8kHz$ assessments indicate clearly the higher propagation in the x -direction, and also the flattening of the radiation lobes in the z -direction.

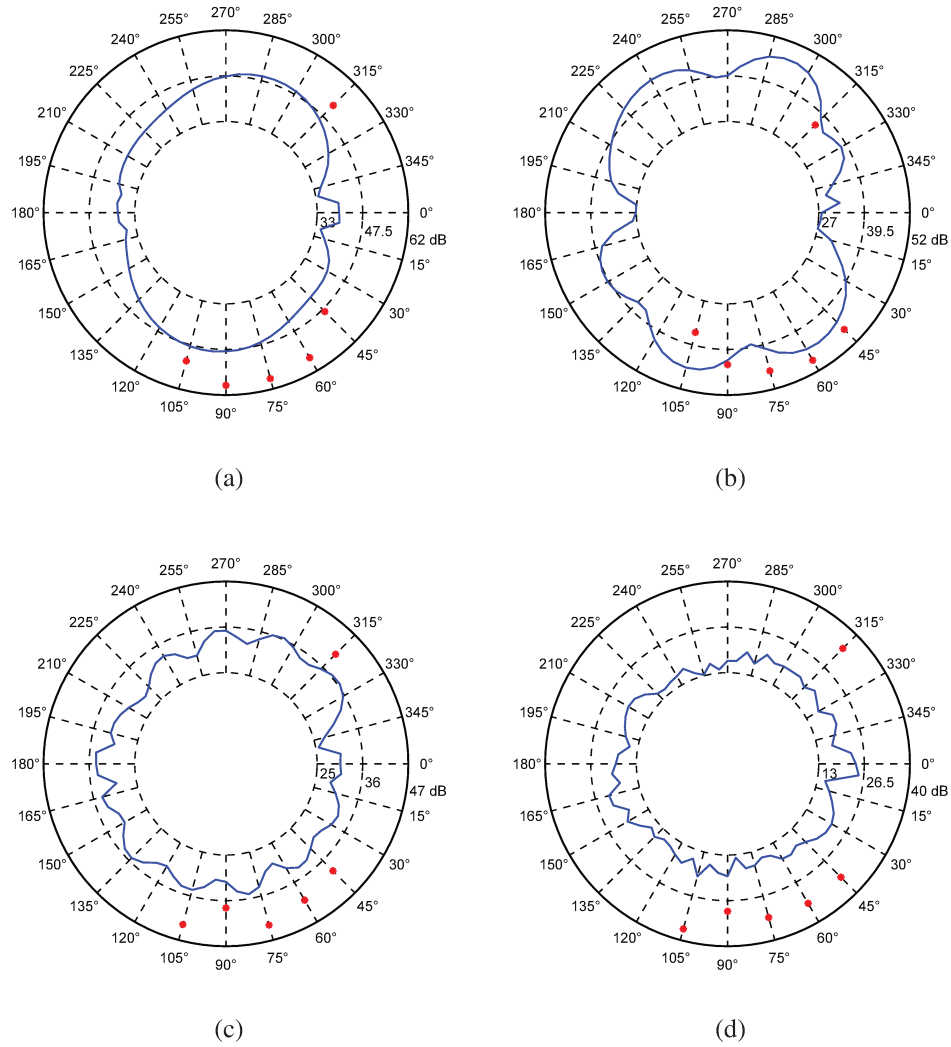


Figure 7.78: Directivity experimental results ($r=2m$) for structures with 20° angle and flow at 35m/s, far-field microphones level in red, frequencies: (a) 1kHz; (b) 2kHz; (c) 4kHz; and (d) 8kHz.

The analysis at 1kHz, on the second data set, flow at 35m/s and angle of 20° , shows that the maxima is farther from the z-axis, despite the convection, but deviations of the estimated directivity to the far-field readings are higher, probably caused by a higher turbulence. The other frequencies present even worst deviation, and up to 20dB deviations are found in the 8kHz comparison.

On the third data set, flow at 70m/s and angle of 7.5° , the convection effect is more clear, twisting the lobes towards the flow axis. The maxima are on the first and fourth quadrants for all frequencies.

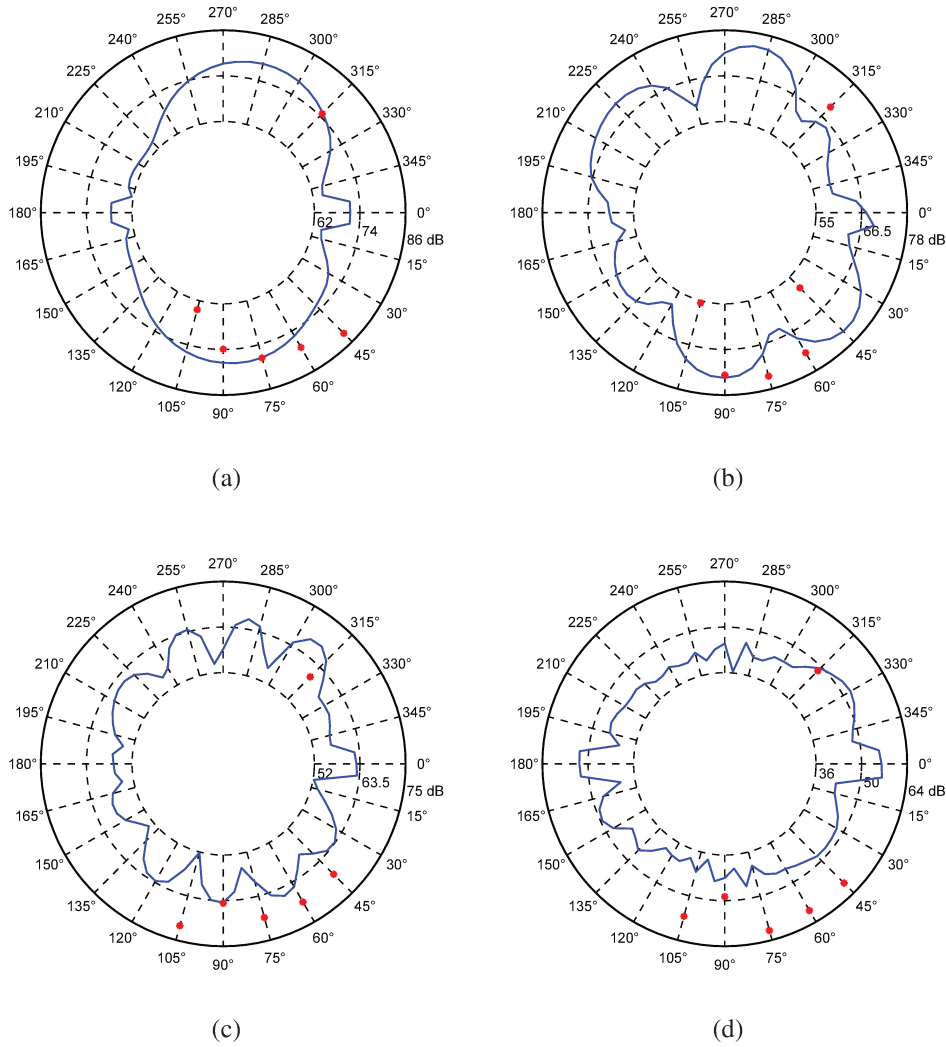


Figure 7.79: Directivity experimental results ($r=2\text{m}$) for structures with 7.5° angle and flow at 70m/s , far-field microphones level in red, frequencies: (a) 1kHz ; (b) 2kHz ; (c) 4kHz ; and (d) 8kHz .

On the last data set, flow at 70m/s and angle of 20° , despite the higher flow speed, due to the higher turbulence level, the maxima on the 1kHz case is back to the second and fourth quadrants. For the other frequencies, the general form of radiation is similar but deviations are up to 15dB , as on the 8kHz case.

In summary, considering that the assessment at 2m radius from the upstream bar center is a tremendous challenge to the sources identification, in terms of level and orientation, the overall assessment is that the directional plots, the equivalent pressure mapping, is an important guide, but

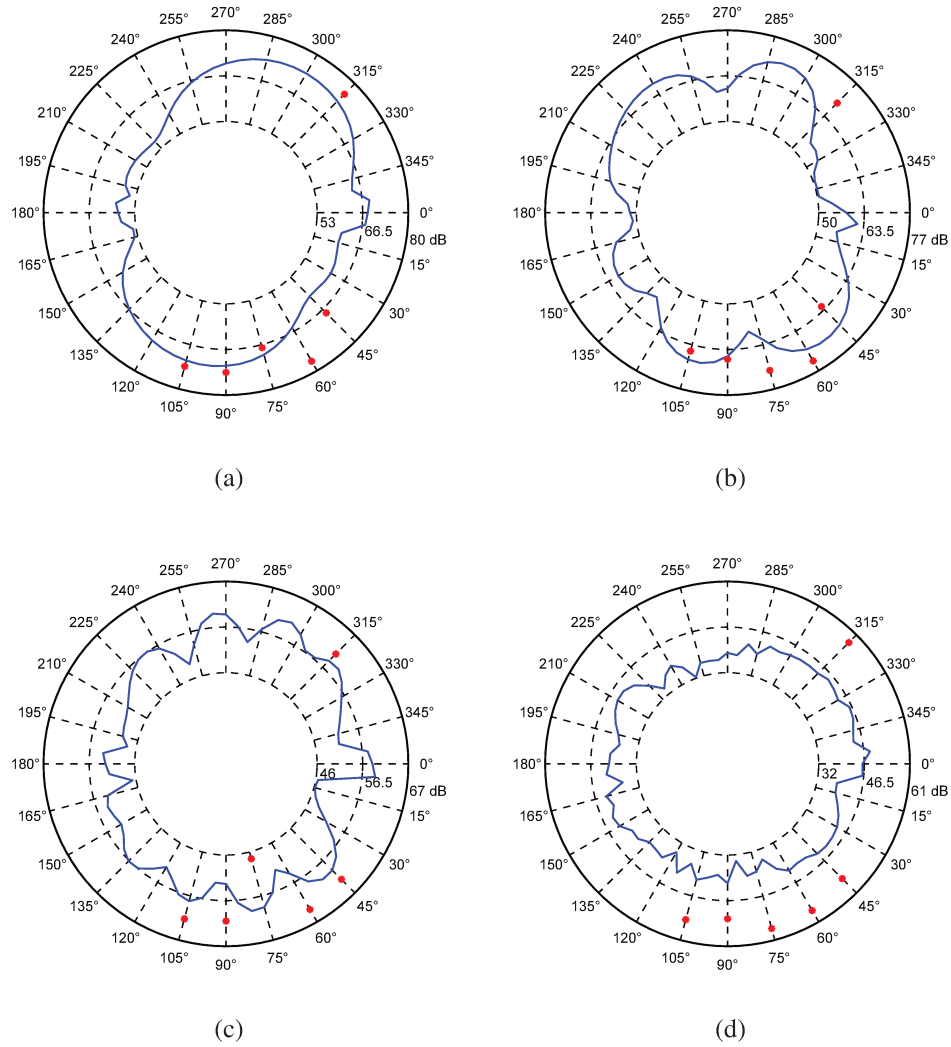


Figure 7.80: Directivity experimental results ($r=2m$) for structures with 20° angle and flow at 70m/s, far-field microphones level in red, frequencies: (a) 1kHz; (b) 2kHz; (c) 4kHz; and (d) 8kHz.

should not be considered precise, before revision of some aspects, as accounting for the shear layer influence and for the non free-field environment.

7.6.10 Line Grid Experimental Results Analysis

In order to assess if the consideration of a simple line of dipoles distribution along the bars centers would be enough, the identifications are also performed for the line grids on the four data sets. The results for dipole source power level for the first data set, flow at 35m/s and angle of 7.5° ,

are presented in Figure 7.81.

It is clear from the plots that they don't bring clear information of main source regions, in all frequency range, despite the fact it seems to capture the rear bar with higher level of source power on three frequencies, 1, 2 and 4kHz analyzes. The worst case identification is found at the 8kHz analysis, where it is not possible to identify the center region along the bar as main region of radiation nor the rear bar for this purpose.

Directivity results are also built, and they are presented for all data sets in Figures 7.82 to 7.85.

Considering the source localization with the line grid as less accurate than the one which uses the 3D grid, surprisingly, the directivity plots bring slightly better results when compared to the 3D grid. Specially at 8kHz, where a closer sound pressure level is reached by the equivalent pressure mapping based on the estimated sources.

The possible explanation is that the accuracy on the 3D grid is higher for the grid points that are closer to the array, as observed on the simulations with a single dipole, where only the closer faces to the array displays the dipole. This preferred location is probably caused by the least squares approach, where the minimization of residue or source strength favors the source locations with shorter distances as a better representation.

The unbiased dipole estimation should be symmetrically represented around the bar since it is at the bar geometrical center. The use of a 3D grid with a plane array is then partially accurate for source localization, and for total efficiency it would maybe require also a 3D array around the test object, which is again beyond the initial scope of this investigation, and left as a suggestion for future work.

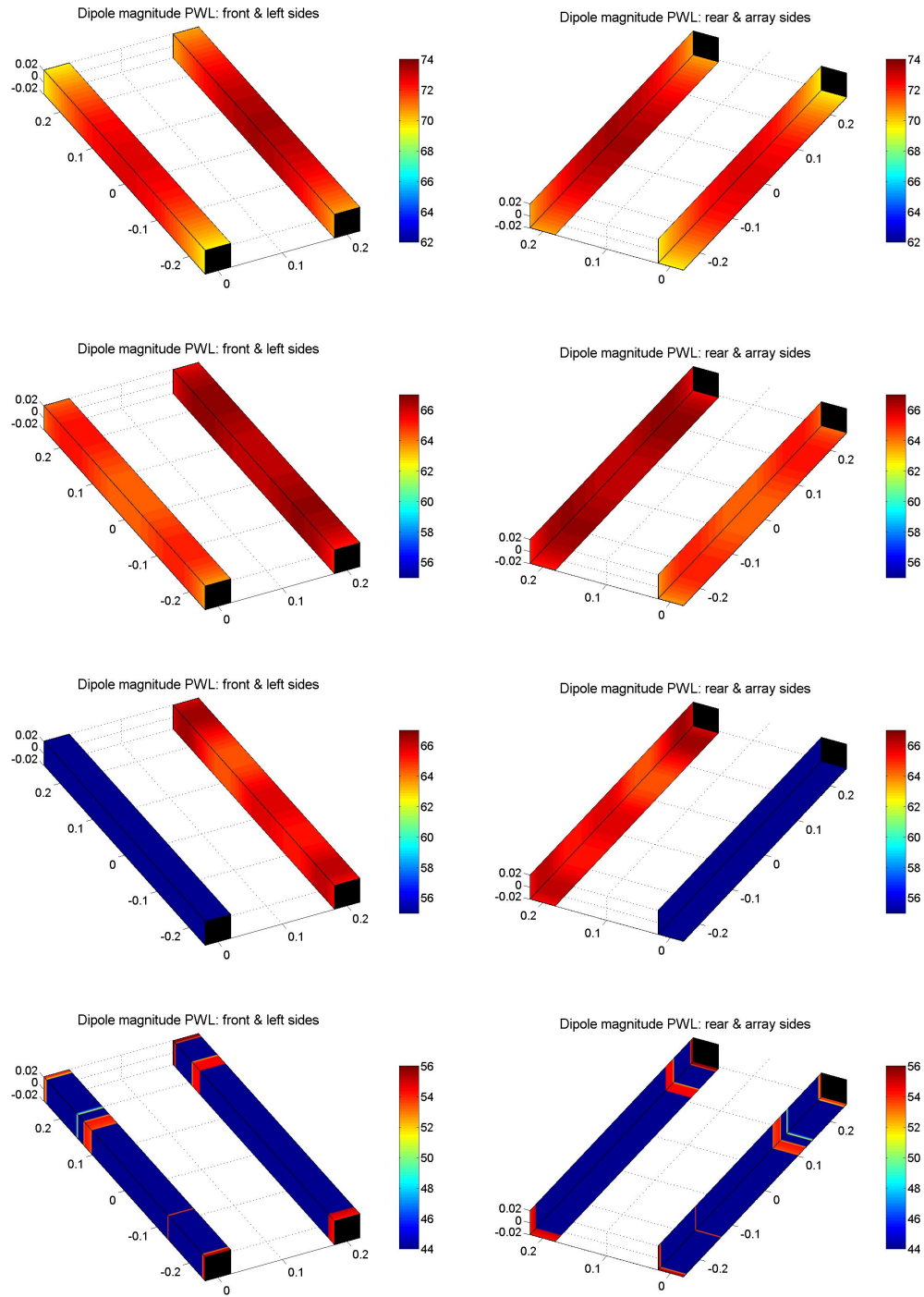
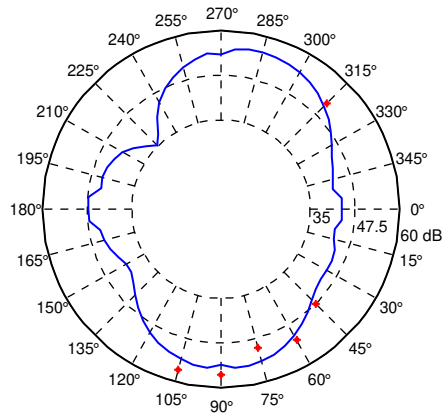
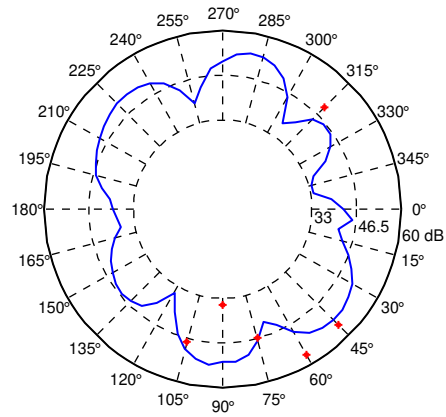


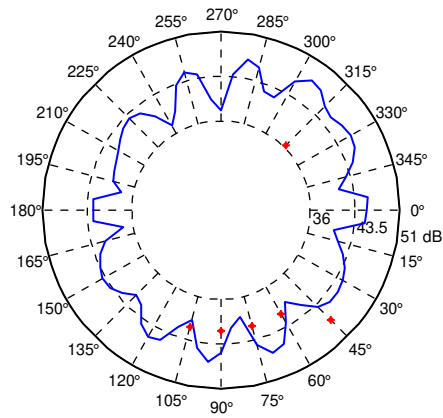
Figure 7.81: Dipole power level using the line grid (experimental results) for structures with 7.5° angle and flow at 35m/s: 1kHz (top); 2kHz; 4kHz; and 8kHz. Mappings are source PWL in dB re 1pW.



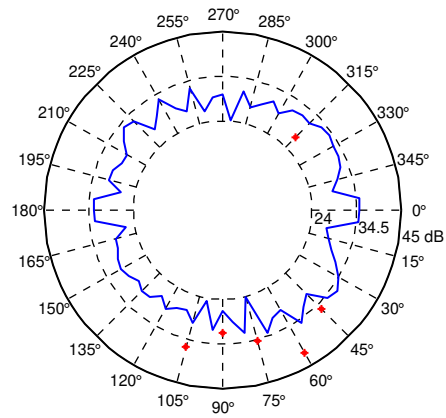
(a)



(b)

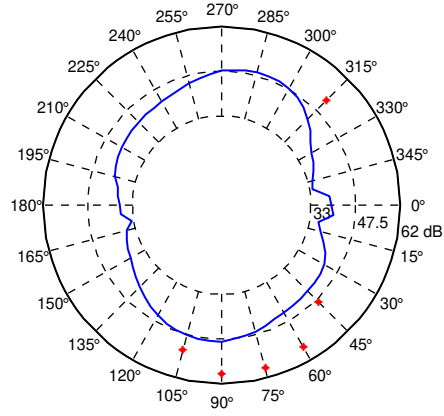


(c)

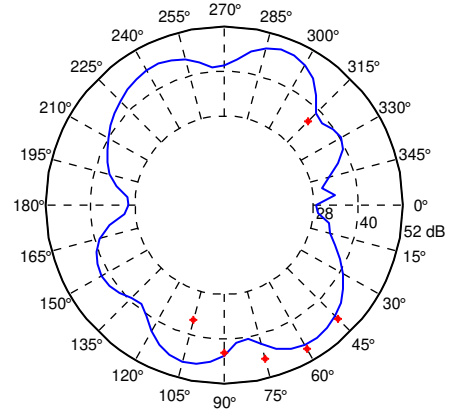


(d)

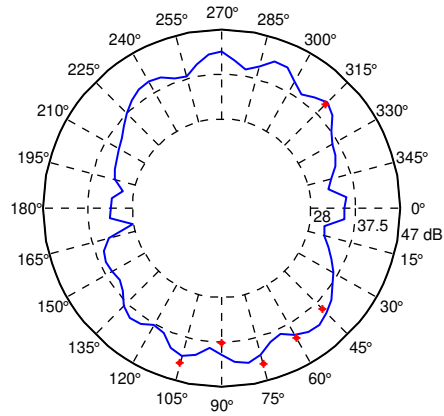
Figure 7.82: Directivity ($r=2\text{m}$) experimental results using the line grid for structures with 7.5° angle and flow at 35m/s , far-field microphones level in red, frequencies: (a) 1kHz ; (b) 2kHz ; (c) 4kHz ; and (d) 8kHz .



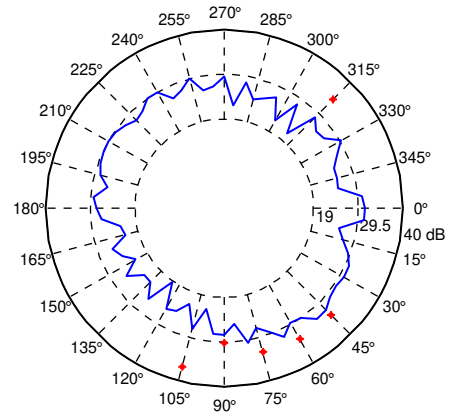
(a)



(b)

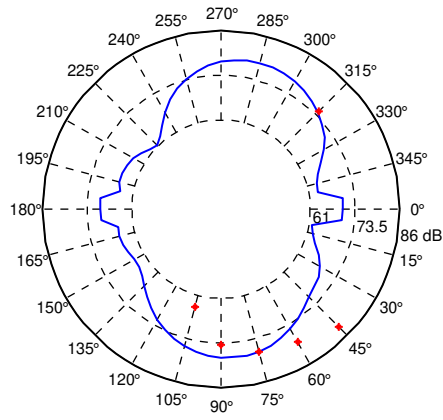


(c)

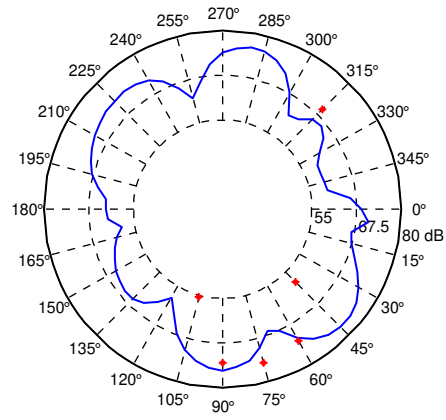


(d)

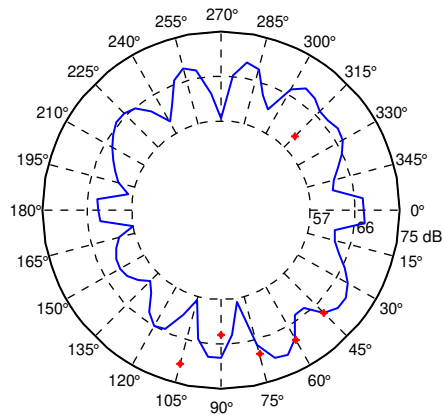
Figure 7.83: Directivity ($r=2m$) experimental results using the line grid for structures with 20° angle and flow at $35m/s$, far-field microphones level in red, frequencies: (a) $1kHz$; (b) $2kHz$; (c) $4kHz$; and (d) $8kHz$.



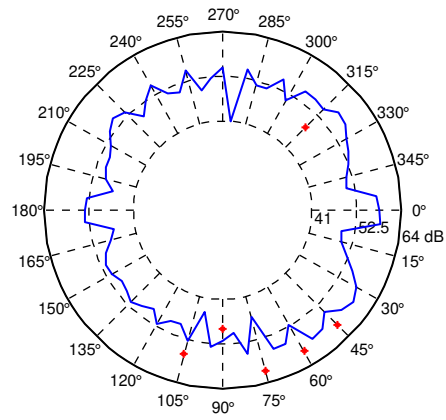
(a)



(b)

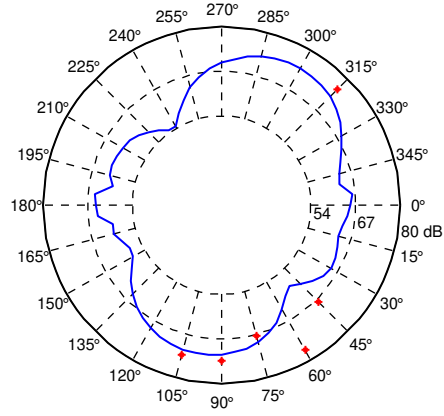


(c)

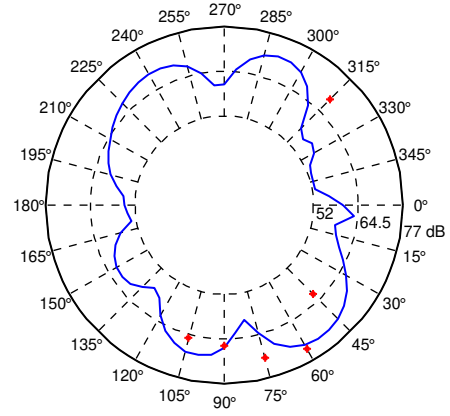


(d)

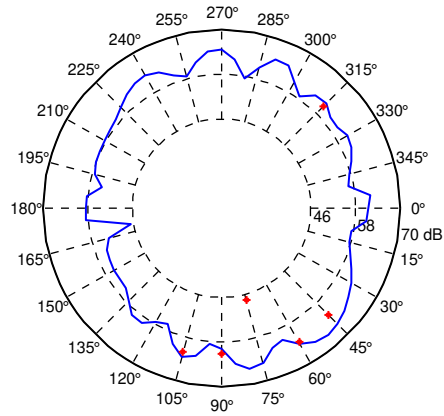
Figure 7.84: Directivity ($r=2\text{m}$) experimental results using the line grid for structures with 7.5° angle and flow at 70m/s , far-field microphones level in red, frequencies: (a) 1kHz ; (b) 2kHz ; (c) 4kHz ; and (d) 8kHz .



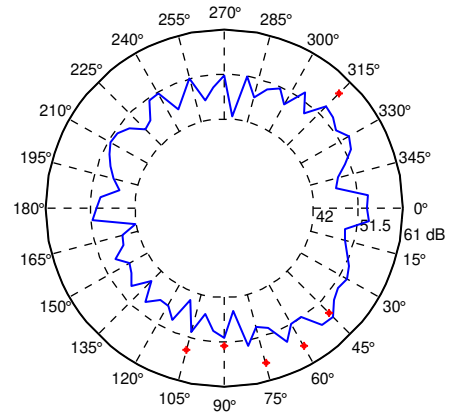
(a)



(b)



(c)



(d)

Figure 7.85: Directivity ($r=2\text{m}$) experimental results using the line grid for structures with 20° angle and flow at 70m/s , far-field microphones level in red, frequencies: (a) 1kHz ; (b) 2kHz ; (c) 4kHz ; and (d) 8kHz .

7.6.11 Auto-Powers Attenuation Influence on Identification

The use of spectrum auto-powers attenuation in the Cross-Spectral Matrix, similarly as the diagonal removal procedure in the conventional beamforming, improves the dynamic range in the source localization resolution. The first data set is used again here, flow at 35m/s and angle of 7.5° , for the analysis at 8kHz, and the mappings for dipole source level with and without the auto-powers attenuation are presented in Figure 7.86.

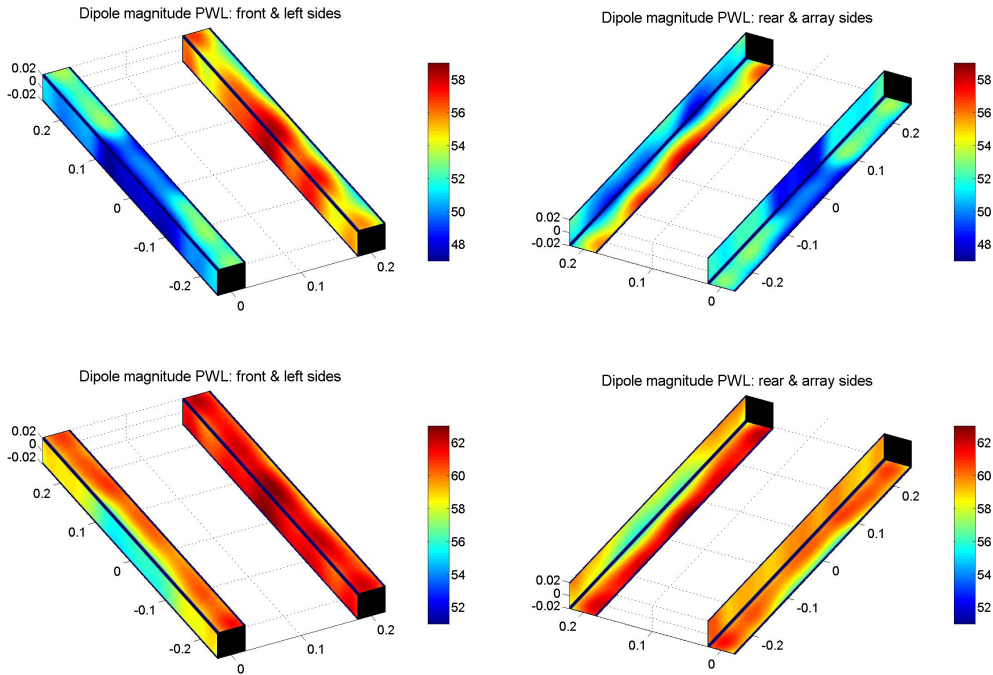


Figure 7.86: Dipole power level hybrid mapping comparison for the 8kHz analysis (experimental results) for structures with 7.5° angle and flow at 35m/s: with auto-powers attenuation (top); and without auto-powers attenuation. Mappings are source PWL in dB re 1pW.

Again, as shown for the conventional beamforming example (Figure 7.14), this proposed procedure improves the identification with the cost of reducing the estimation level. This is well known, due to the coherence loss from the source generation to the microphone location, outside the flow.

Considering that the far-field microphones readings would also suffer from coherence loss, and augment the sound pressure reading, the directivity plots are estimated without the attenuation procedure (original data in the CSM). Results are presented for the 3D grid and for the line grid on

Figures 7.87 to 7.90, and Figures 7.91 to 7.94, respectively.

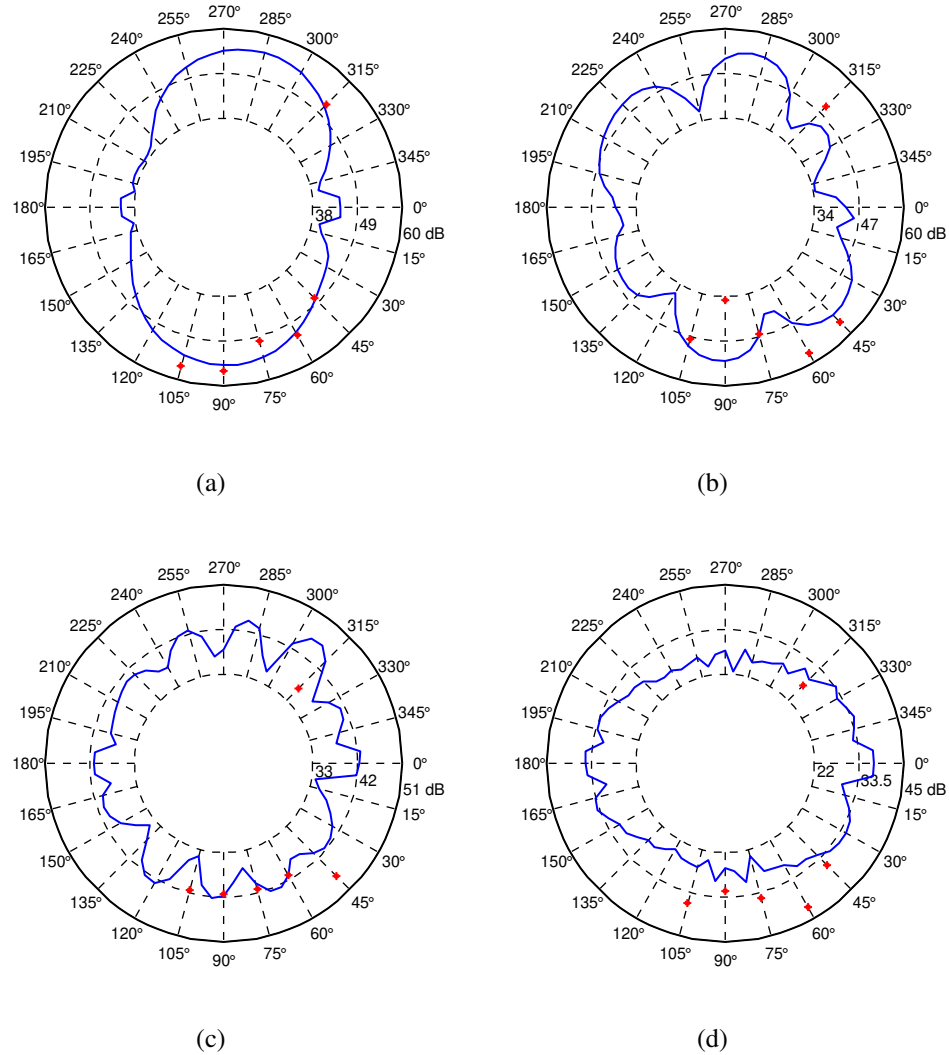
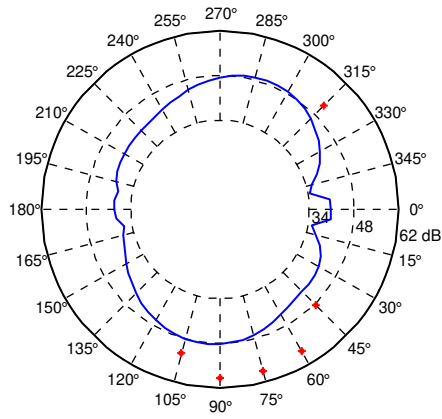


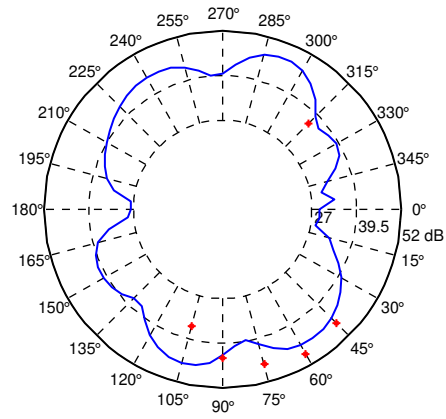
Figure 7.87: Directivity experimental results ($r=2m$) with 3D grid and without attenuation of auto-powers for structures with 7.5° angle and flow at 35m/s, far-field microphones level in red, frequencies: (a) 1kHz; (b) 2kHz; (c) 4kHz; and (d) 8kHz.

for the 3D grid results without the auto-powers attenuation, the changes are observed mainly on the 8kHz analysis, where small improvement is found in the levels. The overall shape of directivity is kept almost the same.

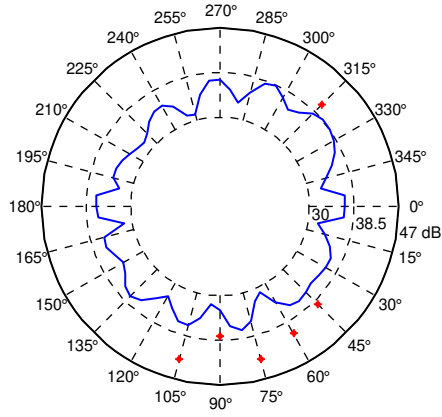
For the directivity plots on the results obtained using the line grid and without the attenuation of auto-powers, the levels on the equivalent pressure based on the estimated source distributions are even closer to the far-field microphones, specially improving the 4kHz and 8kHz cases. The



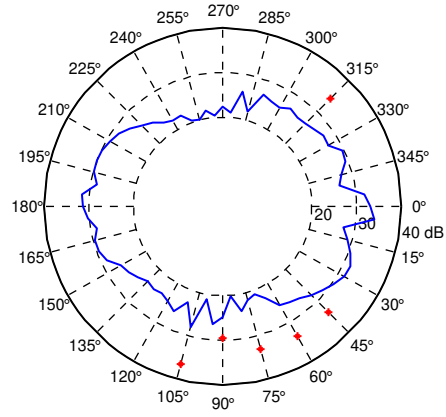
(a)



(b)



(c)



(d)

Figure 7.88: Directivity experimental results ($r=2m$) with 3D grid and without attenuation of auto-powers for structures with 20° angle and flow at $35m/s$, far-field microphones level in red, frequencies: (a) 1kHz; (b) 2kHz; (c) 4kHz; and (d) 8kHz.

general shape is still very similar to the ones obtained with the attenuation, specially for 1, 2 and 4kHz, where it is practically the same.

In summary, in order to reproduce the far-field microphone readings (as an approximation), the use of the original CSM terms is required, and good agreement is then observed between the overall directivity behavior generated by the dipoles distributed over the bar surfaces.

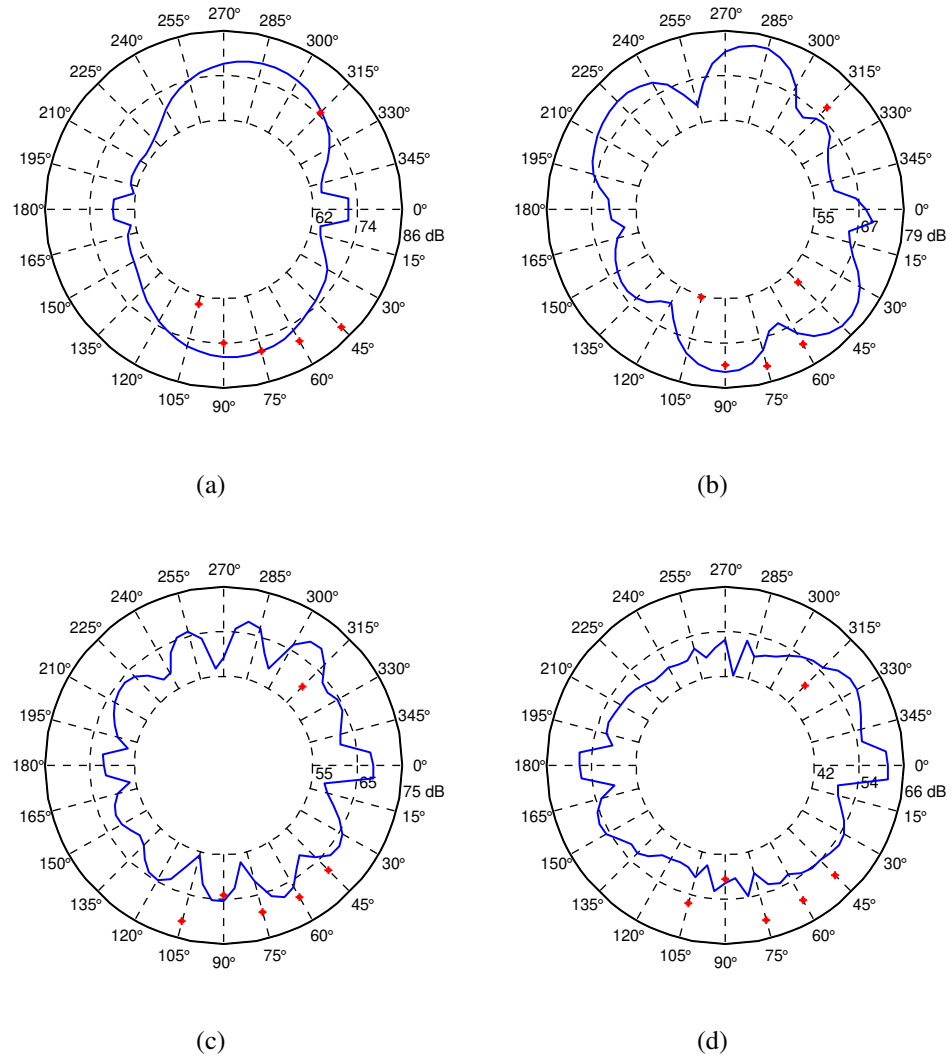
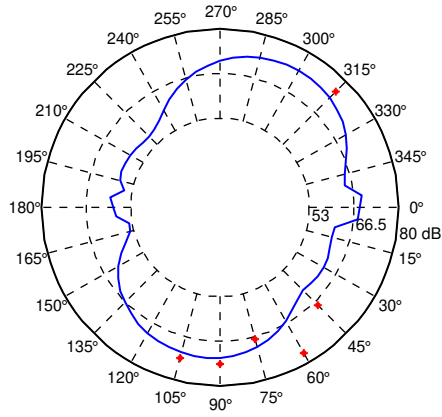


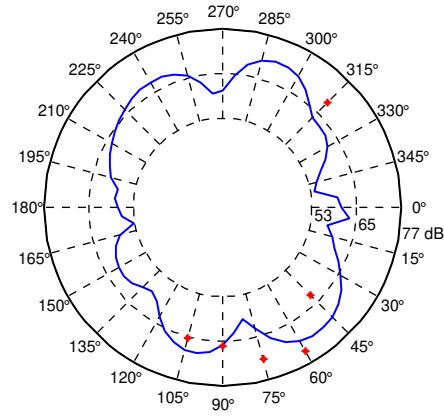
Figure 7.89: Directivity experimental results ($r=2m$) with 3D grid and without attenuation of auto-powers for structures with 7.5° angle and flow at 70m/s, far-field microphones level in red, frequencies: (a) 1kHz; (b) 2kHz; (c) 4kHz; and (d) 8kHz.

7.7 Summary

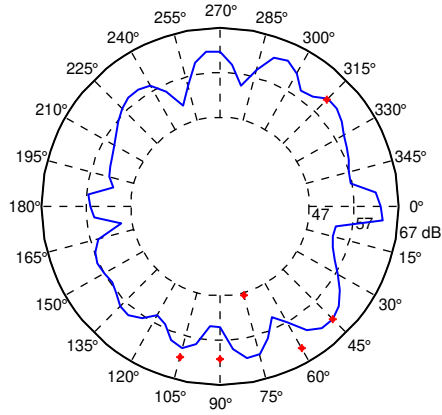
The use of the generalized inverse beamforming for the monopole sources identification using both numerical simulations and experimental data proved to be a valuable technique with higher resolution for source region localization and robust to signals noise influence. Advantages are observed for low frequency analysis, considered in these tests, as 1k and 2kHz frequency range, as well as in the high frequency range of 8kHz. The direct comparison of mappings required



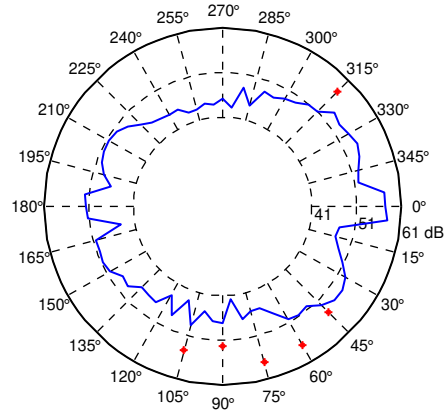
(a)



(b)



(c)



(d)

Figure 7.90: Directivity experimental results ($r=2m$) with 3D grid and without attenuation of auto-powers for structures with 20° angle and flow at $70m/s$, far-field microphones level in red, frequencies: (a) $1kHz$; (b) $2kHz$; (c) $4kHz$; and (d) $8kHz$.

an intermediate step of transformation of the norm based information to a directional mapping information through the use of the Hybrid methodology. The latter allowed the direct comparison and smoothing of the generalized inverse result levels.

On the monopole tests, the Hybrid Generalized Inverse mapping proved to be a reliable approach, being in agreement to all conventional beamforming reference mappings, both to source regions as well as to source power levels.

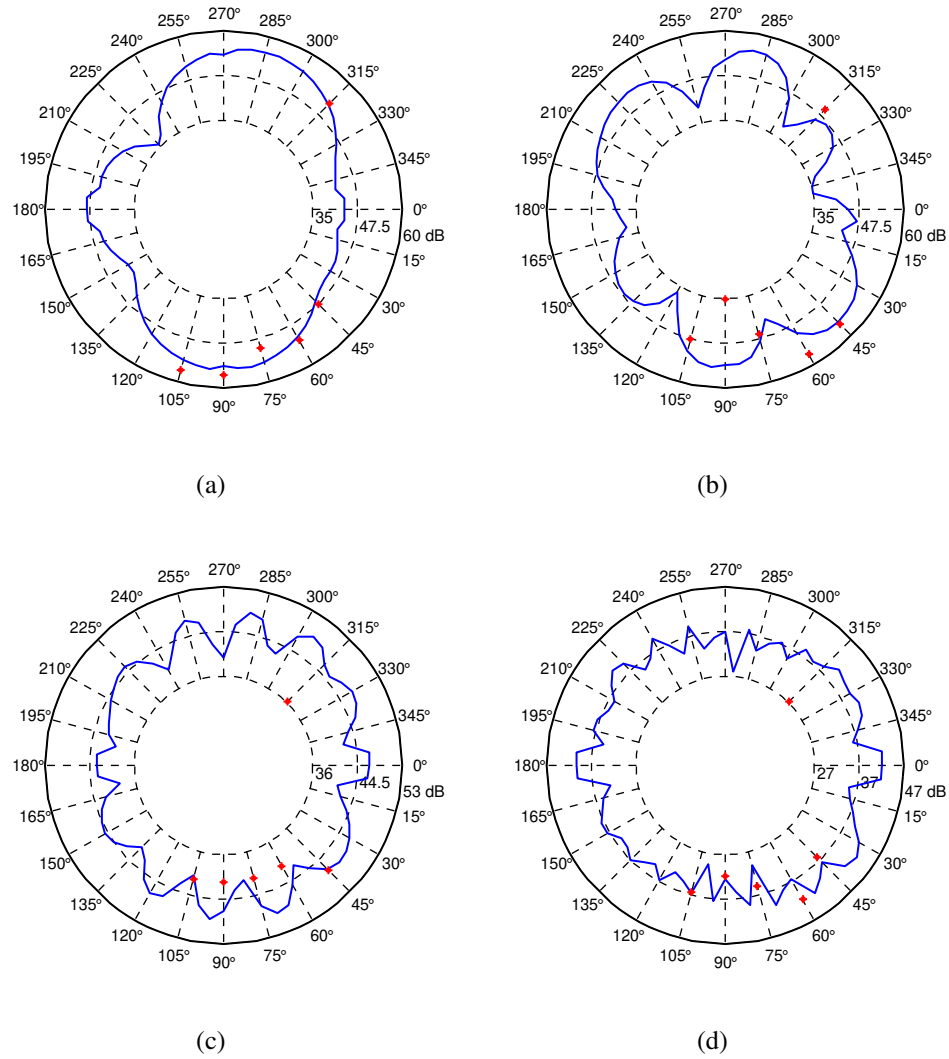


Figure 7.91: Directivity experimental results ($r=2m$) with line grid and without attenuation of auto-powers for structures with 7.5° angle and flow at $35m/s$, far-field microphones level in red, frequencies: (a) $1kHz$; (b) $2kHz$; (c) $4kHz$; and (d) $8kHz$.

On the monopole test cases, the auto-powers attenuation procedure, inspired in the diagonal removal procedure from the conventional beamforming, also proved a valuable counter measure to cases where the cross-power information levels are lower with respect to the auto-powers, as found in aeroacoustics problems. Results demonstrated little or no side effects of the adoption of this proposal in the experimental identifications.

For the dipole identification, the use of a re-scaling procedure proved to be an important artifice in avoiding the anisotropic nature of dipole radiation and its influence in the least squares

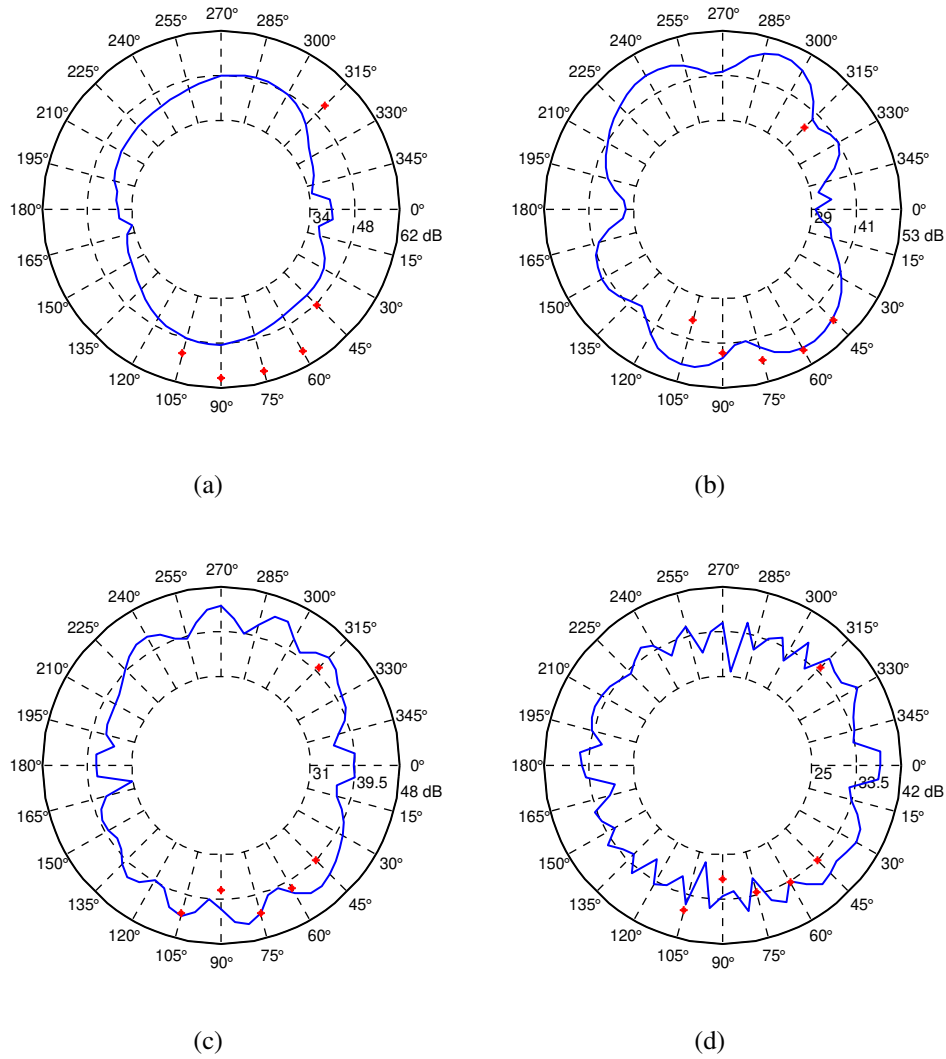
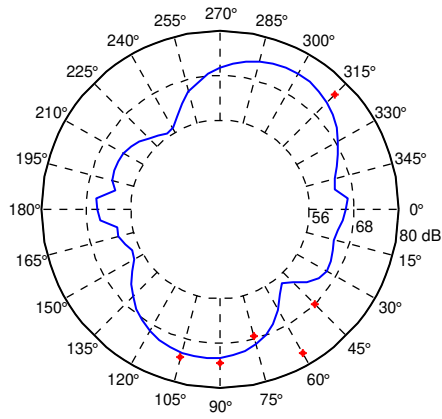


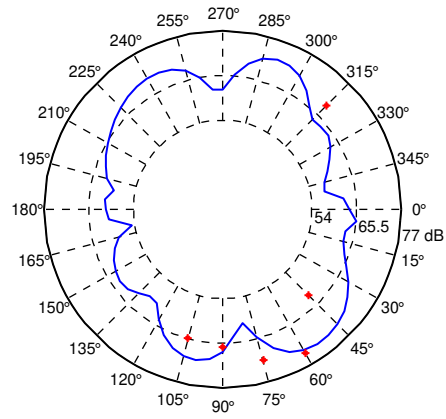
Figure 7.92: Directivity experimental results ($r=2m$) with line grid and without attenuation of auto-powers for structures with 20° angle and flow at $35m/s$, far-field microphones level in red, frequencies: (a) $1kHz$; (b) $2kHz$; (c) $4kHz$; and (d) $8kHz$.

solution determination. Verifications done with simulations are an important step to understand the performance on identification for single and distributed sources, as used on the monopole and on dipole identification sections.

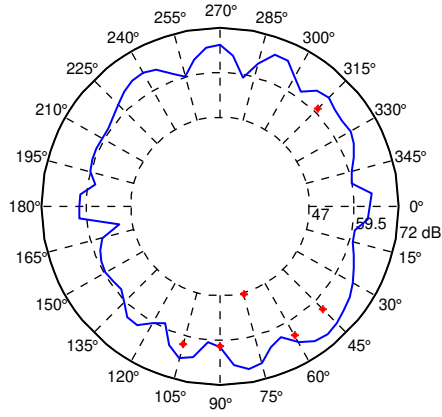
The use of the hybrid generalized inverse mapping and the hybrid mapping for both suggested target grids proved also to be helpful in the visualization of sources distribution. Along with the use of the equivalent pressure distribution calculated to build a directivity assessment, they form an important set of analysis procedures to be used on these kinds of problems.



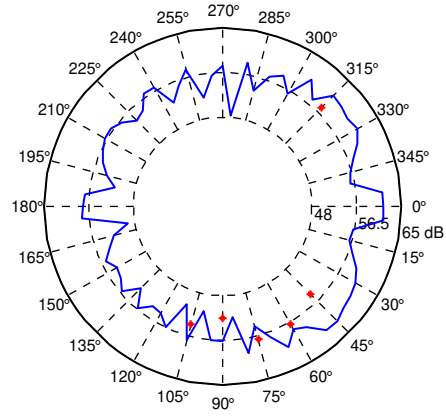
(a)



(b)



(c)



(d)

Figure 7.94: Directivity experimental results ($r=2m$) with line grid and without attenuation of auto-powers for structures with 20° angle and flow at $70m/s$, far-field microphones level in red, frequencies: (a) $1kHz$; (b) $2kHz$; (c) $4kHz$; and (d) $8kHz$.

far-field measurements, considering that the far-field microphones are located in the opposite side of the array and that its assumption is of a free-field condition. On the other hand, the 3D grid is, for sure, the one that provides the most detailed information about source distribution along the structure surfaces, with information about the dipole level and orientation along each structure face.

8 Aeroacoustic Source Identification: NACA-0012 Airfoil in Subsonic Flow

On this Chapter, monopole identifications using three different methods, DAMAS2, conventional beamforming and generalized inverse beamforming, are compared for the testing of an standard airfoil, NACA-0012. Testings are conducted in a closed wind tunnel test facility, and this measurement environment have inherent difficulties such as close reflecting walls, noise from flow turbulence over walls, and sound pressure recordings exposed to flow turbulence. Estimations are compared and discussed with objective to illustrate the generalized inverse method performance on this challenging measurement condition.

8.1 Introduction

The use of an standard airfoil, NACA-0012, for aeroacoustic assessment provides a common basis for different research centers investigation on this type of problem: the noise generation from airfoils. One important work with this objective is the one performed by Brooks *et al.* (1989). In this work from NASA (United States National Aeronautics and Space Administration), a prediction method is developed for the NACA-0012 airfoil to the sound produced by the self-noise mechanisms. The self-noise includes some mechanisms such as: boundary-layer turbulence passing the trailing edge; separated-boundary layer and stalled flow over an airfoil, vortex shedding due to laminar-boundary-layer instabilities; vortex shedding from blunt trailing edges; and the turbulent vortex flow existing near the tip of lifting blades (BROOKS *et al.*, 1989).

Several other studies have been published, and even recent experimental efforts are made to fully characterize and understand the noise generation mechanisms on this specific airfoil configuration, as in (HERRIG *et al.*, 2008). Another interesting study using the NACA0012 airfoil is found in the Doctorate Thesis from Oerlemans (2009), where conventional beamforming is applied on source localization of airfoils and wind turbine blades. Also, recent efforts are made in simulation field in studying the self-noise generated by this airfoil, as studied by Wolf (2011) in his Doctorate Thesis.

The Engineering School of São Carlos (Escola de Engenharia de São Carlos - EESC) from the University of São Paulo (USP), also performed studies on this airfoil configuration, and prepared a

closed wind tunnel for aeroacoustic testing, work which led to a Master Dissertation by Santana (2010). This work presents beamforming mappings using the DAMAS2 method (DOUGHERTY, 2005), for the NACA-0012 airfoil, along with other testings. In a cooperation with the State University of Campinas, the Aerospace Department from EESC, provided the measurement data of the NACA-0012 testings, and results using DAMAS2 are then compared to the implemented conventional beamforming method as well as to the Generalized Inverse Beamforming method, all based on monopole type of source.

The objective is to illustrate the conventional beamforming and generalized inverse methods performance in comparison to the state-of-the-art method, DAMAS2, for two conditions of airflow speeds, 23 and 35m/s (approximately 0.06 and 0.1 Mach numbers), and two conditions of airfoil angle-of-attack, 0° and 5° .

8.2 Test Setup and General Conditions

The closed wind tunnel test facility from the University of São Paulo, at the School of Engineering of São Carlos (EESC), is shown schematically in Figure 8.1, where the installation layout of the closed circuit is shown along with the test section, fan and extractor sections. The test section has dimensions of 1.70x1.20m, and a turntable support structure. The tested NACA-0012 airfoil and a closer view of the testing section are also presented in Figure 8.2.

The array has 106 microphones distributed in a spiral configuration, with a light foam cover for protection. Figure 8.3 has the photos of the array, and Figure 8.4 shows the microphone position coordinates. Acquisition is performed with a sampling frequency of 51.2kHz, and sample blocks of 2048 points are used for the spectrums calculation, leading to a frequency resolution of 25Hz. Approximately 10 seconds are recorded, and the Cross-Spectral Matrix (CSM) are built from spectrums with 50% overlap.

Both methods, conventional beamforming and generalized inverse beamforming used the same target grid strategy based in regular points distribution with a constant width of $1/4$ of a wavelength. This strategy provides a reasonable spatial resolution with a low computational cost. The adopted grids are presented in Figure 8.5, for the three third octave band frequencies of: 1kHz; 1.6kHz; and 2.5kHz.



Figure 8.1: Test facility, test section and installation layout.



Figure 8.2: NACA-0012 airfoil and test section with an airfoil test setup.

The grids are slightly overextended in horizontal and vertical directions to improve the central resolution when using the generalized inverse beamforming method, with limits approximately at 1.00 x 1.20m, this influence is discussed in more details throughout the results analysis in the next sections.

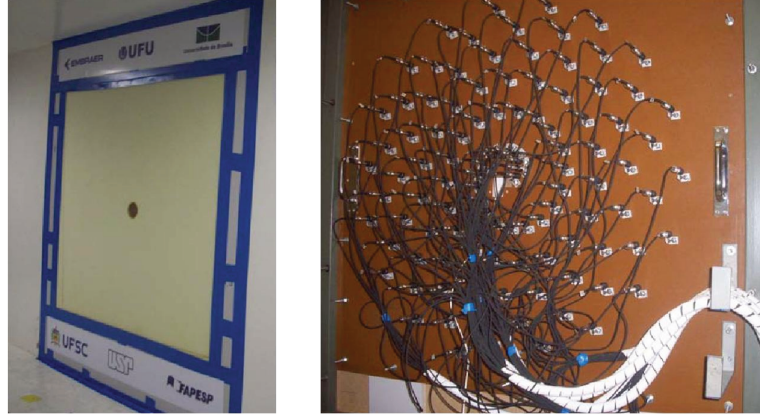


Figure 8.3: Array with 106 microphones in spiral distribution: light foam cover (left); and rear view of installation.

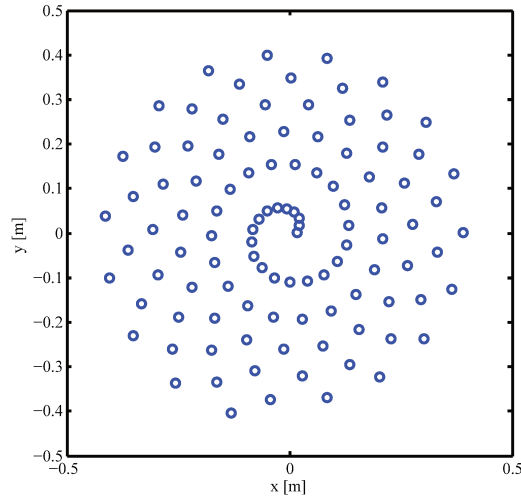


Figure 8.4: Array microphones positions in spiral distribution.

8.3 Beamforming Results Comparison: DAMAS2 and Conventional Beamforming

The conventional beamforming in this Chapter is applied to estimated the average sound pressure level at the array plane, Delay-And-Sum approach, in order to compare with the results obtained by Santana (2010), using DAMAS2. The conventional beamforming estimations are performed without the diagonal of the CSM, and both results are presented in Figures 8.6 to 8.9, for the airflow speeds of 23 and 35m/s, and airfoil angle-of-attack (AOA) of 0° and 5° .

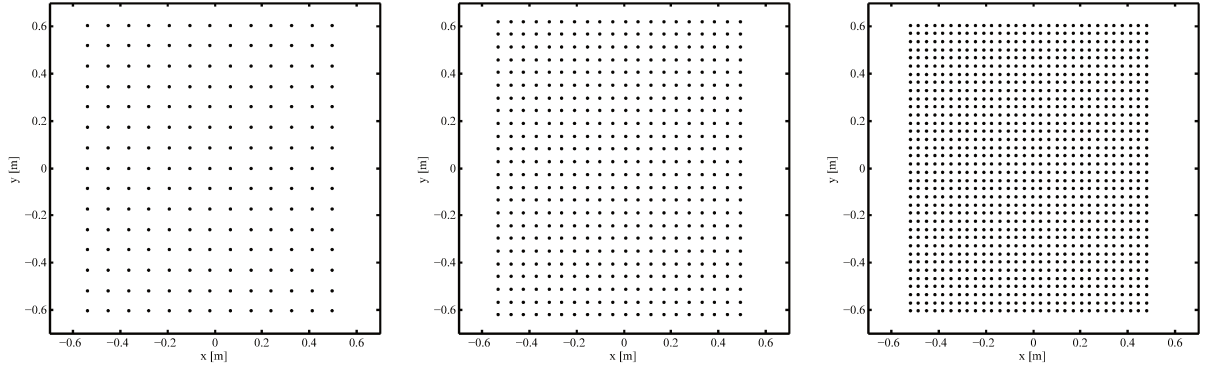


Figure 8.5: Target grid used on beamforming mappings: 1kHz / 195 points (top); 1.6kHz / 480 points; and 2.5kHz / 1080 points (bottom).

From the results, it is clear the advantage in localization dynamic range of the DAMAS2 method compared to the conventional beamforming mappings. Despite of that, the conventional beamforming is able to capture the main locations of noise radiation in all conditions with one exception, the analysis of the 1kHz third octave band, airflow speed of 35m/s and AOA of 0° . At this condition and frequency of analysis, the mapping is not able to distinguish the noise from the airfoil to the noise from the right side of the tunnel, where the fan is located.

In general, the noise center is located at mid-span region for low frequency as 1kHz, and more distributed in spanwise direction for 1.6k and 2.5kHz frequencies of analysis. The radiation center is located at the trailing edge for all conditions, and this is in accordance to the literature expected location for main source region. The sound pressure levels corresponds to the respective third octave band level, and are in fair agreement between methods, with a slight overestimation in the low frequency range for the conventional beamforming as expected considering the lower dynamic range.

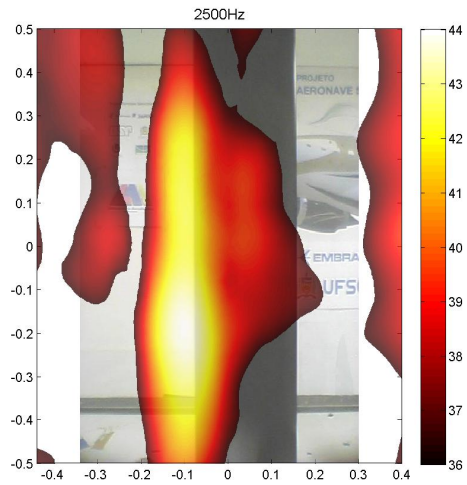
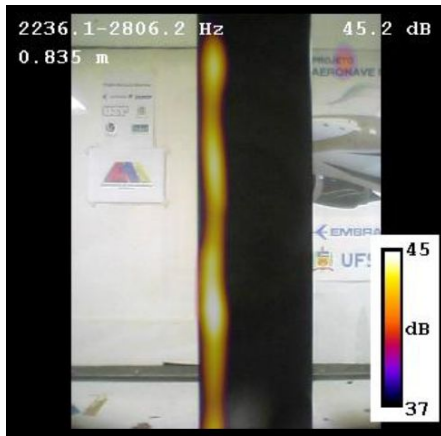
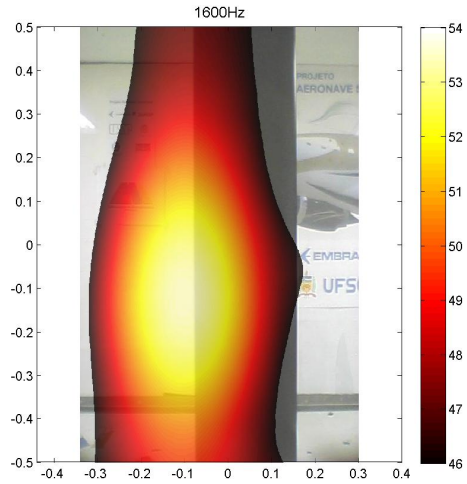
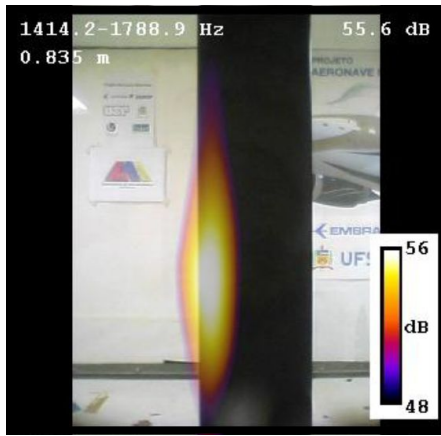
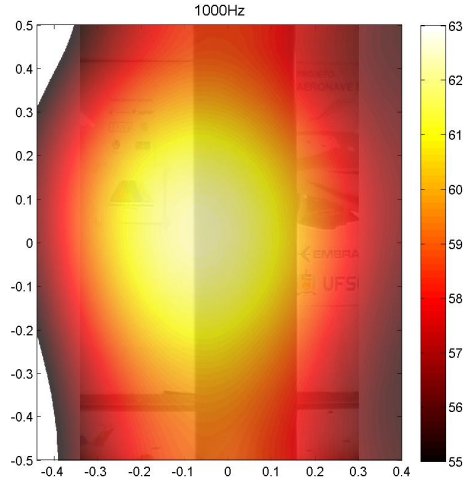
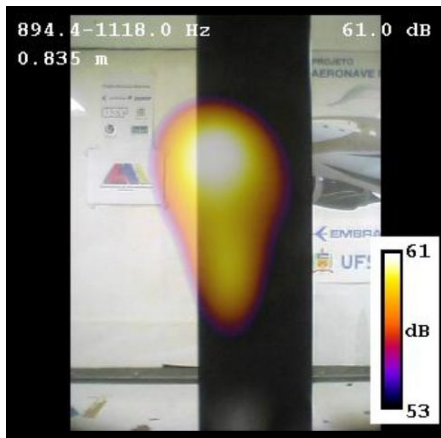


Figure 8.6: Beamforming results comparison for NACA-0012 with air at 23m/s and 0° angle-of-attack, DAMAS2 (left) and conventional beamforming (DAS): 1000Hz (top); 1600Hz; and 2500Hz (bottom). Mappings are SPL at array plane, and flow from right to left.

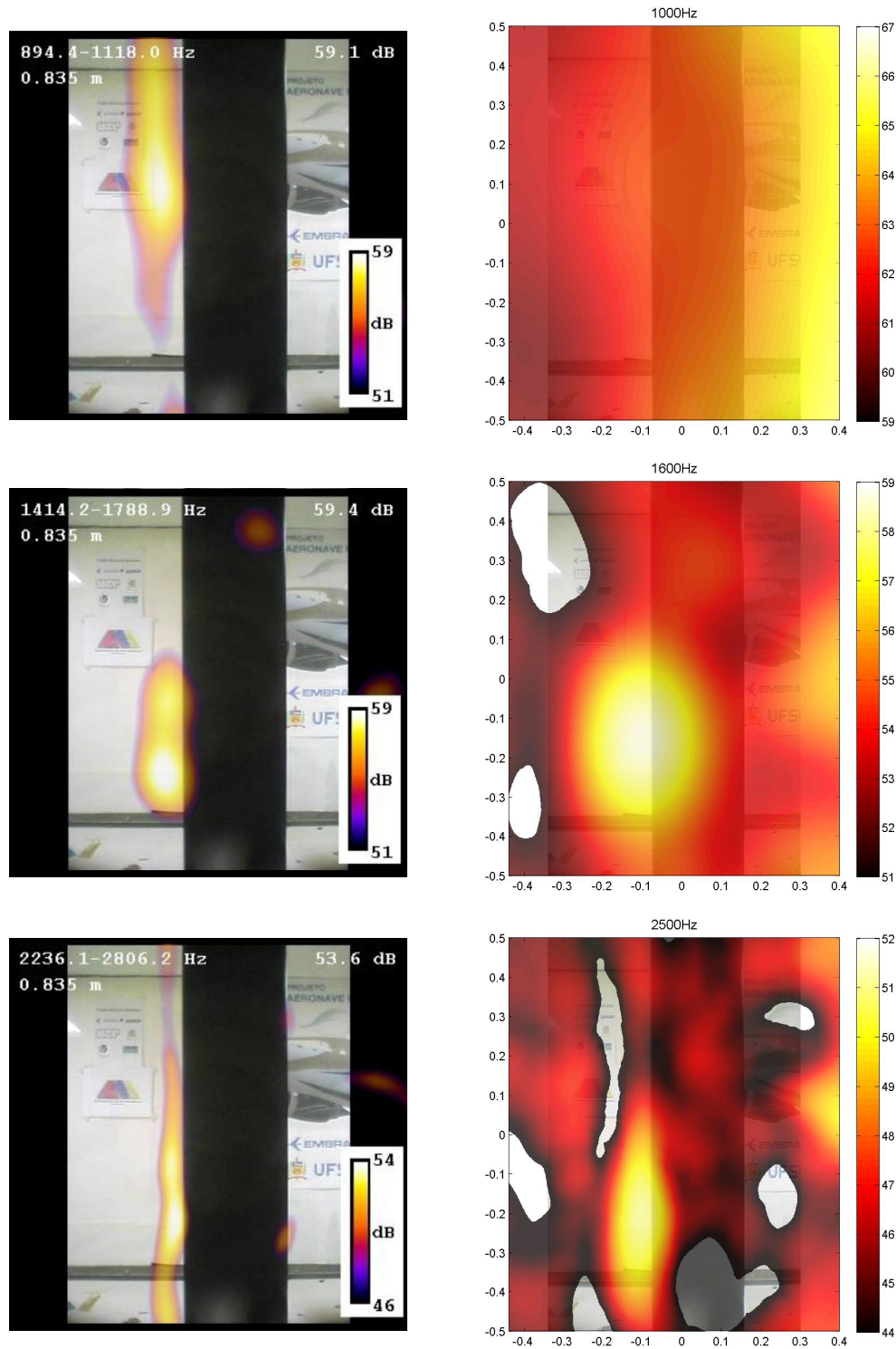


Figure 8.7: Beamforming results comparison for NACA-0012 with air at 35m/s and 0° angle-of-attack, DAMAS2 (left) and conventional beamforming (DAS): 1000Hz (top); 1600Hz; and 2500Hz (bottom). Mappings are SPL at array plane, and flow from right to left.

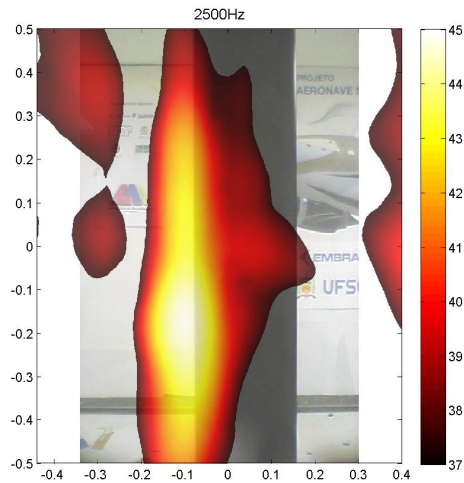
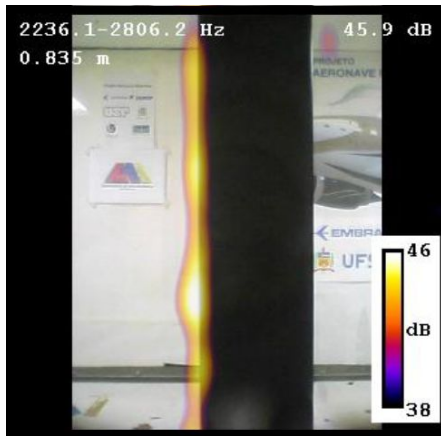
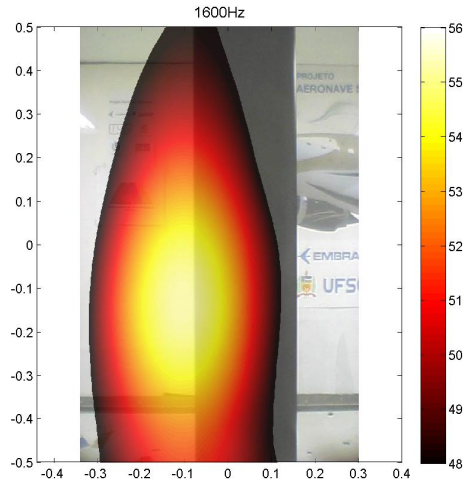
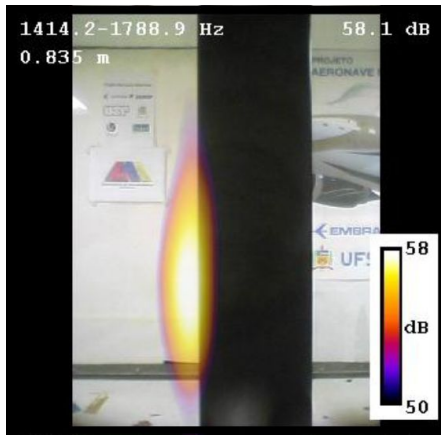
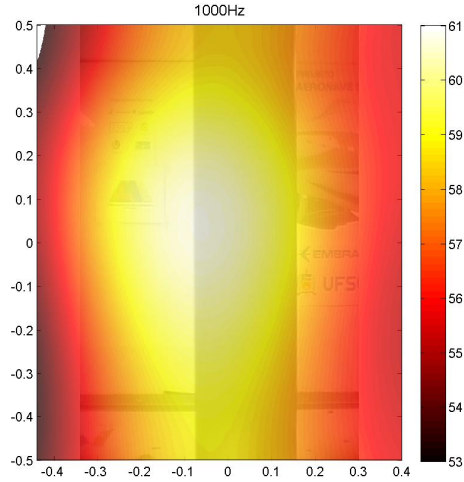
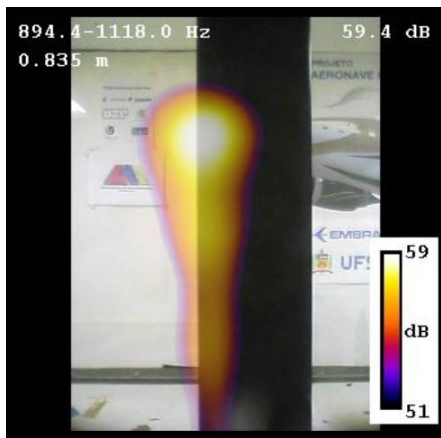


Figure 8.8: Beamforming results comparison for NACA-0012 with air at 23m/s and 5° angle-of-attack, DAMAS2 (left) and conventional beamforming (DAS): 1000Hz (top); 1600Hz; and 2500Hz (bottom). Mappings are SPL at array plane, and flow from right to left.

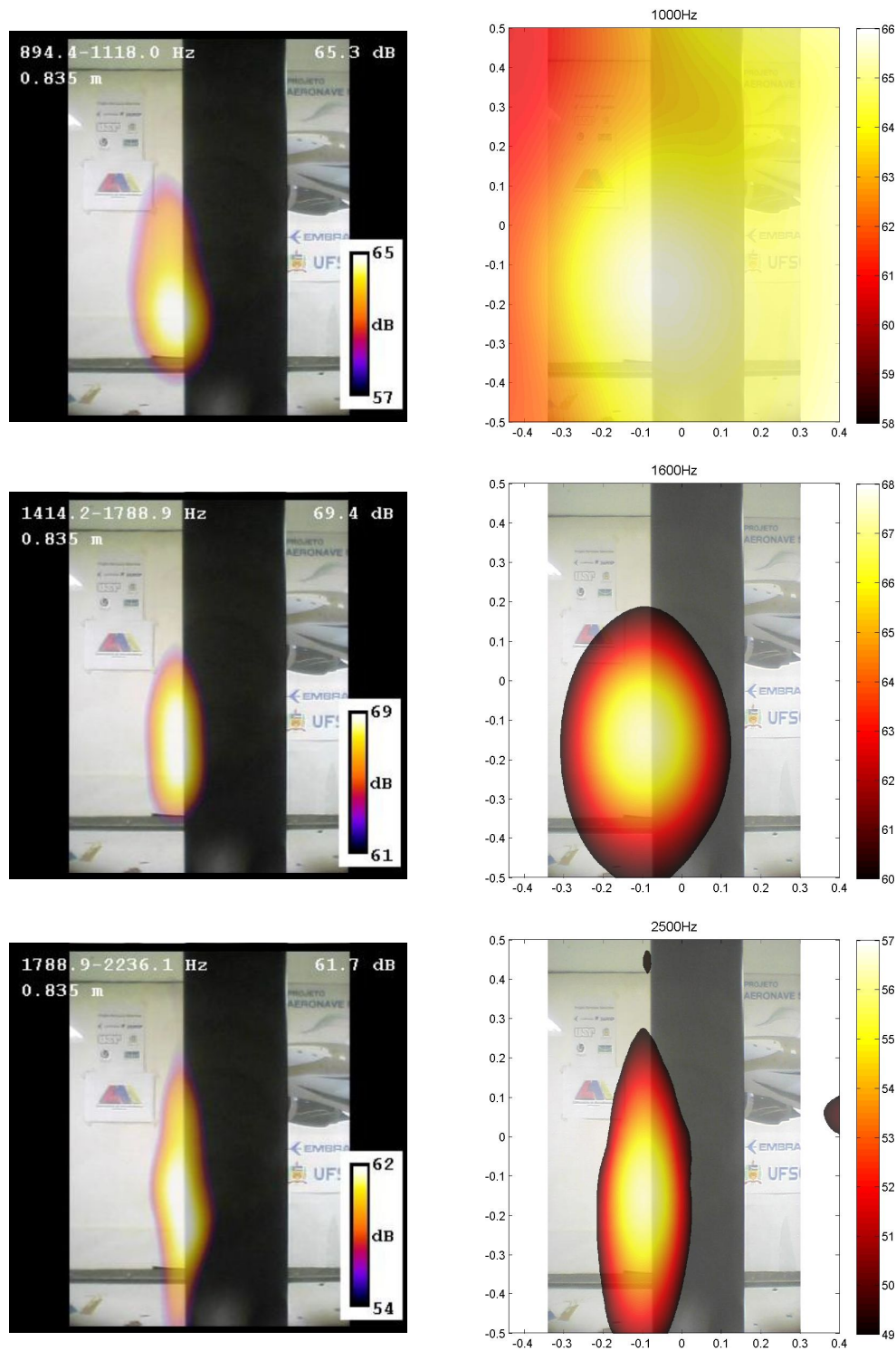


Figure 8.9: Beamforming results comparison for NACA-0012 with air at 35m/s and 5° angle-of-attack, DAMAS2 (left) and conventional beamforming (DAS): 1000Hz (top); 1600Hz; and 2500Hz (bottom). Mappings are SPL at array plane, and flow from right to left.

8.4 Monopole Identification Using Generalized Inverse Beamforming

The generalized inverse method is applied for the sources identification using the monopole type of radiation on the received measurements from EESC. The generalized inverse method is applied with and without the IRLS scheme. Results of estimations are presented in Figures 8.10 to 8.13.

The generalized inverse method required a higher regularization factor than previously used, settled to 20% of the of the greatest eigen-value of $A^\dagger A$ or $A^\dagger W_i A$, and kept fixed throughout the subsequent iterations. This is necessary in order to obtain reasonable mappings under noisy conditions, expected sound coming from the fan, noise from the flow turbulence on walls, and influence from the flow over the microphones. All this extraneous noise sources in respect to the test object, is present in a reverberant environment, since the test section have rigid walls. All these sound radiations pose an extra difficulty to reach the proper source distribution solution by the least squares approach, and only few iterations are applied on algorithm to preserve mapping integrity and avoid divergence of solution. On the generalized inverse without IRLS, the number of iterations ranges from 20 to 30 with 10% truncation on each iteration. For the generalized inverse method with IRLS, only 1 to 3 iterations are used without losing the mapping integrity.

The CSM is adopted without auto-powers attenuation, since it also decreased the localization accuracy and mapping integrity. On these measurements, the ratio of average cross-power term by the average auto-power terms is about 5%, demonstrating a recorded high pressure fluctuation due to the flow turbulence that is not coherent between microphones.

The generalized inverse method failed to clearly estimate the sources location at one condition, the 1kHz band analysis with flow at 35m/s and AOA of 0° , with a clear influence from the sound coming from the right direction of the tunnel, the inlet part, where the fan is located. This also occurred on the conventional beamforming mapping, indicating that the recorded sound is really influenced by external sources in respect to the test object on this measurement data.

The generalized inverse method with IRLS also failed to estimate the sources location at this condition, and also at a second condition: flow at 35m/s and AOA of 5° . These results, illustrates the difficulty of the generalized inverse method to overcome the presence of extraneous sound sources

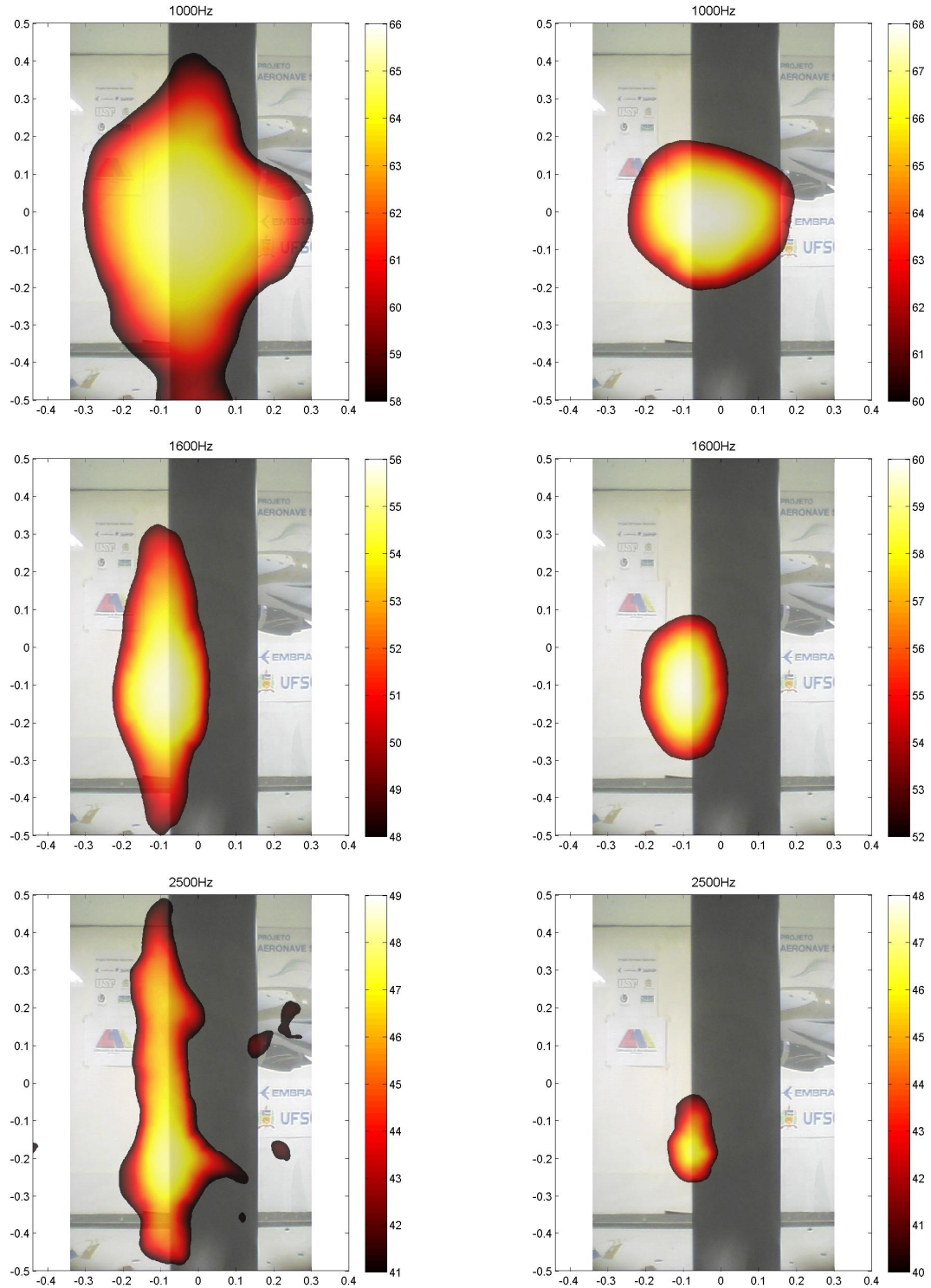


Figure 8.10: Generalized inverse beamforming results comparison for NACA-0012 with air at 23m/s and 0° angle-of-attack, without IRLS (left) and with IRLS: 1000Hz (top); 1600Hz; and 2500Hz (bottom). Mappings are SPL at array plane, and flow from right to left.

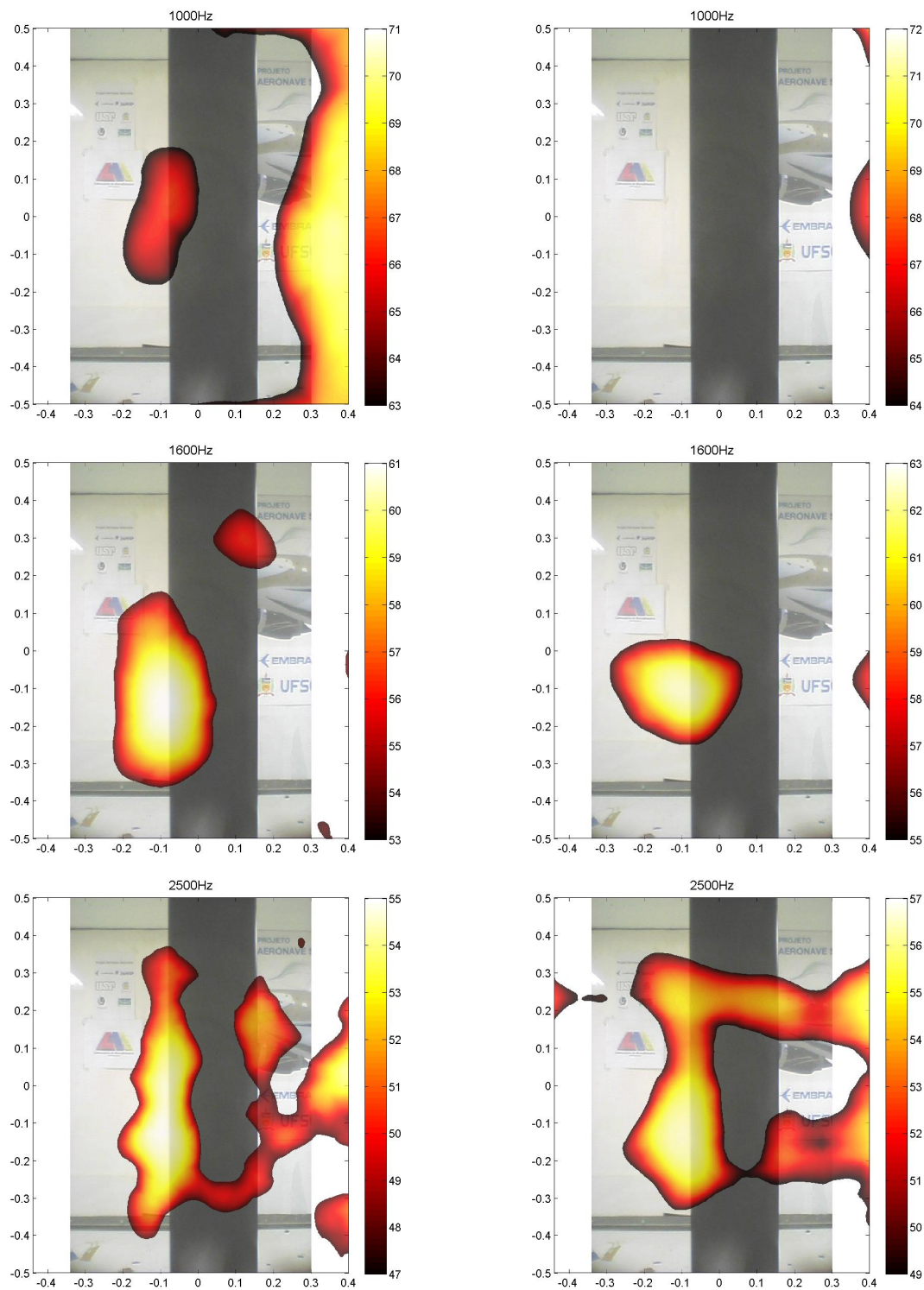


Figure 8.11: Generalized inverse beamforming results comparison for NACA-0012 with air at 35m/s and 0° angle-of-attack, without IRLS (left) and with IRLS: 1000Hz (top); 1600Hz; and 2500Hz (bottom). Mappings are SPL at array plane, and flow from right to left.

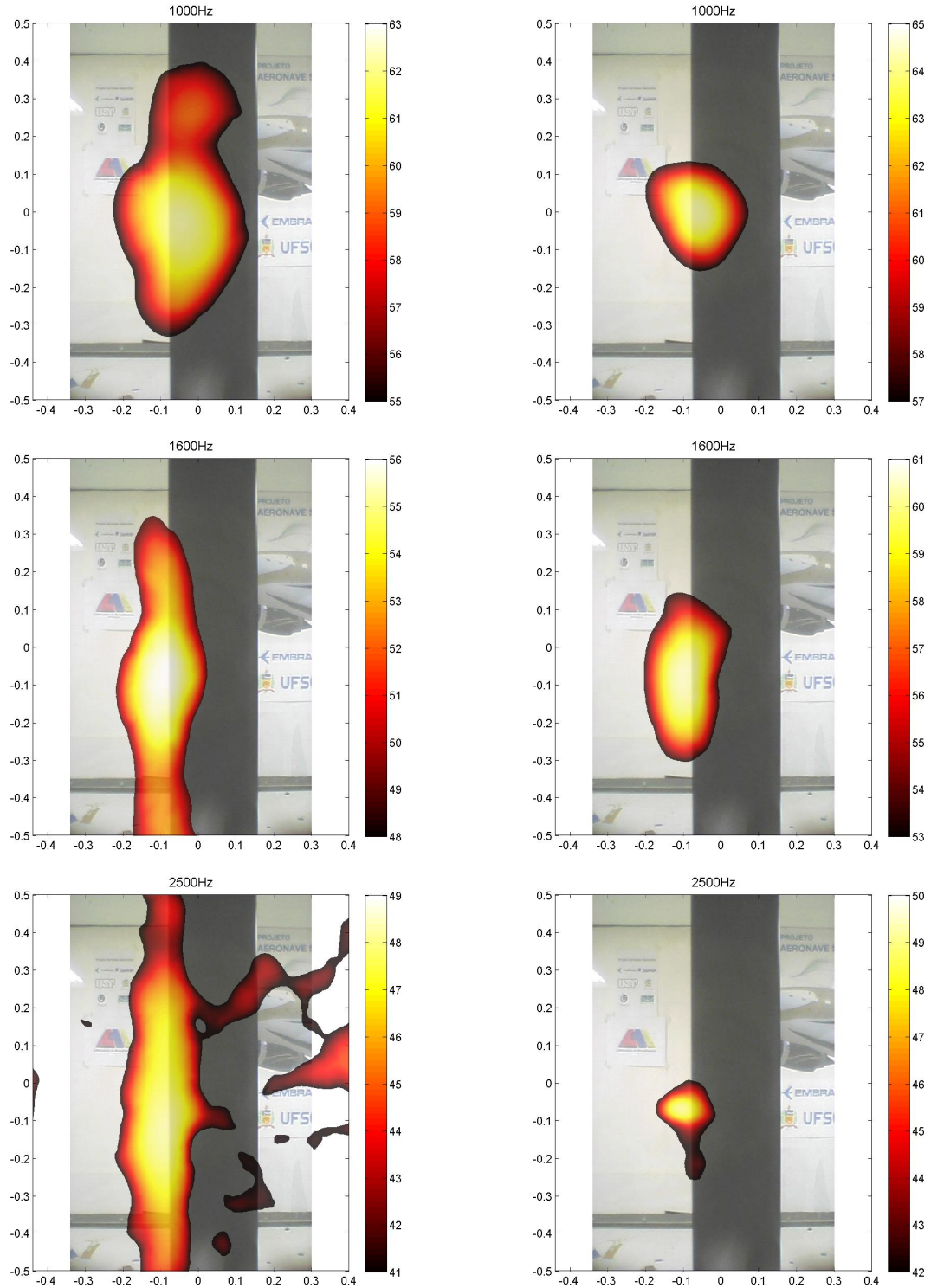


Figure 8.12: Generalized inverse beamforming results comparison for NACA-0012 with air at 23m/s and 5° angle-of-attack, without IRLS (left) and with IRLS: 1000Hz (top); 1600Hz; and 2500Hz (bottom). Mappings are SPL at array plane, and flow from right to left.

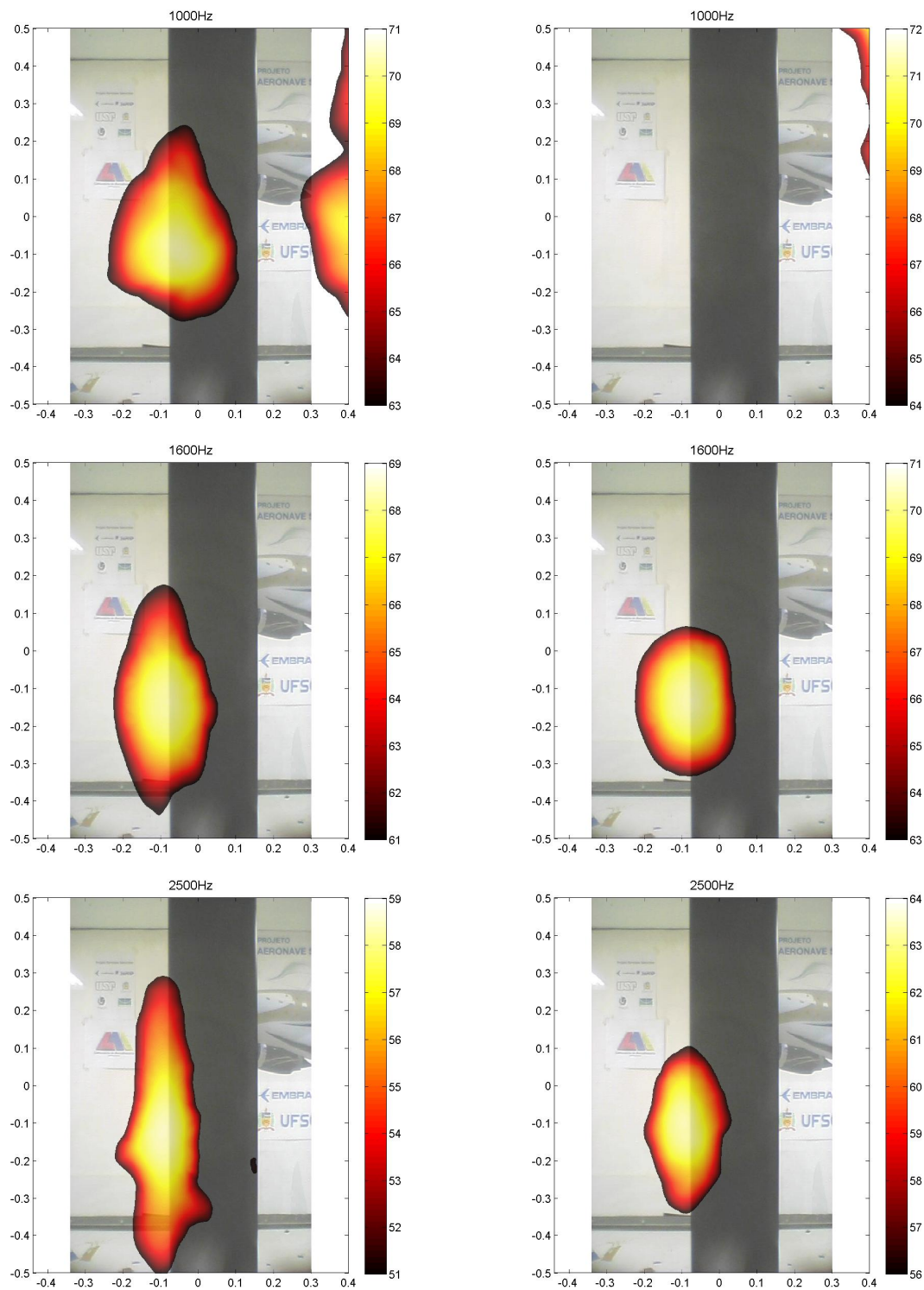


Figure 8.13: Generalized inverse beamforming results comparison for NACA-0012 with air at 35m/s and 5° angle-of-attack, without IRLS (left) and with IRLS: 1000Hz (top); 1600Hz; and 2500Hz (bottom). Mappings are SPL at array plane, and flow from right to left

that are not in the target range. The energy coming from these sources are incorporated in the eigen-modes, and their contributions are spread over the grid locations, in an attempt by least squares to fit the source vector to the array measurements, represented by the eigen-modes. This seems to be one of the biggest challenges of inverse methods when compared to directional assessments as in the conventional beamforming.

Despite these difficulties, in general the generalized inverse method is capable to locate the main source region at the trailing edge, as shown by the DAMAS2 and conventional beamforming results. The results demonstrates that the localization using the generalized inverse without IRLS present a lower dynamic range when compared to the method with IRLS, but in the other hand, it seems to capture with a greater detail the distributed character of the sources at the trailing edge. The generalized inverse method with IRLS, tend to concentrate the localization, clear for higher frequencies, as shown for example in Figure 8.12, for the flow with 23m/s and AOA of 5° .

The closer results to the DAMAS2 mappings are observed in the generalized inverse without IRLS, where the distributed character is preserved, and localization nuances are in agreement between mappings. These nuances are also shown in the conventional beamforming results. In terms of source level, the generalized inverse without IRLS also present the closer estimation to the DAMAS2 results, with a higher overestimation in lower frequencies as 1kHz, with values up to 6dB higher.

Despite the high number of microphones, the generalized inverse method seems to be limited by the presence of reflecting surfaces and external sources, and results present similar localization dynamic range to the conventional beamforming resolution, but with the advantage of less side effects (spurious noise peaks).

8.5 Summary

In terms of aeroacoustic sources localization, both conventional beamforming and generalized inverse beamforming demonstrated its capacity in performing source estimations on this kind of measurement on closed wind tunnel. On the other hand, the generalized inverse beamforming demonstrated limitations to overcome the influence of close reflecting walls and external loud sources in respect to the test object, showing dynamic resolution comparable to the conventional beamforming. This characteristic is observed despite the use of a high number of microphones.

9 Moving Source Identification: Passenger Vehicle Pass-by Noise

Pass-by noise level is an important design criteria for vehicle engineering development, and tools for better understanding of subsystem contribution on the recorded level during passage are of most interest. In this Chapter, generalized inverse beamforming is used to investigate advantages on this approach in a passenger vehicle pass-by noise assessment. A simplified moving source modeling is adopted. Localization performance is investigated using a known source and influence of block size and averaging is also discussed. In the end, passenger vehicle pass-by noise analysis is presented with order and spectrum peak mappings.

9.1 Introduction

The investigation of critical noise sources on pass-by noise tests is demanding development of the current techniques in order to locate and quantify these sources. One recent approach is to use beamforming techniques to this purpose. The phased array information can be processed using several methods, for example, conventional delay-and-sum algorithms, deconvolution based algorithms, such as DAMAS2, and more recently, the generalized inverse beamforming. This later method, presents the advantage of separating coherent sources with better dynamic range than conventional beamforming. Also, recent developments, such as the Iteratively Re-Weighting Least Squares, increases the localization accuracy allowing it to be used in a challenging problem as a fast moving source detection, a non-stationary condition. This Chapter raises the main advantages and disadvantages on this method using a practical case, a passenger vehicle pass-by test.

This section outlines the moving source modeling and the adopted simplifications, such as de-Dopplerization, and separation of time and space in the moving source radiation model.

The test setup is introduced with array details and signal acquisition parameters. Processing details are summarized and the influence of averaging and block size are investigated through the localization of a known source radiating at 3kHz placed on top of the vehicle. Results using conventional focused beamforming and generalized inverse beamforming are compared.

In order to exemplify the dominant source assessment in a passenger vehicle pass-by noise

in one particular test passage, 30km/h entrance and Wide-open-Throttle (WOT) acceleration, beamforming mappings are presented for the third octave peak level and the main engine order using conventional beamforming and the generalized inverse beamforming, these results are also presented in (ZAVALA *et al.*, 2011C,B).

In the end, the main advantages and disadvantages observed on the application of the conventional and generalized inverse beamforming in pass-by noise sources localization are presented.

9.2 Moving Source Modeling

The model adopted in this work is based in (MORSE & INGARD, 1968). The source moves with constant speed, parallel to the array of microphones, and the radiation is calculated with respect to the emission location. Figure 9.1 shows the adopted simplified modeling of a moving source with respect to the array microphones.

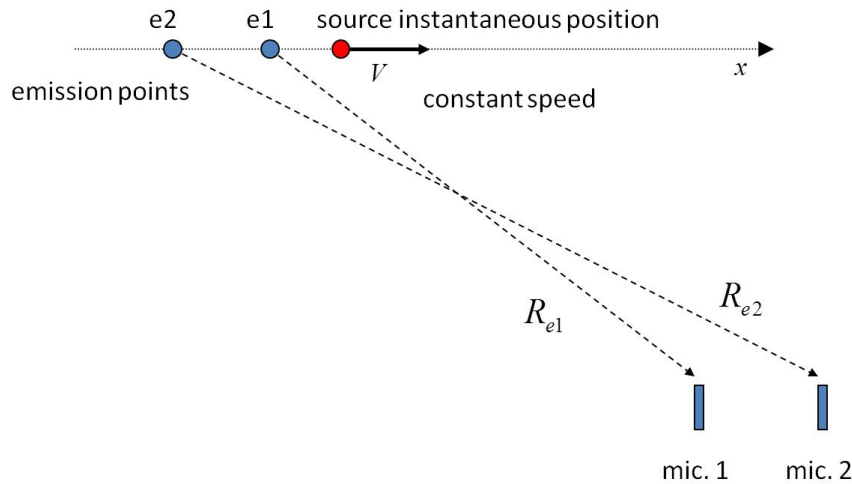


Figure 9.1: Simplified moving source modeling.

The emitted phase and decay which is observed at the microphone positions is calculated as a function of the instantaneous source position. This relationship can be described by the equation

below:

$$R_e = \frac{M_s(x - Vt) + \sqrt{(x - Vt)^2 + (1 - M_s^2)(y^2 + z^2)}}{(1 - M_s^2)}, \quad (9.1)$$

where R_e is the emission source distance; M_s is the ratio between the source speed and the speed of sound; x, y and z , are the coordinates of the instantaneous source position, with x parallel to the array of microphones; V is the source speed; and t is time.

With the representation above, the transfer matrix, A , can be built for each source position candidate using the following equation:

$$Press_{mic_m} = \frac{\rho c k Q}{4\pi R_e} e^{-jkR_e}, \quad (9.2)$$

where $Press_{mic_m}$ is the pressure calculated at each microphone location m ; ρ , c , k and Q , are the air density, speed of sound, source radiation wavenumber and strength, respectively.

The Doppler shift is removed from each of the array microphone signals considering the center of the target grid (source location candidates) as reference, before the CSM is generated.

In summary, the main simplifications are that the source is assumed stationary on each sample block, using the intermediate source instantaneous position to calculate the emission distance and the transfer matrix, and the de-Dopplerized spectra are used to build the CSM.

9.3 Test Setup and General Conditions

The pass-by noise test consist in recording the overall sound pressure level at a particular distance from a vehicle that is accelerated (ISO362). In order to verify the localization performance in similar condition as on a real pass-by noise test, an antenna (array of microphones) with 59 microphones is placed approximately 6m from the center of a track, or approximately 5m from the sideline of a vehicle (reference to the right side of the vehicle). The tests are conducted with

support of LMS International Engineering at the Headquarter in Leuven (in Belgium). The antenna has approximately 3.4m aperture, and is placed 0.6m from the ground. The antenna shape is a 5-arm star configuration, with microphone denser distribution near the center of the array. The vehicle adopted is a Ford Focus Station Wagon TDI 1.8L 2008 (Belgium market model). A loudspeaker is placed on top of the car for the verification of localization performance for a known source.

A target grid (source location candidates) is distributed on a rectangular region with approximately 3000 grid points spaced regularly around the vehicle right side. A new grid is used at each vehicle expected position along the track. Light sensors are used at the track beginning and at the end, as well as a speed radar, to define vehicle position and speed along passages as adopted normally on this kind of testing. The track, antenna, vehicle and target grid can be seen on Figures 9.2 to 9.4.



Figure 9.2: Test track.

LMS Scadas system was used for the microphone signals simultaneous acquisition with 51.2kHz sampling. Standard 1/2" and 1/4" microphones were used in the antenna.



Figure 9.3: 5-arms star antenna layout.

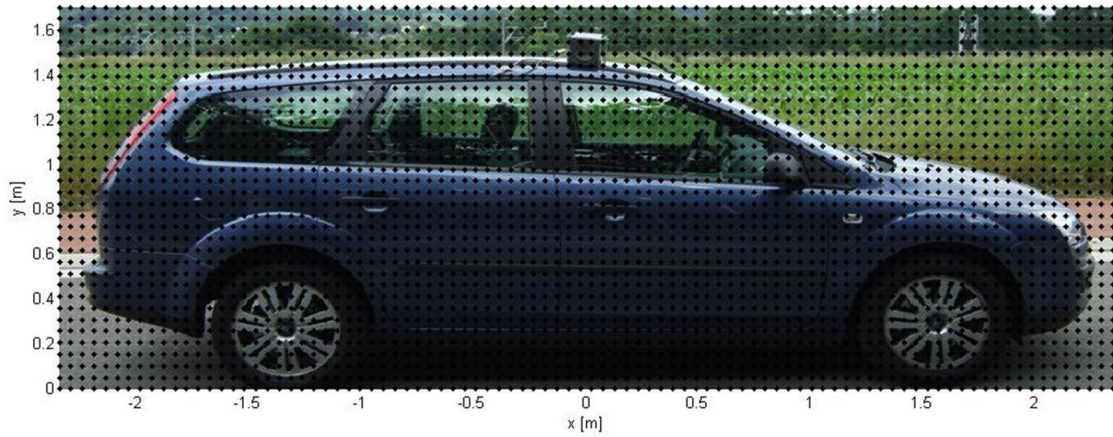


Figure 9.4: Vehicle and target grid distribution.

9.4 Experimental Identification Verifications

A 3kHz tonal radiation is adopted for the loudspeaker sound emission, and a vehicle constant speed of 30km/h used for the localization accuracy assessment with respect to identification parameters such as block size and estimation averaging strategy. The GIB algorithm adopted

used the IRLS scheme shown in (SUZUKI, 2010), with 40 iterations and 10% truncation. Some variation in the source localization is expected due to the uncertainties in vehicle speed, vehicle path distance to array, wind, reflections, signal noise, etc. The results below are with respect to identifications in one vehicle passage, using different number of average of estimations and different sizes of samples block.

# of est.	-6m	-4m	-2m	0m	2m	4m	6m
1	X	0.1	0	0	0.1	0.1	0.1
2	0	0.1	0	0	0.1	0.1	0.1
3	0	0.1	0.1	0	0.1	X	0.1

Figure 9.5: Localization error with respect to the number of estimates and using block of 2048 samples (X means error is higher than 0.4m).

block	-6m	-4m	-2m	0m	2m	4m	6m
1024	X	0.2	0.4	0.1	X	0.3	X
2048	0	0.1	0	0	0.1	0.1	0.1
4096	X	0.2	0.1	0.2	0.3	X	0.4

Figure 9.6: Localization error with respect to block size using 3 estimates (X means error is higher than 0.4m).

The results shown in table 9.5 and 9.6 clearly indicated the strong influence in localization performance due to the number of estimate averages and block size, with best compromise on this particular example with 2 estimates and block size of 2048 samples. For each estimation, the CSM is also averaged using 10 spectrums with 90% overlap. Using this configuration, the error in source center localization is up to 0.1m for the considered track points. The block size sensitivity possibly indicate that the simplifications assumed, namely stationarity along the block period, may not be valid beyond certain block size limit. The sensitivity to the number of estimate averages may indicate that variations or errors in signals, vehicle speed measurement, vehicle distance to array, etc., could be also of important influence on localization accuracy. This localization certainly could be improved if this result is also averaged for repeated passages, which is not considered in this example.

Considering the best configuration, average of two estimates and block size of 2048 samples, source localization mappings are presented in Figures 9.7 and 9.8, for track center and approaching vehicle position (-6m), for generalized inverse beamforming.

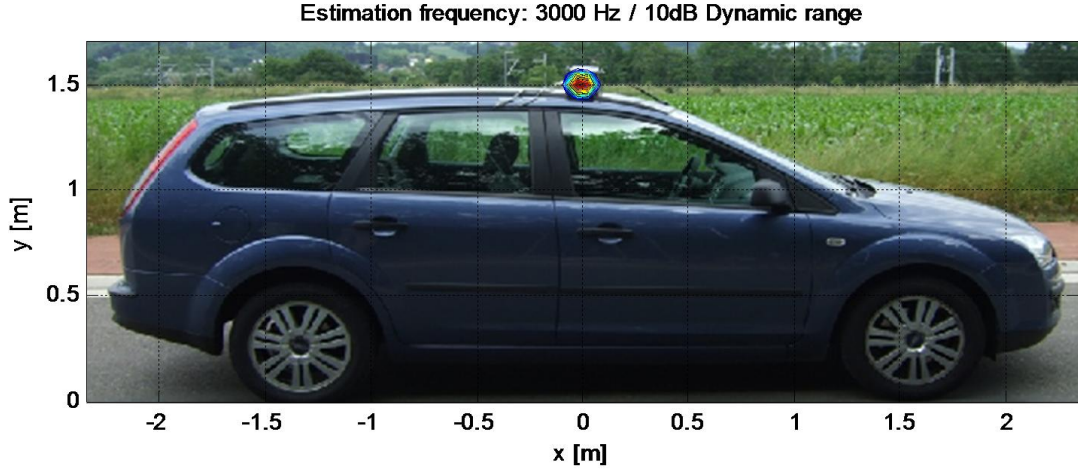


Figure 9.7: Localization example using GIB for vehicle at 0m (in front of array).

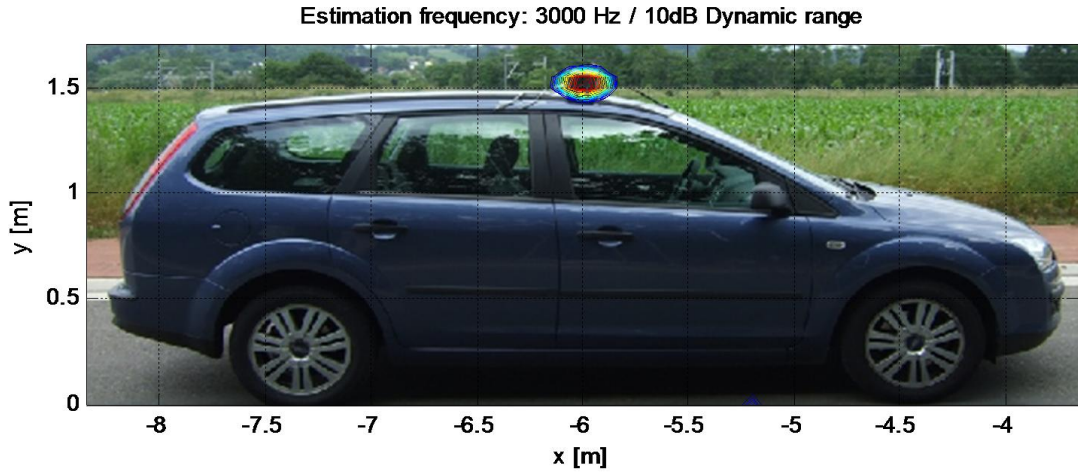


Figure 9.8: Localization example using GIB for vehicle at -6m from track center.

The conventional beamforming considered the diagonal removal to improve accuracy of the mappings. The results for the localization when the vehicle is at the center of the track range and in the approach are shown in Figure 9.9, for conventional beamforming.

The dynamic range on the localization is significantly higher for the GIB compared to the conventional method despite both methods are capable to locate source center in this case. A more

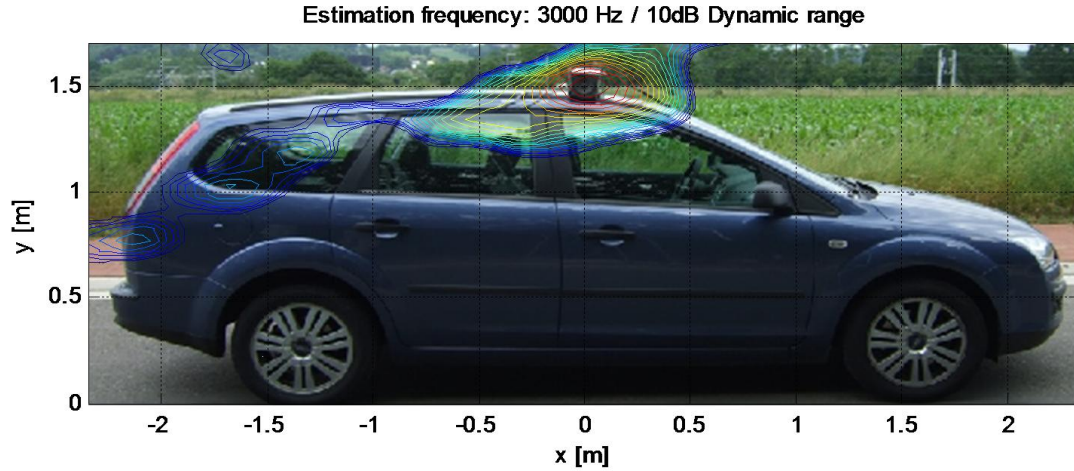


Figure 9.9: CB: Vehicle at 0m (in front of array).

challenging identification for vehicle being at -6m from track center can be seen on Figure 9.10, for conventional beamforming.

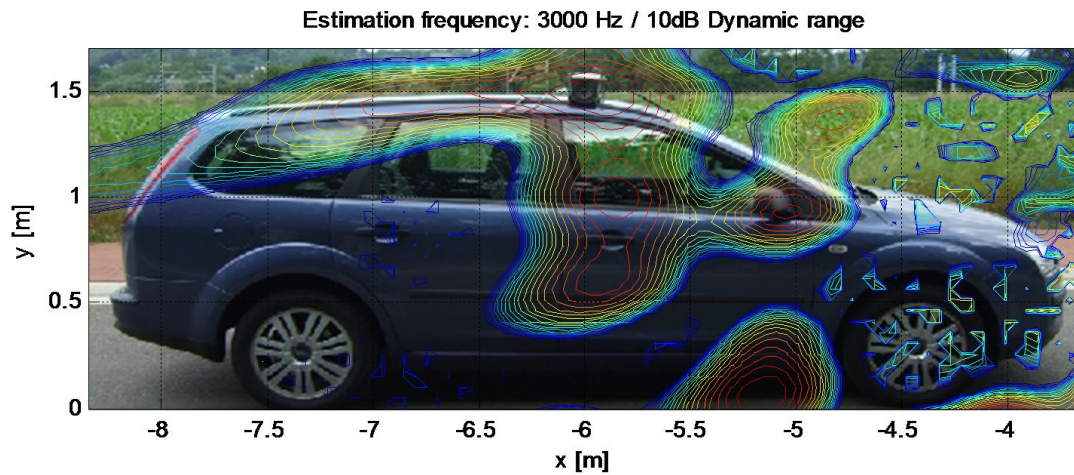


Figure 9.10: CB: Vehicle at -6m.

Now at -6m from the track center, not only the dynamic range is in evidence but also the accuracy on the GIB to locate the source. For investigations over 6m from the track center, is recommended that the array is placed at a higher distance from the target region.

9.5 Passenger Vehicle Noise Identification

To illustrate the localization of vehicle dominant sources in a pass-by noise passage, the 30km/h approach and wide-open-throttle (WOT) condition is chosen as example. The overall dBA level for a microphone position similar to the regulation required position is shown in Figure 9.11, for two types of calculations, the rms Fast Averaging as required by the norm and the identification blocks rms level, both in dBA. The objective is to locate the samples block that would better represent the peak on the Fast Averaging calculation.

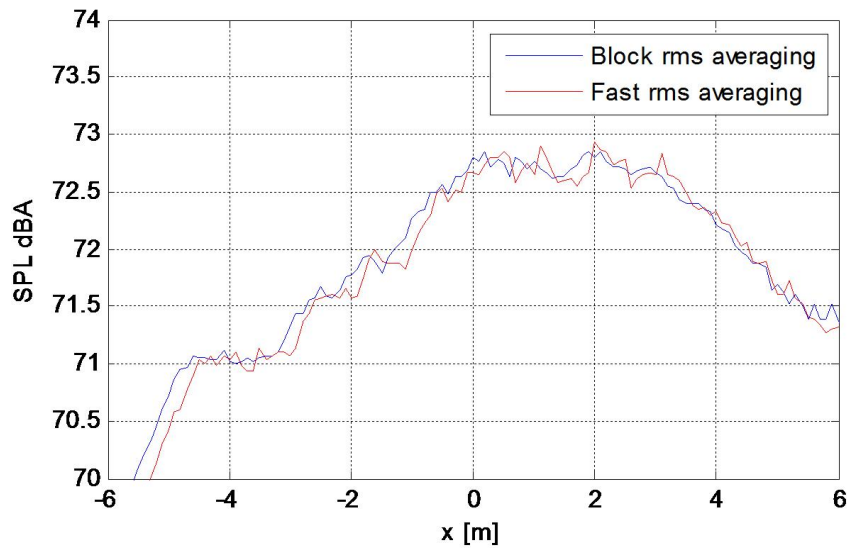


Figure 9.11: Center microphone level along vehicle run.

On this case, the vehicle position that brings the highest level is when its center is at 2m (from track middle position). Two analysis are carried out for this vehicle position, the spectrum peak frequency, and 2nd engine order, to illustrate the frequency range on identifications. Both seems to capture emissions from the exhaust tailpipe. Generalized inverse beamforming mappings are shown in Figures 9.12 to 9.15.

Considering the GIB results, on Figure 9.12, the localization clearly indicate the exhaust tailpipe contribution for that particular order and moment even in the low frequency case of 2nd engine order analysis. It is important to observe that the localization at the ground is related to the presence of reflections in the ground. Figure 9.13 shows the dominant source for that chosen

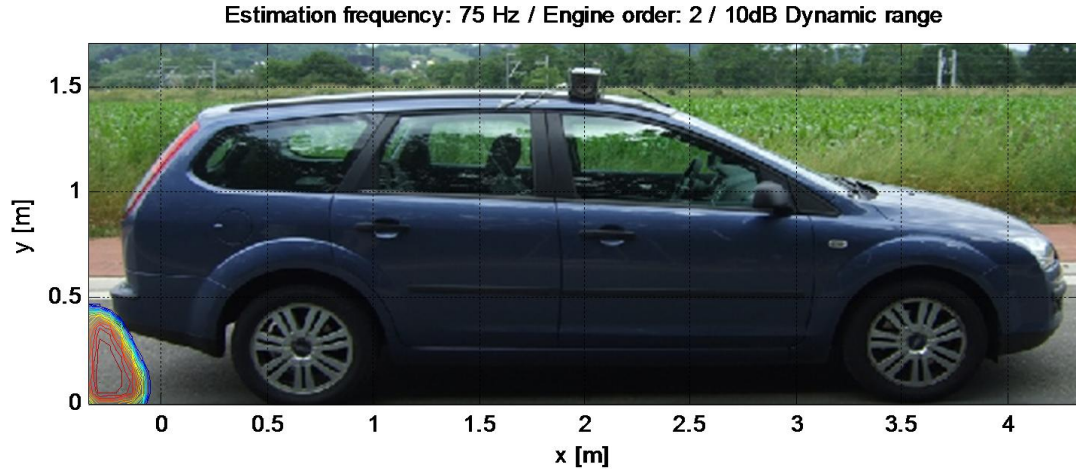


Figure 9.12: GIB: Engine 2nd order (75Hz) localization example for vehicle at 2m from track center.

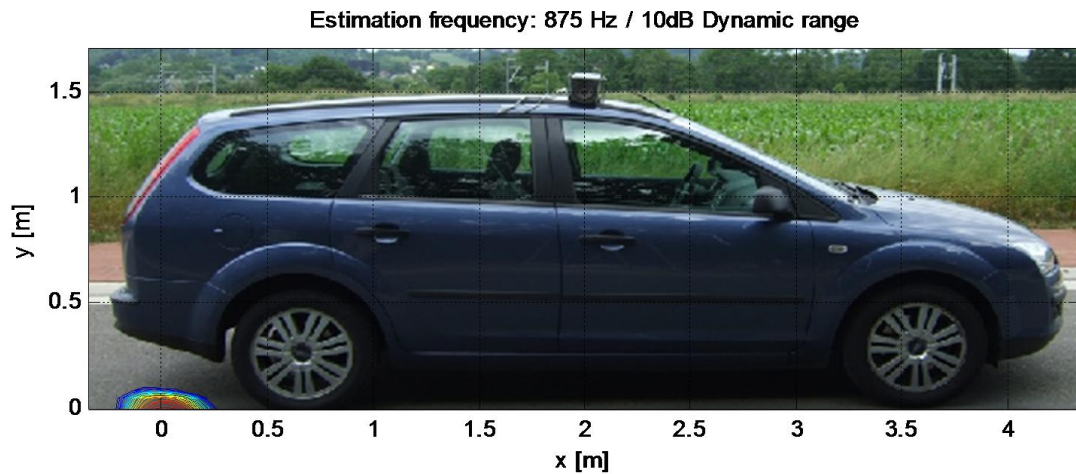


Figure 9.13: GIB: Spectrum peak (875Hz) localization example for vehicle at 2m from track center.

vehicle position (2m), with 875Hz peak, and localization region around exhaust tailpipe, again the reflection in the ground seems to be dominant and no direct exposure of the source is observed.

The shown results considered the first eigenmode from the CSM, meaning that the most significative radiation is used for that selected period. Several other analysis can be done, for example, averaging between repeated passages to improve localization accuracy and reliability, or increased grid density on selected regions per iteration to an increased spatial resolution.

Conventional beamforming results are presented in Figures 9.14 and 9.15.

The observation is that the conventional beamforming totally fail to locate clearly the source

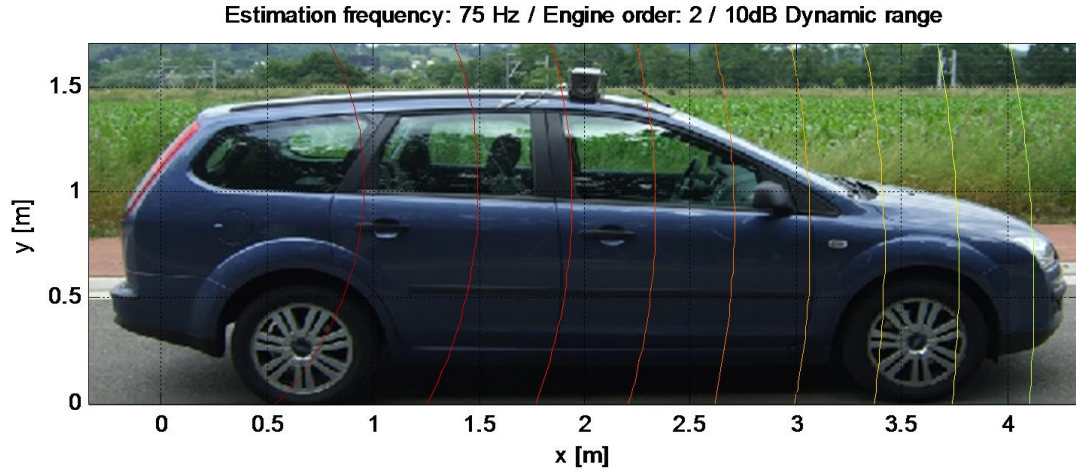


Figure 9.14: CB: Engine 2nd order (75Hz) localization example for vehicle at 2m from track center.

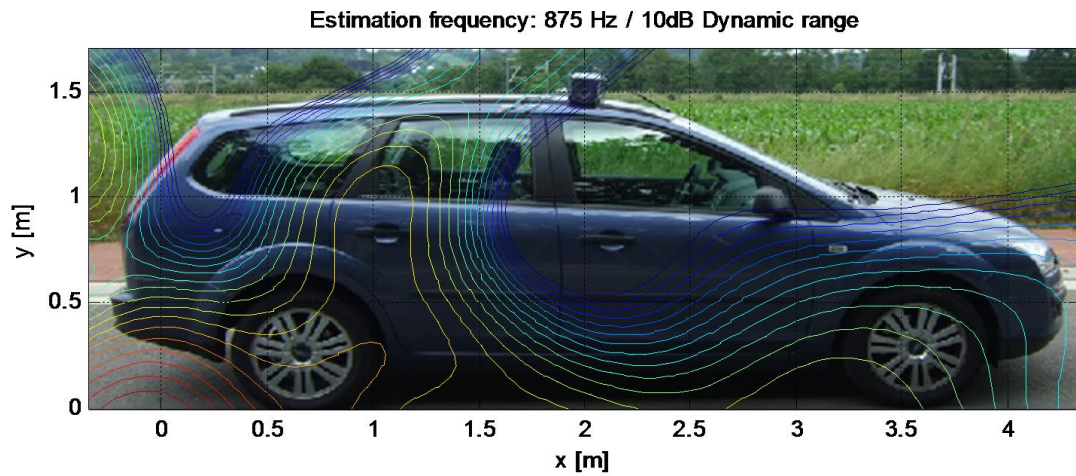


Figure 9.15: CB: Spectrum peak (875Hz) localization example for vehicle at 2m from track center.

center for the 2nd engine order frequency range, and the peak frequency at 875Hz. However, they both indicate also the rear region of the car to have higher levels, confirming the general location as pointed by the GIB.

9.6 Summary

The main advantages observed are: the higher dynamic range in localization obtained with GIB/IRLS, presenting low noise with a 10dB range at 3kHz; the consistency on the localization region observed in the loudspeaker verification; the small and accurate localization region even at low frequency of analysis.

The main disadvantages observed are: the variation in localization for the studied frequency of 3kHz, presenting errors of up to 0.1m in the considered track points; the sensitivity for the averaging strategy, and possible need of averaging between passages (not ideal); and the localization being dominated by the reflections at the ground when no direct exposure from the source is observed.

The investigation on the use of the generalized inverse beamforming on pass-by noise source localization demonstrated that the performance is dependent on several aspects, such as averaging strategy and frequency resolution, but the method can be an important support tool for source localization and proper pass-by noise development.

Other aspects should also be considered in further investigations on the use of the generalized inverse beamforming for pass-by noise tests, such as sensitivity to errors in vehicle position and vehicle speed, antenna distance to vehicle, wind influence, etc. The presented results do not exhaust the potential of the method, and further investigation have to be carried out to completely assess the generalized inverse beamforming as a pass-by noise tool.

10 Moving Source Identification: Truck Pass-by Noise

In this Chapter, generalized inverse beamforming is applied to source identification in a truck pass-by noise test condition. For this, first is developed an special array of microphone distribution which provides the capability to perform identification in very low frequency range, as desired on this kind of testing. The hybrid generalized inverse mapping is used on identification, and two artifices are developed to improve performance: use of an image source in the transfer function; and a focus compensation for low frequency of analysis. Generalized inverse beamforming using the IRLS scheme is applied and its limitations on these testing conditions are illustrated. Conventional beamforming results are obtained for comparison and discussion. In the end, truck peak noise on two passage conditions and one side are analyzed by generalized inverse and conventional beamforming, for peak frequency and main engine order, a very low range of analysis.

10.1 Introduction

The importance on pass-by noise analysis is also critical on truck design development. Heavy structures and powerful power units provide a big challenge to the engineering balance and attendance of the legal requirement. Among the available technical tools, the beamforming source imaging provides some advantages such as simple test setup with low preparation time, simultaneous testing with the pass-by level recording procedure, and fast post-processing and generation of source mappings. On the other hand, the conventional beamforming present the disadvantage of poor resolution in low frequency, where the normal range is above 300Hz to provide good results. This characteristics are well investigated in (GUROVICH *et al.*, 2009).

This frequency range, above 300Hz, is insufficient to most of the cases involving the engine as cause, with main engine orders starting on the range of 50Hz. To address this problem, a new approach has to be developed and tested. Since the generalized inverse beamforming already demonstrated a lower limit in the frequency range when compared to the conventional beamforming, it is a natural candidate to provide the desired full frequency range of analysis on pass-by noise testing.

On this Chapter, first the test setup is introduced, with special attention to the designed

array of microphones, which is intended to support the analysis of very low frequencies by the generalized inverse method. Then, identifications using two loudspeakers for tonal and white noise in coherent and incoherent noise radiation are presented with hybrid generalized inverse mappings. Two artifices to improve the results are presented: image source in transfer matrix; and focus compensation for low frequency analysis. Results with IRLS are presented along with conventional beamforming results for comparison and discussion of verification tests.

In the end, the truck peak noise emission is investigated with generalized inverse and conventional beamforming. To illustrate the performance in the low frequency range, the main engine order is also investigated, with hybrid generalized inverse mappings and conventional beamforming mappings for comparison.

10.2 Test Setup and General Conditions

The pass-by noise test, ISO 362, consists basically in recording the maximum sound pressure level at 7.5m (1.2m height) from the vehicle path, in the range of -10m to 10m from the microphones line (positioned on both sides of the vehicle). The truck tests conditions slightly differs from the passenger vehicle conditions, in gears of testings for example, but in general it remains the same concept. The truck start testing with 30km/h or 50km/h, and then accelerates in full powering condition.

The testing results presented on this work are a collaboration between Mercedes-Benz do Brasil, Trucks Division, and the Computational Mechanics Department of the Faculty of Mechanical Engineering from the State University of Campinas (UNICAMP). On these testings, a heavy truck, Actros Line, is measured and results analyzed for different post-processing techniques. The Actros truck, track, and Array can be observed in Figure 10.1.

The array have 61 microphones distributed in “X” configuration. This concept is developed based in simulations using the generalized inverse beamforming and has three main objectives, the first is to have an extended distribution along track direction, covering about 6m on this direction to improve the low frequency resolution as well as source position resolution along track direction. The second objective is a symmetric distribution to provide identical resolution for both truck testing sides. Despite that on this investigation only one truck side is considered for testing for simplicity of results analysis, this symmetrical behavior is protected in the array design. The third



Figure 10.1: Track, array of microphones and measured truck at track center ($x=0$).

objective is to use the pass-by microphone position in the beamforming mapping and provide results as third octave sound pressure averaged levels corresponding to the pass-by microphone position.

The mapping levels using this averaging to the pass-by microphone position are the closest possible representation of the level contribution from the source to the pass-by level, but have two characteristics that influence level value, first is the third octave band range in the analysis on the beamforming, a fraction of the signal level, and the second is that beamforming mappings applied to distributed sources overestimates source levels based on the sensitivity determined by the mainlobe width. Despite this effects, the mappings can be reliably used to assess source level changes. The microphone position coordinates are presented in Figure 10.2, and built array is presented in Figure 10.3.

The horizontally extended nature of the array is better explained if the whole range of interest is considered: tracking all possible source locations along truck extension when it starts the testing, when it reaches the $x=-10\text{m}$ position, until the full truck leaves the $x=10\text{m}$ track position ($x=0$ is the line of pass-by microphones position, the track center). This desired range of analysis is illustrated in Figure 10.4, where the extended nature of the array distribution still seems insufficient to provide accurate mappings in all test range.

Two loudspeakers are used on top of the truck to provide an experimental verification for source location identification. The loudspeakers are approximately symmetrically positioned in respect to the considered truck center, with approximate distance between speakers as 3.90m . The

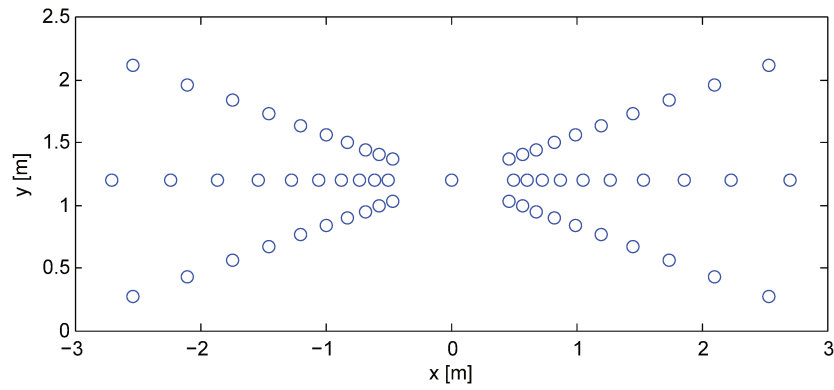


Figure 10.2: Array microphone coordinates, including pass-by noise microphone position at array center.



Figure 10.3: Array assembly with 61 microphones, including pass-by noise microphone position at array center.



Figure 10.4: Test track overall range: left and right cones indicate the truck extension coverage during pass-by test.

front loudspeaker has its center at approximately 0.56m from the ground, and the rear loudspeaker has its center at approximately 1.05m from the ground. The loudspeakers positioning and assembly details are shown in Figure 10.5.



Figure 10.5: Loudspeakers position and assembly details: rear (left); and front speaker.

Tonal signal with frequencies of 500Hz, 300Hz, 200Hz, 100Hz and 50Hz, are used on front speaker for low frequency resolution verification. For high frequency investigation (7kHz range), white noise in coherent and incoherent radiation are used on front and rear loudspeakers. These known sources provide an easy assessment of the beamforming resolution for low frequency and high frequency of analysis, covering all the pass-by noise testing desired range.

To perform the beamforming, a target grid with 3120 points is adopted with squared regular spacing, and kept fixed for all analysis, from conventional beamforming to generalized inverse beamforming, from 50Hz to 7kHz frequencies of analysis. The grid is slightly overextended in the horizontal direction to improve generalized inverse mapping when the source is close to the truck extremity. The full grid is presented in Figure 10.6.

The grid is moved to the truck position for every analysis. The truck position information is based on a photocell trigger signal, placed at -30m from track center, and the speed information is obtained from a Doppler radar positioned in the final track section. With both signals acquired simultaneously with the microphone signals. The sampling frequency is 16.384kHz, and the usage of blocks with 1024 samples implies in a frequency resolution of 16Hz.

The signals are de-Dopplerized in time (PIET *et al.*, 2002) using the position of the center grid point as reference. The averaging strategy is the same for the conventional beamforming and the generalized inverse beamforming, with Cross-Spectral Matrices built from 5 spectrums with 90% overlap respective to each position. The amplitude increase or reduction due to the Doppler effect is also taken into account in the source models for both conventional and generalized inverse beamforming (MORSE & INGARD, 1968).

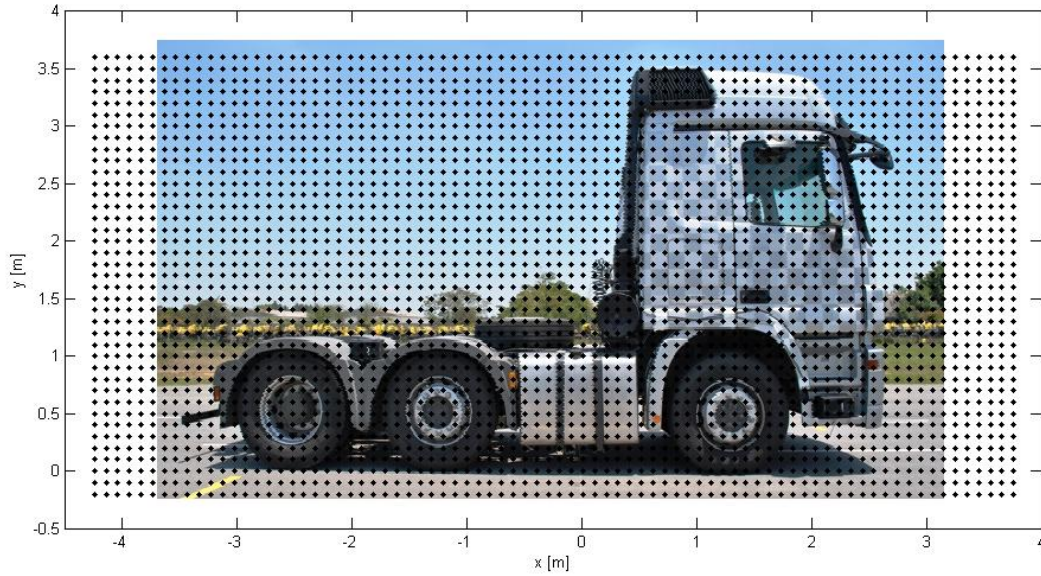


Figure 10.6: Target grid with 3120 points in square regular distribution.

10.3 Experimental Identification Verifications

In this section, identifications of the noise emitted by the loudspeakers are used in constant speed runs to avoid noise from the truck. This testings verify the detection performance in track position range and in frequency range. For this, two types of testings are performed: tonal sound from the front loudspeaker, from 500Hz to 50Hz; and broadband white noise from both loudspeakers in coherent and in incoherent radiation, to be analyzed in the range of 7kHz. These two testings provide a valuable information regarding the antenna combined with the generalized inverse method overall performance in localization and in dynamic range resolution.

The first batch of results to be presented is the generalized inverse results, and two artifices to improve identification are introduced: image source in transfer matrix; and focus compensation for low frequency of analysis. All mappings presented with the hybrid generalized inverse mapping, which is here considered as based on the square of the PSF function to augment the localization detection. Then, the results obtained using the generalized inverse with IRLS scheme are presented. In the end the conventional beamforming results are presented to demonstrate its performance in comparison to the generalized inverse beamforming for the chosen test conditions.

10.3.1 Generalized Inverse Beamforming

The test condition used on the verifications is the passage of the truck with constant speed of 50km/h, and this is done to avoid excessive noise from the truck and mask the noise from the loudspeaker. This condition is done in a relatively high speed to validate detection performance on more representative conditions than used previously. The first batch of tests uses only the front loudspeaker to produce a tonal sound in low frequency. Results for truck positions of $x=0\text{m}$ (truck at track center), -5m , 5m , -10m and 10m , for the speaker sound in 500Hz are presented in Figure 10.7. The algorithm for the generalized inverse method used 30 iterations in all identifications in this Chapter, with the capability to stop truncation if the minimum of the problem cost function (J_1) is reached before the 30 iterations for each of the eigenmodes. When applicable, the result for each eigenmode is summed on its intensity to compose the overall source level. The number of eigenpairs are based on the 10dB range of eigenvalues from the maximum value. Regularization factor is set as 5% of the maximum eigenvalue of the matrix to be inverted.

These points in track are representative of the general performance and they demonstrate that the generalized inverse method is capable to capture the source location on this condition.

Considering that the wavelength for 500Hz is approximately 0.68m, and the reflections of sound in the ground represent an image source separated by less than two wavelengths from the emission center, it creates a mixed perception between the true source and its image. This poses a challenge in any method in trying to separate the true source location from its distorted estimation by the reflection. For the generalized inverse results, this effect can be seen on the more distant positions, where the center of radiation is estimated as closer to the ground than it is in reality.

On the track center mapping is clear the higher resolution of the estimation in horizontal direction which is a result of the array distribution, to better locate the sources on longitudinal aspect. The extreme positions present a bigger localization error with maximum of 0.5m error in the 10m position.

In order to improve the localization center and decrease the influence of the image source (reflections on ground), an artifice is developed and introduced in the next section.



Figure 10.7: Identifications of front loudspeaker with tonal 500Hz and Truck at constant speed of 50km/h for various track positions. Mappings are 3rd oct. SPL (A-Weighted) at pass-by noise microphone position.

10.3.2 Use of Image Source in Transfer Matrix

Reflections on the ground can be very complex to model, since they have dependence in frequency and in angle of incidence. On this work, a simplified approach is adopted, and a reflection of 10% in amplitude is considered as a secondary (image) source in the transfer function for each grid point. No dependence in frequency neither angle of incidence is considered on this simplified model. The results for the previous case, truck at 50km/h and loudspeaker with tonal sound at 500Hz are estimated again and presented in Figure 10.8.

There is a slight improvement in the localization region for the cases where the truck is at $x=0\text{m}$, -5m and 5m , but on the extremes $x=10\text{m}$ and -10m , this is not observed. Since the main region of interest is the region between -5m and 5m , this artifice is kept in the algorithm for the further analyzes.

On the second test, the front loudspeaker is emitting a tonal sound at 300Hz, and results are presented in Figure 10.9.

The localization of the 300Hz source center is rather accurate for the positions of $x=0\text{m}$, -5m and -10m , but the $x=5\text{m}$ and 10m demonstrated an error of about 1m. This could be explained by a wave spreading change due to wave scattering on the truck rear surfaces and/or loudspeaker wave radiation differing from the pure spherical wave radiation.

Since the actual characteristics of the wave emitted by the loudspeaker is not known, it is expected an intermediate wave front between the pure spherical and the plane propagation. This impact the localization that considers a pure spherical radiation in producing a false source location behind the actual source center. This effect is expected to be increased with the angle of detection as on the extreme positions of the truck. This effect can be reduced if the target grid is positioned also behind the actual expected true source location and an artifice is introduced in the next section to improve results on these conditions.



Figure 10.8: Identifications of front loudspeaker with tonal 500Hz using image source in transfer matrix and truck at constant speed of 50km/h for various track positions. Mappings are 3rd oct. SPL (A-Weighted) at pass-by noise microphone position.

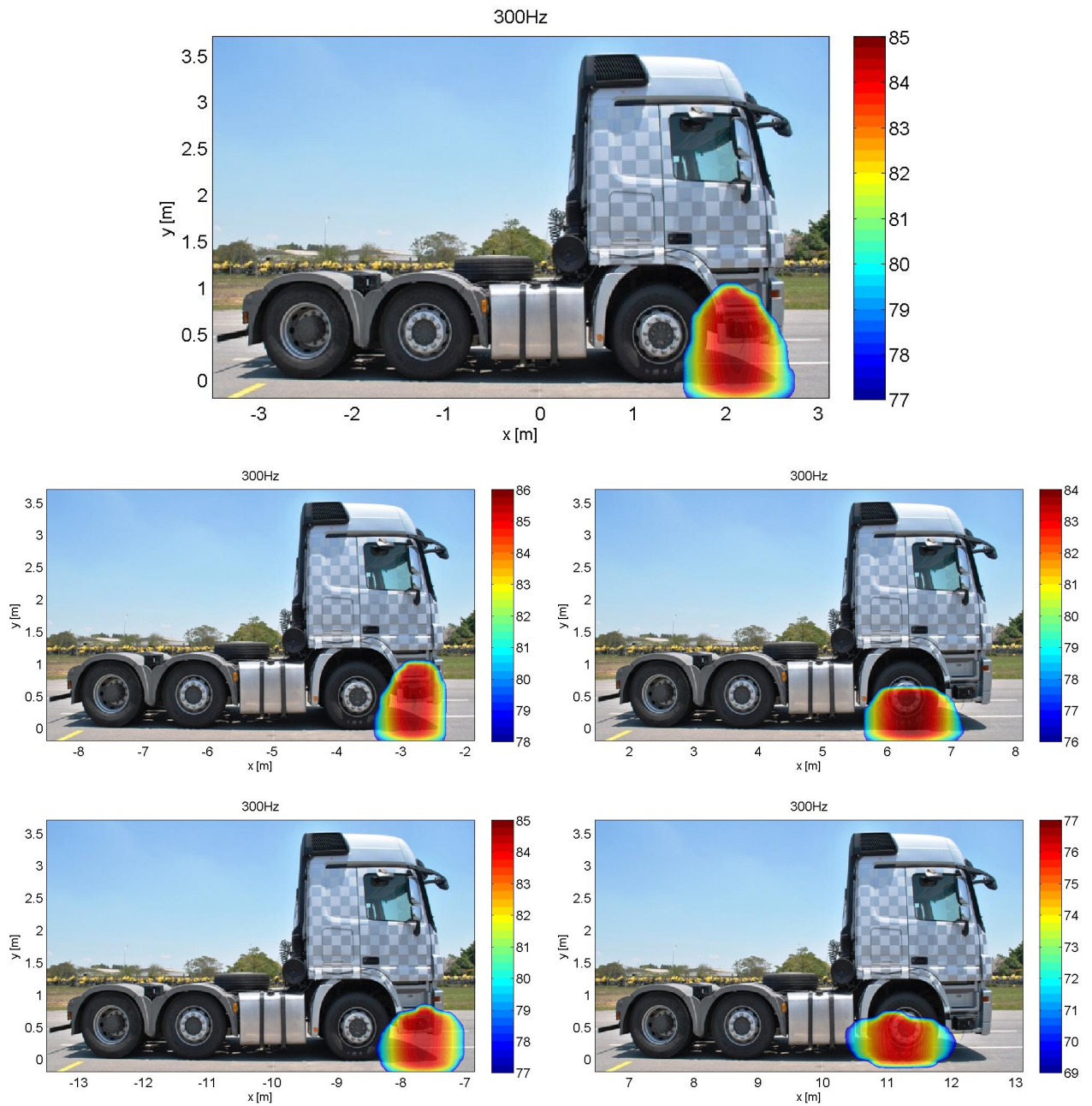


Figure 10.9: Identifications of front loudspeaker with tonal 300Hz and truck at constant speed of 50km/h for various track positions. Mappings are 3rd oct. SPL (A-Weighted) at pass-by noise microphone position.

10.3.3 Use of Low Frequency Focus Compensation

Since the actual loudspeaker directivity is unknown and considering the previous estimation results, a focus compensation is introduced based on the wavelength of analysis, for estimations below 500Hz. This compensation is to move the target grid about 60% of the wavelength in analysis in the direction perpendicular to the truck path. This empirical artifice is tested and results presented in Figure 10.10.

Basically, this artifice of moving the target grid further away improves the localization on the cases where $x=5\text{m}$ and 10m , while slightly deteriorating the localization on the $x=-5\text{m}$ and -10m , with maximum error reduced to 0.6m . This is presented as an option to the analyst, based on the verifications.

One of the possible causes that can explain the localization error is the occurrence of small deviations of the truck path along the passage, with deviations of 0.3m for example, causing source localization errors of similar size. In any case, the focus compensation artifice is kept on the algorithm of identification for analysis below 500Hz as an improvement measure.

The following performed test is for the front loudspeaker with tonal radiation of 200Hz, and results are presented on Figure 10.11. On this case, the localization is quite accurate for truck positions of $x=-5\text{m}$ to 5m , but for $x=10\text{m}$, it presents an error of 1.5m . Since the main range of interest is the -5m to 5m range, the results are considered acceptable.

The following test is for the front loudspeaker with 100Hz tonal radiation, with results shown in Figure 10.12, and again, the major error is found for the truck as $x=10\text{m}$ position. The cases where the truck is at -5m and 5m are still acceptable, with errors of about 0.5m . This is small when compared to the wavelength of radiation, on this case, about 3.4m .

The last low frequency test, with front loudspeaker with tonal 50Hz radiation, have results presented in Figure 10.13. This is the most challenging condition of identification, with wavelength of approximately 6.8m , and comparable to the size of array in horizontal direction. Despite of that, the generalized inverse method is still capable to bring a localization that is quite accurate, with maximum error of 0.8m on the $x=0\text{m}$ truck position. This is an impressive result and new in literature for estimation performance in very low frequency of analysis using beamforming.

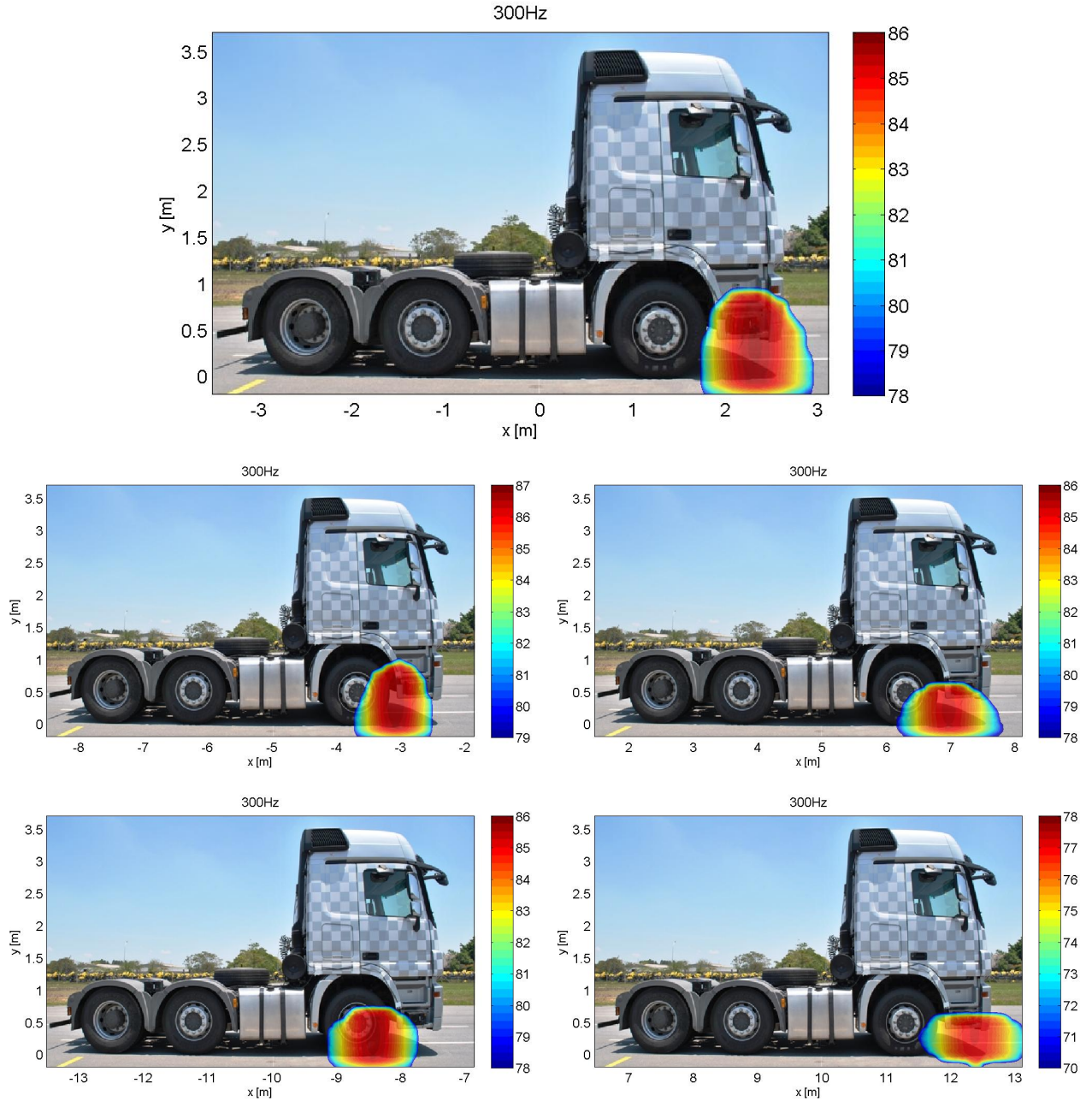


Figure 10.10: Identifications of front loudspeaker with tonal 300Hz using low frequency focus compensation and truck at constant speed of 50km/h for various track positions. Mappings are 3rd oct. SPL (A-Weighted) at pass-by noise microphone position.

The error in the position where the truck is in front of the array suggests that the focus compensation should be even higher to improve the result in this condition, but this study is considered out of the initial scope of this work, and is left as a suggestion for future research: a method to evaluate and determine the best focus distance for low frequency sources with unknown



Figure 10.11: Identifications of front loudspeaker with tonal 200Hz using low frequency focus compensation and truck at constant speed of 50km/h for various track positions. Mappings are 3rd oct. SPL (A-Weighted) at pass-by noise microphone position.

directivities.



Figure 10.12: Identifications of front loudspeaker with tonal 100Hz using low frequency focus compensation and truck at constant speed of 50km/h for various track positions. Mappings are 3rd oct. SPL (A-Weighted) at pass-by noise microphone position.

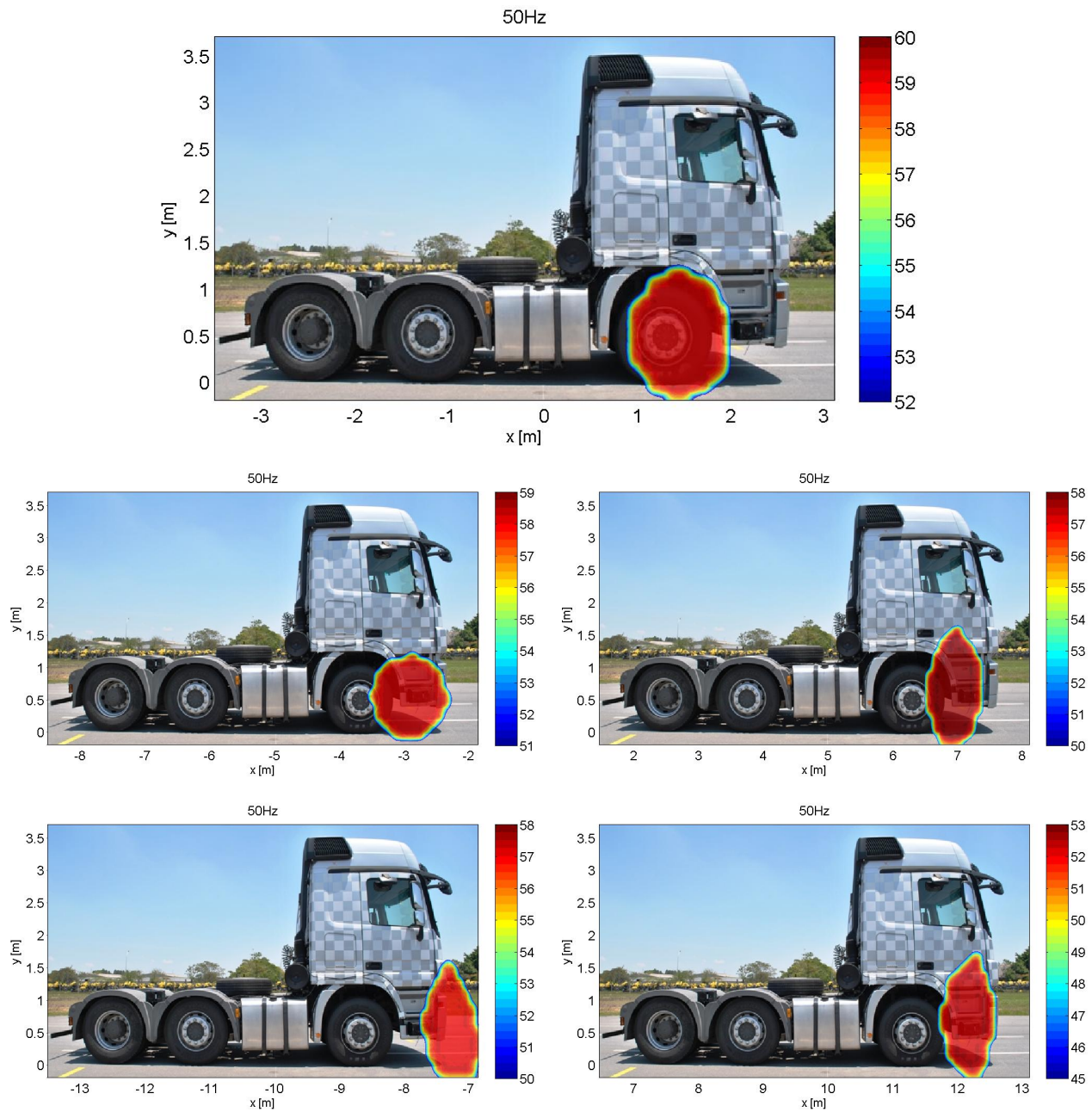


Figure 10.13: Identifications of front loudspeaker with tonal 50Hz using low frequency focus compensation and truck at constant speed of 50km/h for various track positions. Mappings are 3rd oct. SPL (A-Weighted) at pass-by noise microphone position.

10.3.4 Coherent and Incoherent Broadband Sources Identification

In order to demonstrate or verify the identification performance for higher frequency range, two cases are studied, both with truck at constant speed of 50km/h: both loudspeakers with broadband white noise in coherent radiation (same input signal); and both loudspeakers with broadband white noise in incoherent radiation (two incoherent signal inputs). The chosen frequency range is with 3rd octave band centered at 7kHz. This frequency range covers the majority of high frequency desired analysis in pass-by of trucks. The results for the identifications on the first case, coherent radiation from speakers are presented in Figure 10.14.

On the center track position result, both loudspeakers are observed, with a slight difference in level, on the expected range of 2dB. On the $x=-5\text{m}$ and $x=5\text{m}$, the source which is closer to the array is captured, but the other is not identified. This could be explained by the second source being out of the range compared to the primary source level. This is repeated on the positions of $x=-10\text{m}$ and $x=10\text{m}$, where also an increased error is observed, with maximum value of 0.3m on the $x=-10\text{m}$ case.

Those results can be considered exceptionally accurate considering that no relevant spurious peaks are observed in the range of 8dB for the $x=-5\text{m}$ to $x=5\text{m}$ positions, with no significative errors on localization. The second case of loudspeakers radiation is with incoherent emission, and results are presented in Figure 10.15.

On the incoherent case, both sources are still located for truck at $x=0\text{m}$, but rear speaker presents a lower level on the identification that on the coherent case. Also, some spurious peaks appeared on mapping. This result shows more difficulty to track both sources on the incoherent case, maybe because the energy is spread in more eigenpairs than that on the coherent case, reducing the resolution.

The identifications for truck positions of $x=-5\text{m}$ and $x=5\text{m}$, showed similar performance that the coherent case, and positions of $x=-10\text{m}$ and $x=10\text{m}$, showed more distortion on the source localization, with an unclear source center at the $x=-10\text{m}$ position.

These results are considered accurate on the main range of interest, from $x=-5\text{m}$ to $x=5\text{m}$, with no significative errors in localization for the impressive range of 7kHz 3rd octave band.

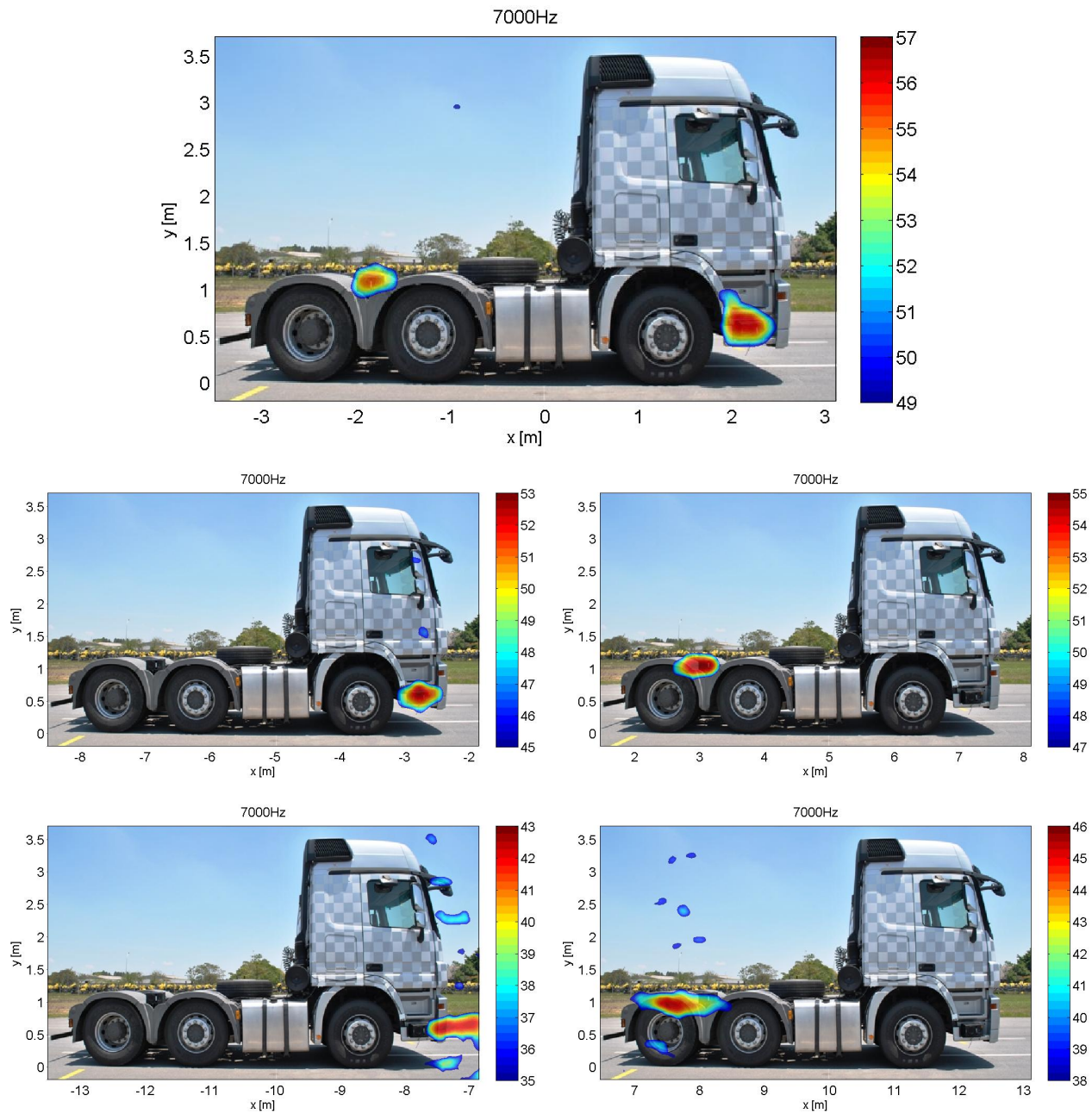


Figure 10.14: Identifications on 7kHz 3rd oct. of front and rear loudspeakers with coherent white noise and truck at constant speed of 50km/h for various track positions. Mappings are 3rd oct. SPL (A-Weighted) at pass-by noise microphone position.



Figure 10.15: Identifications on 7kHz 3rd oct. of front and rear loudspeakers with incoherent white noise and truck at constant speed of 50km/h for various track positions. Mappings are 3rd oct. SPL (A-Weighted) at pass-by noise microphone position.

10.3.5 Generalized Inverse Beamforming with IRLS Scheme

The generalized inverse method is applied with the use of an Iteratively Re-Weighted Least Squares (IRLS) scheme. This section bring the results obtained by this method for the previously shown test cases. The algorithm use 1 iteration only, with regularization of 5% of the matrix to be inverted. Results for the first case, front loudspeaker with tonal sound of 500Hz, is shown in Figure 10.16.

This first result is very similar to the ones which uses the generalized inverse without IRLS scheme, and present accurate source localization for most of the positions, with some deterioration on the $x=10\text{m}$ truck position, failing to clearly estimate the source location center, with probable error of 0.5m. Even though, the localization in the range of $x=-5\text{m}$ to $x=5\text{m}$ present a smaller region of detection, with spreading towards the ground region.

The second considered analysis is the front loudspeaker with a tonal emission of 300Hz, shown in Figure 10.17. On this case, all the identifications are considered acceptable with exception of the $x=10\text{m}$ position, where the source location seems to be placed in a higher position. The use of IRLS seems to locate the source with just one iteration (much faster), on the other hand, it is more fragile to bring accurate results on the cases where the identification is on its limits, on the track extremes for example. The use of more iterations don't improve results and even produce worst localizations than it is shown.

The third considered test case is when the front loudspeaker radiates a tonal sound with 200Hz, shown in Figure 10.18. Results show higher localization error, even in the range of $x=5\text{m}$, where a higher source position is estimated. The results for $x=-10\text{m}$ and $x=10\text{m}$ demonstrates a bigger spreading in localization than the generalized inverse method without the IRLS. Thus, the IRLS scheme is not recommended for analysis below 200Hz on the measured test conditions.

Now, on the case where both loudspeakers are emitting a coherent white noise radiation, analysis for the 7kHz 3rd octave band are presented in Figure 10.19.

The identification presents rather accurate localization on the case where the truck is at $x=0\text{m}$ position, with a slight deterioration in the level estimation for the rear loudspeaker. Is important to note that the same measurement data is used for both analyzes, and source levels seems to be underestimated when compared to the results obtained without IRLS scheme. The identification for



Figure 10.16: Identifications of front loudspeaker with tonal 500Hz using IRLS scheme and truck at constant speed of 50km/h for various track positions. Mappings are 3rd oct. SPL (A-Weighted) at pass-by noise microphone position.

$x=-5\text{m}$ and $x=5\text{m}$ positions, brings an impressively accurate source localization, considering that only one iteration is used. On the other hand, the $x=-10\text{m}$ and $x=10\text{m}$, brings errors of up to 0.4m, but with smaller deterioration when compared to the results without IRLS.



Figure 10.17: Identifications of front loudspeaker with tonal 300Hz using IRLS scheme and truck at constant speed of 50km/h for various track positions. Mappings are 3rd oct. SPL (A-Weighted) at pass-by noise microphone position.

Results for the case when loudspeakers radiation are in incoherent radiation are shown in Figure 10.20. For $x=0\text{m}$ truck position, the rear loudspeaker is not located, and a spurious peak is present on the mapping. For positions of $x=-5\text{m}$ and $x=5\text{m}$ the localization seems quite accurate, and for positions of $x=-10\text{m}$ and $x=10\text{m}$, the method is still capable to locate the source centers, with

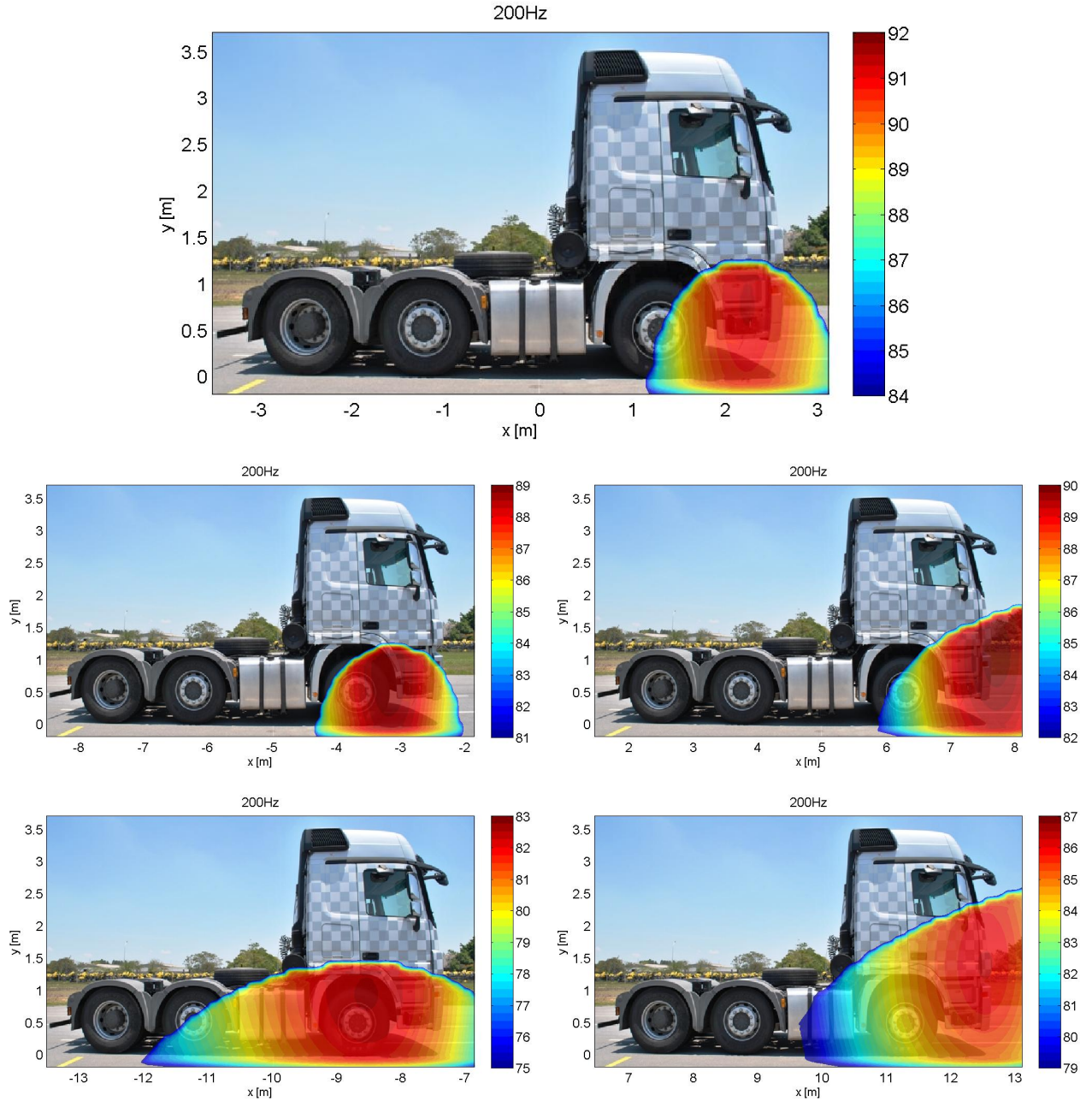


Figure 10.18: Identifications of front loudspeaker with tonal 200Hz using IRLS scheme and truck at constant speed of 50km/h for various track positions. Mappings are 3rd oct. SPL (A-Weighted) at pass-by noise microphone position.

error of approximately 0.6m on the $x=-10$ case, and less deterioration of mapping when compared to the method without IRLS.

In summary, the use of IRLS scheme seems to improve localization of the main region of



Figure 10.19: Identifications on 7kHz 3rd oct. of front and rear loudspeakers with coherent white noise using IRLS scheme and truck at constant speed of 50km/h for various track positions. Mappings are 3rd oct. SPL (A-Weighted) at pass-by noise microphone position.

radiation with the cost of loosing accuracy on secondary source regions. It is recommended to always check both mappings when above 200Hz, with respect to localization and levels estimation, since the use of IRLS scheme seems to be more sensitive to limit conditions of identification as well as to capture the source levels differences along regions of radiation.



Figure 10.20: Identifications on 7kHz 3rd oct. of front and rear loudspeakers with incoherent white noise using IRLS scheme and truck at constant speed of 50km/h for various track positions. Mappings are 3rd oct. SPL (A-Weighted) at pass-by noise microphone position.

10.3.6 Conventional Beamforming

Conventional beamforming mappings are generated for comparison to the ones obtained by the generalized inverse method. It basically uses the same starting point information basis, the same Cross-Spectral Matrix, also with the same de-Dopplerization in time and Doppler amplitude effect compensation, and artifices used on the previous results: image source on transfer function; and focus compensation for low frequency analysis. The same grid is used to generate mappings, and results are presented from Figure 10.21 to 10.24, to cases of front loudspeakers with tonal sound at 500Hz and 300Hz, and analysis at 7kHz for loudspeakers with white noise in coherent and incoherent radiation.

The first result, front loudspeaker with tonal sound at 500Hz present reasonable localizations for the positions of $x=-5\text{m}$ to $x=5\text{m}$, but starts to loose tracking on the passage extremes, $x=-10\text{m}$ and $x=10\text{m}$. The second result, tonal sound at 300Hz (front speaker), present an even worst identification, with a totally lost tracking on the passage extremes. The limitation of the conventional beamforming to detect sources of low frequency of radiation is known and this limit is considered as 300Hz for the measured test setup and conditions.

Now, if the analysis of both sources in broadband radiation in coherent mode is considered, the identification on the 7kHz 3rd oct. band, shown in Figure 10.23, is able to capture both source centers of radiation for position $x=0\text{m}$, but also bring sidelobe effects due to the dynamic range in mapping, 8dB range. On the other positions, the closest source to the array is captured along with the sidelobe effects, which are deteriorated since the identification focus is farther from central array focus.

The incoherent sources radiation case brings slightly worst results than the coherent case, with a totally lost tracking on the position of $x=10\text{m}$. On this case, is rather difficult to separate the true source location from the sidelobe peaks on the mappings.

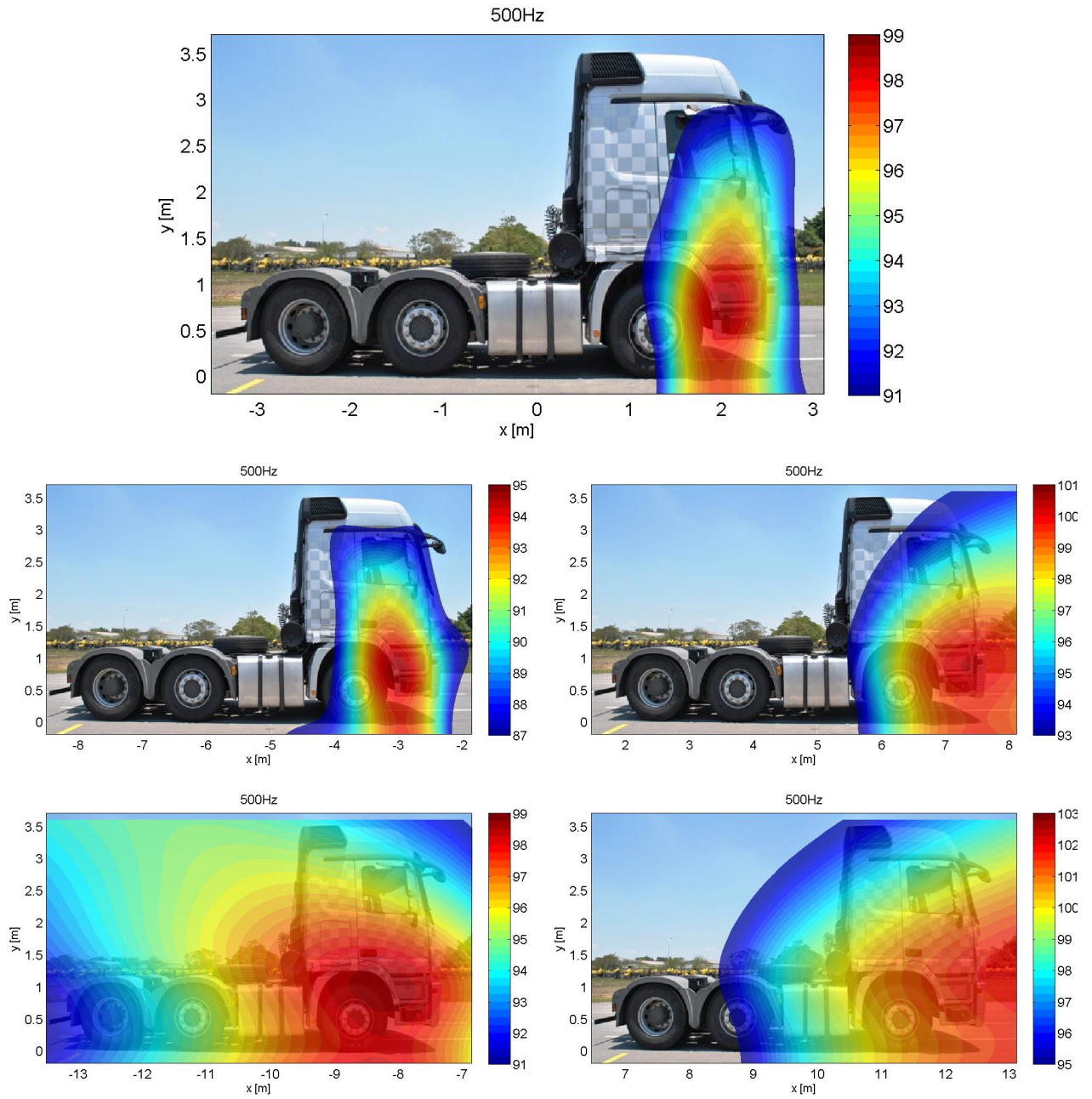


Figure 10.21: Identifications of front loudspeaker with tonal 500Hz using conventional beamforming and truck at constant speed of 50km/h for various track positions. Mappings are 3rd oct. SPL (A-Weighted) at pass-by noise microphone position.

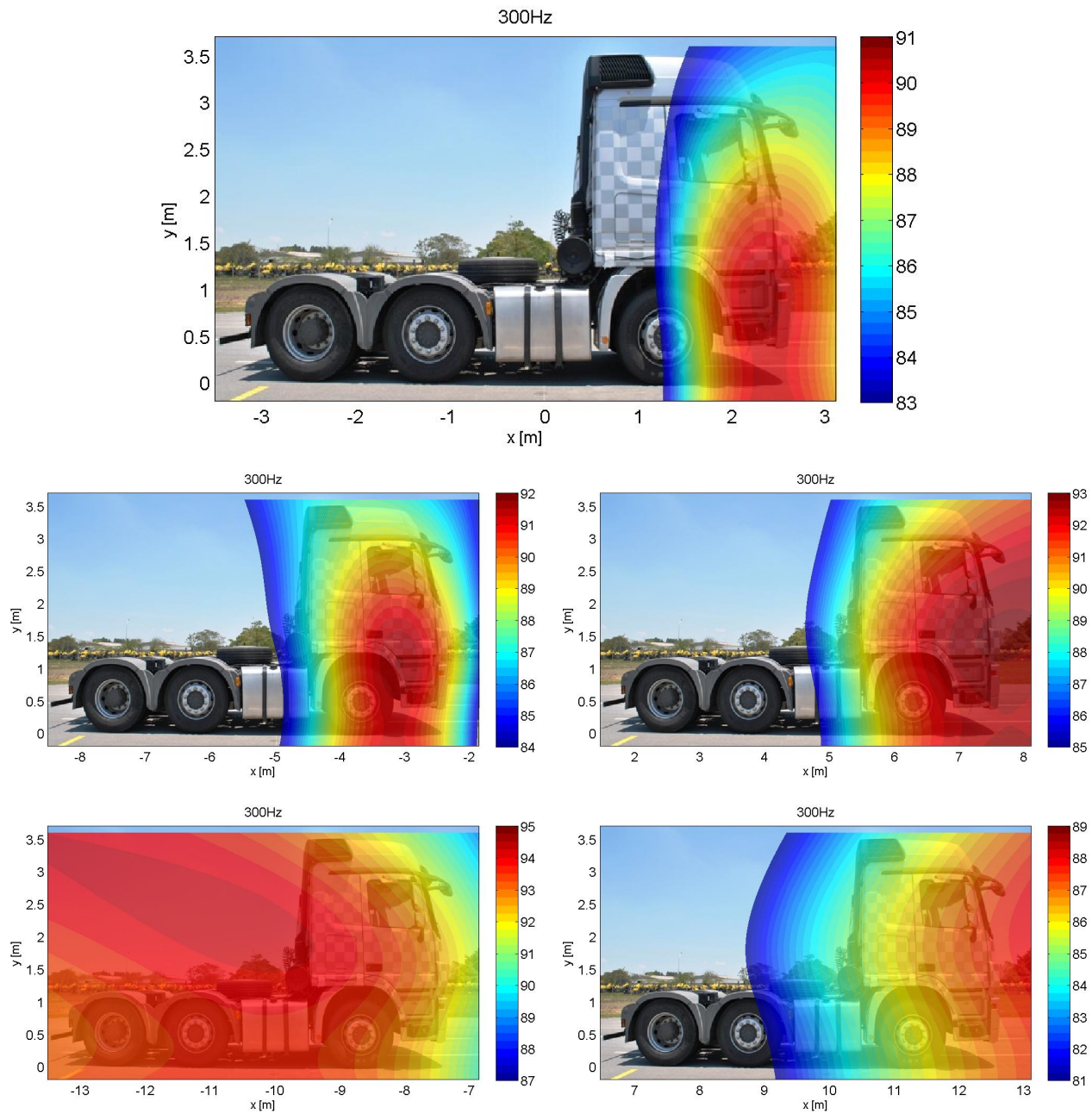


Figure 10.22: Identifications of front loudspeaker with tonal 300Hz using conventional beamforming and truck at constant speed of 50km/h for various track positions. Mappings are 3rd oct. SPL (A-Weighted) at pass-by noise microphone position.

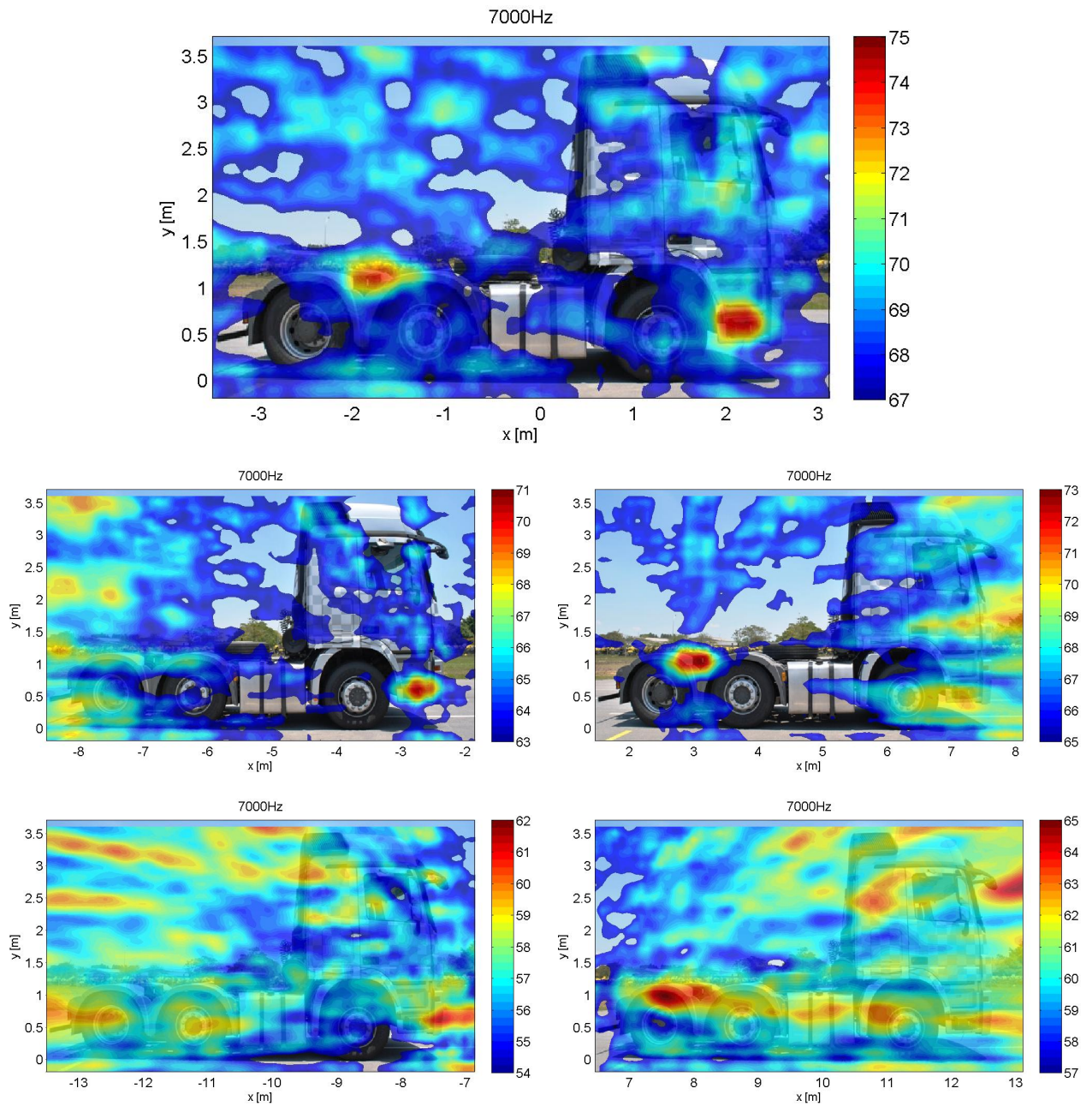


Figure 10.23: Identifications on 7kHz 3rd oct. of front and rear loudspeakers with coherent white noise using conventional beamforming and truck at constant speed of 50km/h for various track positions. Mappings are 3rd oct. SPL (A-Weighted) at pass-by noise microphone position.

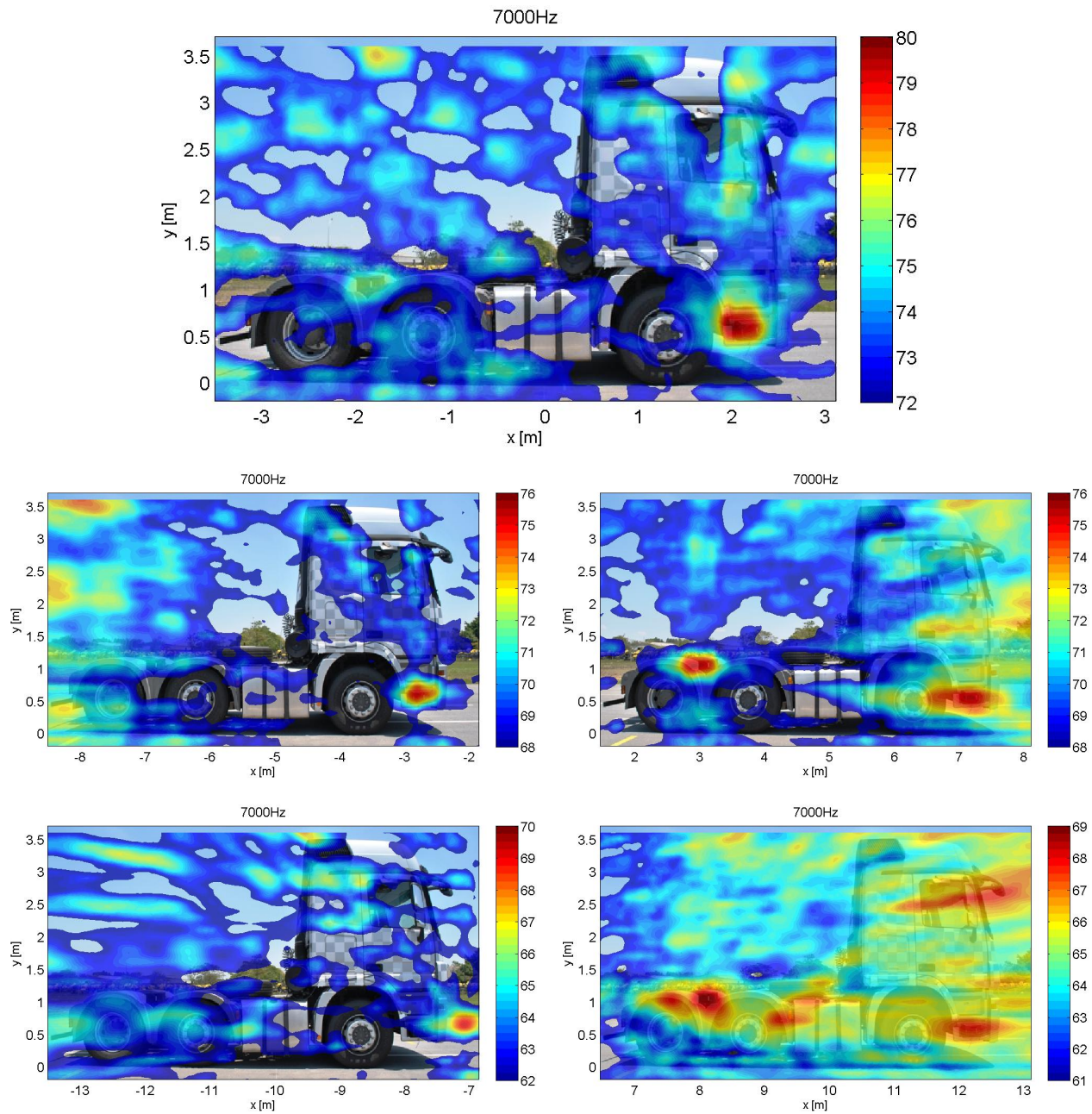


Figure 10.24: Identifications on 7kHz 3rd oct. of front and rear loudspeakers with incoherent white noise using conventional beamforming and truck at constant speed of 50km/h for various track positions. Mappings are 3rd oct. SPL (A-Weighted) at pass-by noise microphone position.

10.4 Truck Noise Identification

After the verifications using loudspeakers and constant truck speeds, real test conditions (accelerating tests) are performed with loudspeakers turned off and with truck start speed of 30km/h and 50km/h, in 10th and 12th gears, respectively. One side of truck assessment is presented for simplicity. Results of the pass-by noise level along passage for these two entry speed conditions are presented in Figure 10.25.

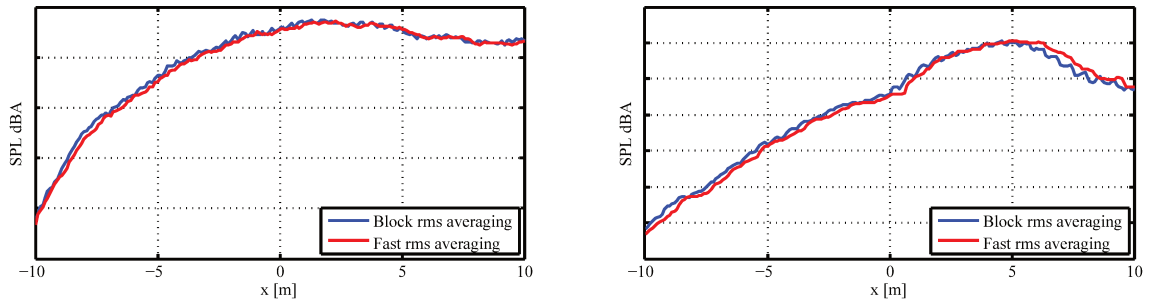


Figure 10.25: Pass-by noise level along runs with start at 30km/h using 10th gear (left) and 50km/h using 12nd gear. Scale on level has 2dBA per division.

On these two examples, the level (A-Weighted) is assessed using the fast averaging mode (standard 125ms time window) and confronted to the related block rms level, showing the small time lapse between them, and supporting the proper truck position to be analyzed. On this cases, the chosen positions are $x=2\text{m}$ for the 10th gear and $x=5\text{m}$ for the 12th gear.

With the two positions corresponding to the pass-by maximum levels, identifications are performed for two types of analysis: considering the peak frequency level and its 3rd oct. band; and as example, the engine 3rd order and its 3rd oct. band.

10.4.1 Identification of Peak Noise Emission

Identifications using the generalized inverse without and with IRLS, and conventional beamforming are generated for the peak noise emission positions. The results for the start speed of 30km/h are shown in Figure 10.26 and for the start speed of 50km/h are shown in Figure 10.27.

All identifications are in agreement in terms of main region of radiation. The conventional beamforming present the biggest region of localization in 8dB dynamic range, and the generalized

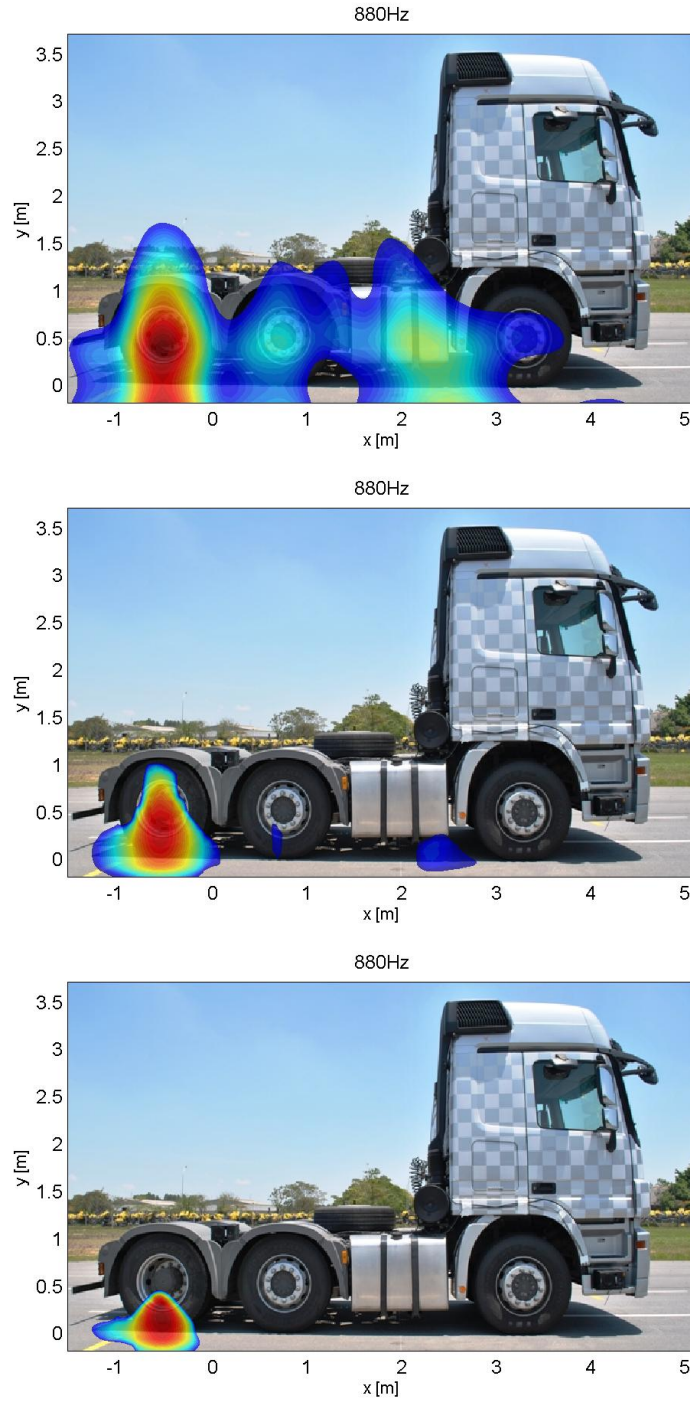


Figure 10.26: Identification for peak frequency level using conventional beamforming (top), generalized inverse without and with IRLS scheme (bottom) for start speed of 30km/h and truck at $x=2\text{m}$ track position. Mappings are 3rd oct. SPL (A-Weighted) in 8dB range at pass-by noise microphone position.

inverse with IRLS, the smallest region of localization. The levels are lower in the hybrid generalized inverse mappings and probably are closer to the real sources level, considering that the hybrid estimation level also suffers from the mainlobe overestimation on distributed sources, as previously discussed for the conventional beamforming.

On the 30km/h start speed case, the hybrid generalized inverse mappings points to the rear tire region which is in contact with the ground, probably the one which is most demanded in the acceleration loading, as expected. For the case of 50km/h start speed, again the same region is identified, but region of localization is slightly deviated towards the rear of the truck. This effect, could be influenced also by the position of the truck starting to be out of the main region of array focus.

10.4.2 Identification of Main Engine Order at Peak Noise Emission Position

Two main engine order noise analyzes are used as example of identification on very low frequency range, around 50Hz. The identifications also used the 3rd oct. band for analysis and results for the two start speeds are presented in Figure 10.28 and 10.29.

On this frequency range, only the conventional and the generalized inverse beamforming without the IRLS scheme are presented. The conventional beamforming identification on the first case, start of 30km/h, totally loose the tracking of the source center, while the generalized inverse present the source center in an intermediate truck position, close to the exhaust tailpipe (behind the fuel tank).

For the test with start speed of 50km/h, again the conventional beamforming loose tracking of the source center, while the generalized inverse shows the same region as found in the 30km/h entry speed test. This result, while not being the responsible for the peak level, demonstrates that very low frequencies can be analyzed for real test conditions, as it was verified by the loudspeaker tests.

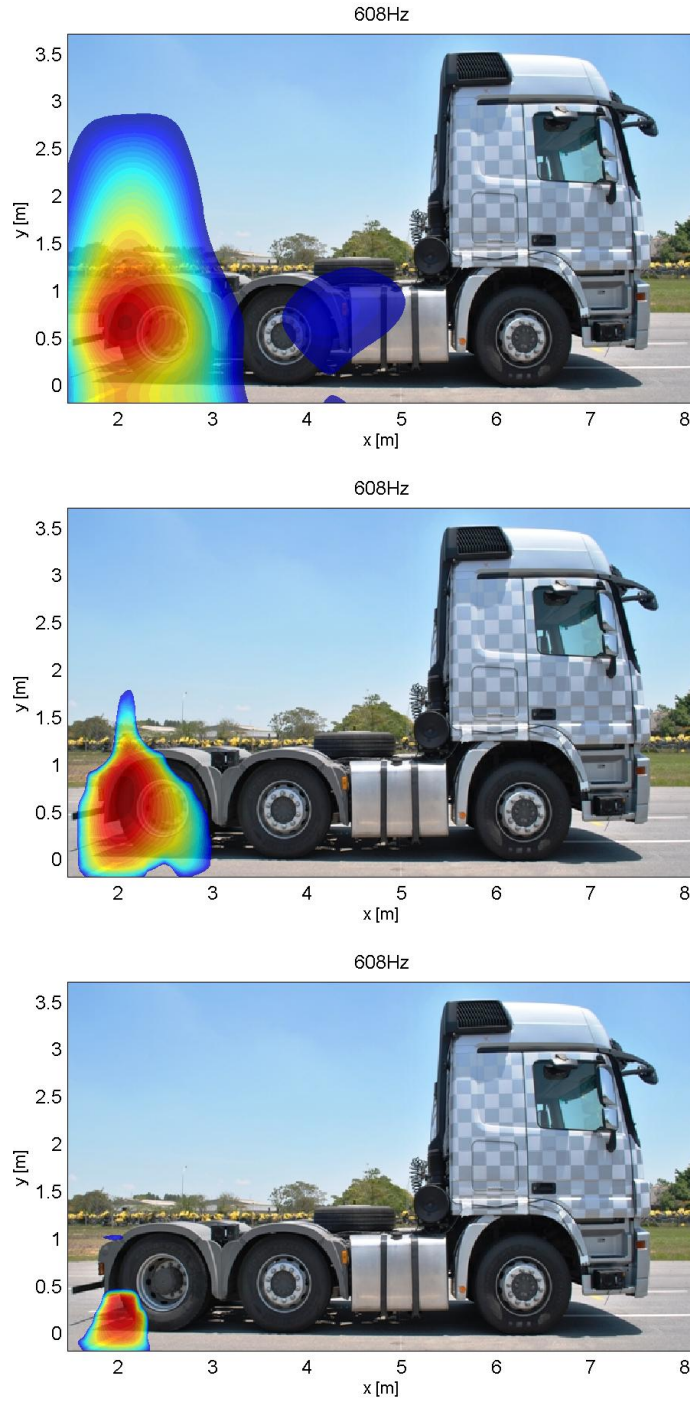


Figure 10.27: Identification for peak frequency level using conventional beamforming (top), generalized inverse without and with IRLS scheme (bottom) for start speed of 50km/h and truck at $x=5\text{m}$ track position. Mappings are 3rd oct. SPL (A-Weighted) in 8dB range at pass-by noise microphone position.

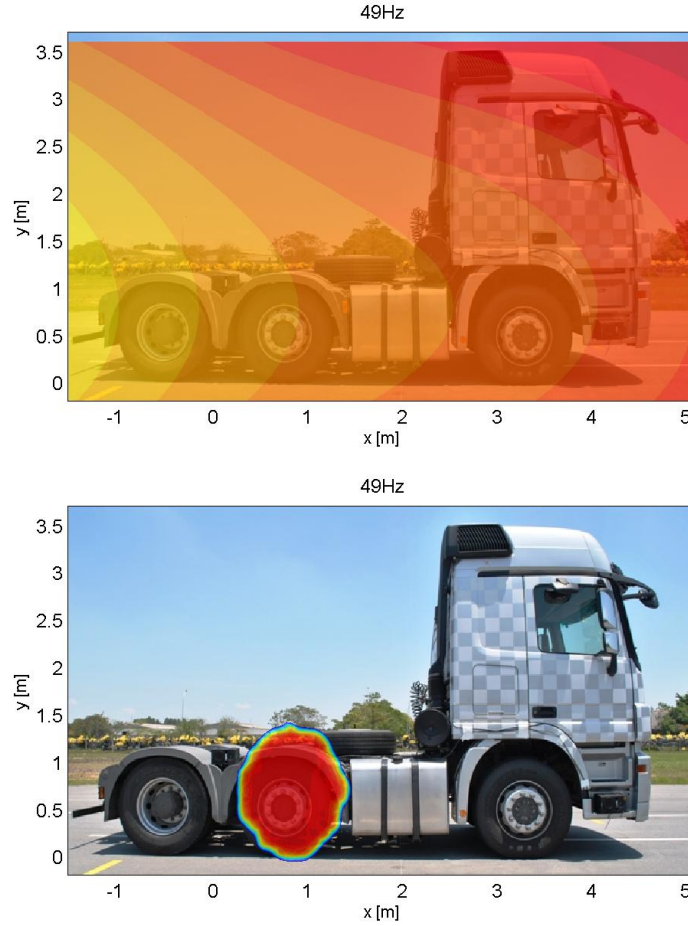


Figure 10.28: Identification for 3rd order level using conventional beamforming (top) and generalized inverse without IRLS scheme for start speed of 30km/h and truck at x=2m track position. Mappings are 3rd oct. SPL (A-Weighted) in 8dB range at pass-by noise microphone position.

10.5 Summary

The proposed artifices to improve localization demonstrated their contributions on source center determination based on the verification tests performed with known sources. Two frequency ranges of analysis provided evidences that the method works in the full desired range, from very low frequencies such as 50Hz, to high frequencies such as 7kHz.

The high quality in identification provided by the generalized inverse methodology is demonstrated when compared to the conventional beamforming on moving source tests, using known sources, and also for real truck noise sources. The objective here is not to discuss these truck

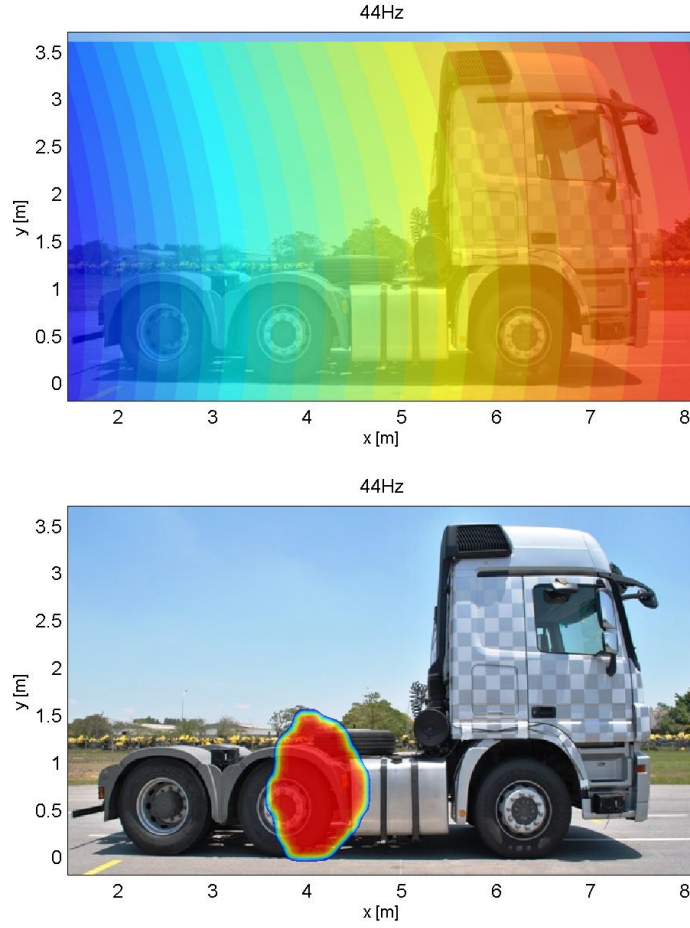


Figure 10.29: Identification for 3rd order level using conventional beamforming (top) and generalized inverse without IRLS scheme for start speed of 50km/h and truck at x=5m track position. Mappings are 3rd oct. SPL (A-Weighted) in 8dB range at pass-by noise microphone position.

sources but to provide evidences that this new methodology, the generalized inverse beamforming, is a reliable and robust approach to these test conditions, identification of truck pass-by noise sources.

11 Conclusions

In this Chapter, the main conclusions on the development of an identification method based on generalized inverse beamforming for aeroacoustic problems and moving source problems are discussed. The main advantages are raised in face of the obtained results, and, on the other hand, the disadvantages, also named areas for improvements, are brought to light and discussed. In the end, the main contributions to the research field in aeroacoustic source identification and in moving source localization are outlined, together with the future work left as suggestion.

11.1 Introduction

The structure behind this research can be summarized as testing the generalized inverse beamforming method initially for simple problems with simulated and experimental data, and, after this phase, the application to more complex test cases, again using simulations and experimental data.

This approach proved to be an important and necessary research practice throughout this research, avoiding jumping into conclusions without prior verifications in simpler cases.

The monopole and dipole identification is first experimentally verified using compact sources in a semi-anechoic test room. This preliminary phase was important to develop, for example, the hybrid estimation.

After this preliminary experimental verification phase, more complex problems were analyzed and a detailed discussion is presented in the following sections.

11.2 Aeroacoustic Source Identification

The second experimental phase consisted in the cylinder section testing, a simple and known in the literature aeroacoustic problem. The third and fourth test phases have more complex source distributions, with tests for two squared profile structures and an standard airfoil under subsonic flow.

11.2.1 Dipole over Cylinder in Subsonic Jet

Aeroacoustic sources generation is basically a stochastic process. However, for deeper source generation mechanism investigation, the identification certainly demands newer approaches than traditional one.

In this work, the dominant sound emission event is separated and treated as an important isolated event when received signals at the array possess enough coherent distribution to be used to characterize important regions of source distribution. These dominant emissions can vary in frequency, in time period, and in location.

The general conclusion is that for higher frequencies, the dipole direction seems to deflect towards the downstream direction, and the region on the obstacle surface also moved in downstream direction. This indicates that detachment of fluid from the cylinder surface, which leads to pressure fluctuations in surface, would cause different radiation frequencies and durations depending on its position along surface.

The observation of single events is a new proposed approach and is helpful to link acoustic radiation to possible fluid characteristics such as turbulence around the obstacle.

If source radiation is taken into consideration as a stationary process, the results showed a spiral like radiation pattern, with two main regions in the cylinder downstream surface, in upper and bottom region, as expected. These two regions are the most probable regions for fluid separation and thus, source generation.

The spiral like pattern, on the other hand, doesn't correspond to a well behaved dipole formation orthogonal to the flow direction as indicated by the literature, but could be associated to a dipole intermittent formation between upper and bottom regions, similar to the vortex shedding generation, also known as Von Kármán Vortex Street (VON KÁRMÁN, 1963). The observed radiation pattern also could be interpreted as a rotating dipole with intermittent center of radiation between upper and bottom cylinder regions.

The identification based on the generalized inverse method demonstrated its quality to allow generation of equivalent far-field pressure mappings (based on identified sources), and directivity plots, of great importance to later development of noise reduction solutions.

The disadvantage is the difficulty to separate a good quality mapping from spurious results, where a good quality mapping is clearly dependent on several aspects, such as source type, location, grid distribution and spacing, frequency resolution, regularization, number of iterations, etc.

11.2.2 Two Structures in Subsonic Flow

The two-structures testing in a open wind tunnel at NLR allowed a direct comparison from conventional beamforming results obtained by that research center to results generated in this thesis with conventional beamforming and generalized inverse beamforming.

The comparison showed that the high quality mappings from the conventional beamforming could be obtained also by inverse methods for monopole identifications, and even a higher resolution is observed for low frequency center of radiation, and high frequency region localization on inverse methods.

With the use of line source distributions based in the literature, coherence length in simulations provided an important mapping interpretation reference to be used on experimental data analysis. The use of auto-powers attenuation proved to be a valuable measure to improve resolution on inverse mappings, comparable to cross-spectral matrix diagonal removal in the conventional method. The hybrid generalized inverse mapping also created a comparable source level reading to conventional mapping, an important analysis tool.

The dipole distribution identification followed the expected surface distribution, represented by two grid strategies: a line grid and a 3D grid. The generalized inverse beamforming with IRLS presented a higher resolution in source localization, with detection of specific structure corners that are probably related to high pressure fluctuations, facing turbulence or with flow separation.

The use of hybrid generalized inverse mapping proved to be a valuable visualization aid for smooth distribution analysis. The transfer matrix re-scaling also proved to be a necessary step to obtain dipole orientation identification when there is significative dipole component towards the array direction.

Directivity assessments were made and comparisons to far-field microphones showed a good agreement if original cross-spectral matrix is considered. The directivity estimation is possible

since dipole orientation identification by the generalized inverse method is done for its orthogonal components, and a full 360° directivity assessment is made. For these cases, the line grid showed slightly better results, and a symmetry is kept in all 360° range.

Wall-pressure transducer analysis showed that regions of high pressure may not directly indicate source center. Despite that, there is coherence between the pressure distribution and dipole distribution as identified by the generalized inverse method.

11.2.3 NACA-0012 Airfoil in Subsonic Flow

Tests conducted with a standard airfoil, NACA-0012, at the closed wind tunnel facility from EESC-USP, allowed a comparison of mappings obtained by conventional and generalized inverse with and without IRLS beamformings. The results are in agreement with the literature results based on DAMAS2. The reverberant condition in this testing setup proved to be a big challenge to the inverse method since all energy contributions are spread over eigenvalues, and identification can be lost if the exact location is not represented on the target grid, as observed for low frequency of analysis, where sound from fan may have caused the method to fail to locate sources.

Despite that, in general, sources are identified distributed in the trailing edge, as it is reported in the literature, and consistency of the localization throughout test speed conditions demonstrate that convection modeling is correctly implemented.

11.3 Moving Source Identification

The last two test phases are passenger and truck pass-by noise source identification. The generalized inverse method is applied to a non-stationary condition in a fast transient test.

11.3.1 Passenger Vehicle Pass-by Noise

The results demonstrated that the adopted simplifications, including de-Dopplerization, are valid, but some attention is required to considered time period, frequency resolution, and averaging strategy in order not to deteriorate results.

High accuracy is achieved for validation with a known source, even considering that the array is close to the vehicle path. A clear source region center is pointed for very low frequencies, such as engine 2nd order, a real breakthrough in the available literature.

The potential is evident in source localization, however, some drawbacks can also be mentioned based on test results: sensitivity of the method to the identification parameters, sensitivity to microphone signals noise, localization dependance on vehicle speed, and distance to array accuracy.

11.3.2 Truck Pass-by Noise

The observed capacity of localization in lower frequencies when compared to the conventional beamforming inspired the application of generalized inverse beamforming in truck pass-by noise source identification.

This application required a special array design, with higher resolution in horizontal direction, and centered at pass-by microphone position, which allowed the report of the source level contribution to the pass-by microphone level. This mapping is only jeopardized by the inherent characteristic of beamforming level overestimation when source is of distributed nature.

Verifications with two loudspeakers were performed, and tonal and broadband white noise used for testings from low frequency as 50Hz, to high frequencies as 7kHz, with extremely positive results. Hybrid generalized inverse mappings with and without IRLS were presented, showing that while the use of IRLS may increase speed of the algorithm and localization region separation, it may degrade faster on low frequency of analysis.

Two artifices, image source on transfer function to account for reflections from asphalt, and low frequency focus compensation to overcome wave spreading differences from pure spherical radiation, proved to be helpful in the identification of source center, in vertical and in horizontal range, respectively.

Conventional beamforming results were presented to demonstrate their lack of accuracy in low frequency and also in high frequency in terms of dynamic range resolution, adopted as 8dB for generalized inverse mappings and conventional mappings.

In the end, truck noise identification at peak emission demonstrated clearly the region of radiation, with consistency between conventional and generalized inverse methods. This is also verified in the 3rd engine order (V6 engine) identification example, despite being far from the peak level frequency, the source region is also captured by the inverse method mappings, with noise from the exhaust (behind the fuel tank) being the probable sound source. This last identification was done in a very low frequency range of analysis of 50Hz.

11.4 Main Contributions to The Research Field

The main contributions of this work can be divided in contributions to the generalized inverse beamforming method, contributions to aeroacoustic source identification, and contributions to moving source identification. These contributions are new to the research field, and certainly advances the identification capabilities. The list of contributions to the generalized inverse identification method in general is presented below:

- 1) Automated regularization factor definition in the optimized regularization strategy
- 2) Criteria to stop truncation iterations in the GIB method based on the optimum J_1 cost function (based on $\ell - 1$ norm)
- 3) Dipole radiation induced by two compact monopole sources identification
- 4) Use of a virtual grid to separate direct and reflected contributions (locating image sources)
- 5) Eigenvalue based strength estimation comparison to conventional and GIB results (with and without floor reflections)
- 6) Direct radiation analytical estimate comparison to eigenvalue based estimate
- 7) Hybrid method strength estimation based in conventional beamforming and GIB mapping
- 8) Hybrid generalized inverse mapping to provide a comparable level mapping to conventional mapping
- 9) Multiple eigenmode solutions consideration based on eigenvalues, 10dB range
- 10) Transfer matrix re-scaling to allow identification of dipole orientation towards array
- 11) 3D grid to represent obstacles and better locate sources

Without these advances listed above, it is not possible to define an accurate strength estimation and also visualize strength from smoothly distributed inverse mapping results, which are

fundamental aspects for the result analyzes. Dipole identification in 3D orientation is an important advance since in general the dipole is not parallel to the microphone array. 3D grid is a novel approach and opens the possibilities to more accurate and realistic source distributions.

The following list brings the main contributions to the aeroacoustic research area, in terms of source over obstacle identification. Specific approaches were developed and comparison to measured data already indicate their accuracy.

- 1) Dipole identification in a jet over obstacle aeroacoustic problem
- 2) Dominant emissions identification based in cross-spectral averaging
- 3) Equivalent pressure mapping generation based in identified source distributions
- 4) Directivity plots considering dipole radiation in convection and refraction propagation
- 5) Directivity assessment comparison to far-field microphone readings

The dominant emission event analysis is a new approach that demonstrates the capacity of the generalize inverse method, using the optimized regularization strategy, to perform identifications in fast events, with results in accordance to the literature. Equivalent pressure mappings and directivity plots are only possible since source multipole character is fully identified, a new analysis tool when using generalized inverse beamforming.

The third list brings contributions to moving source identification, and more specifically to pass-by noise procedure for source identification. The advances developed in this Thesis are certainly a breakthrough from the limitations of the conventional approach.

- 1) De-Dopplerization based on the target grid geometric center as a simplification
- 2) Investigation of the influence of mappings and spectrum averaging in moving source problems (non-stationary)
- 3) Special array design to improve horizontal source detection resolution and pass-by source level estimate
- 4) Image source in transfer function to minimize reflections influence
- 5) Focus compensation for low frequency of analysis to overcome source non-spherical radiation
- 6) Analysis in the frequency range from 50Hz to 7kHz in moving source identification.

The special array design combines advantages of the generalized inverse method for the desired identification performance, leading to breakthrough results. The localization accuracy, frequency range and source level estimation with the developed procedure is impressive when compared to conventional performance, even considering works as recent as Gurovich *et al.* (2009).

11.5 Suggested Future Work

Some suggestions are given throughout the text, and here a summarized list is presented:

- 1) Faster optimum regularization factor definition
- 2) 3D array of microphones to improve 3D target grid identifications
- 3) Develop a method to improve source level information from mapping and avoid overestimation for distributed sources
- 4) Method to improve generalized inverse beamforming resolution in reverberant conditions
- 5) Method to evaluate and determine the best focus distance for low frequency sources with unknown directivities

These suggestions are basically desired improvements on identification performance, despite the fact that they were briefly investigated throughout the text, it is required a deeper analysis in order to further advance and fully explore the method's potential. Another suggestion to improve results is to increase complexity on the model candidate, including, for example, monopole and dipole source types simultaneously, or more complex transfer functions, for example, taking into account reflective surfaces close to sources.

11.6 Summary

In summary, the generalized inverse beamforming identification method demonstrated its capacity to locate multipole distributed sources in aeroacoustic problems of flow over obstacles, and also demonstrated its quality to perform identification with a non-stationary problem, a moving source pass-by noise test.

Important advantages are observed in aeroacoustic and in moving source identifications, but

some concern still exists for the sensitivity of this method to the quality of input data and to algorithm parameters.

Aeroacoustic identification is one of the most challenging scenarios for source localization, and the literature is still lacking research on general methods capable of dealing with fast emission events, with coherent and incoherent regions, and complex transfer paths with convection and refraction. This work is certainly an important step with the objective to better understand aeroacoustic sources generation.

Table 11.1 brings the main practical engineering advantages and limitations on the use of the generalize inverse method on aeroacoustic and moving source problems.

Main advantages	Limitations
Higher localization accuracy	Sensitivity to errors and extraneous sources
Multipole sources identification	Sensitivity to anisotropic radiation
Identification of coherent and incoherent sources	Spectral decomposition favors higher sources
Fast and non-stationary identifications	Hybrid estimation is required to improve inverse results
Higher resolution in low frequencies	Resolution depends on array distribution

Table 11.1: Main practical advantages and limitations on the use of generalized inverse method on aeroacoustic and moving source problems.

Inverse methods are of extreme importance since they can bring unprecedented detailing in identifications. On the other hand, a deeper knowledge is required from the analyst. The inverse method will always adjust the candidate model to the measured data, and this could bring erroneous conclusions when a wrong model, or a wrong algorithm parameter setting, is used in the system resolution. At last, even considering that inversion techniques are developed at an intense pace, numerical challenges in system conditioning have to be taken into account, and their influence on results completely understood.

The generalized inverse beamforming proved to be the right choice even considering that it is a recent method. Part of the investigations carried throughout this text has already been reported to the scientific community and have been cited by the most recent developments in this area of research (SUZUKI, 2011; DOUGHERTY, 2011), confirming its importance to the field.

12 Conclusões

Neste capítulo, as principais conclusões sobre o desenvolvimento de um método de identificação baseado no beamforming inverso generalizado para problemas aeroacústicos e problemas de fonte em movimento são discutidas. As principais vantagens são levantadas em face dos resultados obtidos e, por outro lado, as desvantagens, ou áreas para melhorias, são apresentadas e discutidas também. No final, as principais contribuições para o campo de pesquisa em identificação de fontes aeroacústicas e fontes em movimento são descritas, juntamente com os trabalhos futuros deixados como sugestão.

12.1 Introdução

A estrutura por trás desta pesquisa pode ser resumida em testar-se o método de beamforming inverso generalizado inicialmente em problemas simples, com simulação e com dados experimentais, e após esta fase, a aplicação em casos de testes mais complexos, mais uma vez, através de simulações e dados experimentais.

Esta abordagem provou ser uma prática de pesquisa importante e necessária ao longo do trabalho, evitando-se saltar para conclusões sem verificações prévias em casos mais simples.

A identificação de monopólos e dipólos é primeiramente verificada experimentalmente usando-se fontes compactas em uma sala semi-anecóica. Esta fase preliminar foi importante para desenvolver-se por exemplo, a estimativa híbrida.

Depois destes testes preliminares de verificação experimental, os problemas mais complexos foram analisados e uma discussão detalhada é apresentada nas seções seguintes.

12.2 Identificação de Fontes Aeroacústicas

A segunda fase experimental consistiu no teste de seção de cilindro, um simples e conhecido problema da literatura aeroacústica. As terceira e quarta fases de teste têm distribuições de fontes mais complexas, com testes de duas estruturas de perfil quadrado e um aerofólio padrão sob fluxo de ar subsônico.

12.2.1 Dipólo sobre Cilindro em Jato Subsônico

A geração de fontes Aeroacústicas é basicamente um processo estocástico. No entanto, uma investigação profunda do mecanismo de geração de fontes certamente exige novas abordagens de identificação do que a tradicional.

Neste trabalho, o evento dominante de emissão sonora é separado e tratado como um importante evento isolado, quando os sinais recebidos na malha de microfones possuem distribuição coerente o suficiente para serem usados para caracterizar as regiões importantes de distribuição de fontes. Estas emissões dominantes podem variar em frequência, em período de tempo, e em local.

A conclusão geral é de que para frequências mais altas, a direção do dipólo parece defletir em direção a jusante, e a região sobre a superfície do obstáculo também se move na direção a jusante. Isto indica que o descolamento do fluido a partir da superfície do cilindro leva a flutuações de pressão na superfície, causando frequências e durações de radiação diferentes dependendo da posição do descolamento ao longo da superfície.

A observação em eventos isolados é uma nova abordagem proposta aqui e útil para ligar a radiação acústica com as características do fluido tais como a turbulência em torno do obstáculo.

Se a radiação é considerada como um processo estacionário, os resultados mostram uma espiral como padrão de radiação, com duas regiões principais na superfície do cilindro a jusante, na região superior e inferior, conforme esperado. Essas duas regiões são as regiões mais prováveis de separação do fluido e de geração de fontes sonoras.

A radiação em espiral, por outro lado, não corresponde a uma formação bem comportada dos dipólos na direção perpendicular ao fluxo, como indicada na literatura, mas pode ser associada à uma formação de dipólo intermitente entre a região superior e a região inferior, semelhante à geração de vórtices, também conhecida como “Von Kármán Vortex Street” (VON KÁRMÁN, 1963). O padrão de radiação observado também poderia ser interpretado como um dipólo rotativo com centro intermitente de radiação entre as regiões superiores e inferiores do cilindro.

A identificação com base no método inverso generalizado demonstrou a sua qualidade em permitir a geração de mapeamentos de pressão equivalentes para campo-distante (com base nas fontes identificadas), e diretividade, de grande importância para o desenvolvimento mais tarde de

soluções de redução de ruído.

A desvantagem é a dificuldade para separar um mapeamento de boa qualidade de resultados espúrios, sendo que um mapeamento de boa qualidade é claramente dependente de vários aspectos: tipo de fonte, localização, distribuição, espaçamento da grade, resolução em frequência, regularização, número de iterações, etc.

12.2.2 Duas Estruturas em Fluxo Subsônico

As duas estruturas no teste no túnel de vento aberto da NLR permitiram uma comparação direta dos resultados de beamforming convencional gerados por esse centro de pesquisa com os resultados gerados neste trabalho, de beamforming convencional e beamforming inverso generalizado.

A comparação mostrou que os mapeamentos de elevada qualidade do beamforming convencional podem ser obtidos também com os métodos inversos para as identificações de monopólos, e até mesmo uma resolução mais elevada é observada na localização dos centros de radiação em baixa frequência, e na região de localização em alta frequência, para o método inverso.

O uso de fontes distribuídas em linha em simulações, com base em comprimento de coerência da literatura, forneceu uma referência importante na interpretação de mapeamentos para ser usada na análise dos dados experimentais. O uso de atenuação de auto-potência provou ser uma medida valiosa para melhorar a resolução em mapeamento inverso, comparável à remoção da diagonal da matriz de espectros cruzados no método convencional. O mapeamento híbrido inverso generalizado também criou uma leitura comparável de nível de fontes em relação a mapeamentos convencionais, uma ferramenta de análise importante.

A identificação da distribuição de dipólos seguiu a distribuição esperada sobre a superfície, representada por duas estratégias de grade: uma de grade em linha; e uma de grade 3D. O beamforming inverso generalizado com IRLS apresentou uma resolução maior na localização de fontes, com detecção dos cantos da estrutura específicos que estão provavelmente relacionados com as maiores flutuações de pressão, ou por enfrentarem turbulências ou por terem região de separação do fluido.

O uso de mapeamento híbrido e mapeamento híbrido inverso generalizado provou ser um auxílio valioso para visualização, e o re-escalamento da matriz de transferência, um passo necessário à obtenção da identificação da orientação dos dipólo quando há componente significativa do dipólo na direção da malha de microfones.

Avaliações de diretividade foram feitas e as comparações com microfones em campo-distante mostrou uma boa concordância se a matriz de espectros cruzados original é considerada. A estimativa de diretividade é possível já que a identificação da orientação dos dipólos pelo método inverso generalizado é feita para os seus componentes ortogonais, e uma avaliação em 360° é feita. Para esses casos, a grade em linha mostrou resultados ligeiramente melhores, e uma simetria é mantida nos 360° .

A análise das medições dos transdutores de pressão de parede mostrou que as regiões de alta pressão podem não indicar diretamente os centros de fontes sonoras. Apesar disso, existe coerência entre as distribuições de pressão e as distribuições de dipólos identificados pelo método inverso generalizado.

12.2.3 Aerofólio NACA-0012 em Fluxo Subsônico

Testes realizados com um aerofólio padrão, NACA-0012, no túnel de vento fechado da EESC-USP, permitiram uma comparação de mapeamentos obtidos pelo método beamforming convencional e o método inverso generalizado com e sem IRLS. Os resultados estão em concordância com os resultados de referência da literatura, baseados no método DAMAS2. A condição reverberante nesta configuração de testes provou ser um grande desafio para o método inverso uma vez que todas as contribuições de energia sonora estão representadas nos autovalores, e a identificação pode ser perdida se a localização exata de todas as fontes não estão representadas na grade alvo, como observado para a análise em baixa frequência, onde o ruído vindo do sistema de ventilação pode ter induzido o método a falhar na localização das fontes.

Em geral as fontes são identificadas distribuídas sobre o bordo de fuga, tal como é relatado na literatura, e a coerência da localização para todas as condições de velocidade do teste demonstram que a modelagem de convecção é implementada corretamente.

12.3 Identificação de Fontes em Movimento

As duas últimas fases de teste são as identificações de fontes de ruído em teste de ruído de passagem de veículo de passageiros e de caminhão. O método inverso generalizado é aplicado a uma condição não-estacionária e em um teste transiente rápido.

12.3.1 Ruído de Passagem de Veículo de Passageiros

Os resultados demonstraram que as simplificações adotadas, incluindo a de-Dopplerização, são válidas, mas alguma atenção é exigida para o período de tempo, resolução de frequência, e estratégia de médias, para não deteriorarem-se os resultados.

Alta precisão é atingida para a validação com uma fonte conhecida, mesmo considerando que a malha de microfones está perto da pista. Além disso, um centro de radiação é apontado claramente para as frequências mais baixas, como a segunda ordem de motor, um avanço real sobre a literatura disponível.

O potencial é evidente em localização de fontes, no entanto, alguns inconvenientes também podem ser mencionados com base nos resultados do teste, como é o caso da sensibilidade do método em relação aos parâmetros de identificação, ao ruído nos sinais dos microfones, à correta velocidade do veículo, e à real distância para a malha de microfones.

12.3.2 Ruído de Passagem de Caminhão

A capacidade observada de localização em frequências mais baixas quando comparada com o beamforming convencional inspirou a aplicação do método de beamforming inverso generalizado em identificação de fontes de ruído de caminhões em teste de ruído de passagem.

Esta aplicação exigiu um projeto especial de malha de microfones, com maior resolução no sentido horizontal, e centrado em torno da posição do microfone do teste de ruído de passagem, o que permitiu a geração de mapeamentos com a contribuição direta da fonte no microfone de ruído de passagem. Este mapeamento é apenas comprometido pela característica inerente ao beamforming convencional em superestimar o nível quando a fonte é de natureza distribuída.

Verificações com dois alto-falantes são realizadas, e ruído tonal e de banda larga (branco) são utilizados para testes em baixa frequência, tais como 50Hz, e para as altas frequências, como 7kHz, com resultados extremamente positivos. Mapeamentos híbridos inversos generalizados com e sem IRLS são apresentados, mostrando que, enquanto o uso de IRLS pode aumentar a velocidade do algoritmo e na separação da região de localização, ele pode degradar mais rapidamente em baixa frequência de análise.

Dois artifícios, imagem de fonte na função de transferência para levarem-se em conta os reflexos sobre o asfalto, e compensações de foco em baixa frequência para contornarem-se as diferenças de radiação em relação à onda esférica pura, provaram ser úteis na identificação de centros de fontes nas direções vertical e horizontal, respectivamente.

Resultados de beamforming convencional são apresentados para demonstrar sua falta de precisão em baixas frequências e também em alta frequência em termos de resolução dinâmica, adotada como 8dB para os mapeamentos inversos generalizados e os mapeamentos convencionais.

No final, a identificação de ruído de caminhão para o pico de emissão sonora demonstra claramente a região de radiação, com coerência entre os resultados obtidos pelos métodos convencional e inverso generalizado. Isto também é verificado na análise da 3^a. ordem do motor (motor V6), como exemplo de identificação, que apesar de estar longe de ser o maior nível em frequência, também consegue ser capturado nos mapeamentos, onde o ruído do escapamento (atrás do tanque de combustível) parece ser a fonte do ruído. Esta última identificação feita numa faixa de frequências muito baixa de análise, 50Hz.

12.4 Maiores Contribuições para o Campo de Pesquisa

As principais contribuições do trabalho nesta Tese podem ser divididas em contribuições ao método de beamforming inverso generalizado, contribuições à identificação de fontes aeroacústicas, e as contribuições ao problema de identificação de fonte em movimento. Essas contribuições são novas a esses campos de pesquisa, e certamente avançam os resultados de identificação. A primeira lista, com contribuições gerais ao método de identificação inverso generalizado é apresentada abaixo:

- 1) Definição automatizada do fator de regularização na estratégia otimizada de regularização

- 2) Critério para parar iterações de truncamento no método GIB com base na função de custo J_1 (baseada na norma $\ell - 1$)
- 3) Identificação de dipólo induzido por duas fontes compactas
- 4) Uso de uma grade virtual para separar as contribuições diretas e refletidas (localização de fontes imagem)
- 5) Comparação de estimativa de vazão acústica baseada em auto-valores com resultados obtidos pelos métodos convencionais e GIB (com e sem reflexos no solo)
- 6) Comparação de estimativa analítica com estimativa baseada em auto-valores
- 7) Método Híbrido de estimativa de vazão acústica com base em beamforming convencional e mapeamento GIB
- 8) Mapeamento híbrido inverso generalizado para fornecer um mapeamento de nível comparável ao de mapeamento convencional
- 9) Consideração múltipla de soluções de auto-modos com base em faixa de 10dB dos autovalores
- 10) Re-escalamento da matriz de transferência para permitir a identificação da orientação dos dipólos em direção à malha de microfones
- 11) Grade 3D para melhor representar obstáculos e melhor localizar fontes

Sem os avanços listados acima, não seria possível definir uma estimativa precisa e também visualizar a vazão acústica a partir dos resultados do método inverso, aspectos fundamentais para a análise dos resultados. A identificação de dipólo com orientação 3D é um avanço importante uma vez que em geral o dipólo não está necessariamente num plano paralelo à malha de microfones. O uso de uma grade objetivo 3D é uma abordagem inovadora e abre as possibilidades para distribuições geométricas de fontes mais precisas.

A lista a seguir traz as principais contribuições para a área de pesquisa em aeroacústica, em termos de identificação de fonte sobre obstáculos. Abordagens específicas foram desenvolvidas e comparações com dados medidos revelam a sua precisão.

- 1) Comparação de diretividade com medições de microfone em campo distante
- 2) Identificação de dipólos num problema aeroacústico de jato sobre um obstáculo
- 3) identificação de emissões dominantes baseado em médias de espectros cruzados
- 4) Geração de mapeamento de pressão equivalente com base nas distribuições de fontes identificadas

5) Diretividade considerando radiação de dipólos em propagação com convecção e refração

A análise de eventos de emissões dominantes é uma nova abordagem que demonstra a capacidade do método inverso generalizado, utilizando a estratégia de regularização otimizada, para executar as identificações em eventos rápidos, com resultados em conformidade com a literatura. Mapeamentos de pressão equivalente e diretividade só são possíveis enquanto o caráter multipolar da fonte é devidamente identificado, sendo uma nova ferramenta de análise quando se utiliza o beamforming inverso generalizado.

A terceira lista traz as contribuições para a identificação de fonte em movimento, e mais especificamente, para a identificação de fonte em teste de ruído de passagem. Os avanços desenvolvidos neste trabalho são certamente um avanço sobre as limitações dos métodos convencionais.

- 1) De-Dopplerização com base no centro geométrico da grade de alvo como uma simplificação
- 2) Investigação da influência de médias de mapeamentos e espectros em problemas de fontes em movimento (não-estacionário)
- 3) Projeto especial da malha de microfones para melhorar a resolução horizontal de detecção de fontes e estimativa de nível em teste de ruído de passagem
- 4) Imagem de fonte na função de transferência para minimizar a influência das reflexões
- 5) Compensação de foco em baixas frequências de análise para fontes com radiações não-esféricas
- 6) Faixa de frequências verificadas de 50Hz a 7kHz para identificação de fontes em movimento.

A concepção especial da malha de microfones combina as vantagens do método inverso generalizado com o desempenho de identificação desejado, levando a resultados nunca antes vistos na literatura. A precisão da localização, a faixa de frequências e estimativa do nível de fonte com o procedimento desenvolvido é impressionante quando comparado com o desempenho convencional, mesmo considerando trabalhos recentes quanto em Gurovich *et al.* (2009).

12.5 Futuros Trabalhos Recomendados

Algumas sugestões são feitas ao longo do texto, e aqui é apresentada uma lista resumida:

- 1) Definição mais rápida do fator de regularização ótimo
- 2) Malha de microfones em 3D para melhorar a identificação em grade 3D
- 3) Desenvolver um método para melhorar a informação do nível de fonte no mapeamento e evitar uma superestimação para fontes distribuídas
- 4) Método para melhorar a resolução do método de beamforming inverso generalizado em ambiente reverberante
- 5) Método para avaliar e determinar a melhor distância de foco para as fontes com diretividades desconhecidas em baixa frequência

Estas sugestões são basicamente melhorias desejadas no desempenho de identificação, apesar de que tenham sido brevemente investigadas ao longo do texto, é necessário uma análise mais profunda, a fim de avançar ainda mais e esgotar o potencial do método. Outra sugestão para melhorar os resultados é o de aumentar a complexidade do modelo candidato, incluindo, por exemplo, tipos de fontes monopólo e dipolo simultaneamente, ou funções de transferência mais complexas, por exemplo, tendo em conta as superfícies reflectoras próximas à fonte.

12.6 Resumo

Em resumo, o método de identificação beamforming inverso generalizado demonstrou capacidade em localizar fontes distribuídas e multipólos nos problemas aeroacústicos de fluxo de ar sobre obstáculos, e também demonstrou a sua qualidade para executar identificações num problema não-estacionário, fontes em movimento no teste de ruído de passagem.

Vantagens importantes são observadas nas identificações de fontes aeroacústicas e de fontes em movimento, mas alguma preocupação ainda existe para a sensibilidade desse método em relação à qualidade dos dados de entrada e parâmetros do algoritmo.

Identificação aeroacústica é um dos cenários mais desafiadores para a localização de fontes, e a literatura ainda é carente de pesquisas sobre métodos gerais capazes de lidar com eventos de emissões sonoras rápidas, com regiões coerentes e incoerentes, e caminhos de transferência complexos, com convecção e refração. Este trabalho é certamente um passo importante com esse objetivo, o de entender melhor a geração de fontes aeroacústicas.

A Tabela 12.1 traz as principais vantagens e as limitações práticas de engenharia no uso do

método inverso generalizado em problemas aeroacústicos e de fontes em movimento.

Maiores vantagens	Limitações
Maior precisão na localização	Sensibilidade a erros e fontes estranhas
Identificação de fontes multipólos	Sensibilidade à radiação anisotrópica
Identificação de fontes coerentes e incoerente	Decomposição espectral favorece fontes mais fortes
Identificações rápidas e não-estacionárias	Estimativa híbrida é necessária para melhorar resultados inversos
Maior resolução em baixas frequências	Resolução dependente da distribuição de microfones

Tabela 12.1: Principais vantagens e limitações práticas de engenharia no uso do método inverso generalizado em problemas aeroacústicos e de fonte em movimento.

Métodos inversos são de extrema importância, uma vez que podem trazer detalhamento sem precedentes nas identificações, por outro lado, um conhecimento mais profundo é exigido do analista. O método inverso sempre irá ajustar o modelo candidato aos dados medidos, e isto pode trazer conclusões errôneas quando um modelo errado, ou uma configuração errada de parâmetros do algoritmo, forem usados na resolução do sistema. Por último, mesmo considerando que as técnicas de inversão são desenvolvidas em um ritmo intenso, os desafios numéricos, como o condicionamento do sistema, têm de ser levados em conta, e sua influência sobre os resultados completamente compreendida.

O beamforming inverso generalizado provou ser a escolha certa para esta investigação, mesmo considerando que é um método recente. Em parte, as investigações realizadas ao longo deste texto já foram relatadas à comunidade científica e têm sido citadas pelos desenvolvimentos mais recentes nesta área de pesquisa (SUZUKI, 2011; DOUGHERTY, 2011), confirmando sua importância para o campo.

Bibliography

AMIET, R.K. Correction of open jet wind tunnel measurements for shear layer refraction. In **AIAA 2nd Aero-acoustic Conference, paper number 75-532, Hampton, VA 24-26. March 1975.**

BJORCK, A. Numerical methods for least squares problems. **Society for Industrial and Applied Mathematics**, 1996.

BLAKE, W.K. **Mechanics of flow-induced sound and vibration.** 1986.

BROOKS, T.F. and HUMPHREYS, W.M. A deconvolution approach for the mapping of acoustic sources (damas) determined from phased microphone arrays. **Journal of Sound and Vibration** **294** 856–879 also **AIAA paper 2004-2954**, May 2006.

BROOKS, T.F.; POPE, S. and MARCOLINI, M.A. **Airfoil Self-Noise and Prediction.** NASA Reference Publication 1218, July 1989.

CASTELLINI, P. and SASSAROLI, A. Acoustic source localization in a reverberant environment by average beamforming. **Journal of Mechanical Systems and Signal Processing**, **24**, 796-808, 2010.

CIGADA, A.; RIPAMONTI, F. and VANALI, M. The delay & sum algorithm applied to microphone array measurements: Numerical analysis and experimental validation. **Journal of Mechanical Systems and Signal Processing**, **21**, 2645-2664, 2007.

CURLE, N. The influence of solid boundaries on aerodynamic sound. In **Proc. R. Soc. London, Ser. A** **231**, 505-514. 1955.

DAY, B.J. and SUZUKI, T. Mode identification in a rectangular duct using an l_1 generalized

inverse beam-forming approach. In **17th AIAA/CEAS Aeroacoustics Conference (32nd AIAA Aeroacoustics Conference)**, paper No. 2812, 05-08, Portland, Oregon. June 2011.

DOUGHERTY, R.P. Extensions of damas and benefits and limitations of deconvolution in beamforming. In **11th AIAA/CEAS Aeroacoustics Conference (26th AIAA Aeroacoustics Conference)**, 23-25, Monterey, California, AIAA-2005-2961. May 2005.

DOUGHERTY, R.P. Improved generalized inverse beamforming for jet noise. In **17th AIAA/CEAS Aeroacoustics Conference (32nd AIAA Aeroacoustics Conference)**, 05-08, Portland, Oregon, AIAA-2011-2769. June 2011.

ELDREDGE, J.D. The dynamics and acoustics of viscous two-dimensional leapfrogging vortices. **Journal of Sound and Vibration**, 301 p. 74-92, 2007.

FFOWCS-WILLIAMS, J.E. The noise from turbulence convected at high speed. **Philosophical Transactions of the Royal Society**, Vol. A255 (1963) pp. 469-503, 1963.

FFOWCS-WILLIAMS, J.E. and HAWKINGS, D.L. Sound generation by turbulence and surfaces in arbitrary motion. **Philosophical Transactions of the Royal Society**, Vol. A264 pp. 321-342, 1969.

GERGES, S.N.Y.; FONSECA, W.D. and DOUGHERTY, R.P. State of the art beamforming software and hardware for applications. In **The Sixteenth International Congress on Sound and Vibration (ICSV16)**, Krakow. July 2009.

GUASCH, O. and CODINA, R. An algebraic subgrid scale finite element method for the convected helmholtz equation in two dimensions with applications in aeroacoustics. **Comput. Methods Appl. Mech. Engrg.** 196 4672-4689, 2007.

GUILLAUME, P.; PARLOO, E. and DE SITTER, G. Source identification from noisy response measurements using an iterative weighted pseudo-inverse approach. In **In Proceedings of ISMA**.

2002.

GUROVICH, Y.A.; PLOTKIN, K.J.; ROBINSON, D.H.; BLAKE, W.K. and DONAVAN, P.R. **Acoustic Beamforming: Mapping Sources of Truck Noise**. National Cooperative Highway Research Program (NCHRP) Report 635, Washington, D.C., US, 2009.

HERRIG, A.; WURZ, W.; KRAMER, E. and WAGNER, S. New cpv-results of naca 0012 trailing-edge noise. In **International Conference on Methods of Aerophysical Research, ICMAR**. 2008.

HOGBOM, T. Aperture synthesis with a non-regular distribution of interferometer baselines. **Astron. Astrophys. Suppl** **15** 417-426, 1974.

HUBER, P.J. **Robust Statistics**. John Wiley & Sons, 1981.

JANSSENS, K.; BRITTE, L. and DEBLAUWE, F. Time-domain source contribution analysis of in-room vehicle pass-by noise. In **International Conference in Sound and Vibration, Rio de Janeiro**. July 2011.

JORDAN, P. and FITZPATRICK, J.A. Measurement of an aeroacoustic dipole using linear microphone array. **J. Acoust. Soc. Am.** **111** (3), March 2002.

KING, W. and PFIZENMAIER, E. An experimental study of sound generated by flows around cylinder of different cross-section. **Journal of Sound and Vibration, Ed. Elsevier**, **328** 318-337, 2009.

KINSLER, L.E.; FREY, A.R.; COPPENS, A.B. and SANDERS, J.V. **Fundamentals of Acoustics**. John Wiley & Sons, third Ed., 1982.

KOPIEV, V.F.; ZAITSEV, M.Y.; VELICHKO, S.A.; KOTOVA, A.N. and BELYAEV, I.V. Cross-correlation of far field azimuthal modes in subsonic jet noise. In **14th AIAA/CEAS Aeroacoustics Conference**, 2008-2887. May 2008.

LEE, M. and BOLTON, J.S. Scan-based near-field acoustical holography and partial field decomposition in the presence of noise and source level variation. **J. Acoust. Soc. Am.** **119 (1)**, pages: **382-393**, January 2006.

LEE, M. and BOLTON, J.S. Source characterization of a subsonic jet by using near-field acoustical holography. **J. Acoust. Soc. Am.** **121 (2)**, pages: **967-977**, February 2007.

LEE, M.; BOLTON, J.S. and MONGEAU, L. Application of cylindrical near-field acoustical holography to the visualization of aeroacoustic sources. **J. Acoust. Soc. Am.** **114 (2)**, pages: **842-858**, August 2003.

LIGHTHILL, M.J. On sound generated aerodynamically. i. general theory. **Proc. R. Soc. Lond. A** **211 pp. 564-587**, 1952.

LIGHTHILL, M.J. On sound generated aerodynamically. ii. turbulence as a source of sound. **Proc. R. Soc. Lond. A** **222 pp. 1-32**, 1954.

MARTIN, V.; LE BOURDON, T. and PASQUAL, A.M. Numerical simulation of acoustic holography with propagator adaptation: Application to a 3d disc. **Journal of Sound and Vibration**, **330, 4233-4249**, 2011.

MARTINEZ-LERA, P.; PRADERA, A. and SCHRAM, C. Efficient implementation of equivalent sources from cfd data in curle's analogy. In **13th AIAA/CEAS Aeroacoustics Conference (28th AIAA Aeroacoustics Conference)**, **2007-3569**. 2007.

MÜLLER, B. High order numerical simulation of aeolian tones. **Computers and Fluids**, **37 450-462**, 2008.

MORSE, P.M. **Vibration and Sound**. Chap. VII, McGraw-Hill, Second Edition, New York, 1948.

MORSE, P.M. and INGARD, K.U. **Theoretical Acoustics**. McGraw-Hill, 1968.

MUELLER, T.J.E. **Aeroacoustics Measurements**. Chap. 2 (Chapter Author: R.P. Dougherty), Springer, New York, 2002.

OERLEMANS, S. **Detection of Aeroacoustic Sound Sources on Aircraft and Wind Turbines**. PhD Thesis from University of Twente, The Netherlands, 2009.

PAPAMOSCHOU, D. Imaging of directional distributed noise sources. In **14th AIAA/CEAS Aeroacoustics Conference, 2008-2885**. 2008.

PARLOO, E.; VERBOVEN, P.; GUILLAUME, P. and VAN OVERMAIRE, M. Force identification by means of in-operational modal models. **Journal of Sound and Vibration, 262:161-173**, 2003.

PIET, J.F.; MICHEL, U. and BOHNING, P. Localization of the acoustic sources of the a340 with a large phased microphone array during flight tests. In **8th AIAA/CEAS Aeroacoustics Conference, 2002-2506**. 2002.

PILLAI, U. **Array Signals Processings**. Chap. 2, Springer, New York, 1989.

PLUMBLEE, H.E.E. **Effects of Forward Velocity on Turbulent Jet Mixing Noise**. NASA CR-2702, 1976.

PRESEZNIAK, F.A. **Acoustic Source Identification with Applications in Aeroacoustics**. PhD Thesis at Faculty of Applied Sciences in the Department of Applied Mechanics, Vrije Universiteit Brussel, March 2011.

PRESEZNIAK, F.A.; ZAVALA, P.A.G.; STEENACKERS, G.; JANSSENS, K.; ARRUDA, J.R.F.; DESMET, W. and GUILLAUME, P. Acoustic source identification using a generalized weighted inverse beamforming technique. **Submitted to Mechanical Systems and Signal Processing in 2010 (status:under review)**, 2012.

REBA, R.; SIMONICH, J. and SCHLINKER, R. Measurement of source wave-packet in high-

speed jets and connection to far-field sound. In **14th AIAA/CEAS Aeroacoustics Conference, 2008-2891**. May 2008.

SANTANA, L. D. **A Capacitação do Túnel de Vento de Circuito Fechado da Escola de Engenharia de São Carlos à Realização de Ensaio Aeroacústicos, Levantamento de Suas Características e Potencialidades**. 2010. Master Dissertation from Escola de Engenharia de São Carlos, Universidade de São Paulo (USP).

SCHMIDT, R.O. Multiple emitter location and signal parameter estimation. **IEEE Trans. on Antennas and Propagation, Vol. AP-34, No. 3**, 1986.

SCHRAM, C.F. **Aeroacoustics of Subsonic Jets: Prediction of the Sound Produced by Vortex Pairing based on Particle Image Velocimetry**. PhD Thesis, Eindhoven Technische Univ., 2003.

SEO, J.H. and MOON, Y.J. Aerodynamic noise prediction for long-span bodies. **Journal of Sound and Vibration, 306 564-579**, 2007.

SIJTSMA, P. Clean based on spatial source coherence. In **13th AIAA/CEAS Aeroacoustics Conference (28th AIAA Aeroacoustics Conference), AIAA-2007-3436**. 2007.

SIJTSMA, P. and STOKER, R.W. Determination of absolute contributions of aircraft noise components using fly-over array measurements. In **10th AIAA/CEAS Aeroacoustics Conference, AIAA-2004-2958**. 2004.

STROUHAL, V. Über eine besondere art der tonerregung. **Annalen der Physik und Chemie (Leipzig) Series 3 (5)**, 1878.

SUZUKI, T. Identification of multipole noise sources in low mach number jets near the peak frequency. **J. Acoust. Soc. Am. 119 (6), pages: 3649-3659**, June 2006.

SUZUKI, T. Generalized inverse beam-forming algorithm resolving coherent/incoherent,

distributed and multipole sources. In **11th AIAA/CEAS Aeroacoustics Conference (29th AIAA Aeroacoustics Conference)**, paper No. 2954, Vancouver, British Columbia Canada, 5-7. May 2008.

SUZUKI, T. Noise sources of subsonic round jets investigated using phased microphone arrays. In **16th AIAA/CEAS Aeroacoustics Conference (31st AIAA Aeroacoustics Conference)**, paper No. 3958. 2010.

SUZUKI, T. l_1 generalized inverse beam-forming algorithm resolving coherent/incoherent, distributed and multipole sources. **Journal of Sound and Vibration**, 330, pages: 5835-5851, 2011.

TAKAISHI, T.; MIYAZAWA, M. and KATO, C. A computational method of evaluating noncompact sound based on vortex sound theory. **J. Acoust. Soc. Am.** 121 (3), March 2007.

TAM, C.K.W. The sources of jet noise: Experimental evidence. In **13th AIAA/CEAS Aeroacoustic Conference**, 2007-3641. 2007.

VISSER, R. **A Boundary Element Approach to Acoustic Radiation and Source Identification**. 2004. PhD Thesis, Univ. of Twente, Enschede, The Netherlands.

VON KÁRMÁN, T. **Aerodynamics**. McGraw-Hill, 1963.

WANG, H. and KAVEH, M. Coherent signal-subspace processing for the detection and estimation of angles of arrival of multiple wide-band sources. **IEEE Trans. Acoustics, Speech, and Signal Proc.**, Vol. ASSP-33, No. 4, August 1985.

WOLF, W. **Airfoil Aeroacoustics: LES and Acoustic Analogy predictions**. 2011. PhD thesis from Stanford University, Department of Aeronautics and Astronautics.

YANG, J.F. Adaptive high-resolution algorithms for tracking nonstationary sources without the

estimation of source number. **IEEE Trans. on Signal Processing**, Vol. 42, No. 3, March 1994.

ZAVALA, P.A.G.; ARRUDA, J.R.F.; DE ROECK, W. and DESMET, W. Dipole identification over a cylinder section in subsonic jet flow using generalized inverse beamforming. In **21st COBEM (International Congress of Mechanical Engineering)**, Natal-Brazil. October 2011a.

ZAVALA, P.A.G.; ARRUDA, J.R.F.; JANSSENS, K. and DESMET, W. Passenger vehicle pass-by noise test using generalized inverse beamforming. In **SAE BRASIL Congress and exposition, São Paulo-Brazil**. October 2011b.

ZAVALA, P.A.G.; ARRUDA, J.R.F.; JANSSENS, K. and DESMET, W. Vehicle pass-by noise source localization using generalized inverse beamforming. In **18th International Congress on Sound and Vibration, Rio de Janeiro**. July 2011c.

ZAVALA, P.A.G.; DE ROECK, W.; JANSSENS, K.; ARRUDA, J.R.F.; SAS, P. and DESMET, W. Aeroacoustic source identification using generalized inverse beamforming. In **Proceedings of ISMA, Leuven, Belgium**. 2010a.

ZAVALA, P.A.G.; DE ROECK, W.; JANSSENS, K.; ARRUDA, J.R.F.; SAS, P. and DESMET, W. Generalized inverse beamforming investigation and hybrid estimation. In **Berlin Beamforming Conference**. February 2010b.

ZAVALA, P.A.G.; DE ROECK, W.; JANSSENS, K.; ARRUDA, J.R.F.; SAS, P. and DESMET, W. Monopole and dipole identification using generalized inverse beamforming. In **16th AIAA/CEAS Aeroacoustics Conference, Stockholm, 2010-3740**. June 2010c.

ZAVALA, P.A.G.; DE ROECK, W.; JANSSENS, K.; ARRUDA, J.R.F.; SAS, P. and DESMET, W. Generalized inverse beamforming with optimized regularization strategy. **Mechanical Systems and Signal Processing**, 25, 928-939, 2011d.

ZAVALA, P.A.G. and PAVANELLO, R. Vibro-acoustic modeling of vehicle interiors and exteriors

using finite element method. In **SAE Brazil Congress paper 982939**. 1998.

A DAMAS2

The method proposed by Dougherty (2005) is based on the method from Brooks & Humphereys (2006), DAMAS. Dougherty basically improved the processing time changing the procedure from time to frequency domain and added a low-pass filter to prevent noise amplification. The disadvantage is that the method requires a translationally-invariant point-spread function, or in other words, that the point-spread function doesn't changes too much along the target region, allowing that a constant PSF is used for all target points estimations. Follows the algorithm proposed by Dougherty (2005):

- 1) Compute $psf = \mathcal{F}[PSF]$
- 2) $a_{PSF} = \sum_{x,y,z} |PSF|$
- 3) Set solution $q_D = 0$ for each \vec{x} in the beamforming grid
- 4) Iterate
 - (a) $\tilde{q}_D(k) = \mathcal{F}[q_D]$
 - (b) For each k : $q_D(k) = \tilde{q}_D(k)e^{-k^2/(2k_c^2)}$
 - (c) Let $\tilde{r}_D(k) = psf q_D(k)$
 - (d) $r_D = \mathcal{F}^{-1}[\tilde{r}_D(k)]$
 - (e) $q_D \leftarrow q_D + [P_{cb} - r_D]/a_{PSF}$ for each \vec{x}
 - (f) Replace each negative value of q_D by 0

where PSF is the point-spread function as defined in 5.10; k_c is the cut-off wavenumber; P_{cb} is the conventional beamforming result; a_{PSF} is the summation of PSF absolute value over the grid; q_D is the strength over the grid calculated by DAMAS2; r_D is the strength mapping from deconvolution of $\tilde{r}_D(k)$; and $\tilde{r}_D(k)$ is the result of convolution between estimated q_D and the PSF.

The method consists in searching iteratively the mapping, q_D , that corresponds to the deconvolution of the conventional beamforming P_{cb} by the point-spread function PSF , or in other words, the source distribution behind the conventional mapping. Normally, a few iterations are enough to stabilize solution vector. The cut-off wavenumber has the purpose to apply a spatial gaussian filter in the inverted mapping, r_D , and improve smoothness of mapping, avoiding noise amplification, thus reducing the difference to the conventional beamforming reference mapping.

B CLEAN-SC

The method proposed by Sijtsma (2007), CLEAN based on spatial source coherence (CLEAN-SC), is based on the CLEAN method from Hogbom (1974). CLEAN-SC basically removes iteratively the part of the conventional plot which is spatially coherent with a peak source, and is most efficient when the sources are not too close. Its advantage can be to extract absolute sound power levels from the source plots, again, if sources are not too close.

The algorithm for the CLEAN-SC can be summarized by (SIJTSMA, 2007):

- 1) Calculate the conventional beamforming map ("dirty map"): $P_{cb}^{(0)}$
- 2) Search for the peak location in the dirty map: $P_{cb_{max}}^{(n-1)}$
- 3) Subtract the appropriate scaled spatially coherent region from the dirty map:

$$DM^{(n)} = DM^{(n-1)} - \phi P_{cb_{max}}^{(n-1)} h_c^{(n)} h_c^{*(n)}$$
- 4) Replace this PSF by a "clean beam" (beam without side lobes):

$$CB_j^{(n)} = \phi P_{cb_{max}}^{(n-1)} 10^{-\lambda_{CLEAN} \|\vec{x}_k - \vec{x}_{max}^{(n)}\|^2}$$
- 5) Iterate from 2) to 4) until a predefined level is reached in the subtracted map

where $P_{cb_{max}}^{(n-1)}$ is the maximum level for the dirty map at iteration $(n - 1)$; $DM^{(n)}$ is the cleaned map after each iteration; $h_c^{(n)} h_c^{*(n)}$ corresponds to the coherent distribution related to the peak level being subtracted; ϕ is the loop gain factor; and $CB_j^{(n)}$ is the new source representation related to a dynamic resolution given by λ_{CLEAN} , in respect to locations \vec{x}_k and \vec{x}_{max} (peak level).

This process consists of replacing the peak levels on the dirty map (original conventional beamforming) by their concentrated representations, $CB^{(n)}$, and obtain a cleaned map. The loop gain, ϕ , determines how much from the peak level is subtracted at each iteration. The expression for the spatially coherent component $h_c^{(n)}$ is:

$$h_c^{(n)} = \frac{1}{(1 + w_{max}^{*(n)} H^{(n)} w_{max}^{(n)})^{1/2}} \left(\frac{DM^{(n-1)} w_{max}^{(n)}}{P_{max}^{(n-1)}} + H^{(n)} w_{max}^{(n)} \right), \quad (\text{B.1})$$

where $H^{(n)} = h_c^{(n)} h_c^{*(n)}$ for non-diagonal terms, and with $H_{jj}^{(n)} = 0$ on the diagonal terms; and

w_{max} is the steering vector associated to the peak level location;

This process has the advantage to clean the side lobes and reduce the localization dynamic range at a cost of concentrating the result when the sources are distributed in the range of approximately one wavelength, as observed on the literature problem results in the Generalized Inverse Beamforming Chapter.